Transactions of the ASME®

Technical Editor, **T. H. OKIISHI (1998)**
Associate Technical Editors
Aeromechanical Interaction
R. E. KIELB (1999)
Gas Turbine (Review Chair)
A. KIDD (1997)
Heat Transfer
M. G. DUNN (1999)
Nuclear Engineering
H. H. CHUNG (1996)
Power
D. LOU (1998)
Turbomachinery
R. A. DELANEY (1998)

BOARD ON COMMUNICATIONS
Chairman and Vice-President
R. MATES

OFFICERS OF THE ASME
President, **R. J. GOLDSTEIN**
Executive Director, **D. L. BELDEN**
Treasurer, **J. A. MASON**

PUBLISHING STAFF
Managing Director, Engineering
CHARLES W. BEARDSLEY
Director, Technical Publishing
PHILIP DI VIETRO
Managing Editor, Technical Publishing
CYNTHIA B. CLARK
Managing Editor, Transactions
CORNELIA MONAHAN
Production Coordinator
VALERIE WINTERS
Production Assistant
MARISOL ANDINO

Transactions of the ASME, Journal of Turbomachinery (ISSN 0889-504X) is published quarterly (Jan., Apr., July, Oct.) for $185.00 per year by The American Society of Mechanical Engineers, 345 East 47th Street, New York, NY 10017. Periodicals postage paid at New York, NY and additional mailing offices. POSTMASTER: Send address changes to Transactions of the ASME, Journal of Turbomachinery, c/o THE AMERICAN SOCIETY OF MECHANICAL ENGINEERS, 22 Law Drive, Box 2300. Fairfield, NJ 07007-2300.
CHANGES OF ADDRESS must be received at Society headquarters seven weeks before they are to be effective. Please send old label and new address.
PRICES: To members, $40.00, annually; to nonmembers, $185.00.
Add $24.00 for postage to countries outside the United States and Canada.
STATEMENT from By-Laws. The Society shall not be responsible for statements or opinions advanced in papers or . . . printed in its publications (B7.1, Par. 3).

INDEXED by Applied Mechanics Reviews and Engineering Information, Inc.
Canadian Goods & Services Tax Registration #126148048

Journal of Turbomachinery

Published Quarterly by The American Society of Mechanical Engineers

VOLUME 118 • NUMBER 4 • OCTOBER 1996

TECHNICAL PAPERS

(Contents continued on p. 653)

(Contents continued)

ANNOUNCEMENTS

Heat Transfer Committee Best Paper of 1995 Award

Distribution of Film-Cooling Effectiveness on a Turbine Endwall Measured Using the Ammonia and Diazo Technique

S. Friedrichs

H. P. Hodson

W. N. Dawes

Whittle Laboratory,
University of Cambridge,
Cambridge, United Kingdom

The distribution of adiabatic film-cooling effectiveness on the endwall of a large-scale low-speed linear turbine cascade has been measured using a new technique. This technique is based on an established surface-flow visualization technique, and makes use of the reaction between ammonia gas and a diazo surface coating. A new method of calibration has been developed to relate the result of the reaction to surface concentration of coolant. Using the analogy that exists between heat and mass transfer, the distribution of film-cooling effectiveness can then be determined. The complete representation of the film-cooling effectiveness distribution provided by the technique reveals the interaction between the coolant ejected from the endwall and the secondary flow in the turbine blade passage. Over- and undercooled regions on the endwall are identified, illustrating the need to take these interactions into account in the design process. Modifications to the cooling configuration examined in this paper are proposed as a result of the application of the ammonia and diazo technique.

Introduction

An increase in the cycle efficiency of gas turbines can be achieved through higher turbine entry temperatures. In turn, this requires the development of materials and efficient cooling methods. One cooling method that has gained increasing importance is endwall film-cooling, where coolant air is discharged through discrete holes in the inner and outer endwalls (platforms) of a turbine blade passage. After leaving the holes, the coolant forms a protective layer between the hot mainstream gas and the surface that is to be protected.

The external flow near the endwall, which interacts with the ejected coolant, is three dimensional due to the presence of secondary flow. A general overview of secondary flow in turbine blade passages is given by Sieverding (1984). Harrison (1989) describes the secondary flow structures in the turbine cascade used in this investigation.

The paper by Blair (1974) seems to be the first work published on endwall film-cooling. He found that both heat transfer and film-cooling on the endwall are influenced by secondary flow. A similar observation was made by Takeishi et al. (1990). Their leading edge horseshoe vortex, for example, increased heat transfer and decreased film-cooling effectiveness near the leading edge on the endwall. Granser and Schulenberg (1990) also observed the influence of secondary flow. They ejected coolant from a slot in the endwall upstream of the leading edge and measured higher levels of film-cooling effectiveness near the suction side of the blade than near the pressure side.

Goldman and McLallin (1977) and Sieverding and Wilputte (1981) performed aerodynamic measurements and found a significant effect of endwall film-cooling on the loss and angle distributions downstream of the blade passage, illustrating that endwall coolant ejection influences the passage flow field.

Bourguignon (1985) observed that coolant ejection tends to turn the endwall streamlines toward the inviscid streamlines. In Bourguignon's investigation, endwall film-cooling was effective for up to ten hole diameters downstream of ejection. Both Bourguignon (1985) and Bario et al. (1990) found that ejecting the coolant at an angle to the flow has little effect on the jet trajectory, except in the vicinity of the holes. Despite the strong interactions present in endwall film-cooling, the investigations of Harasgama and Burton (1992) and Jabbari et al. (1996) show that high levels of cooling can be achieved with endwall film-cooling.

In the present study, the effectiveness of a film-cooling configuration is assessed by comparing the temperature T_{aw} that an adiabatic wall would assume under the influence of the ejected coolant, with the one that it would assume without coolant ejection. Since the Mach number in this investigation is small, the uncooled adiabatic wall temperature is approximately equal to the free-stream temperature T_∞. The adiabatic wall temperature T_{aw} is usually expressed as a dimensionless temperature, or adiabatic film-cooling effectiveness η, with T_{jet} being the coolant temperature at the exit of the cooling hole:

$$\eta_{aw} = \frac{T_{aw} - T_\infty}{T_{\text{jet}} - T_\infty} \tag{1}$$

An isothermal film-cooling effectiveness can be defined based on isothermal wall arguments. This is an alternative to the adiabatic film-cooling effectiveness and is used in temperature-based experimental studies with isothermal wall conditions.

Techniques for the experimental determination of adiabatic film-cooling effectiveness can be classed into two groups. In the first group the coolant is ejected at a temperature different from the mainstream and the adiabatic wall temperature is mea-

Contributed by the International Gas Turbine Institute and presented at the 40th International Gas Turbine and Aeroengine Congress and Exhibition, Houston, Texas, June 5–8, 1995. Manuscript received by the International Gas Turbine Institute February 4, 1994. Paper No. 95-GT-1. Associate Technical Editor: C. J. Russo.

sured directly. Thermocouples, thermochromic liquid crystals, or infrared cameras may be used to measure the surface temperature. In these experiments it is often difficult to achieve an adiabatic wall, so corrections are applied to allow for conduction in the wall. The second group of techniques relies on the analogy that exists between heat and mass transfer. Coolant air at the same temperature as the free stream is seeded with a tracer gas, and surface concentrations of the tracer gas are measured. Analogous to the adiabatic film-cooling effectiveness, an impermeable wall effectiveness based on concentration measurements can be defined:

$$\eta_{iw} = \frac{C_{iw} - C_\infty}{C_{\text{jet}} - C_\infty} \tag{2}$$

The conditions for the use of the analogy between heat and mass transfer in film-cooling investigations have been reviewed by Shadid and Eckert (1991). When they are met, the impermeable wall concentration field is similar to the adiabatic wall temperature field and the two effectiveness parameters are equal:

$$\eta_{iw} = \eta_{aw} \tag{3}$$

This is the case in typical film-cooling investigations, where Reynolds numbers are high and turbulent mixing dominates over molecular diffusion. Molecular parameters such as Prandtl and Schmidt numbers have very little influence. The results of Pedersen et al. (1977), for example, illustrate that the impermeable wall effectiveness is practically independent of the Schmidt number over their investigated range. Therefore the C_{iw} distribution in a concentration based film-cooling experiment will be representative of the T_{aw} distribution of a temperature-based experiment having similar Reynolds numbers and coolant-to-free stream property ratios.

To date, surface concentration measurements have been performed by analyzing gas samples taken either through tappings in the wall or through probes or rakes adjacent to the surface. This paper describes an alternative technique for performing surface concentration measurements: the ammonia and diazo surface coating technique.

In both the temperature and concentration-based experiments, different techniques are capable of different degrees of resolution of film-cooling effectiveness. Jabbari et al. (1996), for example, encountered difficulties with their gas sampling technique. The coolant trajectories moved relative to the fixed gas sampling tappings as experimental conditions were varied. In practice, thermocouple techniques and techniques based on sampling gas through wall tappings are only able to measure at predetermined locations. Probe sampling techniques, thermochromic liquid crystal, infrared camera or ammonia and diazo techniques cover a large area of the surface and provide a complete representation of the film-cooling effectiveness.

The Ammonia and Diazo Technique

The use of the ammonia and diazo surface coating technique for measuring adiabatic film-cooling effectiveness is based on an established surface-flow visualization technique. In investigations such as those reported by Joslyn and Dring (1983) and Hodson and Addison (1989), the surface of the test piece is covered with diazo-coated paper. Pure ammonia gas is then either passed slowly through wall tappings or is ejected from an upstream probe. The ammonia gas reacts with the diazo coating, leaving a trace on the paper as it is transported over the surface by the flow under investigation. Dring et al. (1980) and Jabbari et al. (1996) used the same basic technique to visualize coolant flow in film-cooling investigations. The coolant air was seeded with ammonia gas and was passed over a surface covered with diazo paper, leaving traces of varying darkness.

The first suggestion of the use of the ammonia and diazo technique for quantitative effectiveness measurements seems to have been by Soechting et al. (1987). To simulate a realistic density ratio they used CO_2 as coolant, demonstrating the use of the basic technique with coolant gases other than air. They did not develop a quantitative ammonia and diazo technique, as they concluded that extensive calibrations were necessary to correlate the darkness of the trace to the coolant concentration.

The method of calibration described below was developed to allow the calculation of film-cooling effectiveness from the measured darkness. A detailed description of this new method of calibration and of the use and validation of the ammonia and diazo surface coating technique for the measurement of adiabatic film-cooling effectiveness is given in Friedrichs and Hodson (1994).

The Diazo Surface Coating. The chemicals of the diazo surface coating are usually applied to paper or polyester film, which is then fixed to the experimental surface. In the experiments presented here, a polyester film with a thickness of 0.05 mm was used. The film is covered with the chemicals embedded in a resin. The use of film was preferred over the use of paper as it has a smoother surface and is easier to remove from the test piece after being fixed with low-tack double-sided tape. In the study of very complex three-dimensional geometries where paper or film cannot be fixed satisfactorily, they may, however, be applied directly to the surface.

The mixture of chemicals usually consists of ten to fifteen different components, mainly diazos, couplers, and additives. The diazos are light sensitive and react with ammonia and water to form radicals. Exposure to light desensitizes the diazos to ammonia and water. The couplers react with the radicals to form the dyes that darken the surface coating. The additives may include stabilizers, contrast enhancers, and ethylene glycol to absorb moisture.

Experimental Procedure and Processing. The measurement technique relies on the principle that the darkness of the traces on the diazo surface coating is dependent on the surface concentration of the ammonia and water vapor in the coolant gas. Prior to the experiment, diazo film is fixed to the experimental surface. The wind tunnel is started and conditions are allowed to stabilize. The cooling air is then seeded with ammonia gas and water vapor. In the experiments presented here, the average ammonia concentration was ~0.5 percent, the average relative humidity was ~90 percent, and the exposure time was between one and two minutes. These values can be varied to achieve the desired darkness of the traces, as long as both am-

Nomenclature

C = concentration
$I = (\rho_{\text{jet}} \cdot V_{\text{jet}}^2)/(\rho_\infty \cdot V_\infty^2)$ coolant momentum ratio
$M = (\rho_{\text{jet}} \cdot V_{\text{jet}})/(\rho_\infty \cdot V_\infty)$ coolant blowing ratio
$\dot{m}$ = mass flow
P_0 = stagnation pressure
p = static pressure
T = temperature
V = velocity
η = film-cooling effectiveness
ρ = density
τ = surface shear stress

Subscripts

aw = adiabatic wall (temperature)
iw = impermeable wall (concentration)
jet = coolant jet condition
rel = relative to coolant in plenum, percent
∞ = local free-stream value

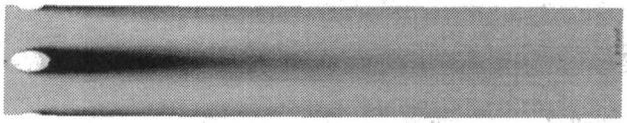

Fig. 1 Coolant traces on a diazo-coated flat plate

monia and water vapor are present for the chemical reaction to take place. After the experiment, the image is fixed by exposure to light to prevent further reaction. An example of the resulting traces on a flat plate is shown in Fig. 1.

A visual inspection of Fig. 1 directly reveals coolant trajectories, but to determine cooling effectiveness the relationship between the darkness of the trace and the surface concentration of coolant has to be found. The reaction between the diazo surface coating and the coolant seeded with ammonia gas and water vapor is dependent on a variety of factors. Increases in ammonia concentration, humidity, and exposure time each result in a darker image. An increase in temperature results in a lighter image, with a temperature difference of merely 3°C resulting a change in relative darkness of about 20 percent.

To avoid individual calibrations for each of these dependencies, a reference experiment is performed parallel to the main experiment. In the reference experiment, a calibration strip such as the one shown in Fig. 2 is produced by mixing the coolant gas mixture with free-stream air from the wind tunnel in known ratios. All these dependencies are automatically taken into account, as the calibration strip is exposed to representative mixtures for the same amount of time as the main experiment.

To create this calibration strip, a mixing box has been designed (see Fig. 3). It provides eleven sampling tubes with coolant-to-mainstream mixtures of 0 to 100 percent, in 10 percent steps. Each of the sampling tubes is fed by a total of ten holes. The 0 percent tube is fed from ten holes ejecting mainstream air, the 10 percent tube is fed from nine mainstream holes and one coolant gas hole, and so on. The air in each of the sampling tubes is passed over a strip of diazo paper or film, creating the calibration strip. The design concentrations in the sampling tubes are achieved with uniform flow rates through all of the holes. The design criteria for the mixing box therefore were uniform hole shapes and diameters, sufficiently large plenum chambers, uniform exit static pressures, and equal pressures in the two plenum chambers. The completed mixing box was calibrated by analyzing gas samples from each of the sampling tubes, and was found to function as designed.

In order to quantify the darkness distribution obtained using the ammonia and diazo technique, both the image and the corresponding calibration strip are digitized simultaneously using an optical scanner. The analysis of the calibration strip gives the relationship between the darkness of the trace and the relative concentration of the coolant. This results in calibration curves such as the one shown in Fig. 4. By applying the calibration using interpolation between the calibration points, the relative concentration of each measurement point is determined.

In the present experiments only the coolant is seeded with ammonia and water vapor. The free-stream concentration therefore corresponds to a value of 0 percent. With the relative coolant concentration in the plenum being 100 percent, the measured relative concentration values are equivalent to the adia-

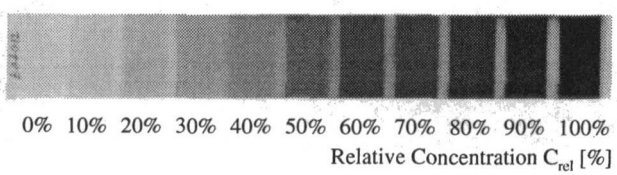

Fig. 2 Calibration strip produced for the trace in Fig. 1

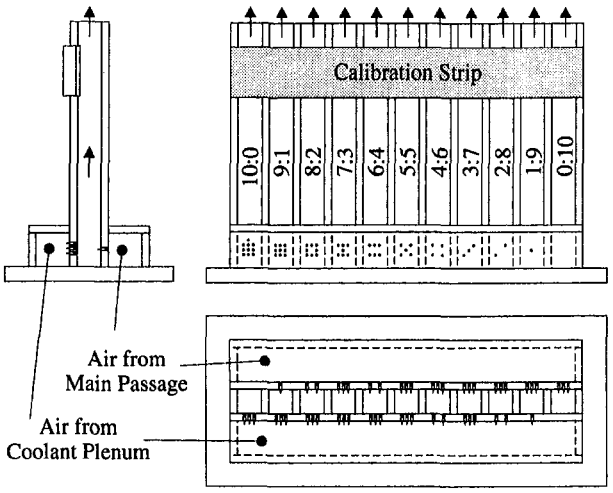

Fig. 3 Mixing box for on-line calibration

batic film-cooling effectiveness. Equations (2) and (3) therefore become:

$$\eta_{aw} = \eta_{iw} = \frac{C_{iw}}{C_{\text{jet}}} = C_{\text{rel}} \tag{4}$$

Validation and Discussion. To validate the ammonia and diazo technique, Friedrichs and Hodson (1994) compared cooling effectiveness data obtained using the ammonia and diazo technique with data obtained using a gas sampling technique. This comparison was performed for a flat plate with a single row of five discrete film-cooling holes. The five holes had a hole length-to-diameter ratio of 3.5, a spacing-to-diameter ratio of 3.0, and were inclined at an angle of 35 deg to the surface in direction of the free stream. The experiments were run at low speed, unity density ratio, and a blowing ratio $M = 0.5$.

Figure 1 shows the coolant trace downstream of the central hole, with traces from neighboring holes visible on either side. In the gas sampling technique, the cooling air was seeded with ethylene gas and samples were taken from surface tappings at fixed locations downstream of the central hole. Using an infrared gas analyzer, the concentration of the tracer gas in the samples of the surface flow was determined. Figure 5 shows the comparison between the results of the gas sampling technique and averaged results from the ammonia and diazo technique. The "spikes" in the ammonia and diazo results are due to holes in the polyester film at the locations of the gas sampling tappings. The comparison shows that the results are in good agreement.

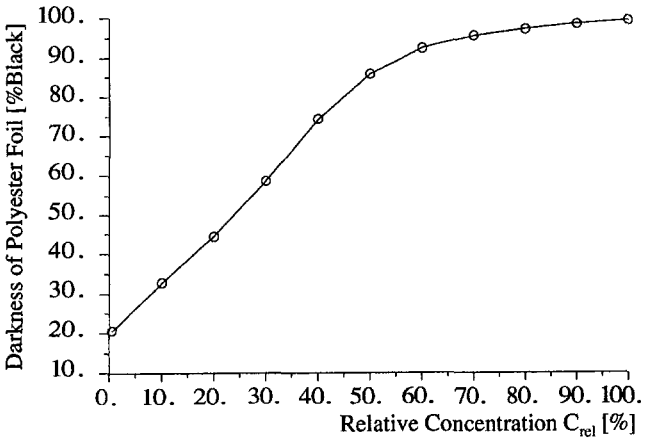

Fig. 4 Calibration curve derived from strip in Fig. 2

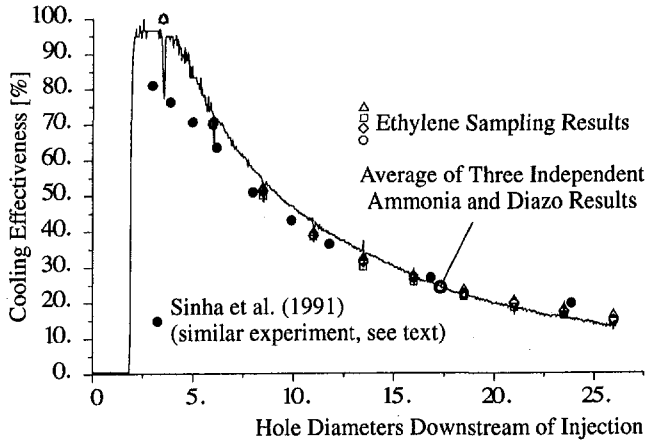

Fig. 5 Centerline cooling effectiveness data obtained using two measurement techniques (Friedrichs and Hodson, 1994); comparison to a similar experiment by Sinha et al. (1991)

Included in Fig. 5 are results from Sinha et al. (1991). They measured centerline cooling effectiveness in a similar experiment using a temperature-based measurement technique. Their experiment differed from the present one in the coolant to mainstream density ratio (1.2 versus 1.0), the coolant hole length-to-diameter ratio (1.75 versus 3.5), and possibly the inlet boundary layer, which was not measured in the present experiment.

Agreement between the results is good, except in the vicinity of the hole where gradients are high. The difference in density ratio is unlikely to be the cause of the discrepancy, as Sinha et al. (1991) showed that density ratio has no noticeable effect at this low blowing ratio. Schmidt et al. (1996) showed that the same is true for the length-to-diameter ratio. Although not measured, the boundary layer is expected to be similar to the one found in the experiments of Sinha et al. (1991). According to Bogard (1995), the discrepancy may be due to conduction problems with the thermal measurements, illustrating a possible limitation of thermal techniques.

The calibration curve shown in Fig. 4 is similar to the curves used in obtaining the results in Fig. 5. It illustrates the nonlinearity of the relationship between darkness and concentration. For these experiments, saturation is reached above 60 to 70 percent coolant concentration. The resolution in that region is significantly reduced. A small change in measured darkness results in a large change in interpreted coolant concentration. The large steps in the regions of high cooling effectiveness of the ammonia and diazo results in Fig. 5 illustrate this effect.

Both the validation experiment and the endwall film-cooling experiment described here were conditioned to give good resolution at low levels of cooling effectiveness. They are therefore well suited to determine the overall distribution of cooling effectiveness. If lighter traces are produced, for example through lower concentrations of ammonia, the experiment can be conditioned to give good resolution at high levels of cooling effectiveness. Details in regions of high cooling effectiveness, for example in the vicinity of coolant jets, can then be studied.

Experiments were performed in two different facilities to determine whether the flow Reynolds number or ammonia or water vapor depletion have an influence on the darkness of the trace. For the depletion experiment, a mixture of ammonia and water vapor was passed through a 2-m-long tube, the inside of which was coated with diazo film. For the Reynolds number experiment, a mixture of fixed concentration was passed over a series of diazo film strips at different flow velocities, covering the range of Reynolds number found in the experiment. Neither the Reynolds number nor ammonia or water vapor depletion had a detectable effect on the darkness.

Sometimes it may not be possible to produce a valid calibration strip such as the one shown in Fig. 2. This may happen when the mixing box and its feed lines are not adiabatic, and the coolant, mainstream, and mixing box temperatures differ. An alternative method of calibration is proposed by Haslinger and Hennecke (1994). For a specific experimental condition, a gas sampling technique such as the one used by Jabbari et al. (1996) may be used to determine concentrations at discrete locations on the surface. An ammonia and diazo trace is produced for the same condition. By comparing the measured surface concentrations to the darkness values of the trace at the same locations, a calibration curve can be derived. By using this alternative method of calibration, the dependencies of the ammonia and diazo reaction are also taken account of, and the advantages inherent in the ammonia and diazo technique remain.

Turbine Cascade and Cooling Configuration

The endwall film-cooling investigation presented here was performed on a large-scale, low-speed, linear turbine cascade. The cascade consists of four blades with a true chord of 278 mm, a span of 300 mm, and a pitch of 230 mm. The flow enters the cascade at an angle of 40 deg and is turned through 105 deg. With the low aspect ratio and high turning angle, the blades produce strong secondary flows. These are stronger than the ones found in high-pressure nozzle guide vanes with a typical turning angle of 70 deg, and therefore allow a more detailed observation of the basic interactions between endwall coolant ejection and the passage flow field. Details of the basic cascade without endwall film-cooling can be found in Harrison (1989).

Figure 6 shows oil and dye surface-flow visualization on the cascade endwall without coolant ejection. The three-dimensional separation lines can clearly be seen. For ease of comparison, they are also shown in Figs. 7 and 8 as dashed lines.

Coolant air is ejected from a common plenum chamber through 43 holes in one endwall of a single passage. Figure 7 shows the cooling configuration that consists of four single rows of holes and four individual holes, all having a diameter of 4 mm and ejecting at an angle of 30 deg to the surface. The thickness of the endwall is 12 mm, giving a length-to-diameter ratio of 6, typical of endwall film-cooling configurations.

This cooling configuration would provide cooling to most of the endwall surface in the absence of secondary flow. It is

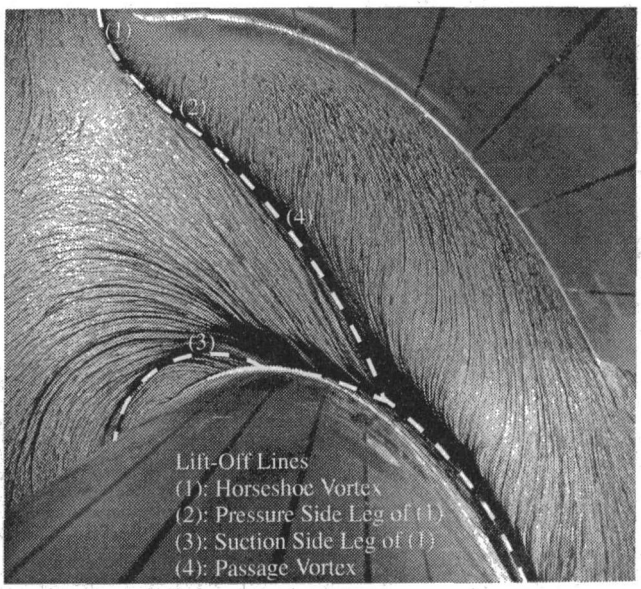

Fig. 6 Oil and dye surface-flow visualization on the cascade endwall without film-cooling

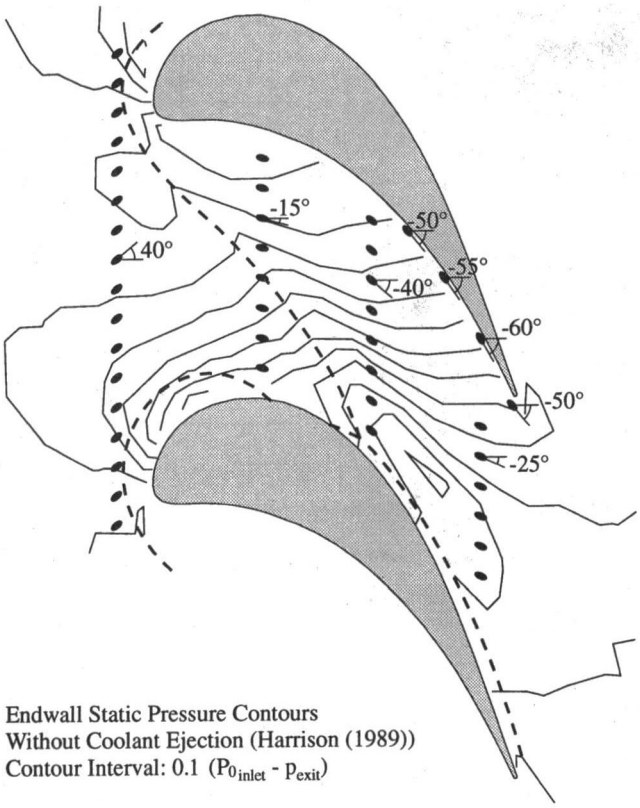

Fig. 7 Cascade endwall with film-cooling holes, endwall static pressure contours, and lift-off lines without film-cooling

therefore well suited to investigate the effect that the interactions between the ejected coolant and the endwall flow field have on the distribution of film-cooling effectiveness. The first row of holes is located upstream of the leading edge, ejecting in the inlet flow direction. The second row of holes is located at 30 percent axial chord and ejects in approximately the inviscid streamline direction. The third row is at 60 percent axial chord, again ejecting in approximately the inviscid flow direction. The fourth row at 90 percent axial chord ejects at an angle to both the inviscid and the actual endwall flow.

The single holes near the blade pressure surface were designed to provide internal cooling. The air is intended to cool the metal of the endwall convectively as it passes through the holes. Upon reaching the surface it is ejected and used for film-cooling purposes. Three of the single holes are located in the corner between the pressure surface of the blade and the endwall in the second half of the blade passage. They eject in the flow direction. The fourth single hole is located just downstream of the trailing edge, and is angled to the flow in an attempt to direct coolant into the wake of the trailing edge.

Each of the cooling holes experiences a different exit static pressure as it ejects into the flow field near the endwall. The undisturbed endwall static pressure field as measured by Harrison (1989) is also shown in Fig. 7. Coolant ejection will affect the pressure field locally in the vicinity of the holes due to the blockage presented by the jet. Due to its interaction with the passage flow field, coolant ejection will also influence the overall passage pressure field. In a first approximation the undisturbed pressure field is used to determine the local hole exit static pressures.

Figure 8 shows the distribution of the mean shear stress coefficient on the endwall. It was calculated by Harrison (1989) from surface shear stress measurements obtained using the oil drop method. Using the Reynolds analogy, this distribution can be viewed as a distribution of Stanton number. From it, one can see that the region downstream of the lift-off line in the first half of the blade passage is one of potentially high heat transfer. Toward the rear of the blade passage the values fall, leaving a local peak where the three-dimensional separation lines reach the blade suction surface. Flow velocities are high in the rear part of the blade passage, especially near the blade suction surface (see Fig. 7). As heat transfer coefficients are proportional to Stanton number multiplied by velocity, this also is a region of potentially high heat transfer.

Test Conditions

In the present experiment, air is supplied to the common plenum chamber at the same temperature as the free stream. As density changes due to the tracer amounts of ammonia gas and water vapor are negligible, this results in a unity coolant-to-free stream density ratio. For the experimental conditions presented here, the coolant plenum pressure equals the inlet stagnation pressure. The ratio of coolant exit velocity to local free-stream velocity is therefore approximately equal for all holes.

An isentropic coolant massflow was calculated based on the experimental conditions, hole diameters, and measured hole exit static pressures. It was compared to the coolant massflow measured during the experiment. The comparison gave an average reduction in massflow by a factor of 0.67. The reduction is caused by flow separation off the inlets of the coolant holes. The separation creates three-dimensional flow structures with counterrotating vortices and large velocity gradients, as can be seen in the computational predictions of Leylek and Zerkle (1994). As a result, all coolant holes operate with a blowing ratio of $M \approx 0.67$ and a momentum ratio of $I \approx 0.45$.

For the passage under investigation, the total coolant massflow was equivalent to 1.64 percent of the passage massflow, if both endwalls had been cooled. The distribution of the coolant massflow for the passage is shown in Table 1.

The results presented in this paper were produced with the cascade operating at a Reynolds number of 8.6×10^5 based on

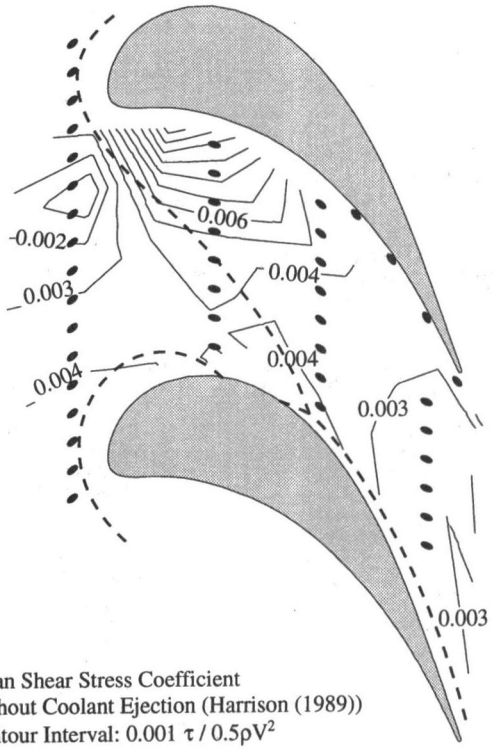

Fig. 8 Distribution of mean shear stress coefficient on the endwall without film-cooling

Table 1 Distribution of the coolant massflow in a single passage

configuration	% of total coolant flow	
row of holes upstream of leading edge	26.6 %	13 holes
row of holes at 30% axial chord	17.3 %	8 holes
row of holes at 60% axial chord	22.5 %	8 holes
row of holes at 90% axial chord	23.4 %	6 holes
single holes	10.2 %	4 holes

exit velocity and true chord, which corresponds to a Reynolds number of 4.5×10^5 based on inlet velocity and true chord. Harrison (1989) measured the inlet boundary layer at a point half an axial chord upstream of the leading edge and found it to have a thickness of 18 mm, a displacement thickness of 2.6 mm, a momentum thickness of 1.9 mm and a shape factor of 1.36. The inlet turbulence level of the free stream was of the order of 0.5 percent.

Discussion of Results

The distribution of cooling effectiveness on the cascade endwall was measured using the ammonia and diazo technique. Two A4 sheets of polyester film were required to cover the relevant regions of the endwall. The traces left by the coolant, which had been seeded with ammonia and water vapor, are shown in Fig. 9.

The darkness distribution on each of the sheets was scanned together with the calibration strip produced during this experiment. Darkness values were measured out of a range of 256 greyscales at a resolution of 75 dots per inch, giving approximately three measurement points per millimetre. After processing, the film-cooling effectiveness results from the two sheets were combined in Fig. 11. A comparison of the results in Fig. 11 with the joint between the two sheets of film seen in Fig. 9 shows continuous contours across the joint, illustrating that possible differences between sheets of film or in scanning and processing are negligible.

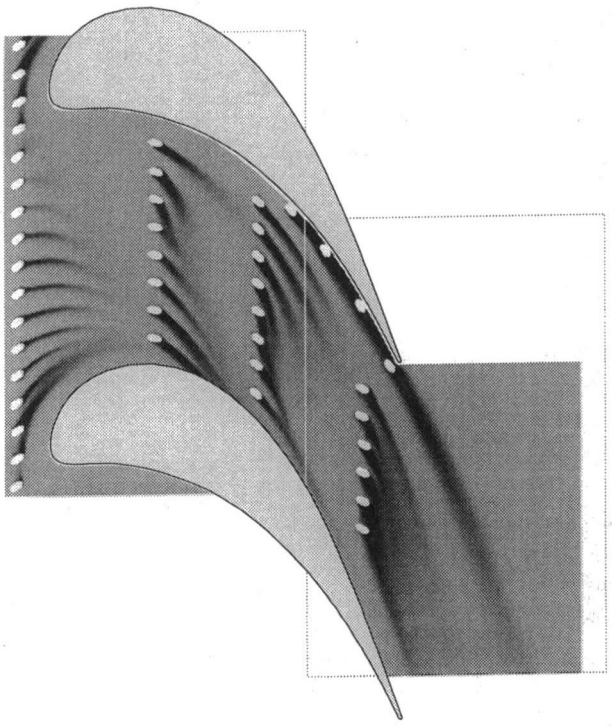

Fig. 9 Traces on the surface coating of the turbine endwall

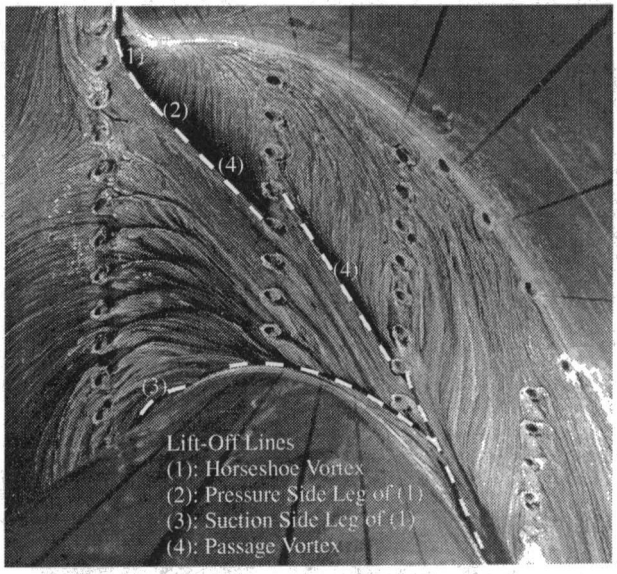

Fig. 10 Oil and dye surface-flow visualization on the film-cooled cascade endwall

Figure 10 shows an oil and dye visualization of the endwall surface flow under the influence of the ejected coolant. Due to the blockage presented by the leading edge, the incoming endwall boundary layer is subjected to a stagnating pressure gradient. This causes the boundary layer to undergo three-dimensional separation and to roll up into a horseshoe vortex. The legs of the horseshoe vortex pass to either side of the blade. The suction-side leg travels around the blade and its lift-off line later intersects the blade suction surface. The pressure side leg moves into the blade passage and merges with the main passage vortex. The passage vortex moves across to the suction surface of the neighboring blade under the influence of the passage pressure field. The incoming boundary layer separates along the lift-off line of the passage vortex. Downstream of the lift-off line, Harrison (1989) found the new boundary layer to be thin, highly skewed, and largely laminar.

A comparison to the case without coolant ejection (see Figs. 6 and 7) shows that the lift-off line of the horseshoe vortex has moved closer to the leading edge. A similar observation is made by taking the two coolant holes at 60 percent axial chord near the blade suction surface as a reference, and comparing the locations of the lift-off line with and without coolant ejection (see Figs. 7 and 10). The comparison reveals that the lift-off line of the passage vortex has moved downstream. In both cases the ejection of coolant seems to have delayed the separation of the inlet boundary layer. The most visible influence of the ejected coolant on the secondary flow can be seen at the row of holes at 30 percent axial chord. The three-dimensional separation of the inlet boundary layer is delayed due to the coolant ejection, resulting in a displacement of the lift-off line. The three-dimensional separation lines shown in Fig. 10 are also shown as dashed lines in Fig. 11 to simplify comparisons.

The Row of Holes Upstream of the Leading Edge. Takeishi et al. (1990) found that the leading edge horseshoe vortex increased heat transfer and decreased cooling effectiveness near the leading edge. In this investigation, Fig. 11 shows that the horseshoe vortex prevents coolant from being effective in the area between its lift-off line and the blade. This area of high heat transfer is therefore virtually unprotected, even with jets aimed directly at the blade leading edge. A possible solution to this problem is to place cooling holes downstream of the lift-off line of the horseshoe vortex, into the corner of the blade with the endwall.

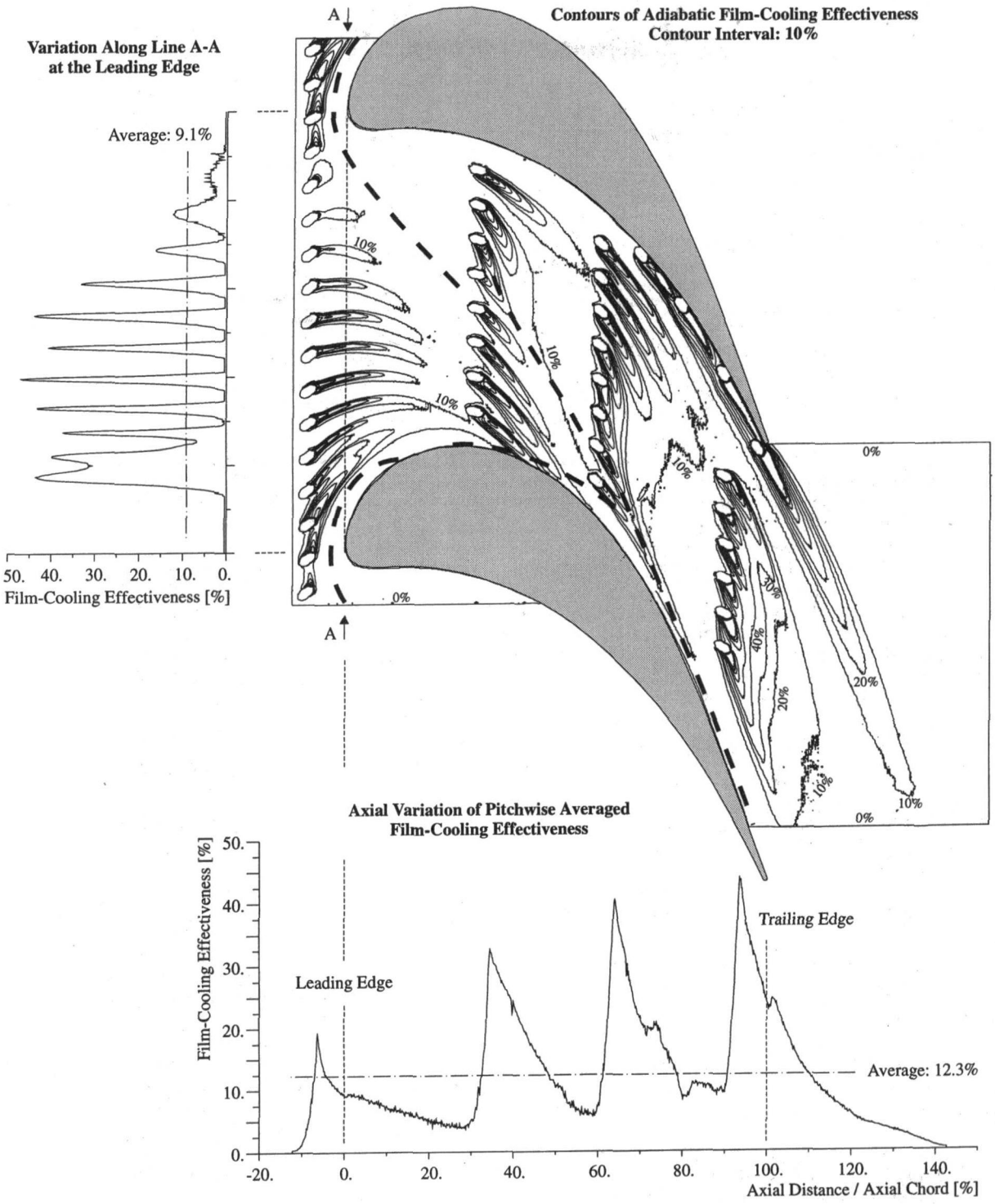

Fig. 11 Endwall film-cooling effectiveness measured using the ammonia and diazo technique

The holes at the leading edge eject coolant into the inlet boundary layer before it separates. Figure 11 shows that cooling is present in the region downstream of the holes and upstream of the lift-off lines, although the levels of cooling effectiveness are not as high as the ones found toward the rear of the passage. The coolant trajectories near the blade suction surface in the mouth of the blade passage display little lateral spreading and high persistence. This indicates reduced mixing, probably due to accelerating flow in this region. Cooling is provided almost up to the row of holes at 30 percent axial chord. An uncooled area remains between the pressure surface of the blade, the lift-off lines, and the cooling holes at 30 percent axial chord. This is unfortunate, as Fig. 8 indicates high levels of Stanton number in this region. Takeishi et al. (1990) and Gaugler and Russell (1984) also measured high heat transfer in this area. The addition of cooling holes in this region is again a possible solution to the problem.

Included in Fig. 11 is the local variation of effectiveness along the leading edge. It shows that even though there are significant gaps between the traces of coolant jets, the integrated average cooling effectiveness is 9.1 percent. The axial variation of pitchwise averages can also be seen in Fig. 11. It shows that

average effectiveness upstream of the row of holes at 30 percent axial chord is lower than the endwall average of 12.3 percent, reflecting the large uncooled area near the pressure surface.

The Row of Holes at 30 percent Axial Chord. The holes at 30 percent axial chord eject into two different regions of flow, which are divided by the path of the passage vortex. The holes near the blade suction surface are upstream of the lift-off line of the passage vortex. They eject into the inlet boundary layer that is thickened as it is "funneled" into the region having the suction side leg of the horseshoe vortex on one side and the passage vortex on the other. The influence of this funneling can be seen in Fig. 11. The trajectories of the affected jets merge and create a blanket of cooling without uncooled gaps. This is beneficial, as heat transfer in this region can be high. Figure 8 suggests a local peak in Stanton number in this region, which combined with high velocities would result in high heat transfer. The comparison between endwall heat transfer and secondary flow given by Gaugler and Russell (1984) also shows a local peak in heat transfer where the three-dimensional separation lines reach the suction surface.

The holes near the blade pressure surface are downstream of the lift-off line of the passage vortex. They eject into the new, thin endwall boundary layer. Figure 11 shows that the trajectory of the coolant from the hole nearest to the pressure surface approximately follows the inviscid streamline direction, leaving an uncooled gap in the blade-endwall corner. A comparison with the surface-flow visualization in Fig. 10 shows that the endwall flow in the trajectory of this jet diverges. This seems to have a positive influence, as both the lateral spreading and the persistence of this trajectory are high. Of all the holes in the endwall, this is the hole that experiences the highest exit static pressure. It therefore has the lowest coolant massflow. The hole next to the suction surface in the same row of holes has approximately three times the massflow. Considering the low massflow, the cooling performance from this hole is very good. However, if the pressure in the plenum is lowered sufficiently, it will be the first hole to experience reverse flow.

The influence of secondary flow is visible in Fig. 11 in the trajectories coming from the second and third holes from the pressure surface. They are turned toward the suction surface as the jets mix out. The fourth hole is located in the vicinity of the lift-off line of the passage vortex. The separation of the inlet boundary layer and the resulting upwash cause the jet to lift off the endwall before it is able to provide much cooling.

Figure 11 shows that due to the strong deflection of the trajectories an area with hardly any cooling is formed upstream of the row of holes at 60 percent axial chord. Figure 8 again shows the uncooled region to be one of potentially high heat transfer. Additional holes are needed to provide cooling in this area, as the new, thin endwall boundary layer downstream of the lift-off line enhances heat transfer to the endwall.

The axial variation of pitchwise-averaged cooling effectiveness in Fig. 11 shows that the row of holes at 30 percent axial chord performs better than the row upstream of the leading edge. Most of the region between 30 and 60 percent axial chord displays an average film-cooling effectiveness higher than the endwall average. Again, the effect of the uncooled region upstream of the next row of holes is clearly seen.

The Row of Holes at 60 Percent Axial Chord. The interaction of the secondary flow with the coolant jets coming from the row of holes at 60 percent axial chord is similar to the one found at 30 percent axial chord. Figure 11 shows that near the pressure surface, jet trajectories are in approximately the inviscid streamline direction. The traces merge at a low level of cooling effectiveness, but retain individual high effectiveness regions downstream of the holes. Toward the middle of the blade passage there again is an influence of secondary flow. The jet trajectories are short and turned toward the suction surface. The coolant leaves the endwall to be entrained into the passage vortex before providing much cooling. The hole nearest to the suction surface provides cooling for a long distance downstream of ejection. Some of its coolant may be entrained in a vortex that forms in the corner of the suction surface of the blade with the endwall, as the endwall crossflow starts to move up the suction surface. Again a large, triangular area upstream of the next row of holes remains practically uncooled due to the influence of secondary flow. Stanton numbers inferred from Fig. 8 are low in this region, but velocities are high (see Fig. 7) and high rates of heat transfer are to be expected. The cooling holes near the lift-off line that are not effective would be better placed in this region.

The pitchwise averages of cooling effectiveness in Fig. 11 show that the effectiveness in the vicinity of the holes at 60 percent axial chord is higher than the one for the row upstream. As the jets mix out, the high effectiveness traces from the single holes in the pressure surface–endwall corner cause a rise in the averages, and keep them from falling below ~10 percent. This masks the effect of the large uncooled area upstream of the row of holes at 90 percent axial chord.

The Row of Holes at 90 Percent Axial Chord. The holes discussed up to now have been ejecting coolant in approximately the inviscid streamline direction. The holes at 90 percent axial chord eject at an angle to this direction, resulting in a large ejection angle to the endwall crossflow. Figure 11 shows that the exit angle is not the direction of the coolant trajectories. The coolant is turned toward the suction surface as soon as it leaves the holes. This corresponds to the findings of Bourguignon (1985) and Bario et al. (1990), who found that ejecting the coolant at an angle to the flow has little effect on the jet trajectory, except in the vicinity of the holes. Although the effect on trajectories is small, there is a large effect on the endwall flow. A comparison of Fig. 10 with Fig. 6 shows that the endwall crossflow has been reduced. The difference in endwall flow angle upstream and downstream of the holes is large, and the amount of overturning near the endwall is reduced.

Figure 11 shows that the coolant jets at 90 percent axial chord merge, forming an insulating layer of coolant that is effective for a large distance downstream of ejection. The regions to either side of this blanket remain uncooled. As these areas lie in regions of potentially high heat transfer, additional holes closer to the blade surfaces are necessary to close the gaps.

Pressure Surface–Endwall Corner. The three single holes in the corner of the blade pressure surface with the endwall eject into the inviscid streamline direction, and the trajectories are oriented accordingly. The lateral spreading of the trajectories is enhanced as the endwall crossflow develops, but not sufficiently so to transport the coolant across the blade passage. The cooling effectiveness is high, and in the context of endwall film-cooling fewer holes would have sufficed.

The cooling effectiveness downstream of the single hole at the trailing edge benefits greatly from the amount of coolant present in the upstream corner. It is angled in an attempt to cool the endwall in the wake of the trailing edge. As this is a region of high levels of turbulence and vortical motion, it was initially expected that providing film-cooling would be difficult. Assisted by the holes in the pressure surface corner, the coolant ejected from the hole at the trailing edge gives high levels of effectiveness, has a high degree of lateral spreading, and is effective for a very long distance downstream of ejection.

Conclusions

The ammonia and diazo surface coating technique has been developed and successfully used to measure the distribution of adiabatic film-cooling effectiveness on the endwall of a large-scale, low-speed, linear turbine cascade. The cooling effectiveness distribution was presented together with surface-flow visu-

alization, revealing the strong interactions between endwall coolant ejection and secondary flow in the blade passage. The turbine cascade was designed to produce very strong secondary flow, stronger than would be found in most engine nozzle guide vanes. This exaggerates the effects, but aids in the illustration and understanding of the basic flow interactions.

The results presented here have shown that the flow structures associated with the three-dimensional separation lines on the endwall can act as barriers to the coolant trajectories on the surface. Coolant ejection underneath the lift-off lines is inefficient, as most of the coolant leaves the surface before providing much cooling. Coolant ejected away from the lift-off lines can provide cooling to a larger area. Ejection near the blade pressure surface into the diverging endwall crossflow is efficient, as it gives traces with a high degree of lateral spreading and penetration. The trajectories of the coolant were not found to be determined by the angle of ejection to the flow, except in the vicinity of the holes.

The endwall surface-flow field has been modified by coolant ejection. The lift-off lines have moved downstream as the ejection of coolant delayed the three-dimensional separation of the inlet boundary layer. The amount of overturning near the endwall downstream of the cascade was reduced, with the endwall crossflow being turned towards the inviscid streamlines.

The tested cooling configuration did not provide a complete coolant coverage of the endwall. Nonetheless, the area-averaged cooling effectiveness for the endwall was found to be 12.3 percent. The uncooled areas have been identified, and modifications to the configuration have been proposed.

In endwall film-cooling studies it is necessary to measure the complete distribution of film-cooling effectiveness or heat transfer. This allows insight into the flow interactions and quickly identifies over- and undercooled regions. With the ammonia and diazo surface coating technique, a technique for measuring adiabatic film cooling effectiveness has been developed that not only gives the complete distribution, but is also easy to use, fast, and low-cost.

Acknowledgments

The authors are grateful for the support provided by Rolls-Royce plc, the Engineering & Physical Sciences Research Council (EPSRC), and the Frankfurt Main Flughafen Stiftung (Frankfurt Airport Foundation). They would also like to thank Ozalid (UK) Ltd., especially Mr. Faiers, for valuable technical advice and for providing Ozalid paper and Ozafilm samples, Prof. Denton for the use of the cascade, the technical staff of the Whittle Laboratory, especially Mr. Saunders, for their assistance, and Prof. Hennecke and Dipl.-Ing. Haslinger in Darmstadt for their useful discussions concerning the measurement technique.

References

Bario, F., Leboeuf, F., Onvani, A., and Seddini, A., 1990, "Aerodynamics of Cooling Jets Introduced in the Secondary Flow of a Low-Speed Turbine Cascade," ASME JOURNAL OF TURBOMACHINERY, Vol. 112, pp. 539–546.

Blair, M. F., 1974, "An Experimental Study of Heat Transfer and Film Cooling on Large-Scale Turbine Endwalls," ASME *Journal of Heat Transfer,* Vol. 96, pp. 524–529.

Bogard, D. G., 1995, private communications, University of Texas at Austin, USA.

Bourguignon, A. E., 1985, "Etudes des Transferts Thermiques sur les Plates-Formes de Distributeur de Turbine avec et sans Film de Refroidissement," AGARD-CP-390, *Heat Transfer and Cooling in Gas Turbines.*

Dring, R. P., Blair, M. F., and Joslyn, H. D., 1980, "An Experimental Investigation of Film Cooling on a Turbine Rotor Blade," ASME *Journal of Engineering for Power,* Vol. 102, pp. 81–87.

Friedrichs, S., and Hodson, H. P., 1994, "The Ammonia and Diazo Surface Coating Technique for Measuring Adiabatic Film Cooling Effectiveness," *Proc. 12th Symposium on Measuring Techniques for Transonic and Supersonic Flow in Cascades and Turbomachines,* Prague, The Czech Republic.

Goldman, L. J., and McLallin, K. L., 1977, "Effect of Endwall Cooling on Secondary Flows in Turbine Stator Vanes," AGARD-CPP-214.

Granser, D., and Schulenberg, T., 1990, "Prediction and Measurement of Film Cooling Effectiveness for a First-Stage Turbine Vane Shroud," ASME Paper No. 90-GT-95.

Gaugler, R. E., and Russell, L. M., 1984, "Comparison of Visualized Turbine Endwall Secondary Flows and Measured Heat Transfer Patterns," ASME *Journal of Engineering for Gas Turbines and Power,* Vol. 106, pp. 168–172.

Harasgama, S. P., and Burton, C. D., 1992, "Film Cooling Research on the Endwall of a Turbine Nozzle Guide Vane in a Short Duration Annular Cascade: Part 1—Experimental Technique and Results," ASME JOURNAL OF TURBOMACHINERY, Vol. 114, pp. 734–740.

Harrison, S., 1989, "The Influence of Blade Stacking on Turbine Losses," Ph.D. Thesis, University of Cambridge; see also Harrison, S., 1990, "Secondary Loss Generation in a Linear Cascade of High-Turning Turbine Blades," ASME JOURNAL OF TURBOMACHINERY, Vol. 112, pp. 618–624.

Haslinger, W., and Hennecke, D. K., 1994, private communications, Technische Hochschule Darmstadt, Germany.

Hodson, H. P., and Addison, J. S., 1989, "Wake-Boundary Layer Interactions in an Axial Flow Turbine Rotor at Off-Design Conditions," ASME JOURNAL OF TURBOMACHINERY, Vol. 111, pp. 181–192.

Jabbari, M. Y., Marston, K. C., Eckert, E. R. G., and Goldstein, R. J., 1996, "Film Cooling of the Gas Turbine Endwall by Discrete-Hole Injection," ASME JOURNAL OF TURBOMACHINERY, Vol. 118, pp. 278–284.

Joslyn, H. D., and Dring, R. P., 1983, "Turbine Rotor Negative Incidence Stall," ASME Paper No. 83-GT-23.

Leylek, J. H., and Zerkle, R. D., 1994, "Discrete-Jet Film Cooling: A Comparison of Computational Results With Experiments," ASME JOURNAL OF TURBOMACHINERY, Vol. 116, pp. 358–368.

Pedersen, D. R., Eckert, E. R. G., and Goldstein, R. J., 1977, "Film Cooling With Large Density Differences Between the Mainstream and the Secondary Fluid Measured by the Heat-Mass Transfer Analogy," ASME *Journal of Heat Transfer,* Vol. 99, pp. 620–627.

Schmidt, D. L., Sen, B., and Bogard, D. G., 1996, "Film Cooling with Compound Angle Holes: Adiabatic Effectiveness," ASME JOURNAL OF TURBOMACHINERY, Vol. 118, this issue, pp. 807–813.

Shadid, J. N., and Eckert, E. R. G., 1991, "The Mass Transfer Analogy to Heat Transfer in Fluids with Temperature-Dependent Properties," ASME JOURNAL OF TURBOMACHINERY, Vol. 113, pp. 27–33.

Sieverding, C. H., and Wilputte, P., 1981, "Influence of Mach Number and Endwall Cooling on Secondary Flows in a Straight Nozzle Cascade," ASME *Journal of Engineering for Gas Turbines and Power,* Vol. 103, No. 2.

Sieverding, C. H., 1984, "Recent Progress in the Understanding of Basic Aspects of Secondary Flows in Turbine Blade Passages," ASME *Journal of Engineering for Gas Turbines and Power,* Vol. 107, pp. 248–257.

Sinha, A. K., Bogard, D. G., and Crawford, M. E., 1991, "Film-Cooling Effectiveness Downstream of a Single Row of Holes With Variable Density Ratio," ASME JOURNAL OF TURBOMACHINERY, Vol. 113, pp. 442–449.

Soechting, F. O., Landis, K. K., and Dobrowolski, R., 1987, "Development of Low-Cost Test Techniques for Advancing Film Cooling Technology," Paper No. AIAA-87-1913.

Takeishi, K., Matsuura, M., Aoki, S., and Sato, T., 1990, "An Experimental Study of Heat Transfer and Film Cooling on Low Aspect Ratio Turbine Nozzles," ASME JOURNAL OF TURBOMACHINERY, Vol. 112, pp. 488–496.

Education Committee Best Paper of 1995 Award

Methods of Classical Mechanics Applied to Turbulence Stresses in a Tip Leakage Vortex

J. G. Moore

S. A. Schorn

J. Moore

Mechanical Engineering Department,
Virginia Polytechnic Institute
and State University,
Blacksburg, VA 24061

Moore et al. measured the six Reynolds stresses in a tip leakage vortex in a linear turbine cascade. Stress tensor analysis, as used in classical mechanics, has been applied to the measured turbulence stress tensors. Principal directions and principal normal stresses are found. A solid surface model, or three-dimensional glyph, for the Reynolds stress tensor is proposed and used to view the stresses throughout the tip leakage vortex. Modeled Reynolds stresses using the Boussinesq approximation are obtained from the measured mean velocity strain rate tensor. The comparison of the principal directions and the three-dimensional graphic representations of the strain and Reynolds stress tensors aids in the understanding of the turbulence and what is required to model it.

Introduction

Flows in turbomachinery blade rows are often complex, three-dimensional, and turbulent. Accurate prediction of such flows is a goal of Computational Fluid Dynamics and a challenge to turbulence modelers. Insights gained from turbulence and Reynolds stress measurements in three-dimensional flows can be useful in developing improved models.

In this paper methods used to analyze and view stress tensors in classical mechanics are applied to the turbulence stress tensors measured in a tip leakage vortex. At any point in the flow the principal directions, as used in mechanics, can be found for a Reynolds stress tensor. When the stress tensor is transformed into this system, the shear stresses are zero and only the normal stresses remain. This principal direction coordinate system is a very different view of the Reynolds stress tensor than is usually considered by turbulence and turbulent boundary layer modelers.

After principal directions have been found, Mohr's circles can then be used to view the normal and shear stresses in the principal planes. These show clearly the relation between the maximum and minimum normal stress and the maximum shear stress.

In mechanics, stress tensors are also viewed as three-dimensional glyphs, the most common being the quadric surface. Here, a different three-dimensional glyph for Reynolds stresses is suggested that gives a more intuitive view of the tensor.

With the goal of using these techniques being to aid in understanding how to model the turbulence in three-dimensional flow, it is appropriate to consider the Boussinesq approximation, which forms the basis of most turbulence models in common use today. In the Boussinesq model, the turbulence stresses are calculated from an isotropic turbulent viscosity, the turbulence kinetic energy, and the mean velocity deformation or strain rate tensor. Here, the turbulence kinetic energy and the turbulent viscosity are calculated from the experimental data, so that the comparison between the measured and modeled Reynolds stress tensors is an assessment of the potential accuracy of Boussinesq based models, rather than an assessment of any particular turbulence model.

Contributed by the International Gas Turbine Institute and presented at the 40th International Gas Turbine and Aeroengine Congress and Exhibition, Houston, Texas, June 5–8, 1995. Manuscript received by the International Gas Turbine Institute March 2, 1995. Paper No. 95-GT-220. Associate Technical Editor: C. J. Russo.

Measurements in VPI&SU Turbine Cascade

The measurements to be used in this study were made by Moore et al. (1994) in the VPI&SU tip leakage turbine cascade. The cascade was raised with a tip gap of 2.2 percent of blade height at the bottom wall. The inlet air flow had a free-stream velocity, U_o = 20. m/s and a free-stream turbulence intensity, Tu = 0.4 percent. The Reynolds number based on blade axial chord and exit velocity was 4.4×10^5.

To gain insight into the dissipation mechanisms, Moore et al. measured the six Reynolds stresses and mean flow velocity on a plane just upstream of the trailing edge at X/c = 0.96, as shown in Fig. 1. The measurements were made throughout the tip leakage vortex using hot-wire anemometry and a rotatable two-wire end-flow probe. Some measurements were also made on a plane upstream of X/c = 0.96 so that mean flow velocity gradients could be determined.

Moore et al. mapped the distributions of Reynolds stresses and turbulence production rate on a cross section of the vortex and evaluated contributions to the turbulence production.

Primary and Secondary Velocities. The x, y, z coordinate system used by Moore et al. for the presentation of the mean velocity data and the Reynolds stresses is shown in Fig. 1. The primary flow direction, x, and the primary flow velocity component, U, are defined in the direction of the mean camber line at the blade trailing edge, β_2 = 26 deg. The secondary velocity components are W in the spanwise direction and V perpendicular to U and W. The corresponding fluctuating velocity components are u, v, and w, respectively.

Contours of the primary velocity component, U, are shown in a y, z view of the measurement plane in Fig. 2; i.e., the measurement plane is viewed looking upstream along the x axis. Superimposed on the primary velocity are the secondary velocity vectors, the resultant of V and W, at the locations of the measurement points.

The secondary velocity vectors show clearly the vortex motion as the tip leakage jet moves across the bottom wall, separates from the endwall, and recirculates around the vortex core.

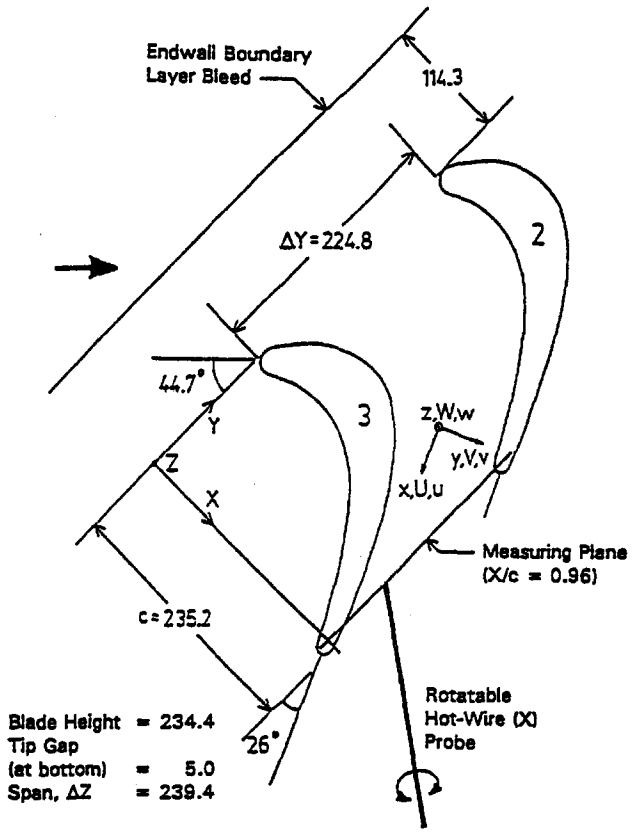

Fig. 1 Tip leakage cascade geometry with coordinate systems for the cascade (X, Y, Z) and for the primary and secondary flow in the tip leakage vortex (x, y, z); linear dimensions in mm

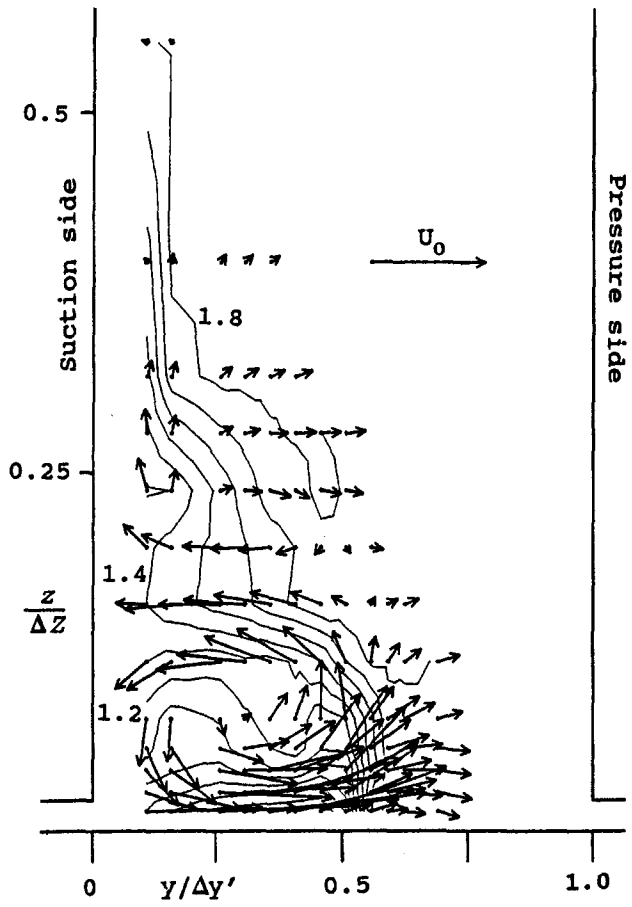

Fig. 2 The mean velocity components in the tip leakage vortex measured at X/c = 0.96 (y, z view); contours of primary flow velocity, U (contour interval, $0.1U_0$) with secondary velocity V, W vectors

Approaching the suction surface, the recirculating flow splits with some fluid remaining in the tip leakage vortex, and some being entrained in a weaker passage vortex above the leakage vortex. This vortex system was discussed by Dishart and Moore (1990) and by Moore and Moore (1991).

The measured primary velocities, U, ranged from $0.6U_o$, near the bottom wall in the separating flow, to $1.8U_o$, above the passage vortex.

Turbulence Kinetic Energy. The distribution of turbulence kinetic energy, shown in Fig. 3, gives a picture of the production and convection of turbulence within the tip leakage vortex. The tip leakage jet has relatively low turbulence, with k less than $0.13U_0^2/2$. This contributes to low turbulence levels around the lower part of the tip leakage vortex. Near the endwall separation there is a region of high turbulence production and the turbulence levels rise to nearly $0.3U_0^2/2$. The turbulence kinetic energy generated in this region is then convected, with some reduction of level, over the core of the tip leakage vortex toward the suction side of the blade.

Stress Tensor Analysis

The stress tensor for the turbulence or Reynolds stresses in Cartesian coordinates is

$$\overline{u_i u_j} = \begin{bmatrix} \overline{uu} & \overline{uv} & \overline{uw} \\ \overline{uv} & \overline{vv} & \overline{vw} \\ \overline{uw} & \overline{vw} & \overline{ww} \end{bmatrix} \tag{1}$$

The principal directions used in mechanics also form an orthogonal coordinate system. When the stress tensor is transformed into this system the shear stresses are zero and only the normal stresses remain.

Methods for Finding Principal Values and Directions. There are several methods for determining the principal stresses and principal stress directions of a symmetric 3 × 3 stress tensor.

Nomenclature

c = blade chord = 0.2352 m
k = turbulence kinetic energy = $\overline{u_k u_k}/2$
$\mathbf{P}_i$ = unit vectors in principal normal stress directions
$\mathbf{p}_i$ = unit vectors in principal normal strain directions
$\mathbf{S}_i$ = unit vectors in maximum shear stress directions
$\mathbf{s}_i$ = unit vectors in maximum shear strain directions
U_i, U, V, W = mean velocity components
u_i, u, v, w = fluctuating velocity components
U_o = upstream free-stream velocity = 20 m/s
X, Y, Z = cascade coordinates, Fig. 1
x, y, z = flow coordinates, Fig. 1
$\Delta y'$ = y component of the blade-to-blade width = 0.0859 m
ΔZ = span = 0.2394 m
ν = laminar kinematic viscosity = 0.000017 m^2/s
ν_t = turbulent viscosity

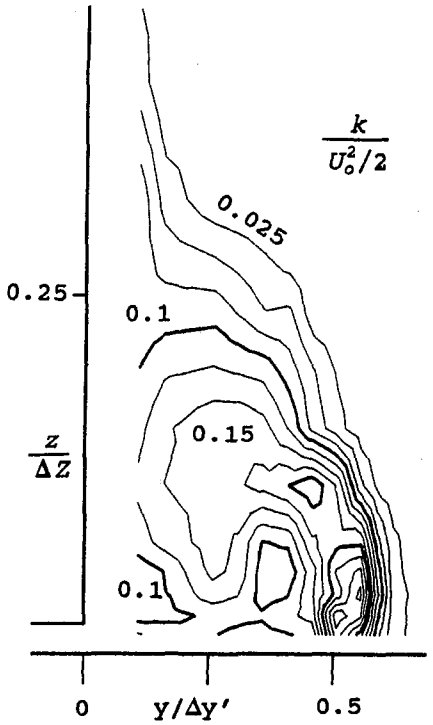

Fig. 3 Turbulence kinetic energy in the tip leakage vortex; contour interval, 0.025

The most common method to find principal values of small matrices is to put the matrix into the standard eigenvalue problem form

$$\underline{\mathbf{A}}\mathbf{x} = \lambda\mathbf{x} \tag{2}$$

The eigenvalue, λ, and eigenvector, $\mathbf{x}$, solutions then correspond to the principal values and the principal directions of the matrix $\underline{\mathbf{A}}$ (see, e.g., Perry, 1988).

Here for simplicity, the principal values were found using the algorithm given in *Numerical Recipes in Fortran* (1992).

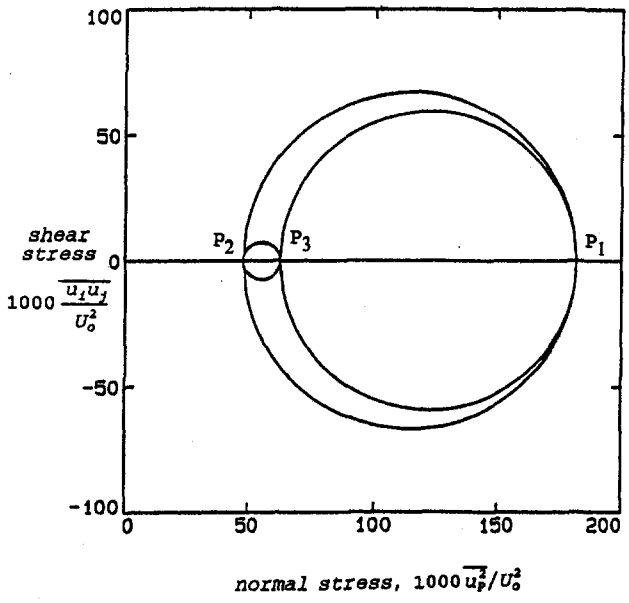

Fig. 4 Mohr circles for the Reynolds stress tensor at the maximum turbulence point

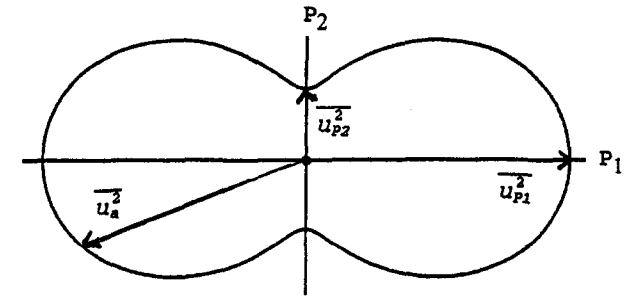

Fig. 5 A two-dimensional section of the Reynolds stress glyph for the maximum turbulence point

This method uses successive transformations of the matrix to create zero values for the off-diagonal elements.

Maximum Turbulence Measurement Point. The point of maximum measured turbulence, at $y/\Delta y' = 0.51$, $z/\Delta Z = 0.027$, in Fig. 3, will be used to demonstrate the transformation of the stress tensor and three-dimensional views of the tensor. On Fig. 2, this data point is on the second line from the bottom wall, and where the tip leakage jet is separating from the wall to form the tip leakage vortex. Here, the secondary flows are large with $(U, V, W) = (0.9, 0.6, 0.4)U_o$. The Reynolds stress tensor for this point is

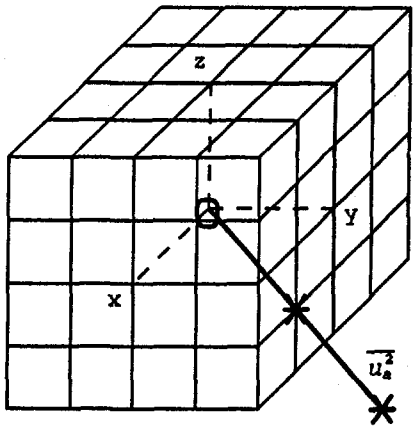

Fig. 6 Sketch of three-dimensional glyph construction

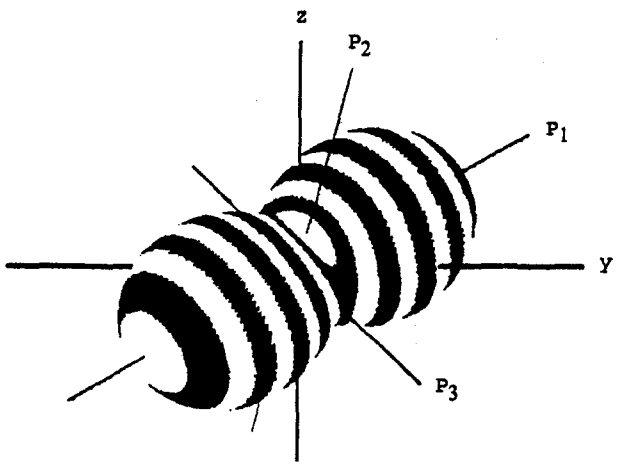

Fig. 7 Reynolds stress glyph at maximum turbulence point

$$1000\,\frac{\overline{u_i u_j}}{U_o^2} = \begin{bmatrix} 89.2 & -48.5 & -34.4 \\ -48.5 & 125.1 & 35.1 \\ -34.4 & 35.1 & 78.2 \end{bmatrix} \tag{3}$$

The shear stresses in the x, y, z coordinates are all of about equal magnitude, $0.2k$ to $0.3k$. The largest normal stress is in the v direction. The turbulence kinetic energy is $1000k = 292.5U_0^2/2$.

Taking the $\mathbf{P}_1$ direction to correspond to the direction of maximum normal stress, and the $\mathbf{P}_2$ direction to correspond to the direction of minimum normal stress, the principal directions for this measurement point are

$$\mathbf{P}_1 = (-0.540,\ 0.727,\ 0.426)$$

$$\mathbf{P}_2 = (0.744,\ 0.175,\ 0.645)$$

$$\mathbf{P}_3 = (0.394,\ 0.665,\ -0.635) \tag{4}$$

The Reynolds stress tensor in the coordinate system of the principal directions can be found by transforming to the fluctuating velocities in these directions

$$u_{Pn} = uP_{n,x} + vP_{n,y} + wP_{n,z} = u_i P_{n,i} \tag{5}$$

and

$$\overline{u_{Pn}u_{Pm}} = \overline{u_i u_j} P_{n,i} P_{m,j} \tag{6}$$

The turbulence stress tensor then becomes

$$1000\,\frac{\overline{u_{Pn}u_{Pm}}}{U_o^2} = \begin{bmatrix} 181.7 & 0 & 0 \\ 0 & 48.0 & 0 \\ 0 & 0 & 62.8 \end{bmatrix} \tag{7}$$

As expected, the shear stresses are zero and the diagonals sum to 292.5. The principal normal stresses are highly nonisotropic with the maximum normal stress being about twice the average

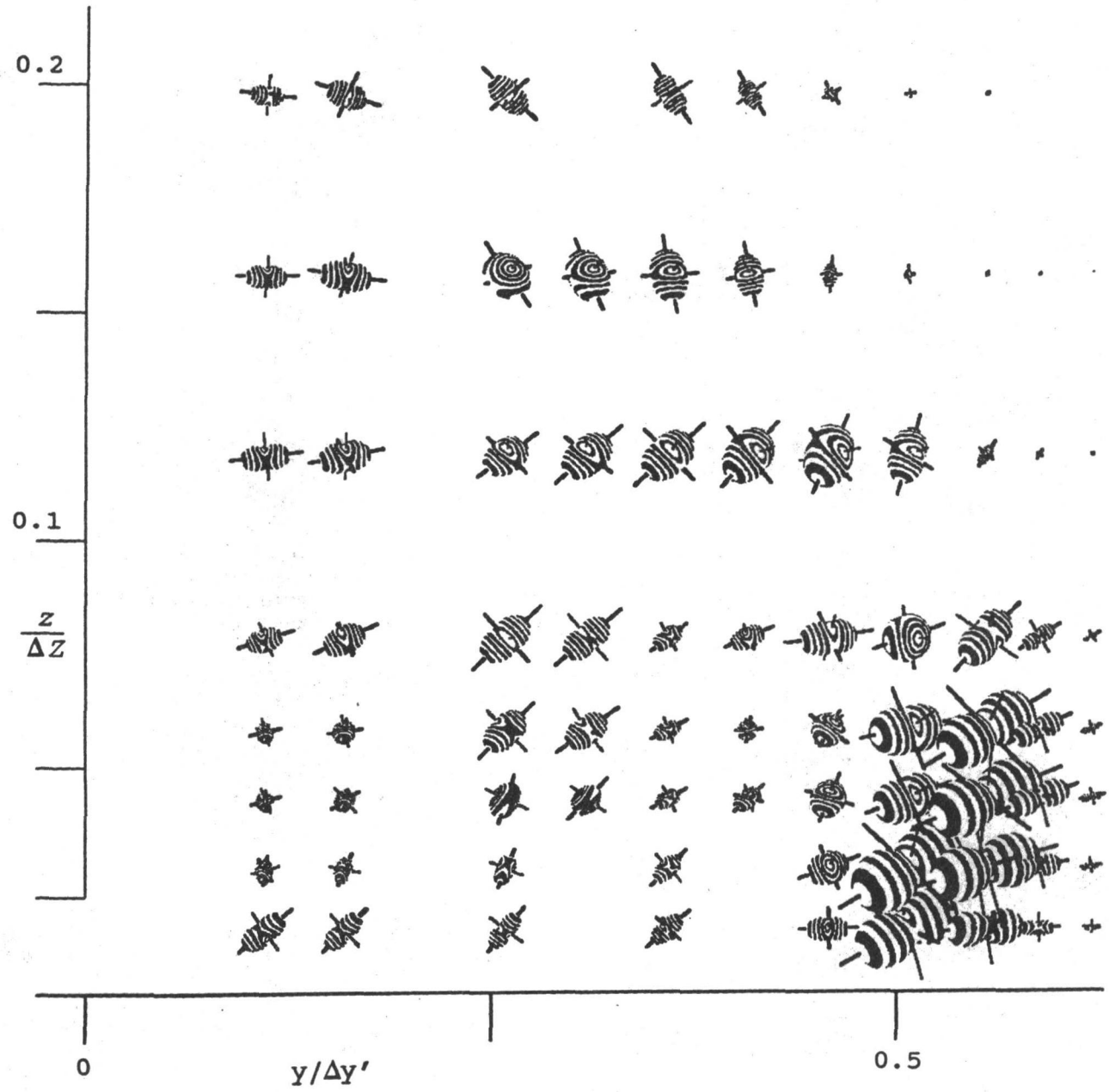

Fig. 8 Reynolds stress glyphs for the data points in the tip leakage vortex

value and the other two being of similar magnitude at about half the average value.

Shear Stresses. In mechanics, Mohr's circles (see, e.g., Beer and Johnston, 1981) are used to determine the shear stresses in the principal planes from the principal normal stresses. Figure 4 shows the Mohr circles for the maximum turbulence point. From the circles, the magnitude of the maximum shear stress is easily obtained as half the difference between the maximum and minimum principal normal stresses. The coordinate directions of the fluctuating velocities in the maximum Reynolds shear stress are in the plane of the principal directions, $\mathbf{P}_1$ and $\mathbf{P}_2$, 45 deg from the principal directions:

$$\mathbf{S}_1 = (\mathbf{P}_1 + \mathbf{P}_2)/\sqrt{2}$$
$$\mathbf{S}_2 = (\mathbf{P}_2 - \mathbf{P}_1)/\sqrt{2} \quad (8)$$

The third coordinate direction, perpendicular to $\mathbf{S}_1$ and $\mathbf{S}_2$, to give an orthogonal coordinate system, is $\mathbf{S}_3 = \mathbf{P}_3$.

For the maximum turbulence point

$$\mathbf{S}_1 = (0.144, 0.637, 0.757)$$
$$\mathbf{S}_2 = (0.908, -0.390, 0.155) \quad (9)$$

and the stress tensor in $\mathbf{S}_1$, $\mathbf{S}_2$, $\mathbf{S}_3$ coordinates is

$$1000\,\frac{\overline{u_{Si}u_{Sj}}}{U_o^2} = \begin{bmatrix} 114.8 & -66.9 & 0 \\ -66.9 & 114.8 & 0 \\ 0 & 0 & 62.8 \end{bmatrix} \quad (10)$$

The maximum shear stress for this point has a magnitude of $0.45k$.

Visual Representation of Second-Order Tensors.

The most common representation of a second order tensor is a quadric surface as discussed by Frederick and Chang (1972) and mentioned in connection with Reynolds stress tensors by Hinze (1975). Quadric surfaces are desirable because they compactly contain information about the total stress on a plane oriented in any direction. Unfortunately, the quadric surface is not intuitive since the magnitude of the normal stress is inversely proportional to the square of the size of the glyph.

Alternatively, Haber (1990) developed a simpler tensor glyph consisting of an elongated cylinder with an elliptical disk about its midlength. The orientation and length of the cylinder along with the dimensions of the elliptical disk are directly related to the magnitude and directions of the principal stresses.

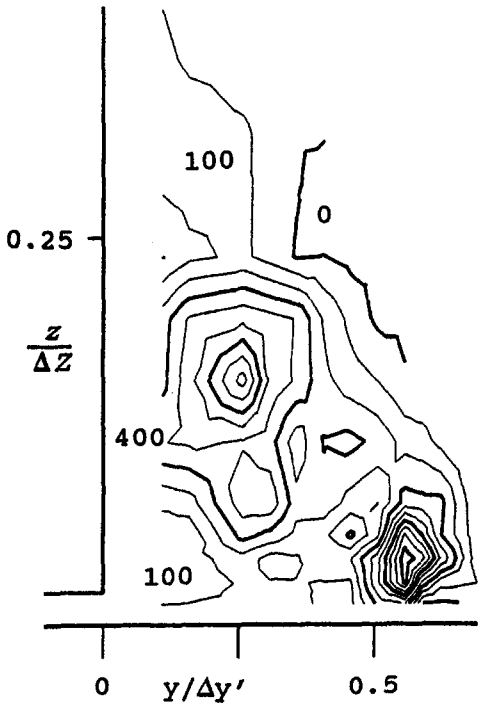

Fig. 9 Turbulent viscosity, ν_t/ν, contour interval 100

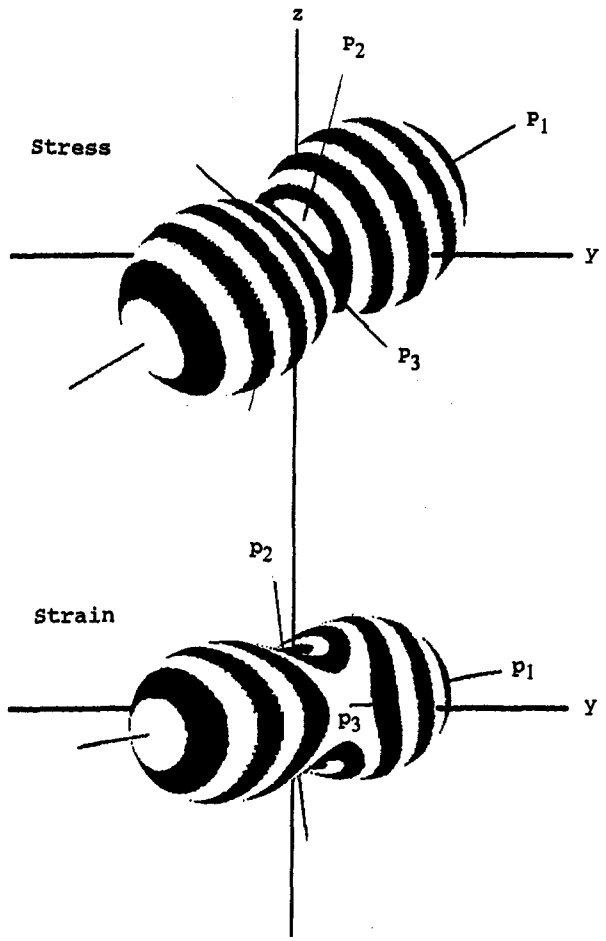

Fig. 10 Comparison of stress and strain glyphs for maximum turbulence point

A Tensor Glyph for Reynolds Stresses. Presented here are glyphs of complexity somewhere between Haber's cylinders and the quadric surfaces. These glyphs are defined such that the distance from the glyph origin to any point on its surface is the magnitude of the normal stress in that direction. A two-dimensional view of this type of glyph can be made by taking a planar cut through the three-dimensional glyph. In Fig. 5, the $\mathbf{P}_1$–$\mathbf{P}_2$ plane is shown for the stress tensor at the maximum turbulence point; this has a maximum to minimum normal stress ratio of 3.8. For comparison, note that the two-dimensional glyph corresponding to isotropic turbulence in all directions is a circle. These glyphs more easily convey the degree of anisotropy than do Haber's cylinders while maintaining a more intuitive representation of the turbulence magnitude than do the quadric surfaces.

To generate the glyphs for the three-dimensional stress tensors, the following method was used. A $(2n + 1) \times (2n + 1) \times (2n + 1)$ cubic grid was constructed around the glyph origin. ($x = -n, \ldots + n$, etc.), as shown in Fig. 6. The vector from the origin to any point on the cube surface, e.g., (i, n, k), is

normalized to a unit vector, **d**. The normal stress in that direction is determined from

$$\overline{u_n^2} = d_x^2\overline{u^2} + d_y^2\overline{v^2} + d_z^2\overline{w^2} + 2(d_x d_y\overline{uv} + d_y d_z\overline{vw} + d_x d_z\overline{uw}) \quad (11)$$

and the point is relocated this distance from the origin along the direction of the unit vector. Relocating all the points transforms the cube into the three-dimensional glyph.

Graphic Presentation of Tip Leakage Data. The glyph for the maximum turbulence point is shown in Fig. 7. To give the surface three dimensionality, contours of constant normal stress are mapped on the surface. Superimposed on the glyph are vectors in the principal stress directions. Note that the $\mathbf{P}_1$ and $\mathbf{P}_2$ vectors protrude from the glyph at the locations of the maximum and minimum normal stress respectively.

The glyphs for all the data points are shown in Fig. 8. The origin of each glyph is the y, z location of the data point. The same scaling is used for each glyph so that the glyphs for the high turbulence points near the bottom wall separation point are significantly larger than the glyphs for the rest of the flow. The differences in orientation clearly show the variation of the main principal direction throughout the vortex. The different shapes of the glyphs show the variation in isotropy of the principal normal stresses. The peanut-shaped glyphs, similar to the glyph for the maximum turbulence point, represent high nonisotropy with one large principal normal stress and two small principal stresses of similar magnitude. As the normal stresses become more equal the shape changes to ellipsoidal then to nearly spherical. There are a few points that are disk-shaped, which represents two high and one low principal stress.

Boussinesq Model for Turbulence Stresses

The Boussinesq model of turbulence stresses forms the basis of most zero, one, and two-equation turbulence models in gen-

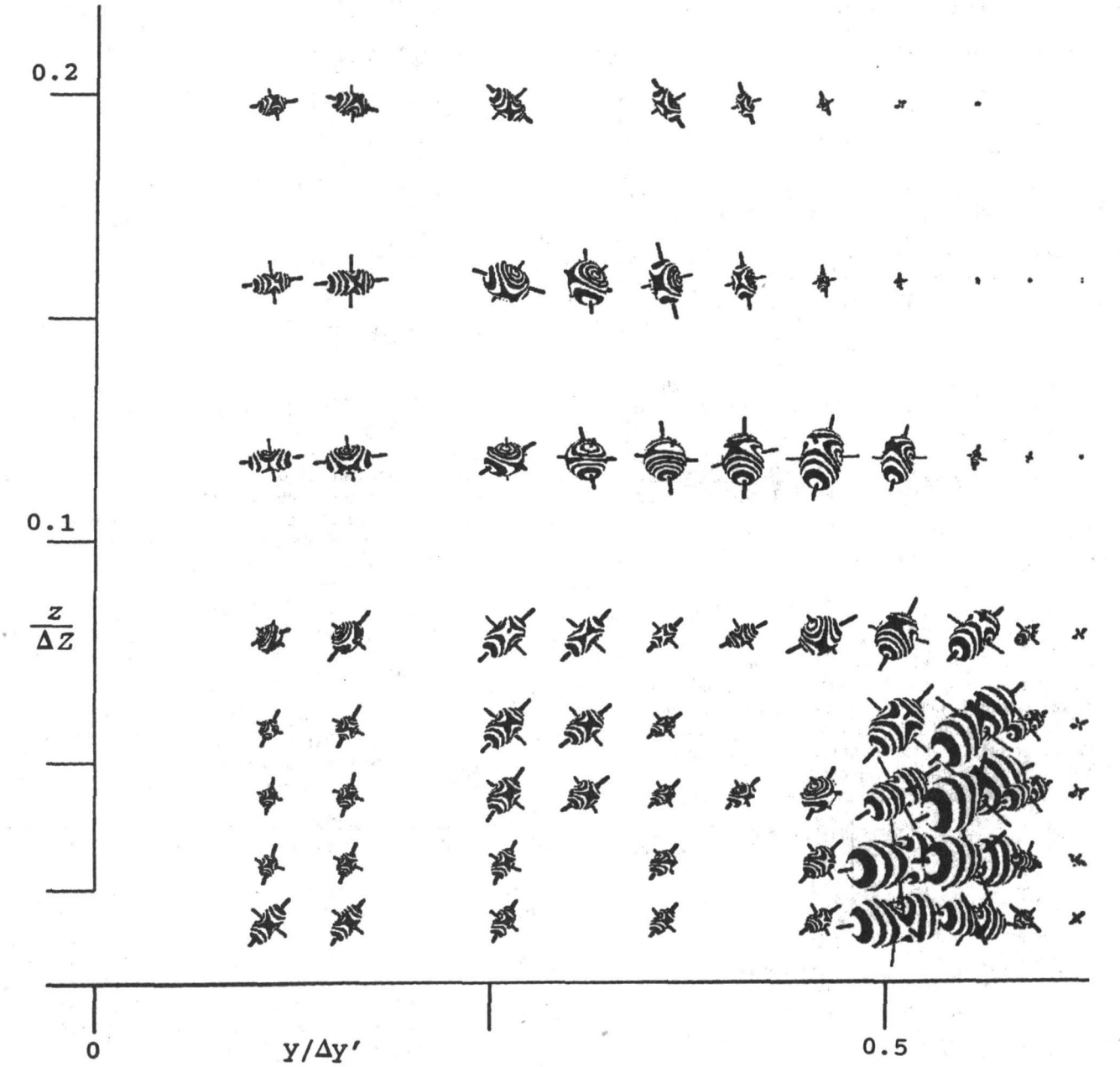

Fig. 11 Strain glyphs for the data points in the tip leakage vortex

eral use today. This model directly relates the turbulence stresses to the velocity deformation. For incompressible flow

$$\overline{u_i u_j} = -\nu_t\left(\frac{\partial U_i}{\partial x_j} + \frac{\partial U_j}{\partial x_i}\right) + \tfrac{2}{3} k\delta_{i,j} \tag{12}$$

The scalars, ν_t and k, are the turbulent viscosity and the turbulence kinetic energy.

Principal directions are not affected by an overall scaling of the tensor or by the addition of a uniform diagonal matrix, therefore the principal directions of the Boussinesq model tensor and the strain rate tensor are the same, and the same for all Boussinesq based turbulence models.

Mohr's circles of the Boussinesq model are the same as for the strain rate tensor except for an overall scaling of the picture, ν_t, and the movement of the axis for the normal stress, the addition of the k term. In terms of the three-dimensional glyphs, ν_t and k affect the size and some aspects of the shape but not the orientation.

Here, to complete the Boussinesq model, k and ν_t are set from the experimental measurements. In particular, the turbulent viscosity, ν_t, is set using the measured strain and Reynolds stress data, so that the model gives the measured rate of turbulence production.

$$\overline{u_i u_j}\frac{\partial U_i}{\partial x_j} = -\nu_t\left(\frac{\partial U_i}{\partial x_j} + \frac{\partial U_j}{\partial x_i}\right)\frac{\partial U_i}{\partial x_j} \tag{13}$$

The turbulent viscosity distribution, determined in this way from the measurements, is shown in Fig. 9. Values around 100 times the laminar viscosity are typical in the tip leakage jet and the lower part of the tip leakage vortex. As the vortex separates from the endwall, the turbulent viscosity rises to its maximum value of 974 times the laminar viscosity. The turbulent viscosity is also high where the flow approaches the suction surface between the tip leakage and passage vortices.

Measured Strain Rate Tensor. The strain rate tensor is determined from the gradients of the mean velocity distributions.

$$\frac{\partial U_i}{\partial x_j} + \frac{\partial U_j}{\partial x_i} = \begin{bmatrix} 2\dfrac{\partial U}{\partial x} & \dfrac{\partial U}{\partial y} + \dfrac{\partial V}{\partial x} & \dfrac{\partial U}{\partial z} + \dfrac{\partial W}{\partial x} \\ \dfrac{\partial U}{\partial y} + \dfrac{\partial V}{\partial x} & 2\dfrac{\partial V}{\partial y} & \dfrac{\partial V}{\partial z} + \dfrac{\partial W}{\partial y} \\ \dfrac{\partial U}{\partial z} + \dfrac{\partial W}{\partial x} & \dfrac{\partial V}{\partial z} + \dfrac{\partial W}{\partial y} & 2\dfrac{\partial W}{\partial z} \end{bmatrix} \tag{14}$$

The flow being considered here is incompressible, so the sum of the normal strains, or diagonal terms, should be zero. The velocity gradients, determined from the measured mean velocities, satisfied continuity over most of the tip leakage vortex. The few points for which continuity was not satisfied have been omitted from the strain rate plots.

The strain tensor for the maximum turbulence point is

$$\frac{c}{U_o}\left(\frac{\partial U_i}{\partial x_j} + \frac{\partial U_j}{\partial x_i}\right) = \begin{bmatrix} -8.5 & 17.7 & 4.5 \\ 17.7 & -19.5 & -7.6 \\ 4.5 & -7.6 & 28.0 \end{bmatrix} \tag{15}$$

This has principal directions

$$\begin{aligned} \mathbf{p}_1 &= (-0.585,\ 0.799,\ 0.141) \\ \mathbf{p}_2 &= (0.057,\ -0.134,\ 0.989) \\ \mathbf{p}_3 &= (0.809,\ 0.587,\ 0.033) \end{aligned} \tag{16}$$

Note that these differ from the principal stress directions.

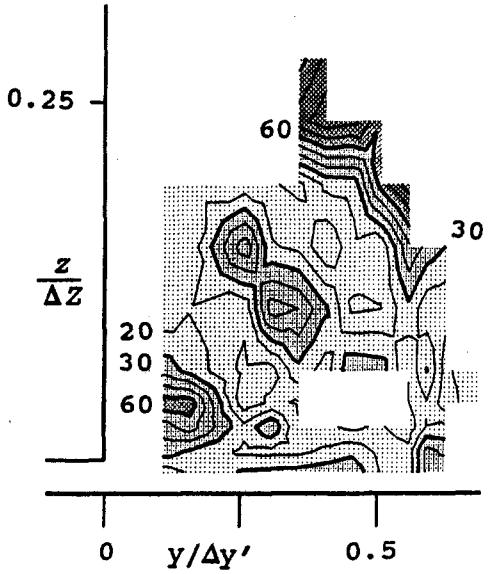

Fig. 12 Angle variation between stress and strain main principal direction, contour interval, 10 deg

The turbulent viscosity for the maximum turbulence point is $\nu_t/\nu = 483$, about half the maximum value. The Boussinesq model tensor in x, y, z coordinates for this point is

$$\frac{1000}{U_o^2}(\overline{u_i u_j})_{\text{Bous}} = \begin{bmatrix} 112.6 & -31.4 & -8.0 \\ -31.4 & 132.0 & 13.5 \\ -8.0 & 13.5 & 47.9 \end{bmatrix} \tag{17}$$

in x, y, z coordinates, and

$$\frac{1000}{U_o^2}(\overline{u_{pn}u_{pm}})_{\text{Bous}} = \begin{bmatrix} 157.4 & 0 & 0 \\ 0 & 45.6 & 0 \\ 0 & 0 & 89.5 \end{bmatrix} \tag{18}$$

in the coordinates of its principal directions, $\mathbf{p}_1$, $\mathbf{p}_2$, $\mathbf{p}_3$.

The glyphs for the stress, and strain in the form of the Boussinesq model stress, are compared for the maximum turbulence point in Fig. 10. The glyphs are quite similar in shape. The strain glyph is slightly shorter, consistent with the smaller maximum normal stress (Eqs. (18) and (7)). The difference in orientation between the stress and strain glyphs can be clearly seen.

The complete set of strain glyphs using the Boussinesq model is given in Fig. 11. These may be compared with the stress glyphs in Fig. 8. The difference in shape in the different regions of the flow is well modeled by the strain glyphs, as least in a qualitative way. The strain glyphs are in general more spherical, indicating more uniform principal normal stresses. The difference in orientation between the maximum normal stress directions is mixed, with some good regions and some poor points.

Quantitative Evaluation of Boussinesq Model. One way to evaluate the potential of Boussinesq-based turbulence models is to compare the orientations of the stress and strain glyphs. In Fig. 12, the difference in orientation is shown as the angle difference between the principal directions corresponding to the maximum normal stress and maximum normal strain, i.e., the angle difference between $\mathbf{P}_1$ and $\mathbf{p}_1$; see Fig. 10. Again, the regions where continuity was not satisfied have been omitted. For about half the measured region the Boussinesq approximation is good with angle variations of less than 20 deg. However, there are some regions with angle deviations in excess of 60 deg. With the symmetry of the tensor, the maximum possible deviation is 90 deg.

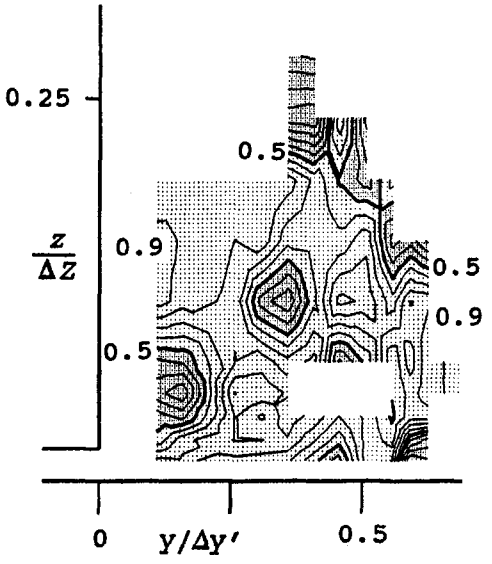

Fig. 13 Ratio of maximum modeled shear stress to the maximum measured shear stress; contour interval 0.1

Another assessment of the potential accuracy of the Boussinesq model is shown in Fig. 13. Here the maximum modeled shear stress is compared with the maximum measured Reynolds shear stress:

$$\frac{|\overline{u_{s1}u_{s2}}|_{\text{Bous}}}{|\overline{u_{S1}u_{S2}}|_{\text{Meas}}} = \frac{\overline{u_{p1}^2} - \overline{u_{p2}^2}}{u_{P1}^2 - u_{P2}^2} = \frac{2\nu_t\left[\left(\frac{\partial U_{p1}}{\partial x_{p1}}\right)^2 - \left(\frac{\partial U_{p2}}{\partial x_{p2}}\right)^2\right]}{\overline{u_{P1}^2} - \overline{u_{P2}^2}} \tag{19}$$

Note that this is not a comparison of the shear stress in the same pair of directions, but a comparison of the maximum magnitude. With ν_t evaluated using turbulence production, the Boussinesq model essentially underestimates the maximum shear stress over the whole tip leakage region. The highest values of the ratio were 1.0 at two points in the flow. The regions where the ratio is less than 0.5 roughly correspond to the regions where the angle deviation was greater than 30 deg.

Conclusions

Stress tensor analysis and Reynolds stress glyphs free one to think in a three-dimensional way rather than looking at components of the stress tensor in arbitrarily chosen coordinate directions.

Transformation of the stress tensors to the principal direction coordinates shows the nonisotropy of the normal stresses. This can also be seen by the shape of the Reynolds stress glyphs. In the present study of turbulence in a tip leakage vortex, the nonisotropy was highest in the tip leakage jet and the highly turbulent region of separation from the bottom endwall. At the maximum turbulence point, the maximum normal stress was 1.9 times the average normal stress and the ratio of the maximum to minimum normal stress was 3.8.

Mohr's circles can be used to show the shear stresses in the principal planes. In the principal direction coordinates, the shear stresses are zero. Rotating 45 deg about the $\mathbf{P}_3$ axis gives the coordinate system corresponding to the maximum shear stress. The magnitude of the maximum shear stress is half the difference between the maximum and minimum normal stresses (in the $\mathbf{P}_1$ and $\mathbf{P}_2$ directions). For the maximum turbulence point in the tip leakage flow, the high nonisotropy gave a maximum shear stress of $0.45k$.

The stress glyph provides a visual way of presenting turbulence stress tensors and comparing modeled and measured tensors. This in turn suggests quite different methods for comparing measurements and turbulence models. Two quantitative methods are used here: the angle difference between the measured and modeled main principal directions, and the ratio of the maximum modeled and measured shear stresses.

The capability of the Boussinesq model to represent the Reynolds stresses in the tip leakage vortex has been evaluated. To complete the model, turbulent viscosities were calculated from the measured turbulence production rates; they varied from about 100 to 1000 times the laminar viscosity in the tip leakage vortex.

The Boussinesq Reynolds stresses then showed reasonable agreement with the measured Reynolds stresses. Over most of the tip leakage vortex, the angle difference between the main principal directions was less than 30 deg and the magnitude of the maximum shear stress was within 50 percent of the measured value.

Acknowledgments

The inspiration for this study came from the graphical representation by Kriz (1994) of a fourth-order stiffness tensor glyph.

References

Beer, F. P., and Johnston, E. R., Jr., 1981, *Mechanics of Materials,* McGraw-Hill, New York, p. 312.

Dishart, P. T., and Moore, J., 1990, "Tip Leakage Losses in a Linear Turbine Cascade," ASME JOURNAL OF TURBOMACHINERY, Vol. 112, pp. 559–608.

Frederick, D., and Chang, T. S., 1972, *Continuum Mechanics,* Scientific Pub. Inc., Boston.

Haber, R. B., 1990, "Visualization Techniques for Engineering Mechanics," *Computing Systems in Engineering,* Vol. 1, No. 1, pp. 37–50.

Hinze, J. O., 1975, *Turbulence,* 2nd ed., McGraw-Hill, New York.

Kriz, R. A., 1994, "Three Visual Methods: Gradients, Function Extraction, and Tensor Glyphs," Class notes for ESM 5174, Virginia Polytechnic Institute and State University.

Moore, J., and Moore, J. G., 1991, "A Computational Study of Tip Leakage Flow and Losses in a Linear Turbine Cascade," AGARD Conference Proceedings No. 510, AGARD meeting on CFD Techniques for Propulsion Applications, San Antonio, TX, May.

Moore, J., Moore, J. G., Heckel, S. P., and Ballesteros, R., 1994, "Reynolds Stresses and Dissipation Mechanisms in a Turbine Tip Leakage Vortex," ASME Paper No. 94-GT-267.

Perry, W. L., 1988, *Elementary Linear Algebra,* McGraw-Hill, New York, pp. 314–316.

Press, W. H., Tuekolsky, S. A., Vetterling, W. T., and Flannery, B. P., 1992, *Numerical Recipes in Fortran,* 2nd ed., Cambridge Univ. Press.

Performance Improvement Through Indexing of Turbine Airfoils: Part 1—Experimental Investigation

F. W. Huber

P. D. Johnson

Pratt & Whitney, Technical,
West Palm Beach, FL 33410

O. P. Sharma

J. B. Staubach

Pratt & Whitney, Technical,
East Hartford, CT 06108

S. W. Gaddis

National Aeronautics & Space Administration,
Marshall Space Flight Center,
Huntsville, AL 35812

This paper describes the results of a study to determine the performance improvements achievable by circumferentially indexing successive rows of turbine stator airfoils. An experimental/analytical investigation has been completed that indicates significant stage efficiency increases can be attained through application of this airfoil clocking concept. A series of tests was conducted at the National Aeronautics and Space Administration's (NASA) Marshall Space Flight Center (MSFC) to experimentally investigate stator wake clocking effects on the performance of the Space Shuttle Main Engine Alternate Fuel Turbopump Turbine Test Article. Extensive time-accurate Computational Fluid Dynamics (CFD) simulations have been completed for the test configurations. The CFD results provide insight into the performance improvement mechanism. Part one of this paper describes details of the test facility, rig geometry, instrumentation, and aerodynamic operating parameters. Results of turbine testing at the aerodynamic design point are presented for six circumferential positions of the first stage stator, along with a description of the initial CFD analyses performed for the test article. It should be noted that first vane positions 1 and 6 produced identical first to second vane indexing. Results obtained from off-design testing of the "best" and "worst" stator clocking positions, and testing over a range of Reynolds numbers are also presented. Part two of this paper describes the numerical simulations performed in support of the experimental test program described in part one. Time-accurate Navier–Stokes flow analyses have been completed for the five different turbine stator positions tested. Details of the computational procedure and results are presented. Analysis results include predictions of instantaneous and time-average midspan airfoil and turbine performance, as well as gas conditions throughout the flow field. An initial understanding of the turbine performance improvement mechanism is described.

Introduction

A series of tests was recently conducted at the National Aeronautics and Space Administration's (NASA) Marshall Space Flight Center (MSFC). The objective of the test program was to experimentally investigate vane wake clocking effects on the performance of the Space Shuttle Main Engine (SSME) Alternate Turbopump Design (ATD) Turbine Test Article (TTA). These tests developed as a result of data analyses from previous baseline ATD aerodynamic rig tests (Gaddis et al., 1992), which indicated possible performance benefits for properly aligning the first vane wakes relative to the downstream vanes. Turbine efficiency contours generated from a complete circumferential mapping of the turbine exit not only showed a 54-cycle pattern corresponding to the second-stage vane count, but also a 2-cycle secondary pattern of ±0.5 percent points. Figure 1 shows the measured efficiency contours along with a Computational Fluid Dynamics (CFD) prediction for the circumferential position of the first vane wake as it approaches the second vane leading edge. The higher efficiency was measured in regions where the first vane wakes were predicted to be in general alignment with the second vane leading edges.

In order to test this theory, the hardware of the baseline ATD Turbine Test Article was modified to allow experimental investigation of the vane clocking effect. Modifications included an increase in the first vane count from 52 to 54 airfoils to match the second vane count and a clocking mechanism to allow the first stage vanes to be moved circumferentially relative to the second stage vanes and the inlet case struts. An external vernier was also incorporated in order to accurately measure first vane circumferential position. These modifications permitted the first stage vanes to be indexed circumferentially in a minimum amount of time without hardware disassembly, or stopping the test program.

Test Overview

Facility. This test series was conducted in MSFC's air flow Turbine Test Equipment (TTE). The TTE is a blowdown facility that operates by expanding high-pressure air from two 6000 cubic feet (170 cubic meters) tanks through a heater section, quiet trim control valve, calibrated subsonic mass flow venturi, and into a plenum section. The air then passes through the test article and an exhaust system to atmosphere. This facility can deliver 220 psia (1517 kPa). The tests described in this paper typically were run with 100 psia inlet pressure. The heater allows a blowdown controlled temperature between 530 R and 830 R (954–1494 K). The TTE has manual set point closed-loop control of the model inlet total pressure, inlet total temperature, shaft rotational speed, and pressure ratio. In addition to these control parameters, the facility can accurately measure mass flow, torque, and horsepower. Facility instrumentation also allows measurement of 400 pressures, 120 temperatures,

Contributed by the International Gas Turbine Institute and presented at the 40th International Gas Turbine and Aeroengine Congress and Exhibition, Houston, Texas, June 5–8, 1995. Manuscript received by the International Gas Turbine Institute Paper No. 95-GT-27. Associate Technical Editor: C. J. Russo.

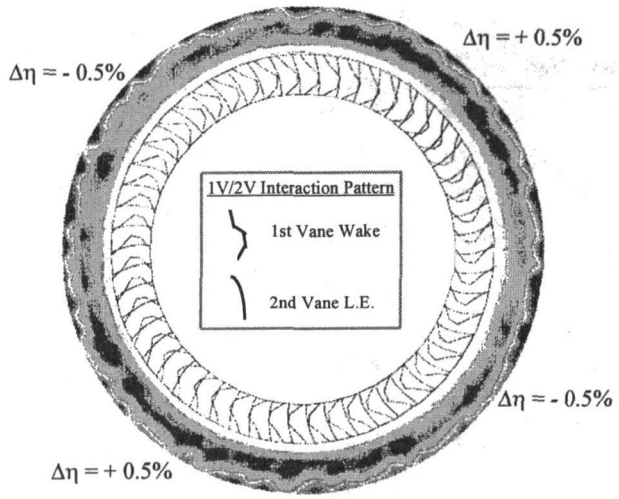

Fig. 1 Circumferential efficiency contours for baseline turbine

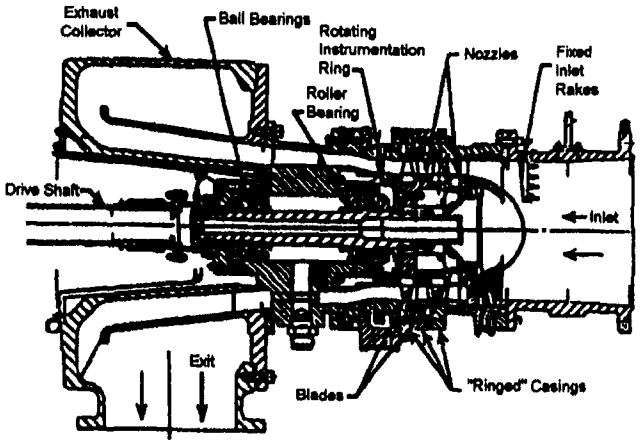

Fig. 2 Turbine test article cross section

and various health monitoring variables (Carter, 1991; Kauffman et al., 1992).

Model. The clocking concept was evaluated in a modified Alternate Turbopump Development (ATD) High-Pressure Fuel Turbopump (HPFTP) Turbine Test Article (TTA), which is a full-scale model of the Pratt & Whitney ATD HPFTP Turbine (Fig. 2). The inlet dome/strut assembly, stators, and rotors accurately duplicate the ATD HPFTP Turbine gas path geometry by utilizing engine hardware fitted and instrumented in the model casings within engine tolerances (Fig. 3). For this series of tests, the first vane count was increased from 52 to 54 airfoils to match the second vane count. The first vane was then restaggered slightly open to maintain the nominal first vane flow area. Also, a first vane clocking mechanism was added along with an external vernier scale to indicate the vane position. This mechanism provided a means for accurately changing the circumferential position of the first stage vanes, while the turbine inlet struts and second stage vanes remained in their original positions. The model flow entered axially into the turbine inlet, and exhausted axially into a collector, which directed the flow downward while diffusing to minimize possible circumferential pressure gradients. This test was designed to evaluate uncooled turbine performance; therefore all internal coolant flow and leakage paths were sealed.

Instrumentation. The turbine inlet was instrumented with four pressure rakes and four temperature rakes, each with five kielheads (Fig. 4). The kielheads were placed at centers of equal annular areas, and aligned pitchwise with the flow about the inlet dome. The turbine exit was also instrumented with four pressure rakes and four temperature rakes with the additional ability to circumferentially traverse. The exit rakes had five kielheads at centers of equal annular areas, and were manually adjustable for varying exit gas swirl angle. The exit instrumentation also included two autonulling cobra probes that were spanwise and circumferentially traversable.

Eight circumferentially spaced static pressure taps were placed on the inner and outer diameter of the flow path at the turbine inlet plane, the turbine exit plane, and between each airfoil row with the exception of the first vane inlet and exit. Other instrumentation included speed pickups, accelerometers, disk cavity pressures and temperatures, and venturi pressures and temperatures.

Test Matrix. The test series was conducted at "cold-air" equivalent conditions in three parts:

- In Part A, the turbine exit flow field was measured in detail for six first vane clocking locations at the aerodynamic design point ($Ptin$ = 100 psia (689 kPa), $Ttin$ = 550 R (990 K), $Ptin/Ptex$ = 1.463, N = 7000 rpm). The six first vane clocking positions were spaced 1°20′ apart, for a total of 6°40′, or one vane pitch (360°/54 vanes = 6°40′, Fig. 5).
- In Part B, the turbine was evaluated off-design at the "best" and "worst" positions, as determined from Part A. The turbine was tested at design pressure ratio over a wide speed range ($Ptin$ = 100 psia (689 kPa), $Ttin$ = 550 R (990 K), $Ptin/Ptex$ = 1.463, N = 2000–10,000 rpm).
- In Part C, the turbine was evaluated at reduced Reynolds number, by lowering the inlet pressure, for the six vane clocking positions of Part A ($Ptin$ = 35 psia (241 kPa), $Ttin$ = 550 R (990 K), $Ptin/Ptex$ = 1.463, N = 7000 rpm).

Turbine Performance

Aerodynamic Design Point Testing. Measured turbine efficiency was used to quantify the effect of vane clocking position on performance. The test program consisted of extensive flow field surveys at the turbine exit plane, approximately two

Nomenclature

$\eta(i)$ = efficiency at circumferential location "i"
$Ttin$ = average inlet total temperature
$Ttex(i)$ = exit total temperature at location "i"
$Ptin$ = average inlet total pressure
$Ptex(i)$ = exit total pressure at location "i"
γ = ratio of specific heats = Cp/Cv
Cp = specific heat at constant pressure
Cv = specific heat at constant volume
N = shaft rotational speed
Γ = shaft torque
W = weight flow
K = (2π rad/rev)/(60 s/min)
J = 778 ft-lb/Btu

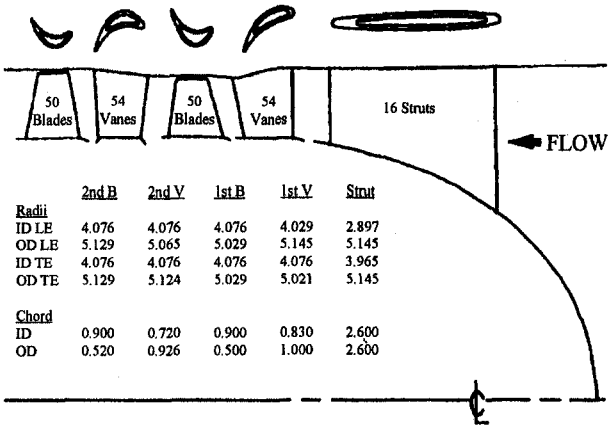

	2nd B	2nd V	1st B	1st V	Strut
Radii					
ID LE	4.076	4.076	4.076	4.029	2.897
OD LE	5.129	5.065	5.029	5.145	5.145
ID TE	4.076	4.076	4.076	4.076	3.965
OD TE	5.129	5.124	5.029	5.021	5.145
Chord					
ID	0.900	0.720	0.900	0.830	2.600
OD	0.520	0.926	0.500	1.000	2.600

Fig. 3 Turbine test article flow path geometry

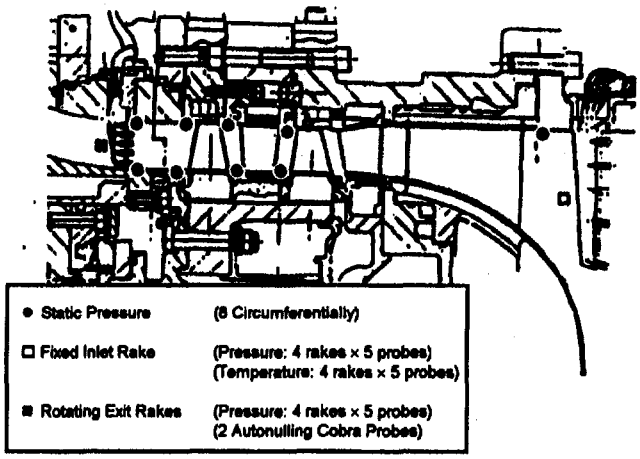

Fig. 4 Turbine test article instrumentation

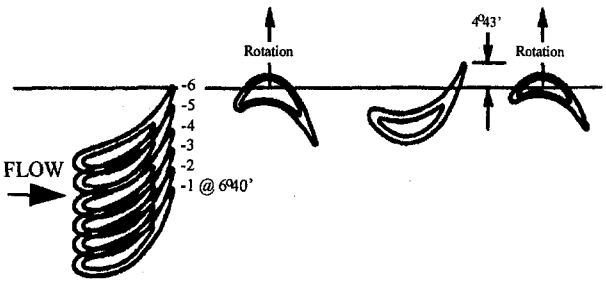

Vane Position	1	2	3	4	5	6
Circ Location	6°40'	5°20'	4°00'	2°40'	1°20'	0°00

Fig. 5 First stage vane clocking positions

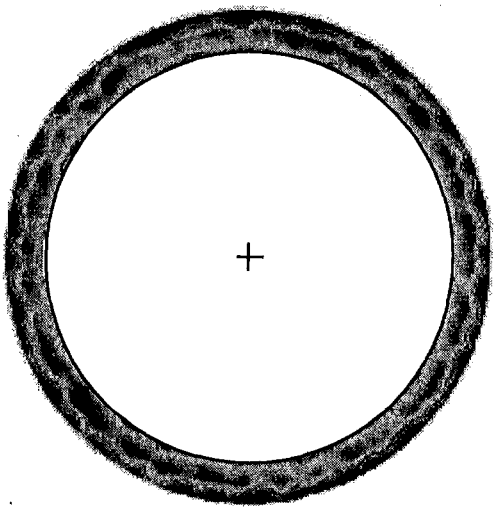

Fig. 6 Efficiency contour for vane position 1

chord lengths downstream of the second rotor. Pressure and temperature measurements were acquired for a full 360 deg at 1 deg increments, and then used to generate efficiency contours. Figure 6 shows the resulting contour map for vane position 1.

The (thermodynamic) method used to calculate efficiency from pressure and temperature measurements is as follows:

$$\eta(i) = \frac{[Ttin - Ttex(i)]}{Ttin\left[1.0 - \left(\frac{Ptex(i)}{Ptin}\right)^{(\gamma-1)/\gamma}\right]}$$

Measured efficiency contours for the six vane clocking positions all showed the 54 cycle pattern associated with the first and second vane count. However, it is noted that the average efficiency at vane position #2 was slightly higher than that at position #4 or #5. An area average of the efficiency contours produces a sinusoidal curve that shows an delta of 0.3 percent points between these vane clocking positions (Fig. 7).

A review of local spanwise efficiency variations with first vane clocking positions reveals local efficiency deltas up to 1.0 percent point. However, the root and tip cyclic variations are out of phase with those of the quarter-root, midspan, and quarter-tip (Fig. 8). A detailed look at the midspan data indicates that if the first vane wake could be properly aligned with the second vane leading edge from root to tip, a 0.8 percent point improvement in turbine performance is possible (Fig. 9).

Turbine performance can also be calculated with the torque and mass flow as follows (mechanical method):

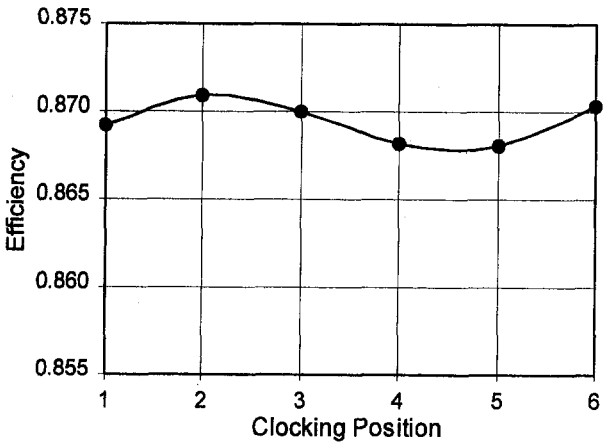

Fig. 7 Measured turbine efficiency versus clocking position

$$\eta = \frac{K*\Gamma*N}{J*Cp*W*Tin*\left(1.0 - \left(\frac{Ptex}{Ptin}\right)^{((\gamma-1)/\gamma)}\right)}$$

Although this method cannot give performance measurements at specific locations in the flow field, it can give an accurate check on the overall average turbine performance.

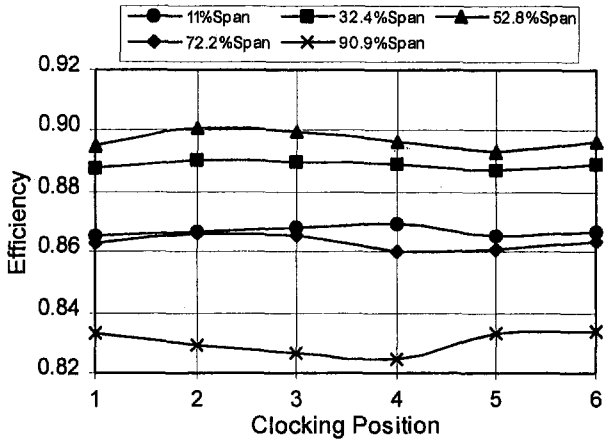

Fig. 8 Spanwise efficiency versus clocking position

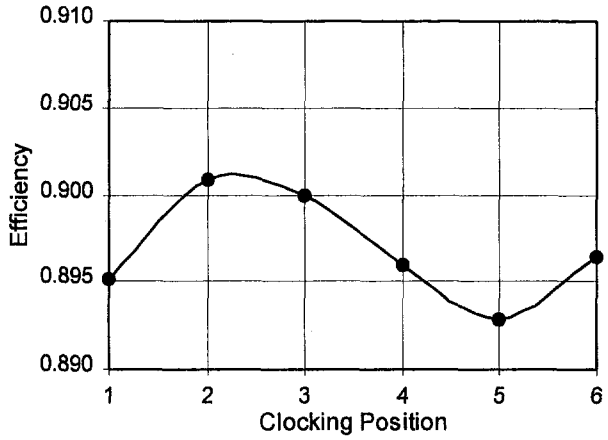

Fig. 9 Midspan efficiency versus clocking position

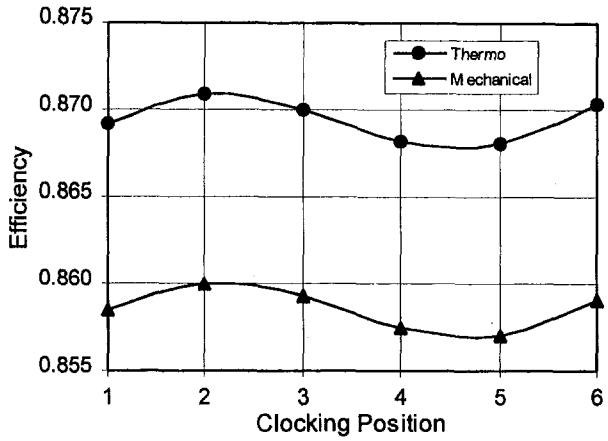

Fig. 10 Efficiency versus clocking position (thermodynamic and mechanical methods)

Comparison with the performance as calculated by the thermodynamic method shows close agreement in the measured trend with vane clocking position (Fig. 10). The offset in levels is probably due to unknown biases in one or both of the performance calculation methods.

Preliminary Analyses. Three-dimensional unsteady Euler calculations were performed to characterize the first vane wake entering the second vane. The computational model consisted

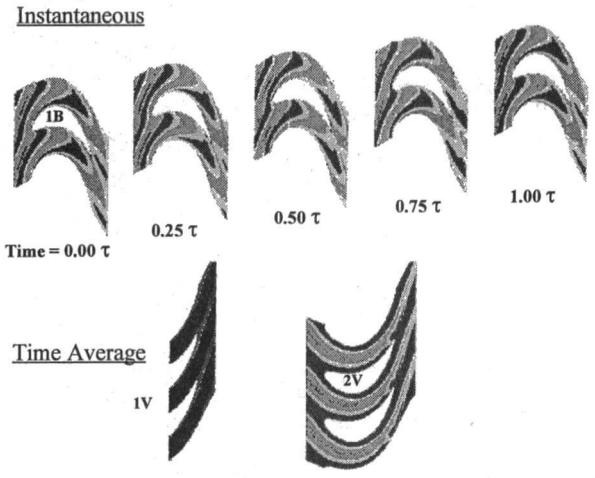

Fig. 11 Predicted instantaneous and time-averaged first vane wake

of the first stage stator and rotor along with the second stage stator. These calculations were used to predict how the first vane wake convects through the rotor and its resulting circumferential position and spanwise shape as it approaches the second vane leading edge. The computational results were then used to correlate first vane wake position to measured performance. The code used for this task was a time marching finite volume solver using Ni's scheme (Ni, 1981; Ni and Bogoian, 1989; Ni et al., 1989; Takahashi and Ni, 1990).

The 16 turbine inlet case struts were not included in the analytical model. The objective of the calculation was to determine how the (circumferential) average first vane wake aligned with the second stage vane leading edge. Since the inlet case struts remained in a fixed position, and the inlet strut count is not an integral multiple of the first vane count, their circumferentially averaged effect on first vane/second interaction was independent of first vane position.

For the Euler calculation, the first vane wake was created by applying a calibrated surface shear model to the momentum equation as a source term. The wake was then allowed to pass inviscidly through the rotor such that its trajectory could be plainly seen with entropy contours (Fig. 11). The first vane wake is chopped by the passing rotor into discrete pulses that exit the rotor passage at a fixed circumferential location relative to the second vane. When this flow field is time-averaged, these pulses appear as a continuous stream into the second vane. It is these time-averaged first vane wakes entering the second vane

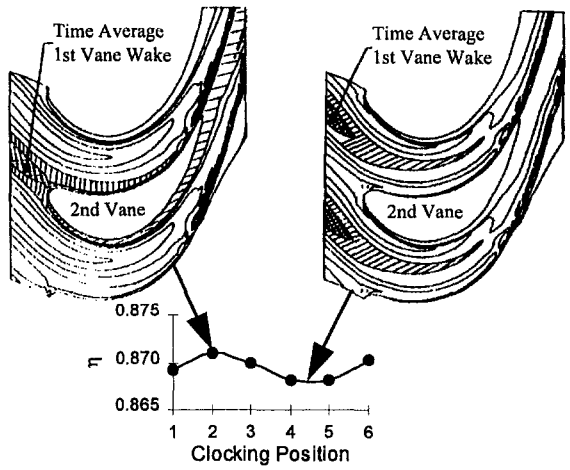

Fig. 12 Predicted time-averaged first vane wake impingement on the second vane

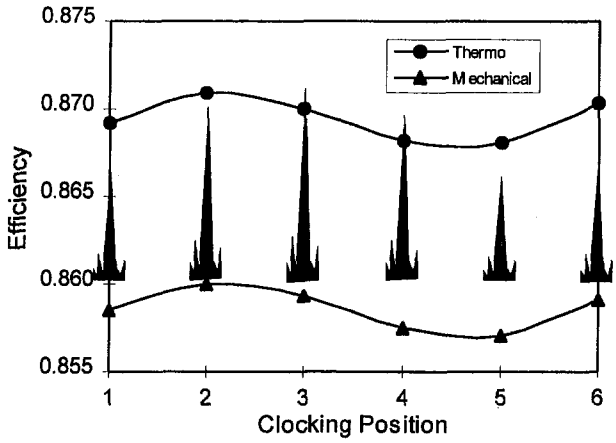

Fig. 13 Relative amplitude of 54E frequency component in measured overall efficiency

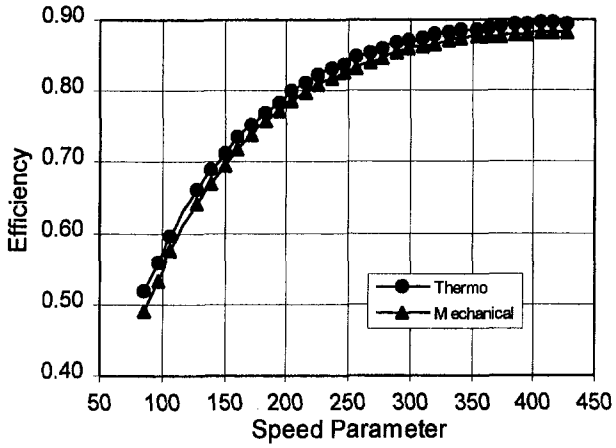

Fig. 15 Off-design performance (thermodynamic and mechanical methods)

that can be clocked by changing the circumferential positioning of the first vane to second vane, or by varying the rotor wheel speed such that the velocity triangles change the first vane wake trajectory.

The measured peak efficiency occurs when the calculated time average first vane wake impinges upon the second vane leading edge. Conversely, the minimum efficiency occurs when the first vane wake is calculated to be in the second vane midchannel (Fig. 12). A Fourier analysis of the full 360 deg of turbine exit data supports this conclusion. The vane count (54 cycle) signal is maximum at peak performance indicating that the first vane and second vane wakes coincide with each other (Fig. 13). Additionally, the spanwise shape of the convective wake entering the second vane tends to explain the variation of the best clocking position versus span. Previously it was shown that the tip and midspan "best" clocking positions were 50 percent pitch out-of-phase with each other. The analytical wake entering the second vane is predicted to be skewed 50 percent pitch between the tip and midspan, which would support this conclusion (Fig. 14).

Off-Design Testing. Off-design testing was done at the "best" (#2) and "worst" (between #4 and #5) vane clocking positions. A plot of turbine efficiency versus speed parameter shows very good correlation between the thermodynamic and mechanical methods of calculation (Fig. 15). As with the aerodynamic design point results, an offset between the two measurement methods exists, which may be due to a bias that has not been identified. However, this bias appears to be constant throughout the off-design envelope.

A detailed review of the turbine off-design performance data shows the effect of changing speed parameter on the clocking phenomenon (Fig. 16). The wakes from the first vane become clocked and unclocked as the turbine operating speed is varied. This test shows the effective speed range in which a particular clocking position is beneficial. As in the aerodynamic design point testing, the efficiency delta was measured to be 0.3 percent overall. The magnitude of the delta at the midspan was measured to be 0.8 percent at the design speed parameter, and as much as 1.0 percent at higher speed parameters, which also verifies the previous aerodynamic design point results (Fig. 17).

Reynolds Number Testing. Testing was also conducted at low Reynolds number by decreasing the inlet pressure to 35 psia (241 kPa). In general the effect of clocking on turbine performance agreed with testing done at an inlet pressure of 100 psia (689 kPa). However, at the lower operating pressure, uncertainties in measured parameters become larger and may cloud the results. The precision in measured turbine efficiency at an inlet pressure of 100 psia (689 kPa), based on measured data, is 0.07 percent for both the thermodynamic and mechanical methods of efficiency calculation. At an inlet pressure of 35 psia (241 kPa), the calculation of turbine efficiency becomes approximately three times less precise. A detailed view of the vane wake indexing effect on midspan efficiency at 35 psia (241 kPa) inlet pressure, shows it is in good agreement with the data obtained at 100 psia (689 kPa) inlet pressure (Fig. 18).

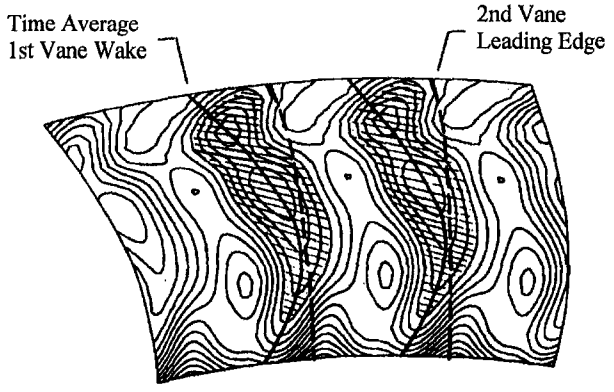

Fig. 14 Predicted time-averaged first vane wake is skewed relative to the second vane leading edge

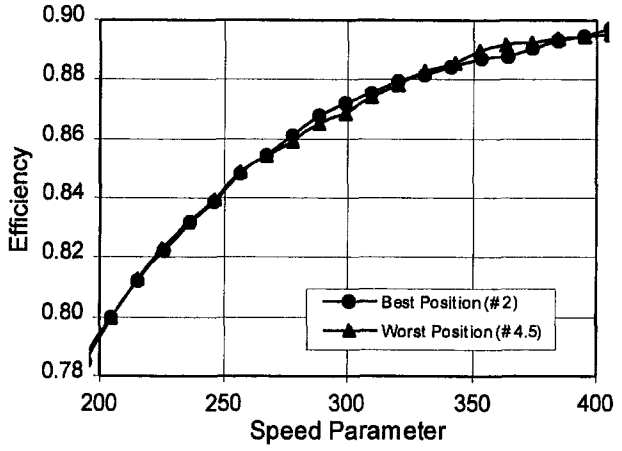

Fig. 16 Off-design performance at "best" and "worst" clocking positions

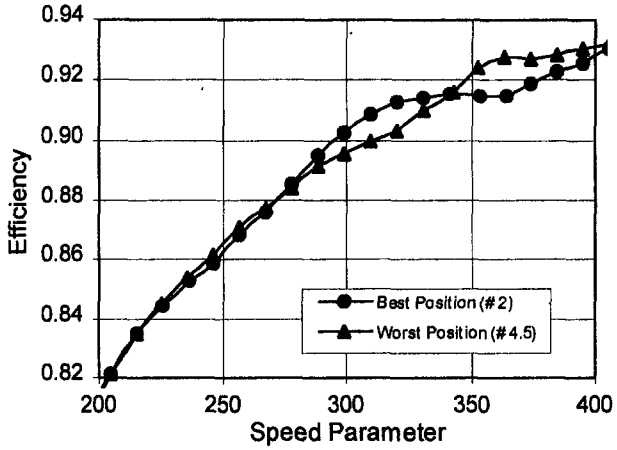

Fig. 17 Off-design performance at "best" and "worst" clocking positions (midspan detail)

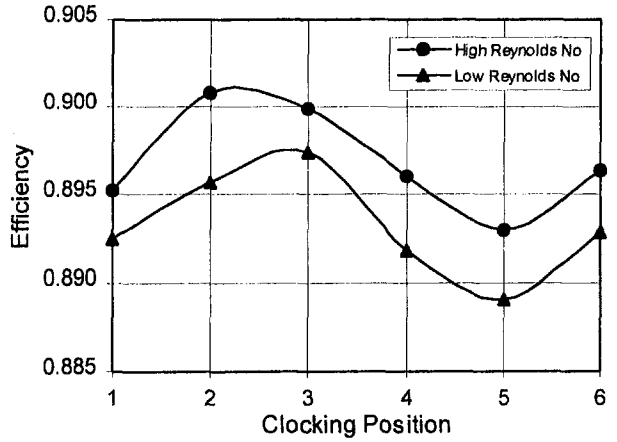

Fig. 18 Efficiency versus clocking position (high and low Reynolds number, midspan detail)

Summary

Testing of the ATD Fuel Turbine Test Article, modified to allow first stage vane circumferential positioning, has provided significant insight into the phenomenon of vane wake indexing. Very detailed turbine exit flow field surveys have been obtained. The effect of vane clocking on turbine performance has been quantified at the turbine aerodynamic design point. Off-design performance mapping has quantified the effective design operating range over which the vane indexing concept can be employed. Low Reynolds number data also confirmed the clocking effect, but with higher data uncertainty. This experiment has demonstrated the vane indexing concept and the associated potential turbine performance benefits.

Acknowledgments

The authors wish to acknowledge the important contributions made to this work by our colleagues. William Kauffman of NASA MSFC and Allen Finke of P & W executed the tests described in this paper, and Adam Fredmonski of P & W performed supporting analyses. Sincere appreciation is also extended to Microcraft and Rotadata for supplying quality hardware in a timely manner.

References

Carter, J. A., 1991, "Blowdown Turbine Test Equipment Design Characteristics," NASA memo ED35-45-91.

Gaddis, S. W., Hudson, S. T., and Johnson, P. D., 1992, "Cold Flow Testing of the Space Shuttle Main Engine Alternate Turbopump Development High Pressure Fuel Turbine Model," ASME Paper No. 92-GT-280.

Kauffman, W. J., Carter, J. A., Heaman, J. P., and Bordelon, W. J., 1992, "The Design and Performance of the Marshall Space Flight Center Turbine Test Equipment," ASME Paper No. 93-GT-380.

Ni, R. H., 1981, "A Multiple-Grid Scheme for Solving the Euler Equations," AIAA Paper No. 81-1025; *AIAA Journal,* Vol. 20, No. 11.

Ni, R. H., and Bogoian, J. C., 1989, "Prediction of 3D Multistage Turbine Flow Field Using a Multiple-Grid Euler Solver," AIAA Paper No. 89-0203.

Ni, R. H., Sharma, O. P., Takahashi, R., and Bogoian, J. C., 1989, "3D Unsteady Flow Simulation Through a Turbine Stage," presented at the 1989 Australian Aeronautical Conference—Research and Technology—The Next Decade, Melbourne, Australia.

Takahashi, R., and Ni, R. H., 1990, "Unsteady Euler Analysis of the Redistribution of an Inlet Temperature Distortion in a Turbine," AIAA Paper No. 90-2262.

Performance Improvement Through Indexing of Turbine Airfoils: Part 2—Numerical Simulation

L. W. Griffin
Fluid Dynamics Analysis,
National Aeronautics and Space Administration,
George C. Marshall Space Flight Center,
Marshall Space Flight Center, AL 35812

F. W. Huber

O. P. Sharma
Pratt & Whitney, Technical,
West Palm Beach, FL 33410; and
East Hartford, CT 06108

An experimental/analytical study has been conducted to determine the performance improvements achievable by circumferentially indexing succeeding rows of turbine stator airfoils. A series of tests was conducted to experimentally investigate stator wake clocking effects on the performance of the space shuttle main engine (SSME) alternate turbopump development (ATD) fuel turbine test article (TTA). The results from this study indicate that significant increases in stage efficiency can be attained through application of this airfoil clocking concept. Details of the experiment and its results are documented in part 1 of this paper. In order to gain insight into the mechanisms of the performance improvement, extensive computational fluid dynamics (CFD) simulations were executed. The subject of the present paper is the initial results from the CFD investigation of the configurations and conditions detailed in part 1 of the paper. To characterize the aerodynamic environments in the experimental test series, two-dimensional, time-accurate, multistage, viscous analyses were performed at the TTA midspan. Computational analyses for five different circumferential positions of the first stage stator have been completed. Details of the computational procedure and the results are presented. The analytical results verify the experimentally demonstrated performance improvement and are compared with data whenever possible. Predictions of time-averaged turbine efficiencies as well as gas conditions throughout the flow field are presented. An initial understanding of the turbine performance improvement mechanism based on the results from this investigation is described.

Introduction

The objective of the ATD program is to provide line replaceable turbopumps for the SSME. These turbopumps are to be more durable than the baseline SSME turbopumps, but should not change the engine balance. A series of aerodynamic rig tests was conducted by Gaddis et al. (1992) to measure the performance of the ATD high-pressure fuel turbopump (HPFTP) turbine. The results would then be compared to the results of the baseline HPFTP turbine tests conducted by Hudson et al. (1991). During the analysis of the data, an interesting phenomenon was uncovered. Turbine efficiency contours generated from a circumferential mapping of the turbine exit showed not only a 54-cycle pattern corresponding to the second stage vane count, but also a two cycle secondary pattern of ± 0.5 percentage points. A CFD analysis was conducted to determine the circumferential position of the first vane wake as it approaches the second vane leading edge. These predictions were compared with the measured efficiency contours. This comparison showed that the higher efficiency was measured at the circumferential locations where the first stage vane wakes were predicted to be in general alignment with the leading edges of second stage vanes. It was therefore theorized that turbine performance benefits are attainable by properly aligning the first stage vane wakes relative to the downstream vanes.

In order to test this theory, an experimental/analytical study was conducted. The ATD HPFTP TTA hardware was modified to allow the investigation of the effects of circumferentially indexing succeeding rows of stator airfoils. The experiment, documented in part 1 of this paper (Huber et al., 1996), demonstrated the potential performance benefits. The turbine exit flow field was measured in detail for six first vane clocking positions. These clocking positions were spaced 0.02327 rad (1.333 deg) apart for a total of 0.11635 rad (6.667 deg), or one vane pitch as shown in Fig. 1. A plot of midspan efficiency versus clocking position (Fig. 2) shows a sinusoidal distribution with a delta of 0.8 percentage points.

Although the tests demonstrated the vane clocking concept and the resulting potential benefits, the reasons the benefits were achieved were unknown. In order to gain insight into the mechanisms of the performance improvement, extensive CFD analyses were performed. The analytical approach and results are the subjects of this paper. The analytical approach taken was to apply a two-dimensional, time-accurate, multistage, viscous code to the turbine midspan for each of the clocked vane configurations. Results from these CFD investigations include time- and circumferentially averaged efficiencies, as well as gas conditions throughout the turbine. An initial understanding of the turbine performance improvement mechanism based on the results of this investigation is offered.

Turbine Description

The clocking concept was tested in a modified version of the ATD HPFTP TTA described by Gaddis et al. (1992). The TTA is a full-scale model of the SSME ATD HPFTP turbine. The inlet dome/strut assembly, stators, and rotors accurately duplicate the ATD HPFTP turbine. In order to evaluate the clocking concept, the number of first stage vanes of the TTA was increased from 52 to 54 to equal the number of second stage

Contributed by the International Gas Turbine Institute and presented at the 40th International Gas Turbine and Aeroengine Congress and Exhibition, Houston, Texas, June 5–8, 1995. Manuscript received by the International Gas Turbine Institute February 11, 1995. Paper No. 95-GT-28. Associate Technical Editor: C. J. Russo.

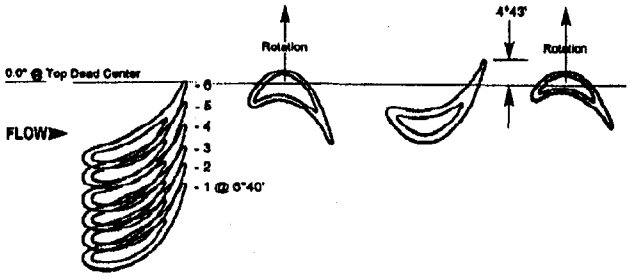

Fig. 1 First vane clocking positions in rig

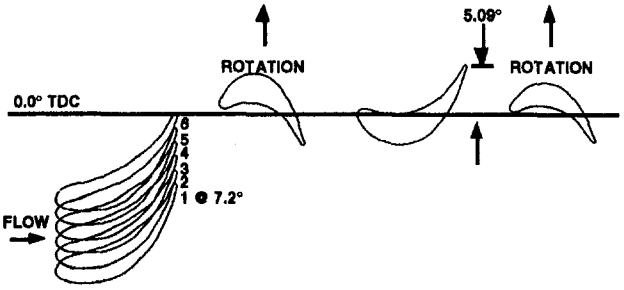

Fig. 3 Numerically modeled first vane clocking positions

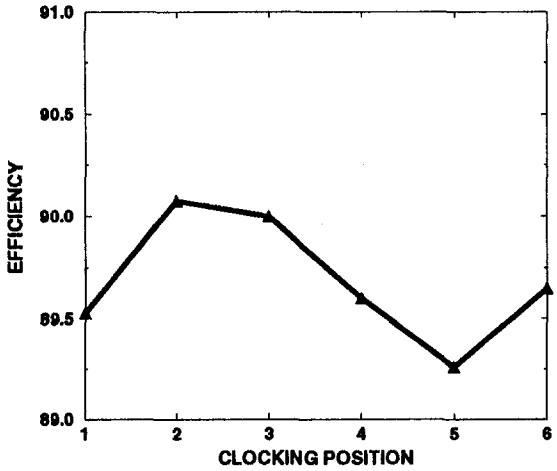

Fig. 2 Experimentally observed efficiency versus clocking position

vanes. The first stage vanes were then restaggered slightly open to maintain the nominal first vane flow area. The modified turbine consists of two stages with an average diameter of 32.60 cm (12.84 in.) and a vane/blade count of 54:50:54:50. The average axial chord is 2.01 cm (0.79 in.) and the average axial gap is 1.05 cm (0.41 in.). Test conditions corresponding to the calculations presented in this paper involve air entering the first vane at approximately 42.89 m/s (140.71 ft/s) and a Mach number of 0.1226. The total pressure (P_{to}) and the total temperature (T_{to}) at the inlet are 687,000 nt/m^2 (99.6 lbf/in.^{2}) and 982.8 K (546 R), respectively. The total-to-static pressure ratio is 1.489, and the Reynolds number (Re) based on axial chord and inlet conditions is 363,500. The rotational speed is 12.19 rad/s (6982 rpm). Additional details on the TTA modifications and the flow conditions for this test series are given by Huber et al. (1996).

Method of Solution

The flow fields for the test series previously described were numerically analyzed using a two-dimensional, time-accurate, viscous code. The methodology, approach, and grid system are discussed in the following sections.

Code Description. The CFD code implemented in this study was STAGE2. STAGE2 predicts the flow through a multistage axial turbomachine with arbitrary blade counts (multiblade) by solving the two-dimensional, unsteady, compressible, thin-layer Navier–Stokes equations. The code is an extension of an algorithm detailed by Rai and Chakravarthy (1988), Rai (1987), and Rai and Madavan (1988). The code features a time-marching, implicit, third-order spatially accurate, upwind finite difference scheme. The flow field is divided into two types of zones. The inner zones are regions near the airfoil where viscous effects are strong. The thin-layer Navier–Stokes equations are solved in these zones. Euler equations are solved in the outer zones where viscous effects are assumed to be weak. This assumption breaks down in the regions of the outer zones between the airfoils where the wakes pass. However, due to the relative coarseness of the outer grids, the numerical dissipation in the outer regions would be much larger than the viscous effects even if the fully viscous Navier–Stokes equations were solved in these zones. Gundy-Burlet et al. (1991) showed excellent agreement with data when calculating wake profiles when the Euler equations were solved in the outer zones and a fine grid system was employed. Rangwalla et al. (1992) also showed excellent agreement with data when calculating total pressure loss. Boundary conditions enforced at the airfoil surfaces are no slip, adiabatic wall, and a zero normal pressure gradient. At the inlet, the flow angle, upstream Riemann invariant, and average P_{to} are specified while the downstream Riemann invariant is extrapolated from the interior. At

Table 1 Predicted total-to-total efficiency—two-stage configuration

POSITION	EFFICIENCY
1	94.82%
2	94.95%
3	94.87%
4	94.74%
5	94.65%
6	94.82%

Nomenclature

AR = Aspect Ratio
C_p = coefficient of pressure
c = axial chord
P = pressure
Re = Reynolds number
s = entropy
T = temperature
u = velocity magnitude
x = axial distance
y^+ = boundary layer parameter
Δ = change in a quantity
γ = ratio of specific heats
η = efficiency

Subscripts

ca = circumferentially averaged quantity
e = exit condition
l = local condition
me = turbine exit measurement plane
o = inlet condition
s = static quantity
t = total (stagnation) quantity
ta = time-averaged quantity
t-t = total-to-total quantity
u = unsteady quantity

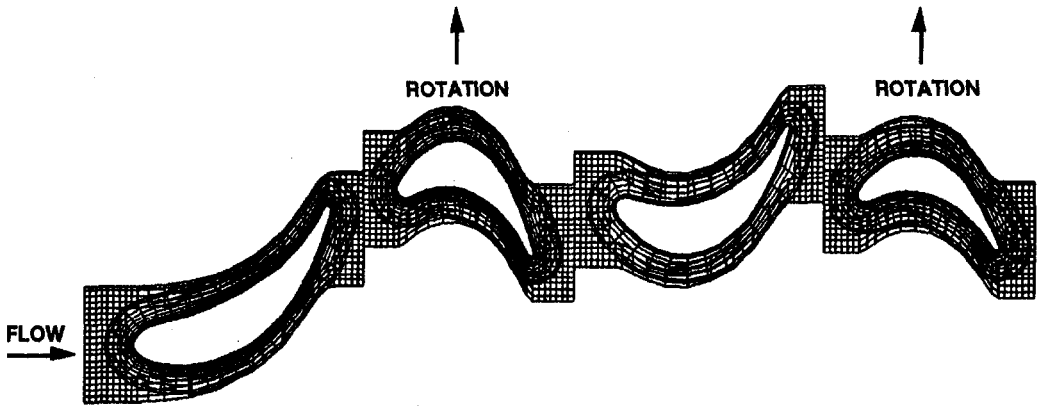

Fig. 4 Modified ATD fuel turbine grid (every fourth point in each direction shown; inflow and outflow grids not shown)

the exit, the average static pressure (P_{se}) is specified, while the upstream Riemann invariant, tangential velocity, and entropy (s) are extrapolated from the interior. The flow is assumed to be fully turbulent. The kinematic viscosity is calculated using Sutherland's law, and the eddy viscosity is estimated using the Baldwin–Lomax (1978) turbulence model implemented in each airfoil's frame of reference. Further details of the STAGE2 code are given by Gundy-Burlet et al. (1989, 1991).

Code Application. The modified SSME ATD TTA has a vane-to-blade ratio of 54:50:54:50. For this numerical study, the turbine was modeled as having a 1:1:1:1 ratio. The vanes were scaled by 54/50 to provide the correct blockage. For the test series, the first vane clocking positions were spaced at 0.02327 rad (1.333 deg) apart for a total of 0.11635 rad (6.667 deg), or one vane pitch. The delta between clocking positions could also be viewed as 20 percent of the vane pitch. Each of these positions provided for a unique flow field. For the analytical investigation, the delta between each clocking position was 20 percent of the scaled vane pitch (Fig. 3). Because of the modeled 1:1:1:1 ratio, the scaled vane pitch is 0.12566 rad (7.20 deg), and the delta between clocking positions is 0.02513 rad (1.44 deg). In addition, because the turbine is modeled with an equal number of vanes and blades, positions 1 and 6 provide an identical flow field.

The 16 inlet struts that were included in the experiment were not modeled. Previous analysis of the ATD HPFTP turbine by Griffin and Rowey (1993) showed that the strut wake persists through the first stage vane and impacts the first stage blade. Its effect on the second stage is unknown. To model the turbine flow path more accurately, the strut and the interaction of its wake with the first stator wake should be modeled. However, with the addition of the struts, the strut-to-vane-to-blade ratio would be approximately 1:3:3:3:3. This larger model would have precluded the analysis of all five test cases due to time and computer memory constraints. The authors believe that the clocking concept can be demonstrated and at least an initial understanding of the mechanism of performance enhancement could be determined without including the inlet struts in this analysis.

Calculations were run on the NASA/MSFC CRAY Y-MP. The grid system density and distribution, boundary conditions, initial conditions, and convergence criteria were consistent from case to case. The ultimate convergence criterion was established to be when the time- and circumferentially averaged, total-to-total efficiency ($\eta_{t\text{-}t}$) stabilized to four significant digits.

Grid System. The grid around each airfoil consists of an inner zone and an outer zone. The inner zone is discretized with a fine "O" grid surrounding the airfoil. The "O" grids are

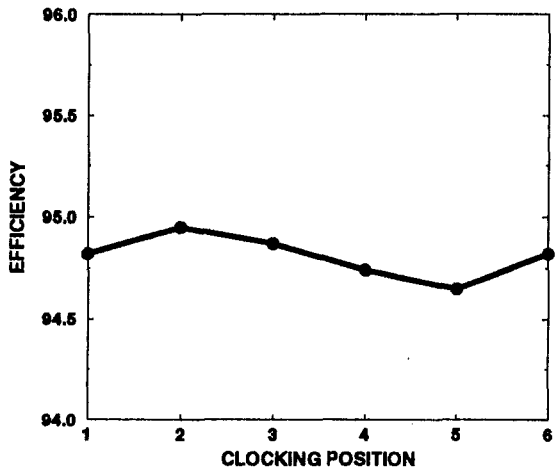

Fig. 5 Predicted two stage efficiency versus clocking position

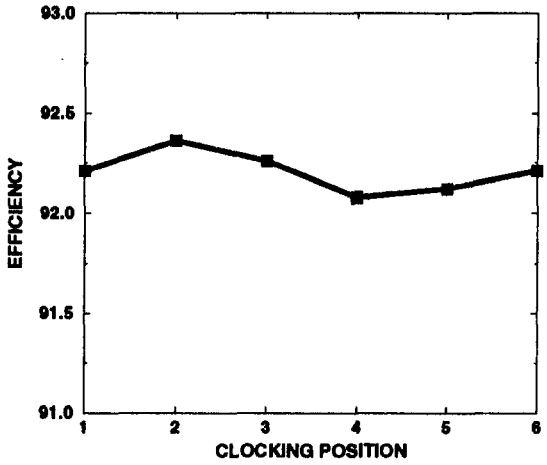

Fig. 6 Predicted $1\frac{1}{2}$ stage efficiency versus clocking position

Table 2 Predicted total-to-total efficiency

POSITION	EFFICIENCY
1	92.21%
2	92.36%
3	92.26%
4	92.08%
5	92.12%
6	92.21%

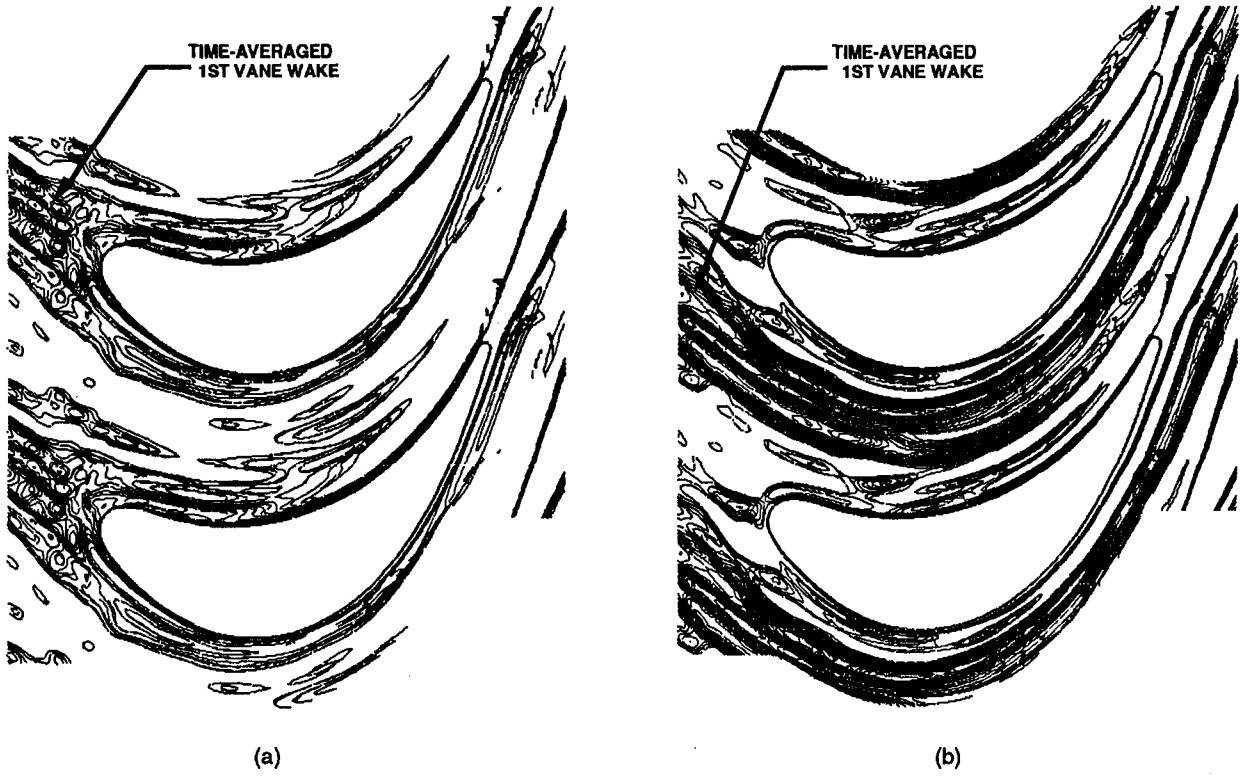

Fig. 7 Time-averaged entropy contours for the second vane with the first vane clocked to (*a*) position 2 and (*b*) position 5

overlaid onto "*H*" grids, which discretize the outer zones. The "*H*" grids are patched between blade rows and the rotor "*H*" grids slide past stator "*H*" grids in time. Each airfoil "*O*" grid contains 201 × 51 points with an average y^+ value of 0.8, and each airfoil "*H*" grid contains 97 × 79 points. Inflow and outflow grids with 36 × 79 and 39 × 79 points, respectively, complete the system. The inflow and outflow grids extended approximately 15 chord lengths upstream and downstream of the turbine, respectively. The axial spacing increases with distance from the turbine to damp the amplitudes of propagating wave modes as prescribed by Rangwalla and Rai (1993). The total number of points in the grid system (shown in Fig. 4) is 77,581.

Grid densities for this study are finer than those used by Rangwalla et al. (1992) who showed excellent agreement with data when calculating midspan total pressure loss for a $1\frac{1}{2}$ stage turbine. The grid dimensions in that study were 151 × 41 and 90 × 71 for the inner and outer grids respectively. The Re per inch based on inlet conditions was 100,000 and the blade pitch was 15.39 cm (6.06 in.). In the current study, the Re per inch is 460,000 so the airfoil wakes should be slightly thinner, which would necessitate a finer grid in the circumferential direction. However, the blade pitch in this study is 1.48 cm (0.583 in.) or 9.6 percent of the blade pitch of the turbine analyzed by Rangwalla et al. Therefore, the authors believe that the grids used in this study were adequate to meet the objectives of the analysis.

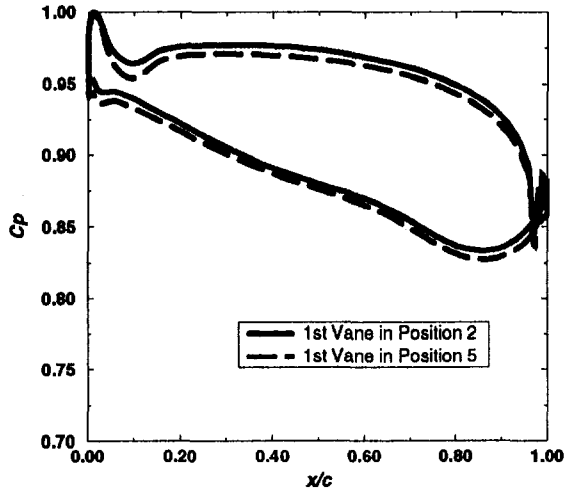

Fig. 8 Pressure coefficients for the second vane

Results and Discussion

Total-to-total efficiency was used to quantify the effect of the vane clocking on turbine performance. The $\eta_{t\text{-}t}$ was calculated by

$$\eta_{t\text{-}t} = \frac{T_{to,ca,ta} - T_{tme,ca,ta}}{T_{to,ca,ta}\left[1.0 - \left(\frac{P_{tme,ca,ta}}{P_{to,ca,ta}}\right)^{(\gamma-1)/\gamma}\right]} \quad (1)$$

where *ta* denotes a time-averaged quantity, *ca* indicates a quantity spatially averaged in the circumferential direction, *o* is the computational inlet, and *me* is the plane that represents the location where the efficiency was measured in the test series. The quantities were time-averaged over 1000 time slices which comprised one periodic rotor passage. The predicted turbine midspan efficiencies are given in Table 1.

A prediction of $\eta_{t\text{-}t}$ at the turbine midspan is shown in Fig. 5. Both the data and prediction show a sinusoidal pattern of $\eta_{t\text{-}t}$ versus clocking position. However, the data show an average efficiency of 89.7 percent with a $\Delta\eta_{t\text{-}t}$ of ± 0.4 percent while the prediction shows an average efficiency of 94.80 percent ± 0.15 percent. The difference in the average level of $\eta_{t\text{-}t}$ can be explained by the types of loss that are generated by the two techniques. For the experiment, the losses are not truly midspan

losses. Because this turbine has small blades with a low aspect ratio (AR = 1.3), the endwalls provide some spanwise mixing. The calculation provides strictly midspan profile loss. A mean-line analysis of the turbine with all losses but profile losses deleted predicted a midspan efficiency of 94.90 percent. There could be several reasons for the difference between the observed and predicted $\Delta\eta_{t\text{-}t}$. The first vane clocking could reduce the endwall losses in the downstream vane or blade row. This effect would not modeled in a two-dimensional calculation. It is also possible that the difference is due to a limitation in the analytical technique due to numerical error. In any event, the difference cannot be explained at this time, and further work is needed.

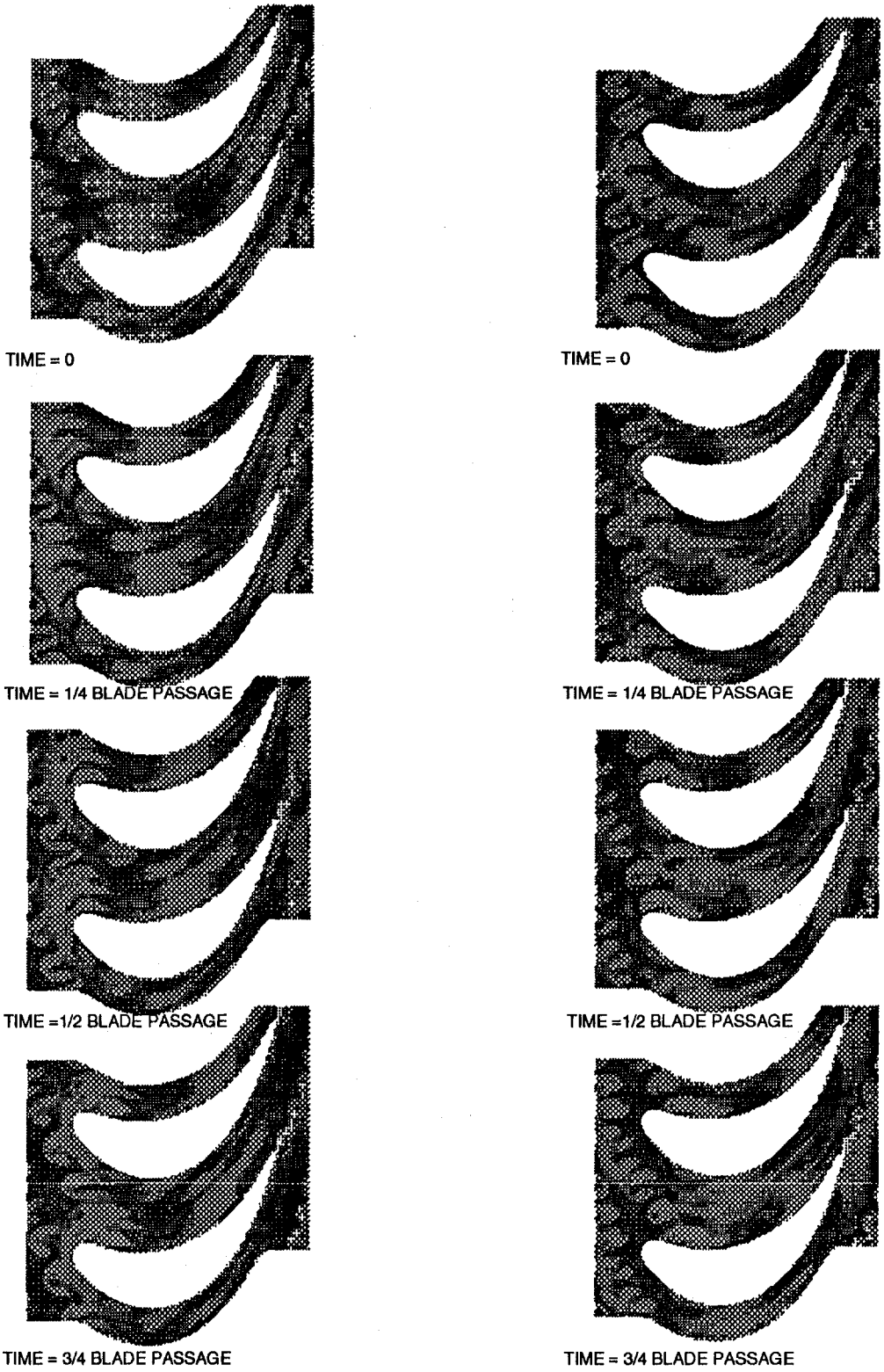

Fig. 9 Instantaneous entropy contours at four time slices for the second vane with the first vane clocked to (*a*) position 2 and (*b*) position 5

In order to isolate whether the performance improvement was due to changes in the flow field of the second vane or the second blade, $\eta_{t\text{-}t}$ was calculated for $1\frac{1}{2}$ stages. The predicted $1\frac{1}{2}$ stage efficiencies are shown in Table 2 and plotted in Fig. 6. The sinusoidal pattern is still evident, and the $\Delta\eta_{t\text{-}t}$ is $\pm$ 0.14 percent. This result indicates that improved second vane performance is a major contributor to the efficiency gain obtained by vane clocking. Therefore, the remainder of the paper will concentrate on performance improvements in the second vane.

Entropy contours were generated in order to visualize the airfoil wakes. The first vane wake is chopped into discrete pulses by the passing first blade. These pulses leave the rotor at fixed circumferential locations relative to the second vane. When the flow field is time-averaged, the pulses appear as a continuous streak into the second vane. Figures 7(a, b) show time-averaged entropy contours (s_{ta}) for the second vane for positions 2 and 5. These vane clocking positions were predicted and measured to produce the highest and lowest turbine efficiencies, respectively. In Fig. 7(a), it is shown that the first vane wake represented by s_{ta} contours impinges upon the leading edge of the second vane when the first vane is clocked to position 2. Figure 7(b) shows that when the first vane is clocked to position 5, its wake passes through the midchannel of the second vane. These results confirm the earlier CFD predictions for wake positions in the baseline SSME ATD HPFTP turbine.

One possible reason for the increased performance of the second vane is reduced surface velocities. When the first and second stage vanes are clocked so that the time-averaged first vane wake is aligned with the leading edge of the second vane (as in position 2), the second vane has lower surface velocities. Figure 8 shows time-averaged pressure coefficients for the second vane, defined in Eq. (2):

$$C_P = \frac{P_{sl}}{P_{T,\text{airfoil}}} \tag{2}$$

for positions 2 and 5. The plot indicates higher surface velocities for the second vane when the first vane is clocked to position 5. In fact, the average surface Mach numbers for the second vane for positions 2 and 5 are 0.437 and 0.471, respectively. Assuming that the dissipation coefficients are constant, the loss can be estimated to be proportional to the difference in the u^3 (Denton, 1993). This estimate indicates that the reduced losses due to lower velocities accounts for 73 percent of the efficiency difference or $\Delta\eta_{t\text{-}t}$ = 0.22.

Another possible reason for increased second vane performance is reduced flow unsteadiness when the vanes are optimally indexed. An increase in unsteadiness would generate additional losses due to increased turbulence. Animation of the unsteady entropy contours shows that the first vane wake is chopped into discrete pulses by the first blade. When the vanes are optimally indexed, these higher entropy regions from the first vane fill in between first rotor wakes at the second vane leading edge. This phenomenon can be seen in Fig. 9, which shows instantaneous entropy contours for the second vane at four different times within a blade passage for clocking positions 2 and 5. The black areas indicate relatively lower regions of loss. Comparison of Figs. 9(a, b) shows that when the vanes are optimally indexed (as in position 2), the second vane leading edge is always in a region of higher loss made up of the chopped first vane wakes along with first blade wakes. When the first vanes are in position 5, their chopped wakes travel midway between second vanes. This results in a more discrete first blade wake passing the second vane leading edge, thus increasing the local variation in entropy. Figures 10(a, b) show unsteady C_p at points near the leading edge of the second vane on the pressure surface and suction surface, respectively, versus blade passage. To aid visualization, the plot is repeated for four blade passages. The increase in the flow field unsteadiness of the position 5 case over the position 2 case is illustrated. On

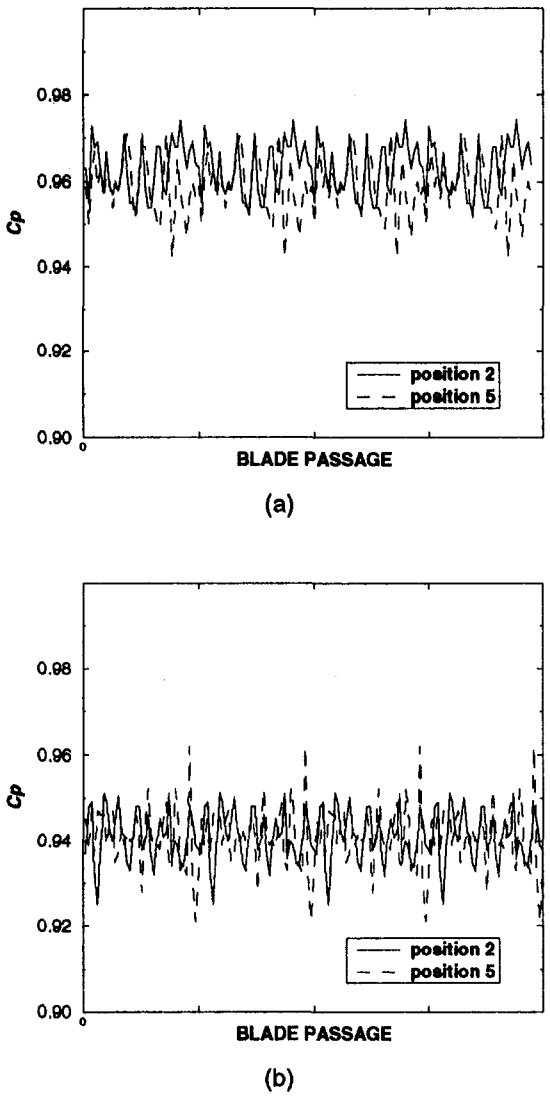

Fig. 10 Unsteady pressure coefficients at the leading edge of the second vane

the pressure side, the standard deviation from the time-average is calculated to be 0.00597 for position 2 and 0.00667 for position 5, demonstrating an increase of 11.8 percent in unsteadiness for position 5 over position 2. On the suction side, the standard deviation from the time-average was 0.00590 for position 2 and 0.00745 for position 5 showing an increase of 26 percent in unsteadiness for position 5 over position 2.

Conclusions

Two-dimensional, time-accurate, Navier–Stokes simulations of the vane indexing experiment have been performed. The primary objective of the investigation was to provide insights into the mechanisms of the turbine performance improvement observed in the experiment. The analysis has provided a vast amount of information that is essential to achieving the objective. Although the results have not been fully interrogated at this time, several candidate mechanisms have been identified.

The numerical analysis correctly predicts the indexing positions of the first and second stage vanes required to produce maximum efficiency. The sinusoidal pattern of turbine midspan efficiency versus clocking position that was seen in the data was also predicted. However, the magnitude of the predicted $\Delta\eta_{t\text{-}t}$ is less than experimentally observed. The most probable reason for the difference is the two-dimensional nature of the

analysis, although limitations in numerical accuracy are possible.

The computational results indicate that improved performance of the second vane is a major contributor to the turbine efficiency benefits achievable through vane indexing. Best performance is predicted to be obtained when the time-averaged first vane wake is aligned with the second vane leading edge. Reduced surface velocities and less large-scale unsteadiness on the second vane are seen as possible reasons for the improved second vane performance.

The results from this numerical investigation show that the turbine airfoil indexing phenomenon is predictable and illustrates how to achieve this phenomenon in the hardware. Questions remain as to the exact mechanisms involved. Further interrogation of the existing results may identify additional candidate mechanisms and provide guidance for further analysis. Three-dimensional analysis will also be necessary for the best and worst clocking positions to investigate possible effects of the vane clocking on endwall losses.

Acknowledgments

The authors wish to acknowledge the important contributions made to this work by our colleagues. Adam J. Fredmonski and Dean Johnson of Pratt and Whitney performed supporting analyses for this work. Karen Gundy-Burlet of NASA/Ames Research Center resolved issues pertaining to STAGE2. We are very appreciative of their support. We are also thankful for the graphics work performed by Catherine Dumas formerly Sverdrup Technology and Denise Doran of NASA/MSFC and for the support for the NASA/MSFC personnel provided by the Office of Advanced Concepts and Technology.

References

Denton, J. D., 1993, "Loss Mechanisms in Turbomachines," ASME JOURNAL OF TURBOMACHINERY, Vol. 115, pp. 621–658.

Gaddis, S. W., Hudson, S. T., and Johnson, P. D., 1992, "Cold Flow Testing of the Space Shuttle Main Engine Alternate Turbopump Development High Pressure Fuel Turbine Model," ASME Paper No. 92-GT-280.

Griffin, L. W., and Rowey, R. J., 1993, "Analytical Investigation of the Unsteady Aerodynamic Environments in Space Shuttle Main Engine (SSME) Turbines," ASME Paper No. 93-GT-362.

Gundy-Burlet, K. L., Rai, M. M., and Dring, R. P., 1989, "Two-Dimensional Computations of Multi-stage Compressor Flows Using a Zonal Approach," AIAA Paper No. 89-2452.

Gundy-Burlet, K. L., Rai, M. M., Stauter, R. C., and Dring, R. P., 1991, "Temporally and Spatially Resolved Flow in a Two-Stage Axial Compressor: Part II—Computational Assessment," ASME JOURNAL OF TURBOMACHINERY, Vol. 113, pp. 227–232.

Huber, F. W., Johnson, P. D., Sharma, O. P., Staubach, J. B., and Gaddis, S. W., 1996, "Performance Improvement Through Indexing of Turbine Airfoils: Part 1—Experimental Investigation," ASME JOURNAL OF TURBOMACHINERY, Vol. 118, this issue, pp. 630–635.

Hudson, S. T., Gaddis, S. W., and Johnson, P. D., 1991, "Cold Flow Testing of the Space Shuttle Main Engine High Pressure Fuel Turbopump Turbine Model," AIAA Paper No. 91-2503.

Rai, M. M., and Chakravarthy, S. R., 1986, "An Implicit Form for the Osher Upwind Scheme," *AIAA Journal,* Vol. 24, No. 5, pp. 735–743.

Rai, M. M., 1987, "Unsteady Three-Dimensional Navier–Stokes Simulations of Turbine Rotor–Stator Interaction," AIAA Paper No. 87-2058.

Rai, M. M., and Madavan, N. K., 1988, "Multi-airfoil Navier–Stokes Simulations of Turbine Rotor–Stator Interaction," AIAA Paper No. 88-0361.

Rangwalla, A. A., Madavan, N. K., and Johnson, P. D., 1992, "Application of an Unsteady Navier–Stokes Solver to Transonic Turbine Design," *Journal of Propulsion and Power,* Vol. 8, No. 5, pp. 1079–1086.

Rangwalla, A. A., and Rai, M. M., 1993, "A Numerical Analysis of Tonal Acoustics in Rotor–Stator Interaction," *Journal of Fluids and Structures,* Vol. 7, pp. 611–637.

Multistage Turbine Simulations With Vortex–Blade Interaction

M. G. Turner
GE Aircraft Engines,
Cincinnati, OH 45215

The average passage approach of Adamczyk et al. (1990) has been used to simulate the multistage environment of the General Electric E^3 low-pressure turbine. Four configurations have been analyzed and compared to test data. These include the nozzle only, the first stage, the first stage and a half, and the first two stages. A high casing slope on the first-stage nozzle causes the secondary flow vortex to separate off the casing and enter the downstream rotor. The detrimental effect on performance due to this vortex interaction has been predicted by the above approach, whereas isolated blade row calculations cannot simulate this interaction. The unsteady analysis developed by Chen et al. (1994) has also been run to understand the unsteady flow field in the first-stage rotor and compare with the average passage model and test data. Comparisons of both the steady and unsteady analyses with data are generally good, although in the region near the casing of the shrouded rotors, the predicted loss is lower than that shown by the data.

Introduction

The use of steady three-dimensional Navier–Stokes solvers has now become routine in the design and analysis of turbomachinery blade rows. Most runs are made assuming the blade is in isolation with prescribed conditions at inlet and exit, as described by Turner and Jennions (1993) and Jennions and Turner (1993). However, most blade rows are not operating in isolation, but are very closely coupled while operating in a multiblade row machine. One approach described by Dawes (1990) uses mixing planes to communicate across blade rows. However, Fritsch and Giles (1993) have demonstrated that a large entropy rise is produced at the interface planes. Also the strength of vorticity is weakened at these interface planes due to the averaging process. Another approach is to run a full unsteady Navier–Stokes multistage calculation using the approach of Rai (1987). This turns out to be impractical in a design process due to the amount of computer time required. The unsteady inviscid solution could be obtained, which has been done by Saxer and Giles (1994), but the absence of viscosity eliminates many of the flow features now addressed by the isolated blade row solvers.

The model equations presented by Adamczyk (1985) have the capability of simulating the blade row interaction effects, and the method presented by Adamczyk et al. (1990) has been extended to be a practical tool for solving the flowfield in a multistage turbomachine. To capture the unsteady interaction, the unsteady solver described by Chen et al. (1994) has been used. It has the capability to be run as a stage solver or as a wake-blade row solver. For efficient solution times, the wake-blade row approach has been used. The average passage solution describes the upstream influences, and is also used to set up the initial solution and periodic boundary conditions. This reduces the number of cycles needed to reach a periodic solution.

This paper will briefly explain both the average passage approach and the unsteady solver. The E^3 low-pressure turbine test program is described, and a discussion of numerical results for this turbine is then presented.

Numerical Approach

To account for blade row interaction, either the Adamczyk (1985) approach can be used or the unsteady flow field can be solved. The Adamczyk approach requires some modeling to get the extra terms, which account for the effect of unsteady and stage-to-stage interactions. Codes that use both approaches are described below.

Average Passage Model. The model equations for the average passage approach were presented by Adamczyk (1985). Due to the circumferential averaging across the passage, extra terms arise due to the nonlinearities in the equations. These are similar to Reynolds stress terms, which result when the Navier–Stokes equations are ensemble averaged. These terms have been modeled and are discussed by Adamczyk et al. (1990). The basic solver is a cell-centered time-marching Runge–Kutta scheme as presented by Jameson et al. (1981). Local time-stepping and implicit residual smoothing are used to accelerate convergence. Both second and fourth-order dissipation are applied to eliminate unstable odd–even modes and to capture shocks. A Baldwin-Lomax (1978) turbulence model is used with wall functions. To allow consistent axisymmetric solutions, and to facilitate the averaging, strict H-grids are required when running the code with more than one blade row.

By using overlapping grids, exchanging body forces from neighboring blade rows, and modeling these extra terms, the interaction effects of a multistage turbomachine can be simulated. The procedure involves running the three-dimensional solver with the body forces from the other blade rows. This is done for each blade row. When all the blade rows have been solved, the new body forces are distributed to each blade row. This is called a flip. By construction, there exists one unique axisymmetric solution. Enough flips are run so that each blade row's axisymmetric solution will converge to this unique solution.

Reduced Model. One drawback to the full model is that a three-dimensional solution of the entire machine domain is required for each blade row. This means the overall size of the problem for solving an n blade row machine is n^2 larger than a single blade row case. To reduce this burden, it was recognized that the interaction effects decay away from the source. Therefore it is realistic to use a reduced three-dimensional solution. For the results presented, this reduced domain extends upstream and downstream one blade row. A meridional view of the three-dimensional domains of the reduced model used for a two-stage machine is shown in Fig. 1. Upstream and downstream of the three-dimensional region is a two-dimensional axisymmetric region, which solves the axisymmetric equations using the body forces that the full model would have used. It is the development

Contributed by the International Gas Turbine Institute and presented at the 40th International Gas Turbine and Aeroengine Congress and Exhibition, Houston, Texas, June 5–8, 1995. Manuscript received by the International Gas Turbine Institute March 10, 1995. Paper No. 95-GT-288. Associate Technical Editor: C. J. Russo.

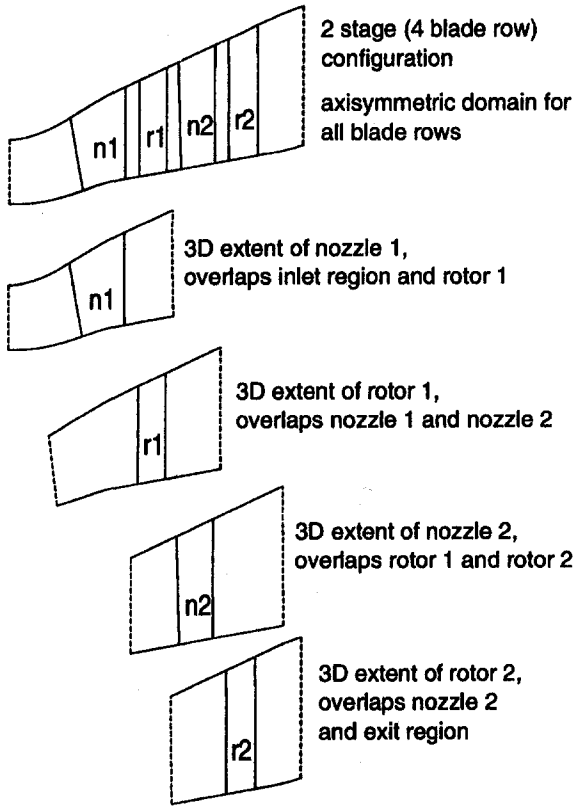

Fig. 1 Meridional view of the three-dimensional domains used in the *reduced average passage approach*

of the reduced model that makes the average passage approach practical for analyzing a multistage machine.

The code for the reduced model was obtained from Adamczyk at NASA Lewis Research Center. It had a novel variable C_p and γ capability, which is explained in Appendix A. The author added a trailing edge treatment, explained in Appendix B. Other modifications were made to improve the ease of use such as dynamic memory allocation and free format input. This code was then used to obtain the results presented later.

Reduced Model Computational Procedure. The starting procedure for running a multistage machine with the average passage code has been greatly simplified by utilizing an existing axisymmetric solution obtained from a code described by Adkins and Smith (1982). This allows the axisymmetric average and the dominant body force terms to be assigned very reasonable initial values. The initial three-dimensional solution is set to the axisymmetric solution. Once these initial files are set up, the average passage code starts up like any other flip in the iterative process. This process is shown schematically in Fig. 2.

Unsteady Solver. The unsteady solver was described by Chen et al. (1994). It is an implicit finite volume scheme capable of using very large CFL numbers. The number of time steps required is therefore dependent on the frequency resolution needed, not due to stability requirements. The solver is therefore very fast. Improvements in solution time are also obtained by starting with good initial conditions. These are derived from the average passage solution and include the initial solution, the initial time-dependent periodic boundary conditions, and the time-dependent inlet boundary condition. Because the average passage solution has the effects from the adjacent blade rows, the initial solution one obtains is only a perturbation from the actual unsteady solution at that time interval.

The code can be run as a stage solver or as a wake-blade row solver. The results presented later are from the wake-blade row calculation. The transmission of unsteady flow information from the downstream blade row to the upstream blades was assumed negligible. Also, using the wake-blade row solver allows the exact blade count to be modeled with only one passage. The current stage solver requires an integral number of blade passages for each blade row. For the first stage presented in this paper, there are 110 rotor blades and 56 nozzles. To model this exactly would require 55 rotor blade passages and 28 nozzle passages. Even though the count is very close to two rotor blades for each nozzle, the implied geometry change would effect unsteady wave propagations. Running as a wake-blade row calculation eliminates this assumption.

E^3 Low-Pressure Turbine Scaled Test

A scaled low-pressure turbine test was conducted as part of the NASA E^3 program. This program consisted of two sets of blading (blocks).

The Block I series had four configurations as listed below, each of which is analyzed in this paper:

1 Stage 1 nozzle only (1 blade row)
2 Stage 1 (2 blade rows)
3 Stage 1 with stage 2 nozzle (3 blade rows)
4 Stage 1 and 2 (4 blade rows, see Fig. 3)

The design, test, and data analyses are described by Bridgman et al. (1983). Figure 3 shows the rig assembly for the Block I two-stage group. The other configurations are similar with different transition ducts downstream of the last blade row.

Plane 42 is the duct inlet plane at which radial and circumferential surveys of total pressure (P_T), total temperature (T_T), and angle were made during configuration 1 testing (Nozzle 1 only). These data demonstrated that inlet T_T and angle were uniform. Slight radial variations in P_T were measured, and are

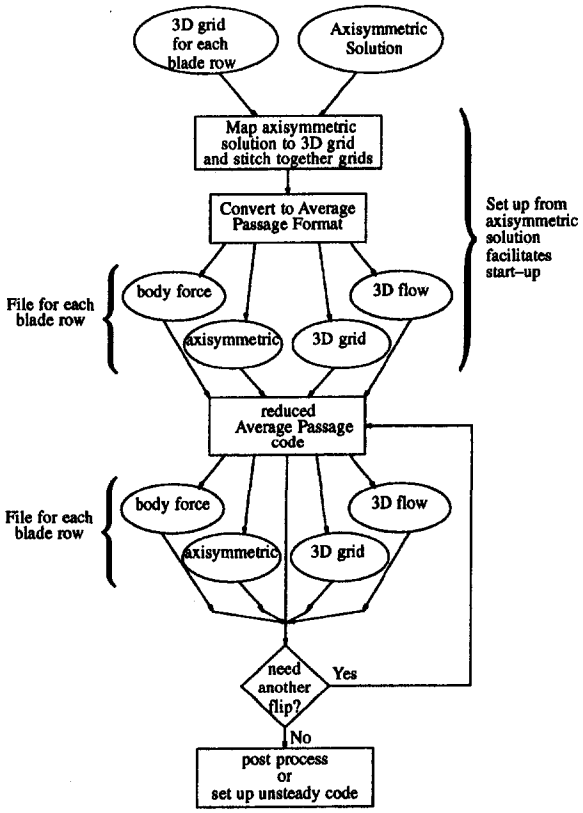

Fig. 2 Schematic of average passage set up and solution

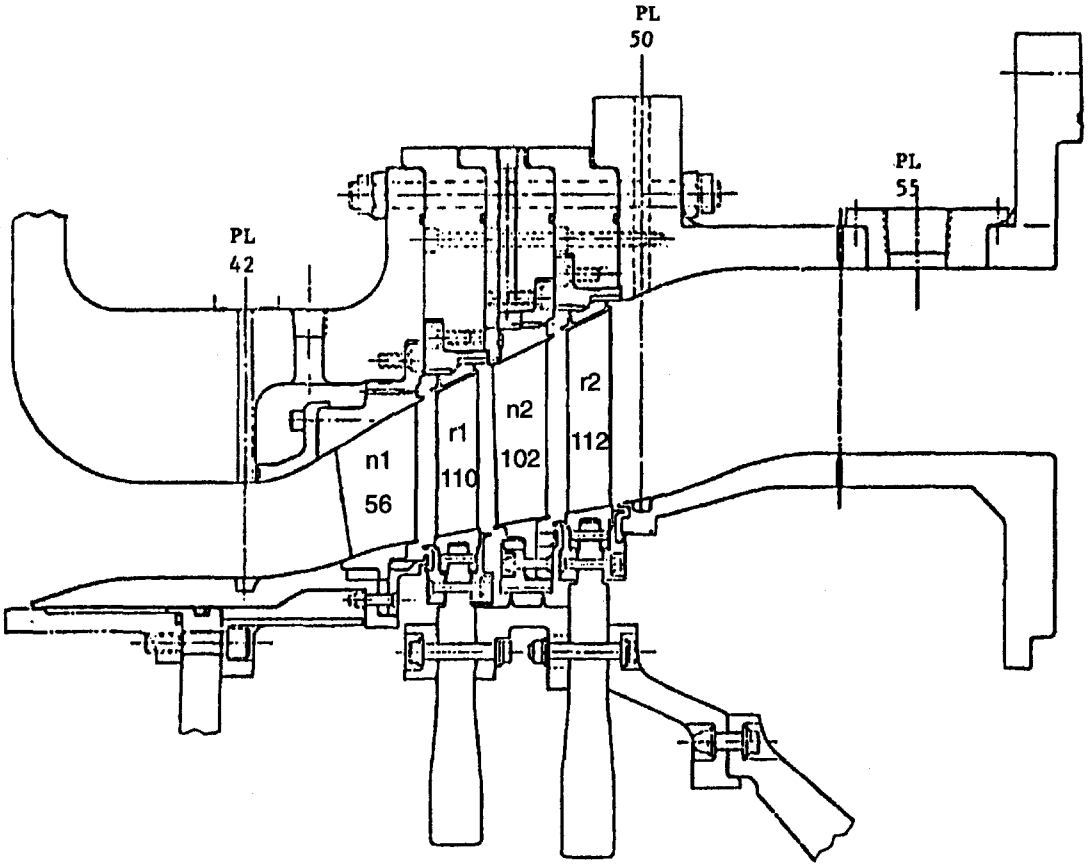

Fig. 3 Configuration four rig assembly

shown in Fig. 4. These profiles of P_T, T_T, and angle served as the inlet boundary conditions for all numerical simulations presented. The level of P_T and T_T are defined by the average values from instrumentation mounted on the leading edge of a strut frame upstream of plane 42.

At plane 50, detailed radial and circumferential traverse surveys were conducted using a combination (Cobra) probe, which measures P_T, T_T, and angle. The precise calibration of the thermocouples on this probe was not critical to the testing procedure. The absolute level of the temperature is adjusted to match the measured torque when quoting efficiency. The temperatures (and calculated efficiencies) presented for comparison purposes are the circumferential averages with the torque corrections. When traversing behind a rotor (configurations 2 and 4 only), the experimental total pressure presented is based on the traverse profile shape adjusted to the level measured at downstream rakes (plane 55). At plane 50, five static taps are equally spaced circumferentially at both the hub and casing. The average of these five pressures define the hub and casing static pressures. It is primarily plane 50 traverses that will be compared to in the following section. Measured temperature profiles were only reduced behind the rotors, so comparisons of temperature and efficiency are not made for configurations 1 and 3.

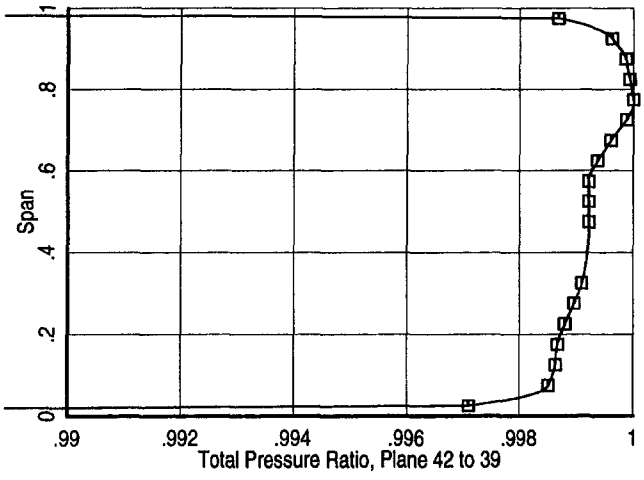

Fig. 4 Measured plane 42 total pressure profile (relative to plane 39) used as the inlet boundary condition for nozzle 1 and stage calculations

The data reduction program performs a circumferential averaging of the traverse data. This averaging uses a mixing analysis similar to that of Stewart (1955). Therefore the temperature should represent a mass-averaged temperature, and the total pressure and angle should represent a mixed out value. Several assumptions are made. One is that the static pressure variation is linear from the hub to the casing, and another is that the mixing occurs only in the circumferential direction and at a constant pressure. It is also assumed that the radial velocity is zero.

Accuracies of the measurements are: 1 rpm on speed, 0.1 percent on torque, 0.15 percent on flow, 1°F (0.13 percent) on temperature, and 0.1 percent on the absolute level of pressure.

At plane 55 are additional hub and casing static pressure taps, and P_T and T_T arc rakes were placed behind the rotors (configurations 2 and 4) only.

The geometry analyzed was based on the aero design intent computer files, which were originally created in 1978. After observing the poor agreement in exit angle for configuration 1 (after all the analyses had been done), it was recalled (and verified in design record books) that nozzle 1 had been rotated

Table 1 Solution time and memory[1] (all grids have 41 spanwise and 33 blade-to-blade points)

config	blade	ni[2]	3D grid	mem.	flips or cycles	iterations	cpu/iter	total cpu/blade	tot. cpu (hours)
1	n1	145	196,185	9.2	-	3600	3.12	11,220	3.12
1 tet[3]	n1	145	196,185	9.2	-	1200[4]	3.12	3740	1.04
2 stage	n1	273	369,369	17.2	59 flips	4720	5.61	26,432	
	r1	273	369,369	17.2	59 flips	4720	5.55	26,196	14.62
2 rotor	r1	153	207,009	9.8	-	1600	3.30	5272	1.59
2 uns[5]	r1	153	207,009	62.9	10 cyc.	640	20.58	13,171	3.66
3	n1	237	320,661	15.7	55 flips	4520	4.73	21,360	
	r1	349	472,197	22.0	55 flips	4520	6.74	30,470	
	n2	253	342,309	16.6	55 flips	4520	4.98	22,490	20.64
4	n1	237	320,661	16.2	60 flips	4920	4.76	23,520	
	r1	335	453,255	21.8	60 flips	4920	7.64	37,570	
	n2	356	481,668	23.0	60 flips	4920	6.87	33,800	
	r2	249	336,897	16.9	60 flips	4920	4.98	24,480	33.16

[1] Computer time is CRAY C90 seconds (hours where noted), and memory is in 10^6 words.
[2] number of axial grid points in 3D domain, [3] trailing edge treatment
[4] restart from case with no tet, [5] unsteady calculation

open one degree. This was done in the manufacturing definition of the nozzle, but was not in the aero design definition. This had the strongest impact when comparing to configuration 1, especially in the angle and mass flow. The effects of this geometry discrepancy decreased when more blade rows were analyzed.

Results

Grids have been set up for each configuration. All calculations have 41 grid points spanwise, and in the three-dimensional domain, there are 33 blade-to-blade points. The number of axial grid points in the three-dimensional domain for each case is shown in Table 1 under the column ni. Table 1 also lists the computer time and memory required for each run. For a single blade row calculation, the whole domain is three dimensional. For configuration 2, this two blade row case is run with the entire three-dimensional mesh overlapping. For the other two configurations, the reduced approach is used, which has an axisymmetric region upstream and downstream of the three-dimensional domain. Table 2 shows the number of axisymmetric grid points upstream and downstream of the three-dimensional region in addition to the number of axial points in the three-dimensional grid. Table 3 lists the mass flow for each case run and compares with the experimental values.

The actual rounded trailing edges are not resolved. Many grid points would be needed to resolve such a small trailing edge. Either solid wedges or a trailing edge treatment (see Appendix B) were used. For configuration 1, both trailing edge options were used. For consistency of geometry for all runs of configuration 2, the trailing edges were modeled as solid wedges due to the inability to use the trailing edge treatment as an option for the unsteady code. For configurations 3 and 4, only the trailing edge treatment was used.

Configurations 1 and 2 had constant properties, whereas configurations 3 and 4 used the variable C_p and γ option. Configuration 1 (the nozzle only) has essentially constant total temperature, so constant properties are a valid assumption. Configuration 2 was run with constant properties since the unsteady solver did not have the option to run with variable C_p and γ.

The inlet plane for each configuration was at plane 42 of the experimental rig. The exit plane was well downstream of the measurement plane (between 77 and 97 percent of the last blade row's hub axial width) to ensure that predictions at this plane were not affected by imposed downstream boundary conditions. The static pressure downstream was set to a linear profile with the level adjusted iteratively until the predicted values at the plane 50 axial location matched the measured value within the desired tolerance. The pressures matched to within 0.35 percent of the upstream total pressure or 0.15 psi, which is much less than the circumferential variation of the measured pressures. On average, three iterations were required to set the back pressure. The unsteady calculation used the stage result to set the downstream boundary conditions.

For the average passage runs, all surfaces were treated as fully turbulent except the suction surface of nozzle 1. Here, transition was set at 60 percent axial chord, which was based on a boundary layer calculation of the midspan section. The grid resolution did not allow the laminar boundary layer upstream of transition to be well defined (the $y^+ \approx 50$ on the blade surfaces in the turbulent region). Cases were run to determine the sensitivity of predicted loss to the prescribed transition location. Although the differences were small (about 10 percent of the total measured loss when going from specified transition at 60 percent to fully turbulent), the trends were physical.

Configuration 1. The nozzle was run using the average passage code as an isolated blade row. Although not required, a pure H-grid was used due to the requirements of the upcoming calculations. It was run both with and without the trailing edge treatment. The case without trailing edge treatment was run first. As described previously, the back pressure was iterated on to obtain the measured values. The case with trailing edge

Table 2 Axial grid points used in reduced code, axisymmetric and three dimensional

config	blade row	2D upstream	3D	2D downstream	total[1]
3	n1	-	237	137	373
	r1	5	349	11	373
	n2	121	253	-	373
4	n1	-	237	248	485
	r1	15	335	137	485
	n2	121	356	10	485
	r2	237	249	-	485

[1] Adjoining edges are counted twice so total is not exactly 2D + 3D.

Table 3 Mass flow rate

Configuration	Experimental lbm/sec	Calculation lbm/sec	difference %	adjusted difference[1] %
1	61.36	58.481	-4.7	-1.6
1 with tet[2]	61.36	59.919	-2.3	+0.8
2 (stage)	63.05	62.008	-1.6	
2 (rotor only)	63.05	62.834	-0.3	
2 (unsteady)	63.05	62.045	-1.6	
3	62.90	63.772	+1.4	
4	61.95	63.058	+1.8	

[1] difference adjusted by 3.1% which is difference in flow rate between 61° and 60°
[2] trailing edge treatment

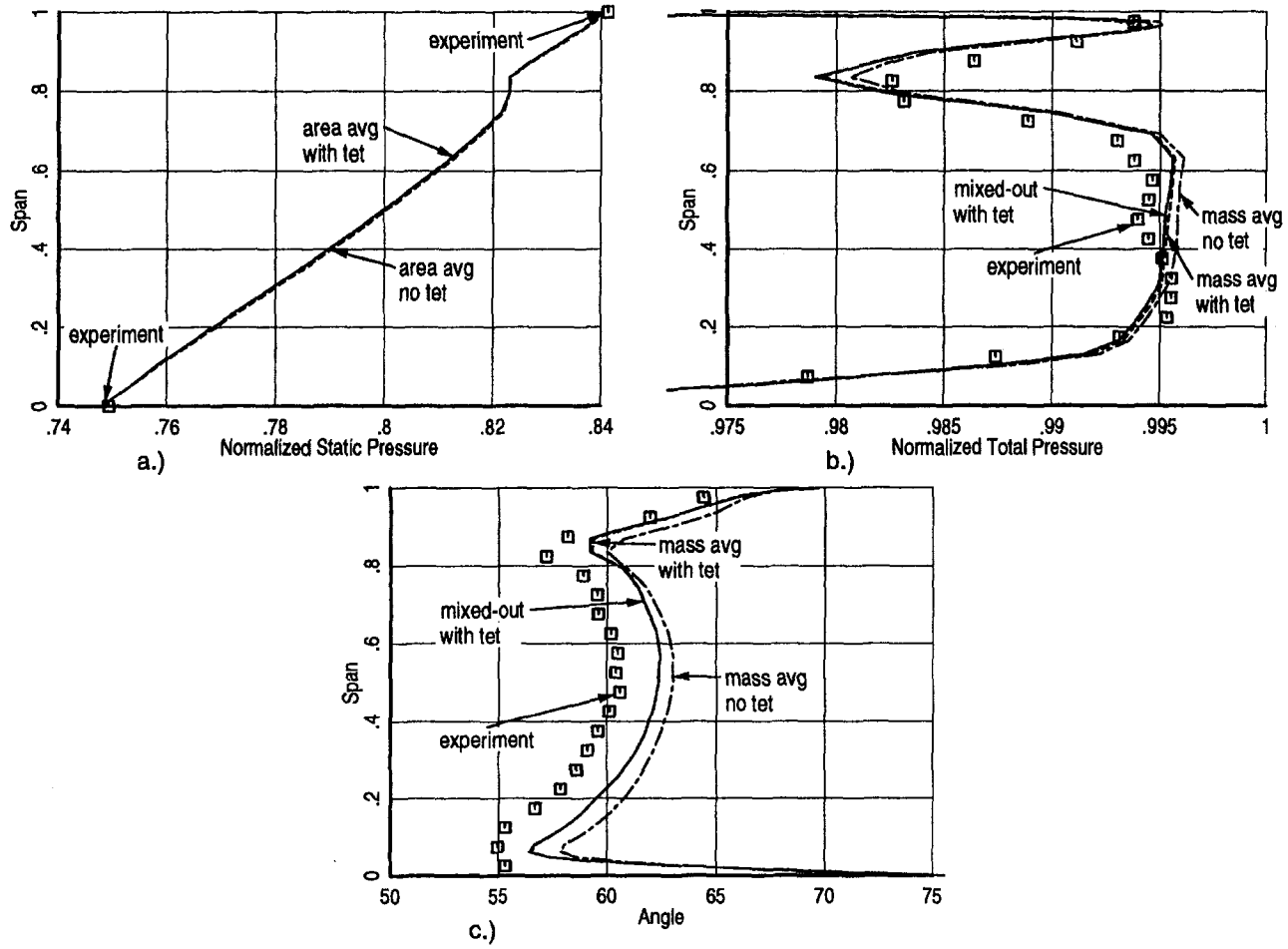

Fig. 5 Comparison of profiles at the measurement plane for configuration 1 (tet is trailing edge treatment). The measured midspan efficiency based on kinetic energy is 97.5 percent.

treatment was then restarted from this converged solution. No further iteration of back pressure was required.

Figure 5 shows the profiles of static pressure (a), total pressure (b), and angle (c) at the measurement plane. Figure 5(a) shows the good agreement with the measured static pressures for both cases. The profile is not linear due to a strong tip vortex which has a low static pressure. The vortex can also be seen in Fig. 5(b), which shows a total pressure hole at the same 80–

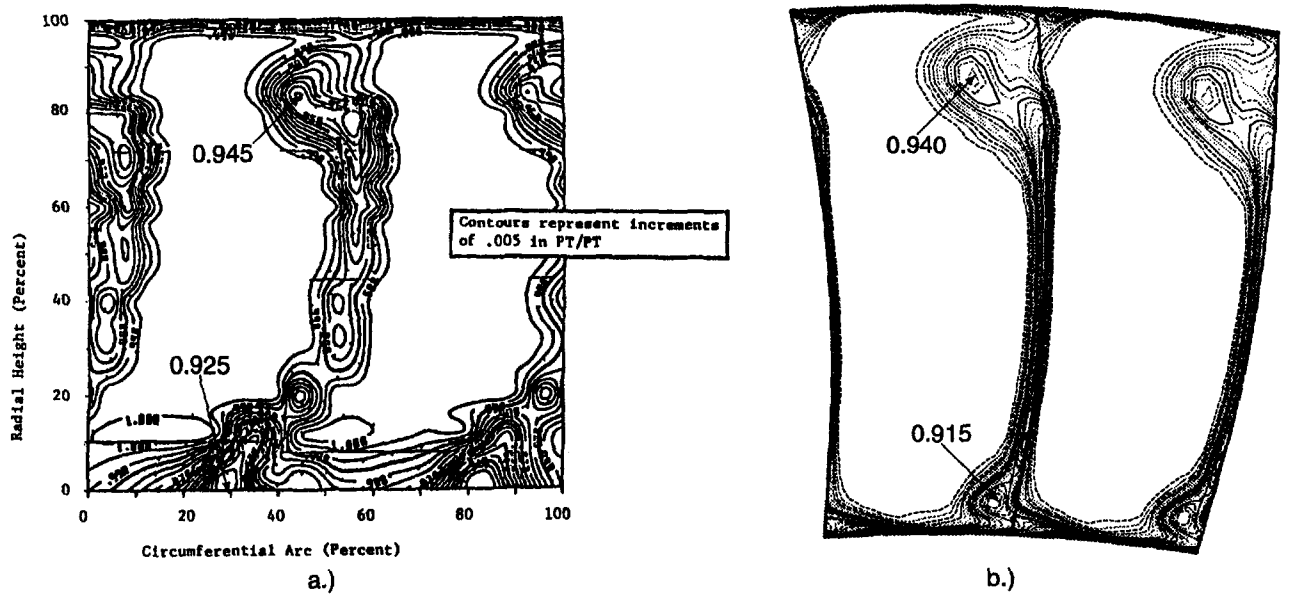

Fig. 6 Comparison of total pressure contours at the measurement plane for configuration 1. Contour intervals are the same for each plot: (*a*) experimental from Bridgeman (1983), (*b*) calculation, with trailing edge treatment.

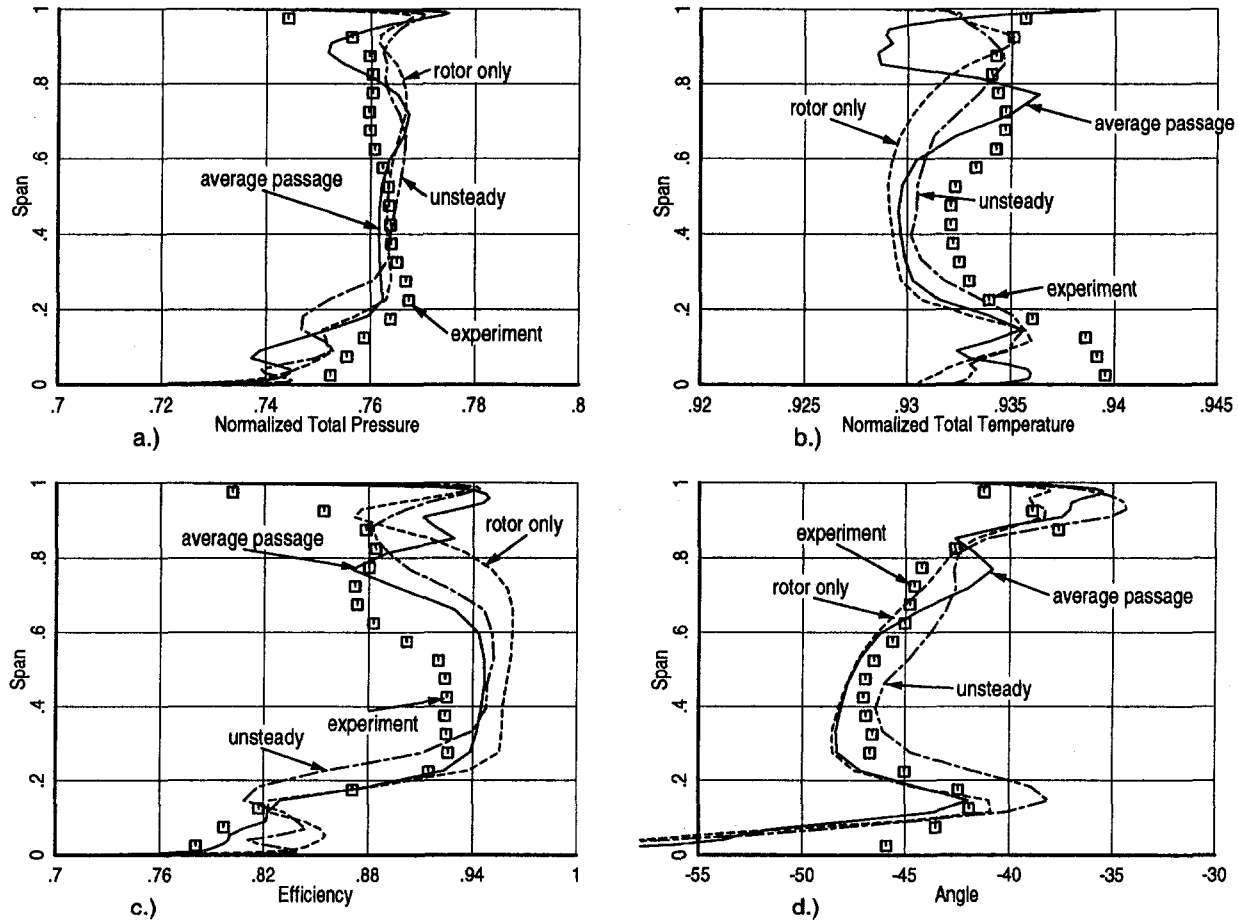

Fig. 7 Comparison of profiles at the measurement plane for configuration 2

90 percent span location. On this plot are three curves compared with measurement points. Two curves are the mass-averaged quantities with and without trailing edge treatment, and the remaining curve is the mixed-out value of total pressure using the trailing edge treatment option. The same data reduction program was used to generate the mixed-out values for the analysis as was used for the test data. As expected, the mixed-out values are less than the mass-averaged values, but the difference is very small. One assumption used in the mixing analysis is that the static pressure profile is linear from hub to casing. From these solutions, it can be seen that this assumption, although not far off, is not strictly valid.

The comparison with data is very good. Away from the endwalls, the absolute level of loss is very small (at midspan, the measured efficiency based on kinetic energy is 97.5 percent) and the scales in the plot are quite expanded so the code has to be quite accurate to pick this up. One reason for this is the low level of numerical dissipation used (the dissipation exponentially goes to zero near solid surfaces).

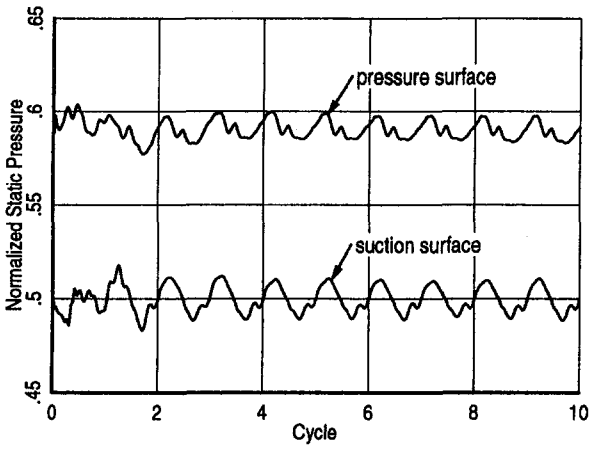

Fig. 8 Time history of static pressure on blade surfaces, midspan, five grid lines downstream of the leading edge

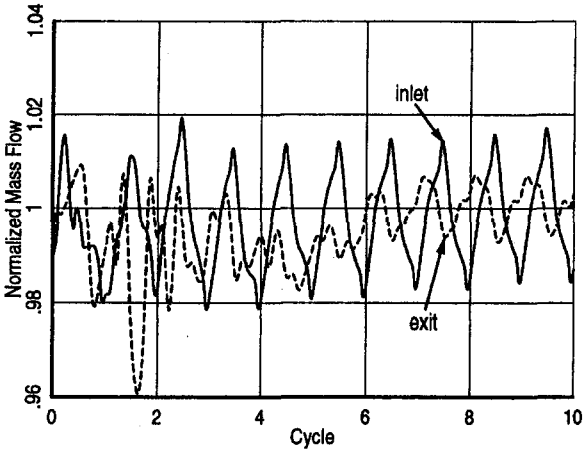

Fig. 9 Time history of inlet and exit mass flow (normalized by the time-averaged inlet mass flow over the last cycle)

Figure 5(*c*) shows the comparison of exit angle. There is very little difference between the mixed-out and mass-averaged angles. The profile shapes are all very similar, with the over and underturning due to the secondary flows being well predicted. At the pitchline, with the trailing edge treatment, the prediction is 1.8 deg. more closed than the experimental results, and without the trailing edge treatment is 2.5 deg more closed. As explained in the previous section, the actual geometry tested had been opened one degree compared to what was analyzed. When this is taken into account, the agreement with the test data is good (less than one degree) when using the trailing edge treatment. The effect of the trailing edge treatment is to produce better exit angle agreement and to add more loss due to the base pressure being applied to a thicker trailing edge.

The mass flow comparisons are listed in Table 3. At an exit angle of 61 deg, one degree of rotation open is a 3.1 percent increase in the throat area. If the angle difference is accounted for, the comparison between the experimental result and the prediction with the trailing edge treatment is good.

Figure 6 is a comparison of total pressure contours at the measurement plane. The comparison between the analysis and measurement is very good. Although a hub vortex is calculated with similar total pressures at the core, the measured contours are more spread out than the calculation. The tip vortex compares very well. It is a dominant feature that has actually separated off the casing. The inlet duct for the nozzle has a high slope, which causes high diffusion and thickens the incoming boundary layer. The vorticity in this boundary layer turns with the nozzle to produce streamwise vorticity and therefore secondary flow. The weaker fluid in this vortex is strongly influenced by the static pressure field induced by the turned flow and high wall slope to cause it to separate off the casing. In the process, good high-momentum fluid ends up toward the casing. This vortex takes up a substantial region of the blade height and can significantly interact with the downstream rotor.

Configuration 2. Configuration 2 was analyzed as a stage with the average passage code, as an isolated rotor and as a wake–rotor interaction calculation using the unsteady code. The isolated rotor case used the results from the stage calculation to define the boundary conditions. At the inlet to the rotor, the mass-averaged total pressure and flow angles obtained from the stage solution were enforced. The upstream uniform total temperature was also enforced. The stage calculations were also used to define the initial solution, the initial time-dependent periodic boundary conditions and the time-dependent inlet boundary condition for the unsteady calculation.

A comparison of the profiles is shown in Fig. 7: the total pressure in (*a*), the total temperature in (*b*), the efficiency in (*c*), and the angle in (*d*). It is hard to define what a steady stationary probe actually "senses" behind a rotor blade, but ideally it would be the time-averaged value. In the relative frame, this is the area average, so for these plots, the area averages are used for the stage and rotor-only calculations. For the unsteady calculation, the area average of the time average is plotted.

A key feature in the experimental results is the efficiency hole (Fig. 7(*c*)) between 60 and 80 percent span, which is a result of the rise in total temperature. This hole, which is felt to be an interaction loss due to the nozzle tip vortex, is predicted by using the average passage model and the unsteady solver, but not in the rotor-only calculation. Although predicted, its spanwise location is too high. Also for all the calculations, the efficiency is too high at the casing, which is a result of both a lower measured total pressure and higher measured total temperature. One physical explanation for this high loss is that the tip of the rotor is shrouded and there is some leakage across the seal, which strongly interacts with the free stream. This leakage is not modeled in the calculations. Besides higher loss, the leakage may be what drives the loss hole to a lower span.

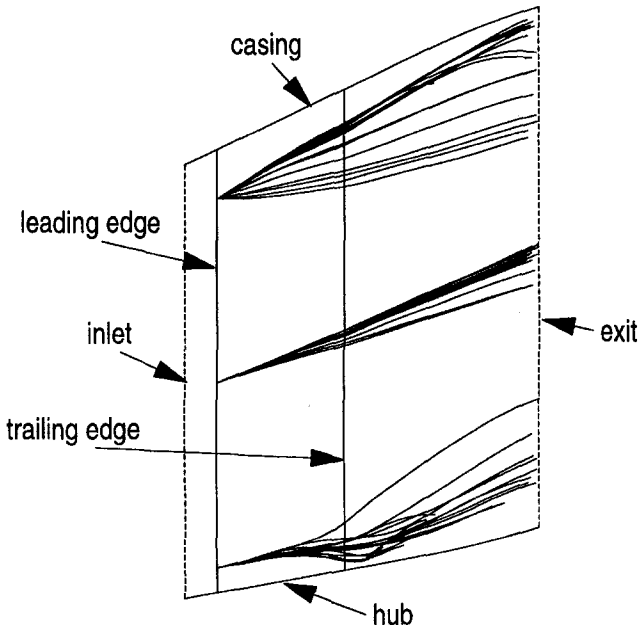

Fig. 10 Meridional view of unsteady particle traces through rotor 1. Particles are spawned at the center of the passage (midpitch), the leading edge plane, and at the three spanwise locations shown.

The levels of total temperature are low because the measurements have been adjusted to the level based on the torque measurements, which has windage and bearing losses. This is also why the efficiency is high compared to the data.

The average passage results of total pressure and temperature have very large oscillations. The total pressure actually swings opposite the direction of the data. One explanation for this is that the average passage model uses turbulent viscosity to model the unsteady mixing process. Because the viscosity coefficient is small, the upstream disturbance (the vortex) has too strong an influence downstream. Therefore the total pressure and total temperature are not correct. But, because little diffusion has been added, the efficiency is very reasonable. The actual unsteady process is not a diffusion process at all; therefore this viscosity coefficient should not be increased. The unsteady results show a more realistic smoothed-out profile of P_T and T_T, and also show the effect of the vortex interaction. Even though some of the interaction effects have been accentuated, the average passage code does pick them up, while the rotor-only calculation did not. It is hoped that the modeling of the unsteady effects can be improved, and through unsteady analysis more insight can be obtained on how to do this.

The unsteady code was run for 10 cycles. The time history of the static pressure on the blade surfaces at midspan and the inlet and exit mass flows are shown in Figs. 8 and 9, respectively. The static pressure has essentially become periodic after three cycles, whereas it took the exit mass flow seven cycles. This is still very fast, and can be attributed to the excellent starting solution obtained from the stage calculation. The solution times are also quite reasonable, even from a design standpoint, less than 3.7 hours on a CRAY C90. It did, however take almost 15 hours to obtain the stage calculation (see Table 1). This could be reduced by almost half if the back pressure were known and would not not have to be iterated on. The other major resource is computer memory, 62.9 million words.

Figure 10 is a plot of unsteady particle traces. Particles were spawned in time from three different spanwise locations at the rotor leading edge plane, each at the center of the passage (midpitch). These are not a line of particles released across the blade pitch, but are at one blade-to-blade location in the relative frame. At the midspan location, the flowfield is fairly steady.

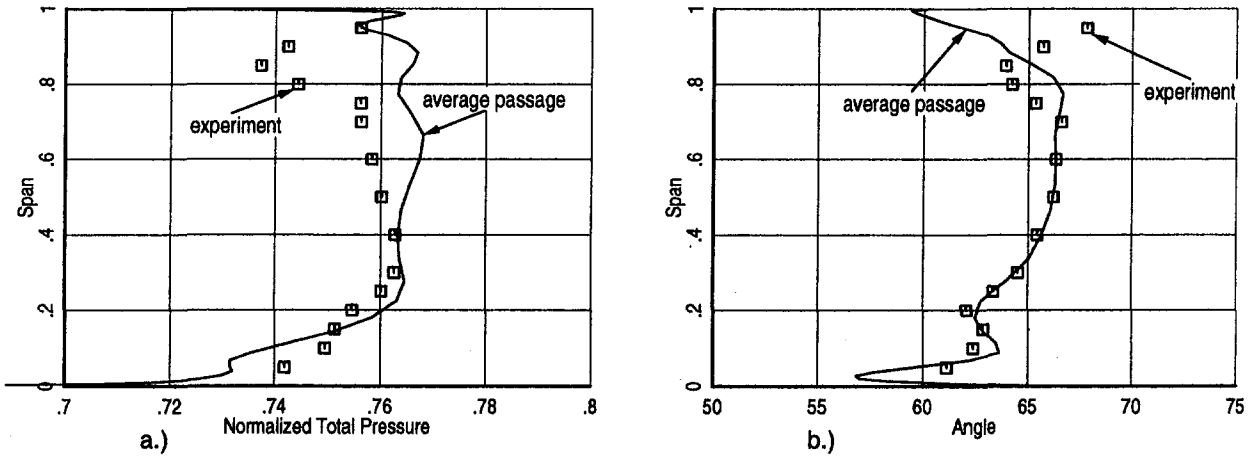

Fig. 11 Comparison of profiles at the measurement plane for configuration 3

But at the hub, it appears that the flowfield is calm for 50 percent of the chord and then the particles get dispersed spanwise. At the tip, the effect of the nozzle vortex is evident with the strong radial flows near the leading edge. This plot clearly shows the spanwise mixing effect due to the unsteady secondary flows interacting with the blade row.

The calculated flow rates are shown in Table 3. The comparison is adequate for all cases, but is hard to quantify considering the error in geometry of nozzle 1.

Configuration 3. The results for configuration 3 are shown in Fig. 11. The agreement in both total pressure and angle is very good between the hub and midspan. However, at the tip, there is a loss hole in total pressure due to the large shear layer, which was measured downstream of the rotor in configuration 2. It is also evident in the angle profiles. Because this shear layer was not predicted in the average passage code, the loss hole is not predicted.

The mass flow is listed in Table 3, and is high (it would even be higher if the real nozzle 1 geometry were used) and is due to total pressures, which are too high in the tip, and angles, which are too low.

Configuration 4. The comparison of the profiles at the measurement plane for configuration 4 are shown in Fig. 12. Although the loss in total pressure at the tip is again underpredicted, the comparison between the hub and midspan is very good. The angle level and shape are also predicted well except near the tip. The shapes of the total temperature and efficiency are also predicted well. Again, the levels are off due to a torque correction applied to the total temperature. The flow rate (see Table 3) is predicted slightly high especially if adjusted for the nozzle 1 geometry difference. Again this is probably due to the lower loss predicted at the tip. Overall, however the agreement is good considering four blade rows are being analyzed at once.

Conclusions

The conclusions from this effort are:

1 The average passage code has been used to analyze a nozzle only, a single-stage, a stage-and-a-half, and a two-stage turbine configuration. The overall comparison with test data was good although the endwall loss was underpredicted at the casing for the single stage configuration. This error in modeling propagates, so details near the casing for subsequent blade rows are also wrong.
2 Blade-row interaction effects due to upstream vorticity and circumferential variations appear to be captured with the average passage code and unsteady solver. These effects are not even modeled with an isolated blade row code or a code that uses mixing planes.
3 The loss mechanisms in a low pressure turbine rotor tip shroud need to be understood better and need to be modeled in order to predict multistage performance better.
4 The start-up of the average passage code using an initial axisymmetric solution greatly facilitates its use.
5 The spanwise mixing due to the unsteadiness of secondary flows is quite extensive.
6 The model used in the average passage code to simulate the chopping of wakes and vortices in the downstream passage needs further development so the simulations are more physical.

The first-stage nozzle tested was rotated open one degree compared to the geometry analyzed. The results presented are consistent with this difference, and re-running these computer-intensive calculations with the modified geometry would not change the conclusions presented above. This mistake was made because of the multiple geometry definitions that existed back in 1978. It is hoped that the number of these mistakes will be reduced in the future with the use of master geometry models where consistent geometry can be guaranteed.

Acknowledgments

The author would like to thank John Adamczyk and Mark Celestina of NASA Lewis Research Center and Jen-Ping Chen of Mississippi State University for their help and advice in running the codes presented in this paper. Thanks are due also to Mark Pearson and Dave Cherry for their help in making the comparisons with the E^3 data. I would like to acknowledge that it was Graham Holmes at GE Corporate Research and Development Center who first put the trailing edge treatment into a three-dimensional flow solver. I would also like to thank GE Aircraft Engines for permission to publish this paper. NAS computer time was used for some of the calculations presented, and was greatly appreciated.

References

Adamczyk, J. J., 1985, "Model Equation for Simulating Flows in Multistage Turbomachinery," ASME Paper No. 85-GT-226.

Adamczyk, J. J., Celestina, M. L., Beach, T. A., and Barnett, M., 1990, "Simulation of Three-Dimensional Viscous Flow Within a Multistage Turbine," ASME JOURNAL OF TURBOMACHINERY, Vol. 112, pp. 370–376.

Adkins, G. G., Jr., and Smith, L. H., Jr., 1982, "Spanwise Mixing in Axial-Flow Turbomachines," ASME *Journal of Engineering for Power,* Vol. 104, pp. 97–110.

Baldwin, B. S., and Lomax, H., 1978, "Thin Layer Approximation and Algebraic Model for Separated Turbulent Flows," AIAA Paper No. 78-257.

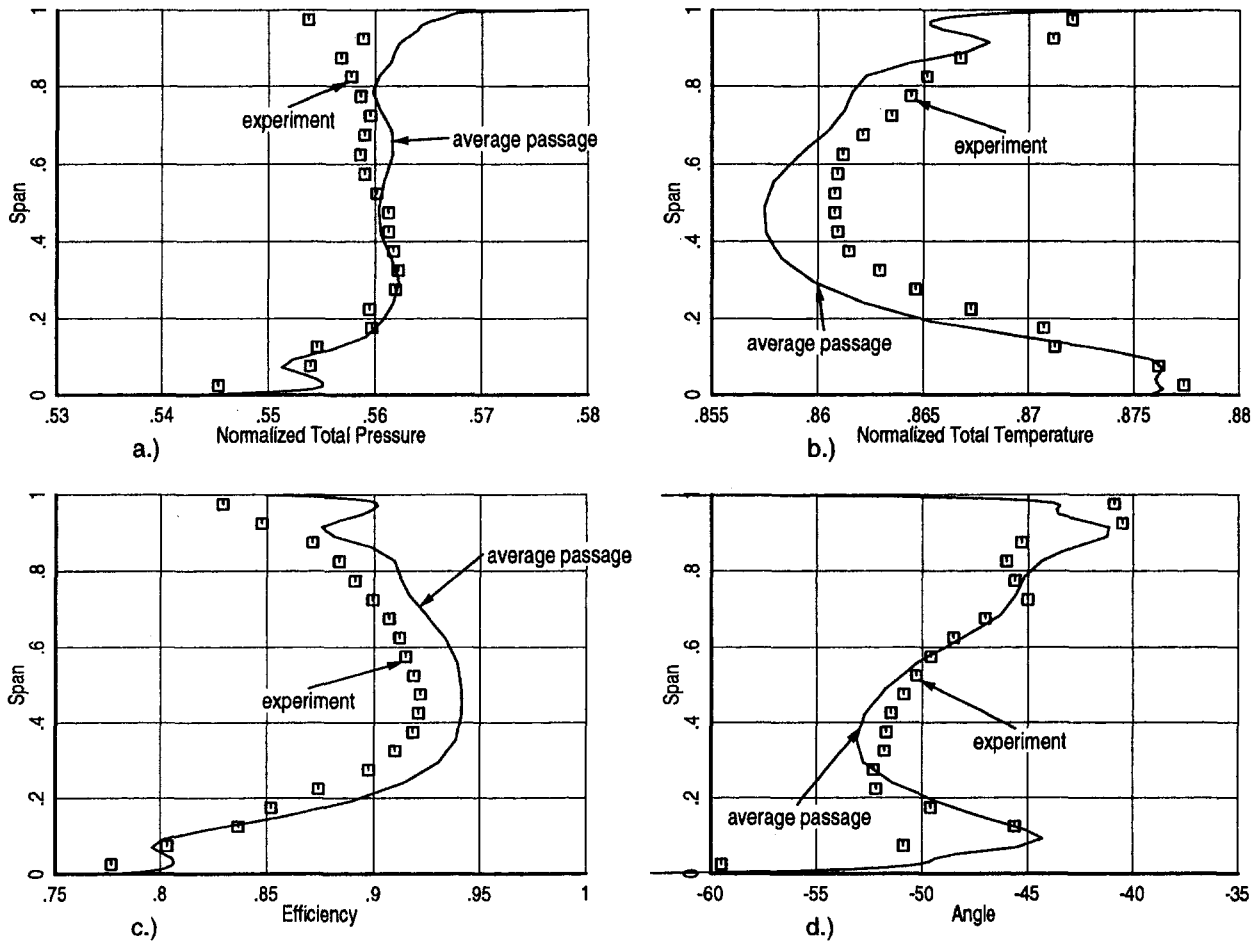

Fig. 12 Comparison of profiles at the measurement plane for configuration 4

Bridgeman, M. J., Cherry, D. G., and Pedersen, J., 1983, "NASA/GE Energy Efficient Engine Low Pressure Turbine Scaled Test Vehicle Performance Report," NASA CR-168290.

Chen, J. P., Celestina, M. L., and Adamczyk, J. J., 1994, "A New Procedure for Simulating Unsteady Flows Through Turbomachinery Blade Passages," ASME Paper No. 94-GT-151.

Dawes, W. N., 1992, "Toward Improved Throughflow Capability: The Use of Three-Dimensional Viscous Flow Solvers in a Multistage Environment," ASME JOURNAL OF TURBOMACHINERY, Vol. 114, pp. 8–17.

Fritsch, G., and Giles, M. B., 1995, "An Asymptotic Analysis of Mixing Loss," ASME JOURNAL OF TURBOMACHINERY, Vol. 117, pp. 367–374.

Jameson, A., Schmidt, W., and Turkel, E., 1981, "Numerical Solutions of the Euler Equations by Finite Volume Methods Using Runge–Kutta Time-Stepping Schemes," AIAA Paper No. 81-1259.

Jennions, I. K., and Turner, M. G., 1993, "Three-Dimensional Navier–Stokes Computations of Transonic Fan Flow Using an Explicit Flow Solver and an Implicit $k-\epsilon$ Solver," ASME JOURNAL OF TURBOMACHINERY, Vol. 115, pp. 261–272.

Rai, M. M., 1987, "Navier–Stokes Simulations of Rotor–Stator Interaction Using Patched and Overlaid Grids," AIAA *Journal of Propulsion and Power*, Vol. 3, pp. 387–396.

Saxer, A. P., and Giles, M. B., 1994, "Predictions of Three-Dimensional Steady and Unsteady Inviscid Transonic Stator/Rotor Interaction With Inlet Radial Temperature Nonuniformity," ASME JOURNAL OF TURBOMACHINERY, Vol. 116, pp. 347–357.

Stewart, W. L., 1955, "Analysis of Two-Dimensional Compressible-Flow Loss Characteristics Downstream of Turbomachine Blade Rows in Terms of Basic Boundary-Layer Characteristics," NACA TN 3515, July.

Turner, M. G., and Jennions, I. K., 1993, "An Investigation of Turbulence Modeling in Transonic Fans Including a Novel Implementation of an Implicit $k-\epsilon$ Turbulence Model," ASME JOURNAL OF TURBOMACHINERY, Vol. 115, pp. 249–260.

APPENDIX A

Variable C_p and γ

When using the average passage code to analyze a machine with more than one stage, the temperature differences can quickly make the constant C_p and γ assumption invalid. A variable C_p and γ capability has therefore been added. Several assumptions are made that do not limit the effectiveness of the method and greatly simplify the calculations and results in few changes to the original code.

The internal energy is

$$e = \int_0^T C_v dT = e_{\text{ref}} + \int_{T_{\text{ref}}}^T C_v dT \tag{1}$$

$$= C_v|_{\text{ref}} T_{\text{ref}} + \int_{T_{\text{ref}}}^T C_v dT, \tag{2}$$

and the enthalpy is

$$h = \int_0^T C_p dT = h_{\text{ref}} + \int_{T_{\text{ref}}}^T C_p dT \tag{3}$$

$$= C_p|_{\text{ref}} T_{\text{ref}} + \int_{T_{\text{ref}}}^T C_p dT, \tag{4}$$

where

$$C_v|_{\text{ref}} = e_{\text{ref}}/T_{\text{ref}},\ C_p|_{\text{ref}} = h_{\text{ref}}/T_{\text{ref}}, \tag{5}$$

e_{ref} is the internal energy at T_{ref}, and h_{ref} is the enthalpy at T_{ref}. From the mean value theorem,

$$e = C_v|_{\text{ref}} T_{\text{ref}} + \overline{C_v}(T - T_{\text{ref}}), \tag{6}$$

and

$$h = C_p|_{\text{ref}} T_{\text{ref}} + \overline{C_p}(T - T_{\text{ref}}). \tag{7}$$

Assume that $\overline{C_v}$ and $\overline{C_p}$ are the arithmetic averages between T and T_{ref}:

$$\overline{C_v} = \frac{C_v|_1 + C_v}{2} - \frac{R}{2}\left(\frac{1}{\gamma_1 - 1} + \frac{1}{\gamma - 1}\right), \quad (8)$$

$$\overline{C_p} = \frac{C_p|_1 + C_p}{2} = \frac{R}{2}\left(\frac{\gamma_1}{\gamma_1 - 1} + \frac{\gamma}{\gamma - 1}\right), \quad (9)$$

where R is the ideal gas constant, C_v, C_p, and γ are values at T, and since

$$C_p - C_v = R, \quad (10)$$

therefore

$$\overline{C_p} - \overline{C_v} = R. \quad (11)$$

$C_v|_1$, $C_p|_1$ and γ_1 are C_v, C_p and γ at T_{ref}. They are not necessarily equal to $C_v|_{\text{ref}}$, $C_p|_{\text{ref}}$, or γ_{ref}, although these values just set the absolute level of internal energy or enthalpy. The absolute level is usually not important; it is the differences that matter. A case for which the absolute level might matter is if a turbine blade row is being analyzed with cooling flow. That flow has different properties in terms of fuel–air ratio and water–air ratio, so R is different. To get the right energy addition without allowing for multiple species requires that the absolute levels be consistent. If this is not necessary, setting $\gamma_{\text{ref}} = \gamma_1$ could be done.

The function for γ could be as complicated as desired, but in the code, it has been chosen to be a linear function of temperature:

$$\gamma = \gamma_1 + \frac{(\gamma_2 - \gamma_1)}{(T_2 - T_{\text{ref}})}(T - T_{\text{ref}}), \quad (12)$$

where γ_2 is γ at T_2. By choosing T_2 and T_{ref} to be the minimum and maximum values expected, γ, C_v, and C_p are very accurately modeled.

The total internal energy is:

$$e_0 = e + q^2/2 \quad (13)$$

$$= e_{\text{ref}} + \overline{C_v}(T - T_{\text{ref}}) + q^2/2, \quad (14)$$

where q is the absolute total velocity. Solving for T

$$T = \frac{e_0 - e_{\text{ref}} + \overline{C_v}T_{\text{ref}} - q^2/2}{\overline{C_v}} \quad (15)$$

$$= \frac{e_0 - q^2/2}{\overline{C_v}} + \left(\frac{\overline{C_v} - C_v|_{\text{ref}}}{\overline{C_v}}\right) T_{\text{ref}}. \quad (16)$$

Applying the ideal gas law

$$p = \rho RT, \quad (17)$$

and defining

$$\bar{\gamma} = \frac{\overline{C_p}}{\overline{C_v}}, \quad (18)$$

an equation for pressure is obtained:

$$p = \frac{\rho e_0 - \rho q^2/2}{\overline{C_v}/R} + \rho RT_{\text{ref}}\left(\frac{\overline{C_v} - C_v|_{\text{ref}}}{\overline{C_v}}\right) \quad (19)$$

$$= (\bar{\gamma} - 1)[(\rho e_0 - \rho q^2/2) + \rho T_{\text{ref}}(\overline{C_v} - C_v|_{\text{ref}})], \quad (20)$$

so that the equation to calculate pressure uses $\bar{\gamma}$ instead of γ and has an extra term, which is a function of $(\overline{C_v} - C_v|_{\text{ref}})$.

When postprocessing, and when applying boundary conditions, it is assumed that the C_p difference is small between the total temperature and the static temperature such that

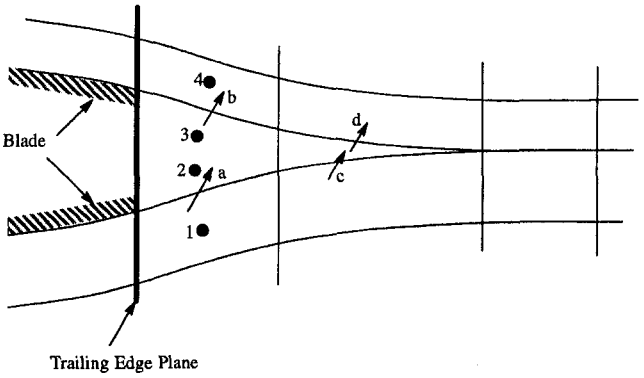

Fig. 13 Schematic of the trailing edge treatment

$$T_T = T + \frac{q^2}{2\overline{C_p}}, \quad (21)$$

where $\overline{C_p}$ is the value at T. To get the total pressure

$$s - s_{\text{ref}} = \int_{T_{\text{ref}}}^{T} C_p \frac{dT}{T} - R\int_{p_{\text{ref}}}^{p} \frac{dp}{p} \quad (22)$$

is valid for an ideal gas. It is assumed that

$$s - s_{\text{ref}} = \overline{C_p} \ln\left(\frac{T}{T_{\text{ref}}}\right) - R \ln\left(\frac{p}{p_{\text{ref}}}\right). \quad (23)$$

Therefore

$$p_T = p\left(\frac{T_T}{T}\right)^{\overline{C_p}/R} = p\left(\frac{T_T}{T}\right)^{\bar{\gamma}/(\bar{\gamma}-1)}. \quad (24)$$

To eliminate extra nonlinear terms that have to be accounted for by averaging across the passage, γ is a two-dimensional array rather than three-dimensional, and is strictly a function of the axisymmetric temperature.

APPENDIX B

Trailing Edge Treatment

The trailing edge treatment is really quite simple and tries to model the blockage due to the trailing edge vortices without actually using a fine grid and resolving the details. Having such a fine grid may also lead to unwanted unsteadiness in a time-marching solver. Worse yet is not having enough resolution to resolve the vortices (this assumes the Reynolds number is high) and the flow stays attached all around the high curvature region of the trailing edge. Any exit angle can be obtained in this case. It should also predict some part of the base pressure loss since the trailing edge is subject to a force normal to the trailing edge. This approach is also superior to fitting the trailing edge with a wedge or cusp, because these essentially act like a flap and large circulation changes can be made with subtle changes to the appended geometry. The trailing edge treatment should only be applied for thin trailing edges in subsonic flow, because the loss mechanisms for blunt trailing edges and shocks are dependent on the details of the trailing edge.

Figure 13 is a schematic of the trailing edge treatment. The blade is cut off at the location where it would otherwise be rounded. For the strict H-grids used by the average passage code, the blade must be cut off at a constant axial location. The grid lines are then cusped to a point some distance downstream. This is usually three to ten times the trailing edge thickness. This region is no longer treated as a solid boundary, but becomes a modified periodic boundary. The normal periodic boundary conditions are applied for a cell-centered code:

$$U_2 = U_4, \quad \text{and} \quad U_3 = U_1 \tag{25}$$

where U represents the dependent variables including static pressure.

If nothing were done, there would be a mass flux error. Although the flow variables are identical at each face, the projected areas are not. Therefore the mass fluxes at (a) and (b) are averaged and the average is applied (likewise for (c) and (d)). The momentum flux is the mass flux times the velocity and the energy flux is the mass flux times the total enthalpy, so these are then identical. It is the pressure force (for a rotor it is also the whirl work) that is different. Essentially normal to the trailing edge plane, the "open cusp" is unloaded. However, through conservation there is a net force that acts against the trailing edge to produce a base pressure loss. This approach is simple, but simulates the blockage, Kutta condition, and base pressure loss without a fine grid.

The Transport of Vortices Through a Turbine Cascade

A. G. van de Wall

J. R. Kadambi

Department of Mechanical and Aerospace Engineering, Case Western Reserve University, Cleveland, OH 44106

R. J. Boyle

J. J. Adamczyk

NASA Lewis Research Center, Cleveland, OH 44135

An experiment was conducted to determine how incident vortices created by upstream blade rows interacted with a downstream turbine cascade. Specifically, the kinematics of the vortex transport through turbine blade passages was investigated. A stationary water table and a flow visualization system using the pH indicator Bromothymol Blue was used to visualize the vortices generated by vortex generators placed upstream of a turbine blade cascade. Two test series were conducted. In the first test series, stationary vortex generators were positioned at various locations along the turbine blade pitch to observe how a steady incident streamwise vortex was transported through the turbine cascade. Observations showed an unsteady vortex response of the streamwise vortex when the incident vortex was located at the stagnation area of the blade. In the second test series, the vortex generators were moved to simulate the relative motion of an upstream blade row. In these tests, the unsteady vortex response was no longer seen at the stagnation region but was instead located at the suction side of the blade. In addition, the breakdown of the vortex varied greatly with the reduced frequency of the incident vorticity and showed an "explosive" type vortex breakdown that occurred at reduced frequencies greater than 8. The dissimilar behavior between the stationary and moving incident vortices indicates that losses and leading edge heat transfer could differ to some degree when determined from a stationary test as opposed to a full-stage simulation.

Introduction

The flows in turbomachines are dominated by complex, unsteady, and three-dimensional flow structures. In addition, these flows are modified as they pass through each blade row. Because of their unsteady and highly three-dimensional structure, these flows are very difficult to predict and measure. An important component of unsteadiness in turbomachines is the vortices that develop in a blade row. These vortices include passage and horseshoe vortices that develop because of the endwall boundary layers, the vortices that form from the leakage flows and scraping effects of rotors, and the trailing edge vortices caused by a variation of spanwise circulation. Figure 1 from Lakshminarayana and Horlock (1963) shows an illustration of the development of these vortices in a compressor rotor. The vortices are similar in a turbine. Even though the development and structure of these vortices are complex and influenced by many factors, their existence has been known for a long time.

Measurements of quantities such as velocity, flow angle, and total pressure can be used to understand the complex secondary flow structures described above. However, useful information regarding secondary flows can also be obtained through the use of flow visualization. While flow visualization does not give quantitative measurements, it can be used to obtain an improved understanding of the flow by obtaining a qualitative perspective. Since various forms of secondary flows occur simultaneously in the blade row, a difficulty is encountered in isolating a particular secondary flow, its cause and effect. Also, recording the phenomena becomes extremely difficult in a high-speed environment. Therefore physical, analytical, and numerical models of the flow in a rotor or stator have been utilized to simplify the analysis.

Most flow visualization experiments on stators, rotors, or vanes have been conducted using a single cascade. The aim of these studies was to improve the understanding of secondary flow production of that blade row. Herzig et al. (1954), using smoke placed in the boundary layer upstream of a cascade, was the first to visualize the passage vortex in a turbine cascade. Recently, Sieverding and van den Bosche (1983) used colored smoke to visualize the evolution of the horseshoe vortex as it merged with the passage vortex to form a single vortex core. Tip leakage flows have also been given attention in recent years. Dishart and Moore (1990) used smoke and particle traces at the endwall to visualize tip leakage flows in a turbine cascade.

The experiments discussed above were all conducted on a single blade row to develop an understanding of the causes and evolution of these secondary flows. However, in addition to the cited isolated blade row studies, interactions that occur between stator and rotor blade rows have also been the focus of some recent experiments. Hebert and Tiederman (1990) placed rods upstream of a linear cascade in a water flow loop to determine the effect of two-dimensional spanwise wakes on the cascade. Both stationary and moving rods were used to determine the steady and unsteady incident wake flow interaction on the linear cascade. They determined that the wake significantly distorted and weakened the passage vortex. Very few experiments, however, have been conducted on the interaction of a streamwise vortex on a downstream blade row. Sharma et al. (1992) referenced unpublished work by LaFleur et al. (1988), who generated streamwise vortices in a water tunnel upstream of a cascade of blades. By using dyes and a sheet of laser light perpendicular to the flow field, the interaction of the vortices with the blade cascade was visualized. Vortex generators were used to generate the streamwise vortices and were moved to different points along the pitch of the cascade to produce an array of steady incident vortices. When the incoming vortex was positioned near the suction side of the blade, the vortex was stable as it passed through the cascade. However, when the vortex was moved to the pressure side of the blade, the vortices collapsed and reformed in an unsteady manner. This result showed that even with an incident flow field that was steady in time, an unsteady flow field developed.

The primary objective of the present study was to expand on the work of Lafleur et al. (1988) by using moving upstream vortex generators to examine the unsteady incident vortex inter-

Contributed by the International Gas Turbine Institute and presented at the 40th International Gas Turbine and Aeroengine Congress and Exhibition, Houston, Texas, June 5–8, 1995. Manuscript received by the International Gas Turbine Institute February 11, 1995. Paper No. 95-GT-240. Associate Technical Editor: C. J. Russo.

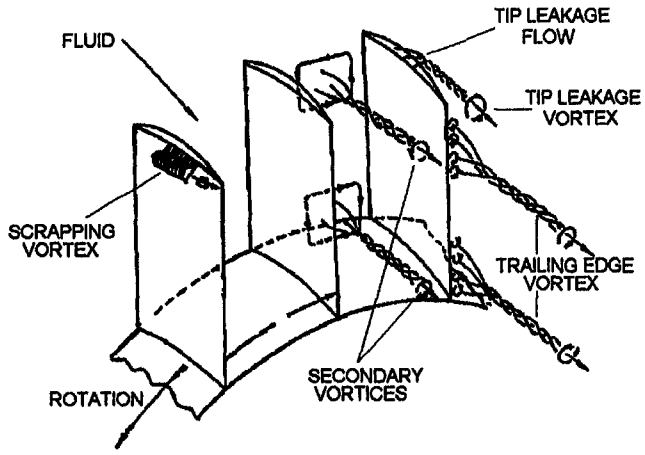

Fig. 1 Streamwise vorticity from Lakshminarayana and Horlock (1963)

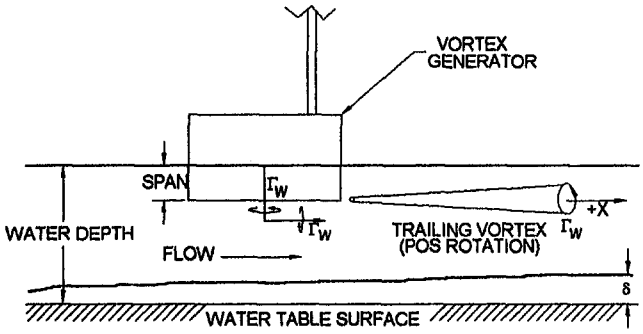

Fig. 2 Experiment vortex production

action of the incoming vortices on a turbine cascade. Secondary objectives were to examine the response of steady incident streamwise vortices moving through a cascade and to determine the difference between the way two-dimensional spanwise vortices (e.g., blade wakes) and three-dimensional vortices (e.g., tip clearance vortices) interact with the downstream blade row. To accomplish the objectives, vortex generators were placed upstream of a cascade of turbine blades in a water table. The vortex interaction was visualized using a pH-based flow visualization technique and photographed using a video camera.

Experimental Development

The experiment was designed to simulate the interaction of vorticity produced by an upstream blade row on a downstream turbine blade row. Specifically, the vortex transport was investigated as a function of pitchwise position, turbine wheel speed, and main flow velocity. Two test series were conducted to characterize this interaction. In the first test series, the incident vortices were positioned at various fixed pitchwise locations with respect to the turbine blade. These tests were conducted to determine whether the incident vortex reacted differently depending on its pitchwise location relative to the turbine blade. These results were then used to help explain the results obtained when the incident vortices were moving with respect to the turbine blade row. The situation with moving vortices simulated the flow in an actual turbine engine where turbine blades see periodic incident vortices. In addition to these two tests, preliminary tests were carried out to determine that the flow structures observed were not caused by any anomalies in the facility.

A water table was used to visualize the interaction of the upstream vortices on a linear cascade of turbine blades. Since the kinematics of the vortex motion was the primary focus of this investigation, centrifugal and compressibility effects were neglected. Only the upstream vortices and not the entire upstream flow field interaction on the turbine cascade was the focus of this study; therefore, a number of vortex generators were used in place of the upstream blade row. The vortex generators were placed above the incoming boundary layer to simulate a vortex operating outside of the endwall boundary layer. Each vortex generator produced a single trailing edge vortex (Fig. 2) with a strength (Γ_w) equivalent to that of the bound vortex. The strength of the vortex was calculated using a two-dimensional circulation calculation using the method and code of McFarland (1993). Schrenk's approximation (1940) was used to correct the two-dimensional circulation of the vortex generator to a three-dimensional circulation distribution. To obtain the periodically changing incident vorticity, the turbine blade cascade was fixed and the vortex generators were moved at a speed that preserved the design velocity triangle. This change of reference simplified photographing of the unsteady flow phenomena since it was desired to visualize the unsteady incident vortex interaction on the turbine blade row.

To classify the operating points of the experiment and obtain results that were representative of a turbine, several nondimensional parameters were used. These nondimensional parameters formed the basis for a nondimensional mapping in which one or more of the parameters were perturbed while maintaining the others constant to observe their effect on the flow field. The governing parameters are given in Table 1, with the reduced frequency and vortex strength described below.

Reduced Frequency, k. The reduced frequency is the ratio of the time for a fluid particle to travel through the blade passage relative to the period of the incoming vorticity field:

$$k = \frac{\text{time for a fluid particle to travel through the blade passage}}{\text{period of the incoming vorticity field}}$$

It can also be expressed in terms of the solidity of the cascade, the interblade phase angle, and the wheel speed ratio, as shown

Nomenclature

C_b = turbine blade axial chord
C_w = vortex generator chord
d = axial gap
h_b = pitch of turbine blades
h_w = pitch of vortex generators
h_n = dimensionless vortex location
k = reduced frequency
Re_b = turbine blade Reynolds number
Re_w = vortex generator Reynolds number
V_g = velocity relative to vortex generator
V_{in} = incident flow velocity for experiment (same as V_{rel} in an actual turbine)
V_r = wheel speed ratio
V_{rel} = velocity relative to turbine blades in an actual turbine
V_w = vortex generator speed (same as rotor tangential speed in an actual turbine)
x = pitchwise coordinate (= 0 @ leading edge)
X = streamwise direction
Γ_n = circulation number
Γ_w = vortex generator circulation
δ = boundary layer thickness of Plexiglas endwall
θ = interblade phase angle
σ_b = turbine blade solidity
σ_w = vortex generator solidity
ω = circular frequency of rotor

Table 1 Governing parameters

Stationary Incident Vortex Test	*Moving Incident Vortex Test*
Inter-Blade Phase Angle $\left(\theta = \frac{h_b}{h_w}\right)$ (1)	Same
Vortex Gen. Solidity $\left(\sigma_w = \frac{C_w}{h_w}\right)$ (2)	Same
Circulation Number $\left(\Gamma_n = \frac{\Gamma_w}{C_w V_{in}}\right)$ (3)	Same
Vortex Location $\left(h_n = \frac{x}{h_b}\right)$ (4)	Wheel Speed Ratio $\left(V_r = \frac{V_w}{V_{in}}\right)$ (5)
	Reduced Frequency $\left(k = 2\pi\sigma_b\theta V_r\right)$ (6)

in Table 1. The experiment was designed to obtain data for various reduced frequencies around a value of 4.7, which is typical for an axial flow turbine. The reduced frequency (k) was very important from the point of ascertaining the transport of unsteady incident vortices through the blade passage (Table 2).

Circulation Number, Γ_n. The circulation number is the total circulation strength of the vortex generator corrected for three-dimensional effects normalized by the chord and the velocity approaching the vortex generators. The circulation number was important in order to determine the effect of the circulation strength on the vortex transport through the turbine blade cascade. The vortex strength was dependent on the solidity of the vortex generators. As the solidity increased, the loading of the vortex generator and therefore the circulation decreased. The vortex generators were designed to model the circulation number of an actual turbine. The model was designed to vary the circulation number about a value of approximately Γ_n = 0.09, which is typical of the blade circulation for an axial flow machine.

Experimental Apparatus

The experimental setup was based on the operating points defined above. Details of the experimental apparatus are given in van de Wall (1994). A short description is given below.

Water Table. A stainless steel stationary water table facility was used. To illuminate the test section, 24 40-W fluorescent light bulbs were mounted below a Plexiglas base. A 50.8 mm (2.0 in.) depth of distilled water was maintained over the Plexiglas base. The water was guided through the wake generators and into and out of the 14-blade turbine cascade by foreboards and tailboards (Fig. 3). Six screens located at the channel inlet were used to minimize the turbulence of the flow approaching the wake generators and cascade. Passages 7, 8, and 9 in the center of the cascade were used to observe the vortex interaction.

Table 2 Importance of unsteadiness

Reduced Frequency (k)	*Importance of Unsteadiness*
$k \ll 1$	Quasi-Steady (Unsteadiness time scale >> Through flow time scale)
$k \sim 1$	Steady and Unsteady effects important
$k \gg 1$	Unsteadiness dominates

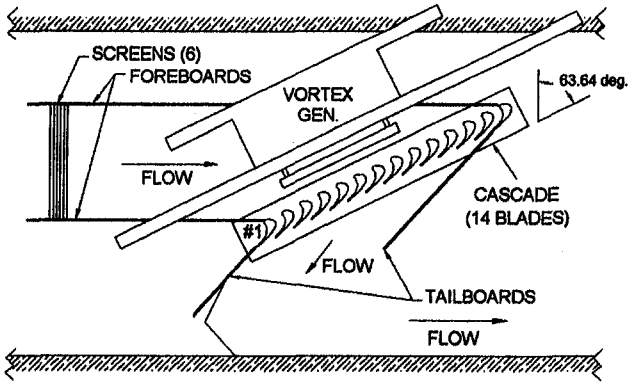

Fig. 3 Channel system—top view

A vortex generation mechanism was built to simulate vortex production by upstream blades (Fig. 4). Vortex generators were attached to a stainless steel chain via plastic rods. The speed of the chain as well as the vortex generator spacing could be varied. To avoid the photographic difficulties associated with surface waves, which formed when the vortex generators entered the water, a maximum of five vortex generators were used with the measurements beginning only after the last vortex generator entered the water.

Vortex Generators. Each vortex generator was required to produce a single strong trailing edge vortex, which remained stable as it passed the trailing edge of the vortex generator. The depth of the vortex generator was adjusted so that the vortex remained outside the endwall boundary layer of the channel but at the same time did not interact with the free surface. The boundary layer thickness was calculated using a Blassius flat plate profile and was verified experimentally using the flow visualization system.

The vortex generator consisted of a 0.64 mm (0.025 in.) thick cambered copper plate with the leading edge aligned with the flow. This configuration removed the leading edge separation problems associated with flat plates. Two chord lengths of 57.2 mm (2.25 in.) and 98.4 mm (3.875 in.) were used. The vortex generators were immersed so 12.7 mm (0.5 in.) was below the free surface. Five vortex generators were generally used. The setting angle of the vortex generator was fixed at 42 deg throughout the tests. Table 3 shows the vortex generator characteristics and Fig. 5 shows the velocity triangles for the vortex generator cascade for both the stationary and moving tests.

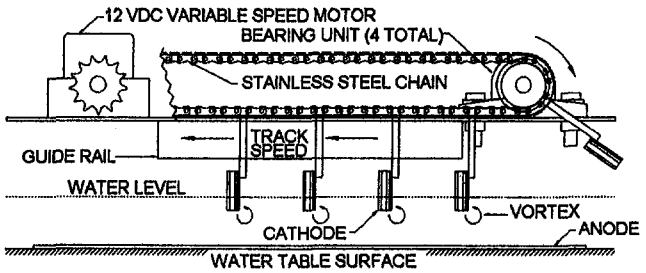

Fig. 4 Vortex generation mechanism

Table 3 Test setup characteristics

Axial Gap - 44.5 mm (1.75 in)	
Vortex Generators	*Turbine Blades*
Chord - 57.2 & 98.4 mm	Axial Chord - 76.2 mm (3.0 in)
Turning Angle - 60 deg.	Turning Angle - 132.25 deg.
Aspect Ratio - 0.13	Solidity - 1.0
Span - 12.7 mm (0.5 in)	Span - 127.0 mm (5.0 in)
Static Set Angle - 35 deg.	Water Depth - 50.8 mm (2.0 in)
Dynamic Set Angle - 42 deg.	

Turbine Blades. The experiments were conducted on a scale model of a high turning turbine blade of current interest. The blades were made of wood and were sealed and painted a dull white. The paint and sealer prevented any bubbles from forming at the surface of the blade because of the porous nature of wood. The foreboards were adjusted so the turbine blades received the relative velocity (V_{in}) at the angle that an actual rotating turbine blade would see. The turbine blade characteristics and installation are shown in Table 3 and Fig. 5, respectively.

Flow Visualization Technique. The flow visualization system used followed the method of Baker (1966), and involved introducing the pH indicator, Bromothymol Blue, into distilled water, which resulted in a solution where the color is dependent upon the pH level (Table 4). By establishing the solution in the water table at a pH of less than 6.0, a color contrast is obtained by applying a potential difference across two electrodes. The solution became basic near the cathode, which changed the fluid color to dark blue. The flow near the cathode was then carried downstream by the flow pattern surrounding the cathode. This dark blue fluid marker was contrasted against the surrounding tank fluid of orange-yellow, which remained at a pH of less than 6.0. Eventually, as the dark blue fluid moved away from the cathode, it was mixed with the surrounding fluid and returned to its original lower pH value. The solution could therefore be used indefinitely. Also, no density difference existed between the dark blue marker and the surrounding fluid; thus, unlike the hydrogen bubble visualization technique, buoyancy is not an issue.

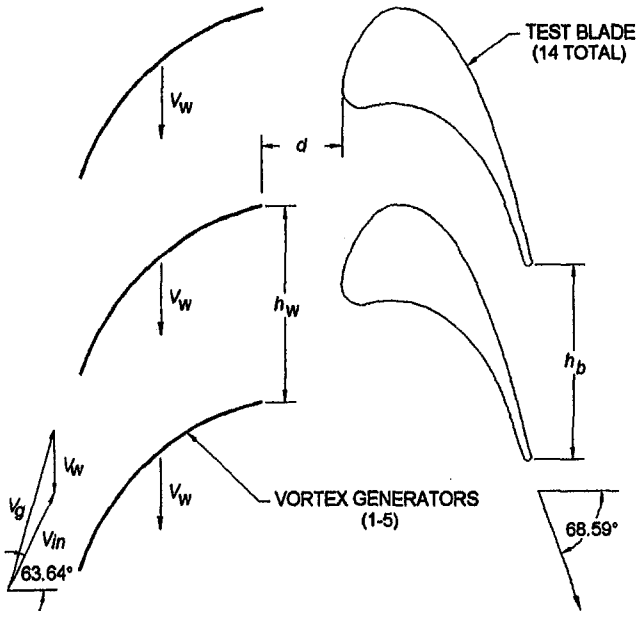

Fig. 5 Test setup characteristics

Table 4 Bromothymol blue colors

pH	*Solution Color*
pH < 6.0	Orange - Yellow
6.0 > pH < 7.6	Transition - Green
pH > 7.6	Blue

The tip of the center vortex generator was used as the cathode, while the remaining portion was insulated. This helped to visualize only the water flowing around the tip. The anode was a 0.13 mm (0.005 in.) thick brass sheet located under the vortex generators. To avoid hydrogen bubble formation, the voltage and current remained below 18 volts and 40 milliamps, respectively, for the entire test. A S-VHS camera with a yellow filter was used to photograph the flow pattern.

Results

Preliminary Tests. Preliminary tests were conducted to determine the undisturbed flow conditions and the interaction of two-dimensional wakes on the turbine blades. Figure 6 is a photograph of the undisturbed mean flow field using six fine wires at 12.7 mm (0.5 in.) pitch placed upstream of the turbine blades. An array of 1.6 mm ($\frac{1}{16}$th in.) diameter rods was also used in place of the vortex generators to generate two-dimensional wakes. As the wakes produced by the fine wires and rods approached the stagnation point of the blade, they flowed smoothly around the leading edge following the mean streamlines. The wakes from the rods showed no difference in structure as their position was varied along the pitch of the turbine blades. The benign behavior of the two-dimensional wakes is in sharp contrast to the results that follow.

Stationary Incident Vortex Tests. The stationary incident vortex test was conducted to determine whether any unsteadiness existed in the limiting case of the reduced frequency, $k \rightarrow 0$. In this limiting case, there is no unsteadiness caused by the relative motion of the upstream blade row.

The flow field that developed varied greatly with the pitchwise location of the incoming streamwise vortex. The sequence of photographs in Fig. 7 is representative of the data set and shows the interaction results from a single steady incident vortex generated from the 57.2 mm (2.25 in.) chord vortex generator. In Fig. 7(a), the vortex was placed at midpitch of the turbine cascade. The vortex followed the main flow streamlines and no unsteady effects were observed. The vortex passed through the cascade as a concentrated vortex core.

Figure 7(b) shows the vortex near the suction surface. The vortex approached the cascade following the streamlines of the main flow. The vortex passed through the cascade as a concentrated vortex core just as at midpitch and similar to the two-dimensional wakes in Fig. 6. As the vortex generator was moved to the stagnation streamline, the vortex displayed an oscillating

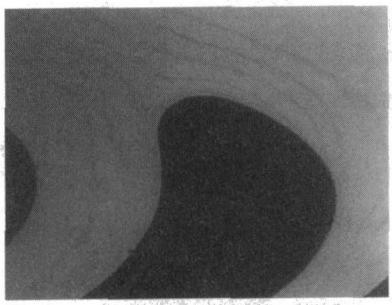

Fig. 6 Preliminary test

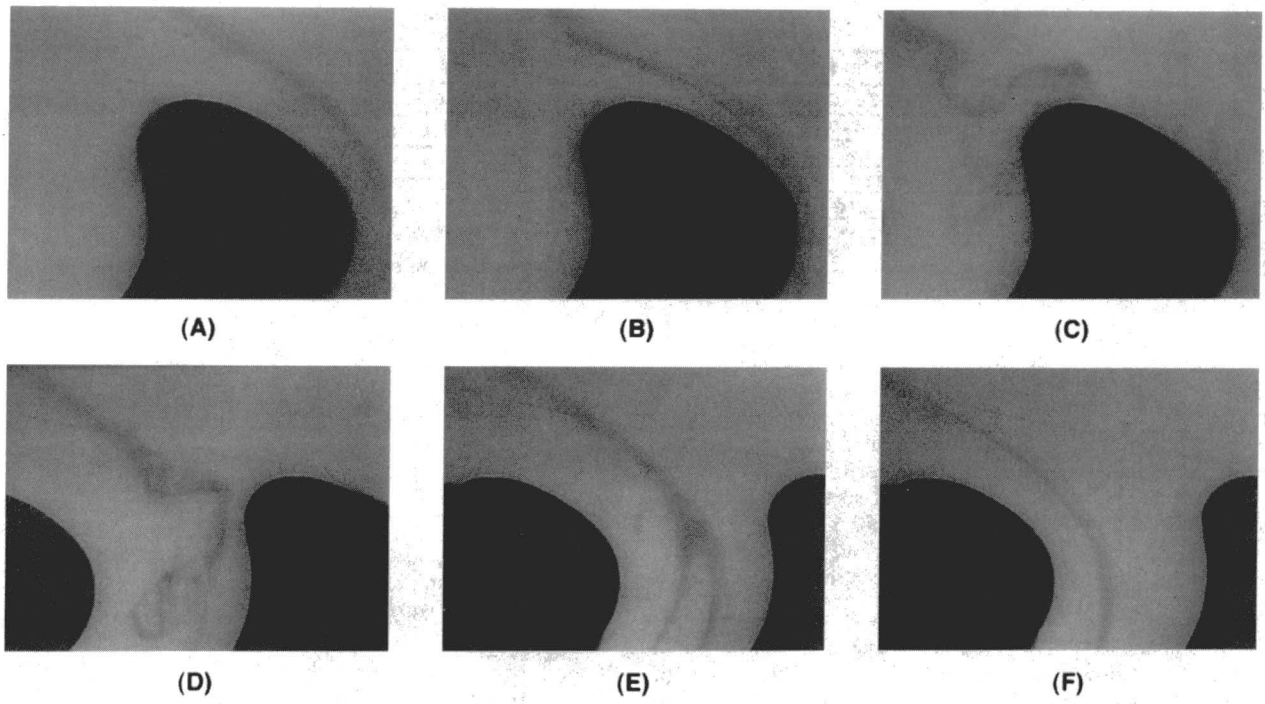

Fig. 7 Stationary vortex interaction

phenomenon as seen in Fig. 7(*c*). The vortex remained initially intact approaching the stagnation point and was convected downstream along both the suction and pressure surfaces. The vortex was stretched and bent around the leading edge of the blade until the vortex line was destroyed. The destruction or bursting of the vortex at the leading edge caused parts of the original vortex to propagate upstream and interact with the periodic oscillation of the vortex. This interaction created a turbulent unsteady flow field very close to the leading edge. The breakdown point followed by the oscillating zone of the vortex is clearly shown in Fig. 7(*d*) where the vortex was located to the pressure side of the stagnation streamline. The entire vortex was convected downstream on the pressure side of the blade.

A closer inspection of the oscillatory behavior of the vortex interaction at the stagnation area revealed a noticeable pattern. The oscillatory behavior of the vortex occurred at a constant frequency. The streamwise vortex approaches the adverse pressure gradient near the stagnation region and is perturbed off of the primary flow streamline. The vortex, which appears in the photographs to oscillate, actually rotates around the initial incident streamline, forming a three-dimensional helical pattern. Considering the rotation as positive in the streamwise direction, the rotation of this vortex around the incident streamline is in the same positive sense as the incoming vortex. This rotation of the helix is in addition to the rotation within the vortex core. This helical form of vortex instability is identical to that observed by Chanaud (1965), reproduced here in Fig. 8. The helical pattern of the vortex induced a reversed velocity opposite to the initial velocity, which therefore produced a stagnation point in the flow field on the axis of the initial streamline.

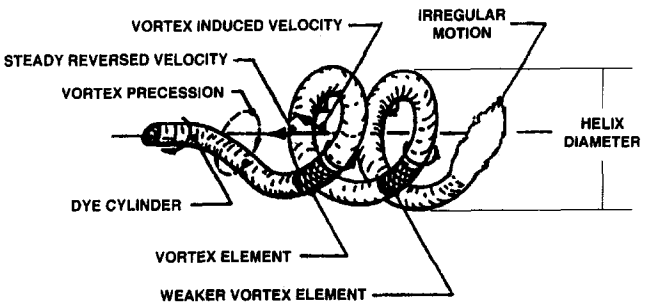

Fig. 8 Helix mode of the vortex approaching stagnation area from Chanaud (1965)

The amplitude of the vortex oscillation decreased as seen in Fig. 7(*e*), when the vortex generator was moved further away from the pressure surface. The amplitude of oscillation was very small and the frequency of vortex oscillation was unable to be determined. Figure 7(*e*) also shows that once the vortex enters the cascade passage, it undergoes a stable breakdown process. This process is similar to that observed by Faler and Leibovich (1977) and was described by them as a type-0 two-tailed vortex breakdown. This breakdown disappeared when the velocity was increased. The breakdown consisted of a stagnation point on the vortex axis followed by an expansion of the vortex core. The bubble is emptied at the rear by the two tails which flowed separately downstream. Further details on classical vortex breakdown can be found in Hall (1972) and Leibovich (1984).

Finally, the vortex is again positioned at midpitch, Fig. 7(*f*), yielding a steady flow pattern identical to Fig. 7(*a*), which confirms the spatial periodicity of the test setup. A summary of the flow structure observed is given in Table 5.

These results supported and expanded upon the data obtained in the water tunnel experiment conducted by LaFleur et al. (1988), which showed that an incident streamwise vortex interacted in an unsteady manner near the pressure side of the blade. LaFleur et al. (1988) also showed the steady vortex transport process near the suction side of the blade, as do the results found in this study. In addition, the present study showed that

Table 5 Streamwise vortex behavior

Vortex Location	*Flow Structure Observed*
Suction Side	Clean Undisturbed Vortex
Stagnation Area	Unsteady Vortex Behavior
Pressure Side	Some Vortex Unsteadiness

Table 6 Moving incident vortex test cases investigated (C_w = 98.4 mm)

Case #	θ (rad)	Γ_n ±0.03	k ±0.15
I	1.0	0.10	6.73
II	1.0	0.10	4.71
III	1.5	0.07	13.46
IV	0.75	0.13	5.05

the periodic collapsing and reforming of the vortex on the pressure surface is associated with a helical breakdown of the incident vortex.

Moving Incident Vortex Tests. Table 6 shows the various cases examined and the values of the parameters used. Cases I and II were used to show the effect of varying reduced frequency, while the holding the circulation number constant. Cases II and IV were used to show the effect of varying circulation, while holding the reduced frequency approximately constant. Case III was used to show the effect when unsteadiness from the upstream blade row dominates the flow field ($k \gg 1$).

General Observations. In the stationary incident vortex tests, an unsteady interaction of the vortex developed in the stagnation region and near the pressure surface as a result of vortex breakdown. With the vortex generator set in motion simulating the preceding blade row, the unsteady vortex motion associated with breakdown is no longer confined to the stagnation region. The vortex breakdown is observed to be near the suction surface of the adjacent blade in the direction of the motion of the vortex generator. In addition, no large-diameter helical breakdown is observed in the moving vortex generator test, as seen in the stationary incident vortex test. Figures 9–12 are the photographs for cases I–IV, respectively. These figures show the vortex generators moving from right to left at a constant speed, V_w, with the primary flow identical to that of the stationary test. In these photographs one vortex, originating from the center vortex generator, is shown as it evolves in time.

Effect of Reduced Frequency. The results for case I (k = 6.73) are shown in Fig. 9. Figures 9(a–d) represent one complete cycle where the vortex moves from the leading edge of a blade to the leading edge of the adjacent blade, with Fig. 9(d) one cycle later than 9(a). In Fig. 9(a), the vortex is stretched around the suction side of the blade to the stagnation region. The incident vortex reaches the stagnation streamline and is aligned with the streamlines of the primary flow. The vortex does not initially develop into a helix at the stagnation streamline as in the stationary incident vortex tests. The start of the breakdown process is at location A of Fig. 9(b), where the incident vortex is on the pressure side of the stagnation streamline. The vortex is no longer aligned with the primary flow and a helical breakdown is initiated. However, a full helix does not develop. The vortex instability is initiated upon reaching the adverse pressure gradient. Because the vortex is moving away from the stagnation point, it spends a finite amount of time in the adverse pressure gradient region. The growth of the breakdown is therefore limited. The time scale for the breakdown to develop is greater than the time scale for the vortex to pass through the adverse pressure gradient associated with the stagnation point. Also, the vortex aligned perpendicular to the stagnation streamline causes it to be stretched, thus damping the instability that prevents the downstream end of the helical vortex from rotating freely as in the stationary incident vortex tests in Fig. 7(c).

The stretching and bending of the vortex on the pressure side of the stagnation region in Fig. 9(b) is similar to that observed by Binder (1985), who used a Laser-2-Focus velocimeter to map the flow field in the rotor of a turbine stage. However, in the present experiment, the vortex remains continuous at the leading edge longer than what Binder (1985) observed. One reason for this could be that the laser velocimeter only provides local measurement at a point; thus, only a pointwise mapping of the flow field can be obtained. Therefore, the whole flow field could not be observed at an instant in time as in the present experiment.

Figure 9(c) shows the vortex still intact as it bends around the stagnation point until it becomes discontinuous (i.e., is cut) at the leading edge labeled location B. This cutting process

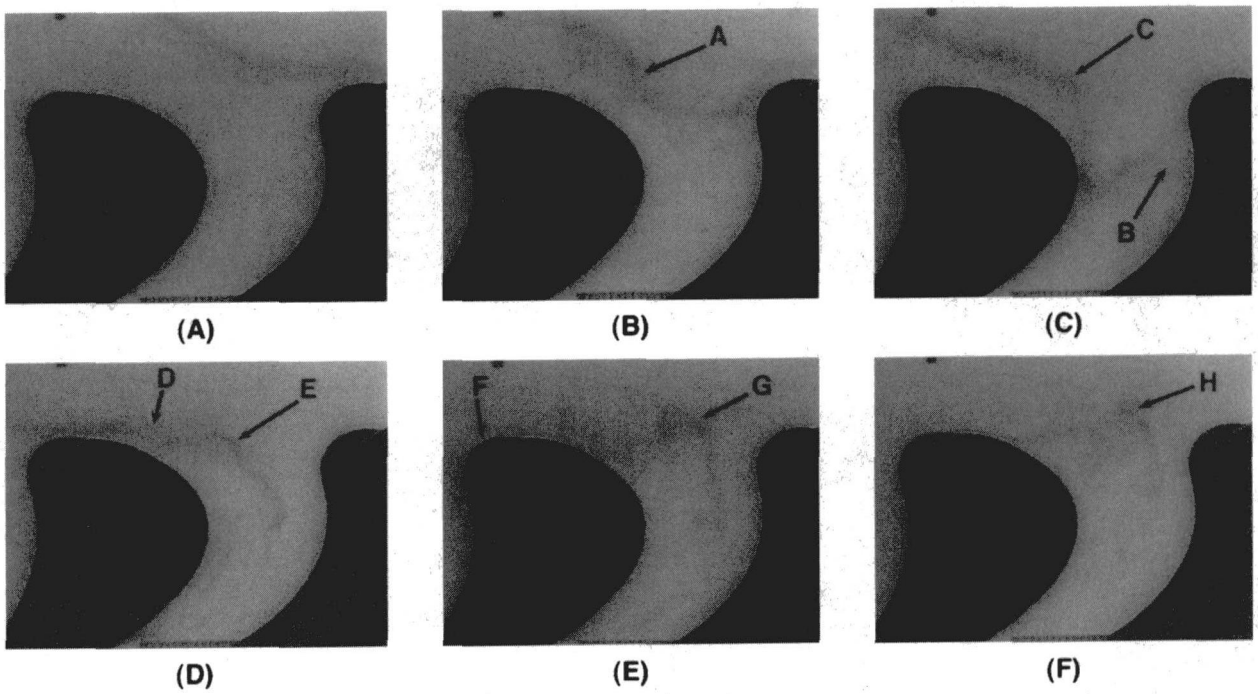

Fig. 9 Moving vortex interaction: case I

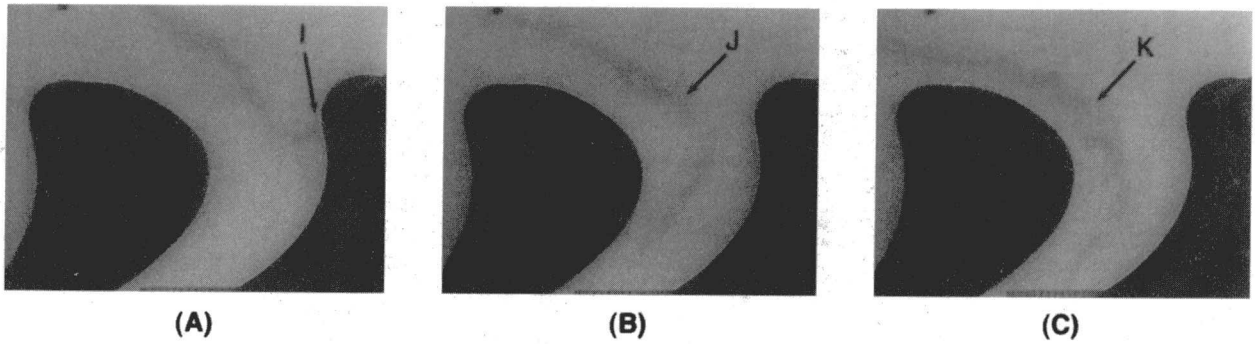

Fig. 10 Moving vortex interaction: case II

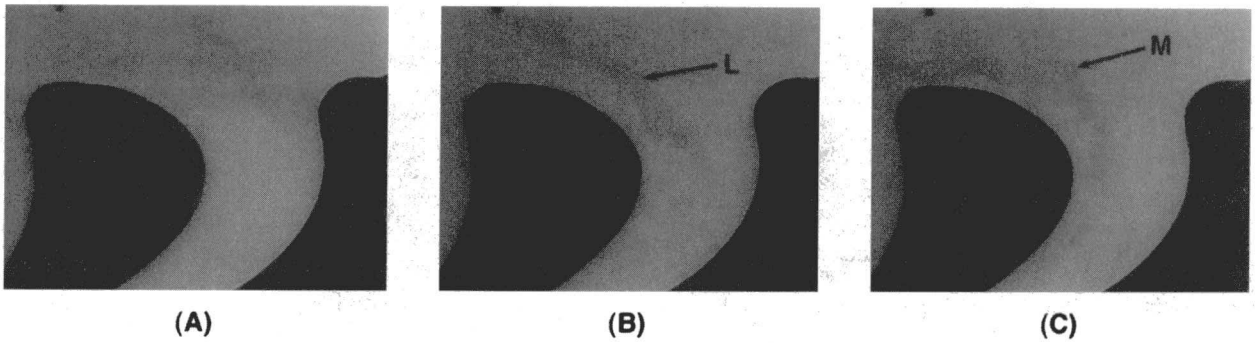

Fig. 11 Moving vortex interaction: case III

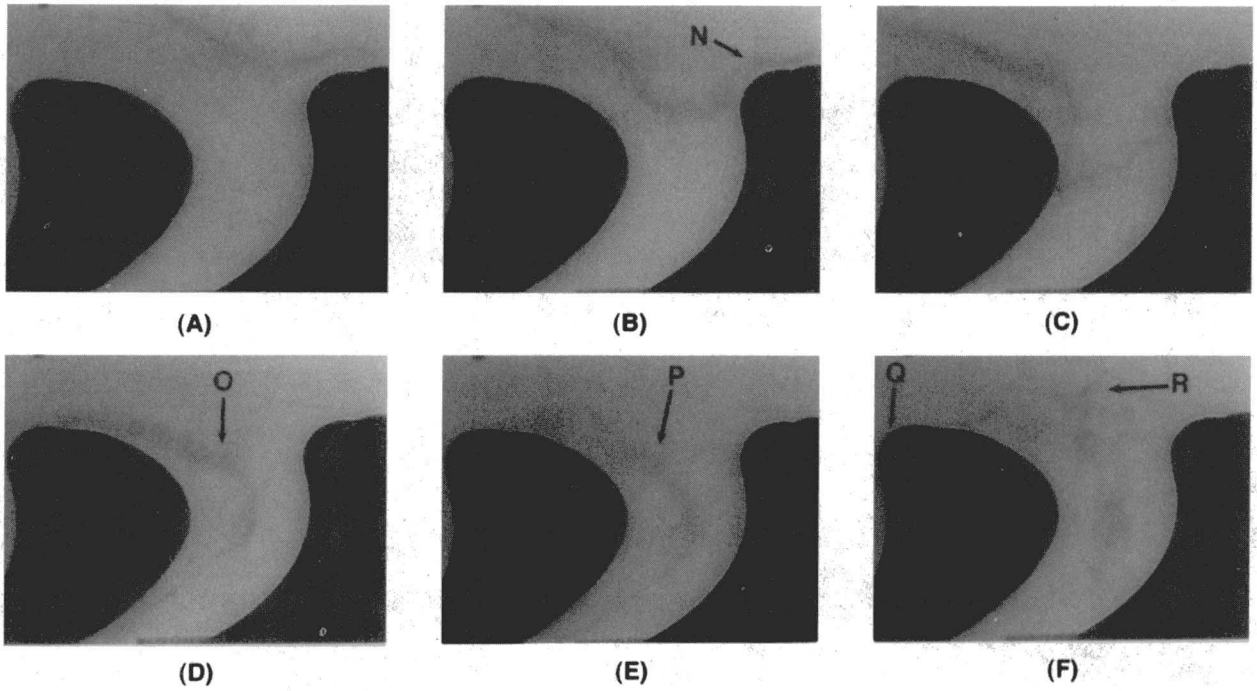

Fig. 12 Moving vortex interaction: case IV

occurs when the vortex is at the middle of the blade passage. During the breakdown process, the upstream part of the vortex remained intact with the helical breakdown point labeled location C.

In Fig. 9(*d*), the end of the vortex that is cut entered the blade passage while its upstream end is at the stagnation point of the adjacent blade (shown on the left in the photograph). The unsteadiness caused by the helical breakdown is located near the suction surface labeled location D. The vortex, upstream of the helical breakdown point, is bending around the leading edge of the adjacent blade aligned with the streamlines of the primary flow. The reduction in helix diameter, labeled locations D and E in Fig. 9(*d*), as compared to the helix diameter in the stationary incident vortex tests, is caused by the vortex moving out of the adverse pressure gradient of the stagnation region. In addition, the vortex position in Fig. 9(*d*) does not

follow the primary flow streamlines near the suction surface, but is underturned relative to the primary streamlines.

Figures 9(*e*) and 9(*f*) show the remains of the vortex after one cycle and are one cycle later than Figs. 9(*b*) and 9(*c*), respectively. In Fig. 9(*e*), the vortex has been cut by the leading edge of the adjacent blade at location F. As soon as the vortex is cut, the fluid that was originally part of the vortex is not observed to have any significant vortical structure and moves across the passage toward the pressure surface. This motion toward the pressure surface is shown as a sequence in time from location E to G to H in Figs. 9(*d*), 9(*e*), and 9(*f*), respectively. This sequence shows a crossflow velocity toward the pressure surface induced by the vortex. The turbulent remains of the vortex in Figs. 9(*e*) and 9(*f*) could be caused by the interaction of the remains of the vortex with the vortex from the next generator. In addition, some of the fluid that was originally part of the vortex migrates around the leading edge of the blade at the right (Fig. 9(*f*), location H).

Figure 10 shows the results of one complete vortex cycle when the reduced frequency was decreased from 6.73 to 4.71, giving more time for a vortex to interact with the cascade. At this lower reduced frequency, the vortex is cut sooner and closer to the stagnation streamline than in case I as seen in Fig. 10(*a*), location I. The cut end of the vortex is no longer bending around the leading edge and is free to convect down the blade passage. There is very little evidence of the helical mode of vortex breakdown at location J in Fig. 10(*b*) and the vortex generally follows the primary flow streamlines. A small diameter helix is seen at location K of Fig. 10(*c*), but the entire helix follows the primary flow streamlines. Also, the vortex is closer to the suction surface than in case I and no crossflow velocity is observed. The higher throughflow velocity relative to the wheel speed assists in sweeping the vortex down the passage.

Effect of Large Reduced Frequency With Low Circulation. In case III, the reduced frequency was 13.46, which gives less time for the vortex to interact with the cascade, and the circulation number was 0.07. This combination of reduced frequency and circulation number was chosen to investigate the case when upstream unsteadiness dominates the flow. Figures 11(*a–c*) show the interaction of the vortex with the cascade at equal increments over the time it takes the vortex generator to traverse a pitch of the cascade. The vortex impacts the suction surface and recoils back from the blade surface in the direction from which it had come. This phenomenon is shown in the sequence from location L to location M in Figs. 11(*b–c*). This flow phenomenon is also clearly evident in the videotape record of the experiment. After the vortex is reflected off the wall and back into the mainstream flow, it seems to "explode," resulting in its destruction. This "exploding" is enhanced by the interaction with the next vortex. The fluid, which was originally part of the vortex, is swept down the blade passage and into the preceding blade passage on the right of the passage in the figures. It was determined that this explosive type of vortex breakdown occurs at a reduced frequency greater than 8.0.

Effect of Vortex Circulation. Figure 12 shows the results when the circulation number is increased to $\Gamma_n = 0.13$ from $\Gamma_n = 0.10$ (case II), while the reduced frequency is maintained approximately constant. Figures 12(*a–d*) show the interaction of the vortex with the cascade at equal increments over the time it takes the vortex generator to traverse a pitch of the cascade. The higher strength vortex remains continuous longer as it bends and stretches around the leading edge of the blades at location N in Fig. 12(*b*), relative to what is observed at location I in Fig. 10(*a*). Because of the stronger vortex, the distorted helical form in case IV, Fig. 12(*c*), has a larger diameter than in case II. Figures 12(*e*) and 12(*f*) show the remains of the vortex after it has passed the leading edge of the blade in the left of Fig. 12. At locations O and P in Figs. 12(*d*) and 12(*e*), respectively, the vortex does not show any signs of a helical breakdown. The vortex formed an acute angle with the primary flow streamlines near mid passage. As in case I, the vortex is cut at the leading edge of the adjacent blade (location Q in Fig. 12(*f*)) and a crossflow velocity similar to location H of Fig. 9(*f*) develops at location R in Fig. 12(*f*), which could be the result of an interaction with the vortex from the next generator.

Summary

Experiments were conducted to obtain a qualitative perspective on the interaction of upstream vorticity on a downstream blade row. In the first series of tests, stationary upstream vortex generators were placed at different locations along the turbine pitch. A difference was found in how two-dimensional spanwise vorticity and three-dimensional streamwise vorticity were transported through the turbine cascade. At all positions along the turbine pitch, two-dimensional spanwise vorticity followed the streamlines of the primary flow. Incident streamwise vorticity did not follow the streamlines of the flow near the stagnation region and underwent a classical helical form of vortex breakdown. From near the suction surface to midpassage, the vortex was aligned with the primary flow streamlines and did not exhibit an unsteady behavior. From midpassage to the pressure surface, the results showed that the steady incident streamwise vortex developed an unsteady response.

In the second series of tests, the upstream vortex generators were moved at a constant speed along the turbine cascade to observe the transport of the incoming vortex through the cascade. At all combinations of reduced frequency and circulation number, the large-diameter helical breakdown observed at the stagnation area of the blade in the stationary incident vortex tests, was not observed in the moving incident vortex tests. The vortex breakdown was not dominated exclusively by the classical helical breakdown, but also by vortex cutting and an explosive type vortex breakdown. As the reduced frequency was reduced toward zero, the helical breakdown occurred along the streamlines of the primary flow. An increase in circulation lengthened the time the vortex remained continuous.

At reduced frequencies greater than 8.0, the incident vortex was destroyed at the suction side of the blade in an "explosive" type vortex breakdown. The vortex recoiled off of the suction side of the blade and traveled back in the direction from which it came. This explosive vortex breakdown needs further investigations, especially in answering the question of whether or not this explosive breakdown leads to an increase or reduction in performance and heat transfer.

Acknowledgments

The authors thank Dr. K. Street for his help in making the Bromothymol Blue flow visualization technique workable, and Dr. Eric McFarland for his two-dimensional analysis of the vortex generators and turbine blades. The help of Mr. J. Kovach and Mr. D. Conger in the construction of the vortex generation mechanism is gratefully acknowledged. The authors also wish to thank the NASA Lewis 10′ × 10′ Supersonic Wind Tunnel technical staff and specifically Mr. N. Lalli for his help in the use of the water table facility, and Mr. J. Sims, Mr. H. Broughton, and Mr. Gary Nolan of the Photographic Services Branch at the NASA Lewis Research Center, for processing the photographs.

Finally, the sponsorship of this research by the NASA Lewis Research Center (Grant No. NCC 3-263) is gratefully acknowledged.

References

Baker, D., 1966, "A Technique for the Precise Measurement of Small Fluid Velocities," *Journal of Fluid Mechanics*, Vol. 26, Part 3, pp. 573–575.

Binder, A., 1985, "Turbulence Production Due to Secondary Cutting in a Turbine Rotor," ASME *Journal of Engineering for Gas Turbines and Power*, Vol. 107, pp. 1039–1046.

Chanaud, R. C., 1965, "Observations of Oscillatory Motion in Certain Swirling Flows," *Journal of Fluid Mechanics,* Vol. 21, Part 1, pp. 111–127.

Dishart, P. T., and Moore, J., 1990, "Tip Leakage Losses in a Linear Turbine Cascade," ASME JOURNAL OF TURBOMACHINERY, Vol. 112, pp. 599–608.

Faler, J. H., and Leibovich, S., 1977, "Disrupted States of Vortex Flow and Vortex Breakdown," *The Physics of Fluids,* Vol. 20, No. 9, pp. 1385–1400.

Hall, M. G., 1972, "Vortex Breakdown," *Annual Review of Fluid Mechanics,* Vol. 4, pp. 195–218.

Hebert, G. J., and Tiederman, W. G., 1990, "Comparison of Steady and Unsteady Secondary Flows in a Turbine Stator Cascade," ASME JOURNAL OF TURBOMACHINERY, Vol. 112, pp. 625–632.

Herzig, H. Z., Hansen, A. G., and Costello, G. R., 1954, "A Visualization Study of Secondary Flows in Cascades," NACA Report 1163.

Inoue, M., Kuroumaru, M., and Fukuhara, M., 1986, "Behavior of Tip Leakage Flow Behind an Axial Compressor Rotor," ASME *Journal of Engineering for Gas Turbines and Power,* Vol. 108, pp. 7–14.

Lakshminarayana, B., and Horlock, J. H., 1963, "Review: Secondary Flows and Losses in Cascades and Axial-Flow Turbomachines," *International Journal of Mechanical Science,* Vol. 5, pp. 287–307.

LaFleur, R. S., Langston, L. S., and Sharma, O. P., 1988, "Flow Visualization Investigation Through a Turbine Cascade With Incoming Streamwise Vortices," unpublished report, University of Connecticut, Storrs.

Leibovich, S., 1984, "Vortex Stability and Breakdown: Survey and Extension," *AIAA Journal,* Vol. 22, No. 9, pp. 1192–1206.

McFarland, E. R., 1993, "An Integral Equation Solution for Multi-stage Turbomachinery Design Calculations," ASME Paper No. 93-GT-41.

Schrenk, O., 1940, "A Simple Approximation Method for Obtaining the Spanwise Lift Distribution," NACA TM 948.

Sharma, O. P., Pickett, G. F., and Ni, R. H., 1992, "Assessment of Unsteady Flows in Turbines," ASME JOURNAL OF TURBOMACHINERY, Vol. 114, pp. 79–90.

Sieverding, C. H., and van den Bosche, P., 1983, "The Use of Colored Smoke to Visualize Secondary Flows in a Turbine-Blade Cascade," *Journal of Fluid Mechanics,* Vol. 134, pp. 85–89.

van de Wall, A., 1994, "An Investigation of the Transport of Streamwise Vortices in a Turbine Blade Cascade Using a Flow Visualization Technique," MS Thesis, Case Western Reserve University.

Time-Accurate Euler Simulation of Interaction of Nozzle Wake and Secondary Flow With Rotor Blade in an Axial Turbine Stage Using Nonreflecting Boundary Conditions

S. Fan
Graduate Assistant.
Mem. ASME

B. Lakshminarayana
Evan Pugh Professor
of Aerospace Engineering.
Fellow ASME

Center for Gas Turbine and Power,
Pennsylvania State University,
University Park, PA

The objective of this paper is to investigate the three-dimensional unsteady flow interactions in a turbomachine stage. A three-dimensional time-accurate Euler code has been developed using an explicit four-stage Runge–Kutta scheme. Three-dimensional unsteady nonreflecting boundary conditions are formulated at the inlet and the outlet of the computational domain to remove the spurious numerical reflections. The three-dimensional code is first validated for two-dimensional and three-dimensional cascades with harmonic vortical inlet distortions. The effectiveness of the nonreflecting boundary conditions is demonstrated. The unsteady Euler solver is then used to simulate the propagation of nozzle wake and secondary flow through the rotor and the resulting unsteady pressure field in an axial turbine stage. The three-dimensional and time-dependent propagation of nozzle wakes in the rotor blade row and the effects of nozzle secondary flow on the rotor unsteady surface pressure and passage flow field are studied. It was found that the unsteady flow field in the rotor is highly three dimensional and the nozzle secondary flow has significant contribution to the unsteady pressure on the blade surfaces. Even though the steady flow at the midspan is nearly two dimensional, the unsteady flow is three dimensional and the unsteady pressure distribution cannot be predicted by a two-dimensional analysis.

Introduction

The flow in a turbomachinery stage is essentially unsteady due to rotor/stator interactions. Many attempts have been made to predict rotor/stator interactions by solving the unsteady Navier–Stokes equations (Rai, 1989, for example). Theoretically, the solution of the Navier–Stokes equations with an adequate turbulence model and enough grid resolution should be capable of fully resolving the three-dimensional unsteady flow due to rotor/stator interaction. In practice, due to the limitation in computer resource, most of the three-dimensional unsteady Navier–Stokes solutions are made with insufficient grid resolution, which limits the accuracy of the solution. For example, insufficient grid resolution for the end-wall boundary layer and tip clearance regions will result in inadequate prediction of the secondary flow and the tip-leakage flow and the unsteady flow field arising from their interactions with the subsequent blade row. The three-dimensional Navier–Stokes solution is impractical for multistage unsteady interactions, especially where uneven blade ratio requires multiblade passage solutions.

An alternative approach to resolve the multistage unsteady interaction is to split the problem into two. The first is a multistage steady Navier–Stokes solution in relative reference frames (being alternatively rotating/stationary in rotors/stators). The unsteady flow in each blade row is then approximated by considering the interaction with the adjacent blade rows. To the first-order approximation, the circumferential nonuniformities (wake, potential field, secondary/tip leakage flows, etc.) from the steady solutions in the preceding and succeeding blade rows become the forcing functions to the current blade row due to the relative motion between the two adjacent blade rows. The idea of splitting a multistage unsteady solution into a multistage steady solution and unsteady solutions in each row originated from the paper by Giles (1993). Giles proposed to obtain the steady base flow by solving the nonlinear Euler equations, and to use the linearized Euler method for the unsteady pressure response in each blade row. While the steady Euler solution can provide the base flow for the linearized Euler solution and the forcing function for the potential interaction, it is unable to provide the forcing functions for the wake/blade interaction and the interactions between secondary flow or tip leakage flow and the succeeding blade row. Since wake, secondary flow, and tip leakage flow are of viscous origin or strongly affected by viscous effects, their definition requires the solution of the Navier–Stokes equations.

Furthermore, the forced response problem is essentially inviscid, despite the fact that the source of the forced response is of viscous origin (viscous wakes, for example). Therefore, if forced response is the major objective of the unsteady solution, unsteady Euler equations are suffice to describe the unsteady interaction in each blade row. Korakianitis (1992) used a three-dimensional Euler approach to predict wake/blade-row interactions. Saxer and Giles (1993) used a three-dimensional Euler approach to simulate the interaction between the blade row and a streamwise vortex.

The key to the success of this approach is the availability of nonreflecting boundary conditions. Since the location of the inlet/

Contributed by the International Gas Turbine Institute and presented at the 40th International Gas Turbine and Aeroengine Congress and Exhibition, Houston, Texas, June 5–8, 1995. Manuscript received by the International Gas Turbine Institute March 2, 1995. Paper No. 95-GT-230. Associate Technical Editor: C. J. Russo.

outlet boundaries of the computational domain is restricted by the physical spacing between the blade rows, in many cases, the inlet/outlet boundaries have to be placed very close to the blade row. The traditional reflective boundary conditions will cause substantial numerical reflections at the inlet and outlet boundaries, thus contaminating the numeral solutions for both steady and unsteady calculations. Giles (1990) developed two-dimensional steady and unsteady nonreflecting boundary conditions for Euler solution of cascade flows. Saxer and Giles (1993) extended the steady nonreflecting boundary conditions into a quasi-three-dimensional formulation and successfully applied to steady Euler solution of axial turbine stages. Three-dimensional nonreflecting boundary conditions for unsteady Euler solution are not available at this time and need to be developed. This is one of the objectives of this paper. Other objectives of this paper are to develop a three-dimensional time-accurate Euler code and to study the interaction of nozzle wake and secondary flow with rotor blades through application to realistic turbine stages.

In the present study, a time-accurate three-dimensional Euler solver has been developed based on a steady Navier–Stokes code (RKCC) developed earlier by Kunz and Lakshminarayana (1992). An explicit four-stage Runge–Kutta scheme is used to integrate the unsteady Euler equations. Three-dimensional unsteady nonreflecting boundary conditions are formulated through extension of the two-dimensional unsteady nonreflecting boundary conditions developed by Giles (1990). The three-dimensional code is first validated for two-dimensional and three-dimensional cascades with harmonic vortical inlet distortions. The effectiveness of the nonreflecting boundary conditions is demonstrated. The unsteady Euler solver will then be used to simulate the propagation of nozzle wake and secondary flow through the rotor blade row and the resulting unsteady pressure field. The configuration chosen is the Penn State Turbine Research Stage. The LDV data from this facility are compared with the prediction.

Unsteady Euler Procedure

This section briefly describe the development of the three-dimensional unsteady Euler procedure. A detailed description is given in Fan (1995). The compressible three-dimensional Euler equations in the rotor frame of reference are written in conservative form in generalized body fitted coordinates as:

$$\frac{\partial \hat{Q}}{\partial t} + \frac{\partial \hat{E}}{\partial \xi} + \frac{\partial \hat{F}}{\partial \eta} + \frac{\partial \hat{G}}{\partial \zeta} = \hat{S} \tag{1}$$

where $\hat{Q}$ is the primary transport variable vector, $\hat{E}$, $\hat{F}$, $\hat{G}$ are the flux vectors, $\hat{S}$ is the source vector.

The standard four-stage Runge–Kutta scheme is used to integrate the governing equations. Central differences are used to discretize the spatial derivatives. Fourth-order artificial dissipation is used to stabilize the Runge–Kutta scheme (see Kunz and Lakshminarayana, 1992, for details).

Periodic boundary conditions are used in the pitchwise direction as in a steady solution. If the rotor and stator have the same number of blades, the unsteady computation can be carried out by solving a single blade passage. When the number of blades differs between the rotor and the stator, multipassage solution is generally necessary. The coding technique in the present program allows for the solution to be carried out for an arbitrary number of blade passages. At the inlet and outlet boundaries, three-dimensional nonreflecting boundary conditions are used. The steady nonreflecting boundary conditions developed by Saxer and Giles (1993) have been implemented in this code. Detailed description of the three-dimensional unsteady nonreflecting boundary conditions will be given in the next section.

Development of Three-Dimensional Nonreflecting Boundary Conditions

The nonreflecting boundary conditions are developed based on the linearized Euler equations. Giles (1990) first used this method to develop two-dimensional steady and unsteady nonreflecting boundary conditions for Euler solution of cascade flows. Saxer and Giles (1993) extended the steady nonreflecting boundary conditions into a quasi-three-dimensional formulation and successfully applied to steady Euler solution of axial turbine stages. The three-dimensional unsteady nonreflecting boundary conditions are developed in this section. The three-dimensional derivation is an extension of the two-dimensional counterpart by Giles (1990). The derivation procedure follows the one by Giles (1990).

Linearized Euler Equations. The nonreflecting boundary conditions are based on the linearized Euler equations. Assuming the periodic unsteady flow is a small perturbation from its steady state, the linearized three-dimensional Euler equations for unsteady, inviscid, compressible flow are,

$$\frac{\partial \mathbf{U}}{\partial t} + \mathbf{A}\frac{\partial \mathbf{U}}{\partial x} + \mathbf{B}\frac{\partial \mathbf{U}}{\partial y} + \mathbf{C}\frac{\partial \mathbf{U}}{\partial z} = 0 \tag{2}$$

Nomenclature

A, B, C = matrices in the linearized Euler equations
c = chord length/speed of sound
c_1, c_2, c_3, c_4, c_5 = characteristic variables
C_p = pressure coefficient = $(p - p_{is})/0.5\rho_{is}q_{is}^2$
C_x = axial chord length
E, F, G = flux vectors
H = total enthalpy, shape factor, normalized blade height = $(r - r_{hub})/(r_{tip} - r_{hub})$
$\mathbf{I}$ = identity matrix
k, l, m = wave number in x, y, z directions
p, p_0 = static pressure, stagnation pressure
p_{is} = steady static pressure at inlet of the midspan
P_b = pitch
q_{is} = total steady relative velocity of inlet to the midspan
Q = primary transport variable vector
r = radius
t = time
T = static temperature/blade passing period
u, v, w = velocity components in x, y, z directions
$\mathbf{u}^L, \mathbf{u}^R$ = left and right eigenvectors
U = rotor traverse speed
V = total velocity in the blade frame of reference
x, y, z = Cartesian coordinates; $x = 0$ at the leading edge
β = relative inlet flow angle
γ = specific heat ratio
Δt = time step
ξ, η, ζ = curvilinear coordinates
ρ = density
ω = wake passing frequency
Ω = reduced frequency = $\omega c_x/u_{is}$

Superscripts and Subscripts

c = chord
is = inlet steady values in blade frame of reference at midspan
m = quantities at midspan
$\hat{}$ = quantity scaled by metric Jacobian
$\tilde{}$ = perturbed variables from steady flow
$\bar{}$ = approximated quantities, time or pitch-averaged quantities

where $\mathbf{U}$ is the vector of perturbed variables from a uniform steady flow,

$$\mathbf{U} = (\tilde{p} \;\; \tilde{u} \;\; \tilde{v} \;\; \tilde{w} \;\; \tilde{p})^T \tag{3}$$

and the coefficient matrices $\mathbf{A}$, $\mathbf{B}$, and $\mathbf{C}$ are constant matrices based on the uniform steady variables,

$$\mathbf{A} = \begin{pmatrix} u & 1 & 0 & 0 & 0 \\ 0 & u & 0 & 0 & 1 \\ 0 & 0 & u & 0 & 0 \\ 0 & 0 & 0 & u & 0 \\ 0 & 1 & 0 & 0 & u \end{pmatrix}, \quad \mathbf{B} = \begin{pmatrix} v & 0 & 1 & 0 & 0 \\ 0 & v & 0 & 0 & 0 \\ 0 & 0 & v & 0 & 1 \\ 0 & 0 & 0 & v & 0 \\ 0 & 0 & 1 & 0 & v \end{pmatrix},$$

$$\mathbf{C} = \begin{pmatrix} w & 0 & 0 & 1 & 0 \\ 0 & w & 0 & 0 & 0 \\ 0 & 0 & w & 0 & 0 \\ 0 & 0 & 0 & w & 1 \\ 0 & 0 & 0 & 1 & w \end{pmatrix} \tag{4}$$

Following Giles (1990), the unsteady perturbations and the steady variables in the coefficient matrices have been nondimensionalized using the steady density and speed of sound. The nondimensionalization will simplify the derivation of the nonreflecting boundary conditions.

Eigenvalues and Eigenvectors. Assume the solution of the linearized Euler equations have the following wave-form solution,

$$\mathbf{U} = \exp[i(kx + ly + mz - \omega t)]\mathbf{u} \tag{5}$$

where $\mathbf{u}$ is a constant vector. Substituting this into the linearized Euler equations gives

$$(-\omega\mathbf{I} + k\mathbf{A} + l\mathbf{B} + m\mathbf{C})\mathbf{u} = 0 \tag{6}$$

where $\mathbf{I}$ is the identity matrix. The existence of nontrivial solutions requires that

$$\det(-\omega\mathbf{I} + k\mathbf{A} + l\mathbf{B} + m\mathbf{C}) = 0 \tag{7}$$

The first three roots are identical:

$$k_{1,2,3} = \frac{\omega - vl - wm}{u} \tag{8}$$

The other two roots are

$$k_4 = \frac{(\omega - vl - wm)(S - u)}{1 - u^2} \tag{9}$$

$$k_5 = -\frac{(\omega - vl - wm)(S + u)}{1 - u^2} \tag{10}$$

where

$$S = \sqrt{1 - (1 - u^2)(l^2 + m^2)/(\omega - vl - wm)^2} \tag{11}$$

For subsonic axial velocity, $u < 1$, k_1, k_2, k_3, k_4 correspond to downstream-running waves, while k_5 corresponds to a upstream-running wave.

For constructing nonreflecting boundary conditions, we need to determine the right eigenvector $\mathbf{u}^R$ and the left eigenvector $\mathbf{u}^L$, which satisfy the equations,

$$(-\omega\mathbf{I} + k\mathbf{A} + l\mathbf{B} + m\mathbf{C})\mathbf{u}^R = 0 \tag{12}$$

$$\mathbf{u}^L\mathbf{A}^{-1}(-\omega\mathbf{I} + k\mathbf{A} + l\mathbf{B} + m\mathbf{C}) = 0 \tag{13}$$

For the repeated eigenvalues k_1, k_2, and k_3, one can obtain three sets of right and left eigenvectors,

$$\mathbf{u}_1^R = (-1 \;\; 0 \;\; 0 \;\; 0 \;\; 0)^T \tag{14}$$

$$\mathbf{u}_2^R = [0 \;\; -u\lambda_1 \;\; (1 - v\lambda_1 - w\lambda_2) \;\; 0 \;\; 0]^T \tag{15}$$

$$\mathbf{u}_3^R = [0 \;\; -u\lambda_2 \;\; 0 \;\; (1 - v\lambda_1 - w\lambda_2) \;\; 0]^T \tag{16}$$

$$\mathbf{u}_1^L = (-1 \;\; 0 \;\; 0 \;\; 0 \;\; 1) \tag{17}$$

$$\mathbf{u}_2^L = [0 \;\; -u\lambda_1 \;\; (1 - v\lambda_1 - w\lambda_2) \;\; 0 \;\; -\lambda_1] \tag{18}$$

$$\mathbf{u}_3^L = [0 \;\; -u\lambda_2 \;\; 0 \;\; (1 - v\lambda_1 - w\lambda_2) \;\; -\lambda_2] \tag{19}$$

where, $\lambda_1 = l/\omega$ and $\lambda_2 = m/\omega$.

For the eigenvalue k_4, the right and left eigenvectors are

$$\mathbf{u}_4^R = \frac{1}{2(1 - u)} \begin{pmatrix} (1 - v\lambda_1 - w\lambda_2)(1 - uS) \\ (1 - v\lambda_1 - w\lambda_2)(S - u) \\ (1 - u^2)\lambda_1 \\ (1 - u^2)\lambda_2 \\ (1 - v\lambda_1 - w\lambda_2)(1 - uS) \end{pmatrix} \tag{20}$$

$$\mathbf{u}_4^L = [0 \;\; (1 - v\lambda_1 - w\lambda_2) \;\; u\lambda_1 \;\; u\lambda_2 \;\; (1 - v\lambda_1 - w\lambda_2)S] \tag{21}$$

For the eigenvalue k_4, the right and left eigenvectors are

$$\mathbf{u}_5^R = \frac{1}{2(1 + u)} \begin{pmatrix} (1 - v\lambda_1 - w\lambda_2)(1 + uS) \\ -(1 - v\lambda_1 - w\lambda_2)(S + u) \\ (1 - u^2)\lambda_1 \\ (1 - u^2)\lambda_2 \\ (1 - v\lambda_1 - w\lambda_2)(1 + uS) \end{pmatrix} \tag{22}$$

$$\mathbf{u}_5^L = [0 \;\; -(1 - v\lambda_1 - w\lambda_2) \;\; -u\lambda_1 \;\; -u\lambda_2 \;\; (1 - v\lambda_1 - w\lambda_2)S] \tag{23}$$

It can be verified that the eigenvectors satisfy the following orthogonality relations: $\mathbf{u}_i^L\mathbf{u}_i^R = 0$ $(i = 2, 3, 4, 5)$, $\mathbf{u}_2^L\mathbf{u}_i^R = 0$ $(i = 1, 4, 5)$, $\mathbf{u}_3^L\mathbf{u}_i^R = 0$ $(i = 1, 4, 5)$, $\mathbf{u}_4^L\mathbf{u}_i^R = 0$ $(i = 1, 2, 3, 5)$, $\mathbf{u}_5^L\mathbf{u}_i^R = 0$ $(i = 1, 2, 3, 4)$.

Approximate Three-Dimensional Nonreflecting BCs. As demonstrated by Giles (1990), the general solution form for $\mathbf{U}$ at the boundary is

$$\mathbf{U}(x, y, z, t) = [\sum_{n=1}^{5} a_n\mathbf{u}_n^R e^{ik_n x}]e^{i(ly+mz-\omega t)} \tag{24}$$

The ideal nonreflecting boundary conditions could be obtained by specifying $a_n = 0$ for each n that corresponding to an incoming wave. It can be shown that this is also achieved by specifying,

$$\mathbf{u}_n^L\mathbf{U} = 0 \tag{25}$$

for each of the incoming wave.

Following the derivation of Giles (1990), to obtain the approximate three-dimensional nonreflecting boundary conditions, we expand $\mathbf{v}_n^L$ into a Taylor series and neglect the second-order terms:

$$\bar{\mathbf{u}}_n^L(\lambda_1, \lambda_2) = \mathbf{u}_n^L|_{\lambda_1,\lambda_2=0} + \lambda_1 \left.\frac{\partial \mathbf{u}_n^L}{\partial \lambda_1}\right|_{\lambda_1,\lambda_2=0} + \lambda_2 \left.\frac{\partial \mathbf{u}_n^L}{\partial \lambda_2}\right|_{\lambda_1,\lambda_2=0} \tag{26}$$

which results in the approximate nonreflecting boundary conditions,

$$\bar{\mathbf{u}}_n^L\mathbf{U} = 0 \tag{27}$$

The approximate left eigenvectors are,

$$\bar{\mathbf{u}}_1^L = (-1 \;\; 0 \;\; 0 \;\; 0 \;\; 1) \tag{28}$$

$$\bar{\mathbf{u}}_2^L = [0 \;\; -u\lambda_1 \;\; (1 - v\lambda_1 - w\lambda_2) \;\; 0 \;\; -\lambda_1] \tag{29}$$

$$\bar{\mathbf{u}}_3^L = [0 \;\; -u\lambda_2 \;\; 0 \;\; (1 - v\lambda_1 - w\lambda_2) \;\; -\lambda_2] \tag{30}$$

$$\bar{\mathbf{u}}_4^L = [0 \;\; (1 - v\lambda_1 - w\lambda_2) \;\; u\lambda_1 \;\; u\lambda_2 \;\; (1 - v\lambda_1 - w\lambda_2)] \tag{31}$$

$$\bar{\mathbf{u}}_5^L = [0 \;\; -(1 - v\lambda_1 - w\lambda_2) \;\; -u\lambda_1 \;\; -u\lambda_2 \;\; (1 - v\lambda_1 - w\lambda_2)] \tag{32}$$

Notice the first three eigenvectors are exact. Multiply by ω and replace ω by $-\partial/\partial t$, l by $\partial/\partial y$, and m by $\partial/\partial z$. This results in the inflow boundary condition:

$$\begin{pmatrix} -1 & 0 & 0 & 0 & 1 \\ 0 & 0 & 1 & 0 & 0 \\ 0 & 0 & 0 & 1 & 0 \\ 0 & 1 & 0 & 0 & 1 \end{pmatrix} \frac{\partial U}{\partial t} + \begin{pmatrix} 0 & 0 & 0 & 0 & 0 \\ 0 & u & v & 0 & 1 \\ 0 & 0 & 0 & v & 0 \\ 0 & v & -u & 0 & v \end{pmatrix} \frac{\partial U}{\partial y} + \begin{pmatrix} 0 & 0 & 0 & 0 & 0 \\ 0 & 0 & w & 0 & 0 \\ 0 & u & 0 & w & 1 \\ 0 & w & 0 & -u & w \end{pmatrix} \frac{\partial U}{\partial z} = 0 \quad (33)$$

and the outflow boundary condition,

$$(0\ -1\ 0\ 0\ 1)\frac{\partial U}{\partial t} + (0\ -v\ u\ 0\ v)\frac{\partial U}{\partial y} + (0\ -w\ 0\ u\ w)\frac{\partial U}{\partial z} = 0 \quad (34)$$

Rewrite these equations using one-dimensional characteristics:

$$\frac{\partial}{\partial t}\begin{pmatrix} c_1 \\ c_2 \\ c_3 \\ c_4 \end{pmatrix} + \begin{pmatrix} 0 & 0 & 0 & 0 & 0 \\ 0 & v & 0 & \frac{1+u}{2} & \frac{1-u}{2} \\ 0 & 0 & v & 0 & 0 \\ 0 & -u & 0 & v & 0 \end{pmatrix} \frac{\partial}{\partial y}\begin{pmatrix} c_1 \\ c_2 \\ c_3 \\ c_4 \\ c_5 \end{pmatrix} + \begin{pmatrix} 0 & 0 & 0 & 0 & 0 \\ 0 & w & 0 & 0 & 0 \\ 0 & 0 & w & \frac{1+u}{2} & \frac{1-u}{2} \\ 0 & 0 & -u & w & 0 \end{pmatrix} \frac{\partial}{\partial z}\begin{pmatrix} c_1 \\ c_2 \\ c_3 \\ c_4 \\ c_5 \end{pmatrix} = 0 \quad (35)$$

$$\frac{\partial c_5}{\partial t} + (0\ u\ 0\ 0\ v)\frac{\partial}{\partial y}\begin{pmatrix} c_1 \\ c_2 \\ c_3 \\ c_4 \\ c_5 \end{pmatrix} + (0\ 0\ u\ 0\ w)\frac{\partial}{\partial z}\begin{pmatrix} c_1 \\ c_2 \\ c_3 \\ c_4 \\ c_5 \end{pmatrix} = 0 \quad (36)$$

where the one-dimensional characteristic variable is defined as

$$\begin{pmatrix} c_1 \\ c_2 \\ c_3 \\ c_4 \\ c_5 \end{pmatrix} = \begin{pmatrix} -1 & 0 & 0 & 0 & 1 \\ 0 & 0 & 1 & 0 & 0 \\ 0 & 0 & 0 & 1 & 0 \\ 0 & 1 & 0 & 0 & 1 \\ 0 & -1 & 0 & 0 & 1 \end{pmatrix} \begin{pmatrix} \tilde{p} \\ \tilde{u} \\ \tilde{v} \\ \tilde{w} \\ \tilde{p} \end{pmatrix} \quad (37)$$

An analysis for well-posedness showed that the approximate inlet boundary conditions are ill-posed, while the outlet boundary condition is well posed. Giles (1990) showed that the ill-posedness on the inlet boundary conditions can be removed by modification of the left eigenvector corresponding to the upstream running pressure wave. Following Giles (1990), the left eigenvector $\mathbf{v}_4^L$ is modified as,

$$\bar{\mathbf{u}}_4^L = [0\ \ (1 - v\lambda_1 - w\lambda_2)\ \ -\tfrac{1}{2}(1-u)\lambda_1\ \ -\tfrac{1}{2}(1-u)\lambda_2\ \ (1 - v\lambda_1 - w\lambda_2)] \quad (38)$$

Also, the first left eigenvector is multiplied by a constant $(1 - v\lambda_1 - w\lambda_2)$,

$$\bar{\mathbf{u}}_1^L = [-(1 - v\lambda_1 - w\lambda_2)\ \ 0\ \ 0\ \ 0\ \ (1 - v\lambda_1 - w\lambda_2)] \quad (39)$$

The modified inlet boundary conditions become

$$\frac{\partial}{\partial t}\begin{pmatrix} c_1 \\ c_2 \\ c_3 \\ c_4 \end{pmatrix} + \begin{pmatrix} v & 0 & 0 & 0 & 0 \\ 0 & v & 0 & \frac{1+u}{2} & \frac{1-u}{2} \\ 0 & 0 & v & 0 & 0 \\ 0 & \frac{1-u}{2} & 0 & v & 0 \end{pmatrix} \frac{\partial}{\partial y}\begin{pmatrix} c_1 \\ c_2 \\ c_3 \\ c_4 \\ c_5 \end{pmatrix} + \begin{pmatrix} w & 0 & 0 & 0 & 0 \\ 0 & w & 0 & 0 & 0 \\ 0 & 0 & w & \frac{1+u}{2} & \frac{1-u}{2} \\ 0 & 0 & \frac{1-u}{2} & w & 0 \end{pmatrix} \frac{\partial}{\partial z}\begin{pmatrix} c_1 \\ c_2 \\ c_3 \\ c_4 \\ c_5 \end{pmatrix} = 0 \quad (40)$$

Dimensional Boundary Conditions. These derivations are in dimensionless form. The boundary conditions are rewritten here in dimensional form.

The definition of the one-dimensional characteristic variables is

$$\begin{pmatrix} c_1 \\ c_2 \\ c_3 \\ c_4 \\ c_5 \end{pmatrix} = \begin{pmatrix} -c_2 & 0 & 0 & 0 & 1 \\ 0 & 0 & \rho c & 0 & 0 \\ 0 & 0 & 0 & \rho c & 0 \\ 0 & \rho c & 0 & 0 & 1 \\ 0 & -\rho c & 0 & 0 & 1 \end{pmatrix} \begin{pmatrix} \tilde{p} \\ \tilde{u} \\ \tilde{v} \\ \tilde{w} \\ \tilde{p} \end{pmatrix} \quad (41)$$

At the inlet boundary, the outgoing characteristic variable c_5 is obtained from the interior flow solution; the four incoming characteristic variables c_1, c_2, c_3, c_4 are determined from the following equation:

$$\frac{\partial}{\partial t}\begin{pmatrix} c_1 \\ c_2 \\ c_3 \\ c_4 \end{pmatrix} + \begin{pmatrix} v & 0 & 0 & 0 & 0 \\ 0 & v & 0 & \frac{c+u}{2} & \frac{c-u}{2} \\ 0 & 0 & v & 0 & 0 \\ 0 & \frac{c-u}{2} & 0 & v & 0 \end{pmatrix} \frac{\partial}{\partial y}\begin{pmatrix} c_1 \\ c_2 \\ c_3 \\ c_4 \\ c_5 \end{pmatrix} + \begin{pmatrix} w & 0 & 0 & 0 & 0 \\ 0 & w & 0 & 0 & 0 \\ 0 & 0 & w & \frac{c+u}{2} & \frac{c-u}{2} \\ 0 & 0 & \frac{c-u}{2} & w & 0 \end{pmatrix} \frac{\partial}{\partial z}\begin{pmatrix} c_1 \\ c_2 \\ c_3 \\ c_4 \\ c_5 \end{pmatrix} = 0 \quad (42)$$

At the outlet boundary, the four outgoing characteristic variables c_1, c_2, c_3, c_4 are obtained from the interior solution; the one incoming characteristic variable is determined by Eq. (36), which is the same in dimensional form.

Equations (42) and (36) are transformed into the generalized coordinates and solved using the same integration scheme for the Euler equations. Central difference is used to discretize the pitchwise derivative. A fourth-order artificial dissipation term, similar in form and magnitude to those for the Euler equation, is found to be necessary to remove odd-even decoupling of the solution due to the use of the central difference.

Validation of Nonreflecting Boundary Conditions

A three-dimensional linear cascade is constructed from a two-dimensional cascade geometry. The geometric parameters and blade profiles for the two-dimensional compressor exit guide vane (EGV) cascade are from Verdon et al. (1991). The major

geometric and flow parameters for this cascade flow is given in Table 1.

Two different computational grids have been used for this cascade, one using a large computational domain and the other a short computational domain. The solution using the large computational domain is used as a reference to evaluate the effectiveness of the nonreflecting boundary conditions. The distance between the leading/trailing edge and the inlet/outlet boundary is 100 percent axial chord length for the large computational domain and 20 percent for the small computational domain. The grid for the small domain solution is 69 × 31 × 31 in the streamwise, pitchwise, and spanwise directions respectively. The grid for the large domain solution is 69 × 31 × 31, with 51 streamwise grid points distributed inside the passage for both cases. The number of time steps in each period is 500 for the unsteady computation.

A three-dimensional vortical gust is specified at the inlet boundary. Details on specifying the inlet vortical gust can be found in Verdon et al. (1991). The three-dimensional vortical wave is shown in Fig. 1 for both the constant K plane cut and the constant J plant cut (midpassage plane). The major difference between the three-dimensional vortical wave interaction and a two-dimensional vortical wave interaction is that the three-dimensional vortical wave is periodic in the spanwise direction and reaches the blade leading edge plane at different phase, whereas the vortical wave in a two-dimensional interaction has no phase difference along spanwise direction.

Three different computations are made for the three-dimensional vortical wave interaction. Two computations are made using the small computational domain. One uses the three-dimensional unsteady nonreflecting boundary conditions, the other uses the three-dimensional unsteady nonreflecting boundary conditions. The third computation, using the large computational domain, is used as the reference for evaluating the effectiveness of the nonreflecting boundary conditions.

Figure 2 shows the comparison of instantaneous unsteady pressure distributions ($t/T = 0$) in a constant K plane ($K = 16$). Although both the solution using the three-dimensional and two-dimensional unsteady nonreflecting boundary conditions (top and bottom figures) appear to have numerical reflection at the inlet and outlet boundaries, the magnitude of pressure reflection for the solution using the three-dimensional unsteady nonreflecting boundary conditions is much smaller than that for the solution using the two-dimensional unsteady nonreflecting boundary conditions. Figure 3 shows instantaneous unsteady pressure contours on constant J plane coinciding with the suction surface. Significant pressure reflections can be found for the solution using the two-dimensional unsteady nonreflecting boundary conditions. The solution using the three-dimensional unsteady nonreflecting boundary conditions indicates little pressure reflections. The comparison clearly indicates the advantage of the three-dimensional unsteady nonreflecting boundary conditions over the two-dimensional unsteady nonreflecting boundary conditions as evidenced by the reduction of numerical reflections at the inlet/outlet boundaries for three-dimensional vortical wave interactions. Another important feature shown in Figs. 2–3 is that the unsteady pressure field is highly three dimensional. In fact, the instantaneous unsteady pressure is periodic along the spanwise direction. This phenomenon does not exist in a two-dimensional vortical wave interaction, where there is no spanwise variation.

Figure 4 shows the distribution of the first harmonic of the unsteady pressure difference across the blade at the $z = 0$ plane. Also included is the corresponding two-dimensional vortical wave interaction solution using the linearized potential method

Table 1 Compressor EGV cascade parameters, from Verdon et al. (1991)

Pitch/Chord (P_b/c)	0.6
Stagger angle	15^o
Steady inflow angle	40^o
Steady inlet Mach number	0.3
Wake number n_w/n_b	1.0
Fractional velocity defect	5%
Reduced frequency (Ω)	11.16

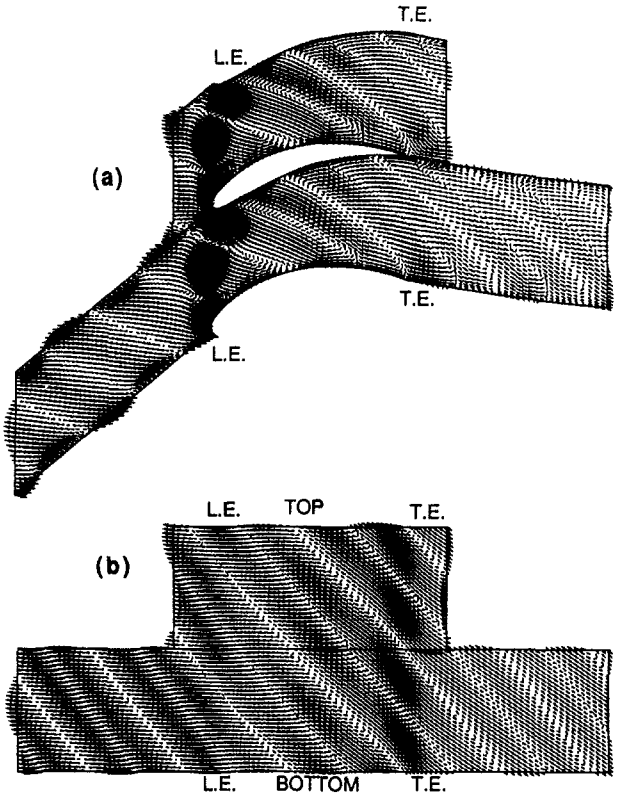

Fig. 1 Unsteady velocity vectors (mean flow subtracted) for three-dimensional vortical interaction: (*a*) constant *K* plane ($k = 16$); (*b*) constant *J* plant ($J = 16$)

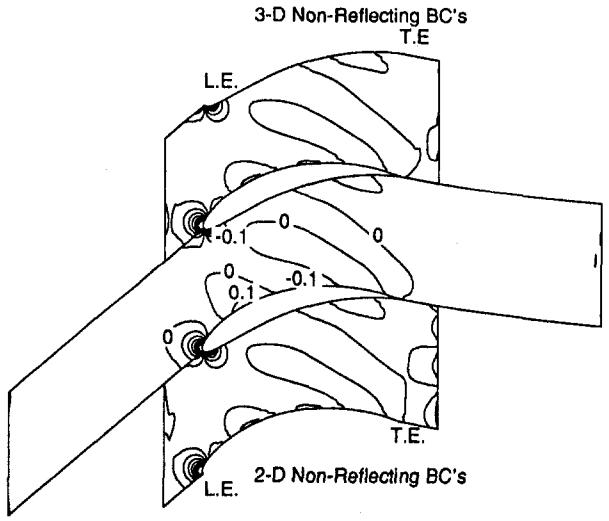

Fig. 2 Unsteady pressure contours (mean flow subtracted) for three-dimensional vortical interaction ($k = 16$ plane), top: small domain with three-dimensional nonreflecting BCs, middle: large domain, bottom: small domain with two-dimensional nonreflecting BCs

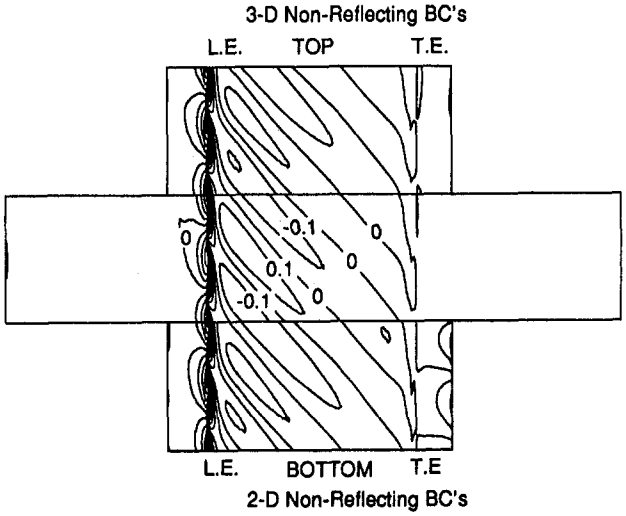

Fig. 3 Unsteady pressure contours (mean pressure subtracted) for three-dimensional vortical interaction (J = 1 plane, pressure surface), top: small domain with three-dimensional nonreflecting BCs, middle: large domain, bottom: small domain with two-dimensional nonreflecting BCs

by Verdon et al. (1991). It is clear that the predicted distributions of the first harmonic of surface pressure difference derived from both the large domain solution and the small domain solution agree very well with each other, indicating the effectiveness of the three-dimensional unsteady nonreflecting boundary conditions. Figure 4 also shows that there is significant difference in unsteady blade pressure response to three-dimensional and two-dimensional vortical waves. This is indicated by the large difference between the unsteady blade pressure distributions from two-dimensional and three-dimensional predictions.

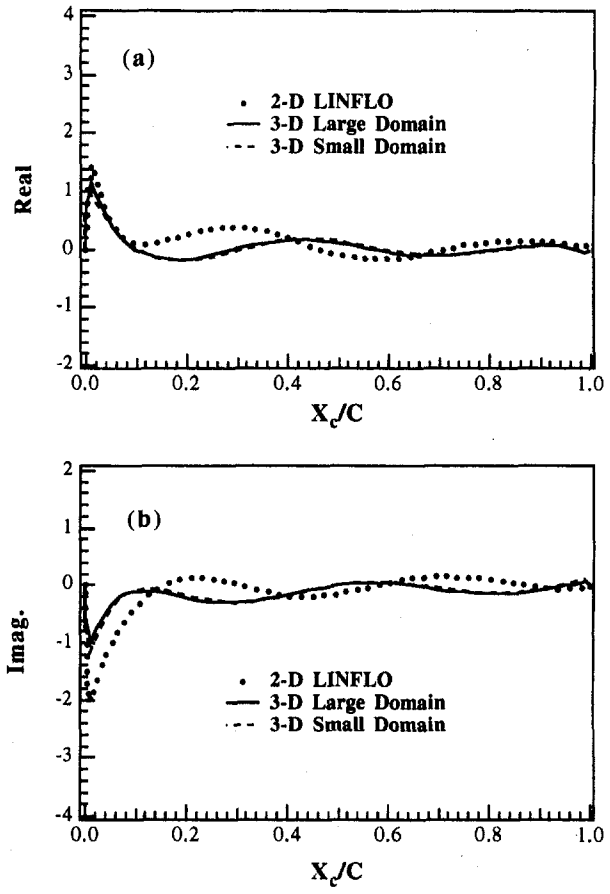

Fig. 4 First harmonic of unsteady pressure difference across the blade (normalized by $\rho_{is}q_{is}q_n$), for three-dimensional vortical interaction

Three-Dimensional Wake and Secondary Flow/Rotor Interaction in a Turbine Stage

Simulation Case and Grid. The code has been used to compute the three-dimensional nozzle wake and secondary flow/rotor interaction in the Penn State large-scale low-speed turbine stage for which extensive data are available. The turbine has a hub tip ratio of 0.73 with an outer casing wall diameter of 0.914 m. The number of blades is 23 for the nozzle and 29 for the rotor. The vane–blade axial spacing is 20 percent of the nozzle axial chord at the midspan. The design mass flow rate and rotational speed are 11.05 kg/s and 1300 rpm, respectively. The loading coefficient ψ ($\psi = \Delta H/0.5\rho U_m^2$) at the midspan is 3.76. The nozzle has a nearly uniform turning of 70 deg, while the rotor has a maximum turning of 120 deg at the hub and a minimum turning of 93 deg at the tip. To accommodate the large spanwise change in blade turning angle, the leading edge of the rotor blade is designed to lean toward the direction of rotation. The reduced frequency Ω based on the midspan quantities is about 9.4. Details of the facility and blade profile data can be found in Lakshminarayana et al. (1992) and Zaccaria (1994).

The computational mesh for the rotor solution is shown in Fig. 5. The three-dimensional H-grid was generated using a interactive program developed by Beach (1990). The mesh is 66 × 39 × 25. In order to apply spatial periodic boundary conditions, five rotor passages are solved simultaneously, corresponding to a nozzle/rotor blade count ratio of 4:5, which is close approximation of the actual number 23:29. For the time-accurate computation, five wake passing periods, with 1200 time steps per period, are computed to achieve periodic solution.

Inlet Flow Properties and Steady Flow Solution. For the steady flow solution, radial distributions of total pressure, total temperature, and flow angle at the inlet of the rotor and radial

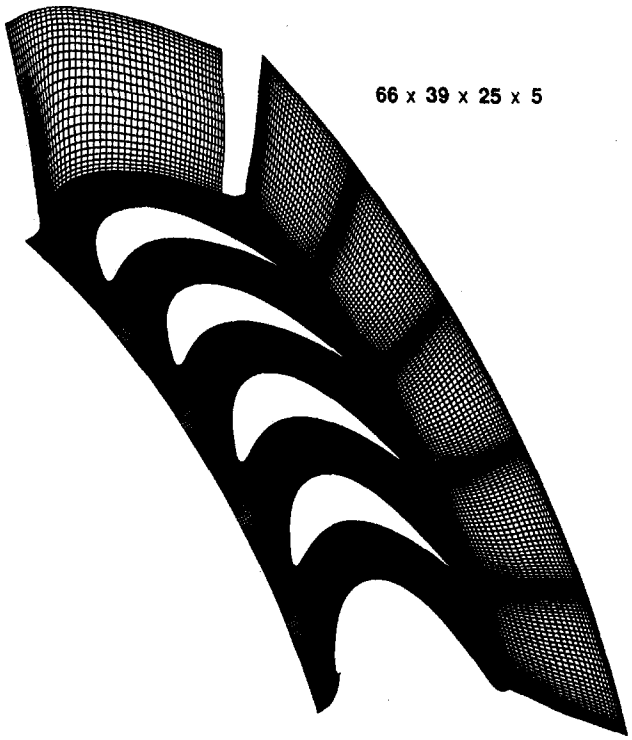

Fig. 5 Computational grid for three-dimensional turbine rotor

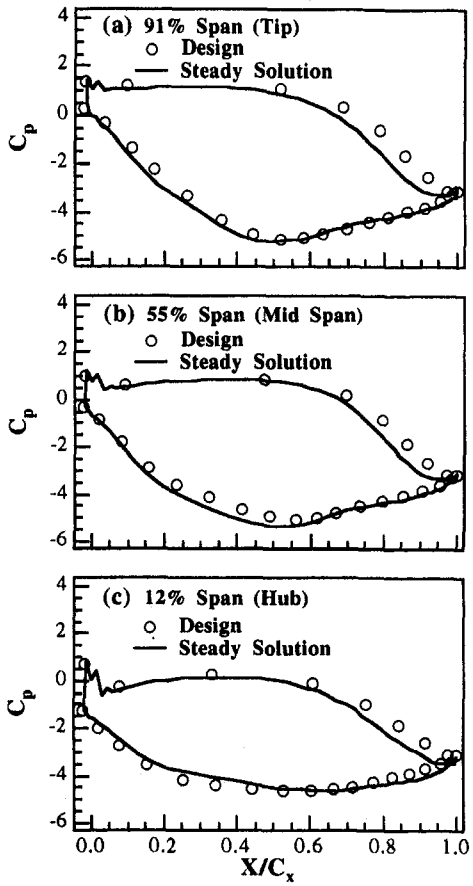

Fig. 6 Comparison of steady pressure coefficient with design values

distribution of static pressure at the outlet of the rotor are specified as the input conditions, which are derived from the experimental data. The data was acquired with a five-hole probe at 21 radial and 80 tangential locations (hub-to-tip, blade-to-blade) at 9 percent axial chord down stream of the nozzle trailing edge. The steady static pressure coefficients on rotor blade are plotted in Fig. 6 for the hub, midspan and tip sections (12, 55, and 91 percent blade height from the hub). The predictions agree well with the design values, except near the trailing edge of the pressure surface. Figure 7 compares the computed blade-to-blade distributions of relative velocity with the LDV data (Zaccaria, 1994) at three axial locations for the midspan section. Good agreement between the computed distribution and the

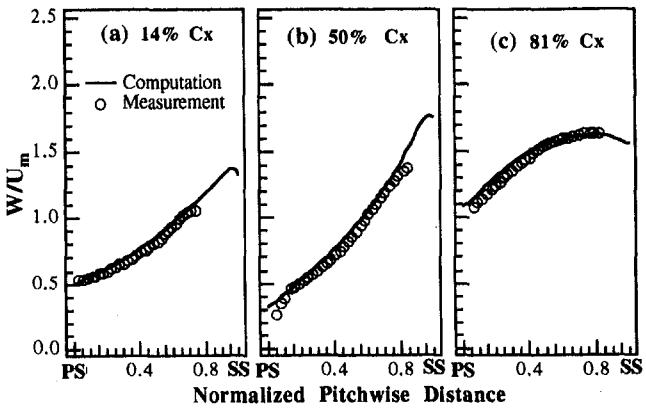

Fig. 7 Comparison of steady relative velocity distribution in the rotor blade passage

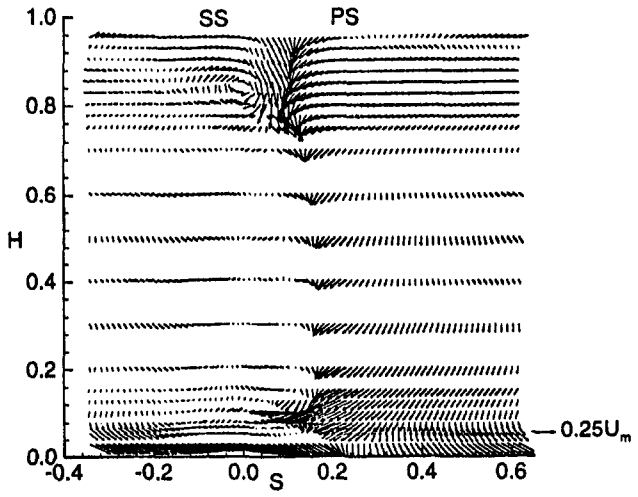

Fig. 8 Secondary flow velocity vectors at 9 percent axial chord down stream of the nozzle (Zaccaria and Lakshminarayana, 1992)

design and measured pressure and/or velocity data suggests that the steady flow field in the rotor passage is captured well.

For the computation of the unsteady rotor flow, the pitchwise and radial distributions of unsteady pressure and unsteady velocity (unsteady in rotor frame and steady in nozzle frame of reference) are specified as the input conditions for the time accurate solution. These properties are derived from the measured data at 9 percent axial chord downstream of the nozzle trailing edge (Zaccaria and Lakshminarayana, 1992). These distributions are shown in Figs. 8 and 9. Figure 8 shows the secondary velocity vectors over a single nozzle passage. The secondary flow is fairly strong in both the annulus wall and hub wall regions and the wakes are thin. The unsteady velocity shown on the top of Fig. 9 is defined as the difference between the instantaneous velocity and the steady velocity. The wakes are indicated by the shadow region. Large unsteady velocities appear at about 10 and 77 percent blade height from the hub on the suction side of the wakes. These originate from the nozzle secondary flow and vortices. The distribution of instantaneous static pressure upstream of the rotor shown in Fig. 9 indicates that both the vortical interaction due to nozzle wake and secondary flow and the potential interaction due to the nozzle pressure field will contribute to the unsteady flow in the rotor blade passages. Furthermore, the flow is highly three-dimensional with differences in wake structure (profile, maxi-

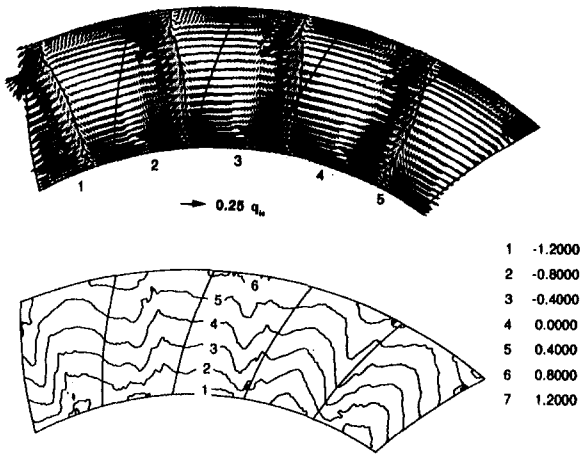

Fig. 9 Unsteady inlet conditions, top: wake and secondary velocity vectors ($V(t) - \bar{V}$), bottom: static pressure coefficient (C_p) contours

mum defect, trajectories), as well as appreciable static pressure gradients in the radial and tangential directions.

Unsteady Wake Transport at the Rotor Midspan. Figure 10 shows the transport of nozzle wakes through the rotor blade passage at the midspan section. At the reduced frequency of 9.4, there are about two wakes in the computational domain at any given instant of time. For this reason, six instantaneous snap shots of the unsteady passage flow over two blade passing periods are shown in Figs. 10(a) and 10(b) to demonstrate the wake transport process through the blade passage. In Fig. 10, the unsteady velocity vectors (steady flow field subtracted) are plotted with the nozzle wakes indicated by the shadow region (positive entropy).

At t/T = 0.0, a new wake comes into the computational domain. In the rotor frame of reference, the wake appears as a negative jet from pressure to suction surface. At t/T = 0.4, the nozzle wake reaches the leading edge of the blade. At this time, the lower part of the wake is not yet influenced by the blade. The part of wake near the suction surface side is deformed considerably and is carried farther downstream along the passage due to high local velocity. In the top passage, the part of wake near the midpassage has been transported much further downstream than the part near the pressure surface, forming a

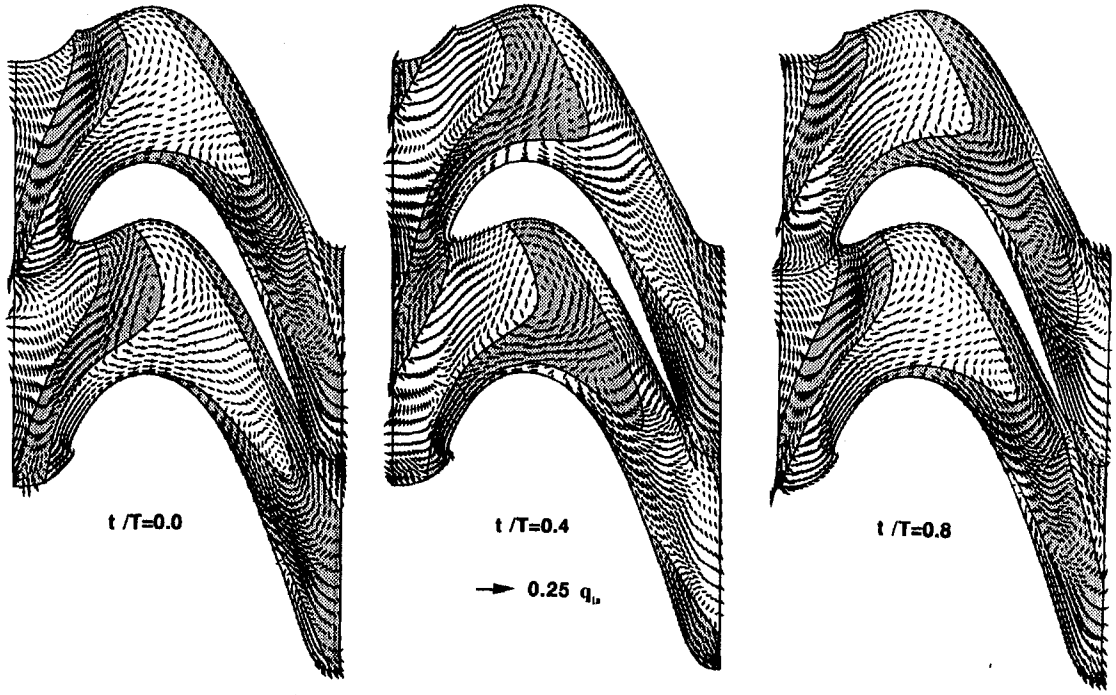

Fig. 10(a) Unsteady wake transport at midspan ($V(t) - \bar{V}$), t/T = 0.0, 0.4, 0.8, wake is indicated by shadow region

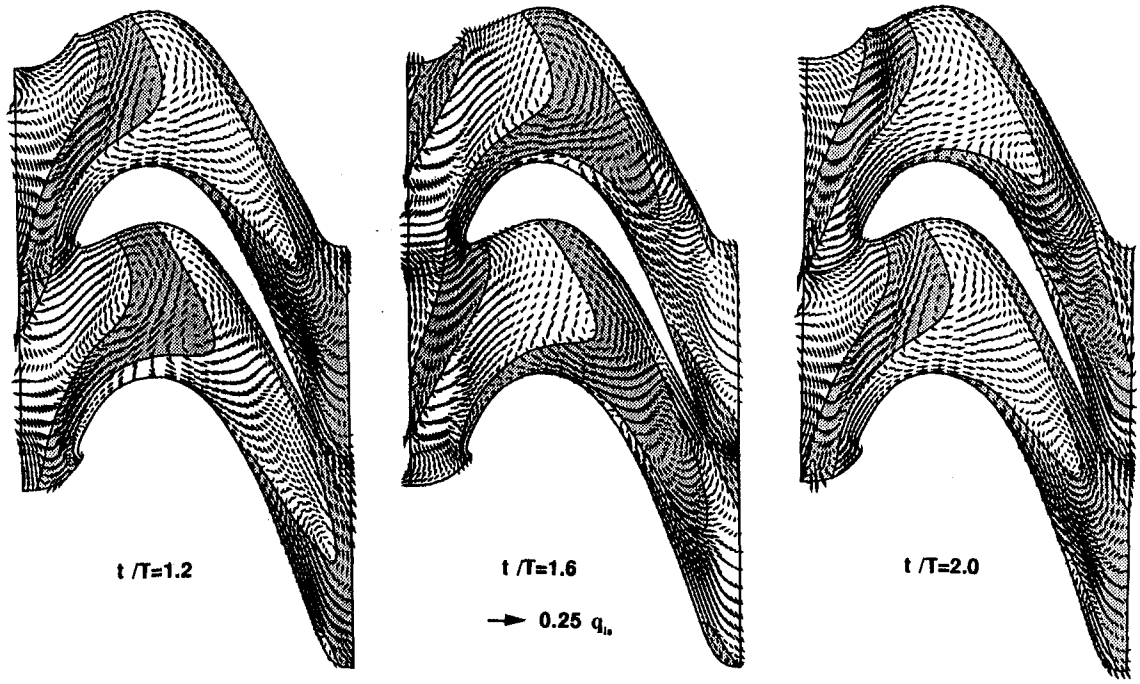

Fig. 10(b) Unsteady wake transport at midspan ($V(t) - \bar{V}$), t/T = 1.2, 1.6, 2.0, wake is indicated by shadow region

bowed and distorted wake. At $t/T = 0.8$, the wake is chopped apart by the leading edge of the blade. The wake segment on the suction surface is stretched to nearly half the blade suction surface length due to very strong flow acceleration at this location. The wake segment in the top passage becomes even more bowed. The wake segment near the pressure surface side also starts to elongate as it reaches the accelerating flow region. During the wake cutting process, recirculating flows are developed on either side of the wake, with a clockwise-rotating vortex upstream of the wake segment and a counterclockwise-rotating vortex downstream of the wake segment. At $t/T = 1.2$, the two wake segments become completely separated and are convected downstream independently. The center part of the wake segment in the top passage already reached the outlet boundary, while the segment in the bottom passage just starts to become bowed. In the top passage, the migration of wake fluid toward the suction surface results in a much wider wake on the suction surface than that on the pressure surface. At $t/T = 1.6$, most part of the wake segment in the top passage has been convected out of the outlet boundary. The wake segment on the pressure surface side is still in the bottom passage. At $t/T = 2.0$, the wake segment in the bottom passage reaches the outlet boundary. In the mean time, in the top passage, a wake segment from the wake that came in one period later almost caught up with the earlier wake segment in the bottom blade passage. This is the result of the very large difference in steady velocity on the suction side and the pressure side of the blade. At 50 percent axial chord, the peak velocity on the suction side is about six times larger than the peak velocity on the pressure side (see Fig. 7(*b*)). Upon passing through the blade passage, the wake is counterclockwisely rotated and the width of the wake segment significantly increased. The above-described characteristics on wake transport qualitatively agree with earlier observations by other investigators in two-dimensional wake/rotor interactions, such as Hodson (1985) and Korakianitis (1993).

Figure 11 shows the instantaneous unsteady pressure distributions at the corresponding six instant of time during two blade passing periods. Close examination and comparison of Figs. 10 and 11 revealed three major features in the unsteady pressure distribution. First, the nozzle potential field, which can be clearly seen near the inlet boundary, has significant influence on unsteady pressure distribution. However, due to its fast decaying nature, its major effects on blade surface unsteady pressure is expected to be confined to the leading edge area. Secondly, no significant generation of unsteady pressure is accompanied by the chopping of wakes by the blade leading edge. This is very different from the case in a compressor cascade, where wake cutting creates very strong unsteady pressure near the leading edge of the blade. The difference is attributed to the different velocity triangles. As demonstrated by Manwaring and Wisler (1993), in the rotor frame of reference, a compressor wake results in large changes in both flow angle (incidence) and transverse velocity, but small change in the streamwise unsteady velocity, while a turbine wake results in large change in the streamwise unsteady velocity, but small changes in the incidence and the transverse unsteady velocity. It can be seen in Fig. 10 that when the wake is cut by the leading edge of the blade, the orientation of the wake and the unsteady velocity vectors in the wake is such that no significant change in incidence is resulted from the unsteady wake. This explains the fact that no significant unsteady pressure is accompanied by the wake. Finally, the unsteady pressure distribution is closely related to the unsteady recirculating vortices. In agreement with Korakianitis' (1993) observation, it is found that the upstream clockwise-rotating vortex causes a local increase in the unsteady pressure near the blade, and the downstream counterclockwise-rotating vortex causes a local decrease in pressure.

Transport of Three-Dimensional Wake and Secondary Flow in the Rotor Blade Passage. The transport of three-dimensional wake and end wall secondary flow through the rotor blade passage is studied through examination of the constant J planes corresponding to the suction and the pressure surfaces from hub to tip. Figure 12 shows the unsteady velocity vectors and trace of wakes and secondary flow on the $J = 1$ plane (suction surface) at six instants of time during two blade passing periods. The wake is indicated by the shadow region corresponding to positive entropy value.

At $t/T = 0.0$, a new nozzle wake and secondary flow comes in from the upper left corner of the domain. This is due to the fact that the rotor blade is leaned toward the direction of rotation. The radial orientation of the blade leading edge results in the fact that the tip of the blade encounters the nozzle wake ahead of the blade near the hub. At $t/T = 0.4$, the part of the new wake near the tip of the blade has been cut by the leading edge and spreads to about 60 percent of the blade axial chord, while the part of the wake near the hub of the blade just reaches the leading edge of the blade. The presence of radial outward flow shortly downstream of the wake and a radial inward flow inside and shortly upstream of the wake can be clearly seen from the unsteady velocity vectors. The radial flow originates from the nozzle exit secondary velocity profiles shown in Fig. 9. In Fig. 9, the unsteady velocity vectors also show large tangential velocity component near the tip and hub on the left hand side of the wake, coinciding with the locations of nozzle secondary vortices. When transported through the blade passage, it is expected that the large tangential velocity component will generate strong flow impingement on the suction surface immediately downstream of the wake. The saddle point flow pattern at about 80 percent of the blade height and shortly downstream of the wake at $t/T = 0.4$ is a clear evidence of this impingement. At this moment the impingement flow near the hub is just starting to form and has a much weaker strength.

At $t/T = 0.8$, the downstream side of the nozzle wake near the blade tip reaches the trailing edge, while the upstream side of the wake near the hub enters the passage. At this instant of time, a strong impingement flow pattern can be seen near the hub of the blade downstream of the wake. At $t/T = 1.2$, the above-mentioned wake reaches the outlet boundary and the corresponding impingement flow pattern near the bottom of the blade is still visible near the trailing edge. At this time, another impingement flow pattern associated with a new wake has been formed at about 80 percent blade height and 40 percent axial chord. Because the two impingement flow patterns occur at different axial locations, strong instantaneous radial flows are induced near the suction surface of the blade, resulting in a complex three-dimensional pattern in the unsteady flow field.

It is thus evident that the three-dimensional nozzle wake and the secondary flow induce strong three dimensionality in the rotor flow field. In addition to counterrotating vortices in the blade-to-blade plane, the rotor flow perceives strong unsteady impingement flow, and radial inward and outward flow (possibly counterrotating vortices in the hub-to-tip plane) upstream and downstream of the wake during its passage. Thus the unsteady flow field is highly three dimensional in nature.

The distributions of instantaneous unsteady pressure on the suction surface of the blade are shown in Fig. 13 for the corresponding six instants of time. Examination of Fig. 12 and Fig. 13 shows that the unsteady pressure distribution is closely related to the impingement flow patterns shown in Fig. 12. First of all, the spanwise locations where the unsteady pressure peaks and troughs occur match the spanwise location of the saddle points of the unsteady impingement flow patterns. A detailed examination of Figs. 12 and 13 reveals that typically a high-pressure peak appears upstream of the impingement flow saddle point and a low-pressure trough appears downstream of the impingement flow saddle point. The strength of the unsteady pressure peaks and troughs appears to increase as the impingement flow moves from the leading edge to the suction surface, and decrease when it moves toward the trailing edge.

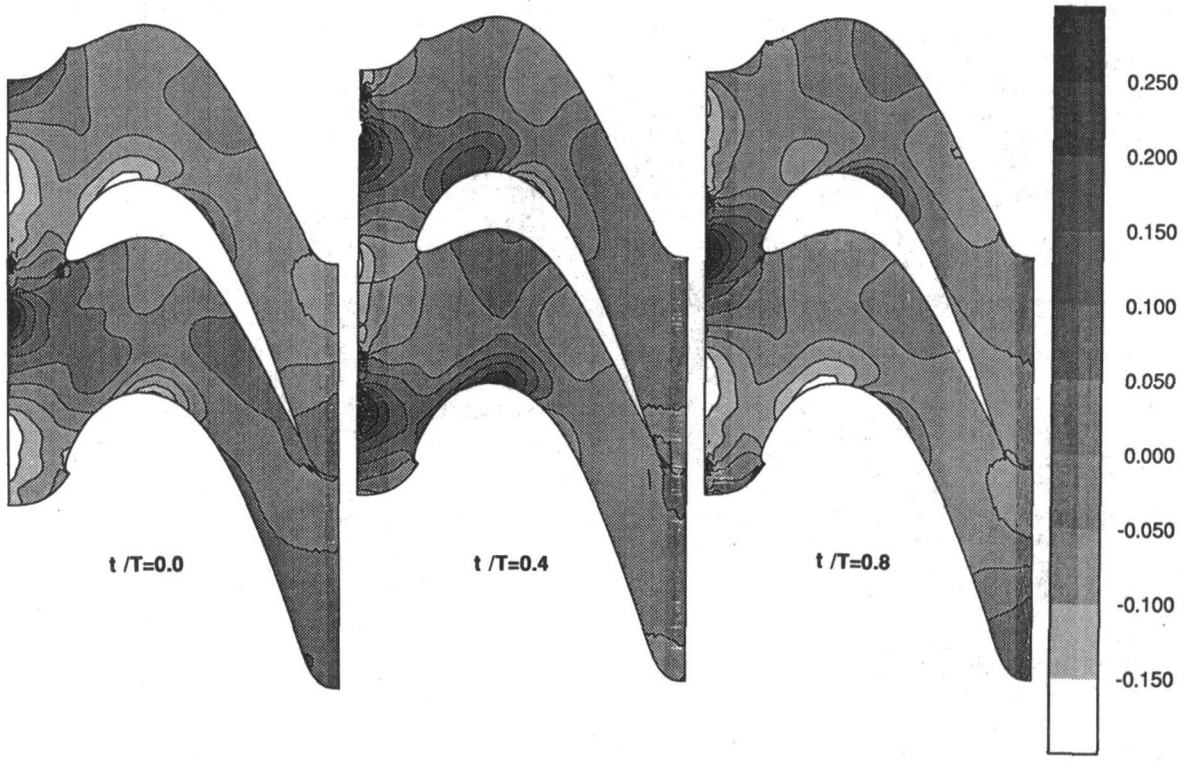

Fig. 11(*a*) Unsteady pressure coefficient ($C_p - \bar{C}_p$) contours at midspan, t/T = 0.0, 0.4, 0.8

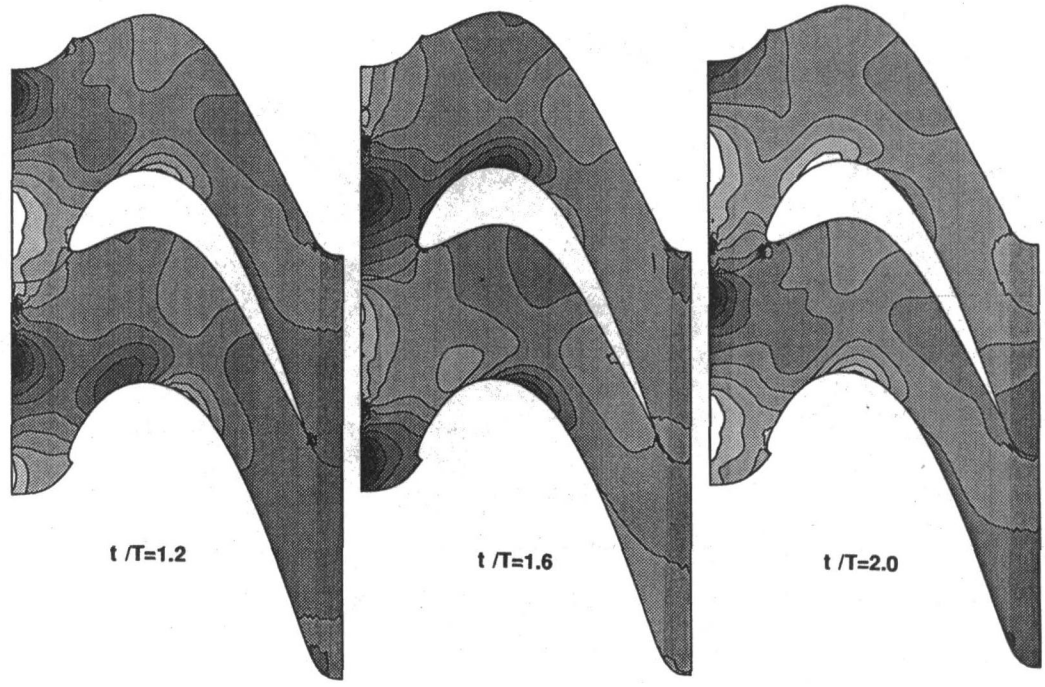

Fig. 11(*b*) Unsteady pressure coefficient ($C_p - \bar{C}_p$) contours at midspan, t/T = 1.2, 1.6, 2.0

Figure 14 shows the unsteady velocity vectors and trace of wakes and secondary flow on the J = 39 plane (pressure surface) at six instants of time during two blade passing periods. One distinct feature evident in Fig. 14 is that there are more wakes and secondary flow regions on the pressure surface at each instant of time; this is due to the fact that local convection velocity is much smaller on the pressure surface than that on the suction surface. Also, the width of the nozzle wake and secondary flow region is much smaller on the pressure surface than that on the suction surface. The width of a wake and secondary flow region remains very narrow until it reaches about 70 percent of the axial chord where the steady flow starts to accelerate significantly. Although the wake and secondary flow region near the tip of the blade reaches the leading edge at an earlier time than the wake and secondary flow region near the hub of the blade, the axial location of the wake and secondary flow in the blade passage is nearly constant on the pressure surface before it reaches the aft-part of the blade. This is also

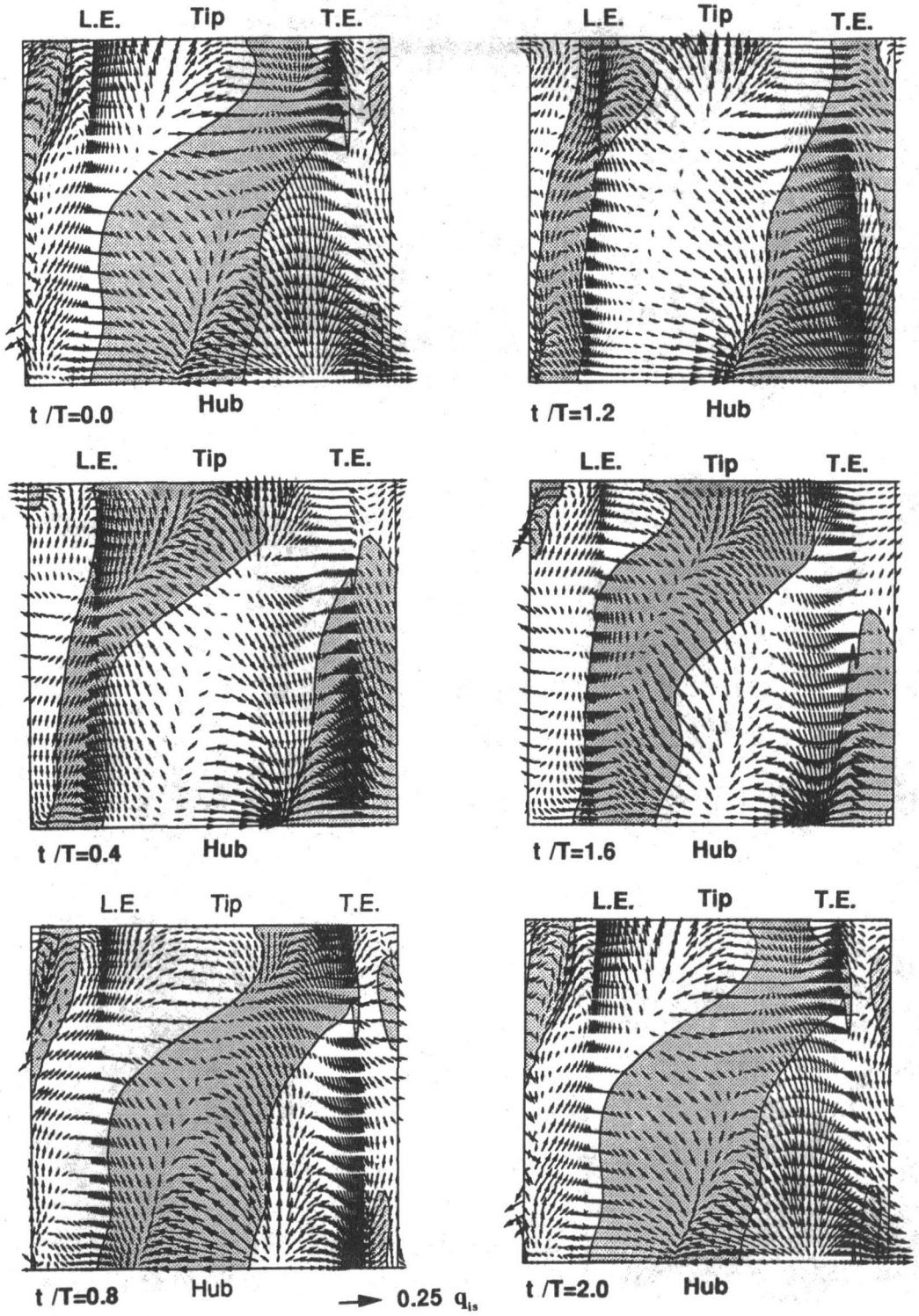

Fig. 12 Unsteady wake transport at $J = 1$ plane (suction surface), $V(t) - \bar{V}$, wake is indicated by shadow region

because of the slow convection speed on the pressure surface. The unsteady flow on the surface is highly three dimensional. Radial flows are generated due to radially inward velocity in the wake, suction and impingement flow patterns due to nozzle wake and secondary flows.

Figure 15 shows the instantaneous unsteady velocity vectors and nozzle wake traces at $I = 36$ (midchord) and $I = 59$ (trailing edge) planes. Very complex three-dimensional flow patterns can be seen in this unsteady velocity field data. Instantaneous suction and impingement flow patterns on both the blade surfaces and the end walls can be identified. Significant unsteady radial velocity appears even at the midspan of the passage. It will be shown that even though the steady flow is nearly two dimensional near the midspan, the unsteady flow is three dimensional in the rotor and cannot be modeled by a two-dimensional analysis. Another important feature shown in this figure is that the unsteady flow field as well as the wake trace differs from one blade passage to another. This is a result of the differing blade numbers between the nozzle and the rotor. The unsteady wake transport in each passage has a phase difference from

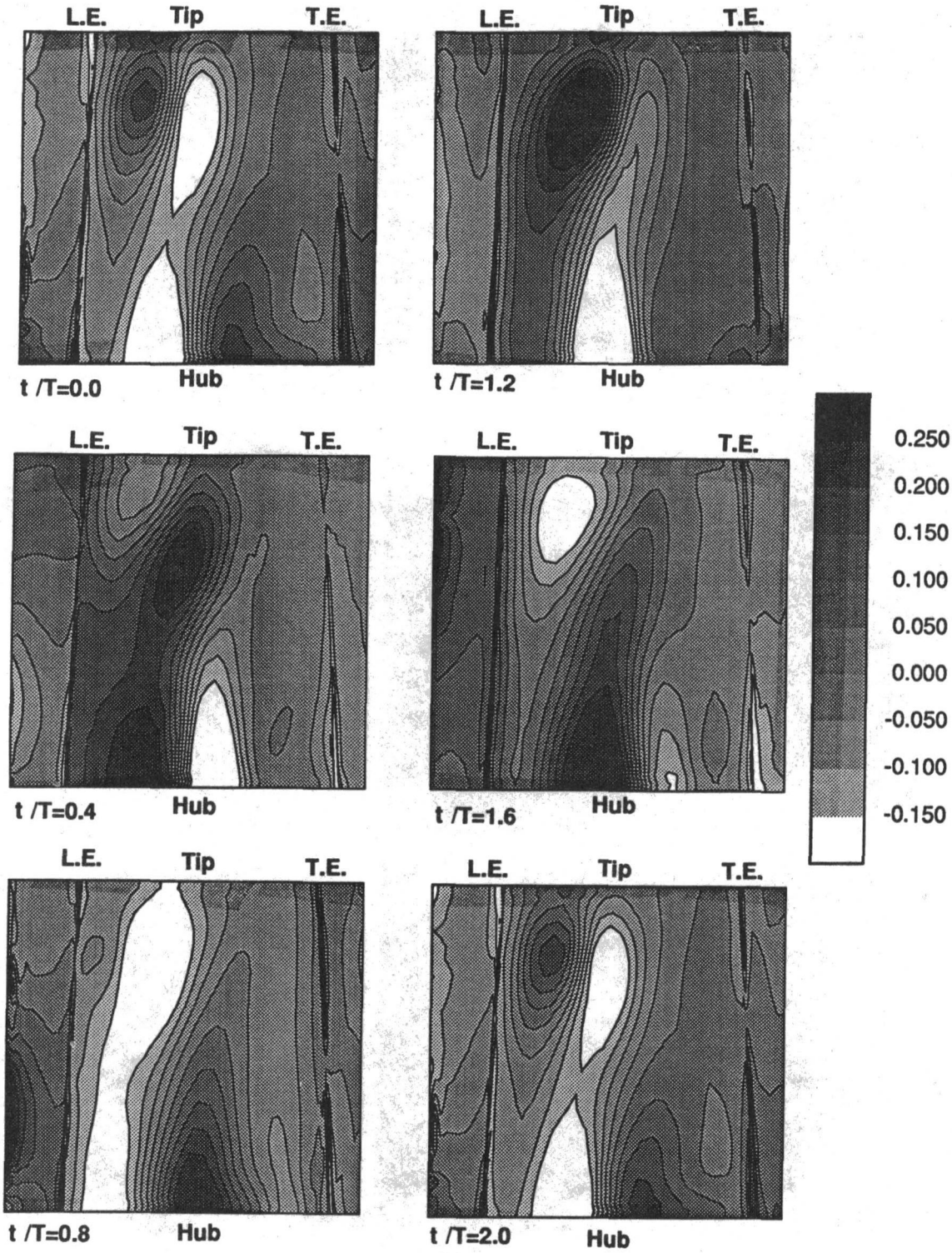

Fig. 13 Instantaneous unsteady pressure coefficient ($C_p - \bar{C}_p$) contours at $J = 1$ plane (suction surface)

the neighboring passages. Even in the same passage, the wake transport differ in phase in the blade-to-blade direction and from hub-to-tip. A large difference in convective velocity between the suction surface and the pressure surface results in distorted wake; the wake near the suction surface reaches the trailing edge plane ahead of the wake near the pressure surface. This results in the discontinuous wake traces across the blade trailing edge.

The wakes and secondary flow patterns are distorted and twisted in both the blade-to-blade plane as well as in the hub-to-tip plane, resulting in highly three-dimensional unsteady flow pattern. The trace of the wake and secondary flow region at any given location is three dimensional in nature. Inward and outward flow exist both within and outside these traces.

The amplitude of unsteady pressure on the blade surfaces is shown in Fig. 16. The amplitude of unsteady pressure is defined as the difference between the maximum and the minimum pressure at a spatial location over a blade passing period. Figure 16 clearly shows that the periodic unsteady pressure fluctuation is much stronger on the suction surface than on the pressure sur-

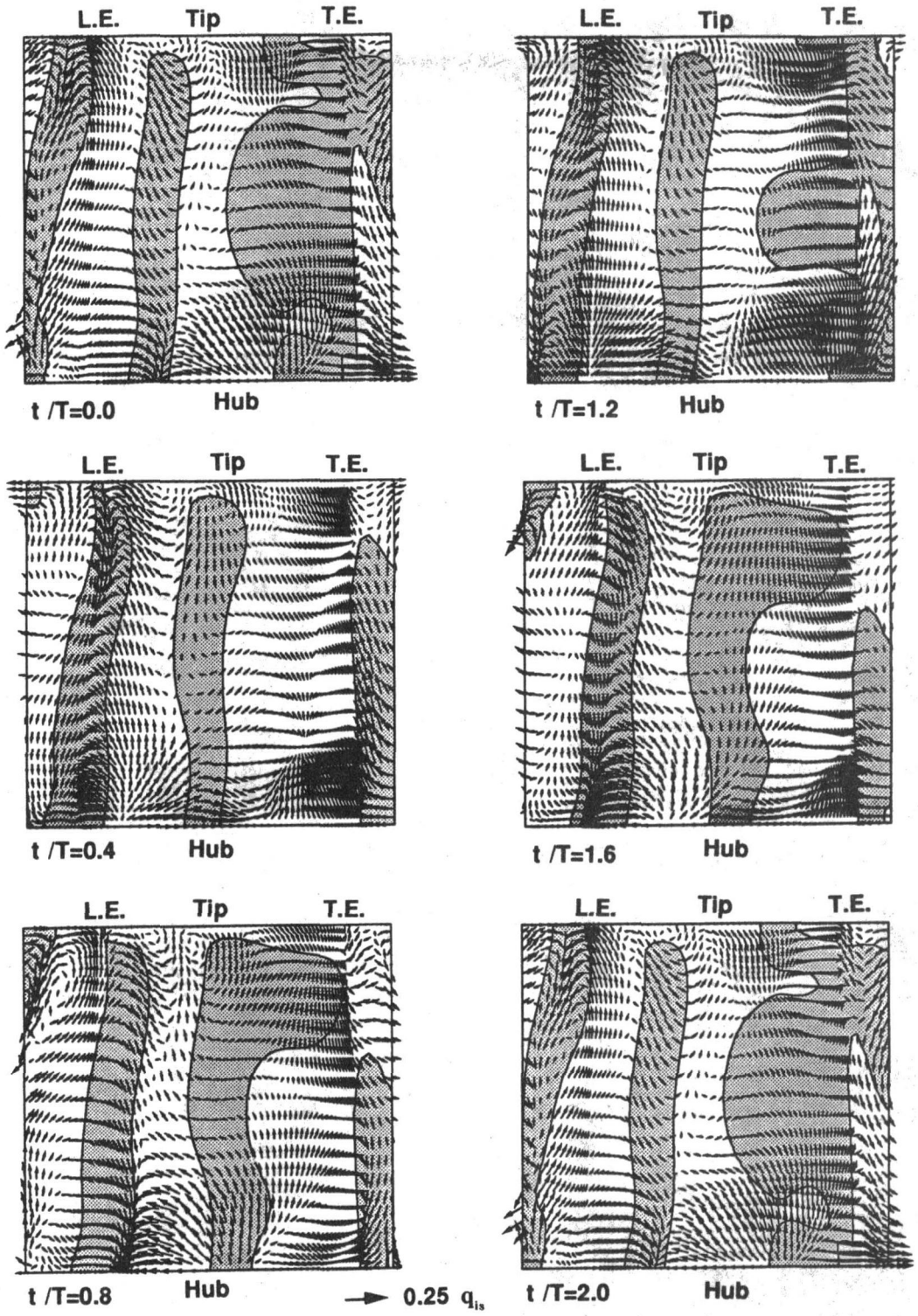

Fig. 14 Unsteady wake transport at $J = 39$ plane (pressure surface), $V(t) - \bar{V}$, wake is indicated by shadow region

face. On the suction surface, two strong peaks appear in the distribution of the unsteady pressure amplitude, one near the hub and the other near the tip of the blade. The spanwise locations of the maximum pressure fluctuation generally match the location of the nozzle secondary vortices at the inlet. Unlike the compressor case, the maximum unsteady pressure occurs further downstream of the leading edge. As discussed earlier, this difference is attributed to the differing velocity triangles encountered in compressors and turbines. The peak values on the pressure surface are much smaller than those on the suction surface.

In order to identify the source of strong unsteady pressure peaks near end wall, a simulation case has been carried out to isolate the effects of the inlet nozzle secondary flow from those due to nozzle wakes. In this simulation case, the measured wake profile at the midspan section has been extended over the entire blade span and used as the unsteady inlet conditions for the three-dimensional Euler solution. The nozzle secondary flow vortices are effectively eliminated from the unsteady inlet condition. Therefore, their effects on the unsteady pressure on the blade surface could be identified through a comparison of the

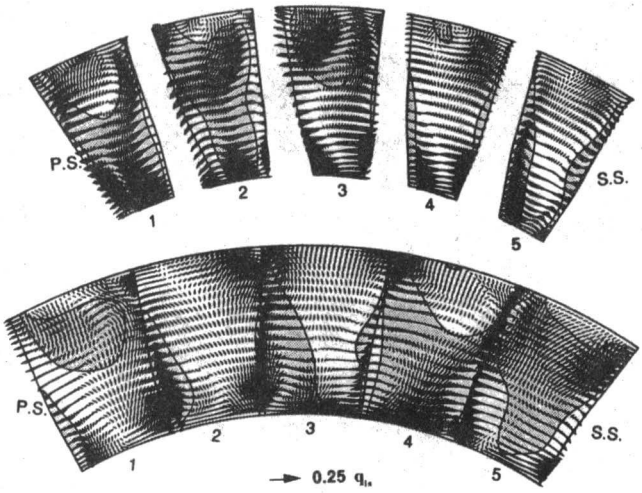

Fig. 15 Unsteady wake transport at constant I plane, top: I = 36, mid-chord, bottom: I = 59, trailing edge, $V(t) - \bar{V}$, wake is indicated by shadow region

computations with and without secondary flow as the unsteady inlet conditions. This study has been carried out to isolate the effects of secondary flow and wake flow from the combined effects observed in Figs. 12–16.

The unsteady pressure contours (amplitude) on the blade surfaces, with only unsteady nozzle wakes (and without the secondary flow vortices), are plotted in Fig. 17 in the same scale as Fig. 16 (wake and secondary flow). It is clear from a comparison between Figs. 16 and 17 that the distributions of unsteady pressure amplitudes are substantially different for the

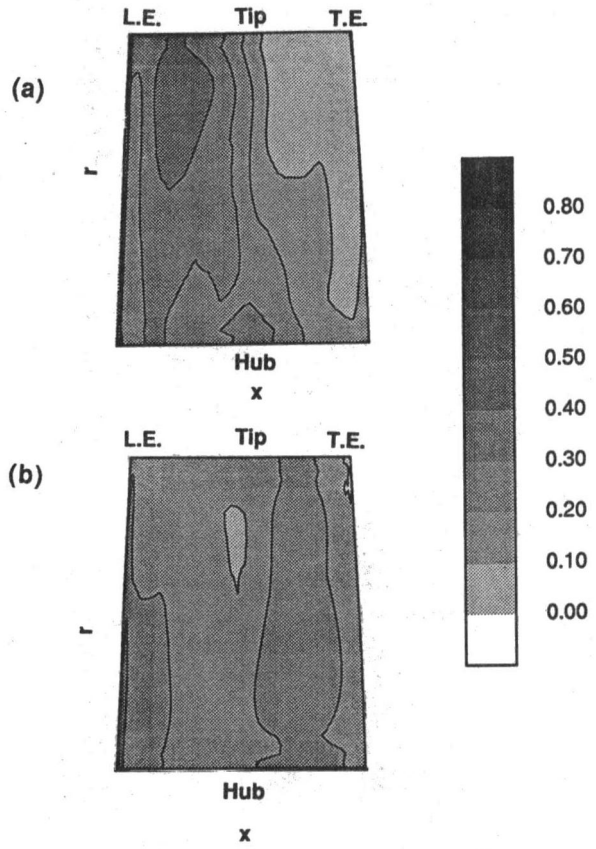

Fig. 17 Amplitude of unsteady pressure coefficient ($C_p - \bar{C}_p$) on blade surfaces (wake only), (*a*) suction surface, (*b*) pressure surface

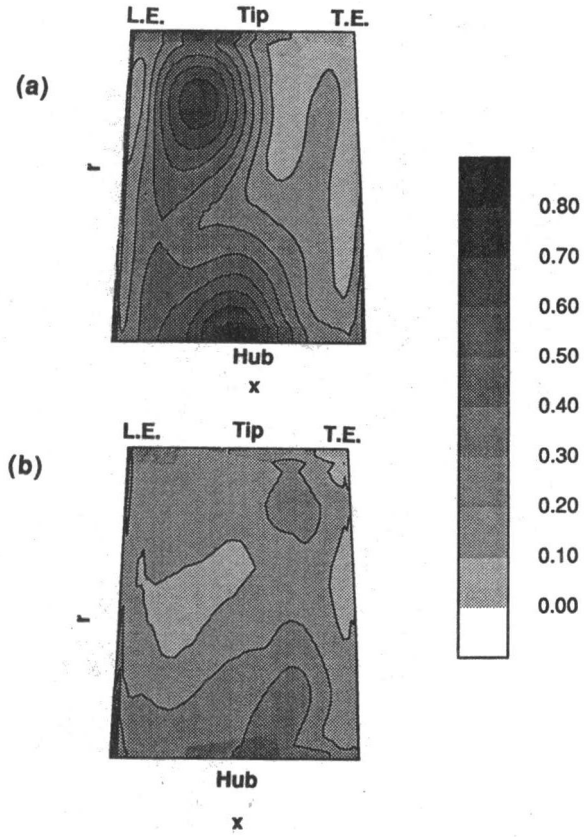

Fig. 16 Amplitude of unsteady pressure coefficient ($C_p - \bar{C}_p$) on blade surfaces (wake and secondary flow), (*a*) suction surface, (*b*) pressure surface

cases with and without inlet nozzle secondary flow. On the suction surface, the magnitude of the two strong peaks of unsteady pressure amplitude, shown in Fig. 16(a), has been substantially reduced with the removal of nozzle secondary flow in the unsteady inlet condition (see Fig. 17(a)). On the pressure surface, the two weaker peaks, shown in Fig. 16(b), almost completely vanish (see Fig. 17(b)). The unsteady pressure amplitude, caused by wake alone, is much more uniformly distributed in the spanwise direction compared with the one with both the nozzle wakes and the nozzle secondary flows. It is evident from this comparison that the nozzle secondary flow vortices have a strong influence on the generation of unsteady pressure on the blade surfaces, especially near the tip and hub of the rotor blade.

Figure 18 shows the predicted chordwise distributions of the amplitude of unsteady pressure on the blade for three representative spanwise locations, for both cases with and without nozzle secondary flows. Also shown in this figure is the unsteady pressure derived from a two-dimensional unsteady solution at the midspan section. Because secondary flows and vortices are present near the tip and the hub of the blade, their effect on the midspan section is expected to be small. This is confirmed by the comparison shown in Fig. 18(b). Near the hub and the tip of the blade, however, it can be seen in Fig. 18 that the nozzle secondary flows contribute significantly to the unsteady pressure on the suction surface of the rotor blade. The peak values of unsteady pressure (amplitude) near the hub and the tip on the suction surface nearly doubled when the nozzle secondary flow is present. This finding has significant engineering implications since the large unsteady pressure resulting from the secondary flow/blade interaction might lead to increased unsteady blade loading and noise production. Such a mechanism has not been considered in the current design and analysis procedures.

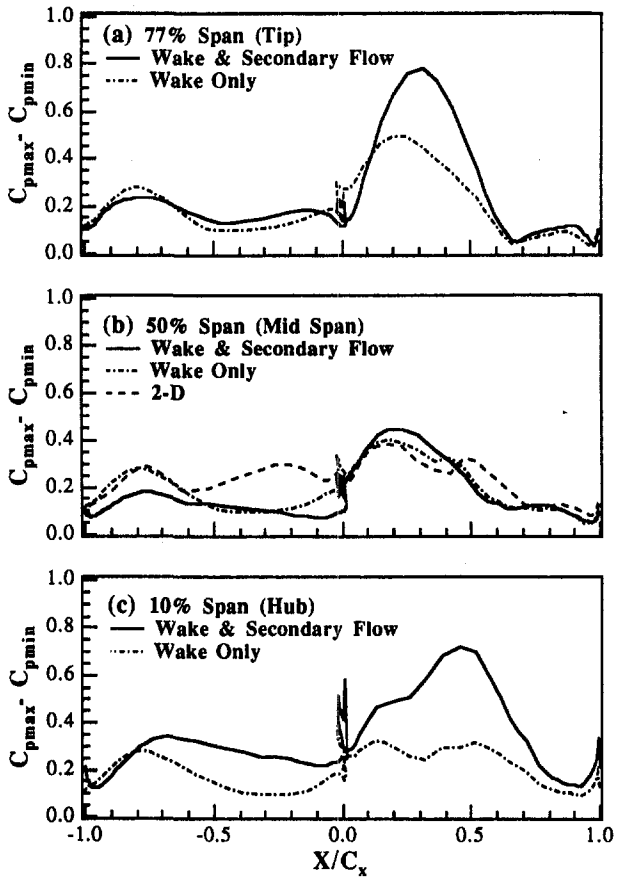

Fig. 18 Amplitude of unsteady pressure coefficient ($C_p - \bar{C}_p$) on blade surfaces, (*a*) tip, (*b*) midspan, (*c*) hub

Comparison between the two-dimensional and three-dimensional solution at the midspan clearly indicate that the unsteady flow at the midspan is strongly three dimensional and the distribution of unsteady pressure coefficient is substantially different. This is clearly shown in Fig. 18(*b*). The unsteady pressure distributions from two-dimensional and three-dimensional computations have significantly different shape on the suction surface. On the pressure surface, the two-dimensional computation results in a much higher pressure amplitude over the entire blade chord. The comparison indicates that unsteady flow field in the rotor cannot be modeled using a two-dimensional analysis, even at the midspan section. Even though the steady flow is nearly two dimensional at the midspan, the unsteady flow is three dimensional. This is mainly caused by the radial velocity in the wake and secondary flow, the phase difference along the span, unsteady flow impingement on the surface of the blade and casings. Thus the two-dimensional unsteady formulation for a rotor can lead to erroneous results and conclusions.

Concluding Remarks

A three-dimensional time-accurate Euler procedure has been developed based on an existing three-dimensional steady Navier–Stokes code. The unsteady Euler procedure has been used to investigate the three-dimensional unsteady interactions in a turbomachine stage. Three-dimensional unsteady nonreflecting boundary conditions have been developed and incorporated in the code to reduce the numerical reflections at the inlet/outlet boundaries. The effectiveness of the three-dimensional unsteady nonreflecting boundary conditions has been demonstrated. The new three-dimensional unsteady nonreflecting boundary conditions show significant improvements over the existing two-dimensional unsteady nonreflecting boundary conditions.

Because the rotor blade leans toward the direction of rotation, the tip of the blade encounters the nozzle wake earlier than the blade near the hub. The wake transport process at different spanwise locations have different phases, resulting in three-dimensional unsteady flow pattern.

Large tangential velocity components exist at the inlet near the nozzle secondary flow region. This is responsible for generating strong instantaneous impingement flow pattern (saddle point) on the suction surface immediately downstream of the wake. The instantaneous impingement flow strongly influences the amplitude of unsteady pressure on the blade surface.

It is evident that the three-dimensional nozzle wake and the secondary flow induce strong three dimensionality in the rotor flow field. In addition to counterrotating vortices in the blade-to-blade plane, the rotor flow perceives strong unsteady impingement flow, and radial inward and outward flow upstream and downstream of the wake during its passage. Thus the unsteady flow field is highly three dimensional in nature.

It is revealed that the nozzle secondary flow vortices have a strong influence on the generation of unsteady pressure on the blade surfaces, especially near the tip and hub of the rotor blade. The peak values of unsteady pressure amplitude near the hub and tip on the suction surface drastically increase due to the effect of the nozzle secondary flows. The numerical simulations suggest that the secondary flow/blade interaction might have a dominant influence on unsteady blade loading and noise production.

Even though the steady flow is nearly two dimensional at the midspan, the unsteady flow is three dimensional. The amplitude of unsteady pressure distribution predicted by two-dimensional and three-dimensional formulations are substantially different for the turbine rotor. Thus the two-dimensional unsteady formulation for a rotor can lead to erroneous results and conclusions.

Acknowledgments

This work was supported by National Aeronautics and Space Administration (NASA) through the contract, NAG 3-1168, with Dr. P. Sockol as the technical monitor. The authors wish to acknowledge NASA for providing the supercomputing resources at NASA Lewis Research Center and NASA Ames Research Center.

References

Beach, T. A., 1990, "An Interactive Grid Generation Procedure for Axial and Radial Flow Turbomachinery," AIAA Paper No. 90-0344.

Fan, S., 1995, "Computation and Turbulence Modeling of Unsteady Flows Due to Rotor/Stator Interaction in Turbomachines," Ph.D. Thesis, Department of Aerospace Engineering, The Pennsylvania State University.

Giles, M. B., 1990, "Non-reflecting Boundary Conditions for Euler Equation Calculations," *AIAA Journal,* Vol. 28, No. 12, pp. 2050–2058.

Giles, M. B., 1993, "A Framework for Multi-stage Unsteady Flow Calculations," in: *Unsteady Aerodynamics, Aeroacoustics, and Aeroelasticity of Turbomachines and Propellers,* H. M. Atassi, ed., Springer-Verlag, pp. 57–72.

Hodson, H. P., 1985, "An Inviscid Blade-to-Blade Prediction of a Wake-Generated Unsteady Flow," ASME *Journal of Engineering for Gas Turbines and Power,* Vol. 107, pp. 337–344.

Korakianitis, T., 1992, "On the Prediction of Unsteady Forces on Gas Turbine Blades: Part 1—Description of the Approach; Part 2—Analysis of the Results," ASME JOURNAL OF TURBOMACHINERY, Vol. 114, pp. 114–131.

Korakianitis, T., 1993, "On the Propagation of Viscous Wakes and Potential Flow in Axial-Turbine Cascades," ASME JOURNAL OF TURBOMACHINERY, Vol. 115, pp. 118–127.

Kunz, R. F., and Lakshminarayana, B., 1992, "Three-Dimensional Navier–Stokes Computation of Turbomachinery Flows Using an Explicit Numerical Procedure and a Coupled k–e Turbulence Model," ASME JOURNAL OF TURBOMACHINERY, Vol. 114, pp. 627–642.

Lakshminarayana, B., Camci, C., Halliwell, I., and Zaccaria, M., 1992, "Investigation of Three Dimensional Flow Field in a Turbine Including Rotor/Stator Interaction, Part 1: Design, Development and Performance of Turbine Facility," AIAA Paper No. 92-3325.

Manwaring, S. R., and Wisler, D. C., 1993, "Unsteady Aerodynamics and Gust Response in Compressors and Turbines," ASME JOURNAL OF TURBOMACHINERY, Vol. 115, pp. 724–740.

Rai, M., 1989, "Three Dimensional Navier–Stokes Simulation of Turbine–Stator Interaction, Part 1—Methodology, Part 2—Results," *Journal of Propulsion and Power,* May–June, pp. 305–311.

Saxer, A. P., and Giles, M. B., 1993, "Quasi-Three-Dimensional Nonreflecting Boundary Conditions for Euler Equation Calculations," *Journal of Propulsion and Power,* Vol. 9, No. 2, pp. 263–271.

Verdon, J. M., Barnett, M., Hall, K. C., and Ayer, T. C., 1991, "Development of Unsteady Aerodynamic Analyses for Turbomachinery Aeroelastic and Aeroacoustic Applications," NASA CR 4405.

Zaccaria, M., and Lakshminarayana, B., 1992, "Investigation of Three Dimensional Flow Field in a Turbine Including Rotor/Stator Interaction, Part 2: Three-Dimensional Flow Field at the Exit of the Nozzle," AIAA Paper No. 92-3326.

Zaccaria, M., 1994, "An Experimental Investigation Into the Steady and Unsteady Flow Field in an Axial Flow Turbine," Ph.D. Thesis, Department of Aerospace Engineering, The Pennsylvania State University.

Rotor–Stator Interaction Analysis Using the Navier–Stokes Equations and a Multigrid Method

A. Arnone
Department of Energy Engineering,
University of Florence,
Florence, Italy

R. Pacciani
Institute of Energetics,
University of Perugia,
Perugia, Italy

A recently developed, time-accurate multigrid viscous solver has been extended to the analysis of unsteady rotor–stator interaction. In the proposed method, a fully implicit time discretization is used to remove stability limitations. By means of a dual time-stepping approach, a four-stage Runge–Kutta scheme is used in conjunction with several accelerating techniques typical of steady-state solvers, instead of traditional time-expensive factorizations. The accelerating strategies include local time stepping, residual smoothing, and multigrid. Two-dimensional viscous calculations of unsteady rotor–stator interaction in the first stage of a modern gas turbine are presented. The stage analysis is based on the introduction of several blade passages to approximate the stator:rotor count ratio. Particular attention is dedicated to grid dependency in space and time as well as to the influence of the number of blades included in the calculations.

Introduction

One of the most challenging aspects in turbomachinery design and analysis is the extensive use of Computational Fluid Dynamics (CFD) to investigate component flow physics in detail. Aspects like heat transfer, secondary flows, leakage flow, and radial mixing can be reasonably predicted on the basis of viscous procedures, and those procedures have become feasible for industrial applications and routinely used in everyday turbomachinery design.

The real flow inside a turbine or compressor is unsteady and strongly influenced by the interaction of pressure waves, shock waves, and wakes between stators and rotors. Three-dimensional, time-accurate simulations of viscous flows are yet to come for practical design purposes. However, with the current trend in computer evolution, the time has come to look at unsteady investigations, and contributions are needed in this field in order to provide efficient tools for the design of the next generation of turbomachinery. In addition, unsteady calculations can be used for fine-tuning steady multirow pitch-averaging techniques, therefore improving the understanding of the multistage environment. The works of Erdos et al. (1977), Rai (1987), Lewis et al. (1987), Jorgenson and Chima (1988), Giles (1988), and Rao and Delaney (1992) are some examples of basic historical contributions to this topic.

Generally speaking, many of the time-dependent approaches used for steady, isolated blade-row analyses can also be used for time-accurate rotor:stator calculations. However, most of these solvers assume periodicity from blade to blade, enabling the analysis of only one blade passage. As modern turbomachines are designed with an unequal number of blades per row, some techniques should be included to address the stage stator:rotor count ratio. Lewis et al. (1987) and Rao and Delaney (1992), presented unsteady calculations using five blade passages. Rai (1987) and Jorgenson and Chima (1988) used approximate stator:rotor count ratios to limit computational cost and storage requirements. Other methods have also been proposed allowing unsteady computations to be carried out on a single blade passage per row for machines with arbitrary stator:rotor pitch ratios. Erdos et al. (1977) proposed phase-lagged periodic conditions implemented by storing the flow variables at the periodic boundaries at each time step for a whole revolution period of the rotor wheel. Fourmaux and Le Meur (1987) devised a particular treatment of the continuity boundary-condition that allows the preservation of the machine geometry. Giles (1988) solved the governing equations on time-inclined computational planes so that simple spatial periodicity conditions were imposed on the analysed blade passage. He and Denton (1994) implemented phase-lagged conditions by storing the temporal Fourier components of the flow variables.

In this paper, a viscous, time-accurate solver (TRAF, Arnone et al., 1993) has been extended to the analysis of rotor–stator interaction. The computational scheme is based on dual time-stepping and on the extension of conventional steady-state acceleration techniques, specifically multigrid and residual smoothing, to unsteady problems. Stability restrictions are removed by means of an implicit time discretization and accelerating techniques are used instead of traditional time-expensive factorizations (i.e., ADI, LU).

In viscous flow calculations, the characteristic time step varies several orders of magnitude inside the computational domain. The time step required for accuracy is quite often similar to the characteristic one of the inviscid core, while in the shear layer, the stability restriction of purely explicit schemes becomes extremely severe. With the proposed method, depending on the time step size, residual smoothing and multigrid can be progressively introduced in order to speed up calculations.

The code has been designed to handle more blade passages per row, and periodic conditions are applied between the first and last passage of each row. The procedure is applied to a typical modern gas turbine first stage. A grid sensitivity analysis is presented, including the influence of time discretization. To check for the accuracy achievable by approximating the stage blade count ratio, several configurations ranging from a few blade passages to the exact one are examined.

With the presented multigrid time-accurate solver, large-scale unsteady problems can be addressed in a reasonable time on a modern workstation.

Contributed by the International Gas Turbine Institute and presented at the 40th International Gas Turbine and Aeroengine Congress and Exhibition, Houston, Texas, June 5–8, 1995. Manuscript received by the International Gas Turbine Institute February 13, 1995. Paper No. 95-GT-177. Associate Technical Editor: C. J. Russo.

Governing Equations

Let t, ρ, u, v, p, T, E, and H denote, respectively, time, density, the absolute velocity components in the x and y Cartesian directions, pressure, temperature, specific total energy, and specific total enthalpy. The two-dimensional, unsteady, Reynolds-averaged Navier–Stokes equations can be written for a moving grid in conservative form in a curvilinear coordinate system ξ, η as

$$\frac{\partial(J^{-1}Q)}{\partial t} + \frac{\partial F}{\partial \xi} + \frac{\partial G}{\partial \eta} = \frac{\partial F_v}{\partial \xi} + \frac{\partial G_v}{\partial \eta} \tag{1}$$

where

$$Q = \begin{Bmatrix} \rho \\ \rho u \\ \rho v \\ \rho E \end{Bmatrix}, \quad F = J^{-1} \begin{Bmatrix} \rho U \\ \rho u U + \xi_x p \\ \rho v U + \xi_y p \\ \rho H U - \xi_t p \end{Bmatrix},$$

$$G = J^{-1} \begin{Bmatrix} \rho V \\ \rho u V + \eta_x p \\ \rho v V + \eta_y p \\ \rho H V - \eta_t p \end{Bmatrix} \tag{2}$$

The contravariant velocity components of Eqs. (2) are written as

$$U = \xi_t + \xi_x u + \xi_y v, \qquad V = \eta_t + \eta_x u + \eta_y v \tag{3}$$

and the viscous flux terms are assembled in the form

$$F_v = J^{-1} \begin{Bmatrix} 0 \\ \xi_x \tau_{xx} + \xi_y \tau_{xy} \\ \xi_x \tau_{yx} + \xi_y \tau_{yy} \\ \xi_x \beta_x + \xi_y \beta_y \end{Bmatrix},$$

$$G_v = J^{-1} \begin{Bmatrix} 0 \\ \eta_x \tau_{xx} + \eta_y \tau_{xy} \\ \eta_x \tau_{yx} + \eta_y \tau_{yy} \\ \eta_x \beta_x + \eta_y \beta_y \end{Bmatrix} \tag{4}$$

where

$$\begin{aligned} \tau_{xx} &= 2\mu u_x + \lambda(u_x + v_y) \\ \tau_{yy} &= 2\mu v_y + \lambda(u_x + v_y) \\ \tau_{xy} &= \tau_{yx} = \mu(u_y + v_x) \\ \beta_x &= u\tau_{xx} + v\tau_{xy} + kT_x \\ \beta_y &= u\tau_{yx} + v\tau_{yy} + kT_y \end{aligned} \tag{5}$$

The pressure is obtained from the equation of state,

$$p = \rho RT \tag{6}$$

According to the Stokes hypothesis, λ is taken to be $-2\mu/3$ and a power law is used to determine the molecular coefficient of viscosity μ as a function of temperature. The two-layer algebraic eddy-viscosity model of Baldwin and Lomax (1978) is used to account for the effects of turbulence.

Spatial Discretization and Artificial Dissipation

The space discretization is based on a cell-centered finite volume scheme. In the present work, due to the extensive use of eigenvalues and curvilinear quantities, it was found convenient to map the Cartesian space (x, y) onto a generalized curvilinear one (ξ, η) where the equation of motion, (Eq. (1), can be easily rewritten in integral form by means of Green's theorem (i.e., Jameson et al., 1981). On each cell boundary, fluxes are calculated after computing the necessary flow quantities at the side center. Those quantities are obtained by a simple averaging of adjacent cell-center values of the dependent variables.

The artificial dissipation model used in this paper is basically the one originally introduced by Jameson et al., (1981). In order to minimize the amount of artificial diffusion inside the shear layer, the eigenvalue scaling of Martinelli and Jameson (1988), and Swanson and Turkel (1987) have been implemented to weight these terms (e.g., Arnone and Swanson, 1993).

Boundary Conditions

In cascadelike configurations, there are four different types of boundary: inlet, outlet, solid wall, and periodicity. In the case of a multistage environment, more than one blade row is taken into consideration, and inlet and outlet refer to the first row inlet and last row exit, while the link between rows must be provided by means of some technique.

According to the theory of characteristics, the flow angle, total pressure, total temperature, and isentropic relations are used at the subsonic-axial first row inlet, while the outgoing Riemann invariant is taken from the interior. At the subsonic-axial last row outlet, the average value of the static pressure is prescribed, and the density and components of velocity are extrapolated.

On the solid walls, the pressure is extrapolated from the interior points, and the no-slip condition and the temperature condition are used to compute density and total energy. For the calculations presented in this paper, all the walls have been assumed to be at a constant temperature equal to a fraction of the total inlet one.

Cell-centered schemes are generally implemented using phantom cells to handle the boundaries. The periodicity is, therefore, easily overimposed by setting periodic phantom cell values. For high turning blade geometries, nonperiodic H- and C-type grids have proven to be effective in order to minimize the mesh skewness (Arnone et al., 1992; Arnone, 1994). On nonperiodic H-type grids, the point-to-point mesh correspondence is broken on the periodic boundaries before the leading edge and on the wake. On nonperiodic C-type grids, the mesh periodicity is removed only on the wake, while it is retained on the external boundary (i.e., Fig. 1). This approach has the advantage of not requiring any interpolation within the blade passage to link blocks. On the periodic boundaries where the grids do not match, the phantom cells overlap the real ones. Linear interpolations are then used to compute the value of the dependent variables.

The link between rows is handled by means of interface lines. Stator and rotor grids have a common interface lines and the match is provided through appropriate calculation of phantom cell values. For the blade passage under examination, the phantom cells relative to the interface line lie on the adjacent blade passage, and linear interpolations are used to provide the flow variable values. This approach, similar to the one used on periodic boundaries, where grids do not match, is not strictly conser-

Table 1 Code performance for the 4:7 case

TIME STEPS PER ROTOR PASSING PERIOD	CFL MINIMUM/ AVERAGE/ MAXIMUM	OPTIMUM NUMBER OF GRIDS	ITERATIONS BETWEEN TIME STEPS	CPU TIME PER CYCLE IBM RISC 590 [h]
50	0.6/3.7/820	3	5-6	5.2
100	0.3/1.9/408	2	4-6	5.8
200	0.15/0.9/204	2	4-5	8.2
400	0.07/0.5/102	1	3-4	11.7

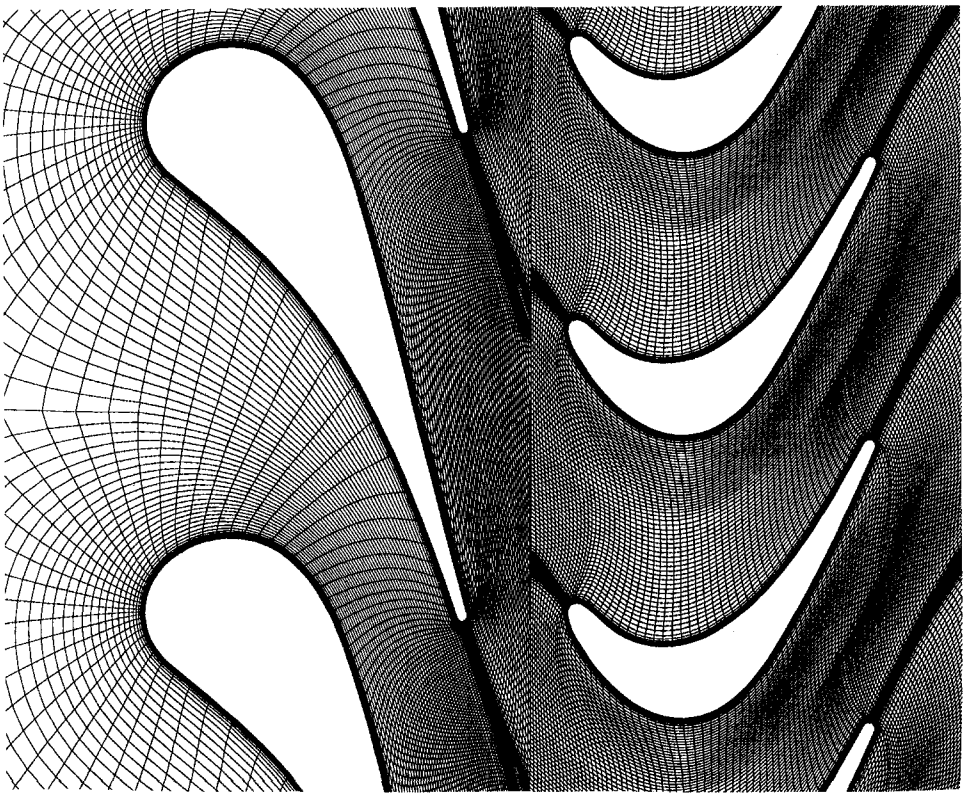

Fig. 1 Mixed C-type and H-type grids for the first stage of the PGT2 gas turbine

vative. However, monitoring of the errors in the conservation of mass, momentum, and energy has indicated a very good level of accuracy. For the practical applications considered up to now, relative errors in conservation were always less then 10^{-4}, which was considered accurate enough.

Basic Multigrid Steady Solver

The system of governing equations is advanced in time using an explicit four-stage Runge–Kutta scheme. A hybrid scheme is implemented, where, for economy, the viscous terms are evaluated only at the first stage and then frozen for the remaining stages. Good, high-frequency damping properties, important for the multigrid process, have been obtained by performing two evaluations of the artificial dissipating terms, at the first and second stages (Arnone and Swanson, 1993).

Three techniques are employed to speed up convergence to the steady-state solutions: (1) residual smoothing; (2) local time-stepping; and (3) multigrid.

Residual Smoothing and Local Time-Stepping. An implicit smoothing of residuals is used to extend the stability limit and the robustness of the basic scheme. The variable coefficient formulations of Martinelli and Jameson (1988) and Swanson and Turkel (1987) are used to obtain effective viscous calculations on highly stretched meshes (Arnone and Swanson, 1993). The time step is then locally computed on the basis of the maximum allowable Courant number, typically 5.0, and accounting for both convective and diffusive limitations (Arnone and Swanson, 1993).

Multigrid. The multigrid technique incorporated in the TRAF code is based on the Full Approximation Storage (FAS) schemes of Brandt (1979) and Jameson (1983). A V-type cycle

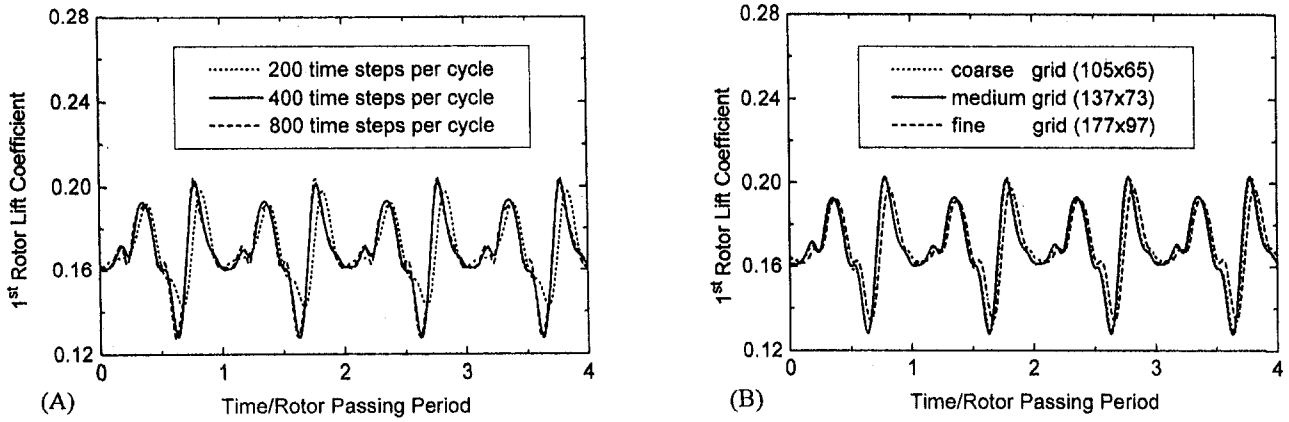

Fig. 2 Effect of the time step size (*A*) and of the grid density (*B*) on the rotor lift evolution for the 4:7 configuration

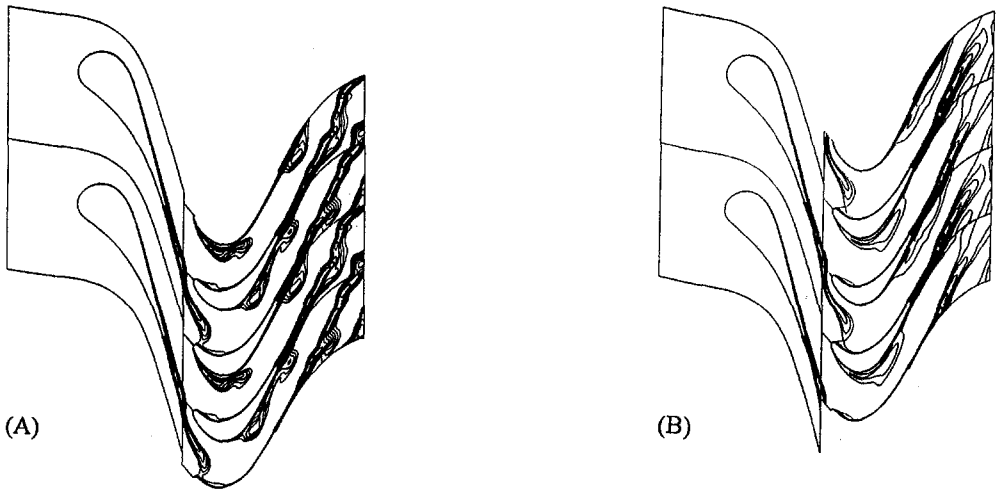

Fig. 3 Effect of the rotor grid density on the instantaneous entropy rise contours for the 1:2 configuration; (*A*) fine grid, (*B*) coarse grid

with coarse grid sweeps (subiterations) is used where the process is advanced from the fine grid to the coarser one without any intermediate interpolation. When the coarser grid is reached, corrections are passed back. One Runge–Kutta step is performed on the fine grid, two on the first coarse grid, and three on all the other coarser grids.

For viscous flows with very low Reynolds numbers or strong separation, it is important to compute the viscous terms on the coarse grids, too (Arnone and Swanson, 1993). The turbulent viscosity is evaluated only on the finest grid level and then interpolated on the coarse grids.

On each grid, the boundary conditions are treated in the same way and updated at every Runge–Kutta stage.

Multigrid Time-Accurate Stepping Scheme

Jameson-type explicit Runge–Kutta schemes in conjunction with residual smoothing and multigrid have proven to be very efficient for steady problems; however, those time-dependent methods are no longer time accurate. As shown by Jameson (1991) for the Euler equations, the system of Eqs. (1) can be reformulated to be handled by a time-marching steady-state solver, and the method can be successfully applied also to the Reynolds-averaged Navier–Stokes equations (i.e., Arnone et al., 1993). Equations (1) are rewritten in a compact form as

$$\frac{\partial Q}{\partial t} = -\mathcal{R}(Q) \tag{7}$$

where $\mathcal{R}$ is the residual, which includes convective, diffusive, and artificial dissipation fluxes. By the introduction of dual time-stepping and a fictitious time τ, the unsteady governing equations can be reformulated and a new residual $\mathcal{R}^*$ defined as

$$\frac{\partial Q}{\partial \tau} = \frac{\partial Q}{\partial t} + \mathcal{R}(Q) = \mathcal{R}^*(Q) \tag{8}$$

Now τ is a fictitious time, and all the accelerating techniques developed in steady-state experiences can be used to reduce the new residual $\mathcal{R}^*$ efficiently, while marching in τ. Following the approach of Jameson (1991), derivatives with respect to the real time t are discretized using a three-point backward formula, which results in an implicit scheme that is second-order accurate in time,

$$\frac{\partial Q}{\partial \tau} = \frac{3Q^{n+1} - 4Q^n + Q^{n-1}}{2\Delta t} + \mathcal{R}(Q^{n+1}) = \mathcal{R}^*(Q^{n+1}) \tag{9}$$

where the superscript n is associated with the real time. Between each time step the solution is advanced in a nonphysical time τ and acceleration strategies like local time stepping, implicit residual smoothing, and multigridding are used to speed up the residual $\mathcal{R}^*$ to zero to satisfy the time-accurate equations.

The time discretization of Eq. (9) is fully implicit. However, when solved by marching in τ, stability problems can occur when the stepping in the fictitious time τ exceeds the physical one. This generally occurs in viscous calculations where core-flow cells are much bigger than those close to solid walls. Based on a linear stability analysis of the four-stage scheme, the stepping in τ must be less then $\frac{2}{3}\,CFL^*\Delta t$. The time step $\Delta\tau$ can then be corrected as follows:

$$\Delta\tau = \text{MIN}\left(\Delta\tau, \frac{\Delta t}{2^{m-1}\,\frac{3}{2}\,\frac{CFL}{CFL^*}}\right) \tag{10}$$

where the contribution of the multigrid speed-up is included through 2^{m-1}, m being the total number of grids used in the multigrid process. After limiting the time step $\Delta\tau$ with Eq. (10) the scheme becomes stable and the physical time step Δt can be chosen safely only on the basis of the accuracy requirement (Arnone et al., 1993).

At the end of each time step in real time, the time derivative $\partial Q/\partial t$ is updated and a new sequence in the fictitious time τ is started.

The method described has recently been used by the authors to compute natural and forced unsteady flows (Arnone et al., 1993, 1994) and has proven to be quite effective. By means of the implicit time discretization, stability restrictions are re-

Table 2 Major parameters of the different stage approximation

#STATORS: #ROTORS	#OF BLOCKS	ROTOR PITCH ERROR [%]	LOWER FREQUENCY LIMIT
1:2	3	-13.0	1/2
3:5	8	+3.6	1/5
4:7	11	-1.3	1/7
7:12	19	+0.76	1/12
11:19	30	0.0	1/19

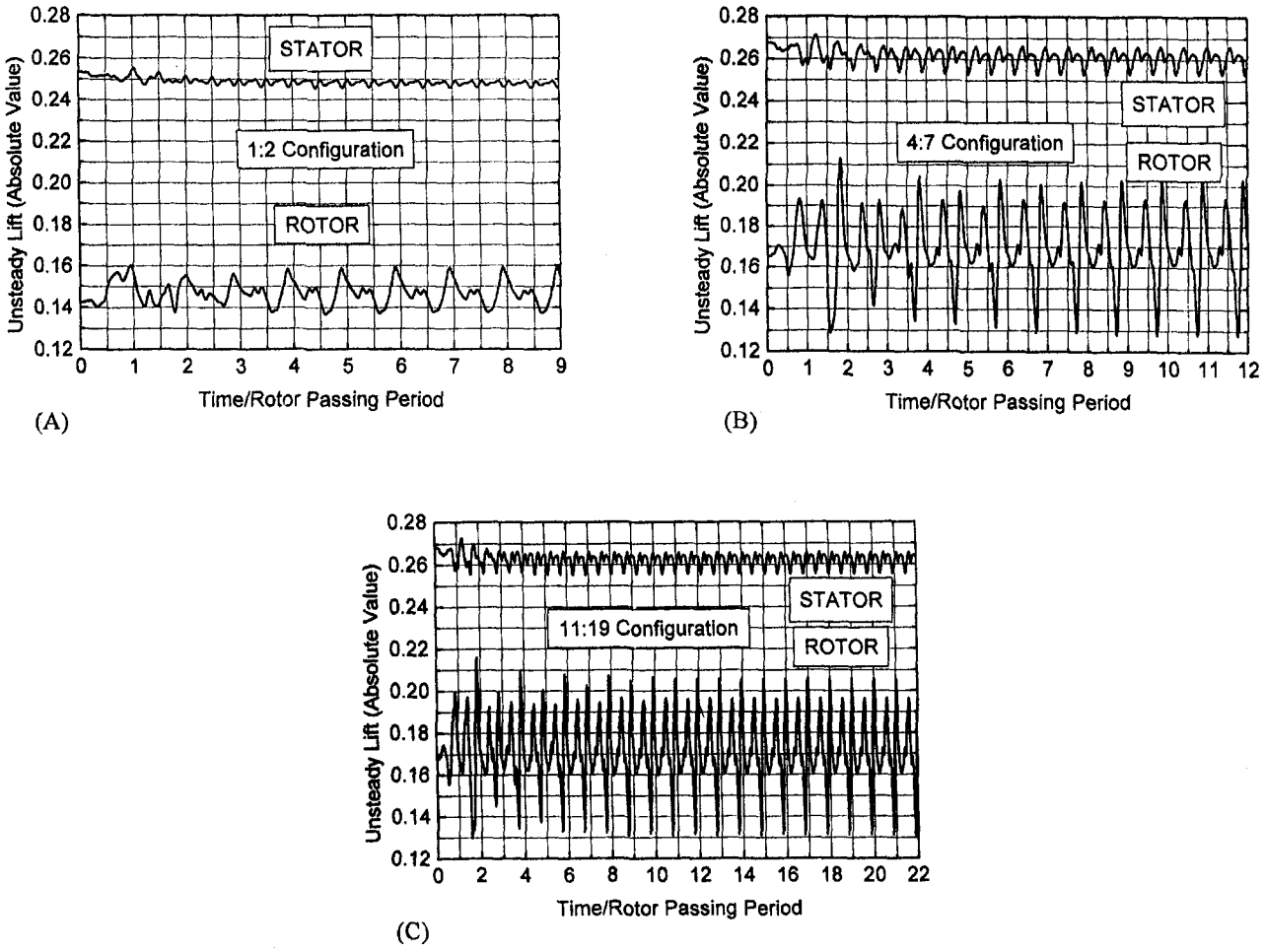

Fig. 4 Unsteady rotor lift evolution for the 1:2 (*A*), 4:7 (*B*), 11:19 (*C*), configurations

moved, while the efficiency of the explicit approach in addressing high-frequency problems can still be maintained by not performing residual smoothing and multigrid. When the characteristic frequency of the problem decreases, accelerating techniques can be gradually introduced to optimize the computational cost.

Application to a Modern Highly Loaded Gas Turbine Stage

As a sample problem to investigate the capability of the procedure, the unsteady release of the TRAF code has been used to study the midspan section of a first-stage transonic blading of a 2 MW gas turbine produced by Nuovo Pignone (PGT2). This turbine features state-of-the-art design with an inlet temperature of 1370 K, and 12.5:1 pressure ratio in two stages. The first stage under investigation has 22 stator blades and 38 rotor blades. The absolute Mach number is slightly above 1.0 at the stator exit, with a Reynolds number of about 1.5 million.

The first issue to address is therefore how to account for the ratio between the number of stator and rotor blades. As mentioned before, the code has been designed to handle more blade passages per each row. Periodic conditions are, therefore, applied only between the first and last block of each row. In our case, assuming steady and uniform inlet and outlet stage boundary conditions, the exact combination would be 11 vanes and 19 rotors. As a consequence, a large number of blocks (30) should be included in the simulation. This circumstance is quite usual in practical stage configuration as designers tend to avoid resonance by using prime numbers of blades on each row or blade count ratios with a small number as the highest common factor. Therefore, several blade passages are needed to reproduce the exact (*stator blade*)/(*rotor blade*) pitch ratio.

It is common in unsteady rotor–stator interaction analysis to limit the number of blade passages included in the calculation in order to end up with reasonable memory and computer time requirements. However, in most cases, the reduction of the number of blocks included in a row produces a pitch alteration. Moreover, an upper limit on the maximum detectable wave length is introduced as

$$\textit{max. wave length} = (\textit{blade pitch}) \times (\textit{No. of blades in a row})$$

This will be reflected in the lowest detectable frequency. For instance, for the rotor row, the lowest detectable frequency will be the one associated with a rotor blade that spans all the stator blade passages included in the discretization.

A practical way of overcoming the problem of pitch alteration is the one of also adjusting the blade chord in order to preserve solidity. This approach has shown to be quite effective in two dimensions but is not extendable to three dimensions and therefore has not been considered herein.

Because of the issues previously mentioned, it was decided to investigate the influence of the number of blades accounted for in the calculation, and all the major stator:rotor combinations were analyzed (1:2, 3:5, 4:7, 7:12, 11:19). This extensive analysis is mainly aimed at producing target solutions for fine-tuning of low-storage approximation and steady pitch-averaging techniques as well as to investigate crucial questions like:

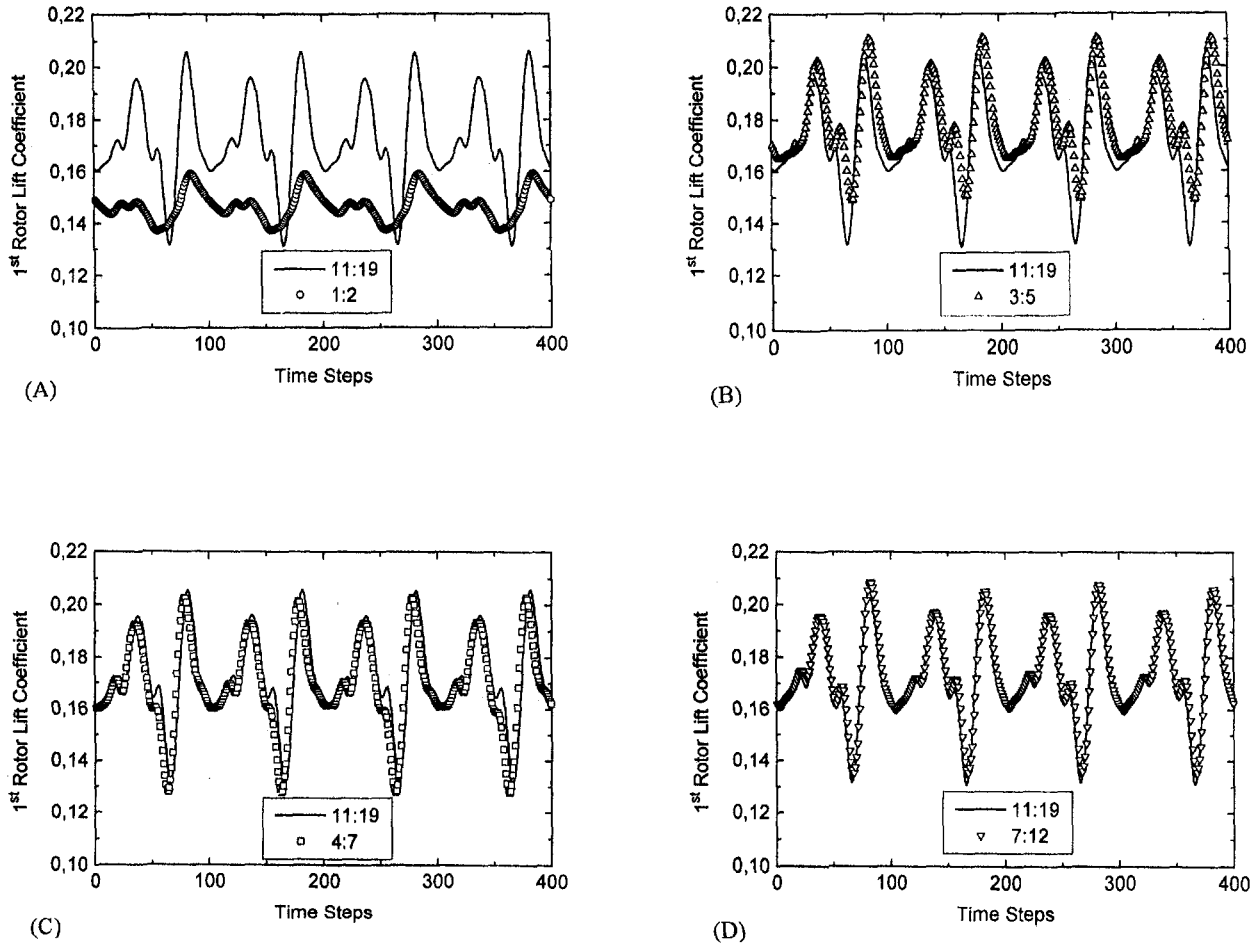

Fig. 5 Effect of the (stator blade):(rotor blade) count ratio on the rotor lift evolution

- In modern turbomachines most of the blade rows work close to the choke condition. What is acceptable in terms of pitch alteration in order to approximate the machine geometry without having a strong impact on the choke mass flow rate and the flow physics?
- Is the lower limit on the detectable frequency restrictive?
- Is the number of time step integrations to achieve periodicity related to the number of blocks included in the simulation?

As no unsteady measurements are available for this sample problem, in order to have more confidence in the indications of the theoretical prediction, a grid dependency study was carried out.

The presentation of the results will be split into two subsections. The first section will be used to discuss the efficiency of the method as well as the dependency of the results on the space and time discretization. The second section will be dedicated to the discussion of the influence of the number of blade passages included in the stage approximation.

Code Performance and Grid Dependence. Before applying the code to the five different stage approximations, the four vanes to seven rotor blades configuration (4:7) was chosen to carried out a grid sensitivity analysis including the dependence on the time discretization. For a transonic stage, like the one under investigation, vanes are basically choked and most of the unsteadiness is expected after the stator throat section. It was therefore decided to chose the stator blade grid on the basis of previous steady-state experience (i.e., Arnone et al., 1992) and only to investigate the influence of the rotor blades' grid density. As the vanes are choked, the various stage configurations have been obtained by using the exact vane pitch while adjusting the rotor one.

Figure 1 shows the computational mesh consisting of mixed C-type and H-type nonperiodic grids. Due to the vane's blunt rounded leading-edge, a C-type grid structure (209×33) was selected for the stators. On the contrary, it was found convenient to use an H-type structure for the rotor blades. Away from the leading edge, the C-type structure tends to increase the grid size and thus induces a smear of the incoming wakes. With an H-type structure, it is much easier to control the uniformity and density of the grid before the blade passage. Three different grid sizes have been tested for the rotors; coarse 105×65, medium 137×73, and fine 177×97. The fine grid has twice as many points as the coarse one on the blade surface. Figure 1 reports the medium grid, which is the one used for most of the calculations presented herein. In order to reduce the grid skewness, both the C-type and H-type grids are of a nonperiodic type (i.e., Arnone et al., 1992; Arnone, 1994).

The nondimensional blade lift coefficient based on pressure distribution was used as a parameter to monitor unsteadiness. Figure 2 reports the rotor lift evolution as function of time for different time step sizes and different grid sizes. The time has been scaled with the one that a rotor blade needs to cross a vane passage (*rotor passing period*), while a *cycle* is defined as the rotor passing period times the number of stator vanes included in the discretization. As can be noticed in Fig. 2(a), 400 time steps per cycle (100 divisions in a rotor passing period) produce a lift evolution that is quite independent of the time discretization. In fact, if the time step is reduced by a

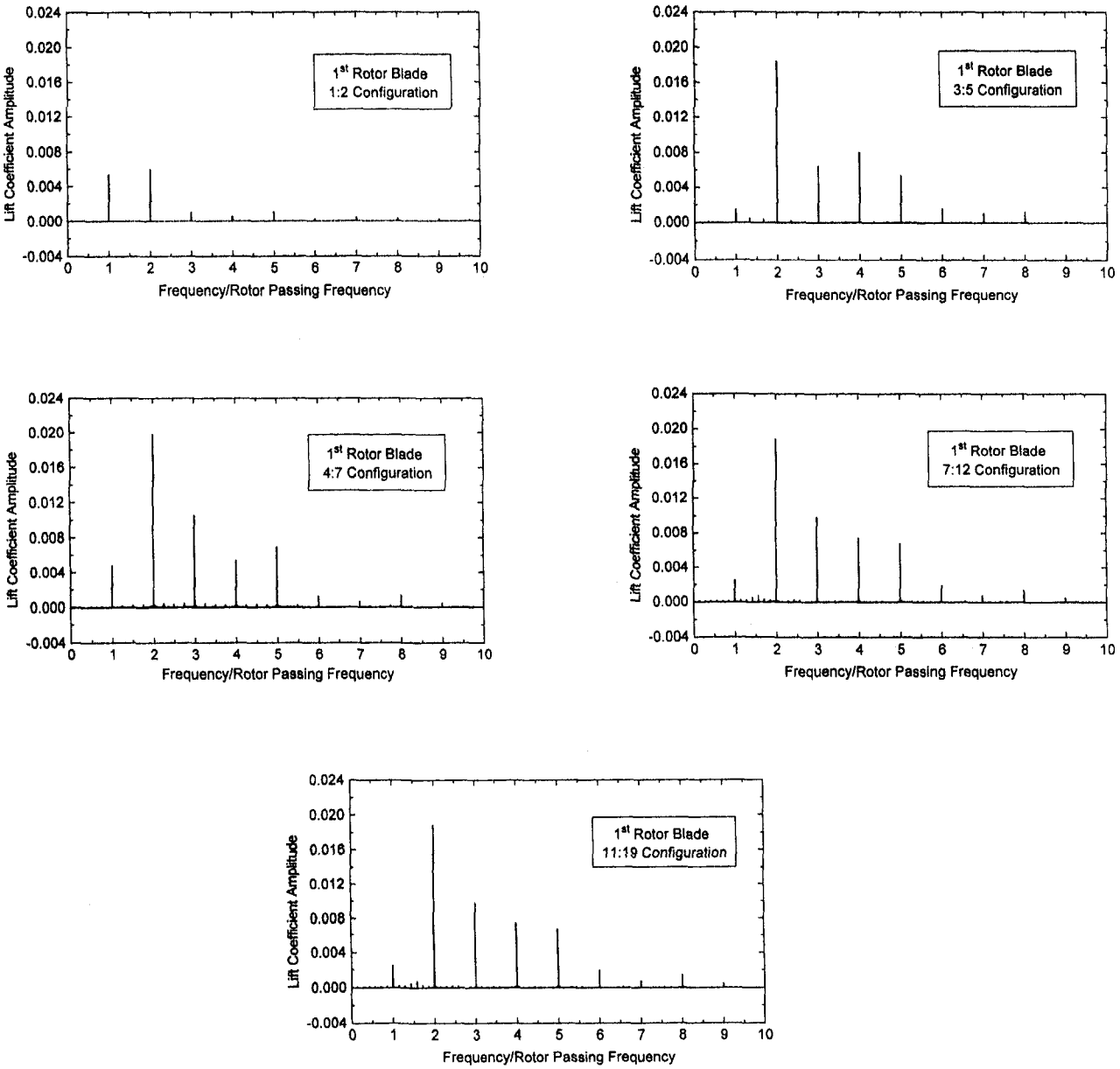

Fig. 6 Effect of the (stator blade):(rotor blade) count ratio on the frequency spectrum of the rotor lift

factor of two, no important effects can be noticed in the rotor lift evolution. The situation is somewhat different in terms of grid dependence (Fig. 2(*b*)). Now the coarse and medium grid look very similar while the fine one indicates some slight differences. We have found that these unsteady lift evolutions are extremely sensitive to the grid density in the axial gap between stators and rotors as well as to the rotor leading edge resolution, and grid independence is very hard to achieve.

Numerical experiments (Arnone et al., 1994) have also indicated that the grid density at the rotor exit may have some impact on the rotor lift evolution. Once stator wakes are chopped by the rotor's leading edge, an entropy spot is generated and convected downstream in the rotor blade passage. Because of the pitchwise pressure gradient, these spots move toward the rotor's suction side and eventually interact with the rotor wakes. As a consequence, the rotor wakes become unstable. It is suspected that, if the space and time resolutions are made fine enough, this mechanism could induce trailing edge vortex shedding and therefore move the target in the dependence analysis. This circumstance is shown in Fig. 3 where plots of entropy rise for fine and coarse grids after the rotor blade passage are reported. By using a fine grid after the rotor blade, one can pick up details of wake unsteadiness that do not show up if a coarse grid is used.

For the present study, interest is focused on the validation of the procedure for practical overall predictions and a large number of calculations need to be performed. Therefore, the level of independence of the calculations from the grid density has been considered satisfactory, and the medium grid was used as reference grid performing 100 time steps per rotor passing period.

The performance of the proposed method is summarized in Table 1. Calculations refer to the medium grid (137×73) for the rotor blades and correspond to a total of about 98,000 grid points to discretize the stage (four stators and seven rotors). In table 1 the maximum, area-averaged, and minimum CFL numbers are reported. Those quantities have been evaluated as the ratios of the physical time step and the characteristic maximum, area averaged, and minimum time step. The code was run in the fictitious time step τ at a local CFL number of 5.0 with

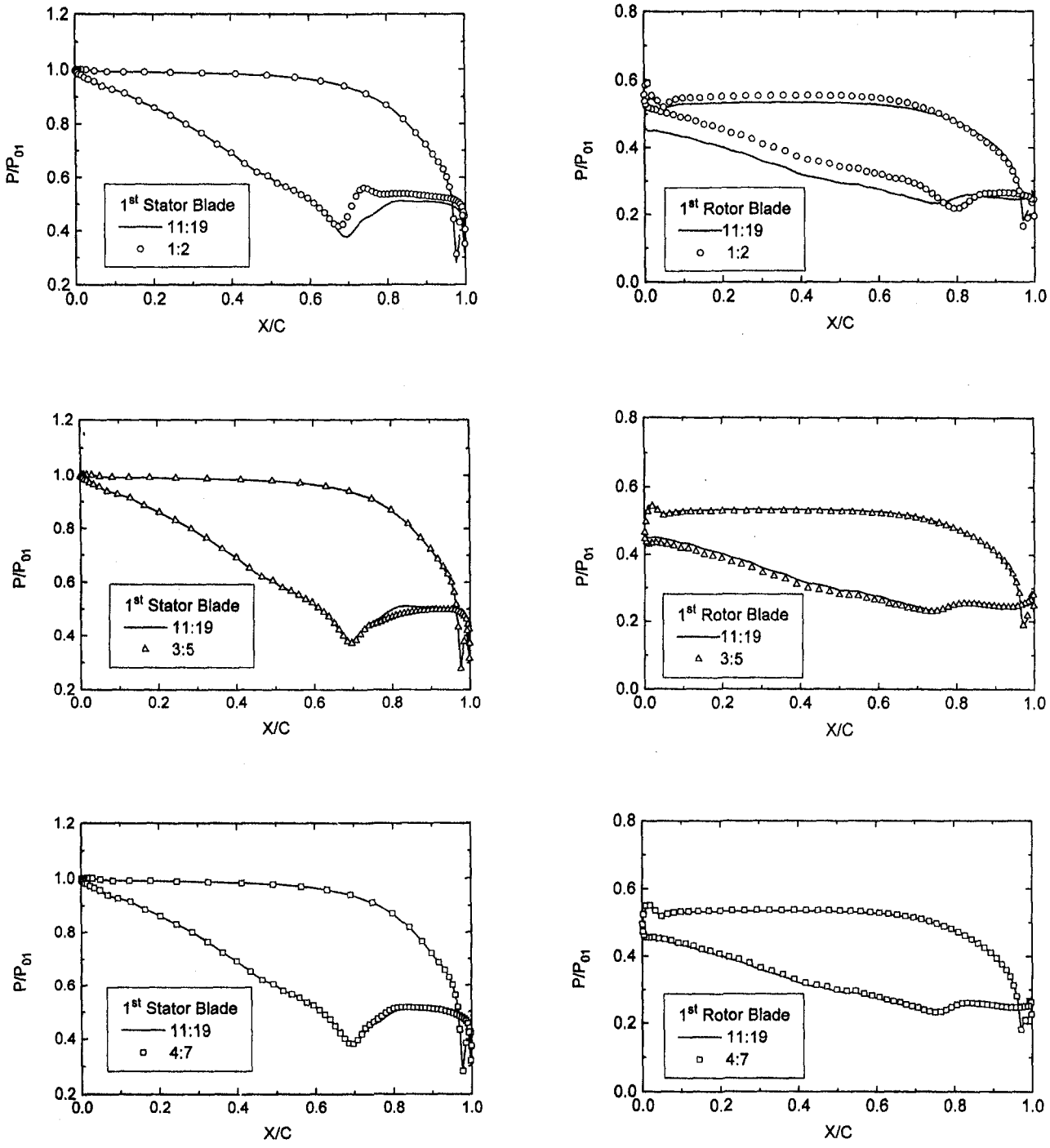

Fig. 7 Effect of the (stator blade):(rotor blade) count ratio on the stator and rotor time-averaged blade surface pressure distribution

implicit residual smoothing adjusting the number of grids (used in the multigrid) in order to optimize the CPU time. Between time steps, iterations are performed until the averaged root mean square of the residuals is less than 10^{-6}, which generally requires from three to six multigrid cycles.

As previously pointed out, the averaged CFL is close to the characteristic one. Using 200 time divisions within a rotor passing period, the CFL number is less than one for most of the computational cells. On the other hand, in the boundary layer, the CFL increases up to several hundreds. In such a circumstance, the advantage of using multigrid is restricted to the viscous layer and decreases when increasing the time step divisions per cycle. As can be noticed in Table 1, if using more than 200 time divisions per rotor passing period, there is no CPU time reduction in running with more than one grid. Although those considerations are related to the particular application and to the grid density, they are believed to give an idea of effectiveness and versatility of the scheme in rotor–stator interaction analysis.

Also an explicit computation with the four-stage Runge–Kutta scheme has been carried out. For the sake of accuracy in time, residual smoothing has not been included in the calculation, which has been performed with a maximum CFL of 2.5. The explicit test required 60,000 time steps per rotor passing period and about 190 h on the IBM RISC/6000 model 590. With the present method and 100 divisions per rotor passing period, the CPU time is $\frac{1}{30}$ of that of the purely explicit code. The extra memory requirement, due to the implicit time discreti-

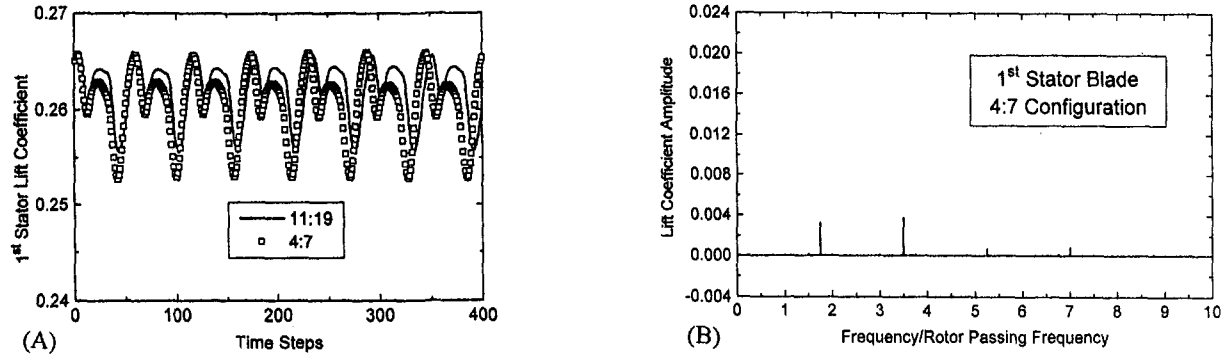

Fig. 8 Unsteady stator lift evolution (*A*) and frequency spectrum (*B*) for the 4:7 configuration

zation, which requires the storage of the flow variables at three time levels, is limited to about 20 percent.

Dependence on the Blade Count Ratio. As previously mentioned, to address the problem of the stage approximation, all the major stator:rotor blade count ratio combinations were analyzed (1:2, 3:5, 4:7, 7:12, 11:19). Table 2 summarizes the major parameters of the five different stage configurations, such as number of stators, rotors, and blocks, rotor pitch approximation, and lower frequency limit. The nondimensional frequency was obtained by scaling the periods with the rotor passing one.

Figure 4 shows the stator and rotor lift evolutions starting from an initial steady-state solution obtained accounting for the rotor blade's motion but without changing the rotor grid's position with respect to the stator vanes. For conciseness only the 1:2, 4:7, and 11:19 configurations are reported. It was surprisingly found that the number of cycles needed to obtain a periodic solution is not linked to the number of blocks included in the calculation. For instance, in the 1:2 (3 blocks) configuration (Fig. 4(*a*)), calculations become periodic after about 5 rotor passing periods, while about 8 rotor passing periods are needed using 11 stators and 19 rotors (30 blocks) (Fig. 4(*c*)). The 11:19 configuration approaches a periodic solution before a complete cycle is performed. An attempt to explain this phenomenon will be provided later.

Figure 5 compares the rotor lift evolution for the 1:2, 3:5, 4:7, and 7:12 configuration to the target 11:19 one. The frequency spectra of the lift evolutions are summarized in Fig. 6. Only the 1:2 configuration seems to be substantially off both in amplitude, mean value, and basic frequency. Figure 7 shows the time-averaged static pressure distribution on stator and rotor blades surfaces for the 1:2, 3:5, 4:7 cases, the solid line being the exact stage configuration (11:19). The 13 percent reduction of the rotor pitch (see Table 1) to assess the 1:2 configuration causes a premature choke in the rotor and a substantial reduction of the vane exit velocity. As a consequence of that, both the rotor and the vane experience a lower lift with respect to the exact configuration. The prediction of the frequency amplitude is also quite rough with two major components of one time and two time the rotor passing one. In contrast, the 3:5 configuration has already most of the frequency well predicted. The differences between the 4:7, 7:12, and 11:19 configurations are really small with a dominant frequency of two times the rotor passing one. The offset in the mean value of the 3:5 and 4:7 configurations is mainly due to the rotor pitch approximation. An increase in the rotor pitch (3:5) causes an increase in the blade load. However, if the pitch adjustment is keep less than about 1 percent, the impact on the lift evolution is negligible (Fig. 5(*d*)).

It can be noticed how, in terms of dominant frequencies, the rotor lift evolution has only multiples of the rotor passing one (Fig. 6), and no appreciable amplitudes can be observed at a frequency lower than the rotor passing one, even in the realistic 11:19 configuration. If it is assumed that the time to obtain a periodic solution is a function of the lower frequency to resolve, it can be predicted that the time to obtain periodicity is not dependent on the number of blocks. In fact, the frequency spectrum of Fig. 6 clearly indicates that the addition of blocks has no influence on the lower frequency. As mentioned before, this circumstance was noticed in the calculations, and is consistent with the Fourier analysis results.

Figure 8 reports the stator lift coefficient and its frequency spectrum for the configuration with 4 stators and 7 rotors. Now the reference period should be computed as (*rotor passing period*) × (*No. of stators*)/(*No. of rotors*). Therefore, in terms of rotor passing frequency the reference one is (*rotor passing frequency*) × (*No. of rotors*)/(*No. of stators*) (see Fig. 8). Once again there is no important frequency below the reference one, and as there are 7 rotor and 4 stator blades the reference frequency is now 1.75 (7/4). A similar behavior in terms of dependence on the number of blocks included in the calculation has been observed for the stator vanes and is not reported for conciseness.

Table 3 summarizes the code performance for the various blade count ratios used to approximate the stage. As discussed, the CPU time to obtain a periodic solution is growing almost linearly with the number of blade passages included in the calculation.

On an IBM 590 workstation, 29 hours are needed to achieve periodicity in the 11:19 configuration using about 270,000 grid points to discretize the stage. A complete cycle would require 41 hours.

Figure 9 shows instantaneous entropy rise, pressure, and absolute Mach number contours for the realistic stage configuration (11:19). As is also evident from the blade pressure distribution of Fig. 7, both the stators and rotors work in transonic conditions. The stators have a throat shock system and a supersonic exit with a fishtail shock. On the rotor blades, the throat shock is very weak and almost disappears when the stator wake enters the rotor blade passage. In terms of velocity gradients, a rotor sees two peaks when spanning the stator passage. One is

Table 3 Code performance for the major blade count ratio

#STATORS: #ROTORS	#OF BLOCKS	PASSING PERIODS TO ACHIEVE PERIODICITY	CPU TIME IBM RISC 590 [h]
1:2	3	5	1.4
3:5	8	6	6.1
4:7	11	6	8.7
7:12	19	7	16
11:19	30	8	29

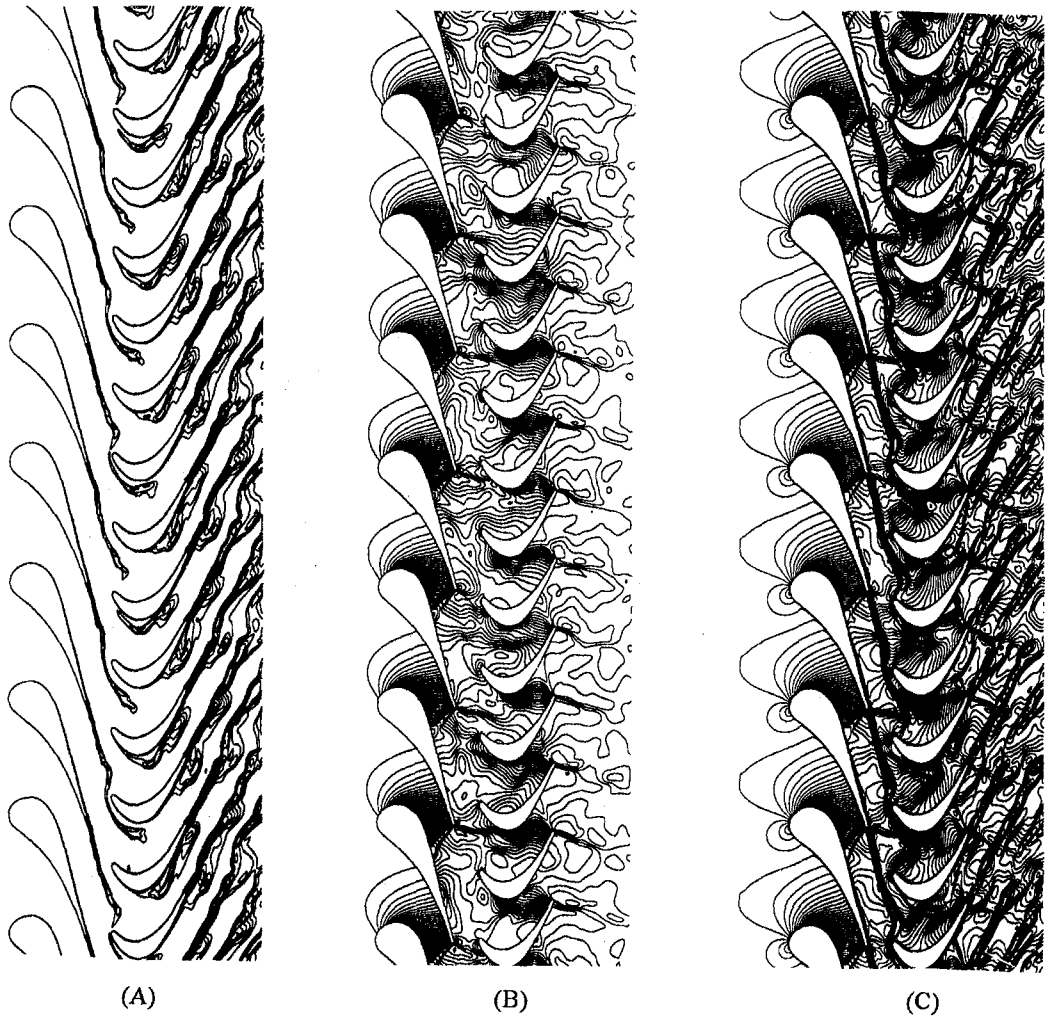

Fig. 9 Instantaneous entropy rise (*A*) pressure (*B*), and absolute Mach number (*C*), contours for the 11:19 configuration

the wake, and the other is the stator fishtail shock. It is suspected that those two contributions are responsible for the large frequency amplitude at twice the rotor passing one. This is also confirmed by the fact that in the 1:2 configuration the stator fishtail shock is much smaller and so is the amplitude of the frequency under discussion.

Several turbine and compressor stage configurations need to be investigated before reliable conclusions can be drawn; however, the information collected in this unsteady rotor–stator interaction study suggests preliminary answers to the three questions raised at the beginning of this section:

- If the adjustment in the blade pitches is less then 1 percent no important deterioration in the stage approximation seems to appear even in a transonic regime.
- The lower limit on the detectable frequency that is introduced when reducing the total number of blocks seems to be not restrictive at all.
- The number of cycles needed to achieve periodicity is not related to the number of blocks included in the simulation as the dominant frequencies are not smaller than the rotor passing one.

Obviously those answers are related to the particular stage under investigation, but if confirmed in the future, they indicate a convenient path in addressing efficiently unsteady rotor–stator interaction. Particularly, stage approximations based on few blocks but with pitch modification can result inaccurate if the pitch adjustments are appreciable. On the contrary, phase-lagged and low-storage techniques that preserve the machine geometry should work nicely even with a small number of blocks. However, they should prove to converge to a periodic solution quite fast; otherwise it would be more convenient to look at parallel computations where a large number of blocks is considered and distributed on several processors.

Concluding Remarks

A multigrid time-accurate Navier–Stokes solver has been extended to the analysis of unsteady rotor–stator interaction. By means of a dual time-stepping, accelerating techniques typical of steady-state solvers have been successfully utilized in unsteady calculations. The application to a first stage of a modern gas turbine has indicated up to 97 percent reduction in the computational effort with respect to classical explicit schemes.

A detailed grid dependence study is presented, including the influence of the time step size. Several stage approximations with different blade count ratios are examined, ranging from few blocks to the exact stage configurations.

The method has proven to be effective in analyzing details of unsteady rotor–stator interactions, and encourages future investigations and three-dimensional extensions.

Acknowledgments

This work has been funded by the Nuovo Pignone Company. The authors would like to express their gratitude to the Nuovo Pignone management and particularly to Drs. E. Benvenuti and

U. Corradini for the numerous and useful discussions. The authors are also indebted to Profs. Ennio Carnevale and Francesco Martelli of the University of Florence, for encouraging and monitoring the research.

References

Arnone, A., Liou, M.-S., and Povinelli, L. A., 1992, "Navier–Stokes Solution of Transonic Cascade Flow Using Nonperiodic C-Type Grids," *Journal of Propulsion and Power,* Vol. 8, No. 2, pp. 410–417.

Arnone, A., Liou, M.-S., and Povinelli, L. A., 1993, "Multigrid Time-Accurate Integration of Navier–Stokes Equations," AIAA Paper No. 93-3361-CP.

Arnone, A., and Swanson, R. C., 1993, "A Navier–Stokes Solver for Turbomachinery Applications," ASME JOURNAL OF TURBOMACHINERY, Vol. 115, pp. 305–313.

Arnone, A., Pacciani, R., and Sestini, A., 1994, "Multigrid Computations of Unsteady Rotor–Stator Interaction using the Navier–Stokes Equations," presented at the 1994 ASME Winter Annual Meeting, Chicago, IL.

Arnone, A., 1994, "Viscous Analysis of Three-Dimensional Rotor Flows Using a Multigrid Method," ASME JOURNAL OF TURBOMACHINERY, Vol. 116, pp. 435–445.

Baldwin, B. S., and Lomax, H., 1978, "Thin Layer Approximation and Algebraic Model for Separated Turbulent Flows," AIAA Paper No. 78-257.

Brandt, A., 1979, "Multi-Level Adaptive Computations in Fluid Dynamics," AIAA Paper No. 79-1455.

Erdos, J. I., Alzner, E., and McNally, W., 1977, "Numerical Solution of Periodic Transonic Flow Through a Fan Stage," *AIAA Journal,* Vol. 115, No. 11.

Fourmaux, A., and Le Meur, A., 1987, "Computation of Unsteady Phenomena in Transonic Turbines and Compressors," presented at the 4th Symposium on Unsteady Aerodynamics and Aeroelasticity of Turbomachines and Propellers, Aachen, Germany.

Giles, M. B., 1988, "UNSFLO: A Numerical Method for Unsteady Inviscid Flow in Turbomachinery," GTL Report #195.

He, L., and Denton, J. D., 1994, "Three-Dimensional Time-Marching Inviscid and Viscous Flow Solutions for Unsteady Flows Around Vibrating Cascades," ASME JOURNAL OF TURBOMACHINERY, Vol. 116, pp. 469–476.

Jameson, A., Schmidt, W., and Turkel, E., 1981, "Numerical Solutions of the Euler Equations by Finite Volume Methods Using Runge–Kutta Time-Stepping Schemes," AIAA Paper No. 81-1259.

Jameson, A., 1983, "Transonic Flow Calculations," MAE Report 1651, MAE Department, Princeton University, July.

Jameson, A., 1991, "Time Dependent Calculations Using Multigrid With Applications to Unsteady Flows Past Airfoils and Wings," AIAA Paper No. 91-1596.

Jorgenson, P. C. E., and Chima, R., 1988, "An Explicit Runge–Kutta Method for Unsteady Rotor/Stator Interaction," AIAA Paper No. 88-0049.

Lewis, J. P., Delaney, R. A., and Hall, E. J., 1987, "Numerical Prediction of Turbine Vane-Blade Interaction," AIAA Paper No. 87-21419.

Martinelli, L., and Jameson, A., 1988, "Validation of a Multigrid Method for the Reynolds Averaged Equations," AIAA Paper No. 88-0414.

Rai, M. M., 1987, "Unsteady Three-Dimensional Navier–Stokes Simulations of Turbine Rotor Stator Interactions," AIAA Paper No. 87-2058.

Rao, K. V., and Delaney, R. A., 1992, "Investigation of Unsteady Flow Through a Transonic Turbine Stage, Part I, Analysis," AIAA Paper No. 90-2408.

Swanson, R. C., and Turkel, E., 1987, "Artificial Dissipation and Central Difference Schemes for the Euler and Navier–Stokes Equations," AIAA Paper No. 87-1107.

Stall Inception Measurements in a High-Speed Multistage Compressor

J. F. Escuret

V. Garnier

Compressor Aerodynamics Dept.,
SNECMA,
Moissy-Cramayel, France

This paper presents unsteady measurements taken in a high-speed four-stage aero-engine compressor prior to the onset of aerodynamic flow instabilities. In this experiment, 40 fast-response pressure transducers have been located at various axial and circumferential positions throughout the machine in order to give a very detailed picture of stall inception. At all the compressor speeds investigated, the stall pattern observed is initiated by a very short length-scale finite-amplitude disturbance, which propagates at a fast rate around the annulus. This initial stall cell leads to a large-amplitude system instability in less than five rotor revolutions. Varying the IGV setting angle is found to have a strong influence on the axial location of the first disturbance detected. In particular, transferring the aerodynamic loading from front to downstream stages moves the first disturbance detected from the first to the last stage of the compressor. Other repeatable features of the stall inception pattern in this compressor have been identified using a simple analysis technique particularly appropriate to the study of short length-scale disturbances. It is found that the origins of instabilities are tied to particular tangential positions in both the stationary and rotating frames of reference. These measurements lead to the conclusion that the stall inception process in high-speed multistage compressors can be characterized by some very local and organized flow phenomena. Moreover, there is no evidence of prestall waves in this compressor.

Introduction

The present trend in aero-engine compressor design is toward higher blade loading to increase the pressure ratio per stage. This objective is clearly limited by the presence of aerodynamic instabilities such as rotating stall and surge in the compressor operating range. As a result, it is more than ever critically important to understand instability inception in order to delay or control it.

Past experimental efforts in this field (Day and Freeman, 1993) have clearly established that the onset of global instabilities, i.e., surge and deep stall characterized by the fall of the annulus-averaged unsteady exit pressure, is always preceded by a circumferential breakdown of the flow in the form of rotating stall. Moreover, two possible routes by which rotating stall can develop have been identified. The first type of stall inception is associated with a modal instability (thus affecting the whole circumference), which starts as an infinitely small circumferential perturbation. It then gradually grows as it rotates until it becomes a fully developed stall cell. Modal perturbations were first observed by McDougall et al. (1990) in a low-speed single-stage compressor and confirmed in a high-speed three-stage compressor by Garnier et al. (1991). Testing from Boyer et al. (1993) and other investigations reported by Tryfonidis et al. (1995) revealed the presence of modal waves in a large variety of machines. The second type of stall inception is initiated by local disturbances (covering about two or three blade passages) of small but finite amplitude when first detected and which rotate very quickly around the annulus. These short length-scale disturbances were first observed by Day (1993a) in two low-speed laboratory compressors and later found in the Viper engine tests by Wilson and Freeman (1994). Day (1993a) as well as Longley et al. (1996) found that the same machine can exhibit the two types of stall inception pattern. In some cases, one type may be dominant, in other cases the other, but there also may be cases in which both types have the capability to cause stall.

The reasons for two different stall inception patterns and the conditions under which they occur are not yet fully understood. It has been suggested by Day (1993a) that the stage matching plays an important role and that well-matched conditions could be more favorable to the development of a modal instability. Also, Franck et al. (1994) found that single-stage compressors with a smooth pressure-rise characteristic near the stall point (corresponding to a progressive stall) tended to exhibit more distinct wave perturbations. Determining which type of stall inception pattern is the most common in modern high-speed machines is a key point as it has major implications on the feasibility of active stall control. The most adverse situation is, of course, that of short length-scale perturbations that present very little warning time (fewer than ten rotor revolutions). Moreover, they can be initiated within a particular blade-row before affecting the whole compressor and are therefore very difficult to "catch" when they are still small. Also, they start as finite amplitude perturbations and are highly nonlinear in nature. The questions of interest for the high-speed compressor designer are therefore:

- Which stall inception pattern predominates in high-speed multistage machines and under which conditions?
- What are the particular features of stall inception in high-speed multistage machines (e.g., spatial origin of instabilities, growth rate of perturbations)?
- Can prestall modal perturbations be detected and which role do they play in comparison with that of short length-scale disturbances?

This paper brings new answers to these questions by presenting measurements from a modern high-speed four-stage compressor with highly resolved fast-response instrumentation. The

Contributed by the International Gas Turbine Institute and presented at the 40th International Gas Turbine and Aeroengine Congress and Exhibition, Houston, Texas, June 5–8, 1995. Manuscript received by the International Gas Turbine Institute February 16, 1995. Paper No. 95-GT-174. Associate Technical Editor: C. J. Russo.

Table 1 Characteristics of the H4 compressor

	IGV	R1	S1	R2	S2	R3	S3	R4	S4
Number of Blades	70	72	108	71	104	69	108	70	82
Tip Diameter (mm)	388.	386.	384.	380.	379.	375.	374.	371.	371.
Hub Diameter (mm)	335.	335.	335.	335.	335.	335.	335.	335.	335.
Mid-height Chord (mm)	18.	21.	17.	20.	17.	20.	17.	18.	40.
Tip Mach Number (Design Point)		0.80		0.77		0.73		0.71	
Axial Spacing (% of stator chord)		50.		59.		63.		28.	

Design Speed (rpm)	13700
Design Pressure Ratio	2.24
Design Flow Rate (kg/s)	3.58
Reynolds Number	$4.0\ 10^5$

effect of stage matching on stall inception is closely examined using variable inlet guide vanes. Also, the influence of fast transients in military engines is reproduced in this experiment with fast throttling tests. Finally, the data is analyzed with a technique particularly appropriate to the study of short length-scale disturbances, which reveals some very local and organized aspects of the stall inception pattern in this compressor.

Experimental Facility and Instrumentation

The stall inception measurements presented in this paper have been obtained from a high-speed four-stage research compressor called the H4 compressor. This machine was designed at SNECMA in the mid-eighties and its most relevant characteristics are given in Table 1. Due to inter-blade-row instrumentation constraints, the axial blade spacing is larger than that usually found in actual aero-engine compressors. Apart from this particular feature, which might have some influence on the stall inception process, the H4 compressor is fairly representative of the last stages of high-pressure compressors present in current civil aero-engines. Also, it is equipped with variable inlet guide vanes, which offers some flexibility in the steady-state matching of the various stages.

Testing of the H4 compressor took place at the CEPr facility in the RACE research bench. A cross-sectional view of the rig is shown in Fig. 1. It is characterized by a very long inlet duct and a large exhaust volute (about 60 times the volume of the compressor), which is terminated by an array of eight throttle valves. It is possible to choose the number of valves to be used (maximum of three during the tests) as well as the closing speed of the valves.

In this experiment, 40 fast-response pressure transducers are located at various axial and circumferential positions throughout the machine in order to give a very detailed picture of stall inception. As represented in Fig. 2, eight transducers are mounted flush with the outer casing wall and as evenly spaced as possible at the upstream plane of each rotor row and at the upstream plane of the IGVs. As far as possible, it was attempted to position each sensor a third of a pitch away from the pressure side of the upstream stator trailing edge. As illustrated by Day (1993a), this pitch location tends to minimize the effects of upstream stator wakes on the measurements.

The signals obtained from the pressure transducers are DC coupled so that the variations of the full pressure signals can be determined. The data is collected at a rate of 32.8 kHz through a 13-bit A-D converter with an analogue anti-aliasing filter at 12.8 kHz. For stall inception measurements, a fine time-resolution is important as it is directly related to the spatial flow field resolution in the rotor blade passages. However, to obtain a clear picture of stall inception, it is desirable to eliminate the relatively high amplitude rotor wake perturbations. The data presented in this paper have therefore been subsequently digitally filtered at 80 percent of the rotor blade passing frequency.

Thirty seconds of data are recorded for each stall inception investigation. This allows standard instability investigations to be conducted with some very slow and repeatable throttle transients, which fully satisfy the quasi-steady-state condition. The fast throttle-closing experiments are carried out using three throttle valves at their maximum closing speed.

Experimental Results

Nature of Stall Inception on the Compressor Map. Figure 3 shows the static pressure signals obtained at the upstream plane of each rotor row during a standard (i.e., quasi-steady throttling) instability investigation at 70 percent of design speed. The traces from the sensors located in the same measurement plane are plotted on the same graph but each pressure signal is translated of a constant equal to its circumferential position. The time axis is represented here using the physical signal from a revolution counter clock in order to provide a reference angle in the relative frame.

As can be seen in Fig. 3, the stall inception process in this machine is initially characterized by a very short length-scale disturbance (i.e., spike localized to 2 or 3 blade passages) of small amplitude (about 1 percent of the mean flow pressure), which propagates at a fast rate around the annulus (73 percent of rotational speed) and which rapidly grows. It then spreads out to the whole annulus circumference while slowing down to 55 percent of rotor speed. This fully developed rotating stall cell finally leads to a global instability as indicated by the fall of the circumferentially averaged static pressure in the last plane of measurement. In this example, the whole stall inception process (i.e., from the first disturbance detected to the system instability) takes less than five rotor revolutions. Another point worth noting is that the first disturbance is clearly detected in the measurement plane upstream of the first rotor, which would seem to indicate a stall initiated by the first stage.

At other speeds, a very similar picture is obtained. The only point of difference consists in the axial location of the first disturbance detected. For example, Fig. 4 shows a standard instability investigation at the design speed for which the first disturbance detected is seen in the last plane of measurement (i.e., upstream of rotor 4). This would in turn indicate a stall initiated by the last stage. For this machine, the off-design stage matching at different speeds is dependent on both compressibility effects and the nominal IGV scheduling. It is therefore difficult to know exactly how the axial distribution of blade loading varies with speed. This point will become clearer when looking more specifically at the influence of different IGV settings.

At all the speeds above 70 percent, the final system instability observed is a low-frequency deep surge cycle. At 50 percent of design speed, the compressor operates in stable operation with a two-cell rotating stall regime at the front (Fig. 5). This pattern evolves into a single-cell deep stall at lower flows, one cell rapidly shrinking while the other grows.

A conclusion of this section is that this machine presents a short length-scale stall inception pattern on all the compressor map whatever the resulting global instability is. Moreover, no wavelike activity is apparent on the raw traces before stall. This question will be further dealt with in the section concerning the analysis of the data.

Effect of IGV Setting. Varying the IGV setting angle modifies the steady-state matching of the various compressor stages. A point of interest is therefore to examine the situation for which a stage has been deliberately more heavily loaded than the others. Another interesting case is that for which all the

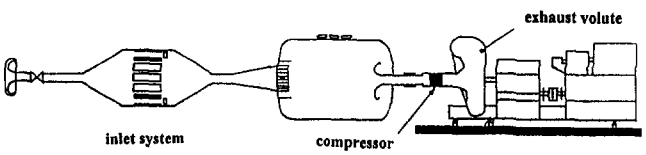

Fig. 1 Cross-sectional view of the rig

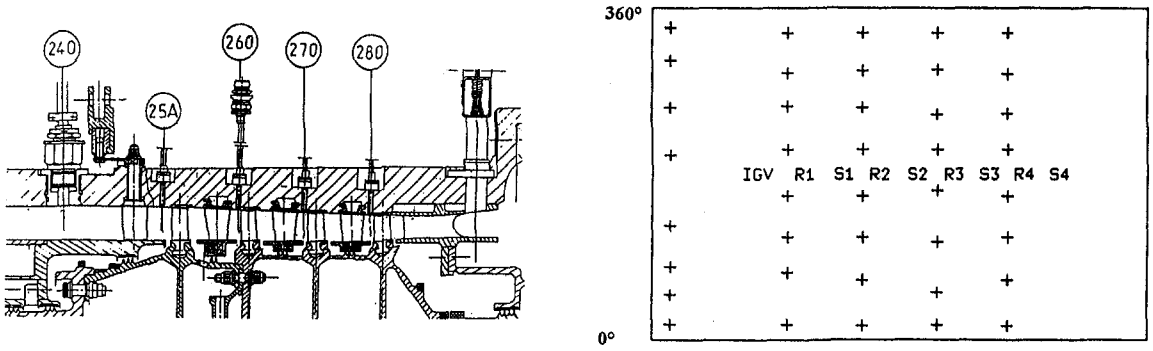

Fig. 2 Axial and circumferential positioning of fast-response pressure transducers

stages are reasonably well matched near the surge point as it might be more favorable to the development of a modal instability (Day, 1993a).

In this experiment, it is found that varying the IGV setting angle has a clear effect on the axial location of the first flow disturbance detected. It is illustrated by Figs. 6 and 7 where the results of standard instability investigations at 92.5 percent of design speed have been plotted for two different IGV setting angles. For an IGV setting angle of +5 deg (Fig. 6), the first disturbance is clearly detected in the plane of measurement upstream of the first rotor, whereas it is in the last plane of measurement on Fig. 7 (IGV angle of +6 deg).

This effect has been studied at three different speeds (87.5, 92.5, and 100 percent) and the same conclusion can be drawn. Opening the IGVs (thus loading the first rotor) tends to move the first disturbance detected to the front stage of the compressor. Closing the IGVs (thus unloading the first rotor) has the effect of moving the first disturbance seen to the last stage. For the three speeds investigated, the IGV setting angle corresponding to the transition between these two situations can be determined with good repeatability. Although there is some measure of uncertainty for events at the transition angle, the compressor presents a very predictable behavior for IGV angles only 2 deg away from the transition angle. These angles are given in Table 2 for the three speeds investigated. As expected, it can be noted that, at higher speeds, IGVs have to be opened to balance the compressibility effects, which tend to load downstream stages.

This is the only apparent effect of varying the IGV setting angle. In particular, no transition from spikes to modal waves can be found on the compressor map, even at midspeeds (87.5 and 92.5 percent) for which the aerodynamic loading was originally thought to be well distributed throughout the compressor near the surge point.

These results have been tested by a throughflow analysis derived from steady-state interrow and traverse measurements.

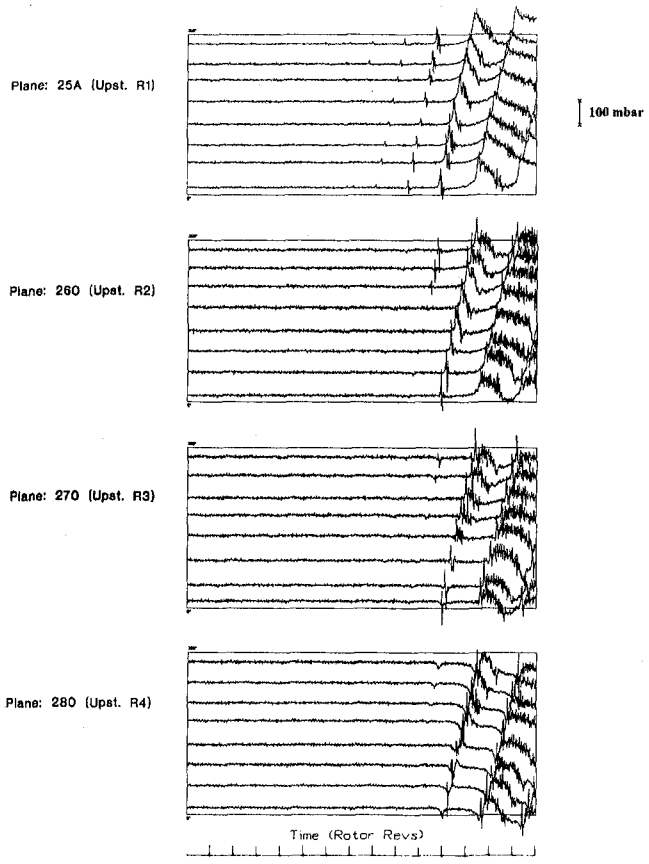

Fig. 3 Instability inception at 70 percent of design speed—IGV setting of +10 deg

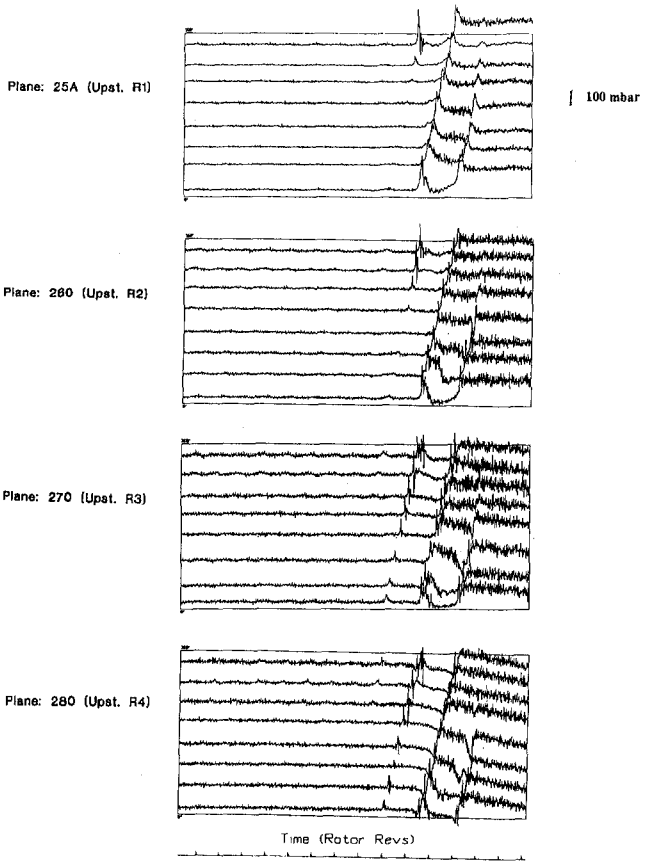

Fig. 4 Instability inception at design speed—IGV setting of −8 deg

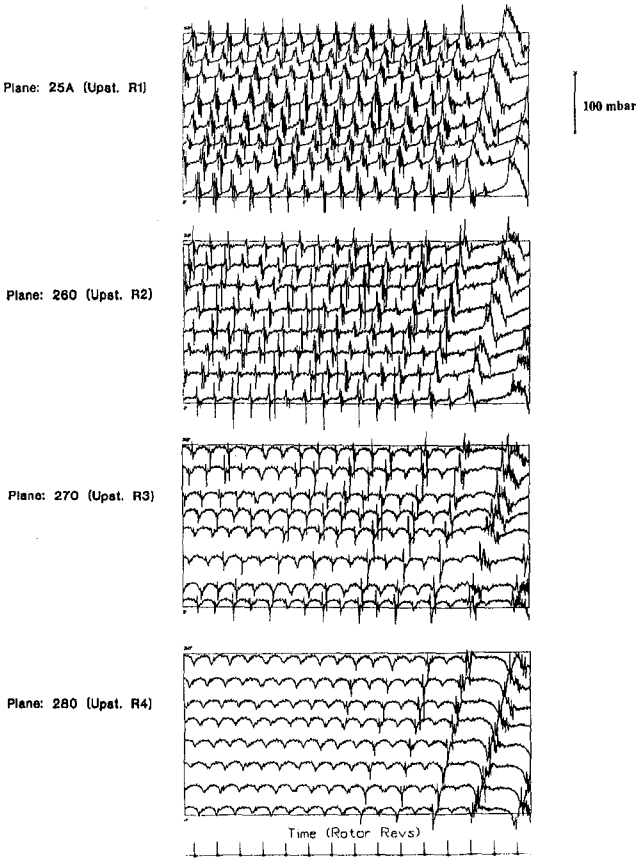

Fig. 5 Instability inception at 50 percent of design speed—IGV setting of +10 deg

Although it is based on some simplifying assumptions, this calculation provides useful trends on the off-design stage mismatching. It is found that, along the surge line, the lowest values of local diffusion ratio are associated with the first rotor and last stator rows. Varying the IGV setting angle does not profoundly alter the situation but decides which row (between the first rotor and the last stator) is the most critical in terms of local diffusion ratio.

This finding is consistent with the axial location of the first disturbance detected. Moreover, it shows that the stages are never really well matched along the surge line (in a two-dimensional sense), which might explain why modal perturbations cannot develop.

Effect of Fast Throttle Closing. The objective of this test is to establish clearly the effect of fast transients on the nature of the stall inception process. The most rapid transients occur in military engine during a fuel injection rise at a given operating speed when a rapid thrust increase is required. A typical value for a transient from the operating line to a point near the surge line is 0.5 second. This situation is reproduced in this experiment by a fast throttling of the compressor outlet which takes 1 s from choke to surge points. This is obtained using three throttle valves at their maximum closing speed. For safety considerations, a stall detection and avoidance system has been set up that fully opens the valves when a flow disturbance above 50 mbars is detected from the unsteady pressure transducers.

For the two speeds investigated in this experiment (80 and 100 percent of design speed), it is found that fast transients apparently have no influence on the nature of the stall inception process. This result is not very surprising as such transients are still comparatively slow in relation to the characteristic time scales involved in rotating stall (of the order of 100 Hz). It nevertheless confirms that the choice of an active stall control strategy is not affected by fast transient considerations.

Analysis of Data

Recently, a fine spectral analysis technique was used by Tryfonidis et al. (1995) to detect the presence of prestall waves (i.e., small-amplitude modal perturbations prior to the formation of a finite stall cell) in a large variety of compressors including those with a localized stall inception pattern. The principle of this technique is to measure the energy of propagating waves in the signals from a circumferential array of sensors during a given period and to see how it varies when approaching stall.

This analysis technique can be applied on the H4 compressor stall inception measurements and for instance, the forward traveling energy of the first spatial harmonic is shown in Fig. 8. This energy spectrum is calculated using a time window of about 50 revolutions positioned just prior to the first flow perturbation detected and a clear peak corresponding to the rotational speed can be seen (230 Hz, design speed). Similar results are obtained for the first spatial harmonic from all the measurements taken (even for steady-state points away from stall) and there is no noticeable change in the peak amplitude along the compressor operating line. For the second and third harmonics, however, no clear peak is visible. One hypothesis from the authors is that this first-order sine wave traveling at the speed of rotation could be associated with a slight whirling motion of the rotor due to shaft misalignment or, more generally, with a circumferential nonuniformity of blade tip radius. Apart from the 1/rev signal, this spectral analysis does not yield any conclusive result and, in particular, there is no clear peak of propagating energy at a fraction of rotor speed. A conclusion of this section is therefore that there is no clear evidence of prestall waves in the H4 compressor stall inception data.

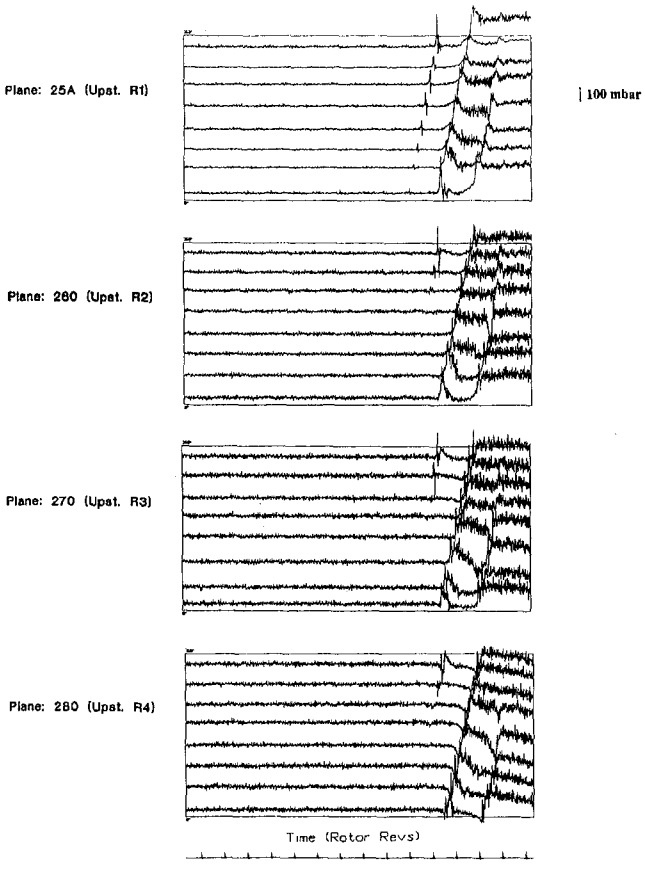

Fig. 6 Instability inception at 92.5 percent of design speed—IGV setting of +5 deg

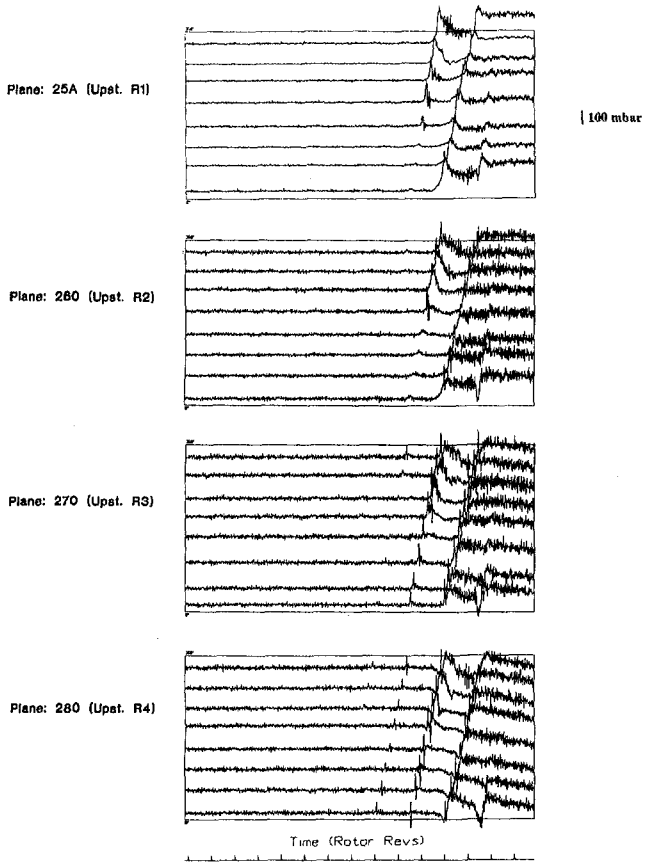

Fig. 7 Instability inception at 92.5 percent of design speed—IGV setting of +6 deg

As the spatial modal analysis is ill-adapted to the study of short length-scale disturbances for lack of adequate spatial resolution and resulting aliasing problems, a simple analysis technique has been specifically developed for the H4 compressor stall inception measurements. It is based on detecting flow perturbations of a certain duration and amplitude in the measurement plane where the instability originates and on plotting their angular positions in both the stationary and rotating frames of reference. The interest of looking at the data in the rotating frame is that the spatial resolution in this frame corresponds in part to the sampling resolution in the stationary frame. The duration of the filtering window is equivalent to two rotor blade passages so that high-amplitude rotor wake perturbations are eliminated. The threshold amplitude is chosen as 8 mbar for perturbations detected in the plane upstream of the first rotor and 16 mbar for perturbations detected in the last plane of measurement (i.e., thresholds proportional to the annulus-averaged pressure). The perturbations detected from all the sensors are represented on the same graph and when more than one perturbation is detected at the same time, only the angular position of the highest amplitude perturbation is kept.

An example of this technique is shown in Fig. 9 where the relative angular positions of flow disturbances detected in the last measurement plane have been plotted for 15 revolutions

Table 2 IGV setting corresponding to the transition between the first disturbance being detected at the front and at the back

Speed (% of Design):	Transition Angle:
100%	-8°
92.5%	between +5 & +6°
87.5%	+11°

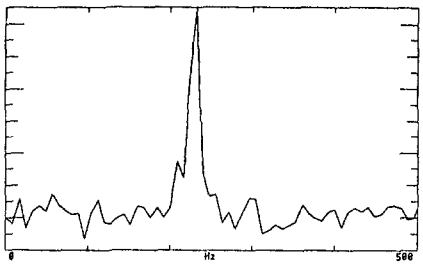

Fig. 8 Prestall forward traveling energy of the first spatial harmonic design speed (230 Hz)—IGV setting of −8 deg

prior to and during stall. This stall inception sample was taken at design speed with an IGV setting angle of −8 deg for which the last stage stalls first. It is worth noting that the growth of a finite-amplitude perturbation appears as an almost continuous line in the relative frame so that the origins (in space and time) of a rotating finite stall cell can be determined. Several flow perturbations can be seen at about the same rotor position prior to stall, which would seem to indicate a particular region of the rotor prone to stall. The corresponding situation in the stationary frame of reference is shown in Fig. 9 where the angular position corresponding to the onset of stall can also be determined (though with less precision). Perturbations can be seen prior to stall from the same three sensors. These perturbations are those also visible on the raw pressure traces (i.e., Fig. 4).

The relative and absolute angular positions corresponding to the onset of stall have been determined for a large number of stall events with different IGV setting angles at design speed (the first disturbance being either detected upstream rotor 1 or rotor 4). As can be seen in Fig. 10, a striking result is that all the tangential positions obtained from the different stall events are very close to each other in both the rotating and stationary frames of reference. This would indicate that there are regions of both the annulus and the rotors (i.e., 1 and 4) that are very

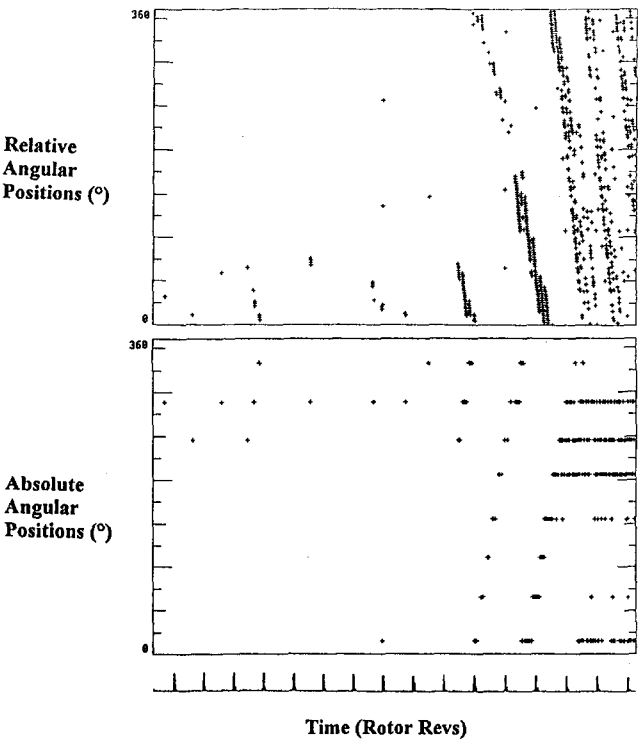

Fig. 9 Relative and absolute angular positions of the disturbances detected in the last plane of measurement design speed—IGV setting of −8 deg

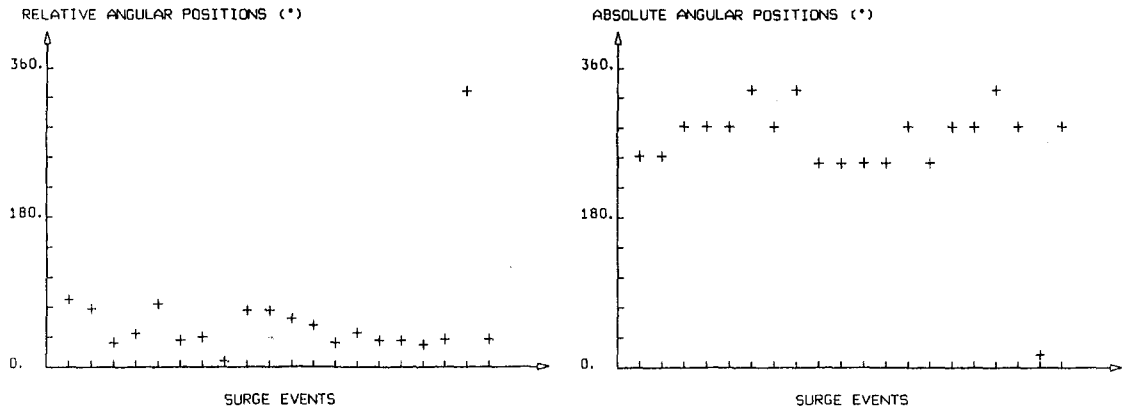

Fig. 10 Relative and absolute angular positions of the first disturbances detected for different events and IGV settings—design speed

favorable to blade stall. Again, one hypothesis is that a small shaft misalignment combined with a slightly oval casing might be responsible for this effect. It would be consistent with the result of the spectral analysis and would demonstrate, for this compressor at least, the strong influence of rotor tip gaps and of any circumferential nonuniformity on the stall inception process. However, no particular effort has been made to identify geometric nonuniformities in this machine. This is a point that therefore requires further investigation.

Discussion

The experimental results presented in this paper have some important implications for stall warning techniques and active stall control strategies.

First, as no prestall waves can be detected and as the raw pressure traces show very little warning time before stall (always fewer than five rotor revolutions), the scope of any stall warning technique is obviously limited and it is more appropriate to talk of an early stall detection technique. An idea developed in this paper is to use the finer spatial resolution in the rotating frame of reference. Moreover, it has been found that some short length-scale disturbances can be detected prior to stall in particular regions of the rotor. It is therefore possible to imagine a technique that would characterize the usual locations for perturbations, then diagnose impeding stall when perturbations are continuously found in regions of the rotor not previously affected.

Second, the requirements for an active stall control technique that could operate satisfactorily on the H4 compressor are quite severe. The rapid development (less than five revolutions) of a localized disturbance, which can either be initiated within the first or the last stage, requires at least two circumferential arrays of sensors and actuators (upstream rotors 1 and 4). Moreover, due to the short length scale of the disturbance, the frequency response of the whole system (i.e., sensors, controller, and actuators) must be of the order of ten times the rotor frequency. Finally, the control technique must accommodate perturbations of finite amplitude (finite energy required) which are highly nonlinear. A linear active stall control technique of the type used by Paduano et al. (1993) and Haynes et al. (1993) to damp modal perturbations would not be very effective in this case. A technique based on very local actuation means (e.g., puffer jets) such as that used by Day (1993b) would seem much more appropriate.

Conclusions and Summary of Results

This paper has presented unsteady measurements from a modern high-speed four-stage compressor with highly resolved fast-response instrumentation. The main results of this experimental investigation can be summarized as follows:

- A localized stall inception pattern was observed on all the compressor maps. As far as the author could ascertain, modal perturbations played no part at all in the instability inception and furthermore, no prestall waves could be clearly detected.
- The effect of stage matching on stall inception was clearly demonstrated using variable inlet guide vanes. The first disturbance detected was found to be associated with the most heavily loaded stage.
- Fast transients as encountered in military engines have apparently no effect on the nature of the stall inception process.
- The stall inception pattern observed in this experiment appeared as very local and organized, starting at particular angular positions in both the stationary and rotating frames of reference. This feature, first observed by Day (1993a), confirms the importance of any circumferential nonuniformity on the stall inception process. Overall, the pattern of stall inception identified in this compressor is very similar to that described by Emmons et al. (1955).
- Severe requirements have been identified for an active stall control technique, which would be applicable to the H4 compressor. A technique based on fast-response local actuation would seem the most appropriate.

Acknowledgments

This test program was conducted within the IMT AC3A Project No. 2031 supported by the Commission of the European Communities. The contributions from all the partners involved in the project are fully acknowledged and particularly that of Ivor Day for his role as coordinator of the various experimental investigations.

References

Boyer, K. M., King, P. I., and Copenhaver, W. W., 1993, "Stall Inception in Single-Stage, High-Speed Compressors With Straight and Swept Leading Edges," AIAA Paper No. 93-1870.

Day, I. J., and Freeman, C., 1993, "The Unstable Behavior of Low and High Speed Compressors," ASME Paper No. 93-GT-28.

Day, I. J., 1993a, "Stall Inception in Axial Flow Compressors," ASME JOURNAL OF TURBOMACHINERY, Vol. 115, pp. 1–9.

Day, I. J., 1993b, "Active Suppression of Rotating Stall and Surge in Axial Compressors," ASME JOURNAL OF TURBOMACHINERY, Vol. 115, pp. 40–47.

Emmons, H. W., Pearson, C. F., and Grant, H. P., 1955, "Compressor Surge and Stall Propagation," *Transactions of the ASME,* Vol. 79.

Franck, B. J., King, P. I., and Copenhaver, W. W., 1994, "Effects of Leading Edge Sweep on Stall Inception in a High-Speed Single-Stage Compressor," AIAA Paper No. 94-2696.

Garnier, V. H., Epstein, A. H., and Greitzer, E. M., 1991, "Rotating Waves as a Stall Inception Indication in Axial Compressors," ASME JOURNAL OF TURBOMACHINERY, Vol. 113, pp. 290–302.

Haynes, J. M., Hendricks, G. J., and Epstein, A. H., 1993, "Active Stabilization of Rotating Stall in a Three-Stage Axial Compressor," ASME Paper No. 93-GT-46.

Longley, J. P., Shin, H.-W., Plumley, R. E., Silkowski, P. D., Day, I. J., Greitzer, E. M., Tan, C. S., and Wisler, D. C., 1996, "Effects of Rotating Inlet Distortion on Multistage Compressor Stability," ASME JOURNAL OF TURBOMACHINERY, Vol. 118, pp. 181–188.

McDougall, N. M., Cumpsty, N. A., and Hynes, T. P., 1990, "Stall Inception in Axial Compressors," ASME JOURNAL OF TURBOMACHINERY, Vol. 112, pp. 116–125.

Paduano, J. D., Epstein, A. H., Valavani, L., Longley, J. P., Greitzer, E. M., and Guenette, G. R., 1993, "Active Control of Rotating Stall in a Low-Speed Axial Compressor," ASME JOURNAL OF TURBOMACHINERY, Vol. 115, pp. 48–57.

Tryfonidis, M., Etchevers, O., Paduano, J. D., Epstein, A. H., and Hendricks, G. J., 1995, "Prestall Behavior of Several High-Speed Compressors," ASME JOURNAL OF TURBOMACHINERY, Vol. 117, pp. 62–80.

Wilson, A. G., and Freeman, C., 1994, "Stall Inception and Development in Axial Flow Aeroengine," ASME JOURNAL OF TURBOMACHINERY, Vol. 116, pp. 216–225.

Modeling Tip Clearance Effects in Multistage Axial Compressors

S. Baghdadi
Pratt & Whitney,
United Technologies,
West Palm Beach, FL 33410

A variety of techniques for simulating the effects of rotor tip clearances in multistage axial compressors is discussed. Proper recognition of stage coupling and rematching effects is shown to be key to successful modeling of the overall behavior of actual engine compression systems. The application of a relatively simple one-dimensional unsteady row-by-row systems analysis is presented and shown to compare well to test data from several engine compressors.

Introduction

The instantaneous clearances between rotating and stationary elements in turbine engine compression systems have critical impacts on the engine's stability. These clearances vary significantly over the engine operating envelope—variations are due to rotor speed changes, to internal temperature and pressure changes, and to differences in the thermal inertias of the elements; variations can also occur due to wear or due to momentary interference between parts ("rubs").

Engine usage, mission, and details of the rotor and case design all influence the operating conditions at which the most open clearances occur; the compression system stability characteristics over the engine power range, when coupled with the clearance characteristics, will dictate the conditions under which the engine stall margin is minimum. Figure 1 compares high-pressure compressor tip clearance distributions near the stability limiting condition for three different engines: a large commercial turbofan shortly after take-off; a fighter engine accelerating from idle to maximum power; and a different fighter engine that has been flown through volcanic ash. These three examples illustrate the variations in tip clearance encountered in modern jet engines. In the first two examples, the open clearances affect the engine stall margin, since the clearance increases occur for relatively short durations; in the third example, both stall margin and fuel consumption are permanently affected.

Observed Trends

It is well known that clearance increases cause substantial degradations in compressor stability margins (Freeman, 1985, for example). However, the sensitivity of multistage machines to this parameter varies considerably; while "rules of thumb" are reasonably useful in projecting the influence of tip clearance on compressor efficiency, they are much less so in projecting the effects of tip clearances on the stability of multistage machines. This is because stage-to-stage interactions play an important role in determining the stability of compressors; it is commonly observed, for instance, that the stall margin degradation of an entire compressor is very different from that of the stage or stage block in which the clearance has been changed. Difficulties in predicting the instantaneous tip clearance distributions throughout the compressor often add to the complexity of the "tip clearance problem," so that most engine development programs devote significant resources to determining and correcting compressor tip clearance-related stability shortfalls.

The impact of tip clearance on the loading capability (i.e., stability) of individual stages or groups of a few low-speed stages is more easily generalized than is the effect on entire high-speed compressors. Single-stage machines (of any speed) and low-speed machines with only a few stages have minimal stage interactions and have been found to produce quite consistent correlations of stability margin[1] with clearance-to-chord ratios. Figure 2 shows such a correlation (Byrne, 1994) together with the supporting research data (Bettner and Elrod, 1983; Fujita and Takata, 1984; Fligg, 1966; Beacher, 1984; McDougall et al., 1990; Baghdadi, 1994). The data, which are from a wide variety of compressors, form a fairly broad band, but are sufficiently organized that the correlating curve can be drawn through the center of the band. The slope of this curve is the stall margin sensitivity to tip clearance. At all but extremely tight clearances, the stall margin sensitivity is seen to vary inversely with tip clearance. This trend is not surprising, in that tip loadings must decrease as clearances increase. One result of the observed trend is that modern machines, which are designed to operate at tighter tip clearances, are more sensitive to that parameter than are older designs. Another interesting feature of the curve in Fig. 2 is that, at very tight clearance, it projects a region of zero sensitivity. Some research machines (McDougall et al., 1990; Fligg, 1966) even show a negative sensitivity at very tight clearance-to-chord rations. McDougall explains that the flow in his test stage separated at the rotor hub; tightening the clearances draws flow away from the hub, thus increasing the loading and the losses in the critical region. Other explanations for the low-sensitivity region at very tight clearances are suggested below.

The nonlinear nature of the curve in Fig. 2 helps explain why many designers, assuming linear behavior, have ascribed widely different sensitivities to different stages.

Modeling Approaches

Aerodynamic instabilities such as surge and rotating stall arise from a complex interaction between the volume dynamics and the pressure/flow characteristics of the entire compression system (Emmons et al., 1955; Greitzer, 1976; Stenning, 1980). Recognition of this systems aspect of compressor stability has led to the creation of unsteady flow models of varying degrees of complexity (Greitzer, 1976; Tesch and Steenken, 1976; Baghdadi and Lueke, 1982; Davis and O'Brien, 1991). In the context of such system models, changing the clearance of one blade row affects the pressure/flow characteristic of the row and therefore of the entire compression system. In addition, experiments and recent Computational Fluid Dynamics efforts have shown that clearance changes within a blade row can have important effects on the performance of the downstream blade row (Dawes, 1994; Howard et al., 1994), thus further affecting the pressure/flow characteristic of the system.

Contributed by the International Gas Turbine Institute and presented at the 40th International Gas Turbine and Aeroengine Congress and Exhibition, Houston, Texas, June 5–8, 1995. Manuscript received by the International Gas Turbine Institute March 10, 1995. Paper No. 95-GT-291. Associate Technical Editor: C. J. Russo.

[1] Surge Margin (SM) is used for high-speed ("real") machines. Throttle Margin (TM) is used for low-speed ("laboratory") machines, which have very low pressure ratios. See Nomenclature for definitions of these terms.

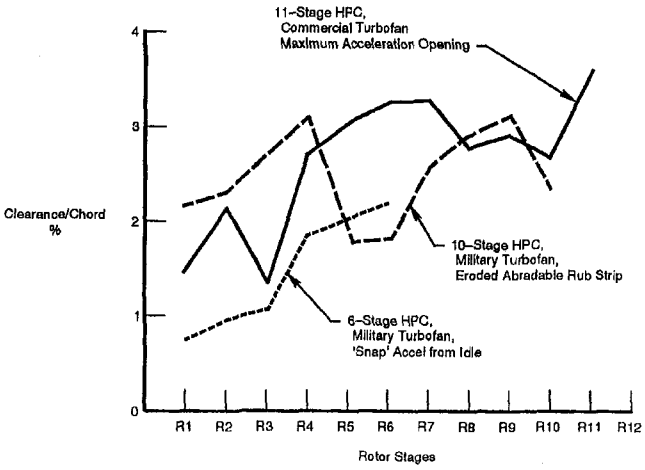

Fig. 1 Clearance distributions near stability limits for three compressors

Modeling the impact of tip clearances on the stability of compressors thus involves predicting the impact of clearance changes on the pressure/flow characteristic of each individual blade row; modeling the impact of clearance changes on the following blade row; and, finally, calculating the response of the entire compression system to the change in the characteristics of each of the individual blade rows.

Modeling the Impact of Clearance Changes on Single and Multirow Characteristics

The effect of increasing tip clearance on the performance of airfoil rows has been the subject of considerable experimental and analytical research (Lakshminarayana, 1970; Adamczyk et al., 1993; Freeman, 1985; Dring et al., 1995). Several of the simple (i.e., non-CFD) models give reasonably accurate estimates of the impact of tip clearances on the operating line efficiencies of many multistage compressors. An example for modern six-stage machine is shown in Fig. 3. The analysis in this example uses a modified version of the clearance loss model of Lakshminarayana (1970). However, in general such models tend to underestimate the impact of clearances on stage stall margin. Since the simple models include data correlations that are "tuned" to achieve good results at the operating line, it is not surprising that they would not work as well at near-stall conditions. . . . The chordwise loading distribution is considerably more "front loaded" near stall than at design conditions, and this will lead to a stronger and more tangential leakage vortex, as has been shown in many CFD studies (Adamczyk, 1984). Moreover, to the extent that simple models are based on analyses or correlations of data from single rows, they will not incorporate the profile/unsteady flow effects on the downstream blade row that become increasingly important at near-stall conditions. Improvements to the simple models that recognize chordwise loading and profile effects on blade row loss, turning, and blockage appear feasible, but, to the author's knowledge, have not been pursued.

The most recent trend has been to use three-dimensional CFD analyses to model tip clearance flows. Advances in this area have been very rapid, and accurate multirow solutions are now achievable (Dring et al., 1995; Dawes, 1994; Adamczyk, 1984). Multirow solutions have a substantial advantage in that they account for the response of both the rotor and the downstream stator-to-rotor clearances. The main disadvantage of this approach is that it is very time and resource intensive, so that it is not yet practical to routinely model an entire multirow compression system this way. Typical "steady" (mixing plane or deterministic stress) models consist of a few (three to seven) airfoil rows. The more accurate unsteady flow models typically consist of only two rows. By contrast, high-pressure compressors have up to 30 rows of airfoils. Efforts to improve the accuracy of these analyses, and also to reduce the computer run times, will likely allow routine executions of "steady" multirow analyses for entire compression systems within the next few years. Such multirow CFD solutions for some or all of the blade rows can provide the characteristics for the individual blade rows in the one-dimensional unsteady system model described below. As an intermediate step between the fully unsteady three-dimensional and the unsteady one-dimensional analyses of the type described below, two-dimensional unsteady solutions are currently being developed. Nonlinear extensions of methods such as those described by Hendricks et al. (1993), and Moore and Greitzer (1986) can be used to address problems involving circumferentially nonuniform clearances and rotating stall formation, and are especially useful in the context of active stability control. This type of model generally requires blade row characteristic inputs similar to those of one-dimensional models.

Three-dimensional solutions that are truly unsteady at both the blade passing frequency level and at the systems dynamic level may eventually replace the current one-dimensional and emerging two-dimensional unsteady system models, but such solutions will not become available for many years, and will not be practical for routine simulations of entire compression and engine systems for many years after that.

An alternative to using three-dimensional CFD analyses to model the effects of tip clearance on the airfoil row and row interaction characteristic is to use simple correlative models calibrated to give the "correct" characteristics for each stage (rotor/stator combination). This approach, while evidently less than general, has proven effective for the several cases of practical interest reported below.

The simple clearance loss model of Lakshminarayana (1970) has been calibrated by reference to carefully controlled clearance tests of a three-stage research compressor rig. The rig ("Rear-Stage" rig) represented three of the rear stages of a commercial turbofan HPC. The rig was tested at several values of clearance-to-chord ratio and has clearance sensitivities typical of the research rig data base, as can be observed in Fig. 2.

The intent of the calibration was to adjust the empirical constant in Lakshminarayana's model to match the change in the

Nomenclature

C_θ = tangential velocity
D_f = diffusion factor = $(V_1 - V_2)/V_1 + (R_2C_{\theta 2} - R_1C_{\theta 2})/(2\sigma R_{av}V_1)$
N_C = corrected speed
P_R = pressure ratio
R = blade mean radius
SM = surge margin = $(\mathrm{Pr}_{surge}/PR_{operatingline} - 1)$ at constant flow
TM = throttle margin = $\Delta\Psi/2\Psi - \Delta\phi/\phi$
V = blade relative velocity
W_C = corrected airflow
σ = blade solidity = chord/spacing
Ψ = pressure rise coefficient
ϕ = flow coefficient

Subscripts

1 = blade inlet
2 = blade outlet
avg = average of inlet and outlet

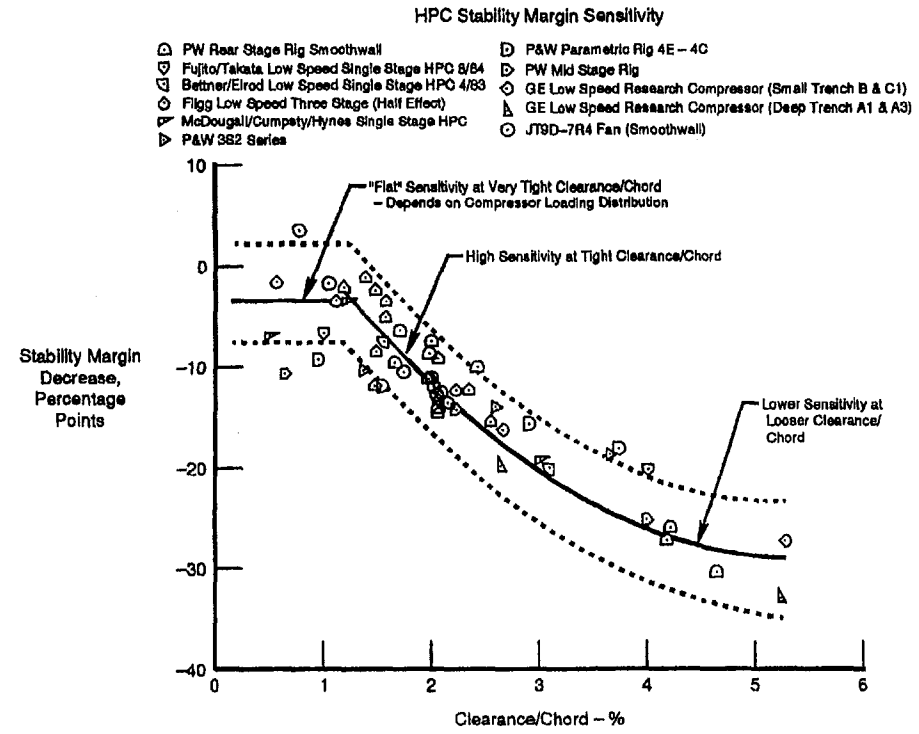

Fig. 2 Correlation of tip clearance effects on stability margins of single-stage and low-speed research compressors

research rig pressure/flow characteristic as clearances were increased from the base (tight) value. The basic model of the compressor (the AXPDY code) is described in the next section. At the base (tight) clearance, this model, which has the empiricism set to match observed operating line efficiency trends with tip clearance (Fig. 3), produced an excellent representation of the research rig; however, at the more open clearance, the basic model showed a smaller degradation in the characteristic than the data. To match the data, the clearance loss had to be adjusted upward at the higher clearance. Figure 4 compares the clearance losses as a function of airfoil loading at the nominal (design) incidence and at the near stall incidence to the basic Lakshminarayana model.

The figure, which is for a typical airfoil row at 2 percent clearance-to-chord ratio, shows that, while the Lakshminarayana model loss is reduced to best match efficiency data near design incidence, it is increased to match the flow/pressure characteristic near stall. This increase in loss can be attributed to changes in the clearance vortex strength and orientation as the airfoil's chordwise loading distribution changes with incidence. The loss increase was applied to the stators as well as to the rotors in order to model the profile/unsteady effect of the rotor clearance on the downstream stator. This calibration resulted in a model that matched the change in the research rig characteristic with tip clearance, as shown in Fig. 5.

The tip clearance model described above is calibrated to be valid in the clearance-to-chord region of greatest interest for large HPCs (up to 4 percent); this model should be amended to extend its validity to larger clearance-to-chord ratios, where clearance sensitivities are reduced (Fig. 2).

The System Model. In order to model the effects of individual blade row clearances on the overall behavior of a compressor, a stability analysis of the entire system is required. A one-dimensional unsteady analysis for assessing the perfor-

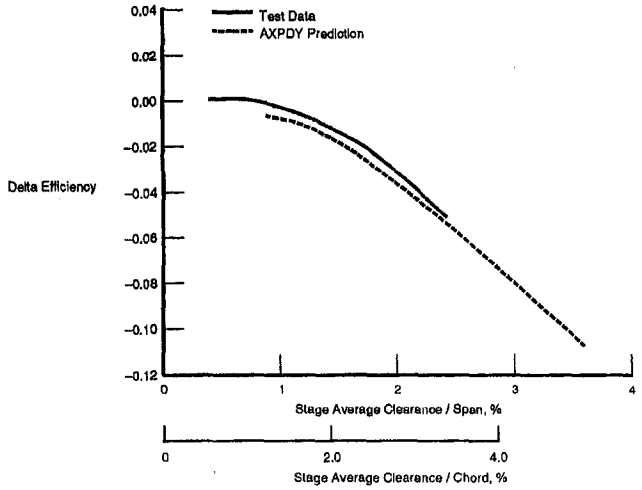

Fig. 3 Effect of tip clearance at operating line conditions

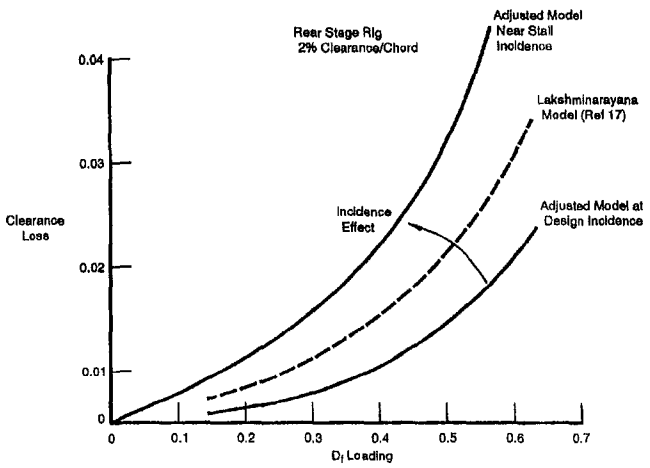

Fig. 4 Clearance loss as a function of airfoil loading

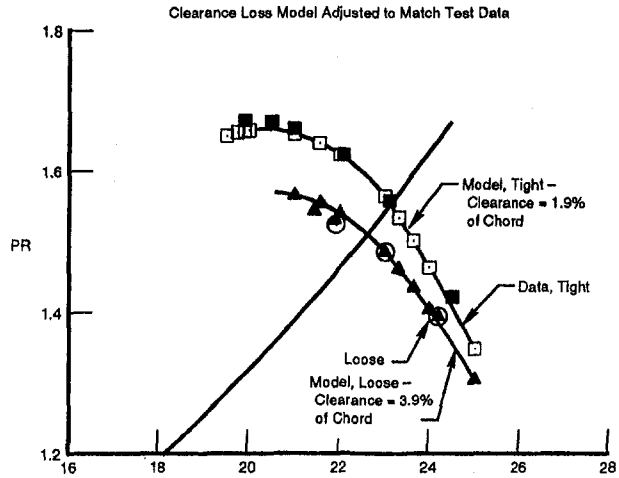

Fig. 5 Three-stage research compressor characteristic at tight and loose clearances

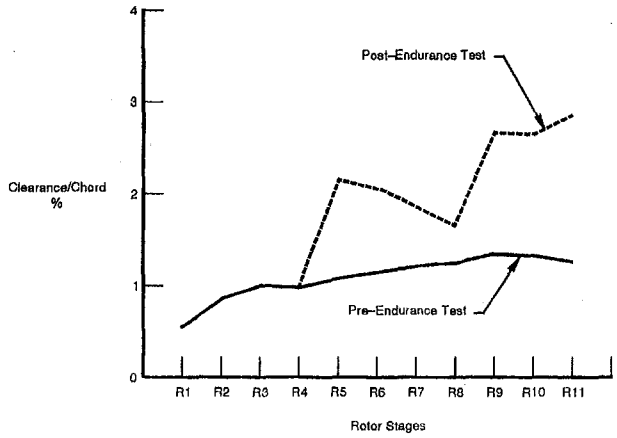

Fig. 7 Pre- and post-endurance tip clearance distributions

mance and stability of axial and axicentrifugal compression systems throughout their operating range has been developed. This analysis, known as AXPDY, combines a row-by-row performance model with an advanced volume-dynamic stability analysis. The stability portion of the analysis uses an unsteady method of characteristics technique to solve the time-dependent flow equations in the individual blade rows and volumes of a turbomachine. The blade row losses, turning, and blockage are determined initially and at each subsequent time step by the performance model. This model includes cascade correlations with incidence, Mach number, Reynolds number, tip clearance, and endwall loss effects. A "design point" blading option is used to select appropriate blading, blade loadings, and incidence at the design point. This blading is then used in the off-design analysis. The blade row characteristics that result from this model are smooth and have no slope discontinuities. These characteristics are generally in fair agreement with test data. As a typical example, Fig. 6 compares flow/pressure characteristics produced by the model to measured data for each of the stator–rotor pairs ("stages," as measured with leading edge instrumentation) of a modern high-speed compressor. The foundations of the analysis and some previous applications have been reported (Baghdadi, 1983, 1987; Baghdadi and Lueke, 1982).

This analysis (AXPDY) has been used to model the effects of aerodynamic design changes, inlet or outlet pressure/temperature pulsations, variable vane and bleed resets, and transient

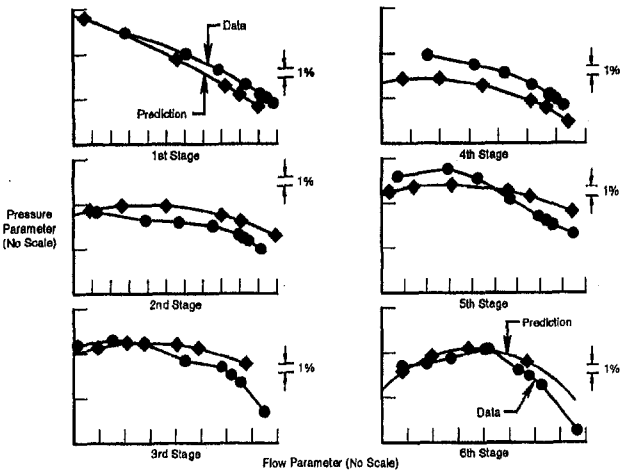

Fig. 6 Predicted and measured pressure/flow characteristics for each stage of a six-stage HPC at design speed

heat transfer on the stability and performance of many fans and compressors. When the analysis is based on "ideal" airfoil row performance, it typically does not match the overall performance characteristics of real machines exactly, but is quite close, as will be shown below. The analysis is consequently best used on a "delta" basis, to predict changes from a baseline. This analysis, upgraded to include the "calibrated" tip[2] clearance model described above, is applied to model the effects of rotor tip clearance on the stability of several multistage compressors, as described in the following.

Applications

(A) Large Commercial Turbofan. Tests aimed at quantifying the HPC stability degradation associated with long service time were conducted at Pratt and Whitney's Willgoos facility. An engine that had been in airline service was stall-tested, then refurbished, stall-tested again, subjected to a long endurance program, and stall-tested again. The high-pressure compressor rub strip dimensions were measured in the as-received condition, in the refurbished condition, and finally at the conclusion of the endurance test. These measurements allowed reasonably accurate estimation of the change in HPC running clearances. A similar endurance test was conducted with a development engine that had not been in service.

The objective of this test and analysis program was to determine how much of the observed stall margin degradation could be attributed to the increase in HPC clearances, as opposed to several other changes that occur in long-service engines.

The high-speed pre- and postendurance tip clearance distributions deduced from the rub strip measurements of the service engine are shown in Fig. 7. The front stages did not rub, so their clearances did not change at a given speed. Figure 8 shows the calculated clearance variation with speed down into the idle range for all the rotors.

The system stability analysis described above was conducted for both undeteriorated and deteriorated clearances. Figure 9 shows the model geometry. Figure 10 compares the predicted and test maps for the tight clearances case, and Fig. 11 compares the predicted stall margin degradation to that measured. The analysis is seen to be in very good agreement with the data at the high and low-power regions, but to overpredict the stability loss in the middle-power range.

(B) Fighter Engine HPC. A model for a six-stage fighter engine high-pressure compressor has been used to simulate the effects of tip clearance. Figure 12 compares the predicted and

[2] The analysis is applied "hands-off," i.e., with no further adjustments, to all the cases discussed below.

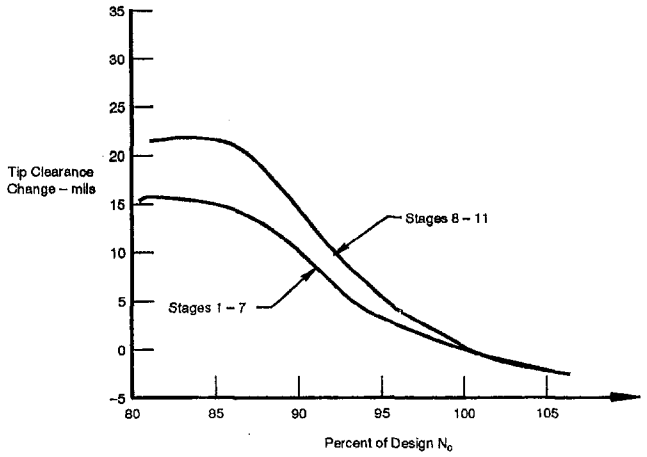

Fig. 8 Tip clearance variation with rotor speed, 11-stage HPC (analysis based on measurements at three axial and three circumferential locations)

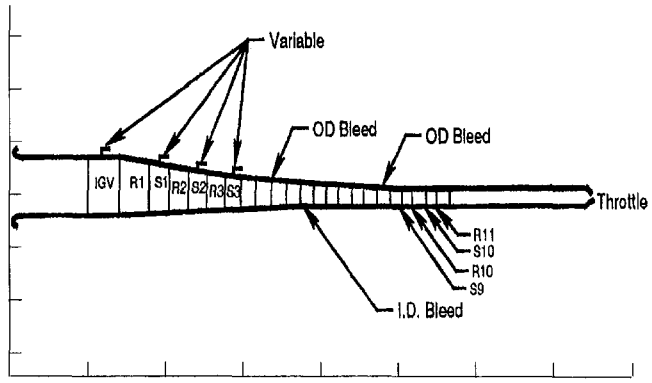

Fig. 9 AXPDY model geometry, 11-stage HPC

measured HPC maps at the nominal (tight) clearances. The model is seen to be in close agreement with the data.

Development tests of the engine are currently under way at Pratt and Whitney facilities in West Palm Beach, FL. Part of the test program has involved stall-testing of the HPC with different levels of rear-stage tip clearance. The clearance variations were accomplished by modulating the compressor bore cooling air, by executing transients with unstabilized rotor disk

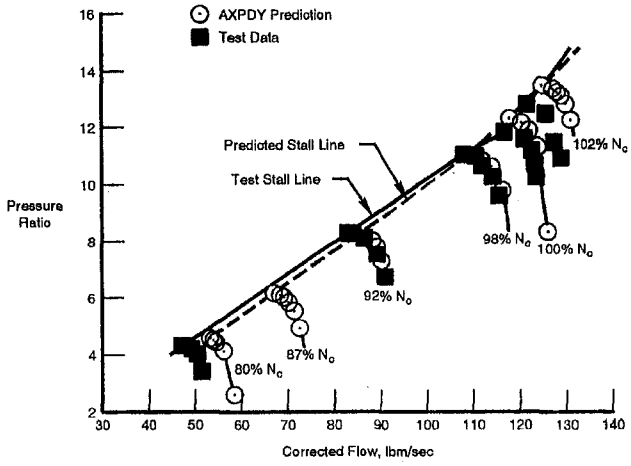

Fig. 10 Predicted and measured maps at tight clearance, 11-stage HPC, nominal vane and bleed schedules, rig test

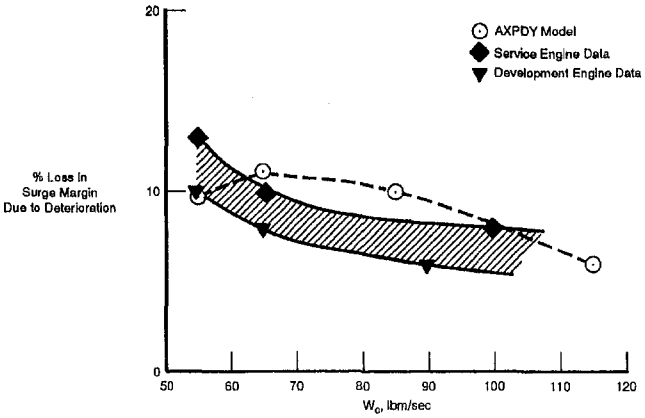

Fig. 11 Predicted and measured stall margin degradation, 11-stage HPC

and case temperatures, and by changing the rotor rub strip dimensions. The tip clearances of the three rearmost rotors were measured transiently by means of laser clearance probes.

Figure 13 shows how this compressor's stall margin responds to tip clearances changes in the rear three stages. There is an indication in the data that the sensitivity at very tight clearances is near zero. Also shown on Fig. 13 is the analytical prediction of tip clearance effects. The prediction gives a linear sensitivity at clearance levels above the design level; for clearances tighter

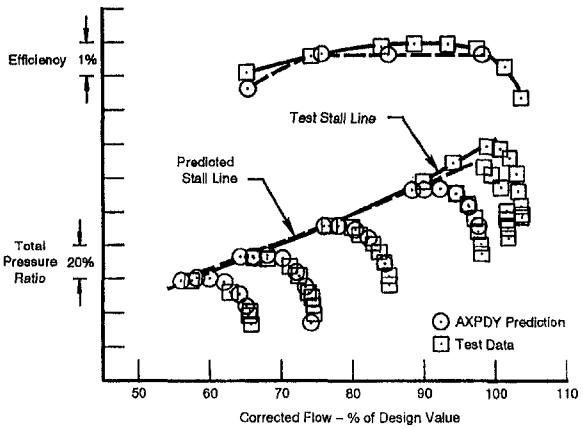

Fig. 12 Predicted and measured performance map, tight clearances, six-stage HPC

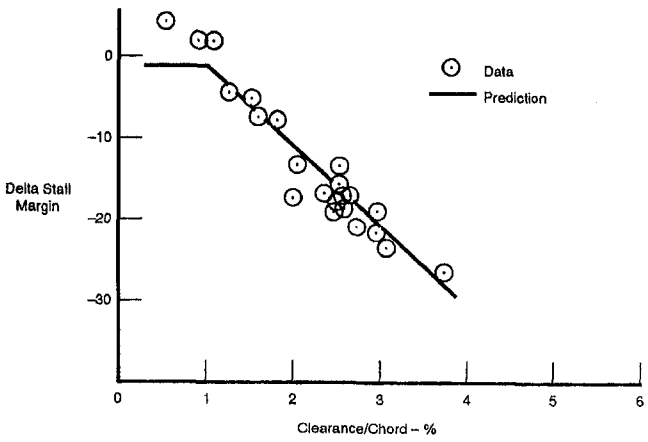

Fig. 13 Predicted and measured effects of rear-stage tip clearances on stall margin, six-stage HPC

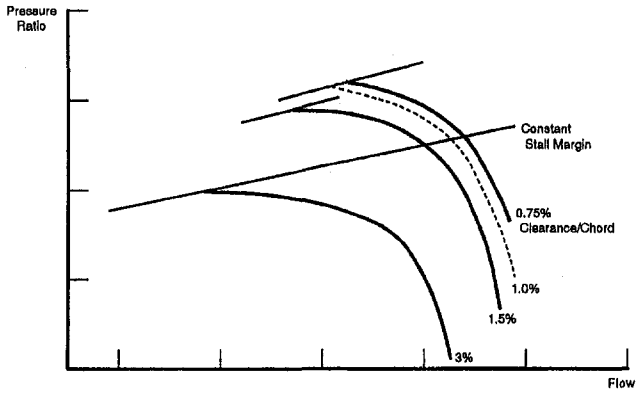

Fig. 14 Compressor stall points as function of clearance

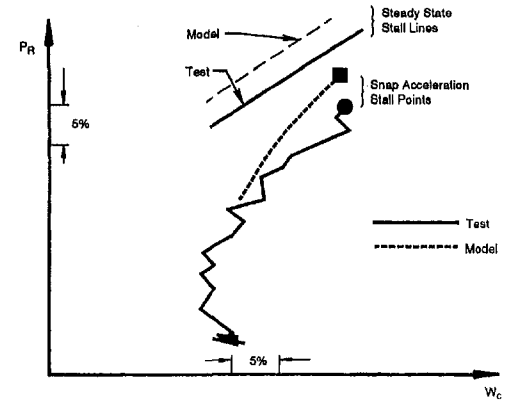

Fig. 16 Predicted and measured stall points, "snap" acceleration with fuel elevation elevated to stall limit

than design, the model predicts a zero sensitivity. Analysis of the results shows that, although the clearance losses decrease as the clearances are tightened, and the overall compressor pressure ratio at stall is increased, these changes are quite small at very tight clearances, and are offset by a flow increase and a redistribution of the stagewise work, so that overall stall margin is not affected. Figure 14 shows the predicted stall points at several clearances on a compressor map.

Military engine acceleration rates are limited by HPC stability considerations; uncontrolled "snap" accelerations from idle to full power can cause surges. This is because the HPC operating point moves up toward the stall line as fuel is added; in this situation tip clearance effects can be critical. Figure 15 shows how the clearance varies in the six-stage compressor during such a transient.

In order to model the behavior of the compression system during a snap acceleration, the compressor model was incorporated into a lower frequency model of the entire engine. This relatively low frequency engine model accounts for the thermal, clearance, and spool inertia effects that occur as the engine accelerates, and also provides the inlet and outlet boundary conditions to the high frequency core engine and HPC model. The high-frequency compressor model was activated periodically during the transient to capture the stalling limits as a function of acceleration rates and tip clearance values. Figure 16 shows that the model replicates the observed characteristics of the engine very well: The difference between the steady state stall line and "snap" acceleration stall point is captured exactly by the model.

Another series of tests was performed to determine the sensitivity of the HPC to variations in clearance of a particular stage (thought to be the "stalling" stage) and also to validate the analytical model. The full engine model incorporating the high frequency compressor model was used to predict the sensitivity of the HPC stall margin to the changes in the fifth (penultimate) stage clearance (Fig. 17(*a*)). Back-to-back tests in which only the fifth stage clearance was varied were conducted; the HPC stalls were induced by a fuel-spiking technique. The result is compared to the engine simulation of the fuel spikes in Fig. 17(*b*). This figure indicates that tightening the clearance on only one stage has a relatively small effect on the overall compressor stall margin. This is true even if that stage is the "critical" or "stalling" stage.[3]

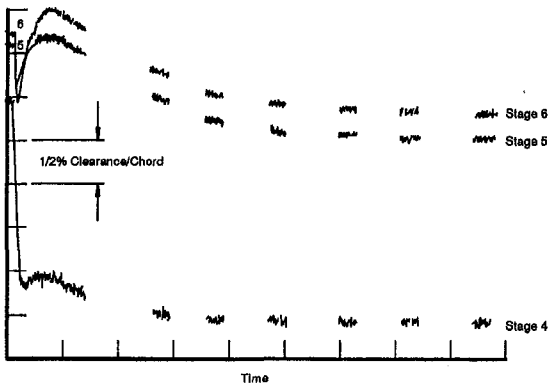

Fig. 15 Rear stage clearance changes during "snap" acceleration, six-stage HPC

A further test series was conducted to evaluate the effects of a "hot reburst" on the HPC's stall margin. In this test, the engine was allowed to warm up thoroughly at high power; then the throttle was chopped to a cruise point, and the engine "fuel spiked" to stall. This maneuver results in very tight clearances throughout the compressor. The model, using instantaneously measured tip clearances, was used to predict the HPC stall margin. Figure 17(*c*) compares the results to data for two "hot reburst" transients. The model is seen to be in excellent agreement with the test data. Figure 17(*a*) shows the measured rotor tip clearance distributions for the two hot rebursts as well as for the tight fifth stage test.

Figure 18 summarizes the predicted and test responses of this six-stage HPC to tip clearance variations.

(C) Ten Stage Military Engine HPC. Engine surges can cause momentary interference between the rotating and stationary elements in the compression system. These "rubs" result in removal of the shroud abradable material, and consequently, in increases in tip clearances. Flight operations in areas contaminated by volcanic ash can lead to erosion of the abradable rub strips, which also results in clearance increases. A program to investigate the consequences of this sort of clearance increase has been conducted as part of the development program for a military turbofan incorporating a ten-stage high-pressure compressor. Tests were conducted on several engines in order to quantify the effects of abradable loss on the HPC stall margin. Five of the engines in the test were representative of nominal (i.e., typical in-service) engines, and another three had the abradable rub strips intentionally and severely "rubbed out" to represent extreme cases. Figure 19 shows the nominal and extreme clearances for these tests. These distributions represent average values for the several engines of each category in the test program. The HPC of each engine in the program was induced to stall by performing slow decelerations from high

[3] In the context of a "systems" model, one can question the concept of a "critical stage" or blade row. All elements of a compressor contribute to the overall system stability. Rows with discontinuous flow/pressure characteristic slopes are destabilizing; but such discontinuities are not required in order for the overall system to be unstable.

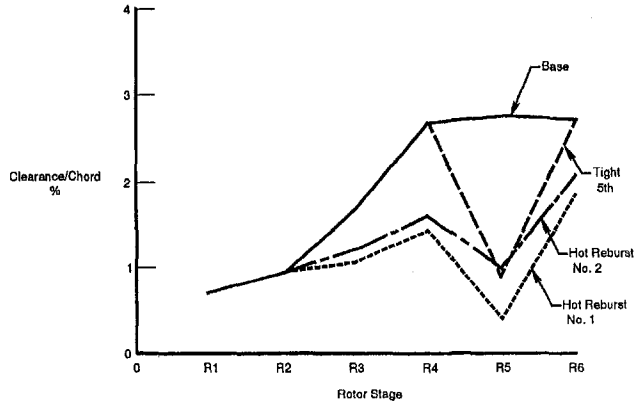

Fig. 17(*a*) Rotor tip clearance distributions near stall-limiting conditions

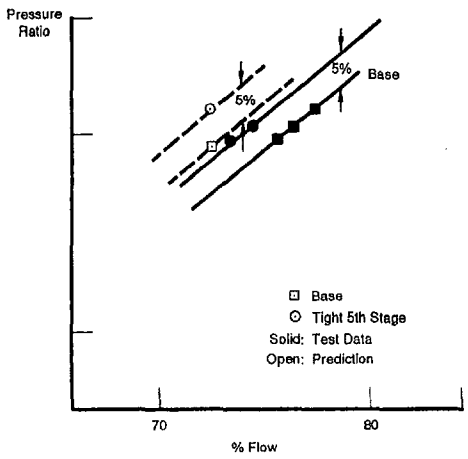

Fig. 17(*b*) Effect of tight fifth rotor on stall line

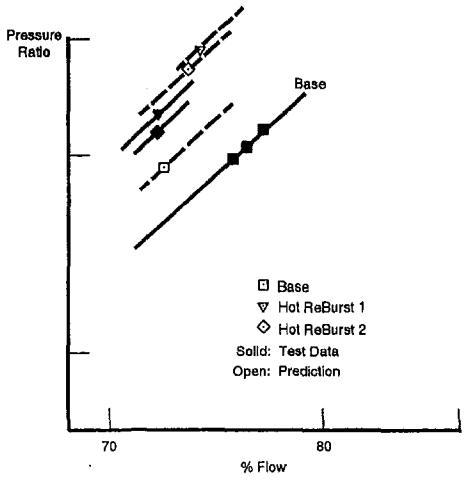

Fig. 17(*c*) Effect of hot rebursts on stall line

power with the HPC variable vanes locked in the fully open (low stagger) position. The speed at which the stall occurred (stall line intersection with the operating line) is an inverse measure of the compressor's stall margin.

Figure 20 depicts predicted locked vane deceleration maps for this compressor at the nominal and extreme clearances. Figure 21 compares the measured locked vane deceleration stall speeds to those calculated by the model. The agreement with the average of the engines of each condition is seen to be excellent, although there is a fair amount of scatter in each data set. One of the interesting observations that the model makes possible is that, although the stall occurs in the front stages of this machine, it is actually caused by the loss of flow capacity of the rear stages, i.e., as the clearances are opened, the rear stages lose flow capacity faster than the front stages do, which tends to back-pressure the front stages into stall. Thus a solution

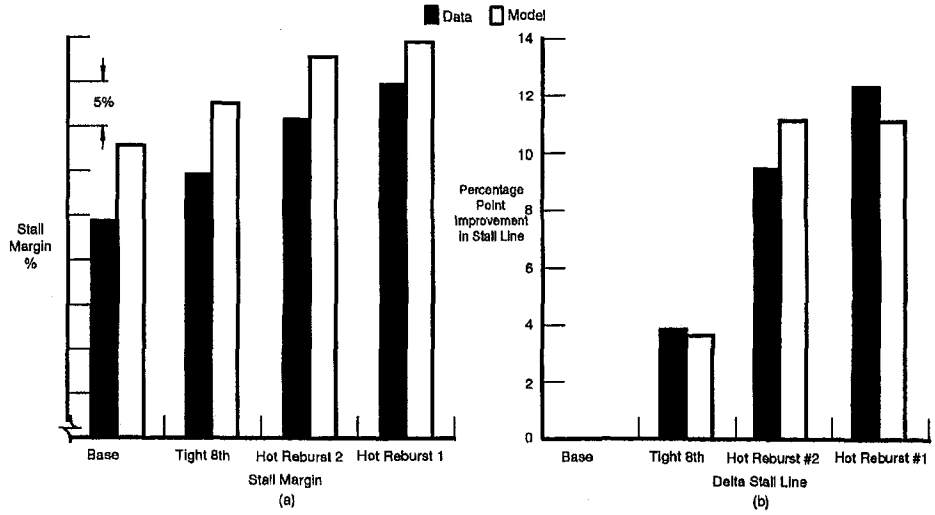

Fig. 18 Summary of tip clearance effects on stall margin, six-stage HPC: (*a*) absolute stall margin; (*b*) change in stall line

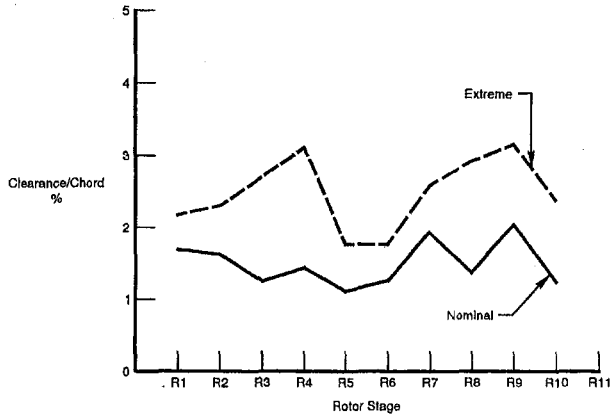

Fig. 19 Tip clearance distributions, ten-stage HPC

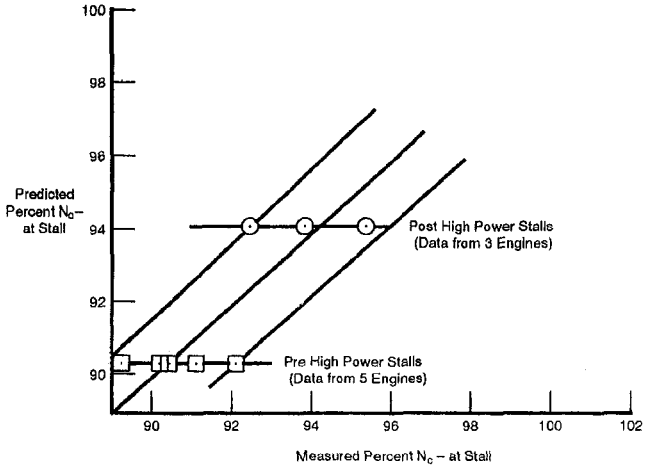

Fig. 21 Predicted versus measured HPC corrected speed at stall, locked vane accelerations, ten-stage HPC

that maintains tight clearances in the rear stages would be more effective than one that maintains tight clearances in the front stages. Tip treatments that improve either front stage stall margin or rear stage flow capacity with large clearances would also be beneficial.

Concluding Remarks

Compressor stability in general is a system dynamics issue, and is best addressed in an environment that recognizes the importance of row-to-row volume dynamic interactions as well as aerodynamic rematch effects. The elements that are critical to modeling the response of compressors to tip clearances changes include the changes in the stage pressure/flow characteristic (including the change induced in the stator by the upstream rotor clearance), and the response of the overall compressor to all of the individual characteristic changes together. This paper presents a relatively simple one-dimensional system dynamic model that incorporates these effects. In such a representation, changes in the highly three-dimensional and unsteady tip clearance flows are represented as changes in the one-dimensional blade row characteristics. Clearly, the accuracy of this representation is a critical element in the simulation. Blade row pressure/flow characteristics may be based on test data, on three-dimensional CFD analyses, or on simple correlative models. This paper has demonstrated that, for many cases of practical interest, even the simplest option—using correlative models—is adequate. The simplicity of this type of model makes it especially attractive for integration into models of entire engines. It is worth noting that the uncertainty in the knowledge of the instantaneous tip clearances is frequently a significant part of the transient stall margin uncertainty; efforts to improve engine stability analysis procedures should therefore include transient tip clearance prediction methods.

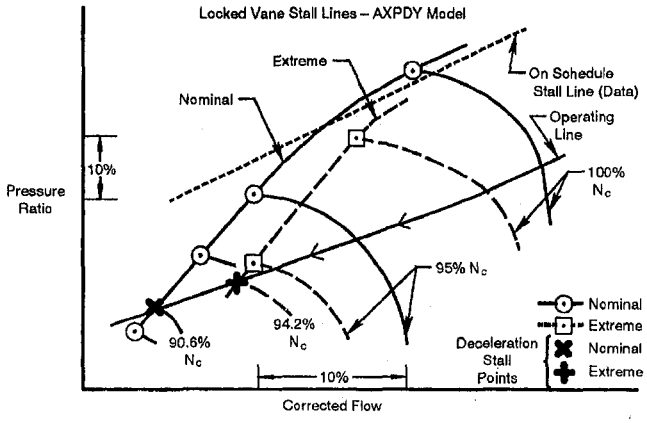

Fig. 20 Locked vane decelerations, ten-stage HPC—predicted stall points

Acknowledgments

The author wishes to thank his colleagues at Pratt and Whitney for their support of the efforts described in this paper; in particular, John Mason and Randy Rosson of the Performance and Systems Analysis group for the full engine transient simulations; and Joe Garberoglio, Kerry Byrne, and Kent Lyons of the Compression Systems Component Center for the compressor simulations and for the research rig data correlations.

References

Adamczyk, J. J., 1984, "Model Equations for Simulating Flows in Multistage Turbomachinery," NASA TM-86869; ASME Paper No. 85-GT-226.

Adamczyk, J. J., Celestina, M. L., and Greitzer, E. M., 1993, "The Role of Tip Clearance in High-Speed Fan Stall," ASME JOURNAL OF TURBOMACHINERY, Vol. 115, pp. 28–39.

Baghdadi, S., and Lueke, J. E., 1982, "Compressor Stability Analysis," ASME *Journal of Fluids Engineering,* Vol. 104, No. 2.

Baghdadi, S., 1983, "Applications of a Compression System Stability Model," AGARD Conference Proceeding No. 324.

Baghdadi, S., 1987, "Compressors for Advanced Turboshaft Engines," *Journal of the American Helicopter Society,* Vol. 32, No. 3.

Baghdadi, S., 1994, "Compressor Stall Margin Sensitivity to Rotor Tip Clearances," Internal Pratt and Whitney Memorandum.

Beacher, B. F., 1984, *Compressor Case Treatment Study,* Air Force Wright Aeronautical Laboratories Report AFWAL-TR-84-2021.

Bettner, J. L., and Elrod, C., 1983, "The Influence of Tip Clearance, Stage Loading, and Wall Roughness on Compressor Casing Boundary Layer Development," ASME JOURNAL OF ENGINEERING FOR POWER, Vol. 105, pp. 280–287.

Byrne, W. P., 1994, personal communication.

Davis, M. W., Jr., and O'Brien, W. F., 1991, "Stage-by-Stage Post-stall Compression System Modeling Technique," AIAA *Journal of Propulsion and Power,* Vol. 7, No. 6, pp. 997–1005.

Dawes, W. N., 1994, "A Numerical Study of the Interaction of a Transonic Compressor Rotor Overtip Leakage Vortex With the Following Stator Blade Row," ASME Paper No. 94-GT-156.

Dring, R. P., Sprout, W. D., and Weingold, H. D., 1995, "A Navier–Stokes Analysis of the Effect of Tip Clearance on Compressor Stall Margin," ASME Paper No. 95-GT-190.

Emmons, H. W., Pearson, C. E., and Grant, H. P., 1955, "Compressor Surge and Stall Propagation," *Trans. ASME,* Vol. 79, pp. 455–469.

Fligg, J., 1966, "Test of a Low-Speed, Three-Stage Axial Flow Compressor With Aspect Ratios of 1, 2, and 4," AIAA Paper No. 66-613.

Freeman, G., 1985, *Effect of Tip Clearance Flow on Compressor Stability and Engine Performance,* Von Karman Institute for Fluid Dynamics, Lecture Series 1985-05.

Fujita, H., and Takata, H., 1984, "A Study on Configurations of Casing Treatment for Axial Compressors," *Bulletin of the JSME,* Vol. 27, No. 230.

Greitzer, E. M., 1976, "Surge and Rotating Stall in Axial Flow Compressors, Part 1: Theoretical Compression System Model," ASME *Journal of Engineering for Power,* Vol. 98, pp. 190–198.

Hendricks, G. J., Bonnaure, L. P., Longley, J. P., Greitzer, E. M., and Epstein, A. H., 1993, "Analysis of Rotating Stall Onset in High-Speed Axial Flow Compressors," AIAA Paper No. 93-2233.

Howard, M. A., Ivey, P. C., Barton, J. P., and Young, K. F., 1994, "Endwall Effects at Two Tip Clearances in a Multistage Axial Flow Compressor With Controlled Diffusion Blading," ASME JOURNAL OF TURBOMACHINERY, Vol. 116, pp. 635–647.

Lakshminarayana, B., 1970, "Methods of Predicting the Tip Clearance Effects on Axial Flow Turbomachinery," ASME *Journal of Basic Engineering,* Vol. 92, pp. 467–482.

McDougall, N. M., Cumpsty, N. A., and Hynes, T. P., 1990, "Stall Inception in Axial Compressors," ASME JOURNAL OF TURBOMACHINERY, Vol. 112, pp. 116–125.

Moore, F. K., and Greitzer, E. M., 1986, "A Theory of Post-stall Transients in Axial Compression Systems: Part I—Development of Equations; Part II—Application," ASME *Journal of Engineering for Gas Turbines and Power,* Vol. 108, pp. 68–97.

Stenning, A. H., 1980, "Rotating Stall and Surge," Chap. 14 in *Fluid Dynamics of Turbomachinery,* ASME Lecture Series, Iowa State University, 1973, reprinted in ASME *Journal of Fluids Engineering,* Vol. 102, pp. 14–21.

Tesch, W. A., and Steenken, W. G., 1976, *Blade Row Dynamic Digital Compressor Program,* Vol. I, J-85 *Clean Inlet Flow and Parallel Compressor Models,* NASA CR-134978.

Simulating the Multistage Environment for Single-Stage Compressor Experiments

J. M. M. Place

M. A. Howard

Rolls-Royce plc,
Derby, United Kingdom

N. A. Cumpsty
Whittle Laboratory,
University of Cambridge,
Cambridge, United Kingdom

The performance of a single-stage low-speed compressor has been measured both before and after the introduction of certain features of the multistage flow environment. The aim is to make the single-stage rig more appropriate for developing design rules for multistage compressors. End-wall blockage was generated by teeth on the hub and casing upstream of the rotor. A grid fitted upstream produced free-stream turbulence at rotor inlet typical of multistage machines and raised stage efficiency by 1.8 percent at the design point. The potential field that would be generated by blade rows downstream of an embedded stage was replicated by introducing a pressure loss screen at stage exit. This reduced the stator hub corner separation and increased the rotor pressure rise at flow rates below design, changing the shape of the pressure-rise characteristic markedly. These results highlight the importance of features of the flow environment that are often omitted from single-stage experiments and offer improved understanding of stage aerodynamics.

Introduction

Low-speed experimental compressors are useful tools for the aerodynamicist. Their mechanical simplicity and low speed means the rig is less expensive to build, maintain, and modify, and can readily be of large scale. The major aero-engine manufacturers regularly use four-stage low-speed compressors to assess blade designs prior to high-speed testing but work is also done on single-stage research compressors. Often the aim of the research carried out on such rigs is to improve blade designs for multistage machines and, if the results from them could be relied upon to achieve this, the validation of design philosophies could become still cheaper and quicker. A conventional single-stage compressor clearly lacks certain features of the multistage flow environment that may be significant in their effect on blade aerodynamics, and it might be the case that a blade design optimized through a series of single-stage tests may be far from the best for a multistage machine.

To make the flow field in a single-stage machine more representative, some features of the multistage environment can be quite easily introduced to the rig: (*i*) First, it is common practice to fit teeth to the casing and hub end-walls upstream of the stage to thicken the boundary layer and ensure that at stage inlet the axial velocity profile is typical of that seen by an embedded stage. (*ii*) Second, the levels of free-stream turbulence measured in multistage machines generally are much greater than those found in a single-stage rig and may have a different length scale; it is supposed that the behavior of blade profile boundary layers and the development of corner separations within blade rows near the end-walls are affected by the free-stream turbulence. Efforts to correct this have been made before: Cyrus (1988) introduced a turbulence-generating grid upstream of a test stage (although in the process this did alter the stage inlet axial velocity profile quite radically). (*iii*) The last feature considered in the work described here is the coupling of the potential field from downstream stages, which affects the flow in all but the rearmost stage. There is evidence that the rearmost stator in a compressor is less able to sustain static pressure rise than stators further upstream, because a downstream stage tends to suppress regions of separation.

The performance effects of wakes and streamwise vorticity from upstream blade rows as they convect through the stage have not been accounted for in this experimental program.

The intention of the work described here is twofold: to modify a single-stage compressor rig so that it simulates the multistage environment adequately, and also to use the opportunity that a single-stage machine offers to assess the influence on stage performance of increased free-stream turbulence and then the pressure field imposed by downstream blade rows. As well as demonstrating improved simulation of the multistage environment, this short series of experiments found significant changes in stage performance and highlighted features of compressor aerodynamics that are inadequately understood.

The paper is structured to provide the reader first with all the information (the rig details, measurement techniques, and results) necessary for discussion. Following discussion of the observations, the paper then closes with conclusions.

Experimental Rig and Multistage Simulation

The experiments to demonstrate improved multistage simulation were performed on the Deverson single-stage axial compressor at the Whittle Laboratory that has been previously described by McDougall (1988). The addition of an auxiliary fan at rig exit well downstream (6.8 rotor midheight radii) of the stator trailing edge allows the mass flow rate to be varied independently of the research-stage pressure rise. The stage has zero inlet swirl, giving high reaction at the design flow coefficient of 0.55. The blades are of C4 section with circular arc camberlines. Details for the mid-height aerofoil sections are given in Table 1. Other stage parameters are given in Table 2.

At the design flow coefficient of 0.55 without multistage simulation features (the baseline build) the stage operates at an efficiency of 87.8 percent with a rotor midheight diffusion factor of 0.44. At this operating point, the Reynolds number based on chord for the rotor at midheight is 324,000 (with a relative inlet Mach number of 0.12) and for the stator 215,000. The rotor tip clearance gap was set to 2 percent of rotor tip chord and the stator hub was sealed. Measurements were taken with the rig in the three configurations shown in Fig. 1 and described below.

Contributed by the International Gas Turbine Institute and presented at the 40th International Gas Turbine and Aeroengine Congress and Exhibition, Houston, Texas, June 5–8, 1995. Manuscript received by the International Gas Turbine Institute February 16, 1995. Paper No. 95-GT-187. Associate Technical Editor: C. J. Russo.

Table 1 Compressor blading geometry at midheight

	Rotor	Stator
Number of blades	51	36
Chord (mm)	111	114
Camber (degrees)	26.5	42.9
Stagger (degrees)	47.9	14.3
Solidity	1.31	0.95
Max thickness/chord	0.10	0.10

Table 2 C4 stage details

Hub / Tip ratio	0.80
Mean radius (mm)	685.8
Rotor rpm	500
Design flow coefficient, ϕ	0.55
Design $\Delta H/U_m^2$	0.45
Axial spacing / rotor chord	0.45

Baseline Build. The baseline configuration is that described by McDougall and consists of the stage with teeth positioned far upstream of the rotor leading edge to generate an appropriate axial velocity profile similar to the thick end-wall boundary layers observed in multistage compressors. The work done on spanwise mixing by Li and Cumpsty (1991) and Goto (1992) used the Deverson rig in this configuration.

Turbulence Grid (TG) Build. The TG build was created by fitting a turbulence grid 5.4 rotor chords upstream of the rotor leading edge (Fig. 1), increasing the free-stream turbulence intensity and reducing the length scale at rotor inlet. The grid was positioned as far upstream as possible to allow the wakes from the bars to mix out while producing at rotor inlet turbulence characteristics typical of the multistage environment as found by Camp and Shin (1995). A series of experiments had been conducted earlier in a wind tunnel to select a suitable geometry for the grid, which consisted of 102 radial bars each of 4 mm square section steel welded to three 6.4 mm square section circumferential bars placed at 18, 53, and 85 percent of the annulus height. Table 3 compares the midheight rotor inlet turbulence of the baseline and TG builds with that at midheight

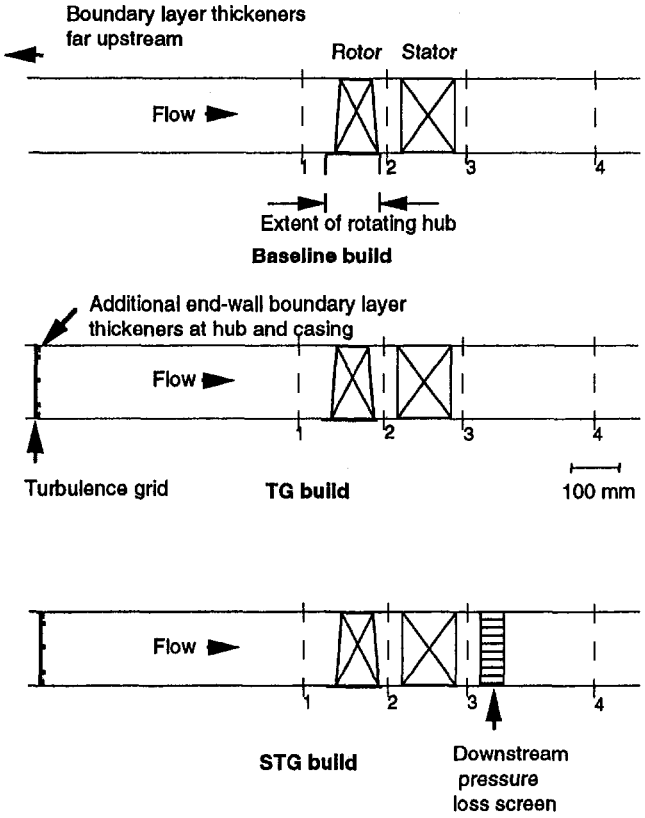

Fig. 1 Experimental arrangements for the Deverson C4 single-stage compressor

Table 3 A comparison of turbulence characteristics

	Baseline	TG	Cranfield 4 stage
turbulence intensity	0.3%	3.7%	4.7%
integral length scale	0.17c	0.06c	0.05c

c is the rotor chord at mid-height

Nomenclature

c = chord
P = static pressure
P_0 = stagnation pressure
P_{0R} = relative stagnation pressure
TG = compressor rig configuration with the turbulence grid fitted upstream of the stage
s = rotor blade pitch
SSHW = single slant hot wire
STG = compressor rig configuration with the turbulence grid fitted upstream of the stage and the pressure loss screen fitted downstream of the stator
U = wheel speed
W = time-mean relative velocity
x = axial coordinate
β_1 = rotor relative inlet angle
β_2 = rotor relative exit angle
ΔH = change in stagnation enthalpy across the rotor at midheight
θ = rotor wake momentum thickness
ρ = air density
Ψ_{TS} = total-to-static pressure rise coefficient = $(\overline{\overline{P_3}} - \overline{\overline{P_{01}}})/\frac{1}{2}\rho U_m^2$
Ψ_{TT} = total-to-total pressure rise coefficient = $(\overline{\overline{P_3}} - \overline{\overline{P_{01}}})/\frac{1}{2}\rho U_m^2$
ϕ = flow coefficient = volume flow rate/annulus area

Subscripts

m = midheight
x = axial
1 = rotor inlet measurement station
2 = rotor exit measurement station
3 = stator exit measurement station
4 = measurement station 2.6 stator chords downstream of the stator trailing edge

Superscripts

$\bar{}$ = pitchwise averaged
$\bar{\bar{}}$ = spanwise and pitchwise averaged
$\hat{}$ = peak value

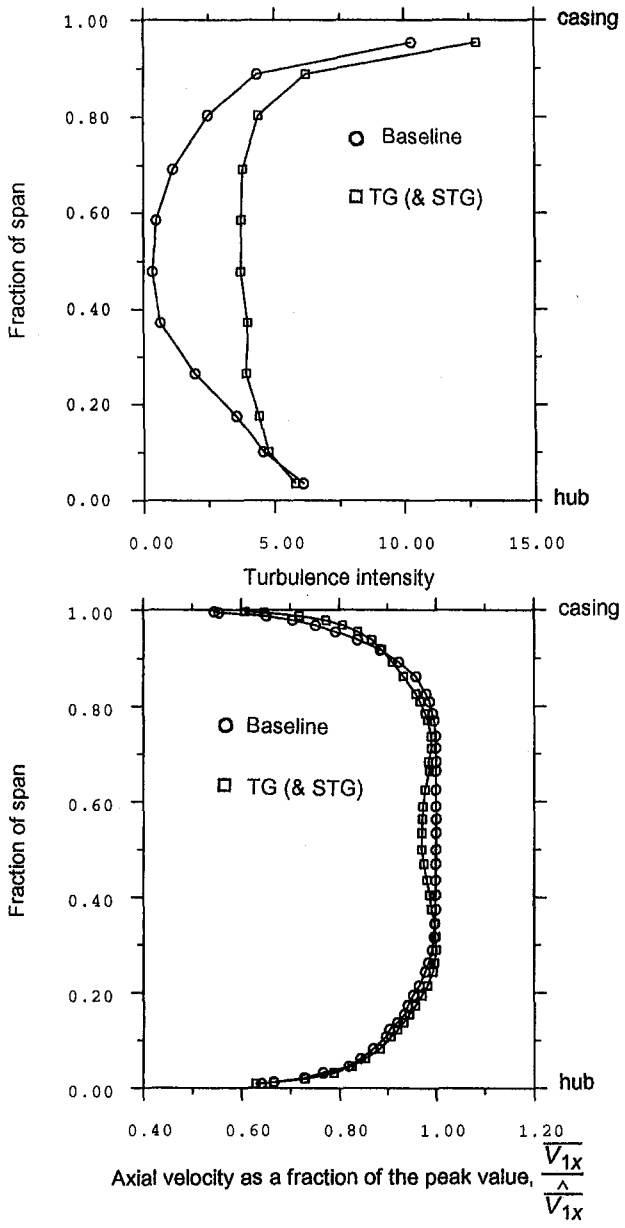

Fig. 2 Stage inlet (station 1) conditions for the three builds

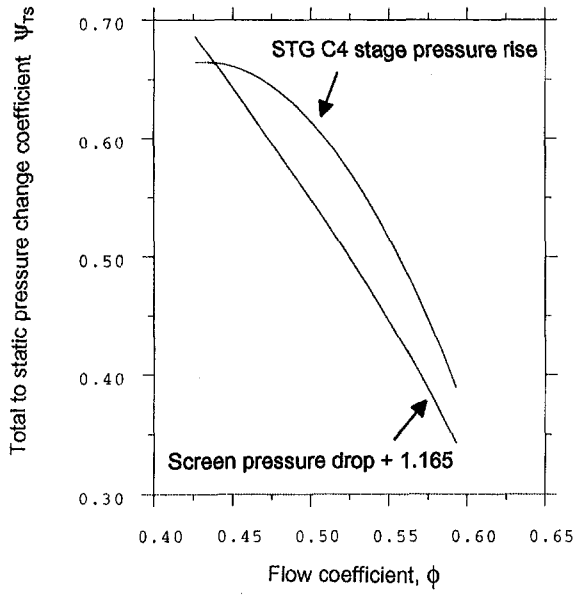

Fig. 3 Simulating the pressure rise of the C4 stage with the downstream pressure loss screen

downstream of stator 3 of the Cranfield four-stage compressor (see Camp and Shin).

It was found that the turbulence grid thinned the end-wall boundary layers and so, to ensure that the axial velocity profile at stage inlet was similar for all builds, additional teeth were fitted at the same axial station as the grid. The incoming axial velocity profiles measured at stage inlet for the baseline and TG builds are compared in Fig. 2 (the profile for the STG build described in section 4.3 is the same as that of the TG build). The profile for the baseline is calculated from the total pressure measured at a single circumferential position while that of the TG build was calculated from an area traverse over one pitch of the turbulence grid. For the TG build (and the STG) the wakes from the radial bars were very shallow at rotor inlet, the velocity deficit being approximately one percent of the free-stream velocity. The wakes from the circumferential bars were deeper, and the midheight bar wake is visible in the figure, but near the end-walls the velocity profiles for the three builds are very similar. The maximum difference in rotor incidence between the baseline and TG build across the span is 0.5 deg at a flow coefficient, ϕ, of 0.57. Since the changes in incidence are small and limited to a small proportion of the span (around midheight where the 0.5 deg maximum occurs) it is reasonable to suggest that differences in performance between the baseline and TG builds are due principally to changes in the turbulence rather than discrepancies in the inlet axial velocity profile.

Screen and Turbulence Grid (STG) Build. The STG build consisted of the TG build with a downstream pressure loss screen positioned 0.5 stator chords downstream of the stator trailing edge (Fig. 1). The intention was to simulate the axisymmetric potential effect of a downstream repeating stage on the research stage. The static pressure field of a healthy downstream stage adjusts to incoming distortion in such a way as to tend to smooth out the nonuniformity. This happens because the pressure rise across the downstream stage is related to the local inlet velocity. Therefore, a region of low velocity flow in, say, the stator wake at the hub (such as might be caused by a corner separation in the upstream stage stator) undergoes a greater rise in static pressure across the downstream stage compared to the fluid at midheight. If the hub fluid is to reach the static pressure enforced at downstream stage exit (where axial flow sets the static pressure to be constant up the span) by means of this greater pressure rise, then the hub static pressure must be reduced at downstream stage *inlet:* This is the "sucking" effect caused by a downstream stage and means that, other factors being equal, an embedded stator is less prone to separation than the final stator in a compressor.

By considering the upstream static pressure field produced by the reaction of the stage to variations in the inlet velocity profile, it can be shown that behavior equivalent to a stage can be obtained from a pressure-loss screen provided the gradient of the screen pressure *loss* characteristic is equal to the gradient of the pressure *rise* characteristic of the stage (see, for instance, Lambie, 1989). (This is true if the gradients of the static-to-static or total-to-static pressure characteristics are equal.) To simulate the correct magnitude of this phenomenon using a pressure-loss screen requires some means of selecting the strength of the screen and finding a suitable axial position for the screen relative to the research stage. Wind tunnel experiments established a design that gave the required loss: A pressure loss screen was constructed from wire mesh with a blockage of 0.57 followed by 50 mm of paper honeycomb to ensure axial flow downstream of the screen. Figure 3 compares the total-to-static

pressure *rise* characteristic curve of the stage in STG configuration with the total-to-static pressure *drop* curve of the screen to show that over the majority of the flow range the gradient is reasonably well matched.

In some respects, the pressure-loss screen is similar to an actuator disk and there have been studies to determine the appropriate axial position for an actuator disk modeling a single blade row (such as Horlock, 1978); these concluded that it should be between the leading and trailing edge, farther aft at low loading and toward the leading edge nearer stall. Bearing in mind that an objective of the experiments was to determine the trends in changes to stage performance as each element of the multistage simulation was added, the front of the screen was fitted in the Deverson rig 0.5 stator chords downstream of the stator trailing edge. This may be a little close for a strictly faithful simulation of a downstream stage at flow rates above design, but was intended to ensure that any changes to the stage aerodynamics would be measurable.

Measurement and Analysis Techniques

Pitot Probe. At stage inlet, pressure measurements were taken 0.6 rotor chords upstream of the rotor leading edge using a flattened pitot probe; velocities were calculated by measuring the casing static pressure and assuming there was no radial variation in static pressure. This assumption is justified because there is no swirl at inlet and the annulus walls are parallel with constant radii.

Ordinary Hot Wire. A straight hot wire normal to the mean flow direction was used upstream of the rotor to measure the stage inlet flow turbulence characteristics. The DC signal was logged at 20 kHz with a low pass filter of 10 kHz to avoid aliasing of data. Definitions of turbulence intensity and integral length scale are those used by Camp and Shin (1995).

Single Slant Hot Wire. To measure the rotor exit flow field, a single slant hot wire (SSHW) was traversed radially at the rotor exit measurement station (0.19 chords downstream of the rotor trailing edge at midheight). For the TG and STG builds the probe was positioned circumferentially 40 percent of stator pitch from the suction surface side of the stator leading edge. For the baseline build the circumferential position was slightly different, at 28 percent of stator pitch from the suction surface side of the stator leading edge. The particular SSHW technique used was described by Goto (1992), a development of the earlier work of Hunter (1979); more details are given by Place (1995).

Phase-locked data from the wire were logged as the rotor passes upstream of the probe at a rate such that 110 data points were taken in the time that 2.8 rotor passages pass; this was repeated 150 times to give an ensemble average. Using this technique it is estimated that the absolute flow angle can be measured to within one degree and the pitch angle to within two degrees, although repeatability is better than this. Velocity measurements depend on the accuracy of the King's law wire calibration as well as the probe calibration, but velocity magnitudes are estimated to be correct to within 2 percent. Circumferentially averaged axial velocities are calculated using area weighting over the central passage measured (i.e., 40 circumferential points). The circumferentially averaged absolute flow angle is defined as the arc tangent of the ratio of the mass-meaned axial and mass-meaned tangential velocity components evaluated from the ensemble average at each of the 40 data points (which covers a single rotor passage) at each spanwise position. In the absence of a measured distribution of static pressure, this procedure gives an approximation to the mixed-out flow angle. The relative flow angle is found by solving the appropriate velocity triangle based on the mean axial velocity and absolute flow angle and the uncertainty in this measurement is ± 1 deg.

The SSHW technique generally captures the midheight rotor wake with between 15 and 20 data points. It is therefore possible to calculate the rotor wake momentum thicknesses with good repeatability. Because there is a pitchwise variation in velocity at rotor exit outside the wakes, it is not straightforward to choose an edge velocity for the momentum thickness calculation. A consistent and plausible wake momentum thickness calculation method that can be automated is required and the following has been found to be effective. The wake is split into suction side and pressure side components and then an appropriate edge velocity must be chosen for each component. The peak velocity is used for the suction side, since this is found to be clear at the edge of this part of the wake. On the pressure side, the edge of the wake is defined arbitrarily as being 10 percent of pitch outboard of the point at which the second derivative of velocity in the circumferential direction is at a minimum. The wake momentum thickness, θ, is then the sum of the two thicknesses calculated for each side of the wake, multiplied by the cosine of the rotor relative exit flow angle, β_2, to transform the parameter into the relative streamwise direction. The two-dimensional profile loss coefficient is then given by

$$\frac{\Delta P_{0R}}{\frac{1}{2}\rho W_1^2} = \frac{2\theta}{\cos \beta_2} \frac{\cos^2 \beta_1}{\cos^2 \beta_2}$$

where β_1 is the rotor relative inlet angle and s is the blade pitch. Uncertainty analysis shows that the rotor profile loss coefficient calculated in this way should be accurate to within 0.3 percent of $\frac{1}{2}\rho W_1^2$.

Three-Hole Probe. Area traverses were performed over a single stator passage using a calibrated three-hole wedge probe at stator exit, 15 percent of stator chord downstream of the stator trailing edge. In combination with a pressure transducer, the stagnation pressure measured by the probe in steady flow conditions at a pressure difference similar to that between the flow at stator exit and atmosphere is estimated to be correct to within 5 Pa.

There is a continuing problem of how to measure the stagnation pressure at rotor exit in the stationary frame where the flow is nonuniform and unsteady. One body of experience suggests that a pneumatic multihole probe, either aligned with the flow by balancing the pressures from the side ports or using a fixed probe setting angle and a calibration, allows good comparisons between builds (e.g., Cyrus, 1986, Howard et al., 1993, and Lewis, 1993). An alternative is to measure the stagnation pressure at stator exit between the stator wakes, where the flow is much steadier, and take this as representative of the rotor exit stagnation pressure. This technique has been regularly used in the Central Institute of Aviation Motors, Russia (Savin, 1993). Since an objective of this study is to compare the performance of different rig configurations, rather than determine the absolute level of rotor performance, it is reasonable to use the stagnation pressures measured at stator exit as a reliable means of assessing changes in rotor pressure rise, especially as there are no blade rows upstream of the rotor.

Stage Pressure Rise and Efficiency Characteristics. In order to compute efficiency both stagnation pressure rise and power input are required. Detailed traverse data were used to obtain stagnation pressure at both inlet and exit because the use of simpler methods were not valid for the build with the downstream screen. For example, stagnation pressure derived from exit static pressure could not be used to compare all three builds since the exit static pressure tappings were downstream of the screen for the STG build. The radial and circumferential traverses were carried out at four flow coefficients at inlet and at three flow coefficients at exit ($\phi = 0.43$, 0.51, and 0.57). The flow at compressor exit (0.15 chords downstream of the stator trailing edge and 0.35 chords upstream of the screen) is

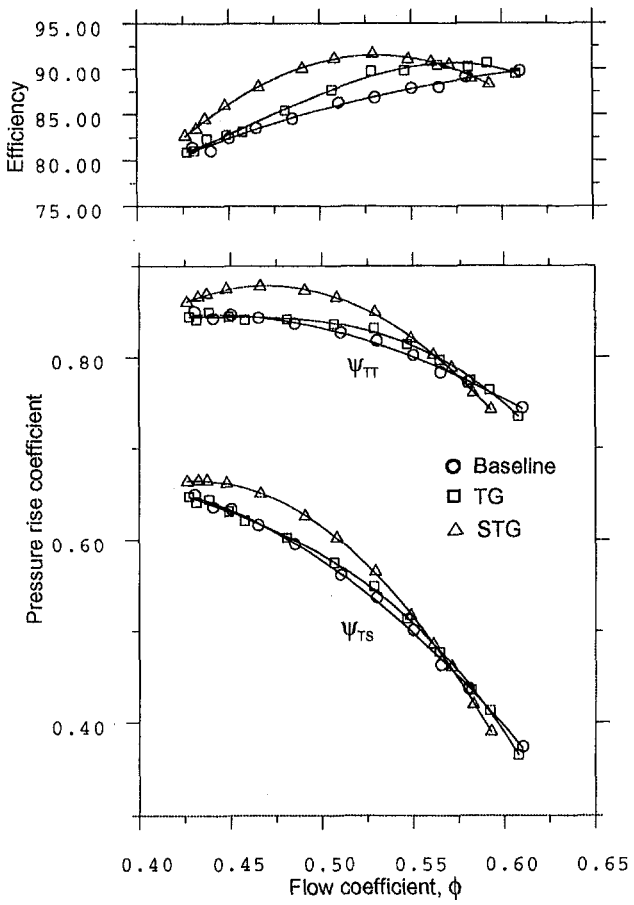

Fig. 4 C4 stage characteristics for the three builds

highly nonuniform and is therefore expected to be sensitive to the form of averaging used. A mixed-out average in the circumferential direction combined with a mass average in the radial direction was chosen after comparison of various methods (see the appendix). The values of average inlet and exit pressure at flow coefficients other than those traversed could then be obtained from appropriately defined interpolations. An exit static pressure representative of the whole annulus was obtained by subtracting the average exit dynamic head from the stagnation pressure.

The power input was derived from the rotational speed and readings from a phase-shift torque transducer. The measured torque was corrected for bearing and windage effects, which were obtained over a range of mass flow rates and drum speeds by measuring the torque with the blades removed.

Uncertainty analysis suggests that the random error appropriate for comparison of efficiency between the builds is approximately ±0.7 percent, which is consistent with the observed scatter. There are, however, significant bias errors additional to this. For instance, due to small nonaxisymmetries at inlet in combination with other sources of uncertainty, the inlet mass flow is estimated to be within ±0.8 percent of the correct value. This implies an increase to the uncertainty when comparing the efficiency of this compressor with others.

Experimental Results

Stage Performance Characteristics. Figure 4 shows the stage total-to-static pressure rise and adiabatic efficiency characteristics for the three builds. The pressure rise characteristics for the baseline and TG builds appear similar, but between $\phi = 0.60$ and $\phi = 0.47$ the TG build has a higher efficiency, with a peak value of 90.4 percent at approximately $\phi = 0.57$. At this operating point, measurements suggest that the TG build is 1.8 percent more efficient than the baseline. This change is so large that a significant proportion of it is felt to be genuine. Introducing the downstream screen causes a major change to the shape of the characteristic curves and below $\phi = 0.55$ the pressure rise is increased significantly relative to the TG build (at $\phi = 0.51$ the total-to-total pressure rise increases by 3.9 percent). Peak efficiency was increased to 91.4 percent and has moved from a flow coefficient of 0.57 to 0.53 and so at $\phi = 0.51$ the stage efficiency has risen by 3.3 percent relative to the TG build.

The stall behavior of the stage for the three builds was not investigated with detailed time-dependent measurements, but it is apparent that only small changes to the stall point resulted from the introduction of the turbulence grid and downstream screen. In passing it should be noted that changes to the inlet velocity profile with flow coefficient that are seen by an embedded stage are not reproduced in this single-stage machine: These could be due to changes in deviation of an upstream stator row as pressure rise increases and may affect stalling behavior.

Flow field measurements were taken at three flow coefficients, 0.57, 0.51, and 0.43, but for brevity comparisons between builds will generally be made at $\phi = 0.51$, the operating point at which differences between the TG and STG builds are greatest.

Rotor Exit Flow Field. Contours of relative velocity for the three builds measured by the SSHW are depicted in Fig. 5 at $\phi = 0.51$ to give an impression of the rotor exit flow field. The wake is thicker near the hub at all flow rates: ammonia and ozalid flow visualization by McDougall (1988) showed that this was the result of separation in the corner region of the hub and the suction surface. Stream-sheet twisting is evident with the lowest energy fluid being swept over toward the suction surface at the hub. The most obvious differences are between the baseline and the other two builds both near the casing and in the form of the corner separation over the lower part of the span. The introduction of free-stream turbulence thinned the rotor wake at around 30 percent height while it remains similar closer to the hub at about 10 percent height.

The circumferentially averaged distributions of flow angle and axial velocity at rotor exit are given in Fig. 6 for all three builds at $\phi = 0.51$ and it is immediately evident that for the bulk of the span there is little difference between the builds. The turbulence grid causes more fluid to be drawn through between 15 and 35 percent of the annulus height, implying an improvement in blade performance over that region of the span, with a reduction near the casing. The circumferentially averaged relative exit flow angle distribution at the same operating point shows small changes that fall within the uncertainty band. Compared to the baseline, the TG build has lower deviation between 20 and 50 percent height but is similar elsewhere. The STG build, however, has a deviation that is lower than the TG build over most of the span.

Rotor Wakes. Increased free-stream turbulence is expected to affect the chordwise position of transition with consequent effects on the development of the blade surface boundary layers. A comparison of the profile losses calculated from wake momentum thicknesses of the baseline and TG builds is made in Fig. 7 at $\phi = 0.57$ and $\phi = 0.51$. For clarity, the data are only shown between 16 and 87 percent of the annulus height, since beyond these bounds the wakes become much thicker (for these to be shown a much larger scale would be required) and their edges less distinct. Also near the end-walls, where the flow is more three dimensional, a two-dimensional momentum thickness becomes less appropriate as a measure of blade behavior. Between 39 and 78 percent height, a region that might be expected to be closest to two dimensional, the TG build has profile losses about 10 percent greater than those of the baseline build at $\phi = 0.57$. Between 10 and 30 percent span, however, in a

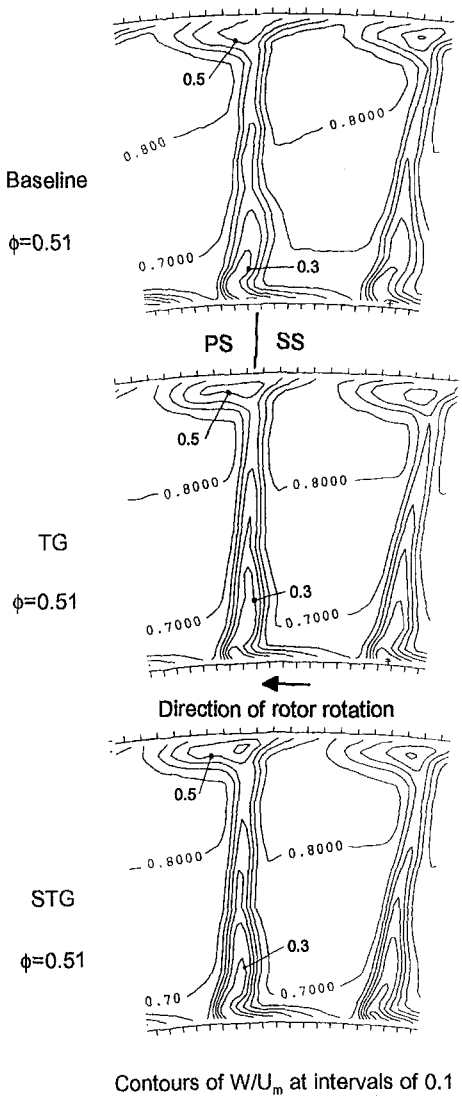

Fig. 5 C4 rotor exit flow field for the three builds at ϕ = 0.51

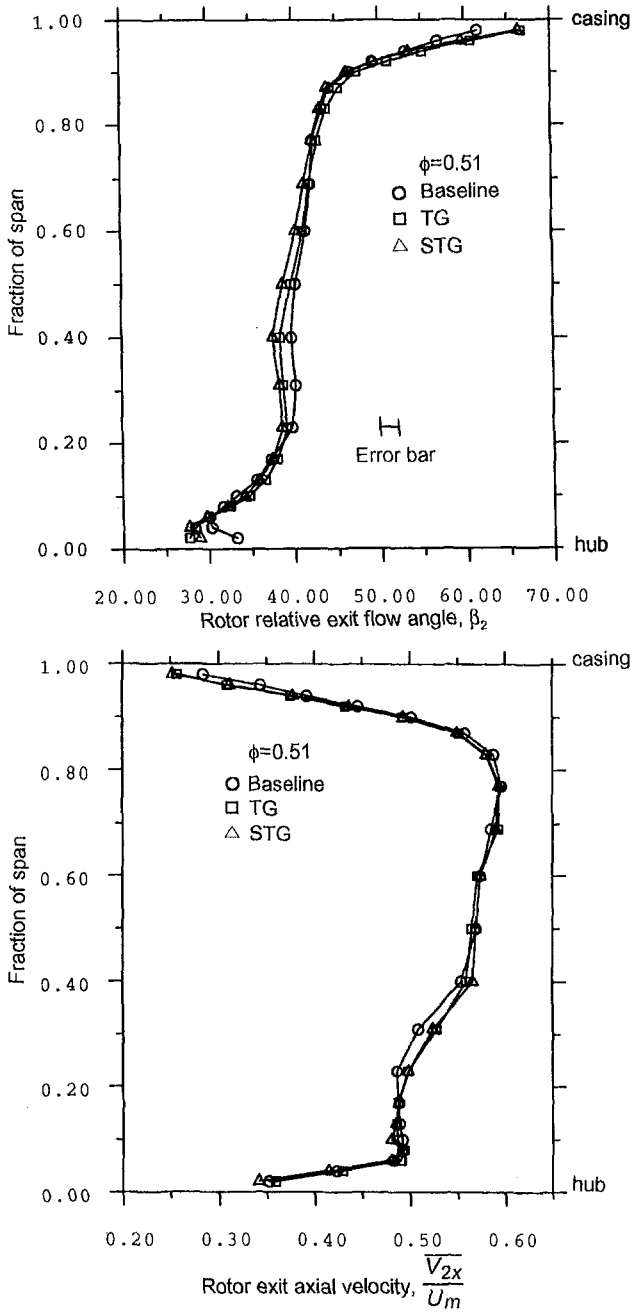

Fig. 6 Rotor exit flow conditions for the three builds at ϕ = 0.51

region of the wake dominated by the hub corner separation, the increased free-stream turbulence has acted to reduce the wake momentum thickness substantially. These trends hold true at increased loading at ϕ = 0.51 and also near stall at ϕ = 0.43 (the latter are not shown), but as the flow coefficient decreases, so the TG build wakes become more similar to those of the baseline.

To summarize the results conveniently, a mean value for the profile loss is calculated by area-averaging the profile loss coefficients between 39 and 78 percent annulus height; results for the three builds are given in Table 4. The STG losses around midspan are similar to those of the TG build at ϕ = 0.57 but about 5 percent greater at ϕ = 0.51.

Rotor Pressure Rise. Figure 8 shows the area-averaged stagnation pressure rise outside of the stator wakes at stator exit for the three builds at ϕ = 0.51. These data were circumferentially area-averaged over the part of the free-stream (i.e., clear of the stator wakes) shown in Fig. 9, and so are representative of the rotor pressure rise. The pressure coefficient plotted is defined as the difference between the mean stage inlet stagnation pressure and that measured at stator exit nondimensionalized by a dynamic head based on the midheight wheel speed. The estimated uncertainty in total pressure measurement using the wedge probe equates to an uncertainty of 0.007 in this pressure rise coefficient value (although repeatability has been found to be better than this). For the baseline and the TG builds the pressure rise around midspan appears generally similar (a difference of 0.006), although near the end-walls the TG build is delivering more pressure rise, significantly greater than the error band. Meanwhile, the STG distribution is similar in shape to that of the TG build but with the level of pressure rise increased at all radii: at 40 percent height the difference in coefficient value is 3.5 percent of the STG pressure rise at this operating point.

Stator Exit Flow Field. Traverses using the wedge probe at stator exit shown in Fig. 9 indicate that the dominating flow feature is the stator suction-surface hub corner separation, which grows steadily as the flow coefficient is reduced (flow reversal was confirmed by oil and dye flow visualization). The pitchwise resolution of the wedge probe area traverse at stator exit was much coarser than that at rotor exit using the SSHW and so

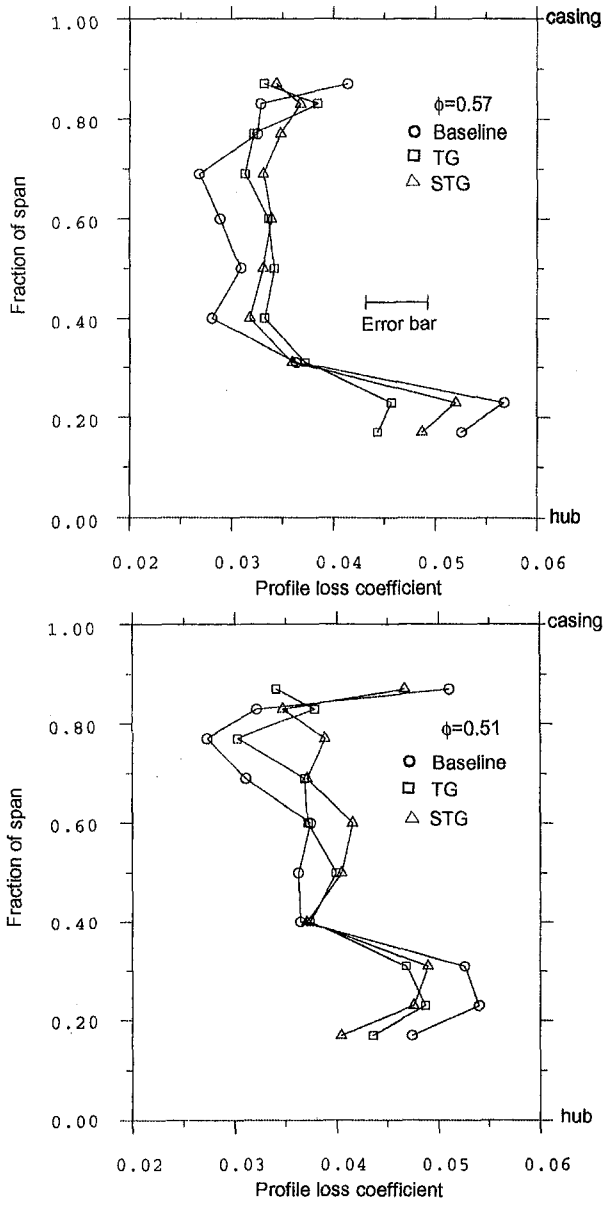

For clarity, data not shown below 16% span nor above 88% span.

Fig. 7 Rotor two-dimensional profile losses for the three builds, calculated from rotor wake momentum thicknesses

Table 4 Area-averaged rotor profile losses as a percentage of inlet relative dynamic head

	Baseline	TG	STG
ϕ=0.57	2.9 %	3.3 %	3.3 %
ϕ=0.51	3.4 %	3.7 %	3.9 %

Uncertainty band is +/− 0.3%

it has not been possible to compare stator wake momentum thicknesses reliably for the baseline and TG builds.

The comparison of the stagnation pressure contours measured at stator exit shown in Fig. 10 demonstrates how the wake width has changed little with the introduction of high free-stream turbulence. Increased free-stream turbulence did not significantly reduce the extent or intensity of the stator corner separation at the hub at $\phi = 0.51$ or closer to stall.

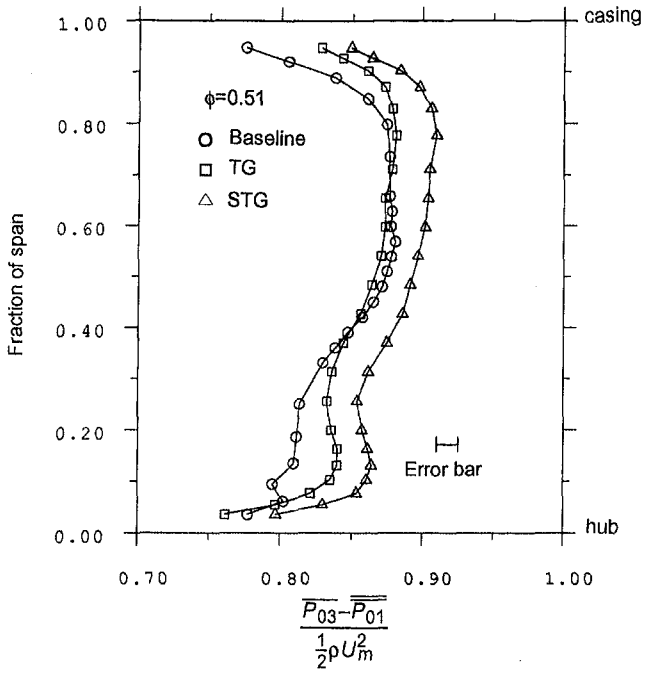

Obtained by area-averaging between the wakes.

Fig. 8 Free-stream stagnation pressure at stator exit at ϕ = 0.51

The downstream screen reduces the severity of the large hub corner separation in the stator at flow coefficients below 0.57. The marked reduction in the size of the stator hub corner separations at flow coefficients of 0.51 and 0.43 are shown in Fig. 11. The stagnation pressure coefficient contours in Fig. 11(*a*) at level 0.90 show that the rotor is delivering more pressure rise in the free-stream region for a flow coefficient, ϕ, of 0.51 in the case of the STG build (as noted in the previous section).

Discussion

Comparison of data from the three builds shows effects of the turbulence grid and the downstream screen that were expected: increased rotor profile loss but reduced rotor corner loss on introducing representative inlet turbulence; a strong effect on the stator separation from the downstream screen. These, together with the changes to stage performance that were not anticipated, notably the increased rotor pressure rise with the downstream screen, are discussed in the subsequent sections.

The Effect of Turbulence on C4 Stage Performance. Although the increased free-stream turbulence of the TG build increased the stage efficiency by 1.8 percent at flow coefficients of 0.57 and 0.51 (these figures are arrived at by comparing curves fitted to the characteristics, Fig. 4), the rotor profile boundary layers thickened and there was no significant improvement in the stator wakes relative to the baseline build. Increased turbulence of the appropriate length scale is expected to cause earlier transition, allowing the turbulent boundary layer to grow over a longer proportion of the chord and so causing it to be thicker by the trailing edge. The experimental results support this with increased rotor profile loss (calculated from the wake momentum thickness) around midspan over the whole operating range, Fig. 7 and Table 4. Increased turbulence also provides for more efficient transfer of energy from the free-stream down to the fluid near the blade surface, making the boundary layer able to withstand a greater adverse pressure gradient before severe separation occurs; this effect is not seen near midspan, even at the lowest flow coefficient tested. The wake is thinned substantially for the TG rotor in the region affected by the corner separation near the hub at ϕ = 0.57, Fig. 7. This reduction

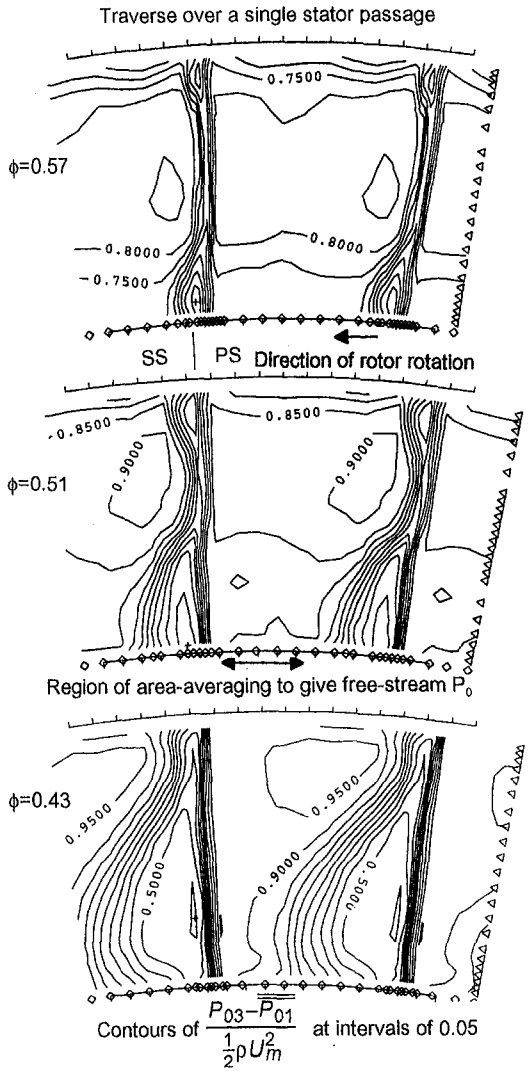

Fig. 9 C4 baseline stator exit flow field

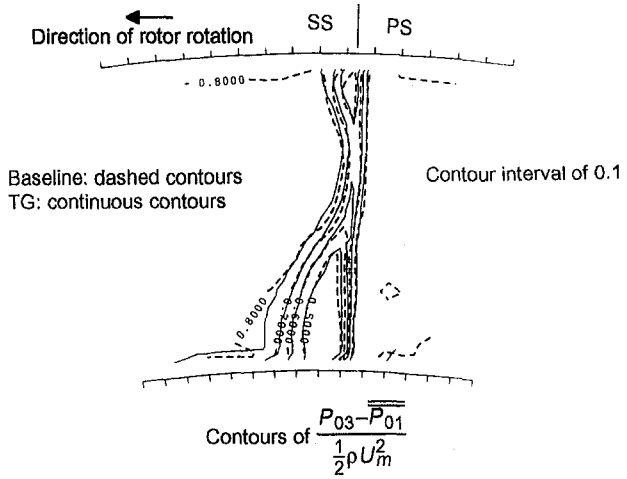

Fig. 10 The effect of increased free-stream turbulence on the stator wake at ϕ = 0.51

in size of the hub corner separation by increased free-stream turbulence diminishes as flow coefficient is reduced, Fig. 7, perhaps because the static pressure rise at ϕ = 0.51 has gone beyond the limit above which increased turbulence is unable to reduce the hub separation substantially.

The increase in efficiency at ϕ = 0.57 attributable to raised inlet turbulence is not accompanied by a greater increase in stage total-to-total pressure rise (Fig. 4) for two reasons. There is a small change in the rotor inlet axial velocity profile between the builds (and hence the rotor exit axial velocity), which leads to a change in rotor work. In addition there is an increase in area-averaged rotor deviation of 0.3 deg (it should be noted that this is well within the uncertainty band) for the TG build relative to the baseline, which seems consistent with higher profile loss.

The different flow pattern observed in the velocity contour plots at rotor exit, Fig. 5, results in a radial redistribution of total pressure when the turbulence grid is introduced (see Fig. 8). In the lower half of the annulus the change in the stagnation pressure levels at stator exit between the wakes can be attributed to a combination of rotor deviation change, rotor loss coefficient change and small differences in the rotor inlet stagnation pressure profile. Between 30 and 40 percent height the deviation is about 1 deg lower for the TG build, Fig. 6; consequently work input is increased here and therefore pressure rise. Nearer to the inner wall the TG rotor losses are reduced relative to the baseline, Fig. 7, and so, even with similar deviation, the pressure rise is increased.

In the region of the casing (85 to 100 percent height) the axial velocity and relative swirl angle shown in Fig. 6 suggest similar work input for baseline and TG builds. It is therefore surprising to see significant differences in the pressure rise attributed to the rotor as seen in the free-stream at stator exit, Fig. 8. The exit stagnation pressure profile changes are also much larger than the small increase associated with the difference in inlet axial velocity profiles that can be seen in Fig. 2. The only hypothesis that can be offered is that the free-stream turbulence is mixing out rotor end wall loss more quickly, before it has undergone the full deceleration of the stator. It has been shown that for simple mixing a streamwise pressure gradient has a large influence on mixing loss (Denton and Cumpsty, 1987) with the loss increasing as mixing takes place after deceleration of the flow. If free-stream turbulence increases the rate of mixing, lower losses by stator exit in the free stream would be expected.

The Effect of the Downstream Screen on Stage Performance. At a flow coefficient of 0.57 the STG build performance is very similar to that of the TG and it is only at flow coefficients of 0.55 or less that the downstream screen increases the pressure rise significantly. Corroborative evidence can be found for this type of change and the clearest example is given by Wisler (1980). The first stage of the GE low-speed research compressor was tested alone and then with the three downstream stages fitted: As Fig. 12 shows, the effect of the downstream stages is to increase the first-stage pressure rise at flow coefficients below 0.37 and reduce it at flow coefficients above 0.4 (the design flow coefficient was 0.408). These trends are similar to those seen on the STG build on the Deverson rig (including the reduced pressure rise at higher flow rates, which remains unexplained), suggesting that the screen has succeeded in simulating important features of the multistage flow field.

The effect of the reduction in the stator corner separation on stage performance at ϕ = 0.51 was calculated by taking the free-stream stagnation pressure at stator exit (Fig. 8) as representative of the rotor exit pressure and then calculating a stator loss for each build using the average total pressure at stator exit. This showed that 25 percent of the difference in total-to-total pressure rise between the TG and STG builds and approximately 1 percent of the 3.3 percent change in efficiency is due to the reduction in stator loss near the end walls. The remainder of the change in pressure rise is due to the stagnation pressure differences seen in Fig. 8. The measured reduction in rotor

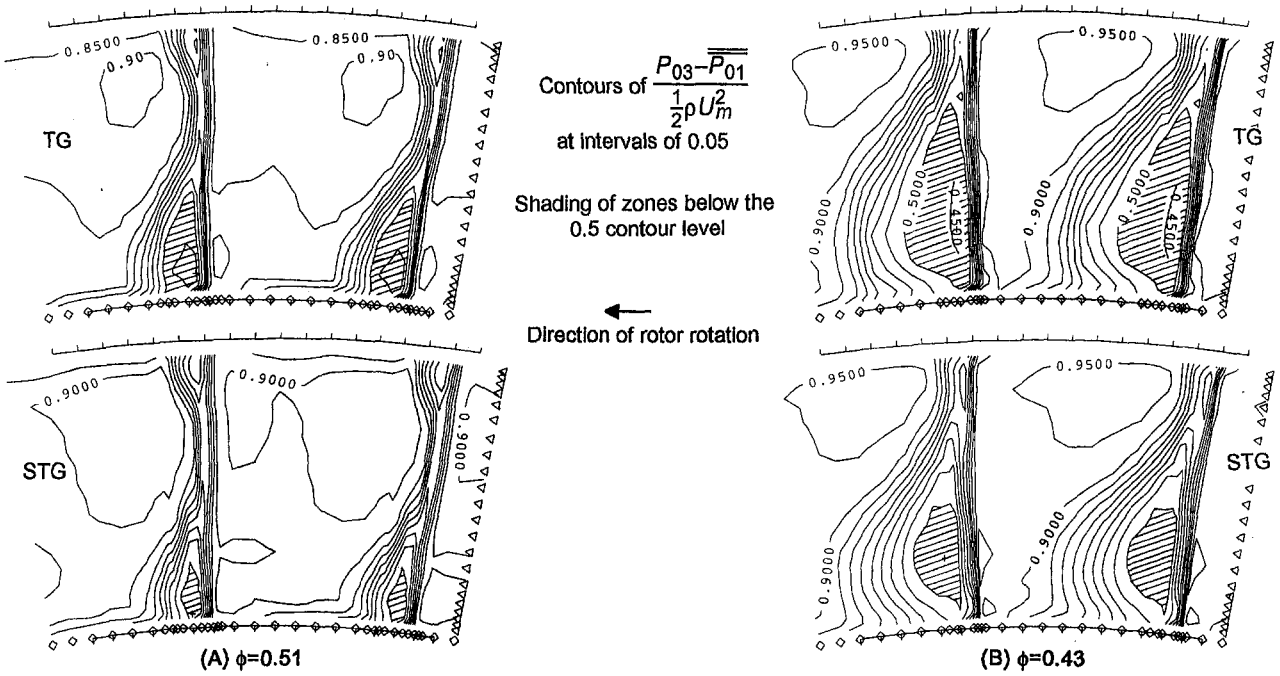

Fig. 11 The effect of the downstream screen on the stator exit flow field

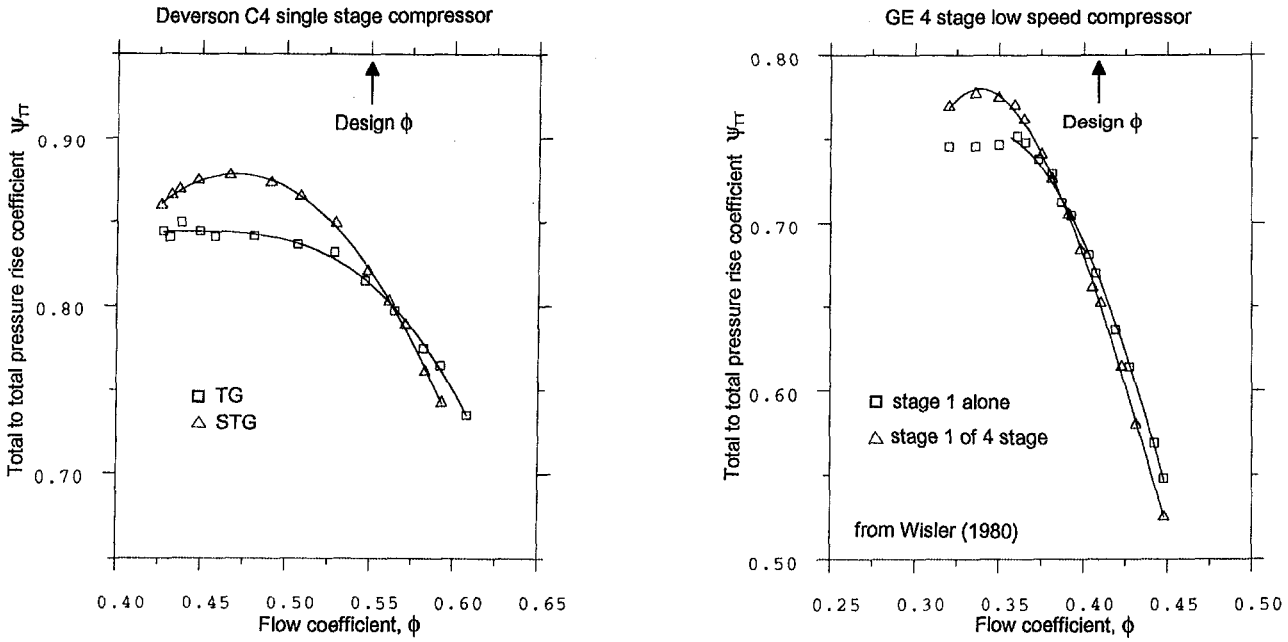

Fig. 12 The effect of downstream stages on the first-stage pressure rise

deviation of approximately one degree at midheight corresponds well with the 0.8 deg change that a simple velocity triangle analysis shows would give the measured 0.025 increase in rotor pressure rise coefficient at $\phi = 0.51$, shown in Fig. 8. This change in deviation is much less than the maximum probable error in rotor exit flow measurement, but the compatibility of the deviation change measured and the deviation required to give the increased pressure rise seems persuasive. Unfortunately, a reduction in deviation and increase in rotor work appears incompatible with the torque measurements: At $\phi = 0.51$, the torque of the STG build was 0.5 percent less than that of the TG, which is a difference a little greater than the observed scatter in this type of measurement. The measured increase in stage efficiency at this operating point is as large as it is because the torque was very similar for the TG and STG builds. Because the alteration in rotor pressure rise was so surprising, a check was performed on the same compressor rig but with a different compressor stage. This was a 50 percent reaction stage with inlet guide vanes. Three Kiel probes, spaced at 120 deg intervals around the circumference, were positioned at midpitch and midheight near the stator outlet (Bolger, 1994). These probes and the compressor were left untouched when the downstream screen was removed: The results showed a small increase in stagnation pressure rise with the screen present downstream of the stator, backing up the trend described in this paper. However, the probes also showed an increase in the nonaxisymmetry

of the flow at stator exit with the screen fitted: It is not known whether this also has been the case for the C4 stage.

Changes to rotor performance with the introduction of the screen were not anticipated. Rotor pressure rise could have increased by the measured difference between TG and STG, while the torque remained unchanged, had the rotor losses decreased along the span. For instance, reducing the midheight loss coefficient from 3.9 to 1.5 percent would result in an increase in midheight pressure rise equal to that measured at stator exit between the wakes. However, the slant hot wire did not measure such a change in rotor loss (which is greater than the error band) and so it is concluded that the screen did not improve rotor performance by reducing profile loss.

Leaving aside the difficulties posed by the small *reduction* in torque, there are possible explanations for the change in rotor work with the downstream screen such as a spanwise redistribution of flow through the rotor (rather than a deviation change), since the stator passage end-wall blockage had been reduced by the screen. The measured stagnation pressure rise is increased all the way up the span, Fig. 8, which suggests that it is not a redistribution that is responsible. In any case the redistribution shown by the axial velocities calculated from SSHW data (see Fig. 6) is insufficient to give this alteration in work.

In the same way that the screen had thinned the stator wakes near the end-walls, so the screen might conceivably have acted on the rotor wakes at all radii and reduced the viscous (as distinct from the inviscid) component of rotor deviation. However, this is not supported by the measured rotor wake momentum thicknesses of the STG build, which are similar to or thicker than those of the TG build (see the profile losses calculated from the wake momentum thicknesses in Table 4).

There is an unsteady, two-dimensional mechanism for the reduction of rotor deviation. Much of the deviation of a C4 profile is inviscid (see Cumpsty, 1989): To follow the curved surface of the aerofoil section, the curvature of the fluid in the blade-to-blade plane must be supported by a cross-passage pressure gradient. Just beyond the trailing edge of an isolated blade the static pressure is nearly uniform in the circumferential direction (since there can be no blade force) and substantial flow curvature cannot be supported. The bulk of the fluid is unable then to follow the blade surface and deviation results. In a multistage compressor the trailing edge of a rotor, for instance, is not moving through a circumferentially uniform static pressure field, but instead through the potential field of the downstream stator. At times the rotor trailing edge will be in a circumferentially varying static pressure field with the sense of the gradient such that it will support the rotor turning and reduce the rotor deviation. At other times, of course, the reverse will be true and the effect of the downstream blade row might be to increase the time-averaged deviation. It is not known whether these effects will cancel out or, if they do not, in which sense they will alter the deviation and pressure rise. The unsteady mechanism just described will be stronger as flow rate is reduced toward stall, since the stator will be more forward loaded and coupling between rotor and stator will be stronger. The downstream screen reduces the stator hub separation and so increases the stator lift and therefore the stator static pressure field, through which the rotor passes. If this phenomenon was sufficient to cause a reduction in rotor deviation of between 0.5 and 1.0 deg it would imply that the rotor–stator interaction for this stage is very sensitive to stator performance. Note that at $\phi = 0.57$, where the stator hub separation is small and relatively unaffected by the downstream screen, there is little difference between the TG and STG builds. This hypothesis could be tested by use of a two-dimensional unsteady inviscid code modeling the midheight rotor and stator blade sections.

It should be mentioned that there are references in the literature to changes to rotor deviation. As an example, Smith (1970) recounts that the measured rotor and stator deviation of blading in the GE four-stage low-speed multistage compressor was lower than cascade data suggested by more than a degree and attributed this to blade-row interaction effects. Reducing the axial gap between blade rows from 0.27 to 0.07 mean chords produced changes to the compressor performance that were consistent with the blade deviation being reduced further by up to 0.5 deg.

The downstream screen in effect has steepened the slope of the stage pressure rise characteristic, resulting in increased pressure rise at low flow rates and reduced pressure rise at high flow rates. It has not been possible to explain this, although it is in part due to the reduced severity of the stator separation. Further progress might be made by modeling this particular stage using first a two-dimensional and then a three-dimensional unsteady code as a means of prompting a theoretical appreciation of the phenomenon.

Conclusions

It has been shown that simulating the effects of a multistage environment alters the behavior of a single-stage compressor rig significantly. The effects introduced, in addition to thickening of the end wall boundary layers, were inlet free-stream turbulence and a downstream screen. It follows that single-stage compressor tests may be inappropriate both for the development of blading and for understanding phenomena in compressors unless steps are taken to represent better the flow conditions that will be met within the multistage environment.

Introduction of the turbulence grid caused a large increase in stage efficiency, measured as 1.8 percent. The increased free-stream turbulence thickened the rotor profile wakes by 10 percent but reduced the severity of the rotor hub corner separation. The stator corner separations seemed to be unaffected by increased free-stream turbulence at compressor inlet. Higher stagnation pressure was delivered near to the casing at stator exit between the stator wakes. This could be due to the influence of free-stream turbulence on the rotor exit end wall flow.

Simulating the potential field of a downstream stage with the screen reduced the extent of stator separation near the hub end-wall, particularly at flow coefficients below that of peak efficiency. At $\phi = 0.51$ this change to stator performance accounted for a 1 percent increase in stage total-to-total pressure rise coefficient and a 1 percent increase in stage efficiency.

Introducing the downstream screen apparently caused the rotor pressure rise to increase at higher loading; this was achieved without increase to the rotor torque, leading to an increase of approximately 2 percent in stage efficiency at $\phi = 0.51$. No satisfactory explanation for this can yet be given.

Acknowledgments

Thanks are due to Dr. J. P. Longley for his interest and suggestions during the course of the experimental work that forms the basis of this paper. The authors are grateful to J. J. Bolger for providing an independent check of the effect of the screen on rotor work. Finally, we would like to thank Rolls-Royce PLC, the Department of Trade and Industry and the Defence Research Agency, Pyestock for both funding and permission to publish this work.

References

Bolger, J. J., 1994, private communication.

Camp, T. R., and Shin, H.-W., 1995, "Turbulence Intensity and Length Scale Measurements in Multistage Compressors," ASME JOURNAL OF TURBOMACHINERY, Vol. 117, pp. 38–46.

Cumpsty, N. A., 1989, *Compressor Aerodynamics*, Longman, United Kingdom, p. 168.

Cyrus, V., 1986, "Experimental Study of Three-Dimensional Flow in an Axial Compressor Stage," ASME Paper No. 86-GT-118.

Cyrus, V., 1988, "Effect of the Inlet Velocity Profile in the Three-Dimensional Flow in a Rear Axial Compressor Stage," ASME JOURNAL OF TURBOMACHINERY, Vol. 110, pp. 434–440.

Denton, J. D., and Cumpsty, N. A., 1987, "Loss Mechanisms in Turbomachines," presented at the Institute of Mechanical Engineers International Conference Turbomachinery—Efficiency Prediction and Improvement, Cambridge, Paper C260/87.

Goto, A., 1992, "Three-Dimensional Flow and Mixing in Axial Flow Compressor With Different Rotor Tip Clearances," ASME JOURNAL OF TURBOMACHINERY, Vol. 114, pp. 675–684.

Horlock, J. H., 1978, *Actuator Disk Theory—Discontinuities in Thermo-Fluid Dynamics*, McGraw-Hill, New York.

Howard, M. A., Ivey, P. C., Barton, J. P., and Young, K. F., 1993, "Endwall Effects at Two Tip Clearances in a Multi-stage Axial Flow Compressor With Controlled Diffusion Blading," ASME JOURNAL OF TURBOMACHINERY, Vol. 116, pp. 635–647.

Hunter, I. H., 1979, "Endwall Boundary Layer Flows and Losses in Axial Turbomachines," PhD Thesis, University of Cambridge, United Kingdom.

Lambie, D., 1989, "Inlet Distortion and Turbofan Engines," PhD Thesis, University of Cambridge, United Kingdom.

Lewis, K. L., 1993, "The Aerodynamics of Shrouded Multi-stage Turbines," PhD thesis, University of Cambridge, United Kingdom.

Li, Y. S., and Cumpsty, N. A., 1991, "Mixing in Axial Compressors: Part II—Measurements in a Single-Stage Compressor and a Duct," ASME JOURNAL OF TURBOMACHINERY, Vol. 113, pp. 166–174.

McDougall, N. M., 1988, "Stall Inception in Axial Compressors," PhD Thesis, University of Cambridge, United Kingdom.

Place, J. M. M., 1995, "Three-Dimensional Flow in Axial Compressors," PhD Thesis, University of Cambridge (to be submitted).

Savin, N. M., 1993, private communication.

Smith, L. H., 1970, "Casing Boundary Layers in Multistage Axial-Flow Compressors," *Flow Research on Blading*, L. S. Dzung, ed., Elsevier, pp. 275–303.

Wisler, D. C., 1980, "Core Compressor Exit Stage Study, Vol. II—Data and Performance Report for the Baseline Configuration," NASA Report No. CR-159498, Nov.

APPENDIX

Averaging of Exit Stagnation Pressure

Combined radial and circumferential traverses were used at stator exit (plane 3, Fig. 1) to define both the detailed distribution of flow and the stage pressure rise.

To define the stage pressure rise, an average value appropriate to the whole annulus is desirable (circumferential and radial coverage). This can readily be obtained from a ring of static pressure tappings distributed around the circumference for the baseline and TG build as described below. This could not be done for the STG build. The stagnation pressure can be derived from the average of the exit casing static pressures by adding an average exit dynamic head derived from the known mass flow. For convenience the average stagnation pressure derived in this way is termed a "continuity average" (since the dynamic head is derived from mass flow continuity). Well-defined preliminary characteristics were derived based on the exit continuity average stagnation pressure for the baseline and TG builds.

A study has been carried out on both the averaging of stagnation pressure and the definition of interpolation procedures necessary to derive pressure at flows between those traversed. The aim of this study was to develop a procedure that can be used for all three builds and that gives similar characteristics to those based on continuity average pressure for the baseline and TG builds.

To choose a suitable means of circumferential averaging, values of average stagnation pressure were calculated using mass weighting, area weighting, and also using a simple mixing calculation (the "mixed-out" pressure). It was found that mass averaging gave efficiency values that were too high close to stall since in the corner separation regions, where the stagnation pressure is low, there is low mass flux and therefore low weighting. Area weighting in the circumferential direction gave improved results near stall and efficiency values close to those derived from the continuity average pressure at a flow coefficient of 0.51 but the rate of change of efficiency with flow rate was much steeper. The best compromise was achieved with the mixed-out value of stagnation pressure (this averaging method was also used by Howard et al., 1993). In the radial direction mass-weighted averaging is fairly standard and was used throughout the study. Consequently a combination of mixed-out circumferentially and mass-averaged radially was used to obtain the compressor characteristics for all three builds shown in Fig. 4.

The Effects of Adverse Pressure Gradients on Momentum and Thermal Structures in Transitional Boundary Layers: Part 1—Mean Quantities

S. P. Mislevy

T. Wang

Department of Mechanical Engineering,
Clemson University,
Clemson, SC 29634-0921

The effects of adverse pressure gradients on the thermal and momentum characteristics of a heated transitional boundary layer were investigated with free-stream turbulence ranging from 0.3 to 0.6 percent. The acceleration parameter, K, was kept constant along the test section. Both surface heat transfer and boundary layer measurements were conducted. The boundary layer measurements were conducted with a three-wire probe (two velocity wires and one temperature wire) for two representative cases, $K1 = -0.51 \times 10^{-6}$ and $K2 = -1.05 \times 10^{-6}$. The surface heat transfer measurements were conducted for K values ranging from -0.045×10^{-6} to -1.44×10^{-6} over five divergent wall angles. The Stanton numbers of the cases with adverse pressure gradients were greater than that of the zero-pressure-gradient turbulent correlation in the low-Reynolds-number turbulent flow, and the difference increased as the adverse pressure gradient was increased. The adverse pressure gradient caused earlier transition onset and shorter transition length based on Re_x, Re_δ^*, and Re_θ in comparison to zero-pressure-gradient conditions. As expected, there was a reduction in skin friction as the adverse pressure gradient increased. In the $U^+ - Y^+$ coordinates, the adverse pressure gradients had a significant effect on the mean velocity profiles in the near-wall region for the late-laminar and early transition stations. The mean temperature profile was observed to precede the velocity profile in starting and ending the transition process, opposite to what occurred in favorable pressure gradient cases in previous studies. A curve fit of the turbulent temperature profile in the log-linear region for the K2 case gave a conduction layer thickness of $Y^+ = 9.8$ and an average $Pr_t = 0.71$. In addition, the wake region of the turbulent mean temperature profile was significantly suppressed.

Introduction

Transition from laminar to turbulent flow causes an increase in both skin friction and convective heat transfer. Accurate predictions of these increases are important in design considerations; inaccurate predictions can have a serious effect on the aerodynamics of compressor and turbine blades, the reliability of turbine vanes and blades, and the thermal efficiency of gas turbine systems. In order to calculate momentum losses and blade heat transfer, one must be able to predict boundary layer development accurately throughout transition.

Transition can be affected by a number of parameters, such as pressure gradients, surface curvature, free-stream turbulence, surface roughness, and acoustic disturbances, to name a few. Each of these parameters can influence the start and length of transition, the flow characteristics, and the structure of the transitional boundary layer. The focus of this research was to study the isolated effect of adverse (positive) pressure gradients on the flow structure and heat transfer in a transitional boundary layer in order to contribute to the understanding of fundamental physics and to increase the data base so that future transition modeling and computational predictions can be improved.

Contributed by the International Gas Turbine Institute and presented at the 40th International Gas Turbine and Aeroengine Congress and Exhibition, Houston, Texas, June 5–8, 1995. Manuscript received by the International Gas Turbine Institute February 4, 1995. Paper No. 95-GT-4. Associate Technical Editor: C. J. Russo.

Schubauer and Skramstad (1948) showed oscillograms of streamwise velocity fluctuations on a flat plate with a nonuniform external velocity distribution. Negative (or favorable) pressure gradients appeared to damp out the oscillations, whereas positive (or adverse) pressure gradients caused a strong amplification and produced earlier transition.

Knapp and Roache (1968) used a smoke-visualization technique and found that an adverse pressure gradient affects the stages of transition differently than does a zero-pressure gradient. Besides a change in the development and shape of the vortex trusses, the formation and breakdown of smoke wave sets occurred at a higher rate than those for the zero-pressure-gradient case, with only a short hesitation between wave sets.

Abu-Ghannam and Shaw (1980) studied natural transition on a flat plate for turbulence intensities of 0.3 to 5 percent and λ_θ ranging from 0.06 to −0.08. With their experimental data, in addition to previous available data, a new family of curves was proposed for pressure-gradient cases where the momentum thickness Reynolds number at the start of transition, $Re_{\theta s}$, is a function of λ_θ and FSTI. From these curves it was deduced that at a given turbulence level, the effect of the adverse pressure gradient for promoting transition is greater than the effect of the favorable pressure gradient for retarding it. In addition, from the plot of $Re_{\theta s}$ versus λ_θ, it can be seen that the effect of the pressure gradients becomes less significant than the effect of FSTI as the turbulence level increases, and that small pressure gradients have incrementally more influence than larger ones have for low-FSTI cases. When they plotted the intermittency

factor against a normalized transition length scale, η ($=(x - x_s)/(x_e - x_s)$), no effect due to pressure gradient could be detected.

The effects of pressure gradient and free-stream turbulence intensity on the length of transition were further studied by Fraser et al. (1988). Their data showed that while the turbulence level remains constant, an increase in the adverse pressure gradient causes a decrease in the transition length Reynolds number. In addition, they found that when the turbulence level is increased beyond 1.4 percent, the free-stream turbulence becomes the dominant controlling parameter. Fraser et al. also concluded that neither the pressure gradient nor the turbulence level has any significant influence on the distribution of intermittency in the transitional boundary layer flows tested, where $\lambda_\theta < -0.06$ and FSTI $\leq$ 1.45 percent. Acharya (1985) found phenomena similar to that described by Fraser et al., but up to a higher FSTI value of about 3 percent.

Walker (1989) developed a minimum transition length model based on a continuous breakdown hypothesis which is similar to forced transition and gives reasonable estimates for transition length in adverse pressure gradients. This transition length correlation, $\mathrm{Re}_L = 2.30\ \mathrm{Re}_{\delta^* s}^{1.5}$, represents the minimum transition length that corresponds to the maximum adverse pressure gradient parameter, $\lambda_{\theta s} = -0.082$, for an attached laminar boundary layer at transition inception. The actual transition length should lie between the values predicted by this model and those of zero-pressure-gradient correlations.

Walker and Gostelow (1989) investigated the effects of adverse pressure gradients on the length of boundary layer transition and introduced a correlation for transition length. The experimental investigations were undertaken at an inlet free-stream turbulence intensity of 0.3 percent. The results indicated that $\mathrm{Re}_{\theta s}$ at the onset of transition declines mildly with a slight increase in the adverse pressure gradient and levels off to a fairly constant value under moderately strong adverse pressure gradients. However, the end of transition occurred much sooner when increasingly adverse pressure gradients were applied. The change in Re_θ at the end of transition was most noticeable when a zero-pressure gradient was replaced by even a weak adverse pressure gradient. This observation is consistent with the conclusions of Abu-Ghannam and Shaw (1980).

Walker and Gostelow (1989) found physical differences in instability waves between zero- and adverse pressure gradients. In a zero-pressure gradient, transition occurs randomly due to the breakdown of laminar instability waves in sets. However, for an adverse pressure gradient, Tollmien–Schlichting waves appear more regularly, and the flow steadily evolves from random to periodic behavior as the pressure gradient becomes more adverse. The results of Walker and Gostelow (1989) indicate that the shape factor, H, is close to the local equilibrium turbulent flow value at the 99 percent intermittency point for the zero-pressure-gradient case, but it increasingly exceeds this value as the pressure gradient becomes more adverse, which suggests the possibility that the shape factor may not be settled at the 99 percent intermittency point.

Gostelow and Walker (1991) evaluated their transitional skin-friction values by using the relationship $C_f = (1 - \Gamma)C_{f,\mathrm{lam}} + \Gamma C_{f,\mathrm{turb}}$. The skin-friction value at the onset of transition was determined in the near-wall region by linear extrapolation of $U^+ = Y^+$, and the skin-friction value at transition completion was obtained by using $\tau_w/\rho = 0.0464(\nu/U_\infty\delta)^{0.25}U_\infty^2/2$. Again, the shape-factor value at the end of transition appears to stabilize only for zero and low adverse pressure gradients, with dH/dx becoming increasingly negative as the pressure gradient becomes more adverse. This means that the shape factor continues to decrease even after intermittency measurements indicate transition completion. Thus, a linear combination of the laminar and turbulent properties in proportion to the intermittency, such as above, may be inappropriate for adverse pressure gradients. Actually, Kuan and Wang (1990) pointed out that even for flow without a pressure gradient, linearly combining the laminar and turbulent properties is questionable, since the nonturbulent part of a transitional flow is highly disturbed laminar flow, and the turbulent part is not fully developed.

Regarding heat transfer within the transition region, Sharma (1987) compared transition lengths between the thermal and momentum boundary layers and found that for flows developing under adverse pressure gradients, the length of transition for the thermal boundary layer is shorter than that of the momentum boundary layer. Sharma modeled the effects of both favorable and adverse pressure gradients on the thermal boundary layer by defining a new thermal intermittency factor that is a function of pressure gradient and momentum thickness Reynolds number for both the thermal and the momentum boundary layers. Although this model gave improved estimates of the heat transfer coefficient on the surface for adverse pressure gradients, not

Nomenclature

C_p = specific heat
C_f = skin friction
FSTI = free-stream turbulence intensity $= \sqrt{(u'^2 + v'^2 + w'^2)/3}/\bar{U}_\infty$
H = shape factor $\equiv \delta^*/\theta$
K = acceleration parameter $= (\nu/\bar{U}_\infty^2)/(d\bar{U}_\infty/dx)$
L = length of transition
Pr_t = turbulent Prandtl number
q_w'' = wall heat flux
Re_x = local Reynolds number
Re_{δ^*} = displacement thickness Reynolds number $= U_\infty\delta^*/\nu$
Re_θ = momentum thickness Reynolds number $= U_\infty\theta/\nu$
St = Stanton number, Eq. (1)
T = instantaneous temperature $= \bar{T} + t$
$\bar{T}$ = mean temperature
$T^+ = (T_w - \bar{T})\sqrt{\tau_w/\rho}(\rho_\infty C_p)/q_w'' = \sqrt{C_f/2}/\mathrm{St}$
U, V = streamwise and cross-stream instantaneous velocity; $U = \bar{U} + u$, $V = \bar{V} + v$
$\bar{U}, \bar{V}$ = mean velocity components
u, v, w = instantaneous velocity fluctuations
u', v', w' = rms value of velocity fluctuations
$U_{\infty 0}$ = free-stream velocity at station 1
$U^+ = \bar{U}/U_\tau$
U_τ = friction velocity $= \sqrt{\tau_w/\rho}$
UHSL = unheated starting length
x = streamwise distance from leading edge
x_0 = unheated starting length
y = normal distance from wall
Y^+ = dimensionless distance from wall $= yU_\tau/\nu$
Γ = intermittency
δ = boundary layer thickness at 0.995 U_∞
δ^* = displacement thickness $= \int_0^\infty (1 - \bar{U}/\bar{U}_\infty)dy$
η = normalized transition distance $= (x - x_s)/(x_e - x_s)$
θ = momentum thickness $= \int_0^\infty (\bar{U}/\bar{U}_\infty)(1 - \bar{U}/\bar{U}_\infty)dy$
λ_θ = pressure gradient parameter $= (\theta^2/\nu)(dU_\infty/dx)$
ν = kinematic viscosity
ρ = density
τ_w = shear stress

Subscripts

cl = conduction layer
∞ = free-stream value
e = end of transition
s = start of transition
w = at the wall
lam = laminar
turb, t = turbulent

much information is available regarding heat transfer inside transitional boundary layers with an adverse pressure gradient. Therefore, in addition to fluid mechanics, detailed experimental investigations of thermal transport are also needed since the Reynolds analogy breaks down when pressure gradients are involved. This paper aims to provide such information. The results of this study, conducted in low free-stream turbulence environments, will serve as the baseline cases for future studies in elevated free-stream environments, which are closer to real gas turbine conditions.

Experimental Program

The test facility used an existing two-dimensional, open-circuit, blowing-type wind tunnel. A detailed description of the wind tunnel and its qualification is given by Kuan (1987) and Wang et al. (1992). A heat exchanger utilizing a continuous fresh supply of city water was used to keep the free-stream temperature uniform and steady. Boundary layer suction was applied at the leading edge in order to initiate a new boundary layer at the leading edge of the test section.

The test section was 0.15 m wide, 0.92 m high, and 2.4 m long. One 0.92 m × 2.4 m vertical face of the test section served as the outer wall. This flexible lexan wall allowed for adjustment of the pressure streamwise gradient along the plate.

The opposing 0.92 m × 2.4 m face functioned as the heated test plate. One hundred and eighty-nine E-type thermocouples, 3 mil in diameter, were embedded in the 0.25-mm 3M-413 tape between the heater and the lexan test wall. Seventy-four of the thermocouples were located along the streamwise centerline of the wall, and the remaining thermocouples were placed in cross-span locations. A foil heater was used, custom-designed such that about 90 percent of the heater area was actively heated. A detailed description of the heated test wall was documented in Wang et al. (1992) and Keller (1993).

Selection of Pressure Gradient. A parameter to characterize the effects of the pressure gradients was sought to perform the experiment. The most common parameters used in the literature are:

$$\beta = \frac{\delta^*}{\tau_w}\frac{dP_\infty}{dx} \quad \text{(Clauser, 1954)},$$

$$\lambda_\theta = \frac{\theta^2}{\nu}\frac{d\bar{U}_\infty}{dx} \quad \text{(Thwaites, 1960)},$$

$$\Lambda = \frac{\delta^2}{\nu}\frac{d\bar{U}_\infty}{dx} \quad \text{(Pohlhausen, 1921)},$$

$$K = \frac{\nu}{\bar{U}_\infty^2}\frac{d\bar{U}_\infty}{dx} \quad \text{(Brown and Martin, 1976)},$$

$$\Delta\tau_w = \frac{\nu}{U_\tau^3}\frac{d\tau_w}{dx} \quad \text{(Patel et al., 1968), and}$$

$$p^+ = \frac{\nu}{\rho u_\tau^3}\frac{dP_\infty}{dx} \quad \text{(Narayanan et al., 1969)}.$$

The first three parameters incorporate the past history of the boundary layer through the use of δ, or through an integral parameter, such as δ^* or θ. For experimental purposes, obtaining constant β, λ_θ, and Λ values requires boundary layer measurements that are undesirably time consuming during setup of the test section. The last two parameters require measurement of the wall shear stress, which is also inconvenient. However, the acceleration parameter, K, sometimes termed the velocity gradient factor, represents the overall free-stream flow-field effect while being independent of the flow history in the boundary layer. The desired constant K value can be simply obtained by adjusting the inlet velocity and the outer wall angle by first keeping the outer wall in a wedge configuration and then fine-tuning it locally to accommodate the effect of the boundary layer growth. Therefore, for this study, the degrees of strength of the various pressure gradients were represented by the use of this acceleration parameter, K. Many researchers attempt to relate the λ_θ value at transition onset to K at transition onset through $\lambda_{\theta s} = \mathrm{Re}_{\theta s}^2 K$, but as pointed out by Zhou and Wang (1992), constant K and constant λ_θ (Falkner–Skan) flows are physically different, and comparing a corresponding location between these two flows based on the strength of the pressure gradient at the single location in the flow field requires caution.

At each wall configuration, the absolute value of K can be increased by decreasing the reference free-stream velocity. The K values and free-stream velocities were chosen so that the complete laminar–turbulent transition was located on the test wall. For the present study, K ranges from -0.045×10^{-6} to -1.44×10^{-6}, and the acceleration parameter was set equal to a constant streamwise value for each test case.

Instrumentation. Two independent, computer-controlled acquisition systems acquired data for both surface heat transfer and boundary layer quantities. One system measured the test plate thermocouple data, and the second system recorded momentum and thermal boundary layer values taken with a thermal anemometry system.

The 189 thermocouples used in the surface heat transfer tests were scanned by a Fluke 2205A Switch Controller at a rate of one reading per second. The average reading of two consecutive scans was obtained for each thermocouple.

A single hot-wire and a three-wire probe were used to make all boundary layer measurements. A single hot-wire TSI model 12185-T1.5 was operated in a constant-temperature mode with an overheat ratio of around 1.8. This single-wire probe was used for velocity measurements as close to the test surface as $Y^+ \approx 3$ for the present study. These near-wall measurements are essential to obtaining skin-friction coefficients.

The three-wire probe contained two velocity wires (2.5-μm, platinum-coated tungsten wire) and one cold wire (1.5-μm platinum wire). The 2.5-μm wires were arranged to measure the streamwise and cross-stream velocity components in a constant-temperature mode while the cold wire, which operated in a constant current mode with a constant current of 0.1 mA, was used to measure temperature variations. The three-wire probe was used simultaneously to measure velocity and temperature signals. Since adverse pressure gradients reduce transition length, low velocities were used in order to "stretch" the transition region so that more measurement stations (15 cm apart) could be located in the transition region. The "cross-talk" between the hot and cold wires becomes amplified at low velocities, so the velocity wires were compromised to operate with low overheat ratios of around 1.3. At this low overheat ratio, the frequency response of the velocity sensors of the three-wire probe was nevertheless satisfactory with a response between 5 and 15 kHz for velocities from 3 to 10 m/s. The frequency response for the temperature wire was experimentally determined by Keller (1993) to be from 4800 to 6400 Hz. The "cross-talk" (or heat contamination) between the cold and hot wires was found to be negligible by comparing the velocity results obtained with and without the cold wire in operation and the temperature results obtained with and without the hot wires in operation. A sampling frequency of 2 kHz for 20 seconds was used for both the three-wire and single-wire probes. For future spectral analysis (not included in this paper), frequencies above 1 kHz were filtered so as to prevent aliasing errors. A detailed description of this three-wire probe is documented in Wang et al. (1996) and Shome (1991). Two additional x-wires were used for measuring v', w', $\overline{uv}$, and $\overline{uw}$, respectively, in the free stream.

The same data-acquisition system was used to obtain signals from both the single hot-wire and the three-wire probes. The

sensors were attached to a probe holder which was held by a single-axis, micrometer-traversing mechanism capable of moving in 0.005-mm increments. Two TSI IFA-100 constant temperature bridges were used for the hot wires, and a DISA constant current bridge was used for the cold wire. A four-channel MetraByte Simultaneous Sample and Hold box (SSH4) and a DAS-20 A/D converter were used to simultaneously take signals from the three wires.

Both the single hot-wire and the three-wire probe were calibrated in situ in the wind tunnel test section. The temperature sensor of the three-wire probe was calibrated by using a heated free jet in a temperature range of 10°C to 50°C against a calibrated *E*-type thermocouple. The calibration for the thermocouples in the test plate was done at four isothermal conditions (no wall heating) of different free-stream temperatures with a constant free-stream velocity of 13 m/s. The uncertainty of the calibrated thermocouples was within $\pm 5\ \mu V$ ($\pm$ 0.08°C).

Experimental Procedure. For the surface heat transfer tests, two consecutive scans of all 189 thermocouples were made for each test. The results were then averaged to reduce the effects of any uncontrollable random errors. Steady state was assumed when the centerline Stanton number values varied less than $\pm$2.0 percent for all measurement locations.

The boundary layer measurements were made at 30 locations across the boundary layer for each station. Baseline tests (zero-pressure gradient) of both surface heat transfer and boundary layer measurements can be found in Wang et al. (1992, 1996) or Keller (1993); these test results will be used for comparison in this paper.

Data Reduction. The surface heat transfer was nondimensionalized in terms of the Stanton number,

$$\mathrm{St} = \frac{q''_w}{\rho_\infty C_{p,\infty} U_\infty (T_w - T_\infty)}. \qquad (1)$$

The free-stream air properties and temperature were corrected for both compressibility effects and humid air conditions.

The above wall heat-flux term, q''_w, was calculated based on an energy balance within the test wall. The heat losses such as upstream and downstream conduction, Q_{cond}, radiation from the test surface, Q_{rad}, and back losses, Q_{back}, were subtracted from the power input, Q_{in}. Thus, the net heat flux was determined by $q''_w\,\Delta A = Q_{in} - Q_{\mathrm{cond}} - Q_{\mathrm{rad}} - Q_{\mathrm{back}}$, where ΔA is the area defined by a 6.45-cm^2 (1-in^2) element centered around each thermocouple in the test plate. The velocity used in determining the local Stanton number at each thermocouple location was calculated by integrating the acceleration parameter, K, which was obtained from 14 measured free-stream velocities along the test section. The upstream conduction loss near the leading edge was not corrected, so the uncertainty is higher at the leading edge.

Since no direct measurement of the wall shear stress was made, the skin friction was determined from the shape of the velocity profiles when plotted in terms of the wall coordinates U^+ and Y^+. For the laminar and turbulent regions, the experimental velocity profiles were converted into wall units and were compared to the numerical results from the STAN5 code (NASA/Lewis version), which is a two-dimensional parabolic solver for boundary layer flows. Using an iterative procedure, the C_f values and the wall configuration (the distance between the first sample location and the actual test wall surface) were fine-tuned for each profile until each individual profile best matched the STAN5 results in the near-wall region. A mixing length model with a correction for van Driest damping coefficient for adverse pressure gradients was used.

For the transitional boundary layer, the determination of C_f is more complicated. One method of determining C_f in transition involves the practice of superimposing weighted laminar and turbulent skin-friction values, but as discussed by Kuan and Wang (1990), this method is at best questionable. A second method involves forcing the two-dimensional momentum integral to close; however, Wang et al. (1985) and Keller (1993) have shown that this method results in unreasonable large values of C_f due to the three dimensionality of the transition region. A third method is to assume that the velocity profile in the viscous sublayer of a transitional flow still behaves like Couette flow. Based on this assumption, the experimental velocity profiles were matched to the inner-wall ($Y^+ \leq 5$) correlation, $U^+ = Y^+$, by using an iterative procedure similar to that used for the laminar flows to determine the skin friction in the transitional flow regime. Velocity data acquired by the single hot wire (not shown in this paper) were used to determine C_f since it could get closer to the wall than could the three-wire probe. However, the practice of forcing the near-wall mean velocity profiles to match the $U^+ = Y^+$ curve in the transition region is not appropriate in early transition for adverse pressure-gradient flows due to the counteracting behavior between adverse pressure gradients and transition on the velocity profiles for $Y^+ < 10$, as will be discussed later.

The boundary layer temperature data were reduced to the form of mean temperature profiles and plotted as T^+ versus Y^+. As with the velocity profiles, this data was compared with the numerical results from the STAN5 code in the laminar and turbulent regions. In addition, the profiles for the turbulent region were compared to the conduction-layer correlation, $T^+ = \mathrm{Pr}Y^+$, in the region very near the wall ($Y^+ < 5$) and to the law-of-the-wall in the log-linear region. For the transition region, the profiles in the near-wall region were matched to the conduction-layer correlation. However, it will be shown later that the data failed to match the log-linear region.

The Reynolds stresses and heat fluxes will be presented in Part 2 of this paper. A detailed uncertainty was performed by Mislevy (1993). Representative uncertainty of the mean quantities is listed in Table 1.

Table 1 Uncertainties of mean quantities and integral parameters

Parameter	Uncertainty (%)
$\bar{U}$	5.83
$\bar{T}/T_w\text{-}T_\infty$	1.23
δ^*	4.2
θ	6.2
H	7.5
Y^+	4.7
U^+	4.7
T^+	3.2

Uncertainty Analysis. Following the methodology of Kline and McClintock (1953), an uncertainty analysis was conducted. In order to determine the propagation of the individual uncertainties into the resultant quantities, the sensitivity coefficient was determined by perturbing each independent variable by its uncertainty value within the data reduction program and noting the change in the resultant quantity (Moffat, 1982).

Using this technique, the resultant uncertainties in Stanton number from both fixed and variable inputs resulted in an overall uncertainty in Stanton number of 5 percent. The uncertainty for the three-wire probe is shown in Table 1 for $y/\delta = 0.2$. The primary contributor to uncertainty in $\bar{V}$, $\overline{uv}$, and $\overline{vt}$ is the angle between the mean flow and the normal to the sensor. The hot-wire calibration equations are the largest contributor to the uncertainty in $\bar{U}$ and u'. The uncertainties in the integral parameters are also summarized in Table 1. The uncertainty in the wall location ($y = 0$) is the major contributor to the uncertainty in displacement thickness, δ^*, and momentum thickness, θ.

Results and Discussion

Surface heat transfer measurements were made for constant K values between -0.045×10^{-6} and -1.44×10^{-6} over five divergent wall angles. In order to compare the experimental results in the laminar and turbulent regions, the STAN5 code was run using the free-stream experimental velocity distributions and corrected wall heat fluxes as boundary conditions. The Stanton number distributions for two representative cases are shown in Fig. 1(a). As the adverse pressure gradient in the laminar region increased, the STAN5 predictions increasingly deviated from the zero-pressure-gradient case ($K = 0$). The largest Reynolds number for each laminar prediction curve is the point where the STAN5 breaks down, which indicates a possible boundary layer separation in the computed flow, although this is not necessarily true for the real flow. The Stanton number at this point, which is also the location of the largest deviation, shows about a 26 percent difference from the $K = 0$ case. In the turbulent region, the STAN5 predictions for adverse pressure gradients also show a deviation from the $K = 0$ curve; however, it should be noted that varying free-stream velocities at a constant K value produce significantly different curves in the low-Reynolds-number region. The same pressure distribution (K value) with different $U_{\infty 0}$ results in different Stanton number distributions. The deviation from the zero-pressure-gradient correlation is greater at higher velocities. This is shown in Fig. 1(a) for $K = -1.05 \times 10^{-6}$ and is not significant in the laminar region.

For comparison, Fig. 1(b) shows the STAN5 skin-friction results. The effect of the adverse pressure gradient on C_f is stronger than it is on the Stanton number, with larger deviations from $K = 0$ in both the laminar and turbulent regions. In other words, the Reynolds analogy ($2\mathrm{St}/C_f$) between heat and momentum transfer is not valid for adverse pressure-gradient flows due to the greater effect of negative K on momentum boundary layer structures, as was modeled by the STAN5. In the laminar region, both the C_f and the St are below the $K = 0$ curve. In the turbulent region, however, the C_f falls below the $K = 0$ curve while the St, although less affected, is higher than the $K = 0$ curve. The C_f is little changed by varying the $U_{\infty 0}$ for the same K value although higher velocities result in the prediction of possible separation further upstream. Clauser (1954) found that adverse pressure gradients have a large effect on skin friction for equilibrium turbulent boundary layers and that even relatively small gradients can reduce skin-friction coefficients by up to 50 percent of zero-pressure-gradient values at the same Reynolds number. For favorable pressure-gradient results, however, the opposite was found to be true. In favorable pressure-gradient cases, Zhou (1993) found both the C_f and the St in the laminar region to be higher than the $K = 0$ curve, and in the turbulent region Zhou found the C_f to be higher than the $K = 0$ curve while the St was lower. In addition, Zhou (1993) showed that favorable pressure gradients also have a larger effect on C_f than on Stanton number.

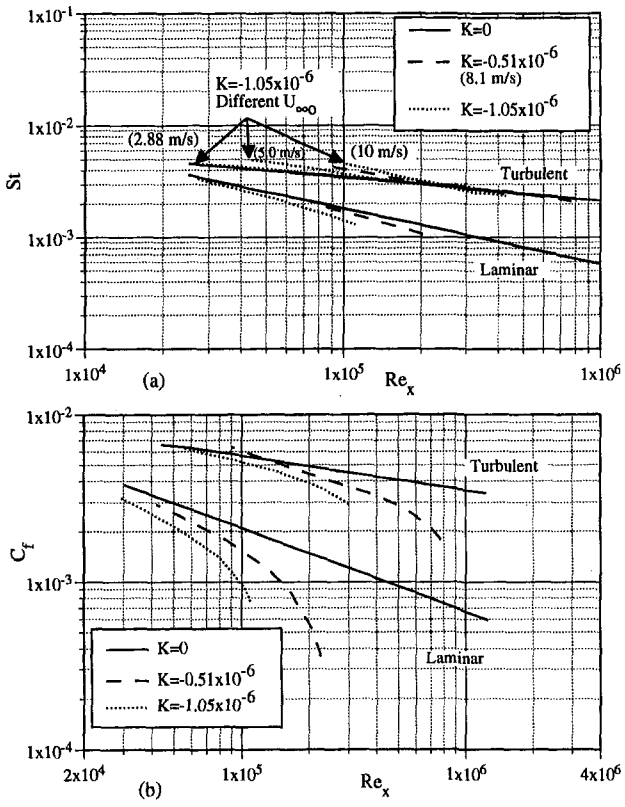

Fig. 1 STAN5 results for (a) Stanton number and (b) skin friction for two constant K cases

Experimental Stanton Number Results. Figure 2 shows the experimental Stanton number distribution for wall configuration 1, which has the smallest divergent angle (1.2 deg) and thus the lowest constant K values. At a fixed divergent wall angle, a lower $U_{\infty 0}$ results in a higher K value, and the corresponding laminar correlation curves differ as well, as shown in Fig. 2 with $U_{\infty 0}$ values of 2 m/s and 16 m/s. For the sake of clarity, instead of plotting every correlation curve for each velocity in the laminar flow region, only one representative curve for the $K = 0$ cases is plotted in the remaining St versus Re_x figures. The laminar and turbulent correlations for zero-pressure gradient can be found in Kays and Crawford (1980) for a constant heat-flux surface:

$$\mathrm{St}_{\mathrm{lam}} = 0.453\ \mathrm{Pr}^{-0.67}\ \mathrm{Re}_x^{-0.5}\left[1 - (x_o/x)^{0.75}\right]^{-0.333} \quad (2)$$

$$\mathrm{St}_{\mathrm{turb}} = 0.03\ \mathrm{Pr}^{-0.4}\ \mathrm{Re}_x^{-0.2}\left[1 - (x_o/x)^{0.9}\right]^{-0.111} \quad (3)$$

The St values in Fig. 2 initially follow the $K = 0$ correlation and begin to deviate from this line as the Reynolds number is increased. Near the leading edge, the St data are lower than the $K = 0$ correlation, possibly due to the uncorrected upstream conduction loss, as discussed earlier in the uncertainty analysis. Transition starts when the St reaches a minimum value, which is at about the same Re_x for all of the cases in this figure due to the low K values associated with this wall angle. In the early transition region, the Stanton numbers for all of the cases follow a well-ordered distribution until midway through transition. At this point, significant scatter develops, which will be discussed later. Although this scatter is present, there is a trend that shows the end of transition occurring at increasingly lower Reynolds numbers as the adverse pressure gradient increases ($|K|$ increases).

Figure 3 shows the Stanton number distribution for wall configuration 2 (divergent angle of 2.6 deg) in which stronger decelerated flows were obtained. As can be seen, the higher K cases result in earlier onset of transition. The Reynolds number at the end of transition could not be determined simply from the wall heat transfer behavior due to the unfamiliar behavior of the Stanton number patterns. There are in fact two noticeable features in the Stanton number distribution in Fig. 3: (1) the local "twist" in the transition region for the smaller K cases (higher velocities) and (2) the overshoot past the turbulent correlation for the larger K cases. As the end of transition is approached, there is an increasing overshoot (about 40 percent) beyond the zero-pressure-gradient turbulent correlation as the pressure gradient is increased. These overshoots are consistent within 5 percent of the STAN5 predictions. For clarity, the STAN5 predictions are not shown in Fig. 3; examples of STAN5 predictions are shown in Fig. 1. However, experimental Stanton number data from Orlando et al. (1974) and Blackwell et al. (1972) for all turbulent, equilibrium adverse pressure-

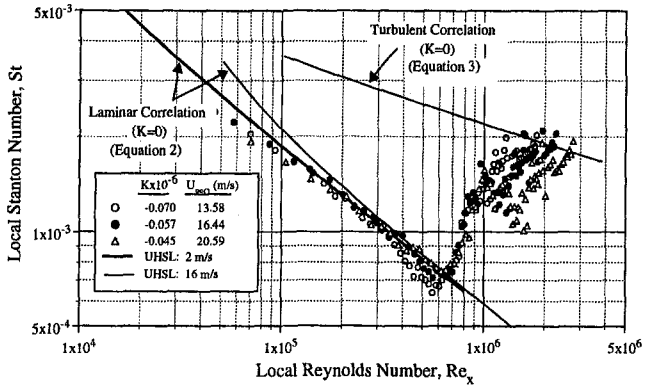

Fig. 2 Local surface heat transfer for wall configuration 1 with a divergent angle of 1.2 deg for various K values

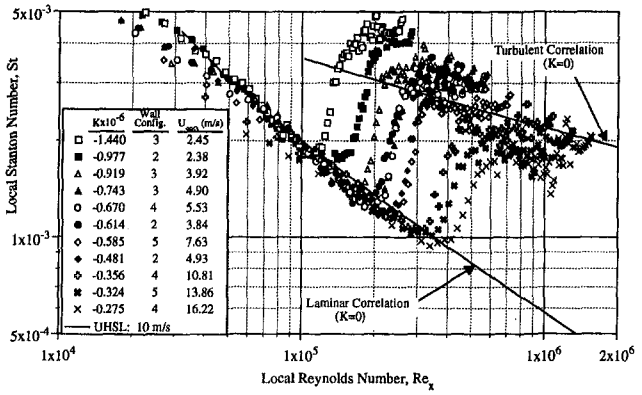

Fig. 4 Comparison of Stanton number for different pressure gradients at wall divergent angles of 1.2, 2.6, 3.5, 4.4, and 5.6 deg

gradient flows show very close agreement with the zero-pressure-gradient turbulent correlation when plotted against enthalpy thickness Reynolds number. However, no data were available in their studies for the Stanton number when explicitly plotted against Reynolds number based on physical x. The limited boundary layer measurements (for two cases) in this present study do not provide sufficient enthalpy thickness information for comparison with their data.

The Stanton number distributions for wall configurations 3, 4, and 5 (divergent angles of 3.5, 4.4, and 5.6 deg, respectively) show the same trends in the presence of increasing adverse pressure gradients as did positions 1 and 2, such as overshooting the zero-pressure-gradient turbulent correlation and an earlier onset of transition. Although the earlier transition onset is apparent at each wall angle for increasing K, Fig. 4 shows the overall effect of constant K flows produced at different angles and $U_{\infty 0}$. As can be seen, stronger negative constant K flows produce earlier transition onset regardless of the wall angle. The sharp "twist" in the transition region for the lower K cases of wall configurations 1 and 2 (Figs. 2 and 3) turns into a broad scatter at the end of transition for cases having larger divergent angles and increasingly higher $U_{\infty 0}$. The overshoot past the zero-pressure-gradient turbulent correlation associated with higher K values disappears as the K value is reduced. The slope of the Stanton number distribution in the early transition region appears to become steeper as the K value increases, reflecting the shorter transition region (based on Re_x) that results from increasing the adverse pressure gradient. The Stanton number appears to be a good parameter for determining the onset of transition, but the peculiar distribution and scatter of the Stanton number within the late-transition and turbulent regions makes it difficult to determine the end of transition.

To determine the cause of this scatter, several possible sources were investigated, such as nonconstant heat flux produced by the heater and separation of the boundary layer from the test surface. However, as explained below, neither nonconstant heat flux nor separation was found to be present.

A single hot wire was used to obtain flow information in the boundary layer and skin-friction measurements on the wall for a flow with a reference free-stream velocity of 20.1 m/s and $K = -0.027 \times 10^{-6}$. Figure 5 shows an overlay of the skin friction and the Stanton number for this case. Both the C_f and the Stanton number show the same location for the onset of transition; however, their locations at the end of transition differ markedly. The C_f overshoots the STAN5 turbulent results by about 5 percent in the early turbulent region and then approaches the turbulent correlation as the Reynolds number increases. However, the Stanton number, as seen before at high $U_{\infty 0}$, develops significant scatter midway through transition with a region that indicates a decrease in the heat transfer coefficient. From information indicated by the flow structures in the boundary layer (such as mean velocity profiles, fluctuating velocities, and shape factors), the turbulent region starts at about 1.3×10^6 (or the location of $C_{f,\max}$). Therefore, if these instabilities are causing the Stanton number scatter, then strangely they are not affecting the mean or fluctuating streamwise velocities (not shown here; see Mislevy, 1993) within the boundary layer. In addition, the C_f distribution does not suggest the existence of a separation bubble since no near-zero value for the C_f was found. The actual cause of this peculiar Stanton number distribution is still not known although it seems to be intensified by the application of increased adverse pressure gradients and increased free-stream velocities. At $K = 0$, the scatter disappears.

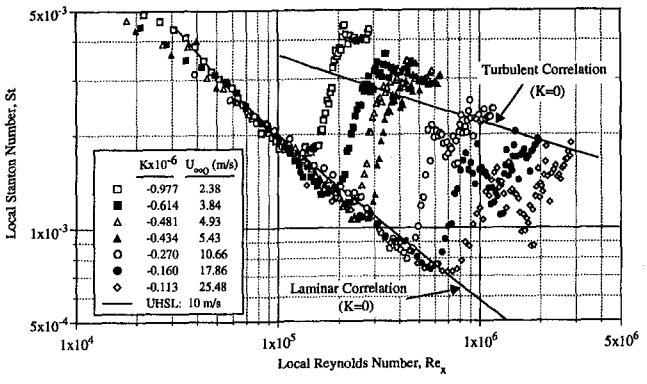

Fig. 3 Local surface heat transfer for wall configuration 2 with a divergent angle of 2.6 deg for various K values; slower $U_{\infty 0}$ results in higher K value

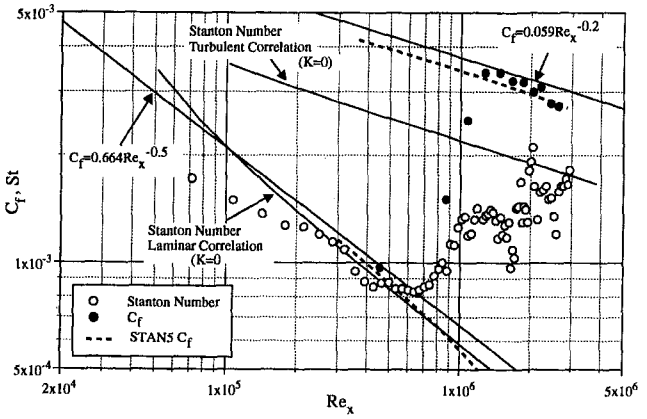

Fig. 5 Centerline Stanton number and skin friction distribution for $K = -0.027 \times 10^{-6}$ ($U_{\infty 0} = 20.1$ m/s)

A direct comparison between two of the adverse pressure gradient and the corresponding baseline results for free-stream velocities of a similar magnitude at $x = 18$ cm are shown in Fig. 6. Both the onset and the end of transition clearly occur earlier for the decelerating cases than for the corresponding baseline cases. K versus Re_{xs} is plotted in Fig. 7, which shows that Re_{xs} decreases sharply in the presence of weak adverse pressure gradients and then seemingly levels off for stronger adverse pressure gradients. It should be noted that the transition onset data in this figure from Gostelow et al. (1992) are based on the intermittency of the momentum boundary layer, rather than surface heat transfer. The strengths of the adverse pressure gradients of Gostelow et al. (1994) were measured based on λ_θ at transition inception. Neither K nor λ_θ values were maintained as a constant in their study. The λ_θ values at the onset of transition for the flows of Gostelow et al. were converted to K values based on the relationship $K = \lambda_\theta/Re_\theta^2$.

Boundary Layer Investigation. In order to gain an understanding of the effects of adverse pressure gradients on the momentum and thermal transport mechanisms in the transitional boundary layer, two representative decelerating cases were chosen for a boundary layer investigation. A medium and a strong adverse pressure gradient were chosen, each at a different wall angle. The obtained K values were $K = -0.51 \times 10^{-6}$ at wall configuration 3 (3.5 deg) and $K = -1.05 \times 10^{-6}$ at wall configuration 2 (2.6 deg), which will be termed $K1$ and $K2$, respectively, for the remainder of the discussion. The K values were determined as described earlier.

The FSTI and the isotropy factors (the ratio of v'/u' and w'/u') for each case are shown in Fig. 8. The FSTI is fairly constant for each of the three cases ranging from 0.3 to 0.6 percent although the decelerating cases show a slight increase

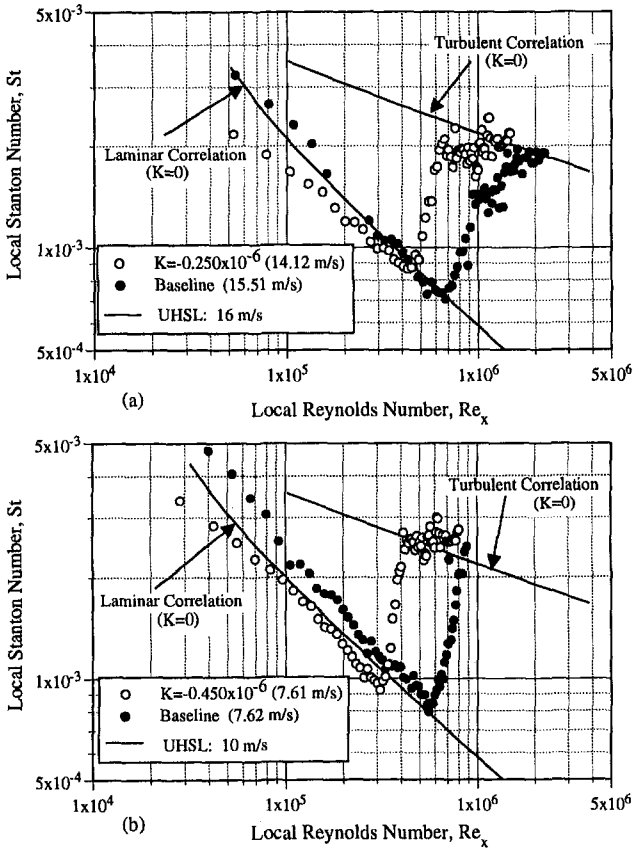

Fig. 6 Comparison of local surface heat transfer behavior between baseline and adverse pressure gradient cases at a similar magnitude of free-stream velocity at $x = 18$ cm

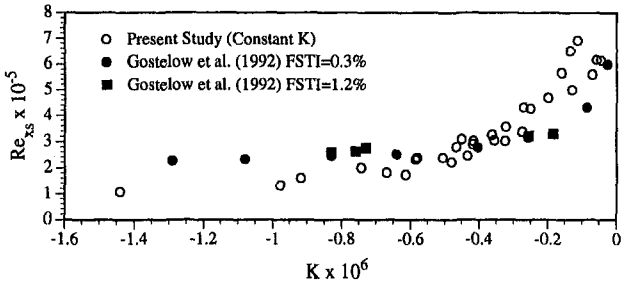

Fig. 7 Comparison of Re_{xs} with different adverse pressure gradients. The data from Gostelow et al. were plotted by converting its λ_θ values at the onset of transition to K values.

in FSTI downstream. The ratio of v'/u', as measured by a uv x-wire, decreases in the presence of increased adverse pressure gradients. The values are not isotropic, and v' appears to be suppressed as the adverse pressure gradient is increased. The ratio of w'/u', as measured by the uw x-wire, is mostly isotropic for the baseline and the $K1$ case. However, for the $K2$ case, w' is also suppressed. This can be explained as vortex compression in a divergent channel with thin boundary layers, similar to the explanation of vortex stretching in a contraction by Uberoi (1956) and Tennekes and Lumley (1972): The velocity fluctuations associated with an "eddy" aligned with the mean flow decrease, and those associated with an eddy perpendicular to the mean flow increase in a contraction. This phenomenon is reversed in a divergent channel. Therefore, both v' and w' decrease in a divergent channel since they are associated with eddies aligned with the mean flow.

The free-stream integral length scales (λ) shown in Fig. 8 vary from 1.9 to 3.0 cm and are consistently larger than the baseline case. The scattered distribution of λ for the $K2$ cases is due to uncertainty in the low-speed flow. The integral length

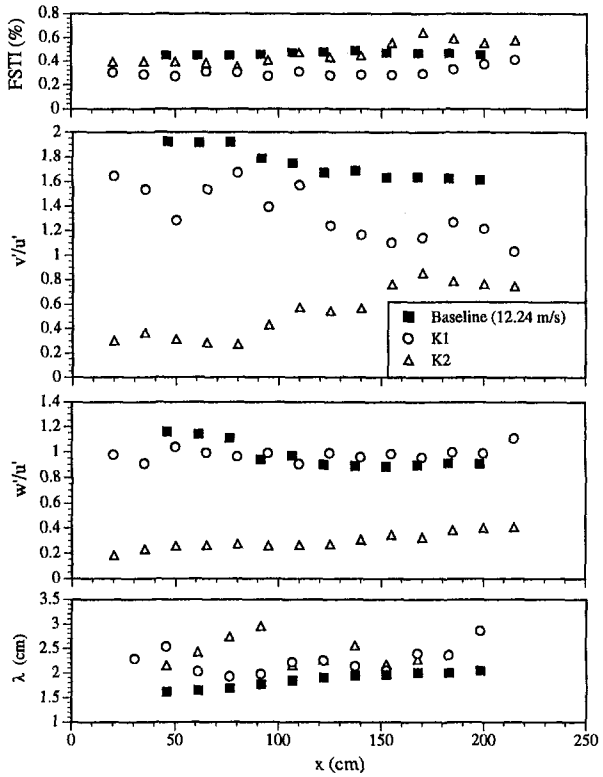

Fig. 8 Streamwise distribution of FSTI, v'/u', w'/u', and integral length scale for $K1$ and $K2$ cases

scales were calculated by integrating the autocorrelation of u' to the first zero crossing, which gives the integral time scale, and then, by assuming that the Taylor hypothesis is valid, multiplying the integral time scale by the mean velocity.

Skin Friction and Integral Parameters. The variation of the skin-friction coefficient obtained from the measurements of both the single hot wire and the three-wire probes is shown in Fig. 9. The skin-friction values for laminar and turbulent flow from the STAN5 solutions are also shown in Fig. 9 for comparison. In both the laminar and the turbulent regions, the experimental skin frictions are higher than the STAN5 predictions but are significantly lower than the baseline C_f values for increasingly adverse pressure gradients. The onset and the end of transition were first chosen at the locations where the skin friction reaches its minimum and maximum, respectively. However, the actual position may occur slightly on either side of the chosen locations due to the space between measurement stations. Therefore, the onset and the end of transition were later cross-checked with the Stanton number distribution, the shape factors, and other mean and fluctuating parameters in the boundary layer. It is also observed that higher negative K values cause earlier transition onset and shorter transition length in terms of Re_x, Re_δ^*, and Re_θ (Table 2).

The integral parameters are shown in Fig. 10. The growth rates of δ, δ^*, and θ for both of the adverse pressure-gradient cases appear to be about the same, but they are larger than those of the baseline cases. The shape factor, H, shows larger values in the laminar region than for the baseline case. The shape factors for the decelerated cases rise to about 3.4 before transition onset and then decrease to between 1.5 and 1.6 in the turbulent region. This tendency for H values to rise at the end of the laminar flow is distinctively different from the tendency for H values to be lower for the baseline case. Increasingly adverse pressure gradients appear to produce higher values of shape factor in both the laminar and the turbulent regions. The tendency for H values to rise at the end of the laminar flow also indicates that the rate of increase for δ^* is faster than it is for θ, as can be seen from the local maximum δ^* values at x = 60 cm for the $K1$ case and at x = 80 cm for the $K2$ case. For all of the cases in this study, the shape factor has reached its turbulent value by the end of transition. However, Gostelow et al. (1992) reported that H continues to fall after transition completion for strong adverse pressure gradients ($\lambda_\theta \approx -0.05$ to -0.07), but that this change is not significant for weak pressure gradients. Gostelow et al. attribute this result to the strong lag effects on the velocity profiles and the shorter transition lengths associated with stronger adverse pressure gradients. Although Gostelow et al. (1994) determined the end of transition based on intermittency (Γ = 0.99), their mean velocity profiles at this intermittency value follow the log-linear turbulent law-of-the-wall in $U^+ - Y^+$ coordinates. It will be shown that although no delay in the shape factor was found in this study, the mean velocity profiles at the determined end of transition also follow the log-linear turbulent law-of-the-wall. In addition, the pressure gradients of Gostelow (1994) were defined by the value of λ_θ at transition onset, and the physical difference between that flow and a constant K flow may be a reason for the discrepancy with the current results.

Table 2 Reynolds numbers at onset and end of transition for cases with boundary layer measurements

		Baseline (K=0)	K1= -0.51×10^{-6}	K2= -1.05×10^{-6}
$U_{\infty 0}$ (m/s)		12.24	8.13	2.88
FSTI (%) at x_s		0.50	0.30	0.35
Onset of Transition	Re_x	5.50×10^5	3.01×10^5	1.35×10^5
	Re_{δ^*}	1294	1227	986
	Re_θ	492	373	294
End of Transition	Re_x	11.2×10^5	4.28×10^5	2.33×10^5
	Re_{δ^*}	1826	1423	1045
	Re_θ	1302	946	679
Length of Transition	$\mathrm{Re}_{x,L}$	5.70×10^5	1.27×10^5	0.98×10^5
	$\mathrm{Re}_{\delta^*,L}$	532	196	59
	$\mathrm{Re}_{\theta,L}$	810	573	385

Mean Velocity and Mean Temperature Profiles. The U^+ versus Y^+ mean velocity profiles for the three-wire probe were determined as described earlier, using the single hot-wire measurements as a guide. The STAN5 predictions for the velocity profiles in the laminar and turbulent regions were obtained and used as a guide in these regions. These profiles are shown in Fig. 11(a) for the $K1$ case. In the laminar region, the adverse pressure gradient causes the velocity profile in the near-wall region to pull away from (move above) the Couette flow $U^+ = Y^+$ curve for locations further downstream. As a result, for station 3 of the $K1$ case the laminar profile matches the $U^+ = Y^+$ curve only for $Y^+ < 2$. Only stations 2 and 3 are obtained in the laminar region since the STAN5 code breaks down after station 3. In the turbulent region, the STAN5 predicts a shortened and steeper log-linear region and stronger wake regions as Re_x increases.

Figure 11(b) shows the STAN5 predictions for the $K1$ case temperature profiles. In the laminar region, the adverse pressure gradient causes the temperature profiles to become increasingly lower than the conduction-layer correlation, $T^+ = \mathrm{Pr}Y^+$, as Re_x

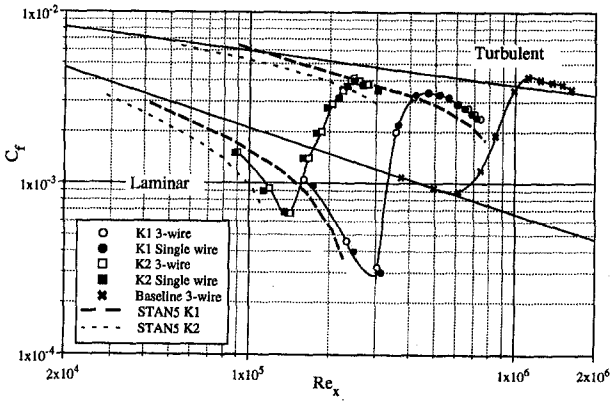

Fig. 9 Comparison of skin friction between the baseline and two decelerating cases with $K1 = -0.51 \times 10^{-6}$ and $K2 = -1.05 \times 10^{-6}$

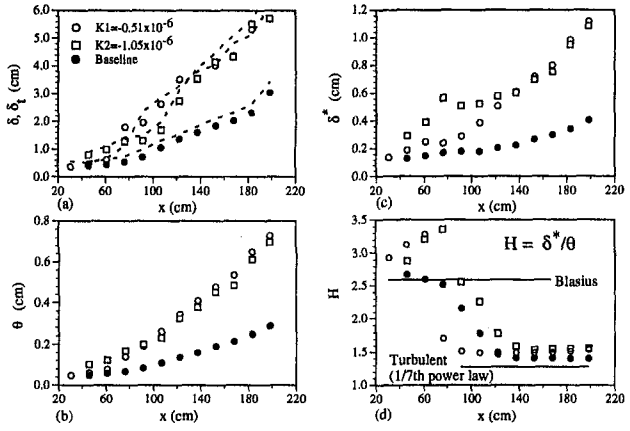

Fig. 10 Boundary layer integral parameters for the baseline, $K1$, and $K2$ cases (--- thermal boundary layer thickness, δ_t)

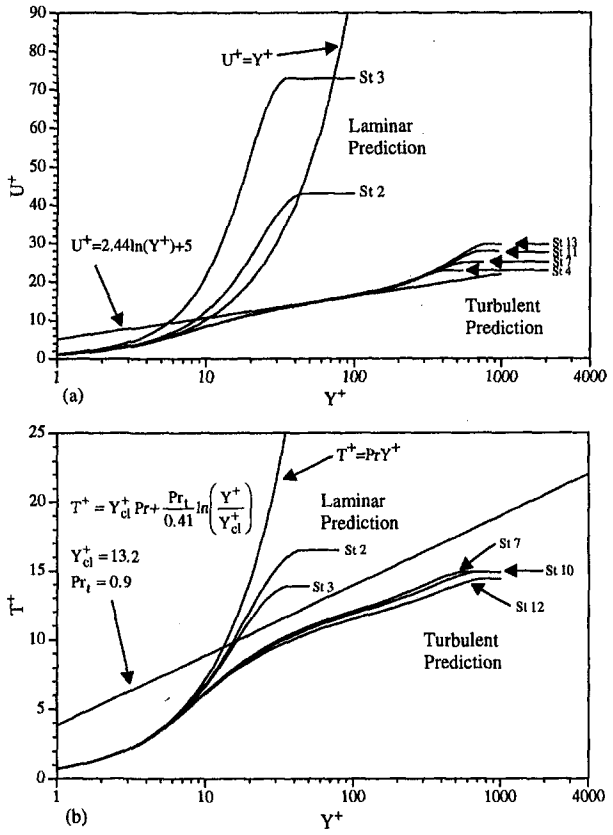

Fig. 11 Results of the STAN5 prediction of (*a*) velocity profiles and (*b*) temperature profiles for corresponding stations of $K1 = -0.51 \times 10^{-6}$

increases. This phenomenon is opposite to the effect of the adverse pressure gradient on the velocity profiles. In the turbulent region, the STAN5 predictions show an increasing undershoot of the thermal law-of-the-wall with an indistinct log-linear region.

Although the STAN5 predicts a possible separation of the laminar boundary layer, no separation was observed in the test section of the present study. Both adverse pressure-gradient cases used in the boundary layer investigation were checked for separation. A 3/4-in.-long tuft on the end of a 2-ft rod was used to probe the near-wall boundary layer over the entire plate, and no separation was detected. In addition, for the region of interest the experimental Stanton number distribution has a smooth distribution well into the transition region, showing no sign of separation. Third, the skin-friction data obtained from the measured velocity profiles do not show a near-zero value (a necessary condition for separation) anywhere along the test plate.

Due to paper length restrictions, the mean velocity and temperature profiles for the $K2$ case only are shown in this paper in Figs. 12 and 13. For the $K2$ case, the mean velocity profiles followed the laminar computational solution up through station 4. Consistent with the Stanton number results, which show that transition does not start until after station 5, the mean velocity profiles indicate that the transition starts between stations 5 and 6. The flow is transitional for stations 6 through 9 and reaches the fully turbulent profile for stations 10 to 13. One problem related to transitional velocity profiles in an adverse pressure gradient is the determination of the near-wall mean velocity profile in the early transition region. Due to the reduction in skin friction relative to the zero-pressure-gradient case, the near-wall laminar profiles of the decelerated flows move higher away from the $U^+ = Y^+$ curve as Re_x increases downstream and then move back toward $U^+ = Y^+$ once transition starts. As a result, there is the question of where the early transitional profiles should lie for $Y^+ < 10$. In the absence of any theoretical velocity profiles or proven numerical predictions as guidelines, the choice of the location of the near-wall velocity profiles relative to the $U^+ = Y^+$ curve can have a significant effect on the determination of the skin-friction coefficient in the early transition region. For the purpose of this study, the location of the first few near-wall data points were chosen to be close to the $U^+ = Y^+$ curve so as to provide a smooth transition in C_f from its laminar to turbulent values. In the turbulent flow region (stations 11–13), the velocity profiles apparently have a shortened log-linear region with a steeper slope.

The mean temperature profiles for the $K2$ case are shown in Fig. 13. The mean temperature profiles are in good agreement with the STAN5 results in the laminar region. The transition of the temperature profiles appears to start between stations 4 and 5, which is earlier than the evolution of the mean velocity profiles. For station 6, the mean temperature profile does not show a trend that would match the conduction-layer correlation, $T^+ = \mathrm{Pr}Y^+$. This can be attributed to increased uncertainty in determining skin friction from the transitional mean velocity profiles and in finding the wall location ($y = 0$) for this station due to the effect of the adverse pressure gradient. The uncertainty in determining C_f affects the uncertainty of the Y^+ and T^+ values. In the turbulent region, the effect of the adverse pressure gradient is to push the mean temperature profiles increasingly below the log-linear curve of a zero-pressure-gradient flow. A curve fit of the turbulent temperature profile in the log-linear region, $T^+ = Y_{cl}^+ \mathrm{Pr}_t + (\mathrm{Pr}_t/0.41) \ln [Y^+/Y_{cl}^+]$, gives a conduction layer thickness of $Y_{cl}^+ = 9.8$ and an average $\mathrm{Pr}_t = 0.71$, while the wake region is apparently suppressed due to the increase in the adverse pressure gradient. Although use of

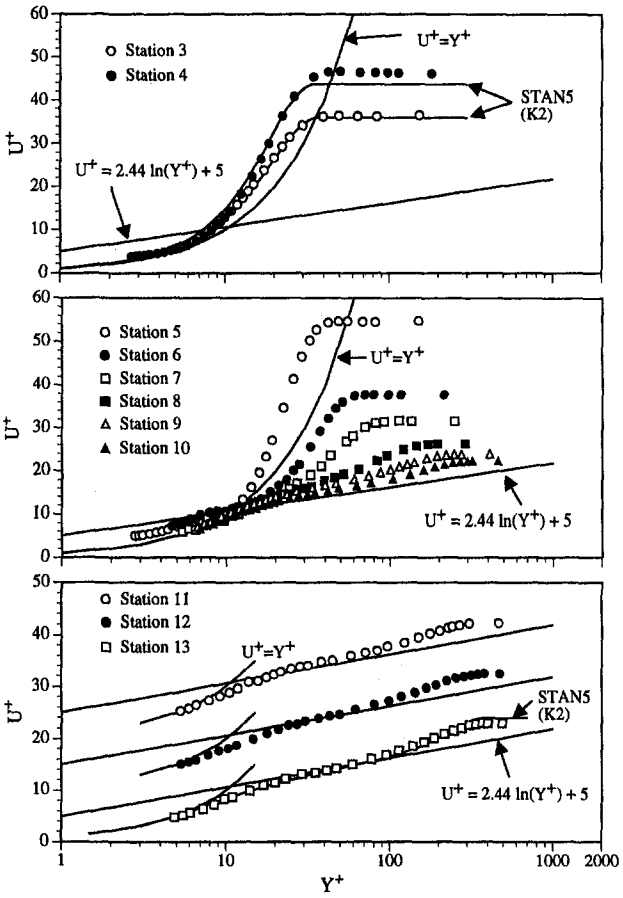

Fig. 12 Mean velocity profiles from the three-wire probe in wall units for $K2 = -1.05 \times 10^{-6}$

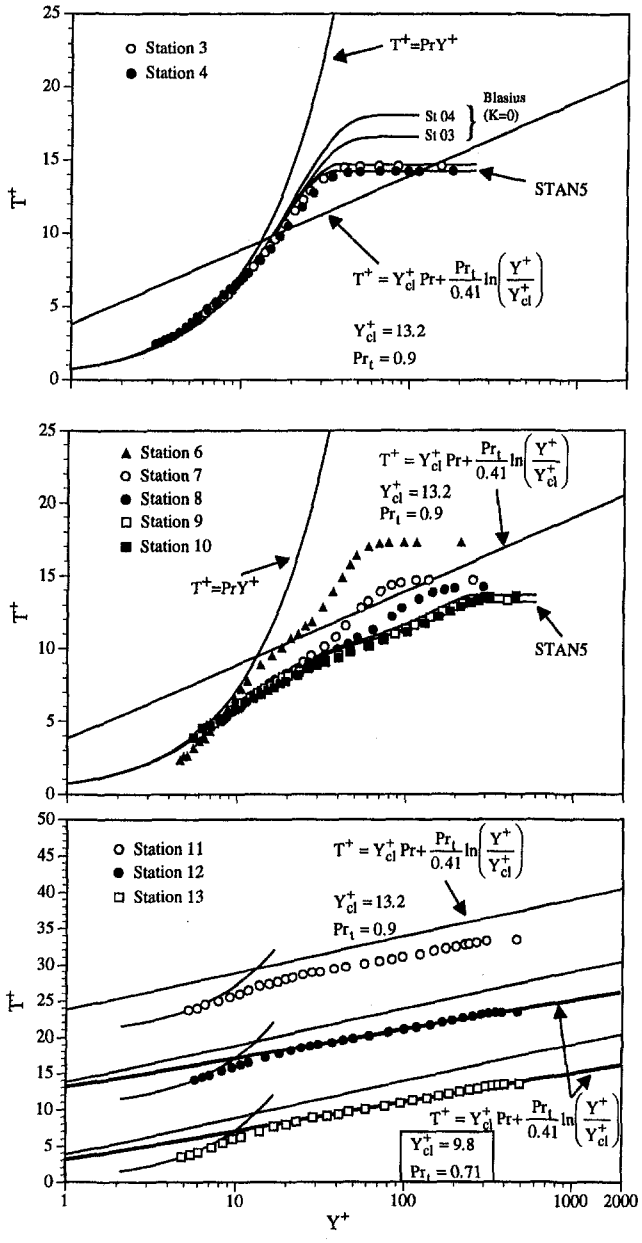

Fig. 13 Mean temperature profiles from the three-wire probe in wall units for $K2 = -1.05 \times 10^{-6}$

the slope of $T^+ - Y^+$ profiles as the average Pr_t has yet to be verified for adverse pressure gradient flows, the value of $Pr_t = 0.71$ is consistent with data from Blackwell et al. (1972). They found that turbulent Prandtl numbers decrease to approximately between 0.6 and 0.8 in the log-linear region with the application of an adverse pressure gradient. It is interesting to note that the velocity profiles in the laminar region under an adverse pressure gradient in $U^+ - Y^+$ coordinates have an upward trend relative to the Couette flow correlation $U^+ = Y^+$ (due to a significant reduction of C_f) as Re_x increases, while the temperature profiles in $T^+ - Y^+$ coordinates move downward from the conduction-layer correlation $T^+ = PrY^+$, which is opposite to the evolution of temperature profiles for zero-pressure-gradient flow.

In addition, for the $K2$ case it is clear that the evolution of temperature reaches fully turbulent flow through the transition region more quickly (at station 9) than does the evolution of velocity, which reaches fully turbulent flow at station 11. The results above indicate that the development of thermal transport in decelerating transitional boundary layers leads the development of momentum transport. Sharma (1987) also found similar results for adverse pressure gradients due to this difference in the thermal and momentum transport and showed that current transitional modeling schemes fail to predict the thermal boundary layer. More experimental results are needed to develop improved transitional flow models.

Conclusion

As seen from the surface heat transfer results, streamwise deceleration caused an earlier onset of transition (smaller Re_{xs}) relative to a zero-pressure gradient. There was a sharp decrease in the transition onset Reynolds number (Re_{xs}) for weak adverse pressure gradients, while for strong adverse pressure gradients, Re_{xs} seemingly approached an asymptotic value. The variation of the Stanton number distribution along the streamwise direction in the early transition region increased faster as the K value increased, reflecting a shorter transition region (based on Re_x).

The Stanton numbers for some cases followed a well-ordered distribution until midway through transition, at which point significant scatter and waviness developed. This region of scatter and waviness increased with decreasing K values (or increasing $U_{\infty 0}$). The C_f distribution obtained from the velocity measurements showed a smooth curve from the laminar to turbulent flow without the scatter and waviness seen in the Stanton number distribution.

In the St versus Re_x figures, the Stanton number distributions are apparently above the zero-pressure-gradient turbulent correlation. This difference increased as the adverse pressure gradient increased. The Stanton number in the turbulent portion decreased with a milder slope downstream than the slope of the zero-pressure-gradient turbulent correlation.

From the boundary layer results, higher negative K values caused earlier transition onset and shorter transition lengths in terms of Re_x, Re_{δ^*}, and Re_θ. Increasing the adverse pressure gradient produced higher values of shape factor in both the laminar and the turbulent regions. Different from the zero-pressure-gradient case, the shape factors for both of the adverse pressure-gradient cases rose to a maximum at the end of the laminar flow. For all cases, the shape factor had almost reached its turbulent value by the end of transition.

For the laminar mean velocity profiles, the adverse pressure gradient induced smaller C_f values and caused the near-wall velocity profiles to pull away from (move above) the $U^+ = Y^+$ curve at locations further downstream. However, for the laminar mean temperature profiles, the adverse pressure gradient caused the near-wall temperature profiles to become lower than the $T^+ = PrY^+$ curve, opposite to its effect on the velocity profiles. The turbulent mean velocity profiles of the decelerated flow show a shortened log-linear region with steeper slopes than the baseline case. The turbulent mean temperature profiles for the decelerated flow have thinner conduction layers (Y_{cl}^+) and lower Pr_t than the baseline case. For the $K2$ case, a curve fit in the thermal law-of-the-wall region results in $Y_{cl}^+ = 9.8$ and $Pr_t = 0.71$. Through the transition region, the streamwise evolution of the temperature profiles achieved fully turbulent flow faster than did the evolution of the velocity profiles. However, this lag of the momentum transport behind the thermal transport in the transition process did not appear to become more pronounced with increasing negative K.

References

Abu-Ghannam, B. J., and Shaw, R., 1980, "Natural Transition of Boundary Layers—The Effects of Turbulence, Pressure Gradient, and Flow History," *Journal of Mech. Engr. Science*, Vol. 22, No. 5, pp. 213–228.

Acharya, M., 1985, "Pressure-Gradient and Free-Stream Turbulence Effects on Boundary-Layer Transition," Brown Boveri Research Center, Baden, Switzerland, Rept. KLR 85-127C.

Blackwell, B. F., Kays, W. M., and Moffat, R. J., 1972, "The Turbulent Boundary Layer on a Porous Plate: An Experimental Study of the Heat Transfer Behavior with Adverse Pressure Gradients," Report No. HMT-16, Ther-

mosciences Division, Department of Mechanical Engineering, Stanford University.

Brown, A., and Martin, B. W., 1976, "The Use of Velocity Gradient Factor as a Pressure Gradient Parameter," *Proc. IMechE,* Vol. 190, pp. 277–285.

Clauser, F. H., 1954, "Turbulent Boundary Layers in Adverse Pressure Gradients," *Journal of the Aeronautical Sciences,* Vol. 21, pp. 91–108.

Fraser, C. J., Milne, J. S., and Gardiner, I. D., 1988, "The Effect of Pressure Gradient and Free-Stream Turbulence Intensity on the Length of Transitional Boundary Layers," *Proc. IMechE,* Vol. 202, No. C3, pp. 195–203.

Gostelow, J. P., and Walker, G. J., 1991, "Similarity Behavior in Transitional Boundary Layers Over a Range of Adverse Pressure Gradients and Turbulence Levels," ASME JOURNAL OF TURBOMACHINERY, Vol. 113, pp. 617–625.

Gostelow, J. P., Blunden, A. R., and Walker, G. J., 1994, "Effects of Free-Stream Turbulence and Adverse Pressure Gradients on Boundary Layer Transition," ASME JOURNAL OF TURBOMACHINERY, Vol. 116, pp. 392–404.

Kays, W. M., and Crawford, M. E., 1980, *Convective Heat and Mass Transfer,* 2nd ed., McGraw-Hill, New York.

Keller, F. J., 1993, "Flow and Thermal Structures in Heated Transitional Boundary Layers With and Without Streamwise Acceleration," Ph.D. Dissertation, Dept. of Mech. Engr., Clemson University, Clemson, SC.

Kline, S. J., and McClintock, J., 1953, "Describing Uncertainties in Single-Sample Experiments," *Mechanical Engineering,* Vol. 75, Jan., pp. 3–8.

Knapp, C. F., and Roache, P. J., 1968, "A Combined Visual and Hot-Wire Anemometer Investigation of Boundary-Layer Transition," *AIAA Journal,* Vol. 6, No. 1, pp. 29–36.

Kuan, C. L., 1987, "An Experimental Investigation of Intermittent Behavior in the Transitional Boundary Layer," M.S. Thesis, Dept. of Mech. Engr., Clemson University, Clemson, SC.

Kuan, C. L., and Wang, T., 1990, "Investigation of Intermittent Behavior of Transitional Boundary Layers Using a Conditional Averaging Technique," *Experimental Thermal and Fluid Science,* Vol. 3, pp. 157–170.

Mislevy, S. P., 1993, "The Effects of Adverse Pressure Gradients on the Momentum and Thermal Structures in Transitional Boundary Layers," M.S. Thesis, Dept. of Mech. Engr., Clemson University, Clemson, SC.

Moffat, R. J., 1982, "Contributions to the Theory of Single-Sample Uncertainty Analysis," ASME *Journal of Fluids Engineering,* Vol. 104, pp. 250–260.

Narayanan, M. A., Badri, X. X., and Ramjee, V., 1969, "On the Criteria for Reverse Transition in a Two-Dimensional Boundary Layer Flow," *Journal of Fluid Mechanics,* Vol. 35, Part 2, pp. 225–241.

Orlando, A. F., Moffat, R. I., and Kays, W. M., 1974, "Heat Transfer in Turbulent Flows Under Mild and Strong Adverse Pressure Gradient Conditions for an Arbitrary Variation of the Wall Temperature," *Proc. 1974 Heat Transfer and Fluid Mechanics Institute,* pp. 91–104.

Patel, V. C., and Head, M. R., 1968, "Reversion of Turbulent to Laminar Flow," *Journal of Fluid Mechanics,* Vol. 34, Part 2, pp. 371–392.

Pohlhausen, K., 1921, "Zur Näherungsweisen Integration der Differentialgleichung der Laminaire Reibungsschicht," *ZAMM,* Vol. 1, pp. 252–268.

Schubauer, G. B., and Skramstad, H. K., 1948, "Laminar Boundary Layer Oscillations and Transition on a Flat Plate," NACA Report No. 909.

Sharma, O. P., 1987, "Momentum and Thermal Boundary Layer Development on Turbine Airfoil Suction Surfaces," Paper No. AIAA-87-1918.

Shome, B., 1991, "Development of a Three-Wire Probe for the Measurement of Reynolds Stresses and Heat Fluxes in Transitional Boundary Layers," M.S. Thesis, Dept. of Mech. Engr., Clemson University, Clemson, SC.

Tennekes, H., and Lumley, J. L., 1972, *A First Course in Turbulence,* MIT Press, pp. 83 and 103.

Thwaites, B., ed., 1960, *Incompressible Aerodynamics,* Oxford University Press, pp. 61–64.

Uberoi, Mahinder S., 1956, "Effect of Wind-Tunnel Contraction on Free-Stream Turbulence," *J. of the Aeronautical Sciences,* pp. 754–764.

Walker, G. J., and Gostelow, J. P., 1989, "Effects of Adverse Pressure Gradients on the Nature and Length of Boundary Layer Transition," ASME JOURNAL OF TURBOMACHINERY, Vol. 112, pp. 196–205.

Walker, G. J., 1989, "Transitional Flow on Axial Turbomachine Blading," *AIAA Journal,* Vol. 27, No. 5, pp. 595–602.

Wang, T., Keller, F. J., and Zhou, D., 1992, "Experimental Investigation of Reynolds Shear Stresses and Heat Fluxes in a Transitional Boundary Layer," *Fundamental and Applied Heat Transfer Research for Gas Turbine Engines,* ASME HTD-Vol. 226, pp. 61–70.

Wang, T., Keller, F. J., and Zhou, D., 1996, "Flow and Thermal Structures in a Transitional Boundary Layer," *Journal of Experimental Fluid and Thermal Science,* Vol. 12, pp. 352–363.

Wang, T., Simon, T. W., and Buddhavarapu, J., 1985, "Heat Transfer and Fluid Mechanics Measurements in Transitional Boundary Layer Flows," ASME *Journal of Engineering for Gas Turbines and Power,* Vol. 107, pp. 1007–1015.

Zhou, D., 1993, "An Experimental Investigation of Transitional Flow With Elevated Levels of Free-Stream Turbulence," Ph.D. Dissertation, Dept. of Mech. Engr., Clemson University, Clemson, SC.

Zhou, D., and Wang, T., 1992, "Laminar Boundary Layer Flow and Heat Transfer With Favorable Pressure Gradient at Constant K Values," ASME Paper No. 92-GT-246.

The Effects of Adverse Pressure Gradients on Momentum and Thermal Structures in Transitional Boundary Layers: Part 2—Fluctuation Quantities

S. P. Mislevy

T. Wang

Department of Mechanical Engineering,
Clemson University,
Clemson, SC 29634-0921

The effects of adverse pressure gradients on the thermal and momentum characteristics of a heated transitional boundary layer were investigated with free-stream turbulence ranging from 0.3 to 0.6 percent. Boundary layer measurements were conducted for two constant-K cases, K1 = -0.51×10^{-6} and K2 = -1.05×10^{-6}. The fluctuation quantities, u', v', t', the Reynolds shear stress ($\overline{uv}$), and the Reynolds heat fluxes ($\overline{vt}$ and $\overline{ut}$) were measured. In general, u'/U_∞, v'/U_∞, and $\overline{vt}$ have higher values across the boundary layer for the adverse pressure-gradient cases than they do for the baseline case (K = 0). The development of v' for the adverse pressure gradients was more actively involved than that of the baseline. In the early transition region, the Reynolds shear stress distribution for the K2 case showed a near-wall region of high-turbulent shear generated at $Y^+ = 7$. At stations farther downstream, this near-wall shear reduced in magnitude, while a second region of high-turbulent shear developed at $Y^+ = 70$. For the baseline case, however, the maximum turbulent shear in the transition region was generated at $Y^+ = 70$, and no near-wall high-shear region was seen. Stronger adverse pressure gradients appear to produce more uniform and higher t' in the near-wall region ($Y^+ < 20$) in both transitional and turbulent boundary layers. The instantaneous velocity signals did not show any clear turbulent/nonturbulent demarcations in the transition region. Increasingly stronger adverse pressure gradients seemed to produce large nonturbulent unsteadiness (or instability waves) at a similar magnitude as the turbulent fluctuations such that the production of turbulent spots was obscured. The turbulent spots could not be identified visually or through conventional conditional-sampling schemes. In addition, the streamwise evolution of eddy viscosity, turbulent thermal diffusivity, and Pr_t are also presented.

Introduction

The previous paper (Part 1) reported the results of an investigation into wall heat transfer, wall friction, and the mean flow structure within the transitional boundary layer under an adverse pressure gradient. In order to understand better the flow structure and the fundamental physics in the transitional boundary layer, information regarding the fluctuating quantities is needed. The fluctuating quantities investigated in this study include typical parameters such as the Reynolds normal and shear stresses (u'^2, v'^2, and $\overline{uv}$), the streamwise Reynolds heat fluxes ($\overline{uv}$ and $\overline{vt}$), the eddy viscosity (ϵ_M), and the turbulent thermal diffusivity (ϵ_H), which are needed for future transitional flow modeling and heat transfer.

Researchers such as Acharya (1985), Gostelow et al. (1994), Gostelow and Walker (1991), and Gostelow and Blunden (1989) have investigated transitional boundary layers subjected to adverse pressure gradients and have determined mean velocity distributions, integral parameters (discussed in Part 1), and intermittency values. These researchers used an on-line intermittency meter with a preset threshold value to determine the intermittency values. Gostelow (1991) presented the velocity traces for what he considered to be zero, moderate, and strong adverse pressure gradients, with corresponding λ_θ values at transition onset of 0, −0.034 and −0.069, respectively. Gostelow (1991) showed that for the strong pressure gradient ($\lambda_\theta = -0.069$), the velocity traces are marked by the continuous appearance of instability waves, which show a greater uniformity of amplitude than is present at lower pressure gradients. The amplitude and frequency of the Tollmien–Schlichting waves are higher than they are at lower pressure gradients and are generally on the same order of magnitude as the fluctuations in the turbulent spots. In addition, Gostelow also stated that the continuous way in which turbulence appears during transition in an adverse pressure gradient makes the turbulent spots much more difficult to characterize, and thus intermittency measurements are open to greater error. In fact, Arnal (1984) stated that intermittency is less apparent even when transition occurs under only a slight adverse pressure gradient since the instability waves exhibit higher amplitudes, making the turbulent spots difficult to distinguish. These previous results seem to indicate that the high turbulent-spot production rate and the shorter transition lengths associated with adverse pressure gradients may be linked to some physical changes occurring in the flow structure in the transition region.

However, very little information regarding the fluctuating quantities under adverse pressure-gradient conditions has been documented in the literature. Recent work by Keller and Wang (1996) and Keller (1993) has provided detailed measurements

Contributed by the International Gas Turbine Institute and presented at the 40th International Gas Turbine and Aeroengine Congress and Exhibition, Houston, Texas, June 5–8, 1995. Manuscript received by the International Gas Turbine Institute February 4, 1995. Paper No. 95-GT-5. Associate Technical Editor: C. J. Russo.

of flow and thermal structures for transitional boundary layers subjected to constant K favorable pressure gradients. Since favorable pressure gradients appear to damp out oscillations and delay transition onset whereas adverse pressure gradients cause strong amplification of instabilities and produce early transition, it would seem reasonable to assume that results obtained under a favorable pressure gradient would be somewhat opposite to those obtained under adverse conditions, and that they would give insight into what might be expected under such conditions.

As might be expected, in the presence of a favorable pressure gradient, the laminar boundary layer can tolerate higher streamwise fluctuations (u') without undergoing transition than it can in the zero-pressure-gradient (baseline) case. With increasing positive K values, the magnitudes of u'/U_∞ and $\overline{uv}/U_\tau^2$ are reduced relative to the zero-pressure-gradient flow at each streamwise location having similar intermittency (Γ) values. In addition, with increasing K values favorable pressure gradients appear to suppress local turbulent shear generation at $Y^+ \approx 100$. The peak magnitude of the Reynolds streamwise heat flux ($\overline{ut}$) in the transition region is approximately 20 times that of the wall heat flux for favorable pressure gradients, while for the zero-pressure gradient it has a magnitude that is 17 times that of the wall heat flux.

The results presented in this paper are intended to provide insight into both the momentum and the heat transfer behavior induced by an adverse pressure gradient. These results include instantaneous velocity signals as well as fluctuating quantities in the form of Reynolds stresses and heat fluxes.

Experimental Program. The same test facility and experimental equipment was used as described in Part 1. Briefly, a two-dimensional, open-circuit wind tunnel was used that had a test section consisting of a heated flat plate and a divergent outer wall for setting constant K pressure gradients. A three-wire probe and a hot-wire anemometry system were used to make instantaneous measurements of velocity and temperature in the boundary layers. The determination of the wall location ($y = 0$) was guided by a single hot-wire measurement.

Detailed boundary layer measurements are made for two cases, $K1 = -0.51 \times 10^{-6}$ and $K2 = -1.05 \times 10^{-6}$. The free-stream turbulence intensities at the onset of transition are 0.3 and 0.35 percent, respectively. The uncertainties of the fluctuating quantities near $y/\delta = 0.2$ are listed in Table 1.

Table 1 Uncertainties of fluctuating quantities

Parameter	Uncertainty (%)
u'	4
v'	24
$\overline{uv}$	11
$\overline{vt}$	12
$\overline{ut}$	4
ϵ_M	11
ϵ_H	12
Pr_t	13

Results and Discussion

Velocity Signals. Instantaneous velocity signals are often helpful in showing flow characteristics and in detecting ambiguous regions between transitional and turbulent flows. The instantaneous streamwise velocity signals were first investigated to see how an adverse pressure gradient affects these signals in comparison to the effect of a zero-pressure-gradient flow (baseline). The baseline case was conducted by Wang et al. (1992, 1996) and is documented in detail in Keller's dissertation (1993). The signals were taken at the y/δ location where the rms streamwise velocity fluctuations reach a maximum in the boundary layer. Figure 1 shows representative velocity signals for the baseline case along with the corresponding intermittency (Γ) values for each station. These intermittency values were determined by Keller and Wang (1995) by using $\overline{uv}$ as the criterion function, $(d\overline{uv}/d\tau)^2$ as the high-pass filter, and the "dual-slope" method on cumulative intermittency distribution to determine the appropriate threshold values. The intermittency value is zero for a laminar flow and 1.0 for a fully turbulent flow. As can be seen, the baseline signals show low-frequency oscillations in the laminar region (stations 4 and 5). These sinusoidal-like oscillations increase in magnitude as transition is approached. In the transition region (station 6), there are distinct turbulent/nonturbulent regions, which show the intermittent passing of turbulent spots or turbulent wave packets. After the spots coalesce into the fully turbulent region, the velocity signal (station 13) shows high-frequency fluctuations characteristic of a zero-pressure-gradient turbulent boundary layer.

In comparison, the velocity signals for the adverse pressure-gradient cases, $K1 = -0.51 \times 10^{-6}$ and $K2 = -1.05 \times 10^{-6}$, are shown in Figs. 2 and 3, respectively. Since these two cases have lower free-stream velocities than does the baseline case, longer time frames are used in Figs. 2 and 3 in order to ensure that the flow travels approximately the same distance as the baseline during the time frame presented. For the $K1$ case, the transition region, determined from the Stanton number distribu-

Nomenclature

K = acceleration parameter = $(\nu/\bar{U}_\infty^2)(d\bar{U}_\infty/dx)$
Pr_t = turbulent Prandtl number
Re_x = local Reynolds number
T = instantaneous temperature = $\bar{T} + t$
$\bar{T}$ = mean temperature
t = temperature fluctuation
t' = rms value of temperature fluctuations
U, V = streamwise and cross-stream instantaneous velocity
$\bar{U}, \bar{V}$ = mean streamwise and cross-stream mean velocity components
u, v, w = instantaneous velocity fluctuations
u', v', w' = rms value of velocity fluctuations
$U_{\infty 0}$ = free-stream velocity at station 1
U_τ = friction velocity = $\sqrt{\tau_w/\rho}$
U_∞ = free-stream velocity
$\overline{uv}$ = Reynolds shear stress
$\overline{ut}$ = streamwise Reynolds heat flux
$\overline{vt}$ = cross-stream Reynolds heat flux
x = streamwise distance from leading edge
y = normal distance from wall
Y^+ = dimensionless distance from wall = yU_τ/ν
δ = boundary layer thickness at $0.995U_\infty$
Γ = intermittency
ϵ_H = turbulent thermal diffusivity = $-\overline{vt}/(\partial T/\partial y)$
ϵ_M = eddy viscosity = $-\overline{uv}/(\partial \bar{u}/\partial y)$
η = dimensionless distance = $(x - x_s)/(x_e - x_s)$

Subscripts

∞ = free-stream value
e = end of transition
s = start of transition
w = at the wall

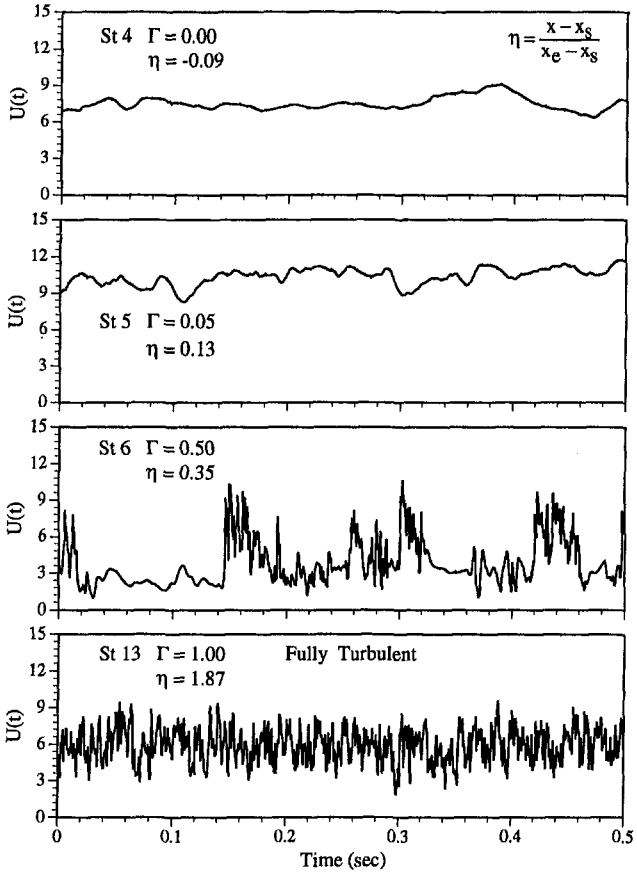

Fig. 1 Representative velocity signals from the three-wire probe for the baseline case taken at u'_{max} ($U_{\infty 0}$ = 12.24 m/s)

tion and the mean velocity profiles in Part 1, starts just after station 4 and ends between stations 6 and 7. The nature of the velocity signals for the $K1$ case are different from those for the baseline case in the following respects: (a) in the pretransition laminar region, no obvious oscillations are observed, (b) in the transition region (stations 5 and 6), there are no distinct turbulent/nonturbulent regions (or intermittency) as were found for the baseline case, and (c) in the turbulent region, the frequencies of the velocity fluctuations are lower than in the transition region for the $K1$ case, whereas for the baseline, the frequencies of the turbulent fluctuations are maintained at about the same level as in the turbulent wave packets of the baseline transition region. Arnal (1984) showed that for decelerated flows, the instability waves in the pretransition region are smaller and look similar to those for a zero-pressure gradient. However, just prior to transition onset (1.5 cm for Arnal, 1984), the unstable waves can reach amplitudes larger than those for a zero-pressure gradient. In the current study, the fast change from pretransition laminar to transitional flow is a likely reason that these high-amplitude waves in the pretransition region were not captured.

The velocity signals for the $K2$ case are shown in Fig. 3. From the Stanton number distribution and the mean velocity profiles in Part 1, transition was determined to start after station 5 and end around station 10. In the pretransition laminar region (station 5), only very weak but relatively uniform sinusoidal oscillations are seen. In the early (station 6) to midtransition region (stations 7 and 8), the velocity signals are obviously dominated by low-frequency fluctuations. However, calculation indicates that these seemingly low oscillation frequencies are much higher than Tollmien–Schlichting wave frequencies due to the low free-stream velocities ($U_{\infty 0}$ = 2.88 m/s). Even in the turbulent region, the velocity signals do not contain the high-frequency fluctuations that were present in both the $K1$ case and the baseline, but, similar to the $K1$ case, the frequencies of the velocity fluctuations in the turbulent region are lower than those in the transition region. For the current study, velocity signals across the boundary layer for the transition region were also investigated in addition to those at u'_{max}. However, there was not any appreciable difference in characteristics between the signals for each station.

An attempt was made to determine the intermittency in the transition region; however, due to the lack of distinguishable turbulent/nonturbulent regions, the method of cumulative power density function used by Hedley and Keffer (1974), Kuan and Wang (1990), and Keller and Wang (1995) for determining intermittency gave unreliable results. Even at stations located far downstream in the turbulent region, this method could not consistently predict an intermittency of 1.00 in the inner boundary layer because some patches of reduced fluctuation frequencies were mistakenly selected as nonturbulent regions by the current method. These lower frequency oscillations were conjectured to be partially due to the lower free-stream velocities ($U_{\infty 0}$ = 8.13 m/s for $K1$ and $U_{\infty 0}$ = 2.88 m/s for $K2$). However, Zhou (1993) used free-stream velocities on the order of 2 m/s with FSTI between 3 and 5 percent in a zero-pressure-gradient flow and found clear turbulent/nonturbulent regions, which yielded consistent intermittency results. Therefore, lower free-stream velocities may be less a cause of the lack of distinctive intermittency than are the adverse pressure gradients.

This raises the question of the nature of natural turbulent spots (in contrast to those artificially generated) in a transitional boundary layer subjected to an adverse pressure gradient. Igarashi et al. (1988) stated that they had observed the formation of turbulent spots in a zero-pressure gradient, but that no spots were observed in the largest adverse pressure gradient case for all of the free-stream velocities tested (~8 to 35 m/s). The

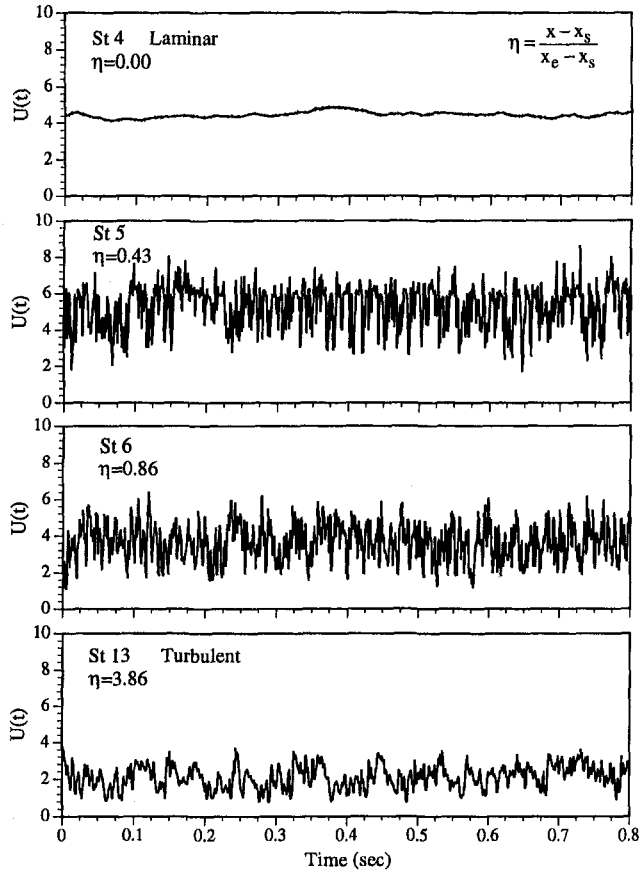

Fig. 2 Representative velocity signals from the three-wire probe for $K1$ taken at u'_{max} ($U_{\infty 0}$ = 8.13 m/s)

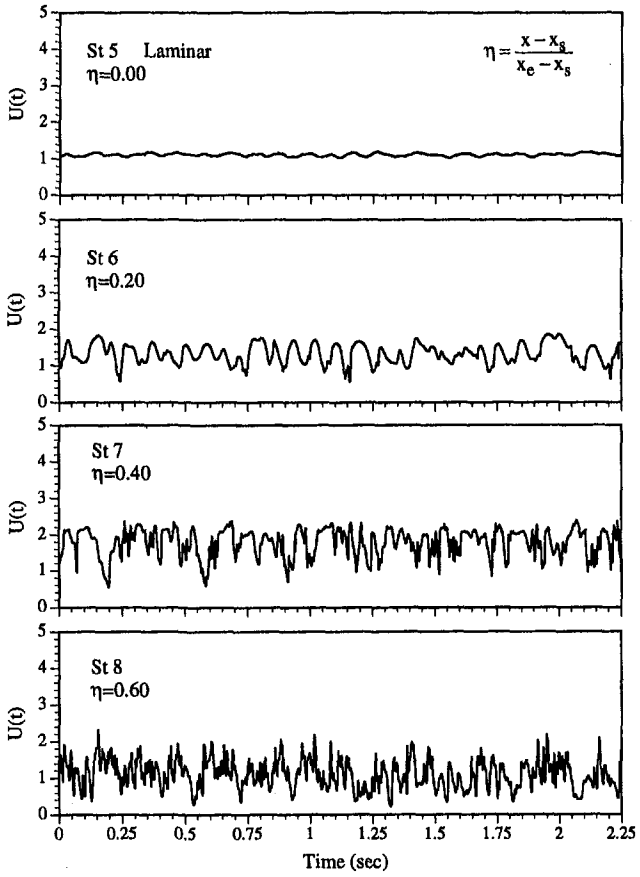

Fig. 3(*a*) Velocity signals from the three-wire probe for *K*2 taken at u'_{max} ($U_{\infty 0}$ = 2.88 m/s)

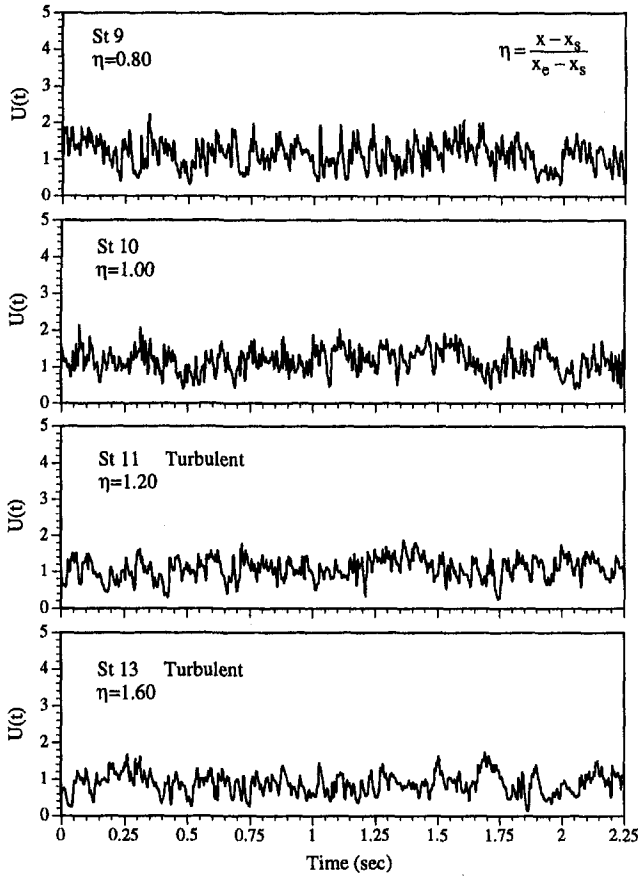

Fig. 3(*b*) Velocity signals from the three-wire probe for *K*2 taken at u'_{max} ($U_{\infty 0}$ = 2.88 m/s)

pressure gradient was defined based on the half-angle of a divergent channel (3.6 deg for the largest pressure gradient), and the free-stream velocity distribution was approximately linear. Arnal (1984) also showed that velocity signals recorded in the middle of the transition region for strong adverse pressure gradients did not present any trace of turbulent spots. For this current study, in which the tests were conducted under a constant K pressure gradient, there also are no clearly defined turbulent/nonturbulent regions in the velocity signals.

Knapp and Roache (1968) stated that there are physical differences between the development of vortex trusses in zero and adverse pressure gradients. Since the initiation of turbulent spots occurs through the appearance of high-frequency fluctuations near the heads of the vortex trusses (or hairpin vortex legs), a change in the development of these trusses could possibly affect the development of turbulent spots through the transition region. In addition, the fact that an adverse pressure gradient causes transition to become a continuous process with only a short hesitation between the breakdown of wave sets may "disguise" any developing turbulent spots, especially for stronger gradients. For the current results, this makes the calculation of intermittency and turbulent spot production rate unreliable. Therefore, a nondimensional length scale, $\eta = (x - x_s)/(x_e - x_s)$, will be used in order to reflect the relative location of each station within the transition region for the decelerating cases (note: $\eta < 0$ indicates the pretransition laminar region and $\eta > 1$ indicates the posttransition turbulent region).

Streamwise Velocity Fluctuations (u'). The streamwise evolution of u' for the $K1$ case is shown in Fig. 4. The zero-pressure gradient (baseline) results are also shown for the sake of comparison. For the $K1$ case, the change of u' along the streamwise direction in the pretransition (or late-laminar) region appears small when compared with the baseline case. However, once transition starts, the production of u' increases faster than in the baseline case (not shown here; see Wang et al., 1996). The u' reaches a maximum value of about 16 percent at station 5. The major difference in the u' distribution between the baseline and the $K1$ case is the broad region ($10 \leq Y^+ \leq 70$) in which the u' value reaches a virtual plateau ($15 \sim 16$ percent) in contrast to the sharp peak of the production region for the baseline case near $Y^+ = 20$. As the end of transition approaches, the u' distribution across the boundary layer becomes similar to that of the baseline but with magnitudes about 5 percent higher than the baseline case between $Y^+ = 20$ and $Y^+ = 200$ and up to 30 percent higher in the near-wall region ($Y^+ < 20$).

The streamwise evolution of u'/U_∞ for the $K2$ case is shown in Fig. 5 in wall units. As for the $K1$ case in Fig. 4, in the pretransition region the change of u'/U_∞ in the streamwise direction is smaller and is of lower magnitude than the baseline. However, once transition starts, there are two distinct peaks of equal magnitude for station 6 at $Y^+ = 7$ and $Y^+ = 30$, respectively. These peaks develop into a broad region of relatively constant u' from $Y^+ = 15$ to $Y^+ = 50$ at station 7 ($\eta = 0.40$), which is similar to $K1$ at $\eta = 0.43$. In the turbulent region (downstream of station 10), the near-wall peak of u'/U_∞ at $Y^+ = 15$ appears to still be changing, while from $Y^+ = 50$ to $Y^+ = 200$, u'/U_∞ does not vary from station to station. Due to the lower free-stream velocity ($U_{\infty 0}$ = 2.88 m/s) of the $K2$ case, more stations are involved in the transition region, and measurements with the three-wire probe can reach $Y^+ = 5$ due to the thicker boundary layer. In general, u'/U_∞ has a broader spread of elevated values across the boundary layer for the adverse pressure-gradient cases than for the baseline case.

Cross-Stream Velocity Fluctuations (v'). The cross-stream evolution of v' for the $K1$ and $K2$ cases is shown in Figs. 6 and 7, respectively. The development of v' for the $K1$ and $K2$ cases is more active than it is for the baseline. Throughout transition, the v'/U_∞ values of the decelerated cases continually exceed the corresponding values for the baseline and remain higher into the turbulent region. In the turbulent region for the baseline case (Fig. 6), the values of v' for $40 < Y^+ < 200$ are fairly constant, with a value of 3.7 percent. However, for the $K1$ case, such a region of constant v' values is only seen immediately after the end of transition at station 7 and is not present in the $K2$ cases (Fig. 7). Farther downstream into the fully turbulent region, a similar region of constant v' values evolves into a distribution with decreasing magnitudes of v' toward the wall. For the zero-pressure-gradient case, the evolution of v' reaches its maximum value in the middle of the transition region and maintains at that maximum value throughout the remaining transition region and into the turbulent region, as will be shown later in Fig. 8. The explanation for this phenomenon provided by Kuan and Wang (1990) is that the increased turbulent energy and dissipation reach equilibrium earlier in the cross-stream direction than they do in the streamwise direction. However, in the decelerated cases, the v' evolution seems to be correlated more closely with the u' distribution. It can be seen in both Figs. 6 and 7 that the v'/U_∞ distribution reaches its maximum value at station 5 ($\eta = 0.43$) for the $K1$ case and station 8 ($\eta = 0.60$) for the $K2$ case. Then, similar to u'/U_∞, v'/U_∞ gradually decreases to its fully turbulent value. This trend of development for v' indicates the significance of increased magnitudes of cross-stream turbulence energy and the involvement of v' in the whole transition process.

The streamwise evolution of the maximum u'/U_∞ and v'/U_∞ at each station for the $K1$ and $K2$ cases is shown in Fig. 8.

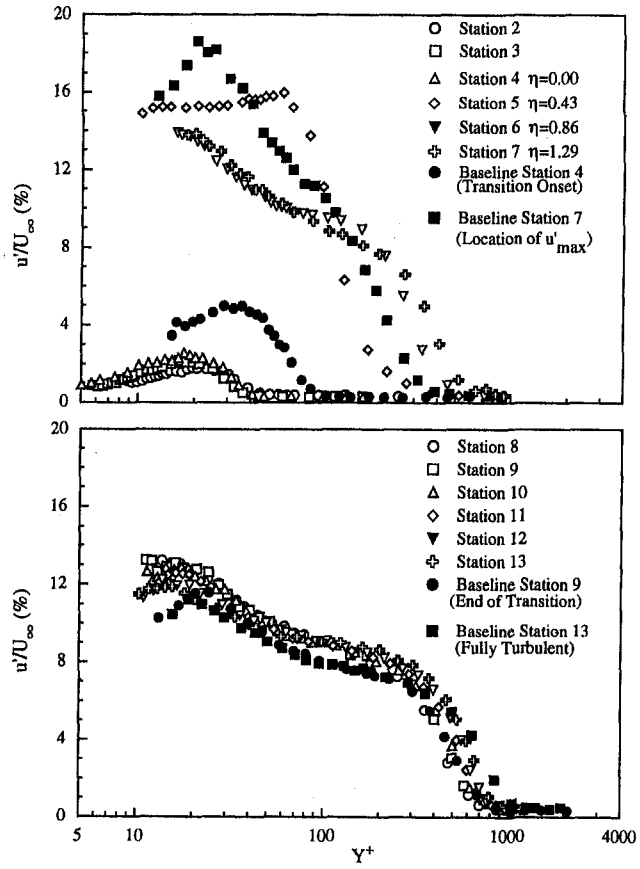

Fig. 4 Streamwise velocity fluctuation distribution for $K1 = -0.51 \times 10^{-6}$ in wall units

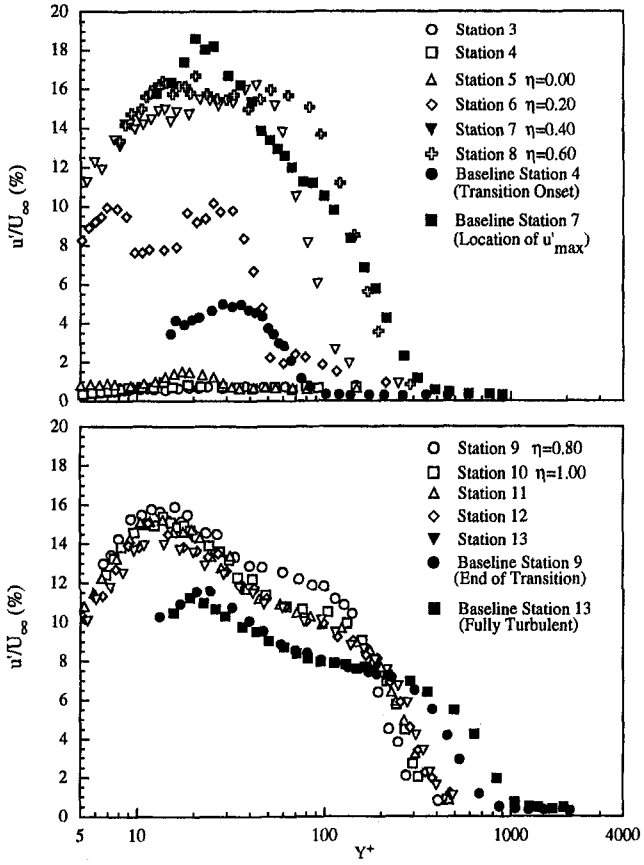

Fig. 5 Streamwise velocity fluctuation distribution for $K2 = -1.05 \times 10^{-6}$ in wall units

The decelerated cases seem to be more effective in transferring turbulence energy from the streamwise direction to the cross-stream direction in the transition and turbulent regions. That this turbulence transfer is more effective is evident from the higher v'_{max} values throughout the transition for both the $K1$ and $K2$ cases as compared to the baseline. In the turbulent region, u'_{max} increases with increased adverse pressure gradients, and for the stronger adverse pressure gradient (the $K2$ case), there is less reduction in u'_{max} from the transition to the turbulent values. Looking at v'_{max}, there is a strong increase in v' in the transition region, and it continues to be higher than the baseline case into the turbulent region. It is also plausible that the increased v' values may not indicate a passively effective energy transfer from u' to v', but rather they indicate an active production of turbulence energy in the cross-stream direction.

Reynolds Shear Stress ($\overline{uv}$). The distributions of the Reynolds shear stresses for the $K1$ and $K2$ cases are shown in Figs. 9 and 10. Baseline Reynolds shear stress distributions at three selected stations (at the onset and the end of transition and at the location with the highest u') are also included for comparison. For the higher adverse pressure-gradient case, $K2$ in Figure 10, the pretransition turbulent shear stress is essentially negligible. However, a sharp increase in the turbulent shear, about 410 percent of the wall shear, occurs at station 6 ($\eta = 0.20$) in the near-wall region at $Y^+ = 7$ with a second peak forming at $Y^+ = 25$ at about 60 percent of the wall shear. At locations farther downstream within the transition region, the near-wall maximum turbulent shear somehow reduces in magnitude while the turbulent shear, between $Y^+ = 10$ and $Y^+ = 100$, rises significantly, as can be seen at station 7 ($\eta = 0.40$). At station 8 for the $K2$ case in Fig. 10, the near-wall region of the turbulent shear decreases to 130 percent of the

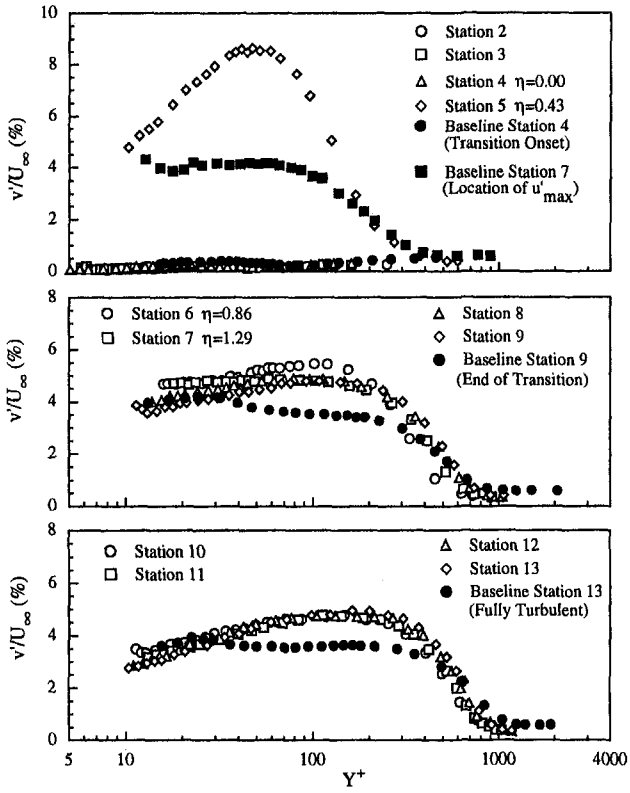

Fig. 6 Cross-stream velocity fluctuation distribution for $K1 = -0.51 \times 10^{-6}$ in wall units

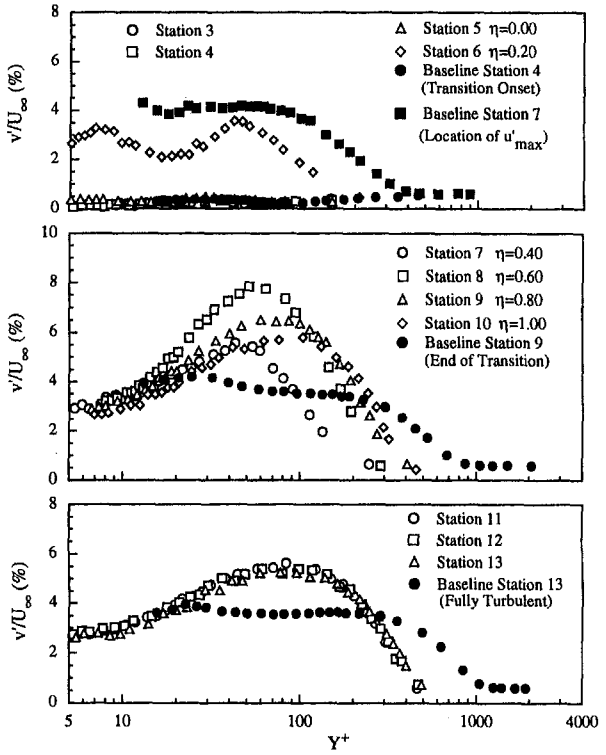

Fig. 7 Cross-stream velocity fluctuation distribution for $K2 = -1.05 \times 10^{-6}$ in wall units

wall shear, but a concentrated high-turbulent shear, about 310 percent of the wall shear, appears around $Y^+ = 70$, which corresponds to the region of maximum turbulent shear at station 7 for the baseline case. It seems that this turbulent shear peak at $Y^+ = 70$ corresponds to the breakdown of the rising vortex tubes away from the wall, and that this is the same mechanism that induces the high-turbulent shear at $Y^+ = 70$ for the zero-pressure-gradient case. Therefore, it is clear that the early near-wall high-turbulent shear generated at $Y^+ = 7$ at station 6 and the subsequent spreading of turbulent shear from station 6 to station 7 are unique characteristics triggered by higher adverse pressure gradients.

It seems that not until the later stages of transition does the increased turbulent shear away from the wall at $Y^+ = 70$ impose on the wall shear and affect the turbulent shear across the boundary layer. As can be seen in Figs. 9 and 10, in contrast to the baseline case, neither the $K1$ nor the $K2$ cases have a region of constant turbulent shear in the fully turbulent boundary layers, although the distribution of $\overline{uv}$ at station 13 for $K2$ is flatter for $Y^+ < 100$ than it is at station 13 for the $K1$ case (Fig. 9). For the $K1$ case in Fig. 9, no near-wall high-turbulent shear (similar to that at $Y^+ = 7$ of station 6 for the $K2$ case) is observed in the transition region, whereas the typical high shear, around $Y^+ = 70$, reaches 500 percent of the wall shear. This may be caused by either (a) a short physical x length over transition due to the associated higher velocities ($U_{\infty 0} = 8.13$ m/s) so that the event of near-wall high-turbulent shear was not captured or (b) the fact that $K1$ is a milder adverse pressure gradient than $K2$ so that the near-wall high-turbulent shear production is not pronounced. In summary, the effect of the adverse pressure gradient significantly increases turbulent shear production throughout the transition region, which is opposite to the effect of favorable pressure gradients (Keller and Wang, 1996), which reduce the ratio of turbulent shear over wall shear in comparison to the zero-pressure-gradient case.

rms Temperature Fluctuations (t'). The distribution of rms temperature fluctuations, t', is shown in Fig. 11 for the $K2$ case only. These rms values are normalized by $T_w - T_\infty$ and are presented in wall units. The evolution of t' for the $K2$ case during transition is similar to that of u' in Fig. 5. Two peaks appear in t' at station 6 in Fig. 11, although the near-wall peak at $Y^+ = 13$ does not exactly correspond to the peak position of u' ($Y^+ = 7$) in Fig. 5. In the later stages of transition, the t' distribution at station 8 maintains a nearly constant value of 12 percent in the region of $10 < Y^+ < 50$ before receding to the asymptotic values in the turbulent boundary layer at station 13. The t' values in the turbulent flow are larger than they are

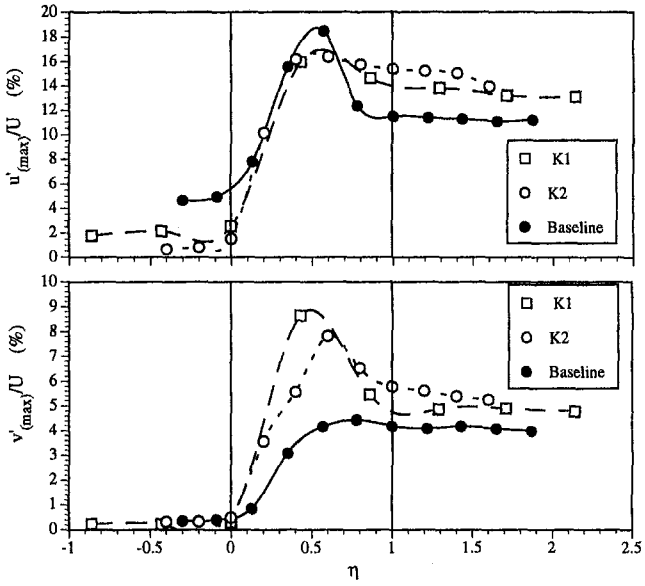

Fig. 8 Distribution of maximum velocity fluctuations

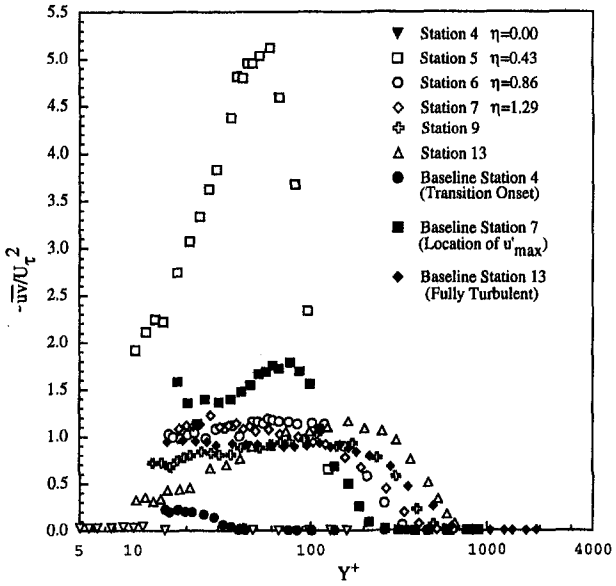

Fig. 9 Reynolds shear stress distribution for $K1 = -0.51 \times 10^{-6}$ in wall units

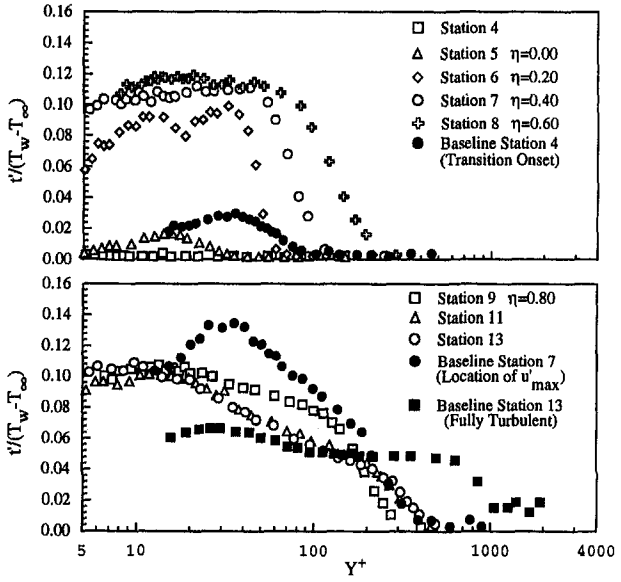

Fig. 11 RMS temperature distribution for $K2 = -1.05 \times 10^{-6}$ in wall units

for both the $K1$ case (not shown, see Mislevy, 1993) and the baseline case in the near-wall region. For the $K2$ case, the t' distribution reaches the value of a turbulent flow at about station 10 or 11. The development of t' lags behind that of mean temperature, which was shown in Part 1 to reach fully turbulent flow at station 9. In other words, the evolution of rms temperature fluctuations under adverse pressure gradients does not appear to keep up with that of the mean temperature. Different from the u' distributions, the t' distributions in the turbulent region for the $K2$ case show a region of constant value, about 10 percent of $T_w - T_\infty$, between $Y^+ = 5$ and $Y^+ = 10$. Stronger adverse pressure gradients appear to produce more uniform and higher near-wall temperature fluctuations in the transition and turbulent regions.

Streamwise and Cross-Stream Reynolds Heat Fluxes ($\overline{ut}$ and $\overline{vt}$). The streamwise Reynolds heat flux, $\overline{ut}$, normalized by the wall heat flux, is shown in Fig. 12 for the $K2$ case. For the baseline case, the magnitude of the peak value of $\overline{ut}$ in the transition region is approximately 17 times greater than the wall heat flux, while for favorable pressure gradients it is 20 times greater than the wall heat flux (Keller and Wang, 1996). However, for the $K1$ and $K2$ cases of this study, the peak magnitude is only five to six times greater than the wall heat flux. As can be clearly seen in Fig. 12, $\overline{ut}$ develops twin peaks at around $Y^+ = 15$ and 50 at station 8 for the $K2$ case and migrates toward the wall in late transition.

In the fully turbulent region for both the $K1$ and $K2$ cases, the maximum $\overline{ut}$ occurs closer to the wall at $Y^+ = 15$ with a magnitude that is about three times greater than the wall heat flux. This $\overline{ut}$ value is larger than that of the baseline case. In comparison to the baseline case in Fig. 12, the adverse pressure gradients increase the near-wall $\overline{ut}$ in the late-transition and turbulent regions, but their effect on the Reynolds heat fluxes is not as great in the outer boundary layer ($Y^+ > 30$). The

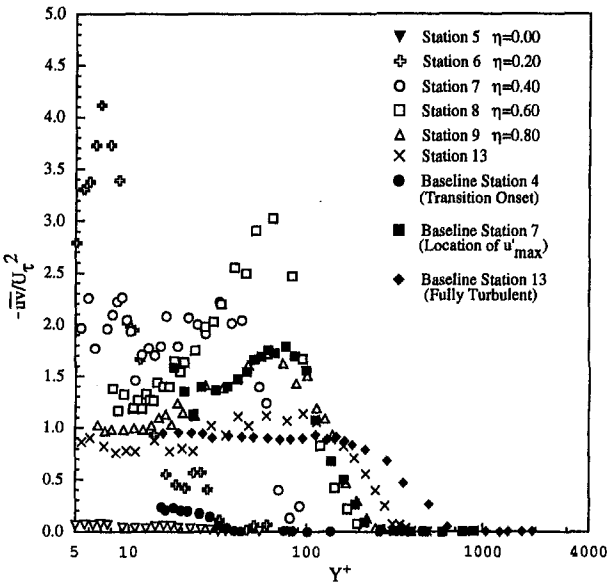

Fig. 10 Reynolds shear stress distribution for $K2$ case

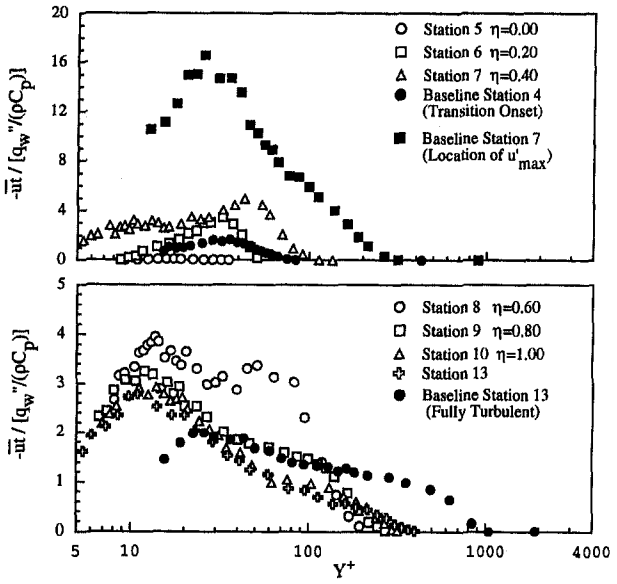

Fig. 12 Reynolds streamwise heat flux for $K2 = -1.05 \times 10^{-6}$ in wall units

term $\partial\overline{ut}/\partial x$ from the energy equation for a two-dimensional, incompressible, turbulent boundary layer is typically considered to be negligible in a fully developed turbulent boundary layer. However, although this term seems to be a significant contributor in the transition region for a zero-pressure-gradient flow, as was pointed out by Keller (1993), it appears to still be negligible for transitional boundary layers developing under adverse pressure gradients.

The $\overline{vt}$ are shown in Fig. 13 for the $K2$ case. For the adverse pressure-gradient case, $\overline{vt}$ reaches a maximum value of 80 percent of the wall heat flux at station 8 ($\eta = 0.60$). This peak value of $\overline{vt}$ for the $K2$ case occurs in the transition region and is about twice as large as that of the baseline case. However, in the turbulent region, the magnitude of $\overline{vt}$ is about the same for both the $K2$ and the baseline cases. Similar to the effect on $\overline{ut}$, increased adverse pressure gradients increase $\overline{vt}$ in the inner boundary layer.

Eddy Viscosity and Turbulent Thermal Diffusivity. The eddy viscosity, ϵ_M, and the turbulent thermal diffusivity, ϵ_H, normalized by their molecular counterparts, are shown in Fig. 14 for the $K2$ case. In the transition region for the $K2$ case, the ϵ_M develops faster with respect to the baseline case with a peak at $y/\delta = 0.4$ because the ϵ_M/ν ratios at $\eta = 0.6$ have peak values similar to those at $\eta = 1.0$, whereas, for the baseline case, ϵ_M/ν at $\eta = 0.57$ is still evolving toward higher values at $\eta = 1.0$. This peak remains fairly constant in magnitude through the turbulent region, although the ϵ_M for the baseline continues to grow in the turbulent region and becomes higher than the ϵ_M for $K2$ by station 13. In the transition region, the ϵ_H also develops faster than for the baseline case, and after reaching a maximum at $y/\delta = 0.4$, it remains relatively constant across the boundary layer with no distinct peak as for the ϵ_M. In the turbulent region, as the flow moves downstream, the ϵ_H develops a small peak between $y/\delta = 0.4 \sim 0.5$. Relative to the same normalized transition length-scale value, η, the adverse pressure gradient seems to cause an earlier and more rapid increase in the development of the ϵ_M and the ϵ_H throughout the transition region than does the baseline. Comparison of the ϵ_M and the ϵ_H for the $K2$ case shows that the ϵ_M increases faster to its maximum value with a distinct peak at $y/\delta = 0.4$.

As also seen in Fig. 14, the Pr_t for the $K2$ case is lower than that of the baseline case in the transition region. However, in the turbulent region, the Pr_t for the $K2$ case becomes larger and decays slower than that of the baseline case. The Pr_t for the adverse pressure-gradient case appears to exhibit a larger region of relatively constant Pr_t value than does the baseline case in both the transition and the turbulent regions. However, as mentioned in Part 1, Blackwell et al. (1972) showed that stronger adverse pressure gradients resulted in lower Pr_t values in the turbulent region. Also, using the slope of the present mean temperature log-linear region gives $\mathrm{Pr}_t = 0.71$ in Part 1. This discrepancy is likely related to the difficulty in experimentally measuring accurate $\overline{vt}$ values. It should be noted that Blackwell et al. did not experimentally measure the Pr_t but determined it by assuming a constant heat-flux region in the turbulent boundary layer and by assuming that the total heat flux in this region was equal to the measured wall heat flux. By subtracting the molecular heat flux from the total heat flux, $\overline{vt}$ was obtained. A detailed discussion and comparison of this method and experimentally determined $\overline{vt}$ values can be found in Keller (1993). Further research is required to specifically investigate the Pr_t measurements and to resolve the discrepancy.

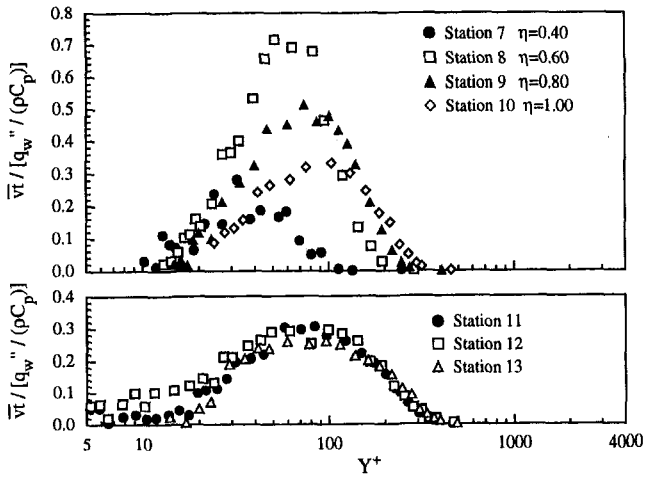

Fig. 13 Cross-stream Reynolds heat flux for $K2 = -1.05 \times 10^{-6}$ in wall units

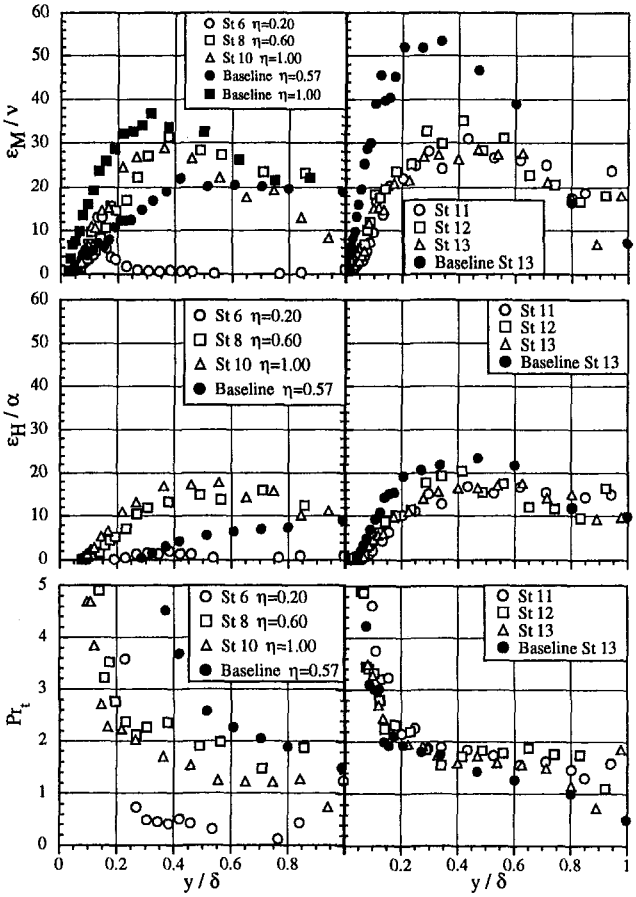

Fig. 14 Streamwise evolution of eddy viscosity, turbulent thermal diffusivity, and Pr_t for $K2$ and the baseline cases

Conclusion

The instantaneous velocity signals taken at the y/δ location where u' is a maximum did not show any clear turbulent/nonturbulent demarcations in the transition region. As a result, reliable intermittency values could not be obtained. It seems that stronger adverse pressure gradients affect and disguise the production of turbulent spots. In fact, even under weak adverse pressure gradients, the magnitude of the waves can be of the same order as the magnitude of the turbulent spots, making the determination of a threshold value difficult.

The u' for the $K1$ and $K2$ cases exhibited a broad region (from $Y^+ \approx 10$ to 65) in which the u' value reached a virtual plateau in the transition region in contrast to a peak-production region for the zero-pressure-gradient baseline case near $Y^+ = 20$. The development of v' for the adverse pressure gradients

was more active than that of the baseline. The v'/U_∞ values for the decelerated cases increased distinctively to approximately twice the baseline value near the onset of transition and continually exceeded the baseline values throughout the transition and turbulent regions. The application of an adverse pressure gradient is apparently effective in transferring turbulence energy from the streamwise direction to the cross-stream direction in the transition region.

The Reynolds shear stress distribution in the early transition region for the stronger adverse pressure gradient ($K2 = -1.05 \times 10^{-6}$) showed a near-wall region of high-turbulent shear generated at $Y^+ = 7$. At locations farther downstream, this near-wall shear reduced in magnitude, while a second region of high shear developed at $Y^+ = 70$. For the baseline case, however, the turbulent shear in the transition region was generated at $Y^+ = 70$, and no near-wall high-shear region was seen.

The peak magnitude of the streamwise Reynolds heat flux ($\overline{ut}$) in the transition region for the decelerated cases was found to be about a third of that for the baseline case. The term $\partial\overline{ut}/\partial x$ (from the turbulent two-dimensional energy equation) is less significant in the transition region when the boundary layer develops under decelerated conditions than under a zero-pressure gradient. However, in the late-transition and turbulent regions, the adverse pressure gradients caused an increase in the near-wall $\overline{ut}$. The $\overline{vt}$ values in a decelerated transitional boundary layer are higher than those in the baseline case.

Both the ϵ_M and the ϵ_H developed faster in the $K1$ and $K2$ cases than they did in the baseline cases and reached equilibrium values in the middle of the transition region. However, the ϵ_M and the ϵ_H of the baseline case eventually outgrew the equilibrium values of the ϵ_M and the ϵ_H in the later part of the decelerated transitional flow and maintained these higher values in the zero-pressure-gradient turbulent boundary layer.

References

Acharya, M., 1985, "Pressure Gradient and Free-Stream Turbulence Effects on Boundary Layer Transition," Brown Boveri Research Center, Baden, Switzerland, Rept. KLR 85-127C.

Arnal, D., 1984, "Description and Prediction of Transition in Two-Dimensional, Incompressible Flow," AGARD-R-709, 2-1.

Blackwell, B. F., Kays, W. M., and Moffat, R. J., 1972, "The Turbulent Boundary Layer on a Porous Plate: An Experimental Study of the Heat Transfer Behavior With Adverse Pressure Gradients," Report No. HMT-16, Thermosciences Division, Department of Mechanical Engineering, Stanford University.

Gostelow, J. P., and Blunden, A. R., 1989, "Investigations of Boundary Layer Transition in an Adverse Pressure Gradient," ASME JOURNAL OF TURBOMACHINERY, Vol. 111, pp. 366–375.

Gostelow, J. P., and Walker, G. J., 1991, "Similarity Behavior in Transitional Boundary Layers Over a Range of Adverse Pressure Gradients and Turbulence Levels," ASME JOURNAL OF TURBOMACHINERY, Vol. 113, pp. 617–625.

Gostelow, J. P., 1991, "Influence of Adverse Pressure Gradients on Chaotic Regimes Encountered During Transition," *Boundary Layer Stability and Transition to Turbulence,* ASME FED-Vol. 114, pp. 145–153.

Gostelow, J. P., Blunden, A. R., and Walker, G. J., 1994, "Effects of Free-Stream Turbulence and Adverse Pressure Gradients on Boundary Layer Transition," ASME JOURNAL OF TURBOMACHINERY, Vol. 116, pp. 392–404.

Hedley, T. B., and Keffer, J. F., 1974, "Turbulent/Non-Turbulent Decisions in an Intermittent Flow," *Journal of Fluid Mechanics,* Vol. 64, Part 4, pp. 625–644.

Igarashi, S., Sasaki, H., and Honda, M., 1988, "Influence of Pressure Gradient Upon Boundary Layer Stability and Transition," *Acta Mechanica,* Vol. 73, pp. 187–198.

Keller, F. J., 1993, "Flow and Thermal Structures in Heated Transitional Boundary Layers With and Without Streamwise Acceleration," Ph.D. Dissertation, Dept. of Mech. Engr., Clemson University, Clemson, SC.

Keller, F. J., and Wang, T., 1995, "Effects of Criterion Functions on Intermittency in Heated Transitional Boundary Layers With and Without Streamwise Acceleration," ASME JOURNAL OF TURBOMACHINERY, Vol. 117, pp. 154–165.

Keller, F. J., and Wang, T., 1996, "Flow and Heat Transfer Behavior in Transitional Boundary Layers With Streamwise Acceleration," ASME JOURNAL OF TURBOMACHINERY, Vol. 118, pp. 314–326.

Knapp, C. F., and Roache, P. J., 1968, "A Combined Visual and Hot-Wire Anemometer Investigation of Boundary-Layer Transition," *AIAA Journal,* Vol. 6, No. 1, pp. 29–36.

Kuan, C. L., and Wang, T., 1990, "Investigation of Intermittent Behavior of Transitional Boundary Layer Using a Conditional Averaging Technique," *Experimental Thermal and Fluid Science,* Vol. 3, pp. 157–170.

Mislevy, S. P., 1993, "The Effects of Adverse Pressure Gradients on the Momentum and Thermal Structures in Transitional Boundary Layers," M.S. Thesis, Dept. of Mech. Engr., Clemson University, Clemson, SC.

Wang, T., Keller, F. J., and Zhou, D., 1992, "Experimental Investigation of Reynolds Shear Stresses and Heat Fluxes in a Transitional Boundary Layer," *Fundamental and Applied Heat Transfer Research for Gas Turbine Engines,* ASME HTD-Vol. 226, pp. 61–70.

Wang, T., Keller, F. J., and Zhou, D., 1996, "Flow and Thermal Structures in a Transitional Boundary Layer," *Journal of Experimental Fluid and Thermal Science,* Vol. 12, pp. 352–363.

Zhou, D., 1993, "An Experimental Investigation of Transitional Flow With Elevated Levels of Free-Stream Turbulence," Ph.D. Dissertation, Dept. of Mech. Engr., Clemson University, Clemson, SC.

Effects of Streamwise Pressure Gradient on Turbulent Spot Development

J. P. Gostelow
Department of Engineering,
University of Leicester,
Leicester, United Kingdom
Mem. ASME

N. Melwani
School of Mechanical Engineering,
University of Technology, Sydney,
Sydney, Australia

G. J. Walker
Department of Civil and Mechanical Engineering,
University of Tasmania,
Hobart, Tasmania, Australia
Mem. ASME

A pressure distribution representative of a controlled diffusion compressor blade suction surface is imposed on a flat plate. Boundary layer transition in this situation is investigated by triggering a wave packet, which evolves into a turbulent spot. The development from wave packet to turbulent spot is observed and the interactions of the turbulent spot with the ongoing natural transition and the ensuing turbulent boundary layer are examined. Under this steeply diffusing pressure distribution, strong amplification of primary instabilities prevails. Breakdown to turbulence is instigated near the centerline and propagates transversely along the wave packet until the turbulent region dominates. An extensive calmed region is present behind the spot, which persists well into the surrounding turbulent layer. Celerities of spot leading and trailing edges are presented, as is the spanwise spreading half-angle. Corresponding measurements for spots under a wide range of imposed pressure gradients are compiled and the present results are compared with those of other authors. Resulting correlations for spot propagation parameters are provided for use in computational modeling of the transition region under variable pressure gradients.

Introduction

Few studies have been made of either natural or artificially initiated boundary layer transition processes under adverse pressure gradient conditions. In earlier work at the University of Technology, Sydney natural transition was investigated over a wide range of free-stream turbulence levels and adverse pressure gradients (Gostelow et al., 1994). In this context "natural" transition also includes bypass transition induced by free-stream turbulence. This earlier work was based on the use of intermittency as a basis for similarity (Narasimha, 1957). This provided a consistent basis for categorizing the development of transition and resulted in the production of correlations for parameters, such as turbulent spot formation rate, for use in computational studies and by designers.

In the course of the studies on natural transition, it had been observed that under conditions of low free-stream turbulence level and strong adverse pressure gradient, the flow was dominated by periodic behavior mainly associated with Tollmien–Schlichting (T–S) waves. Under these conditions it became increasingly difficult to discriminate, on the basis of either frequency or amplitude, between turbulent and merely periodic behavior. This raised practical difficulties with the use of intermittency approaches and serious questions about the nature of turbulent spots under these conditions. A theoretical model of transition under an adverse pressure gradient had been produced (Walker and Gostelow, 1990) and this was predicated on a knowledge of the physics of turbulent spots under an adverse pressure gradient. In particular, assumptions had been made about streamwise and transverse propagation rates of spots and there was a need to validate these.

In turbomachinery the flow is often in a transitional state over much of the blade surface. Prediction of these flows requires a knowledge of transition behavior through regions of rapidly changing pressure gradient. Many predictive approaches for boundary layer transition are predicated on nonexistent knowledge of turbulent spot behavior under varying streamwise pressure gradient. The most usual assumption (cf. Chen and Thyson, 1971) has been to base the spot celerities, and the corresponding spanwise spreading, on information gained from measurements of spots under zero pressure gradient conditions. It will be demonstrated in this paper that this was not a good assumption and that under adverse pressure gradients the spot propagates much more rapidly.

There is a history of successful experimentation on triggered spots under zero and favorable pressure gradients and it was considered appropriate to extend such investigations to adverse pressure gradients. In turbomachinery it is especially important to understand the nature of transition induced by the wakes, from upstream blades, which periodically sweep over the boundary layer and this also motivates an interest in the behavior of triggered turbulent spots (Walker et al., 1993).

The overall purpose of the ongoing program of work is to obtain mappings of developing spots in order to model their physical behavior, growth, and spreading rates, with special reference to the rapid natural transitions that occur under adverse pressure gradients. The resulting models are to be incorporated into boundary layer codes that predict the transition region. Specifically, a developing spot under a strong adverse pressure gradient has been investigated. The pressure distribution chosen replicated that of the suction surface of a controlled diffusion compressor blade.

Apparatus and Data Reduction

The 608 mm × 608 mm octagonal open circuit tunnel at UTS was used for the experimental work. Boundary layer traverses were taken on the upper surface of a 1500 × 608 × 25 mm flat aluminum plate having a high-quality surface finish. The leading edge of the upper surface is of slender elliptical arc form and is located 1200 mm from the working section entrance. The plate has a 0.25 deg negative incidence to avoid leading edge separation. Static taps are located every 25 mm along the plate. Measurement stations are designated to coincide with pressure taps and are listed with corresponding x values in Table 1.

The controlled diffusion pressure distribution shown in Fig. 1 was applied to the flat plate by a fairing, which was purpose-

Contributed by the International Gas Turbine Institute and presented at the 40th International Gas Turbine and Aeroengine Congress and Exhibition, Houston, Texas, June 5–8, 1995. Manuscript received by the International Gas Turbine Institute March 10, 1995. Paper No. 95-GT-303. Associate Technical Editor: C. J. Russo.

Table 1 Station locations and measured free-stream velocities

Station	x mm	U m/sec
7	207	13.07
9	257	12.91
11	307	12.65
12	332	12.53
13	357	12.42
14	382	12.35
15	407	12.28
16	432	12.20
17	457	12.06
18	482	12.00
19	507	11.91
20	532	11.83
21	557	11.78
22	582	11.70
23	607	11.66
24	632	11.60
25	657	11.55

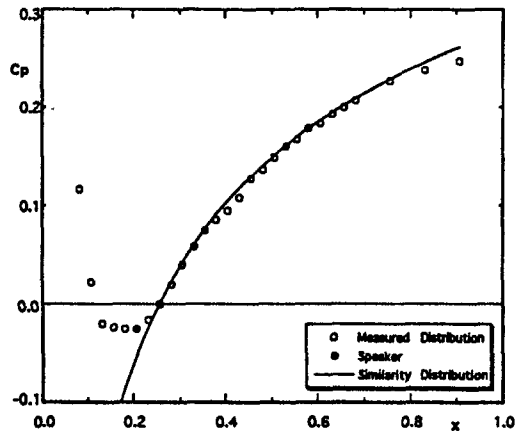

Fig. 1 Controlled diffusion pressure distribution

designed using CFD techniques. The pressure distribution provided a locally self-similar laminar boundary layer downstream of a reference location, which was taken to be Station 9, some 257 mm downstream of the leading edge. The velocity distribution is described by a Hartree β of -0.223, resulting in strong adverse pressure gradients, beyond the theoretical limit for laminar separation. The reference free-stream velocity (at Station 9) was 12.91 m/s. Measured free-stream velocities at each station are also listed in Table 1. The free-stream turbulence level upstream of the flat plate was 0.3 percent. Over the region of interest in these experiments δ_L grew from 3.4 mm to 4.5 mm with an average value of 4.0 mm.

Wave packets and spots were triggered by jets of air injected at Station 7, 207 mm downstream of the leading edge. The jets were produced by a speaker driven by a 1 Hz sharp-edged pulse, which also served to trigger data acquisition. Spot growth by natural amplification of instabilities was achieved using a low-amplitude jet of 0.4 ms duration. Injection ports were available at 20 spanwise locations on either side of the centerline. These were used for triggering off-center spots, facilitating a complete three-dimensional mapping.

Streamwise velocities were measured using a Dantec 55M01 anemometer with a 5 μm single wire platinum probe. The probe was traversed in streamwise and normal directions, its normal position being monitored by a dial gage having a least count of 0.01 mm. A telescope was used, with a fiber optic light source, for zero positioning accurate to 0.02 mm. Traverses took place at streamwise intervals of 25 mm between Stations 7 and 25, representing x values of 207 and 657 mm, respectively.

Each trace, comprising 900 readings, was digitized with 12-bit accuracy at 5 kHz using Labview software on a Macintosh IIfx computer with a National Instruments NB-MIO-16 analog-to-digital convertor. Analog low-pass filtering was applied at a frequency of 2.5 kHz. A Yokogawa DL1200A digital oscilloscope was used for on-line monitoring and provided immediate hard copy of voltage traces.

To obtain consistent velocity data, a phase-averaging procedure was adopted using the rising edge of the triggering pulse as a reference. The velocity was formed by averaging 128 realizations and applying the hot-wire calibration. The correction of Wills (1962) for wall proximity was applied to traces close to the wall. The ensemble of averaged velocity traces was intercepted at each time interval; velocity profiles were plotted throughout the spot and its surrounding region and integral properties were derived. Variations between raw traces were separately analyzed in a procedure that evaluated the root mean square fluctuation level of 30 individual traces.

Results

Phase-averaged contours of velocity perturbation, $(u - u_L)/U$, in the z–t plane for seven streamwise locations are presented in Fig. 2. Each plot is identified by its station number and streamwise location. The contours were taken at a height of $y = 1.2$ mm. Phase averaging has resulted in contours that reveal consistent structural features of the spot while smoothing out most of the variability between realizations.

It is clear from this figure that Station 13 represents wave packet behavior that is not particularly symmetric; Cohen et al. (1991) also observed similar asymmetries. Instability first develops at around Station 14 in the vicinity of the centerline. This becomes a region of turbulence, which is already seen to be propagating outward along the wave packet by Station 16. By Station 18 the wave packet has become swamped by the turbulence and at Station 19 the spot moves in a boundary layer, which has reached an advanced stage of natural transition.

In the early stages of amplification and formation under an adverse pressure gradient spot, and for much of the span, the perturbations can be characterized as wave packets rather than turbulent spots. The adverse pressure gradient has provided an environment permitting strong amplification of the T–S wave prior to breakdown to nonlinearity and the high-amplitude wave

Nomenclature

aU = spot leading edge velocity
bU = spot trailing edge velocity
Cp = static pressure coefficient
t = time
u = local velocity
U = free-stream velocity
x = distance in streamwise direction
y = normal distance from plate surface
z = spanwise distance
α = spot spreading half angle
β = Hartree parameter
δ = boundary layer absolute thickness = $u/U = 0.99$
λ_θ = pressure gradient parameter = $(\theta^2/\nu)(dU/dx)$
θ = boundary layer momentum thickness
ν = kinematic viscosity
σ = dimensionless spot propagation parameter

Subscript

L = pertaining to laminar or ambient boundary layer

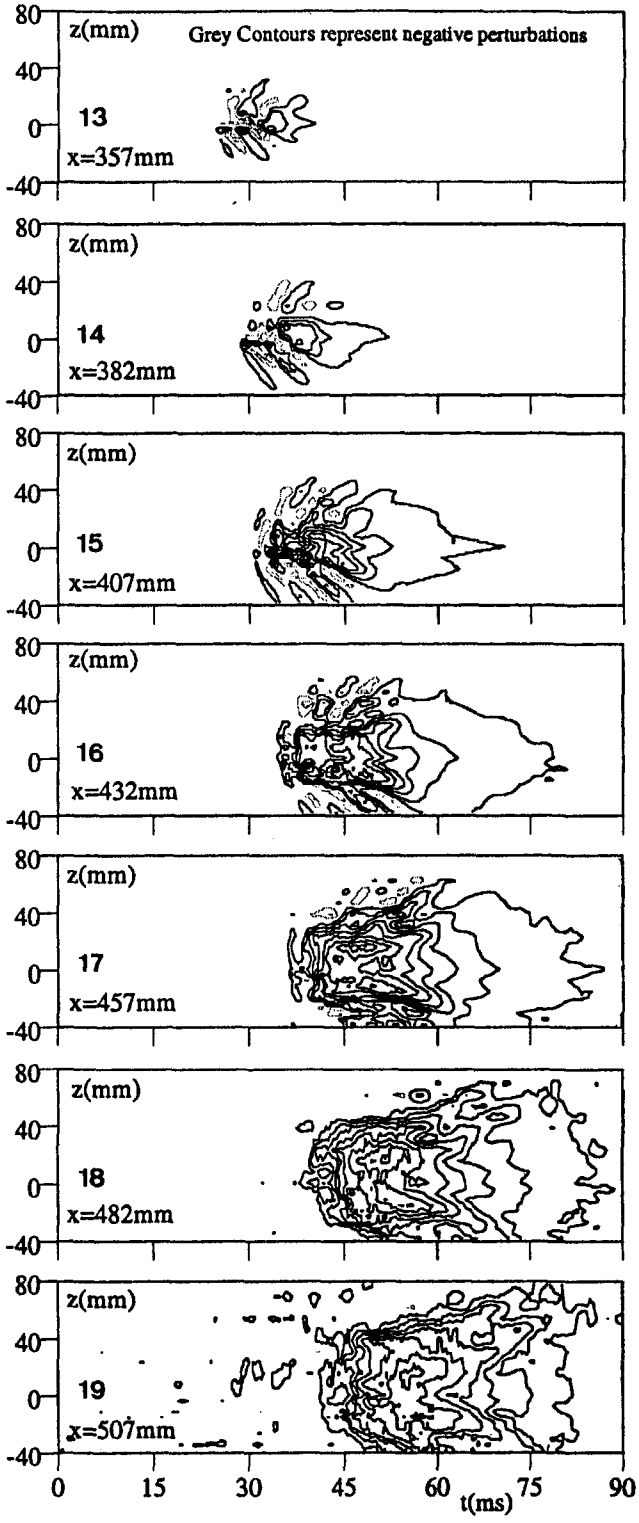

Fig. 2 Contours of velocity perturbation, $(u - u_L)/U$, in z–t plane at y = 1.2 mm; contour interval is 0.04

packet, which forms the lateral extension of the spot, occurs at a wavelength consistent with the predicted T–S value.

High-frequency disturbances tend to be eliminated by phase averaging and are therefore not well-represented in the velocity perturbation plots. Inspection of raw data traces indicated that significant high-frequency activity was confined to inboard locations at the early stages of breakdown (up to Station 15).

The z–t plane plots make it clear that the topography cannot readily be described by the "arrowhead" models used for spots under zero and favorable pressure gradients. Adverse pressure gradient spots have a relatively blunt nose. This geometry is accentuated by the tendency for a small "bow wave" to lead the spot. The disturbance starts close to the centerline of the highly amplified wave packet and spreads laterally along the regions of strong shear associated with the wave packet, eventually swamping it. Gostelow et al. (1993) observed a wave packet that remained abreast of the spot during the transition process. Figure 2, however, which represents more stations than the earlier work, indicates that the wave packet is swept back and begins to drop behind as the spot becomes more mature. This behavior may help to explain the wave packets observed behind the tips of zero pressure gradient spots.

Velocity perturbation contours on the centerline of the y–t plane are presented in Fig. 3 for the same streamwise locations. These show the evolution from wave packet to turbulent spot. The gray contours in the forward region represent negative velocity perturbations. At Station 13 there is first a region of lower velocity than the laminar level, followed by a higher velocity region; this represents wave packet behavior. As the turbulence develops at downstream stations the developing spot is characterized by a turbulent velocity profile with a relatively high velocity near the surface and a low one further out. The calmed region following the spot tends to have a fuller velocity profile than that of the ambient laminar layer.

Figure 4 represents rms fluctuation levels in the same plane. At Station 16 the spot stands alone, but by Station 18 it is moving into a highly disturbed ambient boundary layer. The fluctuation level is higher in the forward regions of the spot than in the ambient layer at locations up to Station 18.

By Station 20 the fluctuation level of the ambient layer has become higher than that of the spot. Figure 5 represents both fluctuation level and velocity perturbation over the longer time interval of 180 ms. It shows clearly the persistence of an extensive calmed region within a turbulent layer. Since the velocity perturbation now shows variations from an ambient layer that has undergone natural transition the velocity profile in the calmed region is relatively laminar in character, with a negative perturbation near the wall and a positive one further out. By Station 21 (not shown here) the spot has become virtually submerged in the encroaching turbulent boundary layer, only the calmed region standing out as a reminder of the spot's passage. The spot and calmed region interact with the turbulent layer. The leading region of negative velocity perturbation projects toward the wall and weakens as the spot is incorporated into the surrounding turbulent layer. By Station 23 this process is more advanced but the calmed region is still present and will yet persist for a good distance downstream. By Station 25 the still extensive region of negative velocity perturbation represents a region of low skin friction near the surface. The only remaining vestige of this triggered spot is therefore, paradoxically, the calmed region. The triggering of the disturbance has had the effect of producing a local reduction in skin friction.

Figure 6 presents spot arrival times on the centerline. The leading edge is characterized at a height of 1.2 mm (y/δ_L = 0.3) by a fairly sensitive 2 percent velocity perturbation. Although over the first 150 mm after the speaker port, the wave packet has a relatively slow propagation speed, in the subsequent region of spot development a linear fit represents the leading edge well. Because the free-stream velocity is decreasing in a streamwise direction, the arrival times are differenced at each station and the local leading edge propagation velocity $\Delta x/\Delta t$ compared with the local free-stream velocity. The results are averaged over the region of interest (Stations 13 to 19) to give the celerity, a. A value of $a = 0.872$ was determined for this leading edge celerity.

Establishing the trailing edge of the turbulent region is more problematic. Velocity perturbations cannot be used because the velocity levels at the trailing edge of the turbulent region have not begun to relax to the laminar values. The rms fluctuation

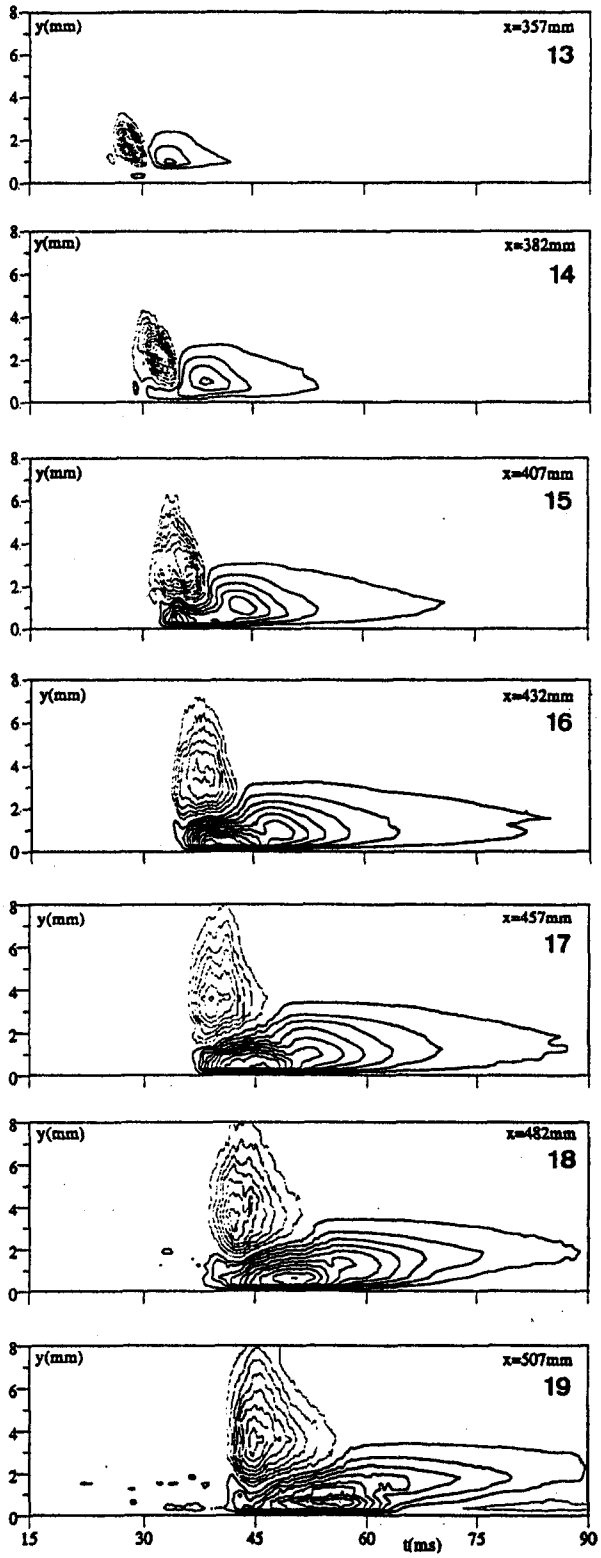

Fig. 3 Contours of velocity perturbation, $(u - u_L)/U$, on centerline in $y-t$ plane; contour interval is 0.04

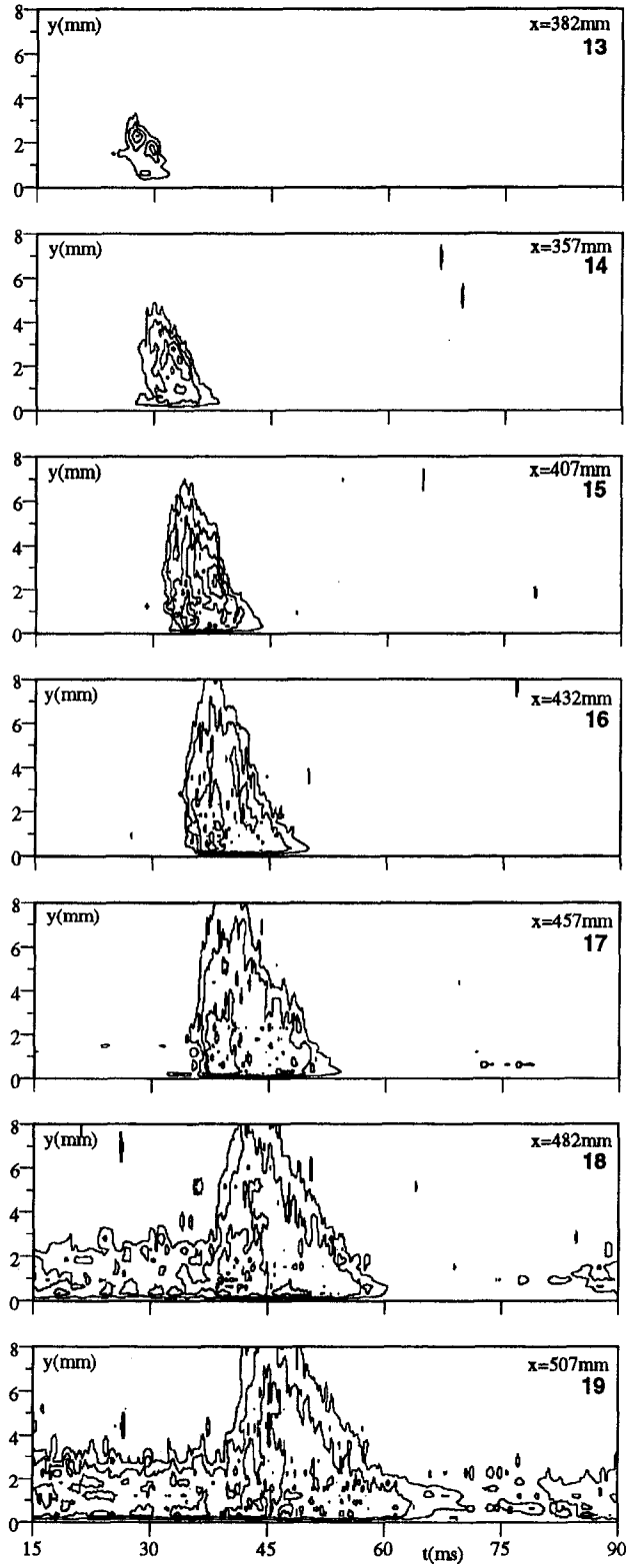

Fig. 4 Contours of rms fluctuation level on centerline in $y-t$ plane; contour interval is 0.04

level was considered to be the most relevant parameter, but it was necessary to reduce any arbitrariness with regard to threshold level chosen and elevation from the surface. It was found that at some heights from the surface, the measured propagation rate was very sensitive to the threshold rms selected. This was not the case close to the surface at $y = 0.3$ mm; at that height the arrival time $x-t$ lines were essentially parallel for different threshold levels, indicating a low sensitivity of trailing edge celerity, b, to the threshold rms selected. This is a result of the topology of the turbulent region of the spot, which, as seen in Fig. 4, sweeps down to the surface at the trailing edge. The arrival times for each rms threshold level were well represented by straight lines and a rms fluctuation level of 4 percent was selected as representative of the trailing edge propagation veloc-

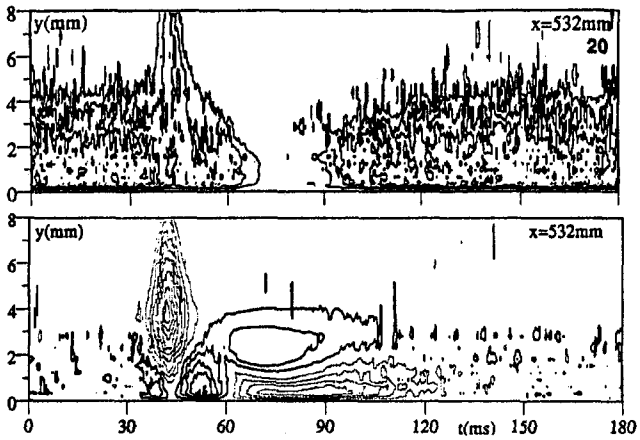

Fig. 5 Contours of fluctuation level (upper) and velocity perturbation (lower) on centerline in y–t plane at Station 20; contour interval is 0.04

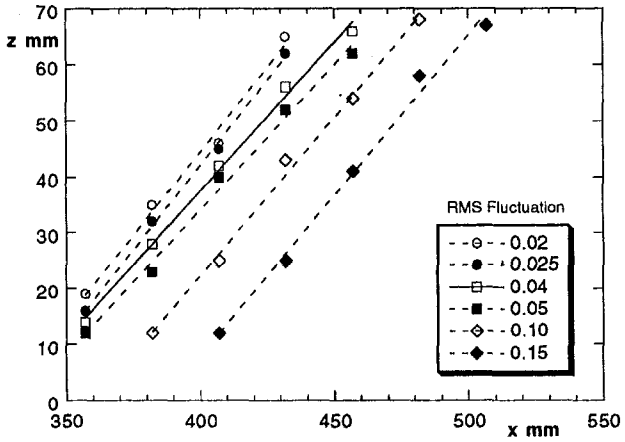

Fig. 7 Dependence of perceived extent of spot lateral spreading on rms fluctuation level threshold

ity. This level is applicable to a wide range of streamwise locations, being present in the wave packet as early as Station 14 and still discernible in the turbulent flow as far back as Station 25. Its use is therefore considered to be representative and robust. Again the local arrival times were normalized by local free-stream velocity and the resulting celerity averaged over the region of interest. This resulted in a value for b of 0.431.

Because local velocities relax gradually and monotonically to the velocity of the ambient boundary layer, a 2 percent velocity perturbation was found to be a reasonable and consistent indicator of the trailing edge of the calmed region. Unlike the leading and trailing edges of the spot itself, the closure of the calmed region is not at all linear with x in the later stages. As the surrounding boundary layer becomes turbulent the calmed region does persist, as an "island" of laminar flow for a significant distance, but is eventually swamped by the turbulence. Similar behavior has been observed on turbomachinery blading. An average celerity for the trailing edge of the calmed region, while it is still unaffected by a surrounding turbulent layer, is of the order of 0.25.

In Fig. 7 the lateral spreading rate of the spot is presented. In this case the furthest extent of the root mean square fluctuation level contours at a height of 0.9 mm above the surface is plotted. The local gradient of this plot gives tan α and the plot demonstrates that the gradient is not particularly sensitive to the fluctuation level threshold selected. Using a fluctuation level detector of 4 percent, a value of $\alpha = 29.2$ deg is obtained. The same exercise was repeated on the opposite side of the centerline and a virtually identical result was obtained. The high spreading angle is consistent with the observation of Watmuff (1989) that under a strong adverse pressure gradient "the spanwise propagation . . . is extraordinarily rapid, i.e., the spotlike flow develops a width greater than its length after streamwise development of about one only spot-length." This implies a half-angle greater than 26.6 deg.

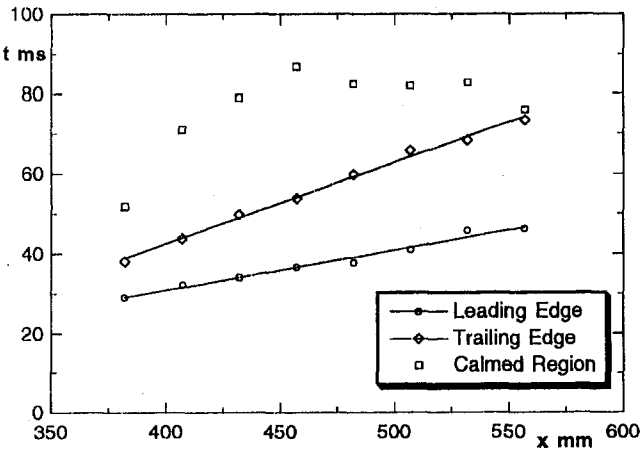

Fig. 6 Arrival times on centerline for spot leading edge, trailing edge, and end of calmed region

Correlations for Spot Characteristics

In Table 2 a compilation has been made of spot celerities and spreading rates from a number of sources. The pressure gradient parameters presented are the Hartree β and the Thwaites λ_θ. The investigation of a triggered spot is time consuming and each investigator tends to limit the investigation to one condition. This has hitherto resulted in a preponderance of results for zero pressure gradient conditions with three qualifying investigations for favorable pressure gradients. Only in the last year have investigations been made of spots under adverse pressure gradients, but it is now possible to report four such results. The subject condition is seen to represent the strongest adverse pressure gradient of those tested. This makes it possible, for the first time, to present spot parameters over a wide range of pressure gradients for attached laminar flows.

All quoted results were obtained under low free-stream turbulence levels and there has been no systematic attempt to cover independent parameters such as free-stream turbulence level and Reynolds number although some investigators (e.g., Wygnanski, 1981) have addressed the Reynolds number question. Accordingly there is some scatter between the results of the different investigators. Each investigator has used a different facility and a different approach to instrumentation, detection, and analysis, but these differences are relatively minor and reasonable comparisons can be made.

A previous compilation was performed by Gutmark and Blackwelder (1987) for zero pressure gradient spots. They chose to do this at heights of 0.1 δ_L and δ_L. Comparisons at a height of 0.1 δ_L are quite meaningful and especially relate to the heat transfer characteristics of the spot. There is a strong argument for comparing spots at a height of around 0.3 δ_L, where fluctuations tend to be strongest, and which tend toward the outer edge of the intermittency plateau (Johnson, 1994). Qualifying investigations have been restricted to those spot measurements for which celerity and spanwise spreading rate are both available and, since results are available from different investigators at different heights, to the range $0.05 < y/\delta_L < 0.35$, encompassing the plateau of highly turbulent activity.

In Table 2 celerities a and b correspond to leading and trailing edge propagation velocities, respectively. α is the half angle of

Table 2 Turbulent spot spreading and celerities, $0.05 < y/\delta_L < 0.35$

	β	λ_θ	a	b	α^o	σ
Present work	-0.223	-0.0573	0.872	0.431	29.2	0.656
van Hest (1994)	-0.14	-0.036	0.92	0.38	17.0	0.472
Gostelow *et al.* (1993)	-0.173	-0.031	0.8	0.5	24.0	0.334
Seifert and Wygnanski (1994)	-0.1	-0.018	0.9	0.49	21.0	0.357
Sankaran *et al.* (1986)	0.0	0.0	0.74	0.53	9.0	0.084
Wygnanski *et al.* (1982)	0.0	0.0	0.89	0.57	9.2	0.102
Schubauer and Klebanoff (1956)	0.0	0.0	0.88	0.5	10.0	0.152
Sankaran *et al.* (1986)	0.095	0.018*	0.79	0.69	7.3	0.024
Wygnanski (1981)	0.12	0.022*	0.98	0.68	5.0	0.039
Katz *et al.* (1990)	1.0	0.059	0.9	0.61	5.0	0.04

*assumes global similarity

spanwise propagation and σ is the Emmons (1951) propagation parameter in simplified form for a triangular spot,

$$\sigma = \tan \alpha(b^{-1} - a^{-1}). \quad (1)$$

Figure 8 gives a comparison of spot leading and trailing edge celerities over a wide range of values of pressure gradient parameter λ_θ. The scatter is significant for all pressure gradients and for both leading edge and trailing edges. In part this reflects the different techniques and indicators used by the investigators listed in Table 2. Nevertheless, it has proved feasible to provide linear fits to the data.

Insufficient data exist to provide quantitative information on the extent of the calmed region over a range of pressure gradients; it is clear that nonlinear interactions predominate in defining the extent of the calmed region. Further study of this is required if the calmed region is to be incorporated into prediction approaches for the transition region.

A comparison of spot spreading half-angles from the investigations of Table 2 is presented in Fig. 9. The spreading half-angle increases strongly as adverse pressure gradients become more intense, approaching a value of 30 deg at the laminar separation limit. A correlation curve has been fitted and an expression for spreading angle as a function of pressure gradient parameter is obtained in the form:

$$\alpha = 4.0 + (22.14/(0.79 + 2.72 \exp(47.63\ \lambda_\theta))). \quad (2)$$

In Fig. 10 the information given above for parameters a, b, and α has been combined according to Eq. (1) to give values of σ. It has again been found possible to provide a reasonable curve fit, despite a degree of scatter. The correlation is:

$$\sigma = 0.03 + (0.37/(0.48 + 3.0 \exp(52.9\ \lambda_\theta))). \quad (3)$$

It is intended to use the resulting correlation, in conjunction with the previously published correlation for spot formation rate

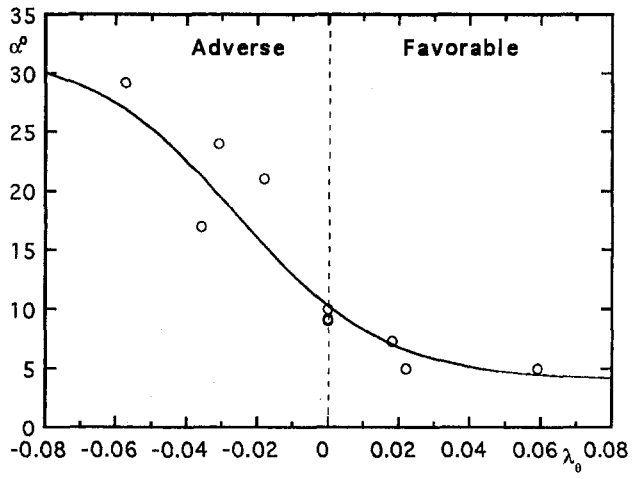

Fig. 9 Compilation of spot spreading angles as a function of pressure gradient parameter

under an adverse pressure gradient (Gostelow et al., 1994), to provide a more adequate model of transition length and the associated spot behavior under a range of pressure gradients; this development is described in the companion paper by Solomon et al. (1996).

Conclusions

Measurements of turbulent spot evolution were made under a controlled diffusion pressure distribution. The principal objective was to obtain sufficient information to give a more accurate model of the spot and its environment under an adverse pressure gradient. This was to be used to provide essential correlations for incorporation into the transition region predictions of boundary layer codes. Phase-averaged velocity traces and root mean square fluctuation level distributions were obtained.

Under an adverse pressure gradient the conditions are conducive to the rapid growth of Tollmien–Schlichting waves. Wave packet behavior is highly amplified and the breakdown to turbulence appears initially in the central region of the triggered disturbance. The turbulent region propagates rapidly in a transverse direction along the wave packet. The calmed region behind the spot is extensive and exhibits a complex interaction with the encroaching ambient turbulent layer.

Propagation rates of spot leading and trailing edges and spanwise spreading rates were evaluated. Corresponding measure-

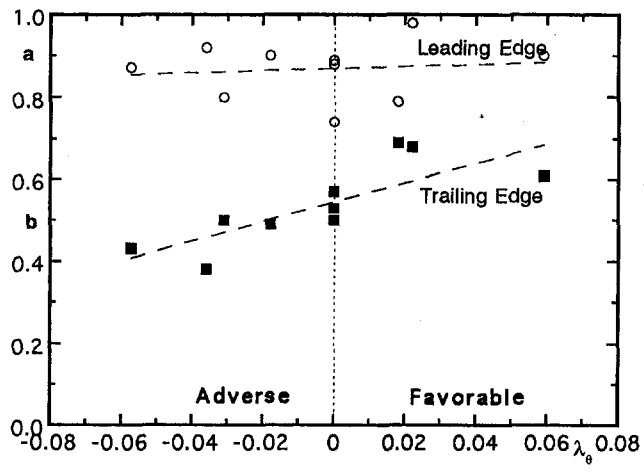

Fig. 8 Compilation of spot leading and trailing edge celerities as a function of pressure gradient parameter

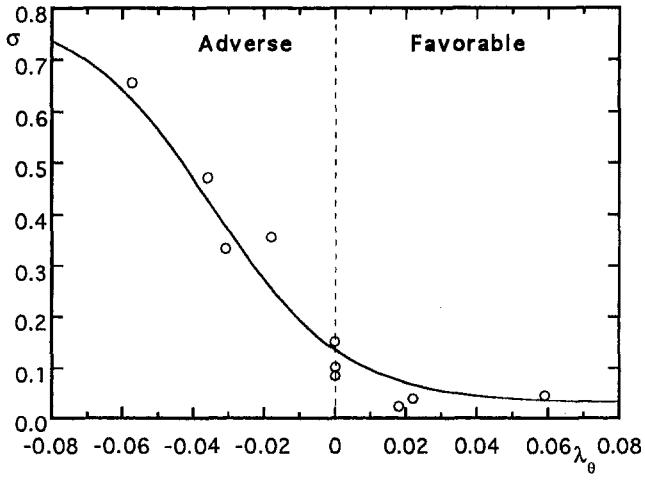

Fig. 10 Comparison of spot propagation parameters as a function of pressure gradient parameter

ments by other researchers for spots over a wide range of pressure gradients were compiled. These have been expressed in correlations of spot propagation parameters for use in computational modeling of spot behavior under variable pressure gradients. Spot propagation parameters indicate that zero pressure gradient data alone do not provide a satisfactory basis for transition predictions. The available literature on the behavior of triggered spots, subject to a wide range of pressure gradients, however, provides a rich resource for understanding and predicting transitional flows.

Acknowledgments

The authors acknowledge the financial support of the Australian Research Council and Rolls-Royce plc. The theoretical contribution of Mr. W. J. Solomon is appreciated.

References

Chen, K. K., and Thyson, N. A., 1971, "Extension of Emmons' Spot Theory to Flows on Blunt Bodies," *AIAA Journal,* Vol. 9, No. 5, pp. 821–825.

Cohen, J., Breuer, K. S., and Haritonidis, J. H., 1991, "On the Evolution of a Wave Packet in a Laminar Boundary Layer," *Journal of Fluid Mechanics,* Vol. 225, pp. 575–606.

Emmons, H. W., 1951, "The Laminar–Turbulent Transition in a Boundary Layer—Part 1," *Journal of Aero. Sciences,* Vol. 18, No. 7, pp. 490–498.

Gostelow, J. P., Hong, G., Melwani, N., and Walker, G. J., 1993, "Turbulent Spot Development Under a Moderate Adverse Pressure Gradient," ASME Paper No. 93-GT-377.

Gostelow, J. P., Blunden, A. R., and Walker, G. J., 1994, "Effects of Free-Stream Turbulence and Adverse Pressure Gradients on Boundary Layer Transition," ASME JOURNAL OF TURBOMACHINERY, Vol. 116, pp. 392–404.

Gutmark, E., and Blackwelder, R. F., 1987, "On the Structure of a Turbulent Spot in a Heated Laminar Boundary Layer," *Experiments in Fluids,* Vol. 5, pp. 217–229.

Johnson, M. W., 1994, "A Bypass Transition Model for Boundary Layers," ASME JOURNAL OF TURBOMACHINERY, Vol. 116, pp. 759–764.

Katz, Y., Seifert, A., and Wygnanski, I., 1990, "On the Evolution of the Turbulent Spot in a Laminar Boundary Layer With a Favourable Pressure Gradient," *Journal of Fluid Mechanics,* Vol. 221, pp. 1–22.

Narasimha, R., 1957, "On the Distribution of Intermittency in the Transition Region of a Boundary Layer," *Journal of Aero. Sciences,* Vol. 24, No. 9, pp. 711–712.

Schubauer, G. B., and Klebanoff, P. S., 1955, "Contributions on the Mechanics of Boundary-Layer Transition," NACA Rep. 1289.

Seifert, A., and Wygnanski, I. J., 1994, "On Turbulent Spots in a Laminar Boundary Layer Subjected to a Self-Similar Adverse Pressure Gradient," private communication.

Sankaran, M., Chambers, A. J., and Antonia, R. A., 1986, "The Influence of a Favourable Pressure Gradient on the Growth of a Turbulent Spot," *Proc. 9th Australasian Fluid Mechanics Conference,* Auckland, pp. 342–345.

Solomon, W. J., Walker, G. J., and Gostelow, J. P., 1996, "Transition Length Prediction for Flows With Rapidly Changing Pressure Gradients," ASME JOURNAL OF TURBOMACHINERY, Vol. 118, pp. 744–751.

van Hest, B. F. A., Pesschier, D. M., and van Ingen, J. L., 1994, "The Development of a Turbulent Spot in an Adverse Pressure Gradient Boundary Layer," *Proc. IUTAM Symposium,* Sendai, Japan.

Walker, G. J., and Gostelow, J. P., 1990, "Effects of Adverse Pressure Gradients on the Nature and Length of Boundary Layer Transition," ASME JOURNAL OF TURBOMACHINERY, Vol. 112, pp. 196–205.

Walker, G. J., Solomon, W. J., and Gostelow, J. P., 1993, "Observations of Wake-Induced Turbulent Spots on an Axial Compressor Blade," ASME Paper No. 93-GT-378.

Watmuff, J. H., 1991, "An Experimental Investigation of Boundary Layer Transition in an Adverse Pressure Gradient," *Proc. ASME Symposium, Boundary Layer Stability and Transition to Turbulence,* Portland, OR, pp. 129–136.

Wills, J. A. B., 1962, "Correction of Hot Wire Readings for Proximity to a Solid Boundary," *Journal of Fluid Mechanics,* Vol. 12, pp. 388–396.

Wygnanski, I., 1981, "The Effect of Reynolds Number and Pressure Gradient on the Transitional Spot in a Laminar Boundary Layer," *Lecture Notes in Physics: The Role of Coherent Structures in Modelling Turbulence and Mixing,* Vol. 136, p. 304.

Wygnanski, I., Zilberman, M., and Haritonidis, J. H., 1982, "On the Spreading of a Turbulent Spot in the Absence of a Pressure Gradient," *Journal of Fluid Mechanics,* Vol. 123, pp. 69–90.

Transition Length Prediction for Flows With Rapidly Changing Pressure Gradients

W. J. Solomon

G. J. Walker
Mem. ASME

Department of Civil and Mechanical Engineering,
University of Tasmania,
Hobart, Tasmania, Australia

J. P. Gostelow
School of Mechanical Engineering,
University of Technology, Sydney,
Sydney, New South Wales, Australia
Mem. ASME

A new method for calculating intermittency in transitional boundary layers with changing pressure gradients is proposed and tested against standard turbomachinery flow cases. It is based on recent experimental studies, which show the local pressure gradient parameter to have a significant effect on turbulent spot spreading angles and propagation velocities (and hence transition length). This can be very important for some turbomachinery flows. On a turbine blade suction surface, for example, it is possible for transition to start in a region of favorable pressure gradient and finish in a region of adverse pressure gradient. Calculation methods that estimate the transition length from the local pressure gradient parameter at the start of transition will seriously overestimate the transition length under these conditions. Conventional methods based on correlations of zero pressure gradient transition data are similarly inaccurate. The new calculation method continuously adjusts the spot growth parameters in response to changes in the local pressure gradient through transition using correlations based on data given in the companion paper by Gostelow et al. (1996). Recent experimental correlations of Gostelow et al. (1994a) are used to estimate the turbulent spot generation rate at the start of transition. The method has been incorporated in a linear combination integral computation and tested with good results on cases that report both the intermittency and surface pressure distribution data. It has resulted in a much reduced sensitivity to errors in predicting the start of the transition zone, and can be recommended for engineering use in calculating boundary layer development on axial turbomachine blades.

Introduction

The importance of laminar–turbulent transition in determining the aerodynamic characteristics of immersed bodies is well known. The transition behavior has a dominant effect on the evolution of losses, the appearance of separation and stall, and other factors of practical significance such as the distributions of wall shear stress and surface heat transfer. A comprehensive discussion of boundary layer transition phenomena and transition zone modeling has been given by Narasimha (1985). The practical significance of transition in relation to gas turbine engines has recently been surveyed by Mayle (1991).

For turbomachine blades operating at relatively low Reynolds number, a useful method of analysis must give reasonable estimates for the transition onset point, the length of the transition zone (i.e., region of intermittently turbulent flow) and the conditions of the turbulent boundary layer at the end of transition. Other important effects that need to be considered include separation, relaminarization, free-stream turbulence effects, and unsteadiness associated with periodic wake passing. The present paper is principally concerned with the problem of predicting transition length.

Many factors can influence the length of the transition zone. Dhawan and Narasimha (1958) introduced a correlation for Re_λ in terms of Re_{xt}, based mainly on zero pressure gradient data. Potter and Whitfield (1962) and more recently Clark et al. (1994) have demonstrated the effects of Mach number on transition. Effects of pressure gradient on spot development have been studied by Gostelow et al. (1994a), Clark et al. (1994), and others; free-stream turbulence by workers such as Blair (1982); surface roughness by Feiereisen and Acharya (1986); and surface curvature by Kim and Simon (1991).

The early transition length correlation of Dhawan and Narasimha (1958) was based on a limited range of data and essentially represents the transition behavior in constant pressure flows. Chen and Thyson (1971) subsequently used the turbulent spot theory of Emmons (1951) to develop a transitional flow model, which purported to allow for the influence of pressure gradient on the intermittency distribution and transition length. This is incorporated in the popular boundary layer computation method of Cebeci and Smith (1974).

Walker et al. (1988) reported a complete breakdown in low Reynolds number airfoil computations with the Cebeci–Smith method due to the Chen–Thyson model predicting excessive transition lengths for flows with laminar separation. It was pointed out that the Chen–Thyson method predicted a transition length little different from that in zero pressure gradient, whereas the theoretical study of Walker (1989) had suggested the transition zone should be almost an order of magnitude shorter in positive pressure gradient situations.

The observations of Walker and Gostelow (1990) confirmed the markedly different nature of transition in decelerating flow. Experiments by Gostelow et al. (1994a) subsequently produced transition length correlations covering a wide range of positive pressure gradients and free-stream turbulence levels. The new correlations gave reliable predictions of transition length for strongly decelerating flows typical of turbomachine blade operation in cases where the pressure gradient did not alter significantly over the transition zone. However, as shown in the present paper, they are still inadequate for cases such as a turbine airfoil suction surface where the pressure gradient changes markedly throughout the region of intermittently turbulent flow.

The latter problems have been ascribed to an unexpectedly large influence of local pressure gradient on turbulent spot propagation, as revealed by recent experiments of Gostelow et al.

Contributed by the International Gas Turbine Institute and presented at the 40th International Gas Turbine and Aeroengine Congress and Exhibition, Houston, Texas, June 5–8, 1995. Manuscript received by the International Gas Turbine Institute February 27, 1995. Paper No. 95-GT-241. Associate Technical Editor: C. J. Russo.

(1996). The authors have used these results, together with correlations for spot inception rates from Gostelow et al. (1994a) and Fraser et al. (1994), to produce a modified Chen–Thyson model for the intermittency distribution in flows with rapidly changing pressure gradient.

The present paper commences with a brief review of transition zone modeling. The new method of determining intermittency distributions is then outlined and compared with experiments for which reliable intermittency and surface pressure distribution data are available. Finally, the new transition zone model is incorporated in a linear combination integral boundary layer computation code and tested against flow cases typical of turbine airfoil suction surfaces.

Transition Zone Models

Introduction. Both integral and differential boundary layer calculation techniques can be applied to transitional flows for a given distribution of turbulent intermittency γ through the transition zone. In the integral codes, laminar and turbulent boundary layer calculations are combined according to the intermittency. In the differential codes the eddy viscosity in the transitional zone is modified according to the intermittency.

Three transition zone models, all based on the turbulent spot theory of Emmons (1951) and the concentrated breakdown hypothesis of Narasimha (1957), are considered in this paper. The first model, referred to here as "Narasimha, Dey," uses Narasimha's universal intermittency distribution with essentially zero pressure gradient transition length correlations. The second method, "Gostelow," also uses the universal intermittency distribution, but with a transition length correlation related to the local pressure gradient parameter at transition onset. The new proposal discards the universal intermittency distribution and allows the spot propagation characteristics to react to changes in local pressure gradient through the transition zone.

As well as transition length correlations, all of these models require a specification of the transition onset location, x_t. The transition zone models should all be started at the point where γ first exceeds zero. At least one commonly used transition onset correlation (Abu-Ghannam and Shaw, 1980) gives predictions for x_t that more closely correspond to the point where $\gamma = 0.25$ (Dey and Narasimha, 1988). To avoid such sources of bias, all the test cases shown here have used (where possible) manually selected onset points that closely match the experimental intermittency distribution.

Narasimha, Dey. Narasimha (1957) showed that the transition zone model of Emmons (1951), when modified by the concentrated breakdown hypothesis, gave a good description of experimental streamwise intermittency distributions. The expression obtained by Narasimha was

$$\gamma = \begin{cases} 1 - \exp[-(x - x_t)^2 n\sigma/U] & (x \geq x_t) \\ 0 & (x < x_t) \end{cases} \quad (1)$$

where x_t is the transition onset point, n is the spot generation rate (the number spots per unit length, per unit time generated at x_t), and σ is the spot propagation parameter.

Defining the transition length in terms of $\lambda = x|_{\gamma=0.75} - x|_{\gamma=0.25}$ leads to Narasimha's universal intermittency distribution

$$\gamma = \begin{cases} 1 - \exp[-0.412(x - x_t)^2/\lambda^2] & (x \geq x_t) \\ 0 & (x < x_t) \end{cases} \quad (2)$$

Equation (2) generally agrees well with experimental results, even in flows with nonzero pressure gradient, provided the pressure gradient parameter remains nearly constant through the transition zone and λ and x_t are chosen correctly (Gostelow et al., 1994a). It also leads to a linear plot of $F(\gamma) \sim x$, which has been used by Narasimha, Gostelow, and co-workers to provide a consistent basis for determining the transition onset point x_t from experimental data.

Narasimha (1985) demonstrates that the most appropriate nondimensional breakdown parameter is of the form

$$N = n\sigma\theta_t^3/\nu \quad (3)$$

This expression is obtained from Eq. (1) and Eq. (2) using the Blasius boundary layer relationship, $\mathrm{Re}_{\theta t} = 0.664\sqrt{\mathrm{Re}_{xt}}$, and a transition length correlation of the form $\mathrm{Re}_\lambda = 9\,\mathrm{Re}_{xt}^{3/4}$.

Dey and Narasimha (1988) tested several correlations for λ with experimental data from various sources. Their study was hampered by the different definitions for the start and end of transition used by different authors, but useful suggestions for converting between definitions were made. For zero pressure gradient flows with levels of free-stream turbulence above around 0.3 percent, N was found to be constant. Pressure gradient effects were only considered for favorable pressure gradients and correlated with the pressure gradient parameter at transition onset, $\lambda_{\theta t}$. The correlation proposed was

$$N = \begin{cases} 0.7 \times 10^{-3} & (\lambda_{\theta t} \leq 0) \\ 0.7 \times 10^{-3} + 0.24(\lambda_{\theta t})^2 & (0 < \lambda_{\theta t} \leq 0.10) \end{cases} \quad (4)$$

This expression was used with Eq. (1) and Eq. (3) at a given x_t to obtain the intermittency distribution and the resulting transition length.

For the cases considered in this paper where x_t occurred in a region of favorable pressure gradient, $\lambda_{\theta t}$ was generally small and the transition length values predicted by this procedure differed little from those for zero pressure gradient flow.

Nomenclature

aU = spot leading edge velocity
bU = spot trailing edge velocity
C_f = skin-friction coefficient
$F(\gamma)$ = Narasimha intermittency function = $[-\ln(1-\gamma)]^{1/2}$
H = velocity profile shape factor = δ^*/θ
N = nondimensional breakdown rate parameter = $n\sigma\theta_t^3/\nu$
Re_{xt} = transition start Reynolds number = $x_t U/\nu$
Re_λ = transition length Reynolds number = $\lambda U/\nu$
Re_θ = momentum thickness Reynolds number = $\theta U/\nu$
U = local free-stream velocity
n = spot generation rate, $\mathrm{m}^{-1}\mathrm{s}^{-1}$
q = local free-stream turbulence level, percent
q_t = free-stream turbulence level at x_t, percent
u = local velocity in boundary layer
x = streamwise distance from stagnation point
x_t = transition onset point
y = distance normal to surface
γ = intermittency factor
δ = boundary layer thickness
δ^* = displacement thickness = $\int_0^\delta (1 - u/U)dy$
θ = momentum thickness = $\int_0^\delta (1 - u/U)u/U dy$
λ = characteristic transition length = $x|_{\gamma=0.75} - x|_{\gamma=0.25}$
λ_θ = pressure gradient parameter = $(\theta^2/\nu)(dU/dx)$
$\lambda_{\theta t}$ = pressure gradient parameter at x_t
σ = spot propagation parameter

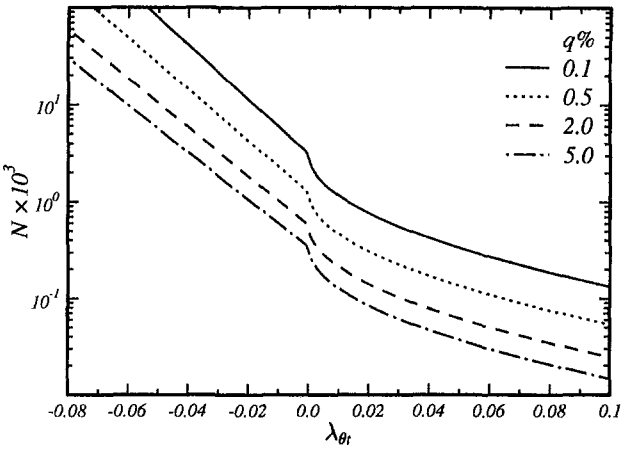

Fig. 1 Nondimensional breakdown rate parameter as a function of free-stream turbulence and pressure gradient parameter at transition onset. Data of Gostelow et al. (1994a) for $\lambda_{\theta t} \leq 0$; Fraser et al. (1994) for $\lambda_{\theta t} > 0$.

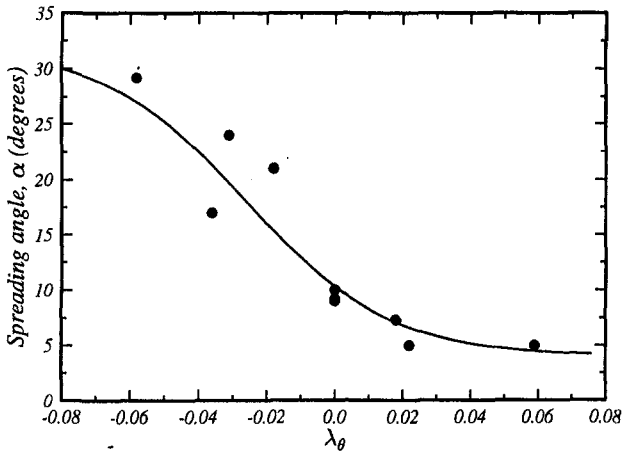

Fig. 2 Fit to turbulent spot spreading data from various sources compiled by Gostelow et al. (1996)

Gostelow. An extensive set of boundary layer transition length measurements in adverse and zero pressure gradients has been reported by Gostelow et al. (1994a) for a range of free-stream turbulence levels. Correlations of these measurements are variously presented as functions of boundary layer thickness, predicted minimum transition length, and spot formation rate. The spot formation rate correlation was obtained using the expression

$$N = 0.412\ \mathrm{Re}_{\theta t}^3/\mathrm{Re}_\lambda^2 \tag{5}$$

which is an alternative form of Eq. (3) for zero pressure gradients. The resulting correlation was

$$N = 0.86 \times 10^{-3} \exp(2.134\lambda_{\theta t} \ln(q_t) - 59.23\lambda_{\theta t} - 0.564 \ln(q_t)) \tag{6}$$

Gostelow et al. (1994b) have proposed a calculation method based on the linear combination integral boundary layer technique of Dey and Narasimha (1988), but using Eq. (6) in place of Eq. (4). However, Eq. (6) is not valid for flows that have a transition onset point in a region of favorable pressure gradient and some modification is required to cover this case. This has been done here on the basis of correlations presented by Fraser et al. (1994) who suggest

$$N = N_0 \times \exp(-10\sqrt{\lambda_{\theta t}}) \tag{7}$$

where N_0 is the value of N at $\lambda_{\theta t} = 0$.

For the current work, therefore, N for the "Gostelow" method is found from Eq. (6) for $\lambda_{\theta t} < 0$ and Eq. (7) for $\lambda_{\theta t} > 0$. The full correlation for N is plotted in Fig. 1. The corresponding intermittency distribution and transition length are then determined from Eq. (1) and Eq. (3) as for the "Narasimha, Dey" method.

New Method

Turbulent Spot Propagation Characteristics. The development of the new transition model has been prompted by recent experiments of Gostelow and co-workers, which provide new data on turbulent spot propagation characteristics in adverse pressure gradients. The variation of spot spreading angle α and propagation parameter σ with pressure gradient parameter λ_θ, as compiled by Gostelow et al. (1996), is shown in Figs. 2 and 3. Both parameters are seen to vary markedly for $\lambda_\theta < 0$. This unexpectedly large variation with adverse pressure gradients clearly invalidates the widely held assumption (e.g., Chen and Thyson (1971) and Mayle (1992)) that spot propagation characteristics should not vary significantly with pressure gradient through the transition zone.

The values of spot propagation parameter shown in Fig. 3 have been derived from experimental data for the leading and trailing edge celerities, aU and bU, and the spreading half-angle α using the relation

$$\sigma = (b^{-1} - a^{-1}) \tan \alpha \tag{8}$$

This relation implies a triangular spot planform as assumed by various workers (McCormick, 1968; Chen and Thyson, 1971).

The following tentative correlations for the variation of α and σ with λ_θ have been made from the data assembled by Gostelow et al. (1996):

$$\alpha = 4 + (22.14/(0.79 + 2.72 \exp(47.63\lambda_\theta))) \tag{9}$$

$$\sigma = 0.03 + (0.37/(0.48 + 3.0 \exp(52.9\lambda_\theta))) \tag{10}$$

Ideally the correlations of α and σ should also allow for the influence of free-stream turbulence q and Reynolds number Re_θ. However, the available data are too sparse to do this at present.

Development of the New Model. Various hypotheses have been used to explain departures from the universal intermittency distribution (or "subtransitions") observed when the pressure gradient changes significantly through the transition zone. Narasimha (1985) has suggested that boundary layer stability may be a factor. Mayle (1991) has proposed a variation in spot generation function through the transition zone.

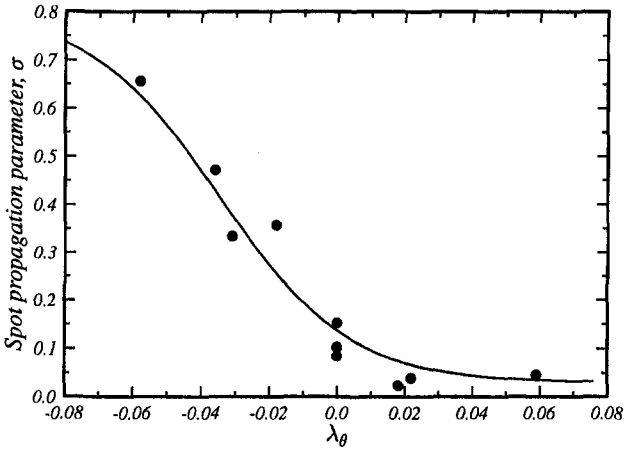

Fig. 3 Fit to turbulent spot propagation data from various sources compiled by Gostelow et al. (1996)

Based on the new data of Gostelow et al. (1996), we abandon these ideas and propose that subtransitions are essentially caused by the influence of local pressure gradient on turbulent spot propagation characteristics. The basic features of the new model are as follows:

(*a*) the concentrated breakdown hypothesis of Narasimha is retained;
(*b*) the spot inception rate is assumed to depend only on the local conditions at transition onset, x_t;
(*c*) the spreading rate of turbulent spots is allowed to vary continuously through the transition zone in response to changes in the local pressure gradient parameter λ_θ.

The new model can easily be implemented by simple modifications to the original model of Chen and Thyson (1971). For two-dimensional flow Chen and Thyson give

$$\gamma = 1 - \exp\left[-G(x - x_t)\int_{x_t}^{x}\left(\frac{dx}{U}\right)\right] \tag{11}$$

for the intermittency distribution in the transition zone, where $G = n(b^{-1} - a^{-1})\tan\alpha = n\sigma$ and σ has been assumed constant through the transition zone. This reduces to Narasimha's universal distribution, Eq. (1), if U is constant.

Chen and Thyson's model, Eq. (11), should give slightly better results than Eq. (1) since it does account for effects of changing U on the spot convection velocities. But as pointed out by Narasimha et al. (1984) and Walker et al. (1988), this effect is small and is unable to account for the large changes in transition length with pressure gradient that are actually observed. The major problem is that the Chen–Thyson formulation for G does not allow for any variations in spot inception rate, or relative spreading celerities, with pressure gradient.

Incorporating the new model assumptions in the original Chen–Thyson formulation leads to the modified intermittency distribution

$$\gamma = 1 - \exp\left[-n\int_{x_t}^{x}\frac{\sigma}{\tan(\alpha)}\left(\frac{dx}{U}\right)\int_{x_t}^{x}\tan\alpha\,dx\right] \tag{12}$$

In the present paper this is applied by using a value of the spot inception rate n inferred from Eqs. (6), (7), and (3) by using the local value of λ_θ at transition onset x_t. The values of α and σ are obtained from Eq. (9) and Eq. (10) using the local value of pressure gradient parameter from the laminar boundary layer component in the linear combination integral computation. This implies that the spot propagation parameters respond instantaneously to changes in pressure gradient, although some lag must be expected in practice.

Results and Discussion

Boundary Layer Code. Dey and Narasimha (1988) present a simple linear-combination integral boundary layer method that is a convenient test-bed for the new intermittency distribution (a version of this code was also used by Gostelow et al. (1994b)). The method uses a modified Thwaites method for the laminar boundary layer and a lag-entrainment method (Green et al., 1973) for the turbulent boundary layer. Within the transition zone the laminar and turbulent solutions are combined as follows:

$$\delta^* = (1 - \gamma)\delta_L^* + \gamma\delta_T^* \tag{13}$$

$$\theta = \gamma(1 - \gamma)\int_0^\delta [u_L(1 - u_T) + u_T(1 - u_L)]dy + (1 - \gamma)^2\theta_L + \gamma^2\theta_T \tag{14}$$

$$C_f = (1 - \gamma)C_{fL} + \gamma C_{fT} \tag{15}$$

where the subscripts L and T refer to laminar and turbulent values, respectively. The value of intermittency γ is determined from one of the transition models above.

It was necessary to continue calculation of the laminar boundary layer component through separating flow for a few of the test cases. This was done crudely by fixing $H_L = 3.70$, $C_{fL} = 0$ and continuing with evaluation of the momentum integral equation to determine θ_L. Any errors arising from this approach will only have a small effect on the final solution provided the intermittency is reasonably large at the laminar separation point. An obvious imperfection in the linear combination method is the assumption of instantaneous switching between the laminar and turbulent velocity profiles. It is well known that there is a significant lag in recovery of the laminar profile following the passage of a turbulent spot. The linear combination method nevertheless gives useful results and is certainly no less realistic than using a turbulent boundary layer calculation method with modified eddy viscosity in the transition zone.

General Test Cases—Narasimha et al. (1984). The experimental cases of Devasia reported by Narasimha et al. (1984) provide convenient benchmarks for testing transition models under conditions of changing pressure gradients. Since intermittency is reported, it is possible to make direct comparisons of the predicted intermittency with experiment. There is also little uncertainty in specifying the transition onset point. In the absence of intermittency data it is necessary to infer the performance of the transition model from comparisons of predicted and measured boundary layer parameters; that introduces additional uncertainty because of imperfections in boundary layer modeling that appear in combination with errors in intermittency prediction.

For this work three cases designated DFU1, DFU3, and DAU1 will be presented. The surface velocity distributions and corresponding variations in pressure gradient parameter for the laminar boundary layer component in the transition zone are shown in Fig. 4. Comparisons of measured intermittency with the predictions of the three transitional flow models are shown in Figs. 5, 6, and 7, respectively.

Case DFU1 involves an increasing acceleration over the forward part of the transition region. This is subsequently relaxed so that the pressure gradient is near zero at the end of transition. As indicated by Narasimha et al. (1984), this produces a relatively mild subtransition (as indicated by a discontinuity in slope of the $F(\gamma)$ distribution) around $x = 1.15$ m. In this case the Narasimha–Dey transition length is much too short; however, the shape of the predicted intermittency distribution is seen to be a reasonable match near the end of the transition zone where the conditions of near zero pressure gradient approximate those of the model. The Gostelow model, which is based on the local pressure gradient parameter at the start of transition, gives a good prediction of the transition length; but this is somewhat fortuitous, as the predicted and measured intermittency diverge significantly with increasing acceleration toward the center of the transition zone and subsequently approach each other again as the pressure gradient is removed. The new model clearly performs best overall, giving credible predictions for both transition length and intermittency distribution; the minor systematic deviations from the measured intermittency that are still evident may arise partly from uncertainties in the correlations of spot properties for the accelerating regime and partly from neglecting the influence of Reynolds number on spot propagation.

Case DFU3 involves a change from accelerating flow over the forward part of the transition zone to a slightly decelerating flow toward the end of transition. This produces a much more marked subtransition effect around $x = 1.05$ m. The Narasimha–Dey model is even less accurate in this case; the transition length is again underestimated, and the shape of the intermittency distribution is not matched in any part of the transition

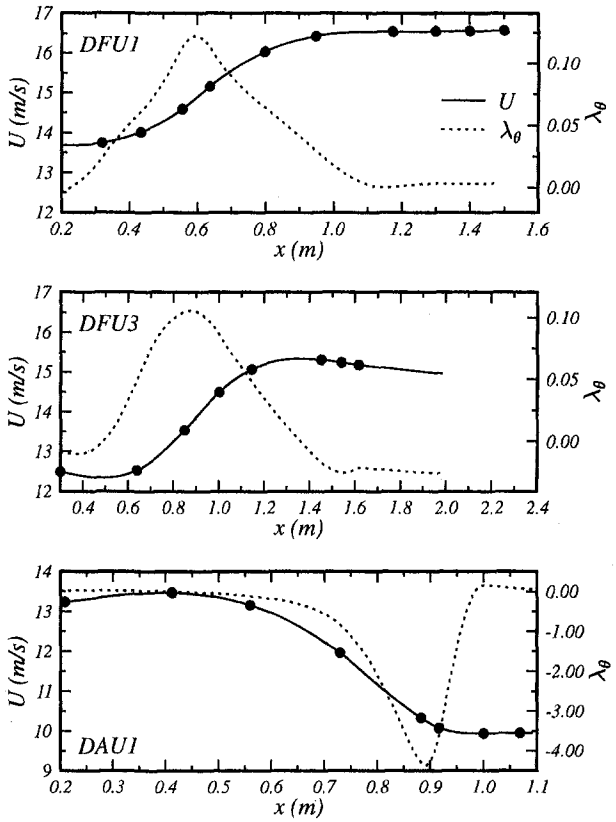

Fig. 4 Velocity and laminar pressure gradient parameter distributions for the Devasia test cases (data scaled from figures of Narasimha (1985))

zone. The Gostelow model captures the shape of the intermittency distribution quite well in the forward part of the transition zone where the pressure gradient parameter is essentially constant; but the predicted intermittency diverges considerably and the transition length is significantly overpredicted as the pressure gradient subsequently becomes slightly negative. The new model again performs credibly, albeit with the same slight systematic deviations in predicted intermittency exhibited in case DFU1.

Case DAU1 involves an even more marked subtransition as the pressure gradient changes from mildly favorable to strongly adverse. The Narasimha–Dey model performs rather better here due to the steepening of the experimental intermittency distribution toward the end of transition. In these circumstances, however, the Gostelow model fails quite spectacularly; its divergence from experiment clearly illustrates the subtransition around $x = 0.7$ m. The new model again gives a very good prediction of transition length, although the divergence from measurement is somewhat greater around the center of the transition zone. The latter effect may be partly due to experimental uncertainty, as the scatter in measured intermittency values appears rather greater in this case.

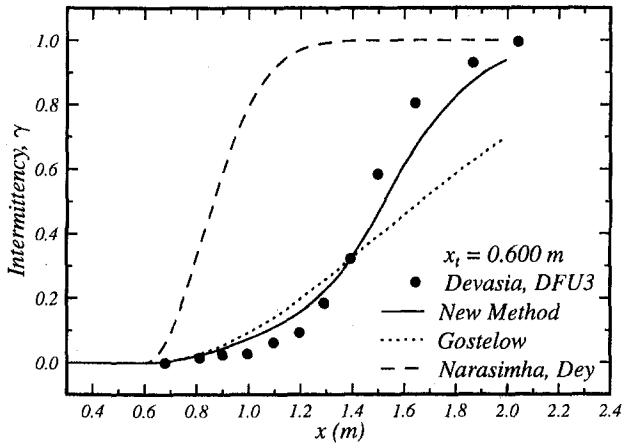

Fig. 6 Devasia case DFU3: intermittency distributions

Forward-Loaded Turbine Airfoil—Sharma et al. (1982). Sharma et al. (1982) have presented detailed measurements of the boundary layer on a plate subjected to a pressure distribution typical of a forward-loaded (or "squared-off") turbine airfoil design. As indicated in Fig. 8, this has a region of nearly constant pressure up to about $x = 0.5$ m, followed by a region of decelerating flow. The inlet turbulence level for this case is 2.4 percent, and the Reynolds number based on exit velocity and test section length is 8×10^5. Intermittency data from flush-mounted hot-film probes indicate that transition commences in the region of decelerating flow between $x = 0.45$ m and $x = 0.50$ m, with intermittency values closely following Narasimha's universal distribution (i.e., there is no significant subtransition evident in this case).

Figure 9 compares the experimental data of Sharma et al. (1982) with the results of boundary layer calculations using the three different transition zone models of the present paper. All computations assume the same transition onset point of $x = 0.45$ m, which is slightly upstream of the experimentally observed location. In this case the Gostelow correlation gives the best prediction of the intermittency distribution through the transi-

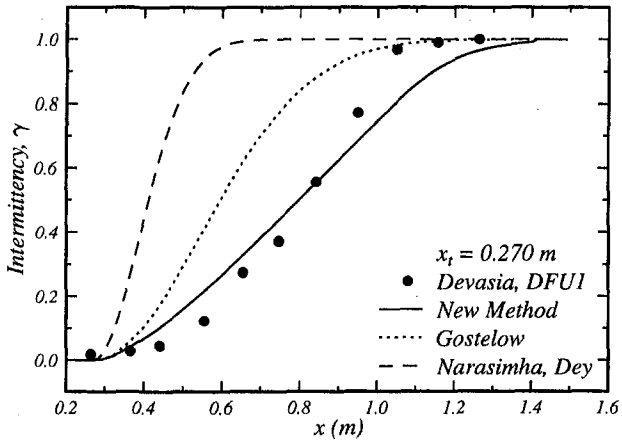

Fig. 5 Devasia case DFU1: intermittency distributions

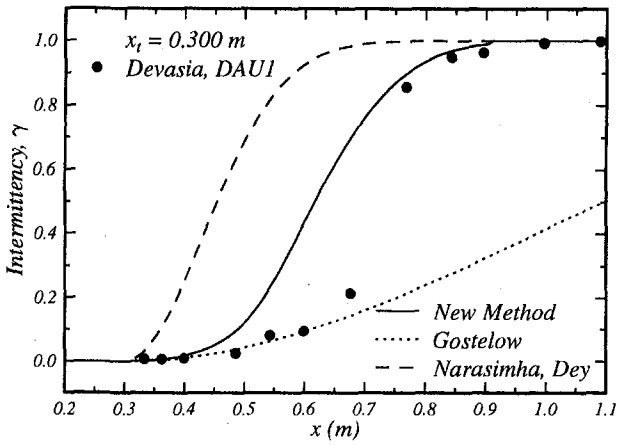

Fig. 7 Devasia case DAU 1: intermittency distributions

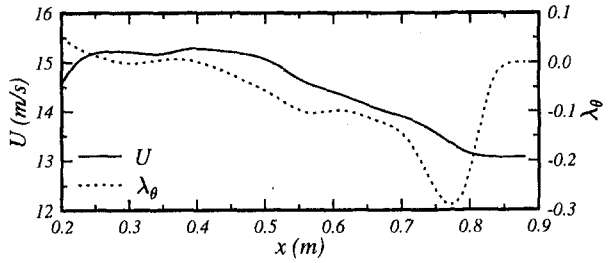

Fig. 8 Sharma et al. (1982) squared-off turbine blade; velocity and laminar pressure gradient parameter distributions

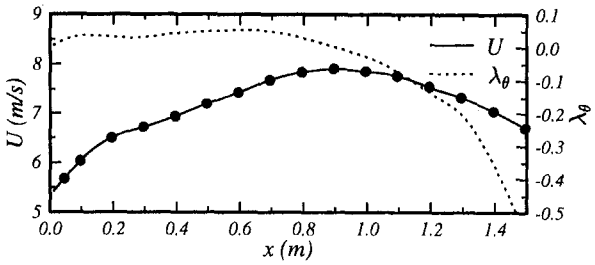

Fig. 10 ERCOFTAC case T3C2, aft-loaded turbine blade; velocity and laminar pressure gradient parameter distributions

tion zone. The Narasimha–Dey method, being based essentially on zero pressure gradient data, gives too long a transition length. The current method gives a transition length that is a little short, the intermittency again rising a little too rapidly with increasing deceleration as was noted for the general test cases of Narasimha et al. above. It should be borne in mind, however, that the intermittency indicated by wall gages will be lower than the near-wall values in the boundary layer under adverse pressure gradient conditions.

The decay in experimental shape factor values through transition is rather more protracted than indicated by the intermittency distributions. This is probably due to:

(*a*) the influence of free-stream turbulence on the laminar boundary layer prior to transition onset, which produces a noticeable decrease in H below the predicted values for a steady laminar flow; and

(*b*) a lag in response of the boundary layer velocity profile to the introduction of turbulent mixing, which is not incorporated in the calculation.

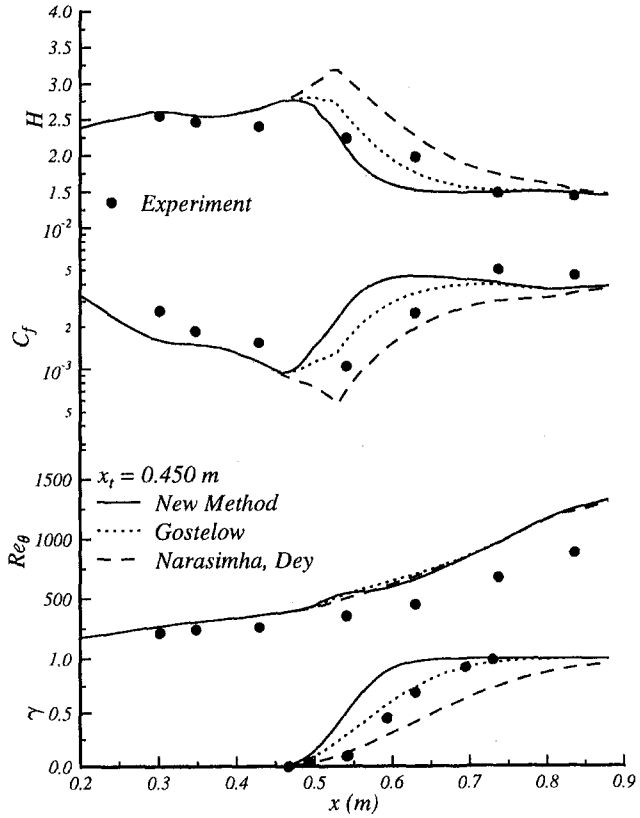

Fig. 9 Sharma et al. (1982) squared-off turbine blade; comparison of methods, all started at the same transition onset point close to the experimentally observed location

The influence of free-stream turbulence on the boundary layer is also reflected by the somewhat higher values of measured skin friction coefficient prior to transition.

The predicted momentum thickness, as indicated by the values of Re_θ, is consistently high throughout the calculation. There is evidently some initial deviation for the laminar values that propagates through the whole calculation. Matching of Re_θ values for the fully turbulent region can only be achieved by imposing a totally unrealistic delay in the transition onset.

Aft-Loaded Turbine Blade—ERCOFTAC Case T3C2. The ERCOFTAC Special Interest Group on Transition uses a set of test cases from the Rolls Royce Applied Science Laboratory described by Coupland (1993). Case T3C2 corresponds to a pressure distribution typical of the suction surface on an aft-loaded turbine blade, as shown in Fig. 10. This consists of a long region of acceleration followed by an increasing deceleration, which is strong enough to promote separation of the laminar boundary layer component in the transition zone. The situation is similar to that of Devasia DAU1, and a strong subtransition effect is again expected. The upstream turbulence level for the T3C2 case is 3 percent and the Reynolds number based on exit velocity and test section length is 6.56×10^5.

No intermittency data have been published for this case. There is therefore some uncertainty about the transition onset location, and the performance of transition zone models can only be checked by comparison with measured values of integral properties. For this reason, a parametric approach is adopted and the sensitivity of calculation methods to variations in the specified transition onset point is investigated. The results are shown in Figs. 11, 12, and 13. Values of H, C_f, and Re_θ are compared; the predicted intermittency distributions are also presented to indicate the assumed extent of the transition zone.

Figure 11 shows the computed boundary layer development for x_t = 0.60, 0.75, and 0.95 m using the Narasimha–Dey transition model. The first two assumed values of x_t lie in the accelerating flow region, while the latter falls slightly after the suction peak. The transition length, being derived essentially from constant pressure flow data, varies only slightly with the boundary layer properties at x_t and is quite insensitive to the value of x_t chosen; however, the predicted variation of boundary layer properties through the transition zone is markedly affected. For x_t = 0.60 m the chosen transition onset is clearly too early; x_t = 0.75 m gives the best overall agreement; x_t = 0.95 m is clearly too late for the transition onset, and the adverse pressure gradient causes the laminar component to separate in the transition zone, giving values of H and C_f that are too high and too low, respectively. In all cases, there is a noticeable tendency for the predicted shape factor to be too high prior to transition onset; this is again ascribed to the influence of free-stream turbulence on the laminar boundary layer, as for the squared-off turbine airfoil case above.

As seen from Fig. 12, the predicted boundary layer behavior with the Gostelow transition length correlation is far more sensitive to the assumed transition onset. For x_t prior to the suction peak, the estimated transition length is much too long; the pre-

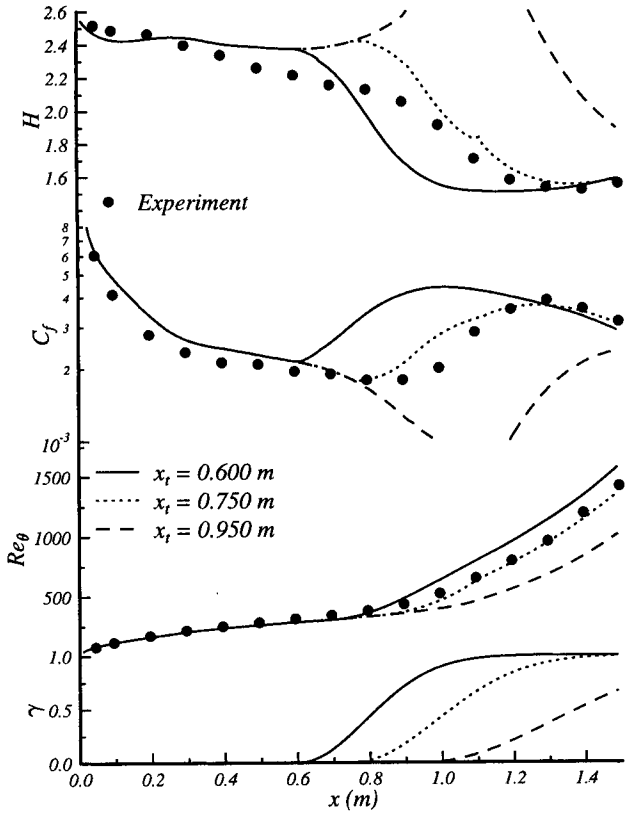

Fig. 11 ERCOFTAC case T3C2: solutions using the "Narasimha, Dey" transition model; various onset positions

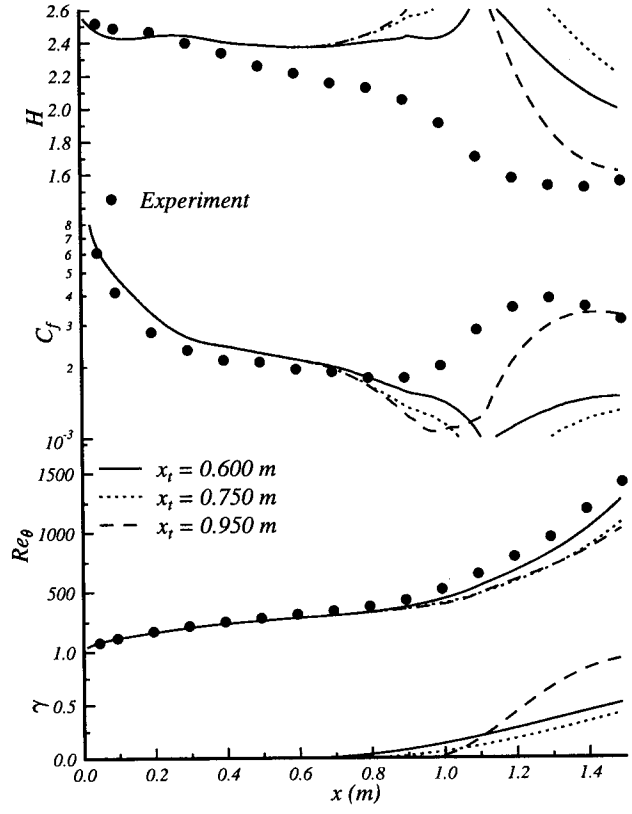

Fig. 12 ERCOFTAC case T3C2: solutions using the "Gostelow" transition model; various onset positions

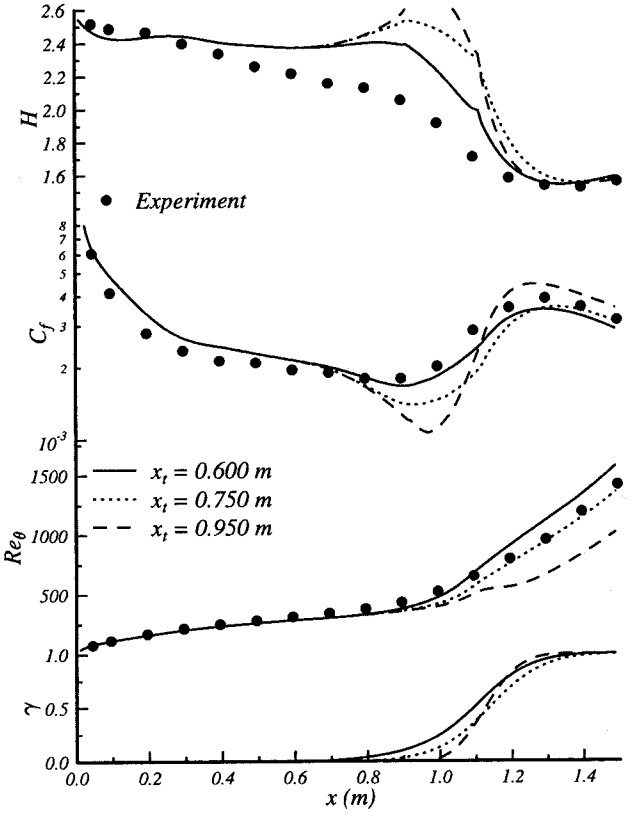

Fig. 13 ERCOFTAC case T3C2: solutions using the new transition length method; various onset positions

dicted boundary layer still has a major laminar component in the decelerating flow region and is thus very prone to separation. Locating x_t after the suction peak gives better agreement for the distribution of C_f, but still allows separation to occur.

Computations using the current method of intermittency prediction are shown in Fig. 13. The results are surprisingly insensitive to variations in the assumed transition onset position. The wall shear stress distribution is particularly good. Best overall agreement is obtained for $x_t = 0.60$ m; however, the predictions remain quite good for values of x_t up to 0.95 m. The end of transition is dominated by the effects of decelerating flow from about $x = 0.9$ m onward; transition is completed by around $x = 1.2$ m regardless of the assumed onset point.

Conclusions

The length of transitional flow in regions of rapidly changing pressure gradient is not adequately predicted by correlations of data from flows in which the pressure gradient parameter remains essentially constant through the transition zone. The turbine airfoil suction surface, on which transition may commence in a region of accelerating flow and end in a region of decelerating flow, provides a particularly severe test of calculation methods. Here the transition length predicted from constant pressure gradient correlations may vary greatly depending on the location of the assumed transition onset in relation to the pressure minimum. This may cause significant variations in computed skin friction and surface heat transfer distributions; the stability of iterative methods used to couple viscous and inviscid flow solutions might also be threatened if the transition onset moves between favorable and adverse pressure gradient regions on successive iterations.

A new method of computing transitional flow length, based on recent experimental results for the variation of turbulent spot spreading rates with local pressure gradient, has been success-

fully demonstrated for typical turbine airfoil test cases. It is considerably more robust in relation to errors in predicting transition onset, and is recommended for immediate engineering use.

The present computations have also shown that rapid changes in pressure gradient may cause significant deviations from the universal intermittency distribution of Narasimha through the transition zone. This provides an explanation for the anomalous behavior generally referred to as "subtransition." For flows involving subtransition, the start of the transition zone inferred by assuming a standard intermittency distribution may differ significantly from the true onset point. A re-examination of existing transition data in the light of this observation and the new computation method is considered desirable.

In particular, it would be useful to reprocess the data of Gostelow et al. (1994a) with the new model to produce revised values of transition length and spot inception rates. The data processing techniques adopted by Gostelow et al. ignored the slight subtransitions evident in those experiments; thus the values of transition length obtained from the resulting correlations such as Eq. (6) may be a little low. To that extent, there may have been some double accounting for subtransition effects through using the original correlations of Gostelow et al. with the new model. This could partially explain the tendency of the new method to give slight underestimates of the transition length where strong subtransitions occur.

The present work has produced results of immediate practical value despite the fact that it has been mainly confined to studying the effects of changing pressure gradient. In the longer term, however, the new transitional flow model could benefit from extensions to incorporate additional factors such as:

(a) the influence of changing turbulent spot shape on the values of spot propagation parameter σ;
(b) a possible replacement of the concentrated breakdown hypothesis with a Gaussian source density function for turbulent spots;
(c) the influence of Reynolds number, free-stream turbulence, and periodic unsteadiness on spot propagation characteristics;
(d) improved modeling of the emerging turbulent boundary layer and an allowance for relaxation effects in the laminar layer following the passage of a turbulent spot; and
(e) the influence of free-stream turbulence on the laminar boundary layer prior to transition inception.

Acknowledgments

The authors wish to acknowledge the support of the Australian Research Council and Rolls-Royce plc.

References

Abu-Ghannam, B. J., and Shaw, R., 1980, "Natural Transition of Boundary Layers—the Effects of Pressure Gradient and Flow History," *Journal of Mechanical Engineering Science,* Vol. 22, No. 5, pp. 213–228.

Blair, M. F., 1982, "Influence of Free-Stream Turbulence on Boundary Layer Transition in Favorable Pressure Gradients," ASME *Journal of Engineering for Power,* Vol. 104, pp. 743–750.

Cebeci, T., and Smith, A. M. O., 1974, *Analysis of Turbulent Boundary Layers,* Academic Press, New York.

Chen, K. K., and Thyson, N. A., 1971, "Extension of Emmons' Spot Theory to Flows on Blunt Bodies," *AIAA Journal,* Vol. 9, No. 5, pp. 821–825.

Clark, J. P., Jones, T. V., and LaGraff, J. E., 1994, "On the Propagation of Naturally-Occurring Turbulent Spots," *Journal of Engineering Mathematics,* Vol. 28, pp. 1–19.

Coupland, J., 1993, *Private Communication Concerning Rolls-Royce Applied Science Laboratory Flat Plate Transitional Boundary Layer Results,* Test Cases used by the ERCOFTAC SIG on Transition.

Dey, J., and Narasimha, R., 1988, "An Integral Method for the Calculation of 2-D Transitional Boundary Layers," Fluid Mechanics Report 88 FM 7, Indian Institute of Science, Bangalore.

Dhawan, S., and Narasimha, R., 1958, "Some Properties of Boundary Layer Flow During the Transition From Laminar to Turbulent Motion," *Journal of Fluid Mechanics,* Vol. 3, pp. 418–436.

Emmons, H. W., 1951, "The Laminar–Turbulent Transition in a Boundary Layer—Part I," *Journal of Aerospace Sciences,* Vol. 18, No. 7, pp. 490–498.

Feiereisen, W. J., and Acharya, M., 1986, "Modeling of the Transition and Surface Roughness Effects in Boundary-Layer Flows," *AIAA Journal,* Vol. 24, pp. 1642–1649.

Fraser, C. J., Higazy, M. G., and Milne, J. S., 1994, "End-Stage Boundary Layer Transition Models for Engineering Calculations," *Proceedings of the Institution of Mechanical Engineers, Part C,* Vol. 208, pp. 47–58.

Gostelow, J. P., Blunden, A. R., and Walker, G. J., 1994a, "Effects of Free-Stream Turbulence and Adverse Pressure Gradients on Boundary Layer Transition," ASME JOURNAL OF TURBOMACHINERY, Vol. 116, pp. 392–404.

Gostelow, J. P., Hong, G., Walker, G. J., and Dey, J., 1994b, "Modeling of Boundary Layer Transition in Turbulent Flows by Linear Combination Integral Method," ASME Paper No. 94-GT-358.

Gostelow, J. P., Melwani, N., and Walker, G. J., 1996, "Effects of Streamwise Pressure Gradient on Turbulent Spot Development," ASME JOURNAL OF TURBOMACHINERY, Vol. 118, this issue, pp. 737–743.

Green, J. E., Weeks, D. J., and Brooman, J. W. F., 1973, "Prediction of Turbulent Boundary Layers and Wakes in Compressible Flow by a Lag-Entrainment Method," Tech. Report 72231, RAE, Farnborough.

Kim, J., and Simon, T. W., 1991, "Freestream Turbulence and Concave Curvature Effects on Heated Transitional Boundary Layers," NASA CR187150.

Mayle, R. E., 1991, "The Role of Laminar–Turbulent Transition in Gas Turbine Engines," ASME JOURNAL OF TURBOMACHINERY, Vol. 113, pp. 509–537, The 1991 IGTI Scholar Lecture.

Mayle, R. E., 1992, "Unsteady Multimode Transition in Gas Turbine Engines," AGARD PEP 80.

McCormick, M. E., 1968, "An Analysis of the Formation of Turbulent Patches in the Transition Boundary Layer," ASME *Journal of Applied Mechanics,* Vol. 35, pp. 216–219.

Narasimha, R., 1957, "On the Distribution of Intermittency in the Transition Region of a Boundary Layer," *Journal of Aerospace Sciences,* Vol. 24, No. 9, pp. 711–712.

Narasimha, R., Devasia, K. J., Gururani, G., and Badri Narayanan, M. A., 1984, "Transitional Intermittency in Boundary Layers Subjected to Pressure Gradient," *Experiments in Fluids,* Vol. 2, pp. 171–176.

Narasimha, R., 1985, "The Laminar–Turbulent Transition Zone in the Boundary Layer," *Progress in Aerospace Science,* Vol. 22, pp. 29–80.

Potter, J. L., and Whitfield, J. D., 1962, "Effects of Slight Nose Bluntness and Roughness on Boundary-Layer Transition in Supersonic Flows," *Journal of Fluid Mechanics,* Vol. 12, pp. 501–535.

Sharma, O. P., Wells, R. A., Schlinker, R. H., and Bailey, D. A., 1982, "Boundary Layer Development on Turbine Airfoil Suction Surfaces," ASME *Journal of Engineering for Power,* Vol. 104, pp. 698–706.

Walker, G. J., Subroto, P. H., and Platzer, M. F., 1988, "Inviscid Interaction Analysis of Low Reynolds Number Airfoil Flows Involving Laminar Separation Bubbles," ASME Paper No. 88-GT-32.

Walker, G. J., 1989, "Transitional Flow on Axial Turbomachine Blading," *AIAA Journal,* Vol. 27, No. 5, pp. 595–602.

Walker, G. J., and Gostelow, J. P., 1990, "Effects of Adverse Pressure Gradients on the Nature and Length of Boundary Layer Transition," ASME JOURNAL OF TURBOMACHINERY, Vol. 112, pp. 196–205.

Transition in a Separation Bubble

E. Malkiel

R. E. Mayle
Professor Emeritus.

Department of Mechanical Engineering,
Rensselaer Polytechnic Institute,
Troy, NY 12180

In the interest of being able to predict separating–reattaching flows, it is necessary to have an accurate model of transition in separation bubbles. An experimental investigation of the process of turbulence development in a separation bubble shows that transition occurs within the separated shear layer. A comparison of simultaneous velocity traces from probes separated in the lateral direction suggests that Kelvin–Helmholtz waves, which originate in the laminar shear layer, do not break down to turbulence simultaneously across their span when they proceed to agglomerate. The streamwise development of intermittency in this region can be characterized by turbulent spot theory with a high dimensionless spot production rate. Moreover, the progression of intermittency along the centerline of the shear layer is similar to that in attached boundary layer transition. The transverse development of intermittency is also remarkably similar to that in attached boundary layers. The parameters obtained from these measurements agree with correlations previously deduced from turbulence intensity measurements.

Introduction

Modern improvements in compressor efficiency are contingent upon extending compressor blade performance through off-design operating conditions. A blade subject to higher incidence angles or lower Reynolds numbers than for which it is designed can be accompanied by drastic losses if stall occurs. Stall, characterized by a loss of lift and increase in drag, is associated with boundary layer separation. When it occurs, reattachment of the boundary layer is delayed (or may never take place), so that massive separated (and recirculating) regions exist on an airfoil's suction side, which cause the flow to deviate substantially from that predicted from purely inviscid calculations (Fig. 1). One way this happens, which is prevalent in today's controlled diffusion design type blades, is through the process of separation bubble bursting, where a short bubble will transform into a long one when operating conditions are changed very slightly. Although Gaster (1967) determined a criterion for bursting and Horton (1967) clarified some of the important parameters behind it, there is still motivation for improved models of separation bubble behavior. This is because of the importance of predicting operating limits of airfoils, when designing compressors, turbines, or wings.

Transitional bubbles, distinguished by shear layers that transition to turbulence, are of the type that burst. The forward portion of a transitional bubble is a constant pressure region (Fig. 2). It is comprised of a laminar shear layer, which because of its inherent instability, promotes the growth of disturbances, which eventually break down into turbulence at X_t. The transition process is nominally complete at X_T, so with the shear layer being turbulent thereafter it reattaches under an adverse pressure gradient. According to Horton's (1967) classic model of a separation bubble, the length of transition is considered negligible and the "transition point" corresponds to the end of the pressure plateau. The data of Gaster (1967) and Malkiel (1994) show that contrary to this model, short bubbles can be dominated by relatively large transition regions and long bubbles complete transition well before the end of the constant pressure region.

In the first attempts to predict separation bubble behavior, von Doenhoff (Tani, 1964) showed that by geometry, the location of transition was a critical parameter for determining the extent of a bubble, because it affected whether the turbulent shear layer (which has greater lateral spread than the laminar one) could reach the airfoil surface and subsequently reattach. Horton (1967) reaffirmed the importance of transition location through a semi-empirical analysis of turbulent shear layer reattachment in separation bubbles, by showing that the position of reattachment (and thus bursting) was strongly dependent on the streamwise location of the turbulent shear layer's origin (X_t). It is now generally believed that the increased entrainment in the rapidly growing turbulent shear layer is responsible for sucking itself toward the surface and bringing about reattachment (Cebeci and Bradshaw, 1977). Shear layer transition plays a major role, because if it does not begin early enough (allowing the shear layer to become far removed from the surface) or proceed quickly (Walker et al., 1988), entrainment may not be sufficient to bring about reattachment. This has been evidenced in separation bubble experiments (Roberts, 1980; Walraevens and Cumpsty, 1995) where decreased turbulence levels in the free stream dramatically increased the size of the separation bubble, presumably by delaying transition.

Early experiments showed that the distance from the point of laminar boundary layer separation to the transition "point" (laminar shear layer length) was characterized by a constant Reynolds number

$$\mathrm{Re}_{sT} = \frac{U_s(X_T - X_s)}{\nu}, \qquad (1)$$

where U_s is the free-stream velocity at separation. Later compilations (Tani, 1964; Horton, 1967) showed much scatter in this constant, with Re_{sT} varying between $3(10)^4$ and $6(10)^4$. Roberts (1980) removed some of this scatter by scaling Re_{sT} with a turbulence factor, which not only depended on turbulence levels, but on length scales as well, fashioned after the parameter used to collapse critical Reynolds numbers for the flow about a sphere (Goldstein, 1965), a number that indicates when the flow changes from being separated without reattachment to that with a separation bubble. Schmidt and Mueller (1989) were the first to correlate Re_{sT} against $\mathrm{Re}_{\theta s}$, the Reynolds number based on momentum thickness at separation. Although they also reported large scatter, they believed it was largely associated with the variety of techniques different researchers used to evaluate the location of transition.

Contributed by the International Gas Turbine Institute and presented at the 40th International Gas Turbine and Aeroengine Congress and Exhibition, Houston, Texas, June 5–8, 1995. Manuscript received by the International Gas Turbine Institute February 11, 1995. Paper No. 95-GT-32. Associate Technical Editor: C. J. Russo.

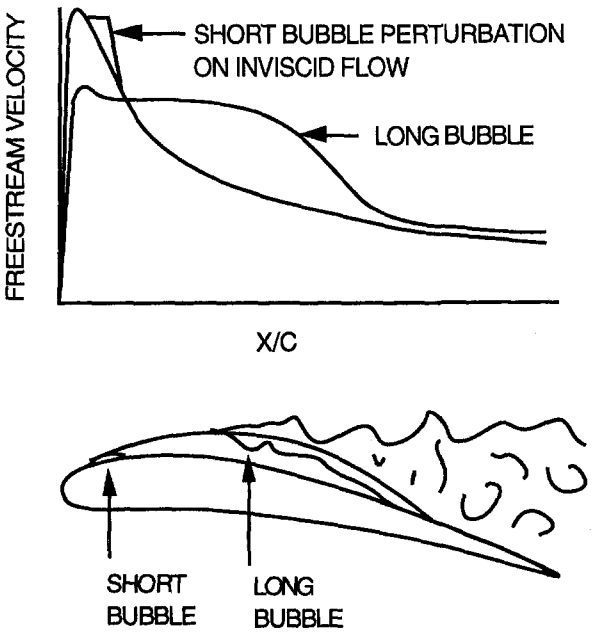

Fig. 1 Separation bubble effects on suction side velocity distribution

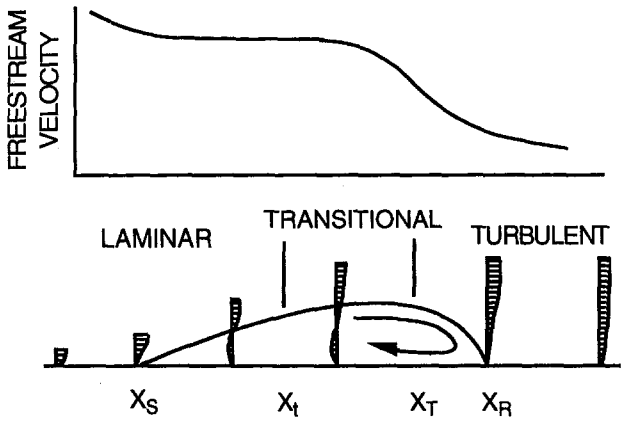

Fig. 2 Velocity distribution over a separation bubble

Mayle (1991), believing that transition took place over an extended regime, 1991 as it does in attached boundary layers, made separate correlations for Re_{st} and Re_{sT}, the difference of which is Re_{LT}, the Reynolds number based on the length of transition. He also used $Re_{\theta s}$ as a correlating parameter, but made sure that it was experimentally measured, since its growth near separation is not well predicted by boundary layer theory. He found that Re_{sT} was well correlated with $Re_{\theta s}$. For the determination of the onset of transition, Mayle used Gaster's (1967) and Bellows' (1985) data on the development of turbulence intensity along a shear layer. Assuming that the growth was due to the propagation of turbulent spots, he reduced the high-frequency turbulence intensity measurements into a corresponding intermittency and extrapolated the location of transition onset using methods borrowed from attached boundary layer transition. He was thus able to make a correlation between $Re_{\theta s}$ and Re_{st} and use this relation to find the length of transition, Re_{LT}. A subsequent investigation (Malkiel, 1994), some results of which are presented in this paper, was undertaken to substantiate Mayle's assumptions and check his correlations.

Empiricism is common to all separation bubble analyses that utilize inviscid–viscid interaction techniques, especially in connection to transition. Often the models of transition are extensions of that used in attached boundary layer flows: analysts may use an e^n method to predict transition location (Gleyzes et al., 1985; van Ingen and Boermans, 1985) or an intermittency factor to model the length of transition (Crimi and Reeves, 1976; Platzer et al., 1993). These models are often validated by comparing the predicted pressure distribution or momentum thickness variation in a separation bubble with that in experiments. Direct experimental measures of the transition process are lacking. Although transition has been scrutinized in free shear layers (Huang and Ho, 1990) and in attached boundary layers (Wygnanski, 1993), besides the present investigation, only a few (Gleyzes et al., 1985; Batill and Mueller, 1981) have concerned themselves with transition in leading edge separation bubbles.

An experimental investigation of a "generic" leading edge separation bubble was undertaken with the primary goal of qualitatively and quantitatively describing the transition within it. This was done with the analysis of hot-wire traces, spatial correlations, intermittency measurements and conditional sampled measurements. This was backed up with a comprehensive look at the entire separation bubble in terms of velocity profiles, fluctuation intensities and pressure distributions in Malkiel (1994).

Experimental Setup

The experimentation was performed in a wind tunnel in a 56 cm wide by 38 cm high test section (Fig. 3). To produce a separation bubble that would burst in size with a change in angle of incidence, a 90 mm thick, 495 mm long flat plate with a semicircular leading edge was constructed. It was mounted vertically in the test section so that blockage effects would not impede the development of a large bubble as it had in preliminary attempts to simulate a bursting bubble. Despite the body's low aspect ratio, two dimensionality was indicated across 90 percent of the span through flow visualization and measurement. An acutely angled tail, nominally 508 mm long, was attached to the originally bluff trailing edge to subdue trailing edge vortex shedding and supposedly prevent any effect it may have had on the separation bubble's behavior. Although the addition did not seem to change the bubble's behavior over the range of incidence investigated, the tail remained attached for all the reported measurements. Pressure taps were installed on the suc-

Nomenclature

C = chord length
$\hat{n}\sigma$ = dimensionless spot production rate
R = leading edge radius
Re = Reynolds number
Tu = turbulence intensity
U = mean velocity in X direction
X = surface coordinate in streamwise direction
Y = coordinate normal to the surface
Y' = coordinate normal to incident flow
α = angle of attack
γ = intermittency (probability flow is turbulent)
θ = momentum thickness
ν = kinematic viscosity

Subscripts

freestream = outside boundary layer
LT = length of transition
max = maximum
NT = nonturbulent
r = reattachment
s = separation
t = beginning of transition
T = end of transition, turbulent

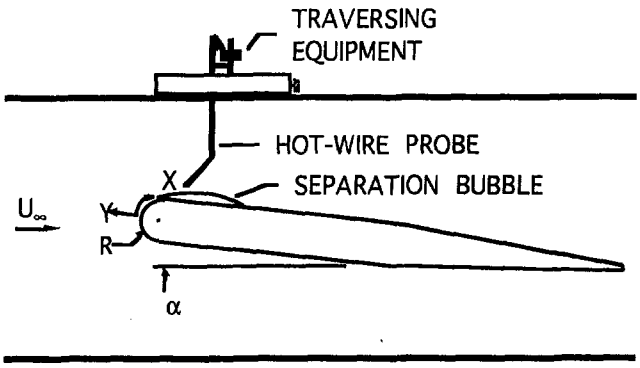

Fig. 3 Test section and body

tion side of the plate for the purpose of measuring mean static pressures and thus freestream velocity.

The wind tunnel was run at a speed of 7.9 m/s with an undisturbed free-stream turbulence level of 0.3 percent just upstream of the body. Under these conditions ($Re_R = 29{,}000$) and with the body at angles of incidence below 4 deg, a classically short separation bubble formed near the leading edge. Increasing the incidence by only 2 deg caused the bubble to burst so that its length increased by an order of magnitude. Preliminary results didn't show any substantial difference in the character of turbulence transition between the shorter bubble and the longer one, so the longer one was studied in more detail since it was less likely to suffer from probe interference effects. The body's angle of incidence was not disturbed from 6 deg during the course of experimentation to eliminate any inconsistencies that could have arisen from slight changes in the angle of incidence and misalignment of the body. Periodic checks on incident speed and frequent measures of the velocity distribution about the body (which varied by less than 1 percent during the entire investigation) were also used to ensure repeatability.

The primary mode of investigation was through the use of hot-wire anemometry. The hot-wire was specially calibrated for very low velocities, enabling accurate measurements in the forward portion of the separation bubble. Because the hot wire is sensitive to temperature as well as velocity, free-stream temperature was recorded along with velocity measurements to correct for its variations. The hot-wire sensor prongs were inclined roughly 45 deg to the surface to minimize probe interference, which was of special concern in the region where the boundary layer was close to separating. The curvature of the surface in this region required that the angle of the probe (with respect to the test section) be changed for traverses at different streamwise locations. The sensor was positioned within 50 μm of the surface by projecting its shadow and examining it through a microscope. The evaluation of this distance was essential in order to correct for hot-wire conduction losses to the surface so that accurate velocity profiles in the laminar boundary layer could be obtained. Measures were also taken to further reduce an almost imperceptible probe vibration, because in thin shear layers, probe movement can and in this case (before corrections) did, produce low-frequency oscillations that might be mistakenly identified as fluid dynamic phenomena. The result of all these steps is that the accuracy and repeatability of mean and fluctuation profiles each falls within 2 percent. Careful interpretation of these results is required, however, because being single sensor measurements, they only indicate the magnitude of the flow velocity in the direction perpendicular to the sensor, which is somewhat different from the velocity component in a single (e.g., stream-wise) direction, especially in regions with reverse flow.

Intermittency (γ) measurements, defined as the fraction of the time that the flow is turbulent at a location, were made using conventional techniques of turbulence discrimination. Turbulence discrimination is accomplished by differentiating the velocity signal with respect to time $|\partial u/\partial t|$ and comparing it to a threshold, above which it is considered turbulent. In practice one needs to evaluate $|\partial^2 u/\partial^2 t|$ as well and/or utilize a hold time to compensate for times when a truly turbulent portion of a signal fails to meet the former criteria. This temporal discrimination scheme relies on the selection of appropriate thresholds. The thresholds and hold time were originally set in the transitional region of the shear layer. The resulting criteria were selected so that a distinction could be made between high-amplitude Kelvin–Helmholtz waves that were present and three-dimensional turbulent fluctuations. A hold time equal to the period of a Kelvin–Helmholtz wave was also employed. Once determined, the same thresholds were applied at all locations. This was later found not to be sufficient in the case of separation bubbles.

The temporal discrimination scheme had to be supplemented with a spatial method in order to determine the threshold objectively. Since the threshold $|\partial u/\partial t|$ is related to $U_T|\partial u/\partial x|$ from Taylor's frozen turbulence hypothesis, the threshold should change with the local convective velocity U_T and turbulent fluctuation strength and scale. A threshold change is especially important in regions with relatively low convective velocities. The absence of threshold change may be the root of the apparent (Mayle, 1991) discrepancy between shear stress gage and hot-wire determinations of near-wall intermittency in turbulent boundary layers. In a separation bubble, threshold change is even more crucial because the low-velocity region is quite extensive.

A boundary layer x-probe was used as an indicator of the spatial correlation of fluctuations in the flow as a means of discriminating turbulent fluctuations from nonturbulent fluctuations. The sensors in this probe are spaced 1 mm apart in the spanwise direction (which is roughly equivalent to the thickness of the laminar shear layer at $X/R = 1.24$) so that any significant, uncorrelated fluctuation was deemed to be turbulent. Mere phase differences were not considered to be marks of uncorrelated signals. Intermittency evaluations made with the x-probe, covering the entire range of the separation bubble, were used as benchmarks to help set appropriate thresholds for a single sensor.

By labeling the flow as turbulent or nonturbulent, a conditional sampling routine could determine mean and root mean square velocities for each region. Consider a typical velocity signal in Fig. 4. The signal's turbulent portions have their individual averages denoted by a line segment. The mean (U_T) of these averages is different from the overall mean velocity (U) of the entire signal. The same is true of the nonturbulent mean velocity (U_{NT}). The weighted average of these two is the mean velocity

$$U = \gamma U_T + (1 - \gamma) U_{NT}, \tag{2}$$

where γ is the intermittency (probability or fraction of time that flow is turbulent).

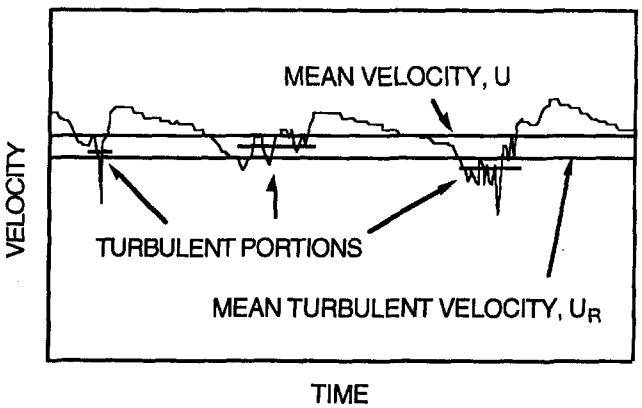

Fig. 4 Conditional velocity schematic

Results

The coordinate system used to present the majority of results is curvilinear, with X representing the distance along the model surface and Y the distance normal to it. The origin of this system, as shown in Fig. 3, is located at the nose of the plate.

Figure 5 shows the free-stream distribution for the standard configuration compared to that in which its boundary layer is tripped. In the latter, the boundary layer is forced to transition by attaching a 0.8-mm-dia wire at $X/R = 0.5$. Subsequently, the boundary layer remains attached when experiencing an adverse pressure gradient and the data reflect the velocity distribution without the presence of a separation bubble (Gaster, 1967).

In both situations, acceleration of the flow at stagnation and around the leading edge reverts to deceleration when the flow encounters an abrupt decrease in surface curvature ($X/R = 1.57$). The resulting velocity maximum, unbalanced elsewhere on the test body, gives rise to a net circulation and is partly responsible for the stagnation point shift away from the geometric origin $X/R = 0$. The shift is greater for the tripped case because of the greater maximum. The maximum is less in the untripped case because the laminar boundary layer separates with a small adverse pressure gradient at $X/R = 1.18$. Since the flow external to the boundary layer is no longer constrained to follow the surface of the test body from this point to reattachment, the overall curvature of the streamlines is relaxed so that a much weaker suction peak is induced. The near absence of streamline curvature outside the forward portion of the separation bubble is also evident from the constant pressure in this region. Farther downstream, reattachment of the shear layer causes a pressure rise. In this case, the rise in pressure occurs far downstream of transition, presumably because the entrainment necessary to attach the flow is large (and thus the length of the shear layer) when the flow's separating angle to the reattachment surface is relatively large. The pressure rise began when the free stream began to diffuse at $X/R = 3.3$ (Malkiel, 1994).

This separation bubble may be classified as a long one. Qualitatively, it falls into this category because it has significantly affected the pressure distribution outside of its location by reducing the suction peak (Gaster, 1967) and its length has increased dramatically (Hancock, 1969) with a slight increase in angle of attack. In agreement with this, is the fact that short bubbles, which were apparent at $\alpha = 0$ deg and $\alpha = 4$ deg had lengths close to Young's (1977) criterion for bursting: $Re_{s,r} = 6.4(10)^4$. The $\alpha = 6$ deg bubble also fits the criterion of Walker et al. (1988) that its length be much longer than the extent of the transition region.

The Pohlhausen method (Schlichting, 1979) was used to calculate boundary layer profiles upstream of separation with the help of the free-stream velocity distribution. The agreement with experiment is initially very good (the theory matched the profile at $X/R = 1.03$ within 2 percent), but it failed to match the downstream profiles and predict separation. The velocity profiles from the forward portion of the separation bubble, being the most relevant for the characterization of transition, are shown in Fig. 6. The separated shear layer begins in a laminar state and thus grows rather slowly. Without much entrainment taking place in this region, the fluid below the shear layer is rather stagnant and thus at a uniform pressure. Coupled with this, is the fact that the shear layer cannot support a transverse pressure gradient, so that curvature of the free-stream flow is absent. As a result, the shear layer travels along a straight line (Fig. 7), which makes a local angle of 6 deg with the surface at separation. Van Ingen and Boerman's (1985) correlation for this angle with the Re_{θ_s} predicts this angle rather well. The direction of the shear layer changes once transition ensues, with the renewed growth of the shear layer. Associated with this increased growth is a marked increase in entrainment and thus reverse flow. The latter is evident in the lower portions of the transitional profiles as a positive increase because as mentioned previously, the single sensor hot-wire measurements are of the magnitude of a velocity component perpendicular to the sensor and thus incapable of distinguishing reverse flow. Even in locations where the mean velocity should vanish, velocity fluctuations cause the hot-wire to sense a nonzero mean magnitude.

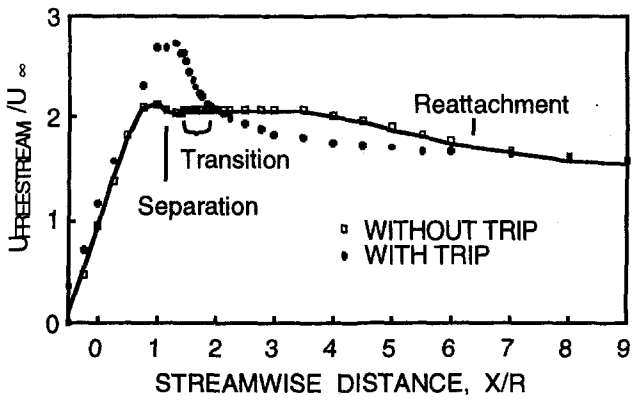

Fig. 5 Free-stream velocity distribution, $\alpha = 6$ deg

As the laminar shear layer becomes increasingly distant from the surface, the velocity profiles become more unstable. Although the shear layer is unstable to small disturbances even before separation (beginning with $X/R = 1.03$) because an inflection point (vorticity maximum) exists in the boundary layer, Kelvin–Helmholtz waves are not detectable until $X/R = 1.24$, somewhat downstream of separation. This is most probably due to the relatively small amplification rates upstream of this point. An instability analysis (Michalke, 1991) of a tanh profile that matches the one at $X/R = 1.24$, reveals that the most amplified disturbances should be ones that have a wavelength of 4.7 mm and a frequency of 1850 Hz. This is in close agreement with the dominant wave in this region which had a length of 5.1 mm and a frequency of 1500 Hz.

The amplification of the Kelvin–Helmholtz wave ensues rapidly. As the waves become progressively stronger, linear stability theory ceases to apply and the growth of these disturbances falls off. This is evident from spectrum analysis of the velocity signal. In the region between $X/R = 1.35$ and 1.45 (Fig. 8(a), 8(b)), the peak of the fundamental has not changed. The fact that this has occurred before the Kelvin–Helmholtz wave could travel more than one wavelength from its point of origin ($X/R = 1.24$) is indicative of the large amplification rates of shear layer instabilities. Apparently, when the fundamental reaches a certain strength, the waves (which act like spanwise vortices) interact with their neighbors and a subharmonic fluctuation will develop. The subharmonic, which is half the frequency of the fundamental (Fig. 8(b), 8(c) is actually due to a rolling over and pairing of the Kelvin–Helmholtz vortices, a process that has been seen in flow visualizations of a separation bubble (Gleyzes et al., 1985). Assuming that the net rate of vorticity convection (shedding) along the shear layer is constant (there aren't any sources or sinks of vorticity in this region), the agglomerated vortex has twice the strength, but the same celerity as its components and can be shed at only half the frequency that the fundamental vortices were shedding. In the transition region of a separation bubble shear layer, the production of turbulence was related to the appearance of a subharmonic, which was most apparent from outside of the shear layer.

In free shear layers, three dimensionality appears before the agglomeration, because the growth of Kelvin–Helmholtz waves causes the shear layer to be unstable to streamwise vorticity. The instability gives rise to counterrotating streamwise vortices, which grow by being stretched between Kelvin–Helmholtz vortices and are eventually comparable in strength to the fundamental vortices. Their spanwise wavelength is theoretically $\frac{2}{3}$ of the

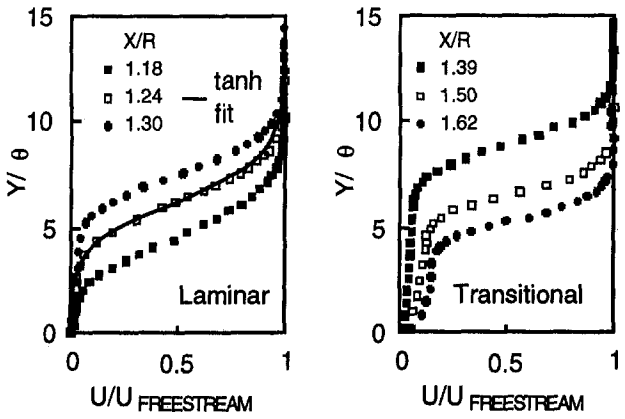

Fig. 6 Velocity profiles in laminar and transitional shear layers

fundamental. Huang and Ho (1990) showed that transition, the generation of small turbulence scales, occurred where these streamwise vortices intersected an agglomerating vortex pair. Although the cause for the breakdown is undetermined, it has been suggested that it is related to compression of the streamwise vortices from the agglomeration of the spanwise vortices. Moser and Rogers' (1993) simulations showed that transition proceeded very quickly in the agglomeration of spanwise vortices when there was strong three dimensionality from the streamwise structures, but they also showed that very strong three-dimensional perturbations were capable of producing turbulence directly, without agglomeration.

In a natural situation (with a predominance of turbulence rather than two-dimensional forcing perturbations in the free stream), one would hardly expect two-dimensional Kelvin–Helmholtz waves, simultaneous spanwise rollover, or the simultaneous spanwise production of turbulence. Even if the first two conditions appear, Huang and Ho's (1990) results show that the last does not occur. Instead of the former conditions, one would expect the Kelvin–Helmholtz wave to be found in wave packets, its rollover to be a stochastic process and the production of turbulence even less deterministic.

High-pass filtered (2 kHz cutoff) hot-wire output was used to perform a visual check on the spanwise correlation of turbulence (which has a smaller scale and thus higher frequency than the Kelvin–Helmholtz waves) production at the onset of transition. Figure 9 shows the simultaneous signals from hot wires positioned within the center of the shear layer and separated by a spanwise distance equivalent to the length of transition. From the perspective of long time scales (a), there is an overall correlation of high-amplitude fluctuations, probably due to selective growth of Kelvin–Helmholtz waves during a phase of low-frequency, shear layer flapping (which was caused by an aperiodic shedding of large scale vortices). Closer examination over a smaller time scale (b) reveals that the production of turbulence is not well correlated. Evidently, Kelvin–Helmholtz waves existed in localized packets and thus confined where turbulence was produced. The three dimensionality of transition has been supported by flow visualizations of a separation bubble performed by Batill and Mueller (1981).

The transition zone of the separation bubble's shear layer was further detailed through intermittency measurements (Fig. 10). Turbulence discrimination schemes based on purely "temporal" methods (constant threshold) and spatial methods, were used to find intermittency profiles in this region and across the entire bubble. In both determinations, the maximum intermittency at a streamwise location falls on the position of maximum vorticity, which corresponds to the center of the shear layer. This is where the turbulence is produced; the center of the conglomerating vortices follows this path. A further indication of turbulence production in this region is shown in Fig. 8(c) where a broad band of higher frequency fluctuations (approximately twice the frequency of the fundamental) appears in the center of the shear layer at mid transition. Below the position of maximum intermittency (beneath the shear layer), the temporal method classifies the flow as nonturbulent (because convective velocity had dropped off and the threshold was not adjusted to compensate) while the more accurate spatial method shows that it tends toward fully turbulent as transition is complete. A visual

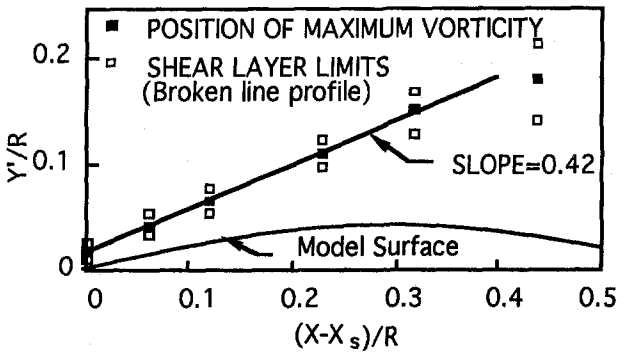

Fig. 7 Location of laminar shear layer in Cartesian coordinates with respect to incident flow direction

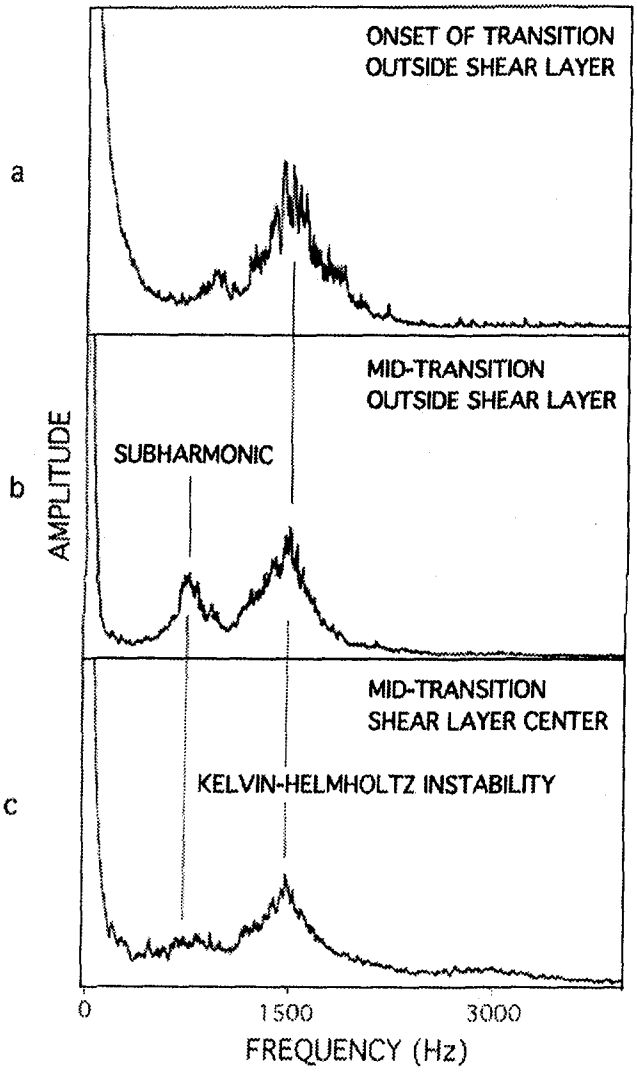

Fig. 8 Velocity spectrum through transition

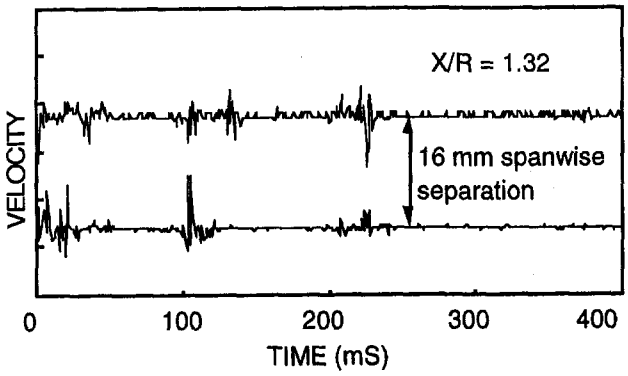

Fig. 9(*a*) Overall view of spanwise correlation of velocity near onset of transition

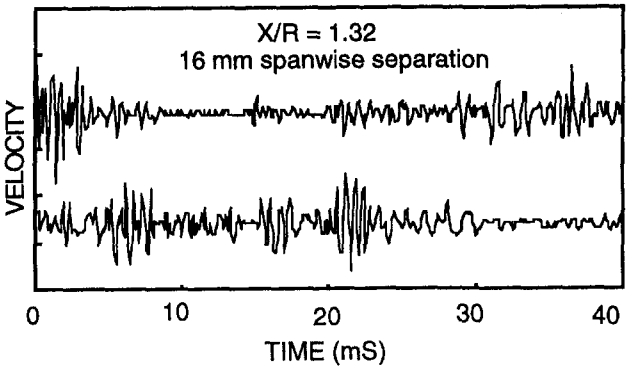

Fig. 9(*b*) Close up view of spanwise correlation in velocity near onset of transition

comparison of simultaneous signals from the middle of the shear layer in midtransition and below it, showed a moderate transverse correlation in the appearance of high-amplitude fluctuations in the latter and turbulent regions below. The cause for this seems to be that the shear layer, because of the growth associated with Kelvin–Helmholtz waves, entrains fluid from downstream, much of which is turbulent and thus gives rise to a sub-shear-layer intermittency. This scenario is supported by conditional averages of turbulent velocity (Malkiel, 1994) and flow visualizations by Arena and Mueller (1980). Relevant in this connection is an experiment done on a free shear layer by Chandrsuda et al. (1978). They found that when a shear layer was allowed to entrain turbulence from downstream (flow over a backward-facing step), "the transitional oscillations became strongly three-dimensional as soon as they appeared," when it would otherwise behave two-dimensional if supplied a nonturbulent flow. This suggests that the turbulent fluid entrained from downstream, which was found intermittently under the shear layer in the forward portion of the separation bubble, may have had an active role in the growth of wave packets and transition of Kelvin–Helmholtz waves. At this point, all that is known is that its appearance is somewhat correlated to the appearance of Kelvin–Helmholtz waves and turbulent flow above it.

In Fig. 11, the magnitude of intermittency is divided by the maximum value in each profile and heights are scaled such that where γ is maximum (Y_{max}) will always lie on zero and the position of $\gamma/\gamma_{max} = 0.5$, ($Y_{1/2}$) will always be at one. In this format, the intermittencies can be compared to a Gaussian curve

$$\gamma/\gamma_{max} = \exp[-0.694(Y/Y_{1/2})^2] \tag{3}$$

and an error curve

$$\gamma/\gamma_{max} = 0.5\{1 - \text{erf}\,[\sqrt{2}(Y/Y_{1/2} - 1)]\} \tag{4}$$

(Mayle, 1991). These equations represent bounds on the intermittency profiles in transition for attached boundary layers; the former approximating early transition and the latter when the boundary layer is almost completely turbulent. From Fig. 11 it appears that the upper portion of the present data fits these curves marginally well in the same manner as the attached boundary layers. This is not too surprising. The Gaussian represents the situation of isolated turbulent blobs being randomly distributed about $Y = Y_{max}$, whereas the error curve represents a turbulent–nonturbulent interface being randomly distributed about $Y_{1/2}$, its mean position. Neither of these representations seem particularly restrictive to attached boundary layer or wake flows. The difference, however, is that there is a reverse flow under the shear layer. In this regard the flow is not symmetric, and turbulence from downstream that is swept forward skews the results on the lower side of the shear layer.

Transition in shear layers is a quick and therefore short process in relation to what occurs in attached boundary layers. One way of clarifying the process is by detailing the streamwise development of the maximum intermittency. Figure 12 shows a plot of the maximum intermittency in the transition zone which was obtained by traversing along the shear layer centerline. The results are plotted in the manner of Narasimha (1957), the usual way for attached boundary layer transition. The ordinate in this type of plot is chosen so that data well represented by the equation

$$\gamma = 1 - \exp[-n\sigma(\text{Re}_x - \text{Re}_{xt})^2] \tag{5}$$

will fall along a straight line. Equation (5) comes from Emmons' (1951) turbulent spot theory, which models the intermittency development as being caused by the merger of growing

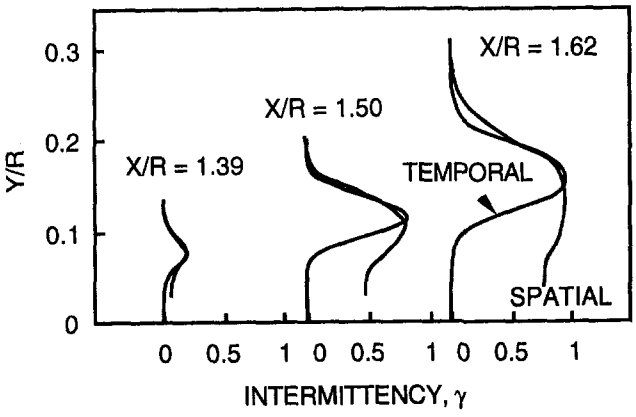

Fig. 10 Intermittency profiles through transition

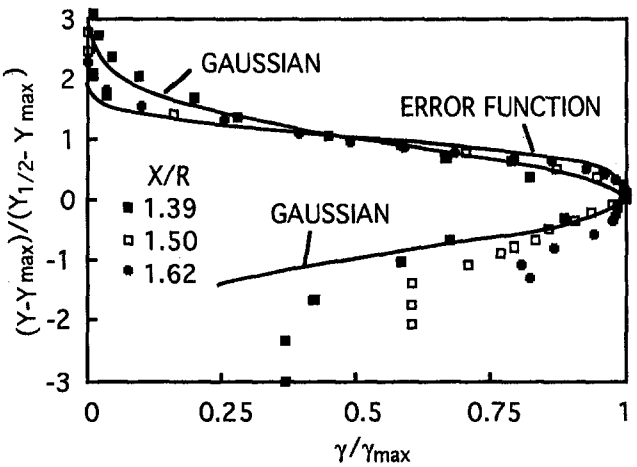

Fig. 11 Intermittency shape comparison at transition

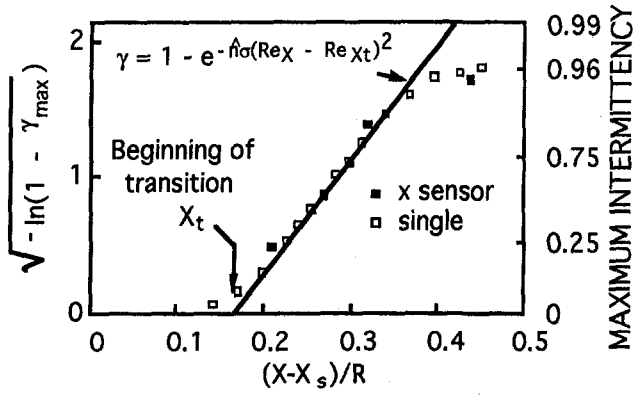

Fig. 12 Maximum intermittency through transition

turbulent spots, and using Dhawan and Narasimha's (1958) stipulation that spots are stochastically produced along one spanwise line at X_t. The dimensionless spot production rate ($\hat{n}\sigma$), which encompasses the rate of spot initiation and spot growth, is given by the slope of the theoretical fit on this plot and is related to the length of transition. Mayle (1991) was the first to suggest that intermittencies in separated flow transition should be plotted in this manner.

It is seen that the data fit this format remarkably well, especially between $\gamma_{max} = 0.25$ and 0.75, where intermittency determinations are least likely to be inaccurate. The tail upstream of transition onset may be an indication of an extended spot production region (Mayle, 1991) possibly caused by the quasi-steady movement of the location of shear layer instability onset with shear layer flapping. At the downstream extreme, intermittency values do not grow as rapidly as predicted, possibly caused by the same phenomenon or because interjections of nonturbulent fluid can penetrate a shear layer more deeply than they can in an attached boundary layer. The maximum intermittency does approach one more closely, farther downstream where the shear layer is thicker. It is also possible that the growing turbulent spots scatter because they are not constrained by a wall. Regardless of what actually occurs, the shear layer may be described as basically fully turbulent when γ_{max} reaches 0.96.

The length of the laminar shear layer, X_{st}, given by the distance between separation and the onset of transition ($X_t - X_s$, as shown in Fig. 2), is compared to a correlation based on momentum thickness at separation (Mayle, 1991) in Fig. 13. The correlation was based on measurements of the development of high-frequency turbulence intensity in short separation bubbles. The maximum turbulence intensity level was plotted in a form similar to that in Fig. 12, based on the assumption that $\gamma = Tu/Tu_{max}$, to give an estimate on the location of transition onset. It should be noted that this method provides a consistent result, which may reduce the scatter of results for laminar shear length. The data points of Gaster and Bellows that underpin the correlation are shown. The present result, which is the only known determination of transition onset from intermittency measurements, is also plotted and compares well.

Figure 14 shows a comparison of the present data with Mayle's (1991) correlation for spot production rate in a separated shear layer. Also presented are production rates derived from Gaster's and Bellows' measurements of turbulence intensity development. The actual correlation was determined by taking Mayle's (1991) correlation for Re_{sT} (which was based on many more points) and subtracting the previous correlation for Re_{st} to get a transition length Reynolds number (Re_{LT}), which is directly related to the dimensionless spot production rate. It is seen that the present data, reduced from intermittency measurements, are quite close to the correlation. As an aside, it should be noted that the dimensionless production rate is several orders of magnitude larger than that found in attached boundary layers without a pressure gradient, but of the same order of those with a strong adverse pressure gradient (Mayle, 1991) when $Tu = 0.3$ percent. This is due to the increased instability of the shear layer, which may allow higher actual rates of spot production and/or larger turbulent spot spread angles.

Conclusion

Laminar shear layers in separation bubbles can be characterized as a cross between attached boundary layers and free shear layers. Therefore, it is not surprising that the transition process they undergo has elements identified with each of these. The intermittency development in separation bubbles is well modeled with the turbulent spot theory used in attached boundary layers and there is also evidence of Kelvin–Helmholtz vortex pairing in the transition region like that found in free shear layers.

The difference in separation bubble transition from each of the above is also notable. The turbulent spot production rate is several orders of magnitude higher than that found in attached boundary layers on flat plates (but the same order of that with adverse pressure gradients). In addition, turbulent spots, which are almost always apparent in attached boundary layer transition, have yet to be clearly identified in separation bubble shear layers, possibly because large spot spreading angles and high rates of spot production make it difficult to distinguish them. Compared with free shear layer transition, the flow was very

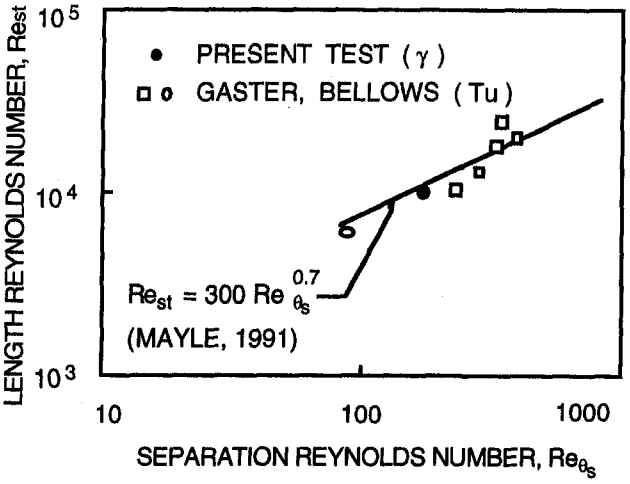

Fig. 13 Correlation for laminar shear layer length

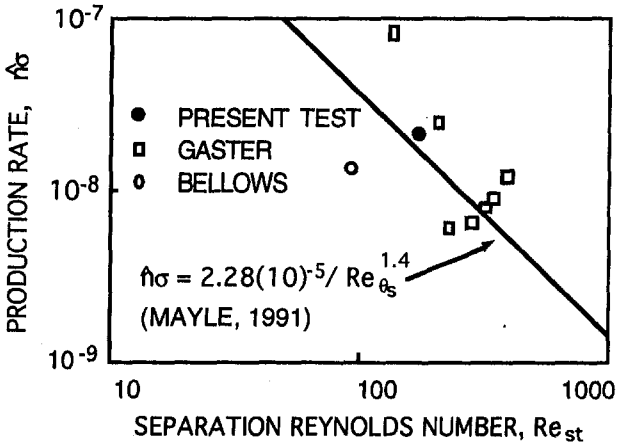

Fig. 14 Production rate of turbulent spots in shear layers

three dimensional and highly complex, with the occurrence of wave packets and localized breakdowns. In addition to this, there seems to be evidence that these wave packets entrained turbulent fluid from downstream which possibly affected their transition.

Measures of intermittency in the separation bubble shear layer corroborated Mayle's (1991) correlations for laminar shear layer length and transition length. These correlations, which are good for low free-stream turbulence levels ($Tu < 1$ percent), need to be checked with experiments at higher turbulence levels to improve their usefulness for turbomachinery. More intermittency measurements in separation bubbles, which objectively define the onset and length of transition, are needed.

References

Arena, A. V., and Mueller, T. J., 1980, "Laminar Separation, Transition, and Turbulent Reattachment Near the Leading Edge of Airfoils," *AIAA Journal,* Vol. 18, No. 7, pp. 747–753.

Batill, S. M., and Mueller, T. J., 1981, "Visualization of Transition in the Flow Over an Airfoil Using the Smoke-Wire Technique," *AIAA Journal,* Vol. 19, No. 3, pp. 340–345.

Bellows, W. J., 1985, "An Experimental Study in Leading Edge Separating–Reattaching Boundary Layer Flows," Ph.D. Thesis, Rensselaer Polytechnic Institute, Troy, NY.

Cebeci, T., and Bradshaw, P., 1977, *Momentum Transfer in Boundary Layers,* Hemisphere Publishing Corporation, Washington, DC.

Chandrsuda, C., Mehta, R. D., Weir, A. D., and Bradshaw, P., 1978, "Effect of Free-Stream Turbulence on Large Structure in Turbulent Mixing Layers," *Journal of Fluid Mechanics,* Vol. 85, pp. 693–704.

Crabtree, L. F., 1959, "The Formation of Regions of Separated Flow on Wing Surfaces," ARC R&M No. 3122, pp. 1–28.

Crimi, P., and Reeves, B. L., 1976, "Analysis of Leading-Edge Separation Bubbles on Airfoils," *AIAA Journal,* Vol. 14, No. 11, pp. 1548–1555.

Dhawan, S., and Narasimha, R., 1958, "Some Properties of Boundary Layer Flow During Transition From Laminar to Turbulent Motion," *Journal of Fluid Mechanics,* Vol. 3, pp. 418–436.

Emmons, H. W., 1951, "The Laminar–Turbulent Transition in a Boundary Layer—Part 1," *Journal of the Aeronautical Sciences,* Vol. 18, pp. 490–498.

Gaster, M., 1967, "The Structure and Behaviour of Separation Bubbles," ARC R&M 3595.

Gleyzes, C., Cousteix, J., and Bonnet, J. L., 1985, "Theoretical and Experimental Study of Low Reynolds Number Transitional Separation Bubbles," *Proc. Conference on Low Reynolds Number Airfoil Aerodynamics,* pp. 137–152.

Goldstein, S., 1965, *Modern Developments in Fluid Dynamics,* Dover Publications, Inc., New York.

Hancock, G. J., 1969, "Problems of Aircraft Behaviour at High Angles of Attack," AGARDograph 136, pp. 1–110.

Horton, H. P., 1967, "A Semi-empirical Theory for the Growth and Bursting of Laminar Separation Bubbles," ARC CP 1073.

Huang, L. S., and Ho, C. M., 1990, "Small-Scale Transition in a Plane Mixing Layer," *Journal of Fluid Mechanics,* Vol. 210, pp. 475–500.

Malkiel, E., 1994, "An Experimental Investigation of a Separation Bubble," Ph.D. Thesis, Rensselaer Polytechnic Institute, Troy, NY.

Mayle, R. E., 1991, "The Role of Laminar-Turbulent Transition in Gas Turbine Engines," ASME JOURNAL OF TURBOMACHINERY, Vol. 113, pp. 509–537.

Michalke, A., 1991, "On the Instability of Wall Boundary Layers Close to Separation," *IUTAM Symposium on Separated Flows and Jets,* Springer-Verlag, Berlin, pp. 557–564.

Moser, R. D., and Rogers, M. M., 1993, "The Three-Dimensional Evolution of a Plane Mixing Layer: Pairing and Transition to Turbulence," *Journal of Fluid Mechanics,* Vol. 247, pp. 275–320.

Narasimha, R., 1957, "On the Distribution of Intermittency in the Transition Region of a Boundary Layer," *Journal of the Aeronautical Sciences,* Vol. 24, pp. 711–712.

Platzer, M. F., Ekaterinaris, J. A., and Chandrasekhara, M. S., 1993, "On the Prediction of Separation Bubbles Using a Modified Chen–Thyson Model," End-Stage Transition Workshop, Syracuse University.

Roberts, W. B., 1980, "Calculation of Laminar Separation Bubbles and Their Effect on Airfoil Performance," *AIAA Journal,* Vol. 18, No. 1, pp. 25–31.

Schlichting, H., 1979, *Boundary-Layer Theory,* 7th ed., McGraw-Hill, New York.

Schmidt, G. S., and Mueller, T. J., 1989, "Analysis of Low Reynolds Number Separation Bubbles Using Semiempirical Methods," *AIAA Journal,* Vol. 27, No. 8, pp. 993–1001.

Tani, I., 1964, "Low-Speed Flows Involving Bubble Separations," *Progress in Aeronautical Science,* Vol. 5, pp. 70–103.

van Ingen, J. L., and Boermans, L. M. M., 1985, "Research on Laminar Separation Bubbles at Delft University of Technology in Relation to Low Reynolds Number Airfoil Aerodynamics," *Proc. Conference on Low Reynolds Number Airfoil Aerodynamics,* pp. 89–124.

Walker, G. J., Subroto, P. H., and Platzer, M. F., 1988, "Transition Modeling Effects on Viscous/Inviscid Interaction Analysis of Low Reynolds Number Airfoil Flows Involving Laminar Separation Bubbles," ASME Paper No. 88-GT-32.

Walraevans, R. E., and Cumpsty, N. A., 1995, "Leading Edge Separation Bubbles on Turbomachine Blades," ASME JOURNAL OF TURBOMACHINERY, Vol. 117, pp. 115–125.

Wygnanski, I., 1993, "The Stability of the Boundary Layer and the Spot," End-Stage Transition Workshop, Syracuse University.

Young, A. D., 1977, "Some Special Boundary Layer Problems," *Zeitschrift für Flugwissenschaften und Weltraumforschung,* Vol. 6, pp. 401–414.

An Investigation of the Effect of Cascade Area Ratios on Transonic Compressor Performance

A. R. Wadia
GE Aircraft Engines,
Cincinnati, OH

W. W. Copenhaver
Wright Laboratory,
Wright Patterson AFB, OH

Transonic compressor rotor performance is highly sensitive to variations in cascade area ratios. This paper reports on the design, experimental evaluation, and three-dimensional viscous analysis of four low-aspect-ratio transonic rotors that demonstrate the effects of cascade throat area, internal contraction, and trailing edge effective camber on compressor performance. The cascade throat area study revealed that tight throat margins result in increased high-speed efficiency with lower part-speed performance. Stall line was also improved slightly over a wide range of speeds with a lower throat-to-upstream capture area ratio. Higher internal contraction, expressed as throat-to-mouth area ratio, also results in increased design point peak efficiency, but again costs performance at the lower speeds. Reducing the trailing edge effective camber, expressed as throat-to-exit area ratio, results in an improvement in peak efficiency level without significantly lowering the stall line. Among all four rotors, the best high-speed efficiency was obtained by the rotor with a tight throat margin and highest internal contraction, but its efficiency was the lowest at part speed. The best compromise between high-speed and part-speed efficiency was achieved by the rotor with a large throat and a lower trailing edge effective camber. The difference in the shock structure and the shock boundary layer interaction of the four blades was analyzed using a three-dimensional viscous code. The analytical results are used to supplement the data and provide further insight into the detailed physics of the flow field.

Introduction

Current trends in aircraft engine compressor designs are toward reduced blade aspect ratios, increased aerodynamic loading and higher throughflow rates to reduce both parts count and inlet cross-sectional areas. A compressor stage of this nature with high specific flow using low-aspect-ratio custom tailored airfoils was documented by Wennerstrom (1984). The rotor was subsequently redesigned to provide a more rugged geometry and yet maintain good aerodynamic performance. The experimental results of this rotor were reported by Law and Wadia (1993). Table 1 summarizes the salient geometric and aerodynamic features of this design.

A comprehensive experimental program aimed at exploring the sensitivity of the performance of low-aspect-ratio compressors to variations in some key design parameters was undertaken. The rotor described in Table 1 was used as a baseline for the program. The specific design parameters investigated included chordwise location of maximum thickness, various cascade area ratios and leading edge sweep. Seven rotors were designed and fabricated for the test program. The experimental results and three-dimensional viscous analyses of Rotors 1 and 2, to evaluate the effect of location of airfoil maximum thickness on transonic compressor performance, have been reported by Wadia and Law (1993).

The objective of the research program presented here was experimentally and analytically to investigate the effect of cascade area ratios on transonic compressor performance. The design of three such rotors is described first, followed by the comparison of the measured performance of the rotors. Three-dimensional viscous analyses of the rotors at their design and 90 percent speed peak efficiency points are used to illustrate the details of the internal flow field and shock structure responsible for the difference in performance between the rotors. Three-dimensional calculations are also used to provide guidance in interpretation of the test data at off-design conditions.

Cascade Parameter Definition. This paper defines the impact of changing various blade cascade parameters. It is therefore important to describe some parameters that will be referenced throughout the paper in describing blade geometric variations. Further details on these concepts are described by Smith and Yeh (1962).

The *mouth area* of a cascade is identified as the quasi-three-dimensional flow area at the mouth of the cascade defined by a straight line from the leading edge of one blade to a point tangent to the adjacent blade suction surface. The location of the mouth is identified in Fig. 1. The mouth area is the product of the two-dimensional passage width times a streamtube lamina thickness determined from an axisymmetric flow calculation.

As with the mouth area, the *throat area* of the cascade is the quasi-three-dimensional flow area at the throat also identified in Fig. 1. The throat is defined at the minimum area along a chord line and the throat area is the product of the two-dimensional passage width times the local streamtube lamina thickness.

The *discharge area* is the quasi-three-dimensional flow area at the discharge shown in Fig. 1. The discharge area is the product of the two-dimensional passage width times the local streamtube lamina thickness.

The inlet two-dimensional passage width is defined as the line perpendicular to the upstream relative flow angle as shown

Contributed by the International Gas Turbine Institue and presented at the 39th International Gas Turbine and Aeroengine Congress and Exposition, The Hague, The Netherlands, June 13–16, 1994. Manuscript received by the International Gas Turbine Institute February 18, 1994. Paper No. 94-GT-286. Associate Technical Editor: E. M. Greitzer.

Table 1 Baseline rotor key design parameters

Specific Flow	43.13 lbm/sec-ft^2
Corrected Tip Speed	1500 ft/sec
Stage Pressure Ratio	1.92
Corrected Flow	61.36 lbs/sec
Inlet Radius Ratio	0.312
Tip Diameter	17 inches
Mean Aspect Ratio (Rotor/Stator)	1.32/1.26
Average Solidity (Rotor/Stator)	2.3/1.68

in Fig. 1. The *inlet area* is the product of the two-dimensional passage width times the local streamtube lamina thickness.

Throat Margin. The ratios of the areas defined above create important parameters to be considered in blade design and are critical to the performance changes noted in this paper. For cascades with supersonic inlet Mach numbers, as those described in this paper, the throat margin is defined as the percent excess area over that required to pass the design flow, assuming losses equal to those of a normal shock at the upstream Mach number that occur between the inlet and the throat. This parameter is defined as a ratio of the throat area (defined above) to the upstream capture area (see Fig. 1) A_T/A_I.

Internal Contraction. There are few, if any, known data concerning the optimum location of the throat for transonic blade rows. Unless the throat is located essentially at the mouth, there will be some internal contraction from the mouth to the throat. This parameter is defined as the ratio of the throat area to the mouth area (A_T/A_M).

Effective Camber. The throat-to-discharge area ratio (A_T/A_D) is herein referred to as "effective camber" of a transonic blade row. The effective camber is therefore a measure of the amount of subsonic diffusion that would be produced by an isentropic diffusion downstream of a sonic condition at the passage throat by the cascade.

Rotor Design Philosophy

The efficiency of a transonic blade is heavily influenced by shock losses; these may exceed the losses due to cascade diffusion and secondary flow effects. The magnitude of the shock losses increases rapidly with rotor inlet relative Mach number, and although this is mainly determined by blade speed, the Mach number just ahead of the leading edge passage shock can be influenced by the shape of the blade suction surface ahead of the shock. Increasing the average suction surface (measured from axial) angle ahead of the shock reduces the average Mach number upstream of the shock through external compression and should reduce the shock losses as was previously described by Kantrowitz (1950) and Klapproth (1961). However, this type of airfoil can result in a reduced cascade throat area. If the throat is too small, the cascade will not pass the design flow and may not achieve the attached shock pattern desired for minimum loss. When the blade suction surface angle is increased ahead of the shock, it may be necessary to have a rapid reduction in blade meanline angle at the cascade mouth to prevent the throat from becoming too small. This rapid change of the suction surface angle will increase the suction surface Mach number ahead of the shock and could increase the shock boundary layer interaction loss.

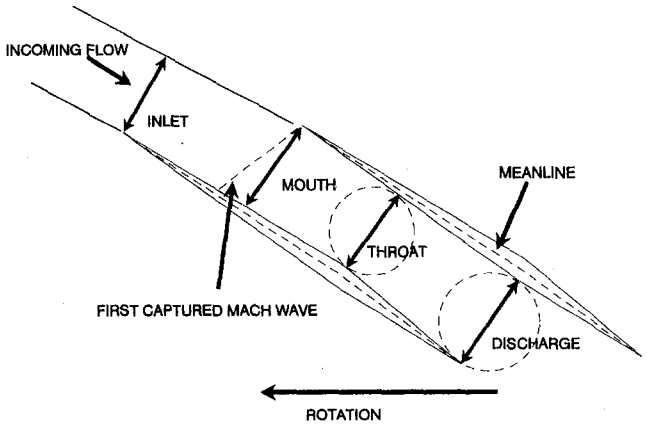

Fig. 1 Definition of cascade parameters

To get more definitive data on the effect of the suction surface shape ahead of the leading edge passage shock, and on the interrelation of the shape of the suction surface and the cascade throat area, two transonic compressor blades (henceforth described as Rotor 3 and Rotor 4) were designed.

Rotors 3 and 4 were designed to have smaller throat areas in the outer part of the blade relative to the baseline blade. This is illustrated by the radial distribution of throat margin in Fig. 2(a). Except locally at the tip, the throat margin was set at about 5 percent. Figure 3 shows the comparison of the tip stream surface sections of the baseline rotor with Rotor 3 and the corresponding axial distribution of the meanline angles. Rotor 4, although nearly identical to Rotor 3, was designed with slightly less external compression. Rotor 3, due to its tight throat margin, also has more internal contraction relative to the baseline rotor. Rotor 4 has even more internal contraction than Rotor 3 as shown in Fig. 2(b). Comparison of Rotor 3 and Rotor 4 test data formed the basis for the evaluation of the effect of internal contraction on compressor performance.

The reason for the trailing edge camber study is explained in the following. The best efficiency at the design speed for transonic rotors normally occurs near the "knee" of the pressure ratio flow characteristics where the flow begins to decrease. This point is reached when the blade no longer has enough circulation capacity or effective camber, to sustain the pressure rise with an attached shock system, and the passage shock must become unstarted and the flow must be reduced so the blade can operate at increased incidence. There is reason to believe that an improvement in useful efficiency might be achieved by adjusting the effective camber such that the "knee" of the characteristics coincides with the operating line point. It was not known if a reduction in the effective camber would reduce the stall line at the design speed, or would have an adverse effect on efficiency at part-speed conditions. Hence, Rotor 5 was designed to obtain experimental data to assess these trade-

Nomenclature

A = area
IMM = radial immersion (0 = tip and 1 = hub)
LE = leading edge
M_{isen} = isentropic Mach number
P = pressure
PS = pressure surface
SS = suction surface
TE = trailing edge
Z = axial distance
θ = tangential distance

Subscripts

D = discharge or exit
M = mouth
T = throat
I = inlet

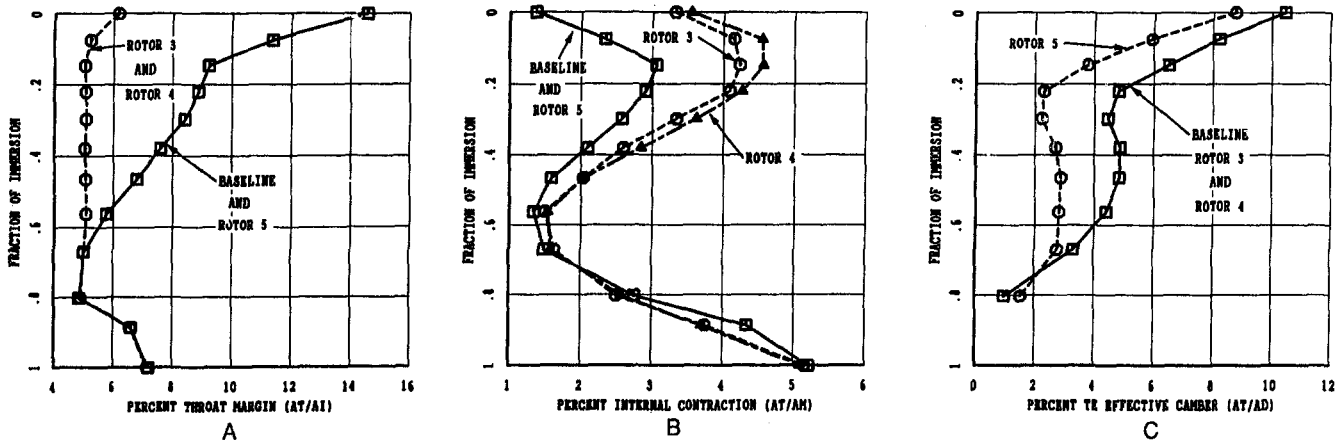

Fig. 2 Comparison of the cascade area ratios investigated in the parametric blade study program

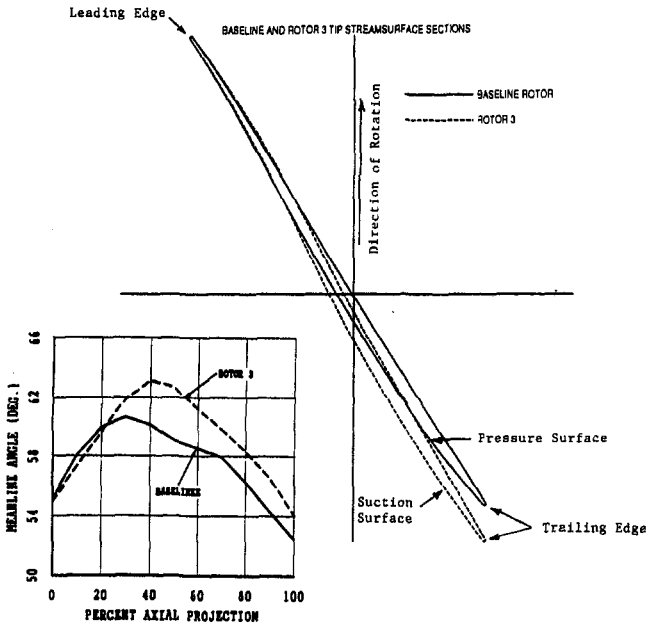

Fig. 3 Comparison of meanline metal angles and tip streamsurface sections of baseline and Rotor 3

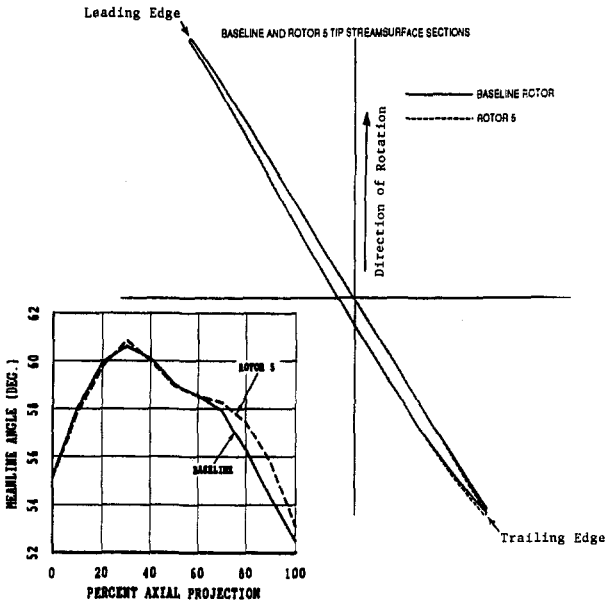

Fig. 4 Comparison of meanline metal angles and tip streamsurface sections of baseline and Rotor 5

offs. Figure 4 shows a comparison of tip streamsurface blade sections and meanline angles of the baseline rotor with Rotor 5. Rotor 5 has the same large throat area and internal contraction as the baseline rotor (Figs. 2(a) and 2(b)), but has reduced trailing edge camber in the outer eighty percent of the blade, as is shown in Fig. 2(c).

Table 2 summarizes the differences between the rotors studied in this series.

The aerodynamic synthesis of the baseline rotor described in the paper by Law and Wadia (1993) served as the basis for the vector diagrams used to design the blading for Rotors 3, 4, and 5. The detailed design procedure was identical to that used to design Rotors 1 and 2 and is presented in the paper by Wadia and Law (1993). To evaluate the performance of the new rotor designs accurately by comparing overall stage performance, the new rotors were designed to produce approximately the same stator inlet conditions in all cases. Further details on the rotor designs are provided by Parker and Simonson (1982).

Table 2 Summary of the comparison of cascade area ratios relative to baseline rotor

Rotors/ Parameters	Rotor 3	Rotor 4	Rotor 5
Throat Margin (AT/AI)	Smaller	Smaller Than Baseline But Same As Rotor 3	Same
Internal Contraction (AT/AM)	Larger	Larger Than Baseline And Rotor 3	Same
Effective Camber (AT/AD)	Same	Same	Smaller

Test Setup and Instrumentation

The tests were conducted in the 2000-hp Compressor Aerodynamics Research Laboratory at Wright Field. The single-stage compressor test vehicle is shown in Fig. 5. It employed a cantilevered rotor to allow for easy exchange of rotor designs with no impact on instrumentation hardware. The rotors designed for this test program were of integral construction machined from single forgings. There were no inlet guide vanes in the experimental setup.

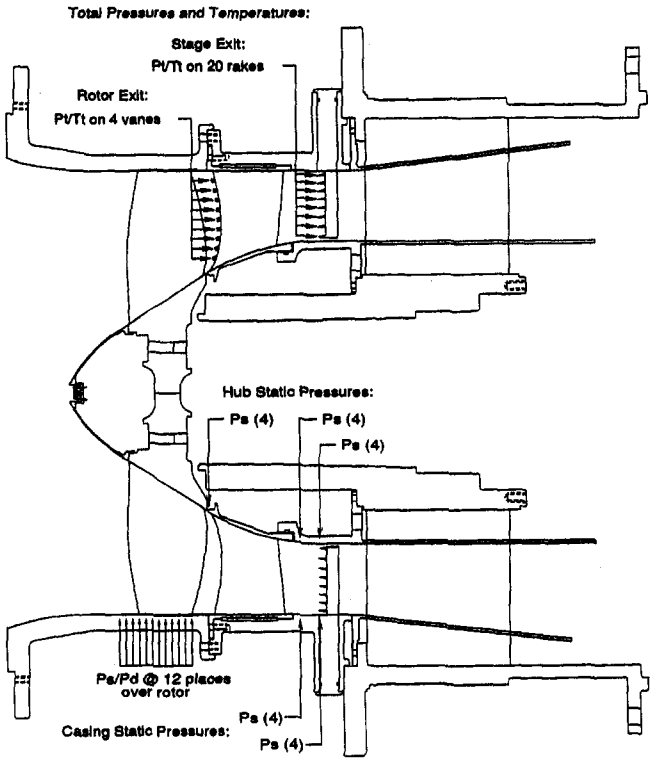

Fig. 5 Single-stage transonic test vehicle

Aerodynamic instrumentation consisted of ten total temperature and ten total pressure stator-exit radial rakes, each with eight measurements at centers of equal area. The rakes were distributed around the circumference and spaced to divide a single vane exit passage into ten equal parts. Vane leading edge total pressure and temperature instrumentation was available, but failed during the test program, and therefore these data are not reported here. Rotor alone performance was extrapolated from the stator exit radial rakes by using the three highest total pressure values. Static pressure taps were located on the inner and outer endwalls at the inlet and exit plane of the stator. Dynamic pressure measurements along the casing over the rotor tip, in conjunction with complimentary steady-state static pressure measurements, were acquired to determine the tip blade-to-blade flow field at selected operating conditions. Measurements of inlet total pressure, temperature, rotor speed, and mass flow were also obtained. All test data were acquired with some degree of depressed inlet pressure and later corrected to standard inlet conditions as reported herein.

The average measured running clearance at design speed for all rotors was approximately 0.025 in. representing a tip clearance-to-chord ratio of about 0.67 percent. Further details on the test setup and instrumentation are described by Law and Wadia (1993).

Discussion of Experimental Results

The test data for 90, 95, and 100 percent of design speed operation are presented in the form of stage performance maps to evaluate the effects of throat margin, internal contraction, and trailing edge camber on transonic compressor performance. Since relative effects between the designs are being considered here, and because the designs were evaluated with the same instrumentation, precision errors are of the greatest importance when considering the results shown here. An estimate of the experimental precision with a *95 percent confidence* level for 100 percent speed is presented below:

Mass flow	0.2 percent reading
Pressure ratio	0.1 percent reading
Efficiency	0.2 points
Pressure	0.012 psi
Temperature	0.36F @ 50°F, 0.54 @ 250°F

In addition, the data were corrected for four erroneous exit total pressure measurements by substituting a neighbor measurement for the ones in error. This procedure was followed identically on all the data presented here to eliminate any bias errors between the data sets. The relative trends for the rotor-alone performance are similar to the stage performance and have not been included in this paper.

The differences in measured performance of the four rotors is discussed in the following paragraphs with analysis provided in the three-dimensional viscous analysis section.

Overall Performance Trends

Levels of efficiency and pressure ratio were determined through mass-weighted averages of the measured exit pressures and temperatures. Figure 6 shows the 90 to 100 percent speed, peak efficiency at flow comparisons of all the rotors studied in this paper. Rotor 4 has the best high-speed performance and the lowest part speed efficiency of the four rotors. This rotor has been discussed some in detail by Hah and Puterbaugh (1990), Copenhaver et al. (1993), and Sellin et al. (1993). The performance of Rotor 5 at high speed was not as good as that of Rotor 3 and 4. However, at 90 percent speed and below (not shown here) Rotor 5 had the highest efficiency of all the rotors investigated.

Throat Margin Effect on Stage Performance. Comparison of the measured stage performance of the baseline rotor with Rotor 3 (smaller throat design) is presented in Fig. 7. The data show that Rotor 3 achieves the same design speed flow as the baseline rotor. At this condition, the leading edge region up to the first captured Mach wave controls the flow induction capability. The suction surface leading edge angles were the same for both rotors and therefore, resulted in nearly identical flows (within the experimental uncertainty) at design speed.

The maximum stage efficiency attained by Rotor 3 is approximately 1.3 points higher at design speed and 0.9 points better at 95 percent design speed relative to the baseline rotor. Also, at both 95 and 100 percent speeds, the stage adiabatic efficiency of Rotor 3 is always equal to or higher than the baseline rotor at all operating flows along the two speedlines. However, these peak efficiency trends are reversed between the two rotors at 90 percent speed and below (not shown here), and the baseline rotor is more efficient. The larger throat baseline rotor has less flow roll back and a slightly lower stall line relative to Rotor 3.

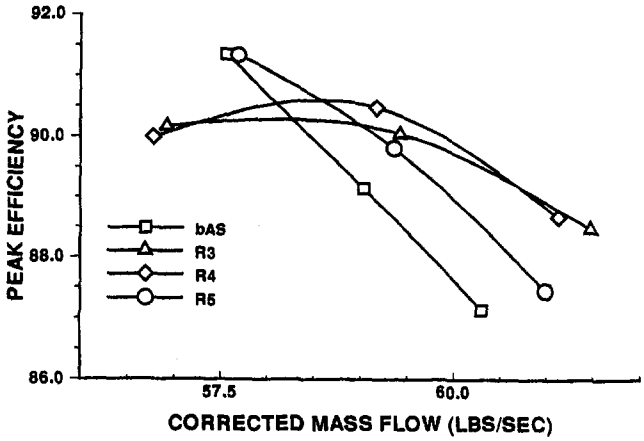

Fig. 6 Peak efficiency characteristics of the four rotors tested

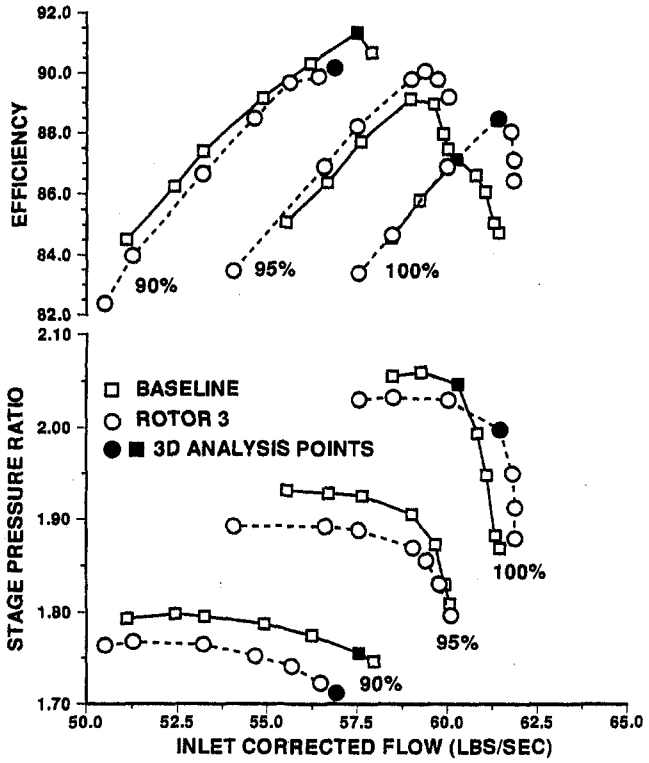

Fig. 7 Baseline and Rotor 3 performance comparisons

Internal Contraction Effect on Stage Performance. Comparison of the measured stage performance of Rotors 3 and 4 is shown in Fig. 8. The flow pumping capability and speedlines for both the rotors are almost identical at all speeds. The maximum stage efficiency of Rotor 4 (larger internal contraction) is higher at 95 and 100 percent speeds by about 0.4 and 0.2 points, respectively. However, the efficiency at 90 percent speed is lower for Rotor 4. This illustrates the tradeoff that can be achieved between high-speed and part-speed performance with internal contraction differences, which alters the shock structure and shock–boundary layer interaction. The data also indicate that there is almost no impact of internal contraction on the compressor stall line. As stated earlier, while the geometric differences between Rotor 3 and 4 were quite small, the transonic compressor performance was sensitive to these changes.

Effect of Trailing Edge Camber on Stage Performance. Comparison of the measured stage performance of the baseline rotor with Rotor 5 (lower camber) is illustrated in Fig. 9. Both rotors achieve similar flow at design speed. The maximum stage efficiency attained by Rotor 5 is equal or higher at all speeds. Rotor 5's peak efficiency at 95 and 100 percent speeds exceeds that of the baseline rotor by 0.7 and 0.3 points, respectively. Rotor 5, with its lower trailing edge camber, does not suffer any loss in stall margin. The lower flow of Rotor 5 over the entire speed range below design speed can be attributed to the lower trailing edge effective camber of Rotor 5. At design speed, the flow is limited by the leading edge suction surface; this is identical for both blades, resulting in similar flow pumping capability. The data suggest that below 95 percent speed, the flow is set by the trailing edge effective camber and the smaller trailing edge passage area of Rotor 5 and therefore results in a lower flow across the entire speed range.

Three-Dimensional Viscous Analysis

The details of the three-dimensional viscous analysis code used to study the flow field in the four transonic compressor rotors have been reported by Jennions and Turner (1993a, b). The analysis code configuration will be described briefly below. The computations were performed with an attempt to resolve the details of the tip clearance flow. The grid consists of 93 nodes in the axial direction, of which 63 were subdivided nonuniformly from the leading edge to the trailing edge: 49 nodes

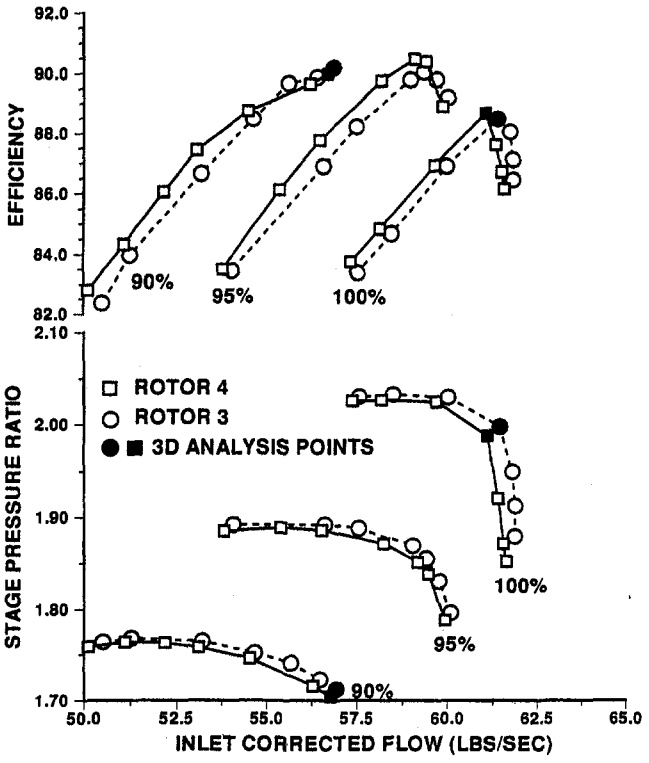

Fig. 8 Rotor 3 and Rotor 4 performance comparisons

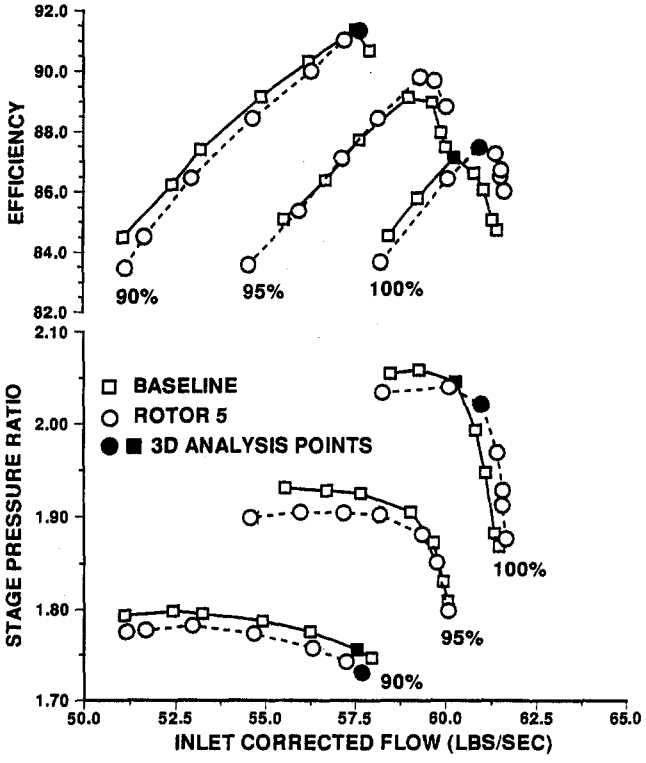

Fig. 9 Baseline and Rotor 5 performance comparisons

in the blade-to-blade direction and 33 nodes in the spanwise direction. A stretching parameter between 1.0 and 1.2 was used in all three directions to model the gradients in the flow field near the endwalls and the blade surfaces. Special care was taken to model the leading edge region accurately to obtain the correct shock structure in the analysis. Five gird cells were used in the analysis within the tip gap. The rotating hub including the spinner was modeled in the three-dimensional analysis. The downstream stator was not included in the analysis.

The inlet boundary conditions for the analysis consisted of uniform inlet total pressure and temperature and the tangential flow velocity (zero in this case). The exit boundary condition consisted of prescribing a radial distribution of the circumferentially averaged static pressure (determined from the experiment) at stator inlet. This approximated the downstream stator effects on the rotors in the three-dimensional viscous analysis. During the analysis the exit static pressure level was adjusted to match the measured flow-pressure ratio operating line. The three-dimensional analysis predicted a flow that was 0.5 to 1.0 percent higher than that measured in the rig test for all the rotors analyzed herein.

The data points selected for the analysis were measured peak efficiency points at design speed and 90 percent speed for all rotors. The main objective of the analysis was to determine where and why the performance differences between the rotors occurred. Some typical comparisons with test data are also shown to illustrate the quality of the three-dimensional calculations. To illustrate the differences between the rotors, the 15 percent immersion location was selected as the point for thermodynamic comparisons. This location was selected because it is sufficiently far from the tip clearance region where significant flow field interactions exists. These interactions at the tip tend to overpower blade design differences. The largest differences in performance, as determined from the analysis, are also found at the 15 percent immersion location.

At 15 percent immersion, comparison of the blade-to-blade isentropic Mach number contours and blade surface isentropic Mach number distribution (determined from the static pressure, an ideal total pressure and isentropic relations) are made to illustrate the differences in structure, strength and shock location. Also at 15 percent immersion, the shock/boundary layer interaction was studied by calculating the blade-to-blade variation in the loss coefficient at the trailing edge. These results identify the free-stream loss, loss associated with the shock/blade surface boundary layer interaction, and also the wake width and depth. The variation of the circumferential average loss coefficient from the inlet to the exit was also computed to illustrate the accumulation of the loss as the flow moves through the passage. Boundary layer separation and reattachment regions are also identified for certain blade rows wherever applicable.

Baseline and Rotor 3 Throat Margin Comparisons

100 Percent Speed. Figure 10 shows a typical comparison of the radial profiles of total pressure and temperature calculated by the three-dimensional viscous analysis with the experimental values. For this comparison the rotor exit total pressures and temperatures were defined as the average of the three highest stator exit plane measurements at a given immersion. The peak efficiency of the baseline rotor occurs at a higher pressure ratio (on a higher operating line) relative to Rotor 3 as seen in the data presented in Fig. 7. The radial profile of total pressure shown in Fig. 10 reflects the operating line differences as seen by the more tip strong radial profile for the baseline rotor. The three-dimensional calculations agree reasonably well with the measured total pressure profile. The calculated work input shown in Fig. 10 is also in reasonably good agreement with the test data with the qualitative trends predicted accurately. As the quality of the agreement between the data and the three-dimensional calculations for the other rotors was similar to that shown in Fig. 10, further comparisons of the radial profiles have not been included herein.

Figure 11 shows the comparison of the calculated shock structure at 15 percent immersion between the baseline rotor and Rotor 3. The figure indicates that both rotors have a two-shock system. The passage shock on the baseline rotor coalesces with the leading edge shock near the suction surface. The passage shock on Rotor 3 near the pressure surface is stronger but bifurcates into shock-free diffusion approximately half way across the passage. The comparison of the corresponding blade surface Mach number distribution is presented in Fig. 11. On the suction surface Rotor 3 diffuses more rapidly from the leading edge to about 30 percent axial distance. Both rotors show a zone of re-acceleration on the suction surface followed by a shock and subsonic diffusion downstream of the shock. The suction surface Mach number before the shock is the same for both rotors. The drop in Mach number across the suction surface shock on both rotors is approximately the same. On the pressure surface Rotor 3 has a stronger shock relative to the baseline rotor and the blade loading 2 percent from the leading edge to 15 percent axial distance is higher.

The analysis indicated that the improvement in efficiency on Rotor 3 occurs almost over the entire span with a predicted 0.6 point overall efficiency improvement relative to about 1.3 points measured in the test. The maximum efficiency difference between the two rotors occurs at about 15 percent immersion. Figure 12(a) shows the comparison of the circumferential distribution of the calculated loss coefficient, at 15 percent immersion from the pressure surface to the suction surface between the rotors at the trailing edge. In the free-stream region near the pressure surface, Rotor 3 with its stronger shock (as seen in Figs. 11(a) and 11(b)) has a higher loss coefficient relative to the baseline rotor. However, as the shocks coalesce on the baseline rotor (Fig. 11(a)), the free-stream loss increases rapidly as shown in Fig. 13(a). The coalesced shock boundary layer interaction near the suction surface results in a thicker wake for the baseline rotor.

The circumferential averaged distribution of the accumulation of loss from about 18 percent upstream of the leading edge to about 10 percent downstream of the trailing edge is shown in Fig. 12(b). The loss from Rotor 3 is slightly higher relative to the baseline rotor up to 50 percent axial distance from the leading edge. The increase in the loss coefficient on the baseline rotor from 40 to 60 percent axial distance (through the coalesced shock) is considerably more than for Rotor 3 and suggests a boundary layer separation induced by the shock. The flattening of the variation in loss coefficient downstream of the shock from 60 to 80 percent axial distance indicates a reattachment of the boundary layer. This notion is supported by the velocity vectors near the suction surface of the baseline rotor (not shown here). For Rotor 3, however, the loss coefficient generally increases smoothly up to the trailing edge with no sign of boundary layer separation downstream of the shock.

Thus from the viscous analysis, the larger shock losses of the coalesced shock structure and the suction surface boundary layer separation downstream of the shock on the baseline rotor results in its poorer performance at high speed.

90 Percent Speed. The comparison of the measured performance between the baseline rotor and Rotor 3 at 90 percent speed peak efficiency (see Fig. 7) shows a loss in performance of Rotor 3 with peak efficiency occurring at a lower flow. The three-dimensional calculations suggest Rotor 3 with its lower flow and consequently higher incidence is unstarted and has higher loss. Figure 13 shows a comparison of the calculated blade-to-blade static pressure distribution at the rotor tip with the measured tip pressures. Both the calculations and the measurements indicate Rotor 3 is operating in its unstart condition at this speed and a second shock (over expansion) has occurred near the blade trailing edge.

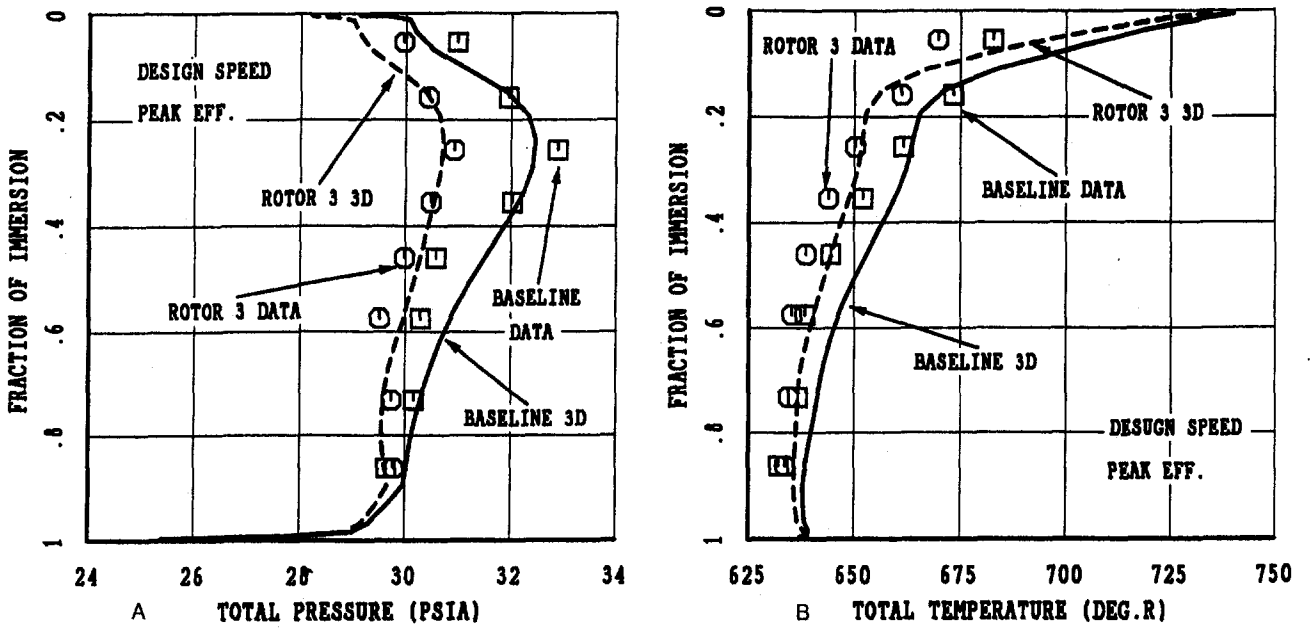

Fig. 10 Comparison of the measured and calculated radial profiles of total pressure and total temperature at design speed and peak efficiency

Figure 14(a) shows the comparison of the blade-to-blade Mach number contours for both rotors at 15 percent immersion. The unstart condition on Rotor 3 still exists away from the blade tip and the overexpanded shock prevails at the trailing edge. The shock remains started at 90 percent speed for the baseline rotor with a strong passage shock and a weak leading edge shock (suction surface Mach number 1.6). Figure 14(b) reinforces the unstart condition observed in the blade-to-blade contours on Rotor 3. The high suction surface Mach number at the leading edge on Rotor 3 (above 1.8) is a consequence of the lower mass flow as shown in the experimental data (Fig. 7) and the corresponding unstart condition. The blade surface isentropic Mach number distribution (Fig. 14(b)) also shows two shocks on the suction surface of Rotor 3 with slightly lower upstream shock Mach numbers relative to the baseline rotor. The shock on the pressure surface of the baseline rotor is stronger and occurs slightly upstream of the pressure side shock on Rotor 3.

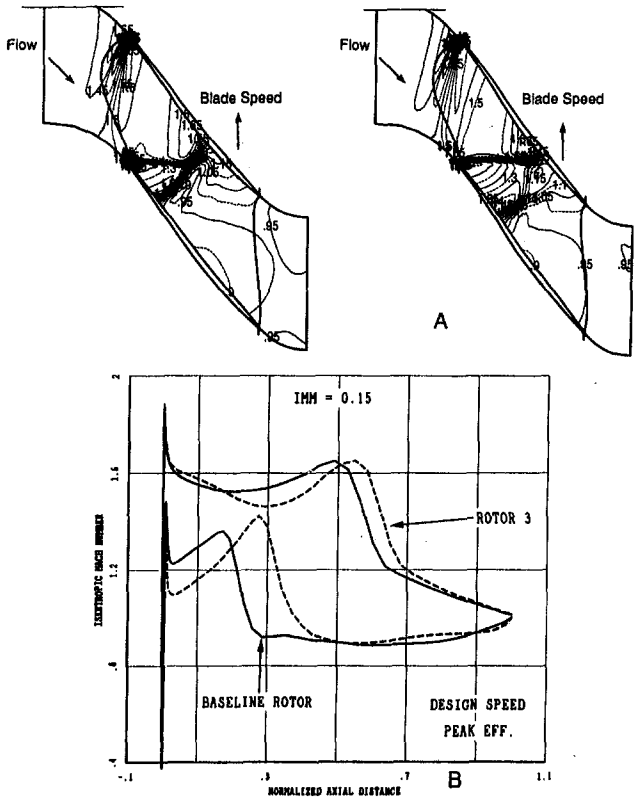

Fig. 11 Comparison of the shock structure and the blade surface isentropic Mach number distribution between the baseline and Rotor 3

Comparison of the calculated radial profiles of efficiency (not shown here) indicate the baseline rotor to be more efficient in the top 40 percent of the blade. The calculated performance difference predicts the baseline rotor to be about 0.35 points better relative to 1.2 points measured in the test.

The comparison of the circumferential variation of the loss coefficient from the pressure surface to the suction surface at the trailing edge is shown in Fig. 15(a). The combined effect of the leading edge detached shock and the overexpanded second shock results in a larger loss coefficient near the blade suction surface for Rotor 3. However, the major penalty in performance is due to the unstarted leading edge shock on Rotor 3 as shown in Fig. 15(b) where the loss begins to accumulate much farther upstream of the leading edge.

While some of the poor performance of Rotor 3 can be attributed to its smaller throat, it seems likely that the consequently higher internal contraction also limits the efficiency at lower speeds by causing the shock to be unstarted.

Summary of Throat Margin Effects. Designers are primarily concerned that the throat margin is sufficient to swallow design flow. The results of the experiments and analysis presented here suggest that the amount of throat margin is critical to the overall performance of the transonic rotor. Low levels of throat margin can produce higher efficiencies at design point, due to shock positioning in the passage, but will result in an unstarted condition at speeds below design negatively impacting efficiency. Higher levels of throat margins will result in reduced design point efficiency, but allow the shock to be started at part speed operation thereby producing higher efficiency at part speed.

Rotor 3 and Rotor 4 Internal Contraction Comparisons. Rotor 4 had the highest design speed peak efficiency of all rotors tested as shown in Fig. 7 and has been the subject of considerable analysis. Some of the detailed three-dimensional

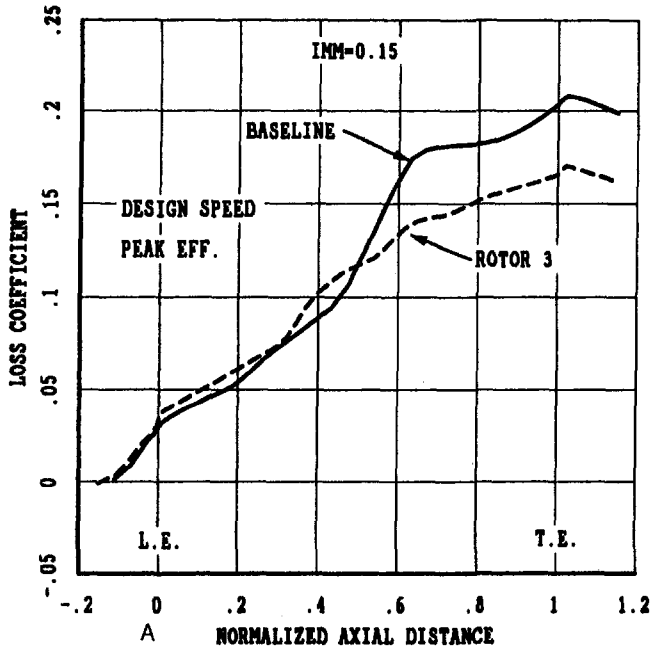

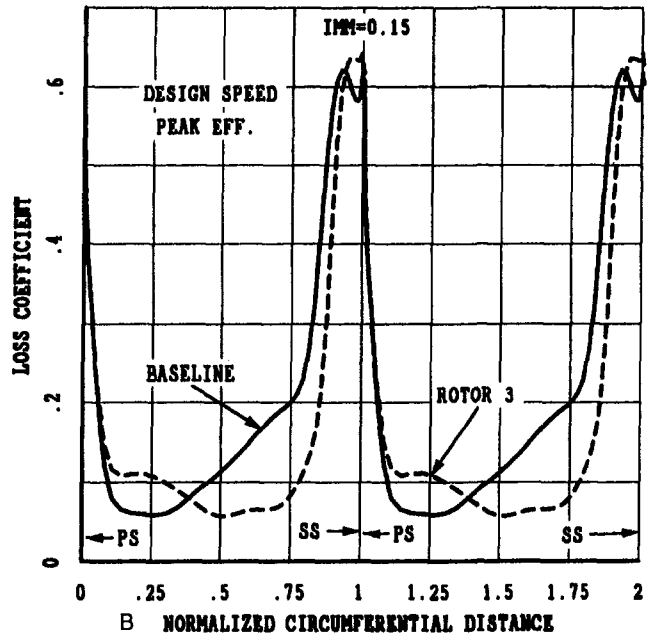

Fig. 12 Comparison of: (*a*) circumferential variation of loss coefficient between two adjacent blades, and (*b*) accumulation of loss from upstream of the leading edge to downstream of trailing edge; between baseline and Rotor 3

studies are discussed in the papers by Hah and Puterbaugh (1990) and Copenhaver et al. (1993). To avoid duplication, only some pertinent three-dimensional results are discussed in this paper.

Both the rotors had lower throat margins than the baseline and Rotor 4 had slightly more internal contraction relative to Rotor 3 as was shown in Fig. 2(*b*). The calculated three-dimensional shock structure for Rotor 4 was very similar to Rotor 3 at both design and 90 percent speeds at peak efficiency. The leading edge shock on Rotor 4 was unstarted (like Rotor 3) at 90 percent speed with an overexpanded second shock at the trailing edge. Even though the internal contraction differences between Rotor 3 and Rotor 4 were small (Fig. 2(*b*)), the three-dimensional calculations were able to distinguish between the performance of the rotors at design and 90 percent speeds. The

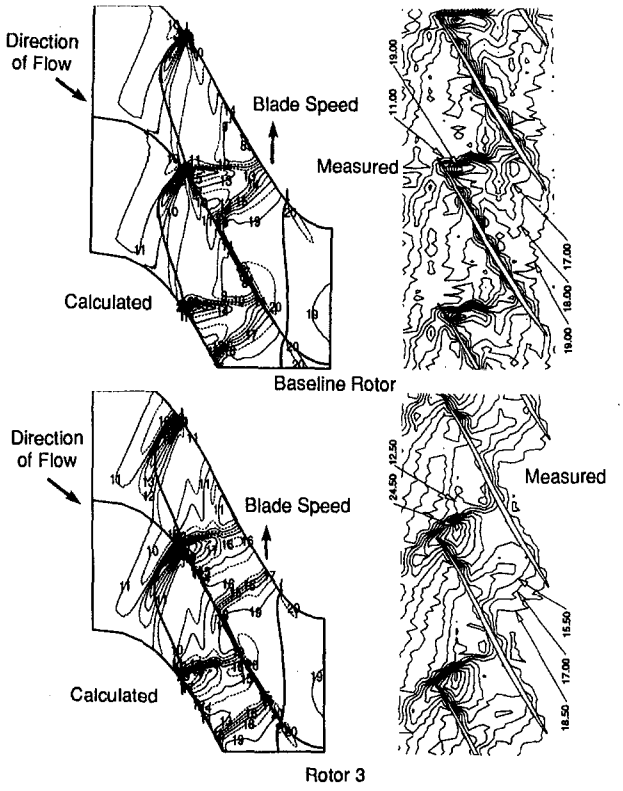

Fig. 13 Comparisons of calculated and measured tip static pressures for baseline rotor and Rotor 3 at 90 percent speed, peak efficiency

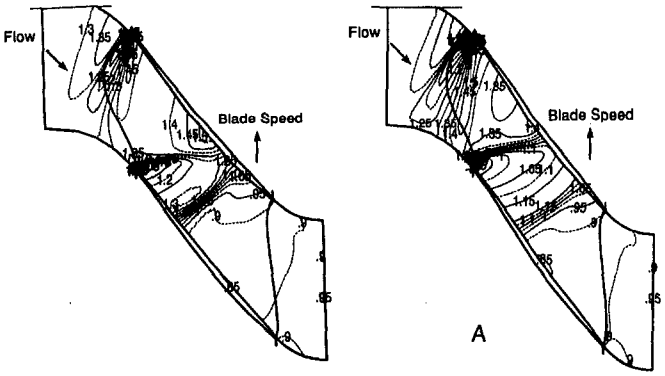

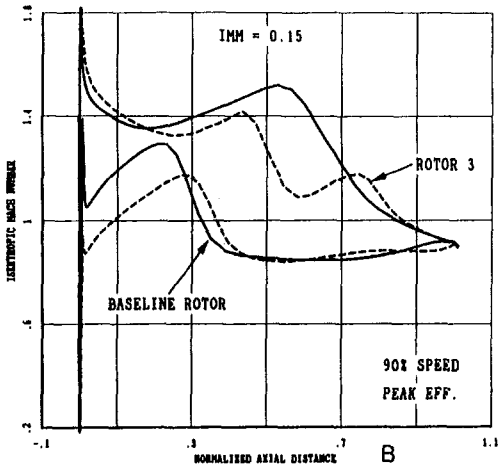

Fig. 14 Comparison of the blade shock structure and the blade surface isentropic Mach number distribution between the baseline rotor and Rotor 3 at 90 percent speed

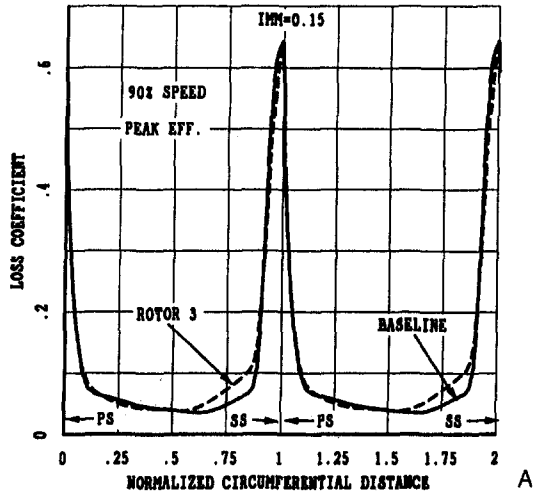

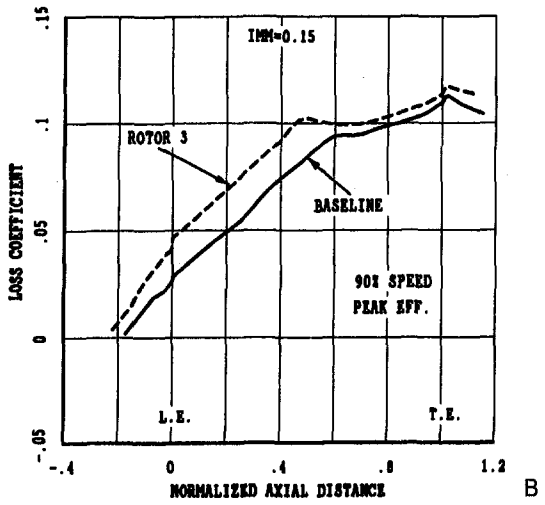

Fig. 15 Comparison of: (*a*) circumferential variation of loss coefficient at the trailing edge and (*b*) accumulation of loss from inlet to exit; between the baseline rotor and Rotor 3 at 90 percent speed

higher contraction Rotor 4 showed about 0.32 points better efficiency at high speed and 0.33 points lower efficiency at 90 percent speed relative to Rotor 3. These differences are small and difficult to detect experimentally. The test data do show trends that match the computation, although the absolute differences (0.2) were slightly less than the experimental uncertainty at a 95 percent confidence level. This may suggest that the uncertainty calculations are somewhat conservative. While both rotors are unstarted at part speed, Rotor 4, due to its larger internal contraction, has the detached shock standing further upstream of the leading edge. Most of the performance differences occur in the top half of the blades.

The measured and calculated results reinforce the fact that higher internal contraction configurations do perform very well at design speed if they achieve a started shock pattern as was the case for both rotors. However, at lower speeds, the blades may run into an unstart condition, which is detrimental to the overall performance as illustrated by the calculations and test data.

Baseline Rotor and Rotor 5 "Effective Camber" Comparisons

Design Speed. Figure 16 shows the calculated isentropic Mach number contours and the corresponding blade surface Mach number distribution at 15 percent immersion for the baseline rotor and Rotor 5. A two-shock system is observed with the leading edge oblique shock slightly stronger in the baseline blade. The suction surface Mach number just ahead of the shock is also calculated to be higher in the baseline rotor. The pressure surface shock is stronger for the baseline rotor. Due to the reduction in trailing edge effective camber, the locations of the pressure and suction surface shocks are about 5 percent upstream for Rotor 5 relative to the respective shocks for the baseline airfoil.

The analysis indicates that the improvement in efficiency on Rotor 5 occurs over almost the entire annulus height. The boundary layer behavior near the pressure surface at the trailing edge is very similar for both rotors, as indicated in Fig. 17(*a*). The figure suggests that Rotor 5 has less loss near the suction surface than the baseline rotor. Rotor 5 has the straighter suction surface downstream of the throat to the trailing edge (Fig. 4) and this results in an improved boundary layer on the suction surface after the shock. Rotor 5 has a lower loss coefficient in the wake and the shock/suction side boundary layer interaction is improved because of the lower upstream Mach number. The circumferentially averaged distribution of the loss coefficient shown in Fig. 17(*b*) illustrates the improvement in the boundary layer characteristics on the less cambered blade downstream of the shock that occurs at about 60 percent axial distance. The loss coefficient on the baseline rotor increases from 80 percent to the trailing edge where as it stays approximately constant for Rotor 5. No separated flow region in the suction surface boundary layer was calculated on Rotor 5.

The three-dimensional viscous calculations at design speed peak efficiency indicate that Rotor 5's efficiency is 0.85 points better than that of the baseline rotor, which is in close agreement with the test data (1.0 point). The slight increase in shock strength and the separated flow downstream of the shock in the suction surface boundary layer is primarily responsible for the lower efficiency on the baseline rotor.

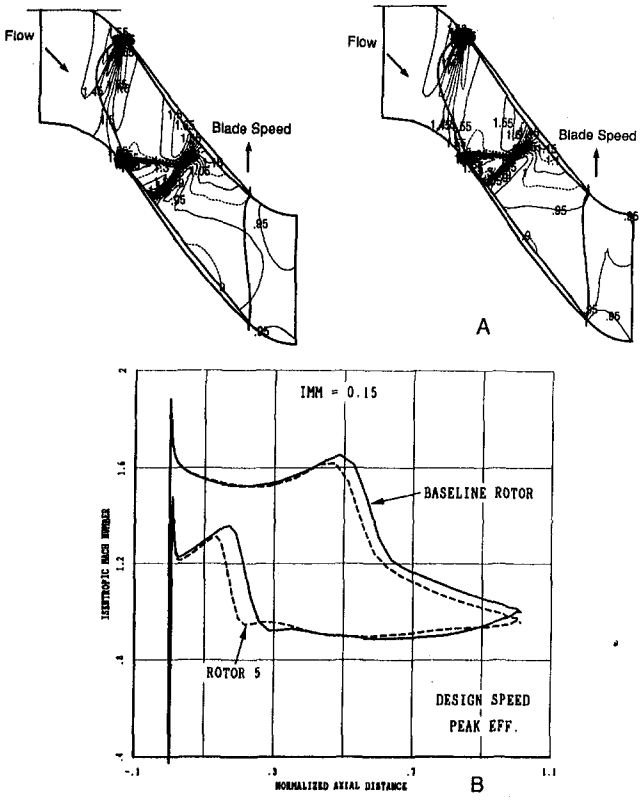

Fig. 16 Comparison of the shock structure and the blade surface isentropic Mach number distribution between the baseline and Rotor 5

90 Percent Speed. Figure 18 shows the calculated isentropic Mach number contours and the corresponding blade surface Mach number distribution at 15 percent immersion. The figure shows a two-shock system with lower Mach numbers than seen at design speed. The upstream Mach number before the shock on both surfaces is lower for Rotor 5 and the shocks occur about 5 percent upstream of the shocks on the baseline rotor. Rotor 5's calculated efficiency is 0.2 points better relative to the baseline rotor, which is in good agreement with the measured performance difference of 0.34 points. The calculated difference in performance between the baseline rotor and Rotor 5 at 90 percent speed (0.2 points) is less than that at design speed (1.0 point). Since the shocks are weaker at the part-speed condition, the boundary layer separation on the baseline rotor observed at design speed does not occur. This is illustrated in Fig. 19(*a*) where most of the relative reduction in loss coefficient at the trailing edge occurs in the free stream region of Rotor 5 which can be attributed to its lower shock losses. While the wake is slightly thinner for Rotor 5, the considerable increase in loss coefficient near the suction surface of the baseline rotor at design speed (Fig. 17(*a*)) is no longer present at part speed. The growth of the loss coefficient shown for both rotors (Fig. 19(*b*)) shows the circumferentially averaged loss to be slightly lower downstream of the shock on Rotor 5. The boundary layer tends to show some improvement through the lower trailing edge camber region of Rotor 5 while it seems to grow uniformly from 60 percent to the trailing edge for the baseline rotor.

The three-dimensional calculations and the test data suggest that the improvement in efficiency for Rotor 5 is most likely due to its lower shock losses and the reduced shock boundary layer interaction. The shocks are started on both blades at the part-speed condition and hence there is lower penalty in performance of these two rotors relative to Rotors 3 and 4 as measured in the test. The improvements in efficiency with the lower trailing edge camber in Rotor 5 did materialize as expected without any of the possible penalty in stall margin that was of concern during the design process.

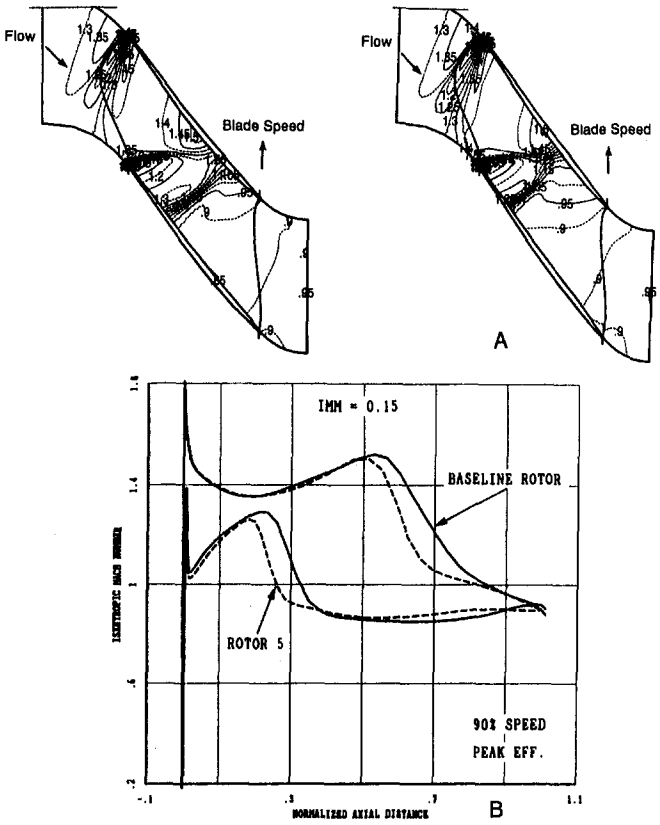

Fig. 18 Comparison of the shock structure and the blade surface isentropic Mach number distribution between the baseline and Rotor 5 at 90 percent speed

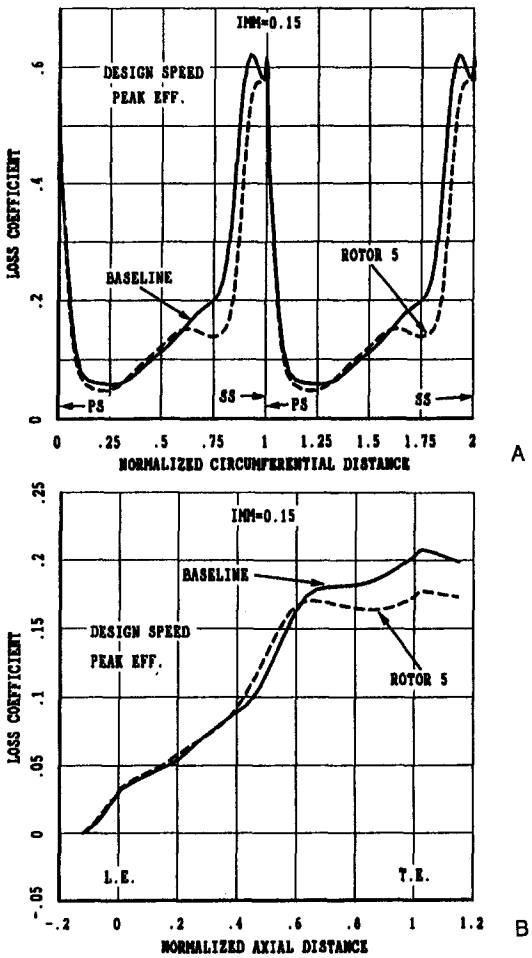

Fig. 17 Comparison of: (*a*) circumferential variation of loss coefficient at the trailing edge and (*b*) accumulation of loss from inlet to exit; between baseline and Rotor 5 at design speed

Summary of Effective Camber Effects. For the designer, effective camber can be useful tool to tailor the part-speed performance of a transonic rotor, without significantly affecting stall margin and still maintaining acceptable design point operation. The experimental results and the analysis show these improvements are possible and they demonstrate that shock position and strength can be altered through the use of trailing edge camber.

Concluding Remarks

Both experimental and detailed analytical results of an investigation of the influence of cascade area ratios on low aspect ratio transonic rotor performance have been presented.

Some conclusions arrived at from the research described in this paper are as follows:

1 Small changes in meanline angles and consequently the airfoil shapes and passage area ratios significantly affect the performance trends of transonic bladerows.

2 A reduction in throat margin increases high-speed performance, but some of the higher internal contraction associated with small throats results in considerably lower part-speed efficiencies as illustrated by the comparisons between the baseline rotor and Rotor 3. The stall line, however, appears to be positively affected (improved stall margin) across the entire op-

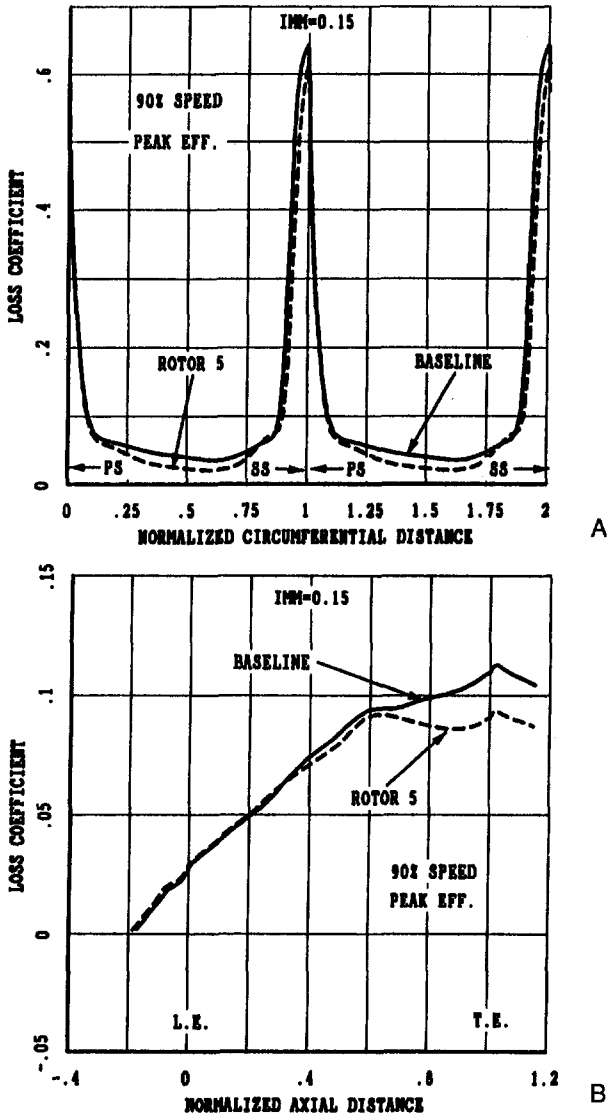

Fig. 19 Comparison of: (*a*) circumferential variation of loss coefficient at the trailing edge and (*b*) accumulation of loss from inlet to exit; between the baseline and Rotor 5 at 90 percent speed

erating range with tight throats that do not result in the flow being choked.

3 Changes in the shape of the suction surface before the shock, which also result in higher internal contraction, improve high-speed efficiency at the cost of part-speed performance as shown by the comparison between Rotors 3 and 4.

4 Lowering the blade trailing edge effective camber results in an improvement in peak efficiency level without significantly lowering the stall line as illustrated by the comparison between the baseline rotor and Rotor 5.

One implication of the study is that the designer can use cascade area ratios very effectively to tailor the design to suit any operating condition requirement. If the engine cycle requires a single point performance target, a design similar to Rotor 4 with tight throats and high internal contraction is very appealing. However, if good performance is to be maintained over a wide range of operating conditions, the merits of Rotor 5 become obvious. With the advent of three-dimensional analysis tools, the consequences of changing area ratios seem to be predicted well.

Acknowledgments

The authors would like to acknowledge the support of all the individuals in the Compressor Aero Research Lab at Wright Patterson AFB for their efforts in performing the experiments presented in this paper. Without their dedication to excellence this research would not be possible. The authors would also like to thank the management at General Electric Aircraft Engine (GEAE) and Wright Laboratory for approving this work for publication. We would also like to specifically acknowledge the assistance of Curt Koch, GEAE, for his insightful comments and suggestions with regard to this paper.

References

Copenhaver, W. W., Hah, C., and Puterbaugh, S. L., 1993, "Three-Dimensional Flow Phenomena in a Transonic, High-Through-Flow, Axial-Flow Compressor Stage," ASME JOURNAL OF TURBOMACHINERY, Vol. 115, pp. 240–248.

Hah, C., and Puterbaugh, S. L., 1990, "A Critical Evaluation of a Three-Dimensional Navier–Stokes Method as a Tool to Calculate Transonic Flows Inside a Low-Aspect-Ratio Compressor," AGARD Conference Proceedings 510, CFD Techniques for Propulsion Applications, pp. 10-1–10-14.

Jennions, I. K., and Turner, M. G., 1993a, "Three-Dimensional Navier–Stokes Computations of Transonic Fan Flow Including a Novel Implementation of an Implicit $k-\epsilon$ Turbulence Model," ASME JOURNAL OF TURBOMACHINERY, Vol. 115, pp. 249–261.

Jennions, I. K., and Turner, M. G., 1993b, "Three-Dimensional Navier–Stokes Computations of Transonic Fan Flow Using an Explicit-Flow Solver and an Implicit $k-\epsilon$ Solver," ASME JOURNAL OF TURBOMACHINERY, Vol. 115, pp. 261–272.

Kantrowitz, A., 1950, "The Supersonic Axial Flow Compressor," NACA Report 974, 1950.

Klapproth, J. F., 1961, "A Review of Supersonic Compressor Development," ASME *Journal of Engineering for Power,* Vol. 83, No. 2, pp. 258–268.

Law, C. H., and Wadia, A. R., 1993, "Low Aspect Ratio Transonic Rotors: Part 1—Baseline Design and Performance," ASME JOURNAL OF TURBOMACHINERY, Vol. 115, No. 2, pp. 218–225.

Parker, D. E., and Simonson, M. R., 1982, "Transonic Fan/Compressor Rotor Design Study, Vols. IV, V, VI," AFWAL-TR-82-2017.

Sellin, M. D., Puterbaugh, S. L., and Copenhaver, W. W., 1993, "Tip Shock Structures in Transonic Compressor Rotors," AIAA Paper No. 93-1869.

Smith, L. H., and Yeh, H., 1962, "Sweep and Dihedral Effects in Axial Flow Turbomachinery," ASME Paper No. 62-WA-102.

Wadia, A. R., and Law, C. H., 1993, "Low Aspect Ratio Transonic Rotors: Part 2—Influence of Location of Maximum Thickness on Transonic Compressor Performance," ASME JOURNAL OF TURBOMACHINERY, Vol. 115, pp. 226–239.

Wennerstrom, A. J., 1994, "Experimental Study of a High-Through-Flow Transonic Axial Compressor Stage," ASME *Journal of Engineering for Gas Turbines and Power,* Vol. 106, pp. 552–560.

Validation of Three-Dimensional Euler Methods for Vibrating Cascade Aerodynamics

G. A. Gerolymos

I. Vallet

LEMFI, URA CNRS,
Université Pierre and Marie Curie,
Orsay, Paris, France

The purpose of this work is to validate a time-nonlinear three-dimensional Euler solver for vibrating cascades aerodynamics by comparison with available theoretical semi-analytical results from flat-plate cascades. First the method is validated with respect to the purely two-dimensional theory of Verdon (for supersonic flow) by computing two-dimensional vibration (spanwise constant) in linear three-dimensional cascades. Then the method is validated by comparison with the theoretical results of Namba and the computational results of He and Denton, for subsonic flow in a linear three-dimensional cascade with three-dimensional vibratory mode. Finally the method is compared with results of Chi from two subsonic rotating annular cascades of helicoïdal flat plates. Quite satisfactory agreement is obtained for all the cases studied. A first code-to-code comparison is also presented.

1 Introduction

Predictive methods for turbomachinery aeroelastic stability have evolved from semi-analytical two-dimensional flat-plate cascade theories (Lane, 1957; Verdon, 1973, 1975, 1977a, b; Verdon and McCune, 1975; Goldstein et al., 1977; Adamczyk and Goldstein, 1978; Ni, 1979; Surampudi and Adamczyk, 1986; Whitehead, 1987) toward time-linearized potential or Goldstein-split (Goldstein, 1978) methods (Verdon and Caspar, 1982, 1984; Whitehead, 1990; Verdon, 1989a, b, 1992, 1993; Usab and Verdon, 1991; Hall, 1993). Methods have later appeared based on the time-nonlinear two-dimensional Euler equations (Gerolymos, 1988; He, 1990; Carstens, 1991; Huff, 1992; Carstens et al., 1993), eventually with boundary-layer correction (He and Denton, 1993a, b), time-linearized two-dimensional Euler equations (Hall and Clark, 1993) and Navier–Stokes solvers (Siden, 1991). The undeniable importance of three-dimensional effects for practical turbomachinery configurations has led to the development of three-dimensional methods. Theoretical semi-analytical methods have been developed for helicoïdal flat-plate cascades (Namba and Ishikawa, 1983; Salaün, 1987; Namba, 1987; Kodoma and Namba, 1990; Chi, 1993). Methods based on the three-dimensional Euler equations have been developed using both time-nonlinear (Gerolymos, 1988, 1993; He and Denton, 1994) and time-linearized (Hall and Lorence, 1993; Hall and Clark, 1993) formulations. He and Denton (1994) also presented results using a thin shear-layer Navier–Stokes solver with Denton's mixing-length turbulence model (Denton, 1992).

Quite a lot of work has been done for the validation of two-dimensional methods for which there exist well-documented experimental and semi-analytical test cases (Bölcs and Fransson, 1986; Fransson and Verdon, 1991). On the contrary very few such data exist for three-dimensional cascades. With the exception of some proprietary on-engine measurements (Halliwell et al., 1984) there are virtually no three-dimensional experimental data available for code validation. The only alternatives are comparisons with theoretical semi-analytical results or code-to-code comparisons.

Contributed by the International Gas Turbine Institute and presented at the 39th International Gas Turbine and Aeroengine Congress and Exposition, The Hague, The Netherlands, June 13–16, 1994. Manuscript received by the International Gas Turbine Institute February 25, 1994. Paper No. 94-GT-294. Associate Technical Editor: E. M. Greitzer.

The purpose of this paper is to validate an existing three-dimensional time-nonlinear Euler code (Gerolymos, 1993) through comparison with theoretical semi-analytical solutions.

2 A Note on the Numerical Method

The unsteady flow due to a prescribed traveling-wave vibration of the blades is computed by numerical integration of the unsteady three-dimensional Euler equations

$$\frac{\partial \rho}{\partial t} + \nabla\cdot(\rho\mathbf{W}) = 0$$

$$\frac{\partial \rho\mathbf{W}}{\partial t} + \nabla(\rho\mathbf{W}\otimes\mathbf{W}) + 2\rho\Omega\times\mathbf{W} + \rho\nabla\left(-\frac{\Omega^2R^2}{2}\right) = -\nabla p$$

$$\frac{\partial(\rho H_R - p)}{\partial t} + \nabla\cdot(\rho H_R\mathbf{W}) = 0$$

$$p = \rho R_g T = \rho\frac{\gamma-1}{\gamma}h = \rho(\gamma-1)e \qquad (1)$$

where ρ is the density, t the time, ∇ the gradient operator, $\mathbf{W}$ the relative flow velocity, H_R the rothalpy ($H_R = h + \frac{1}{2}W^2 - \frac{1}{2}(\Omega R)^2$), h the static enthalpy, Ω the rotational velocity, R the radius with respect to the rotation axis, p the static pressure, T the static temperature, R_g the gas constant, and γ the isentropic exponent.

The method uses a space-centered finite-volume scheme and a five-stage Runge–Kutta integration procedure, which is the three-dimensional extension of the two-dimensional scheme developed by Venkatakrishnan and Jameson (1988). The code was described in detail by Gerolymos (1993) and will not be repeated here. There are only two slight modifications in the code used to obtain the results presented in this paper:

1 The fourth-order smoothing operator is applied only at the end of the Runge–Kutta procedure, and the second-order nonlinear dissipation operator, which is applied at every Runge–Kutta stage, is applied on all variables, as in Gerolymos (1988). This modified dissipation operator with coefficients $q_2 = 0.7$ and $q_4 = 0.03$, for the second order and the fourth order, respectively, gives smoother pressure distributions, eliminating some wiggles present in the results of the original code (Gerolymos, 1993) without significantly altering the results.

Table 1 Configurations studied

case	Verdon_A	Namba	Chi_D	Chi_B
configuration	linear untwisted flat-plate cascade	linear untwisted flat-plate cascade	annular helicoïdal flat-plate wide-chord rotor	annular helicoïdal flat-plate high aspect-ratio rotor
stacking-axis locus	midchord	leading-edge	leading-edge	midchord
N_{blades}	∞	∞	15	30
Ω(RPM)	0	0	265.1	250.29
R_{hub} or z_{hub} (m)	0.	0.	0.35	0.4
R_{tip} or z_{tip} (m)	0.02	0.3	1.	1.
$\theta_{stg,hub}$	59.53°	45°	29.20°	44.70°
$\theta_{stg,tip}$ (deg)	59.53°	45°	67.95°	68°
$M_{rel,hub}$	1.345	0.7	0.57	0.421
$M_{rel,tip}$	1.345	0.7	0.942	0.801
χ_{hub} (m)	0.1	0.1	0.33	0.097
χ_{tip} (m)	0.1	0.1	0.33	0.18
vibratory mode	spanwise constant-amplitude torsion around midchord	spanwise linearly-varying-amplitude torsion around leading-edge	spanwise linearly-varying-amplitude torsion around leading-edge	first-bending mode shape of a cantilever beam
f(Hz)	376.4	361.7	63.3	48.3
β_r (deg)	0°, 180°	0°, 180°	0°	72°

2 Instead of using a moving-grid formulation of the finite-volume discretization by including the grid-velocities in the computation of the fluxes, the grid-projection method described in Gerolymos (1988) was used, because it does not require the accurate computation of grid velocities, but only of grid positions. This option was preferred because the computation of grid velocities in nonharmonically deforming grids is not simple (the grid displacement procedure used is based on the blade positions and not on the blade velocities). In this conjunction it is noted that the exact nonlinear motion was imposed whenever applicable and not the corresponding first harmonics of the displacements, although tests presented in section 3.3 show that, for small amplitudes, the difference in results is insignificant.

The inflow and outflow boundary conditions used for all the computations presented in this work were one-dimensional nonreflecting boundary conditions (Hedstrom, 1979) and have been described in Gerolymos (1993).

3 Results

3.1 Configurations Studied. In order to validate the three-dimensional code, four configurations for which theoretical data are available were studied:

1 A two-dimensional test case for a supersonic linear cascade of untwisted flat plates (Verdon_A cascade).

2 A test case with two-dimensional steady flow, but three-dimensional unsteady flow, through a subsonic linear cascade of untwisted flat-plates (Namba cascade) which has also been studied computationally by He and Denton (1994).

3 A three-dimensional test-case for a subsonic wide-chord rotor of helicoïdal flat plates (Chi_D cascade).

4 A three-dimensional test case for a subsonic large aspect-ratio rotor of helicoïdal flat plates (Chi_B cascade).

Details on these four configurations are given in Table 1.

3.2 Linear Verdon_A Cascade With Two-Dimensional Torsional Vibratory Mode. This is a well-known test case introduced by Verdon (1973) and Verdon and McCune (1975), which has been used by many authors (Fleeter and Hoyniak, 1989; Gerolymos et al., 1990; Whitehead, 1990) and is included in the 8. standard configuration of the updated version of the Standard Aeroelastic Configurations (Bölcs and Fransson, 1986; Fransson and Verdon, 1991). This is a flat-plate cascade at zero incidence, with an upstream Mach number M = 1.345, solidity $\sigma = 1.267$, and stagger angle (with respect to the axial direction) $\theta_{stg} = 59.53$ deg $= \beta$ (where β is the flow angle).

The vibratory motion is torsion around midchord (in the present work the three-dimensional code was used to compute this purely two-dimensional configuration):

$$z(t) = {}^{o}z$$

$$x(t) = {}^{o}x + [{}^{o}x - x_{TC}({}^{o}z)] \cos [\alpha({}^{o}z) \cos \omega t] - [{}^{o}y - y_{TC}({}^{o}z)] \sin [\alpha({}^{o}z) \cos \omega t]$$

$$y(t) = {}^{o}y + [{}^{o}x - x_{TC}({}^{o}z)] \sin [\alpha({}^{o}z) \cos \omega t] + [{}^{o}y - y_{TC}({}^{o}z)] \cos [\alpha({}^{o}z) \cos \omega t] \quad (2)$$

where x, y, z is a Cartesian coordinate system with origin at midchord of the hub section (x in the axial direction and z in the spanwise direction), $\alpha({}^{0}z)$ the torsional vibration amplitude ($\alpha({}^{0}z) = 1$ deg, $\forall {}^{0}z$), $\omega = 2\pi f$ the vibration frequency, $x_{TC}({}^{0}z) = 0$, and $y_{TC}({}^{0}z) = 0$, $\forall {}^{0}z$ the coordinates of the torsional center (located at midchord), and the superscript ${}^{0}(\ )$ denotes the undeflected blade position. The blade height was arbitrarily taken to be $\frac{1}{5}$ of the chord $\chi = 100$ mm (arbitrarily chosen). The flowfield was discretized using an 121 × 25 × 5 computational grid (axial × transverse × spanwise). The number of points in the spanwise direction is of no importance, since both the steady and unsteady flow are strictly two dimensional and computational results were identical at every spanwise station. In order to compare with the results presented in Verdon and McCune (1975) computations were run for two interblade phase angles $\beta_r = 0$ deg and $\beta_r = 180$ deg at a compressible reduced frequency $2\pi f\chi M/(M^2 - 1)V = 1$, which for a total temperature $T_t = 288$ K corresponds to a frequency $f = 376.4$ Hz and a Strouhal number $\mathrm{Sr}_\chi = f\chi/V = 0.096$. The corresponding resonance interblade phase angles (Whitehead, 1987) are $\beta_{res,1} =$

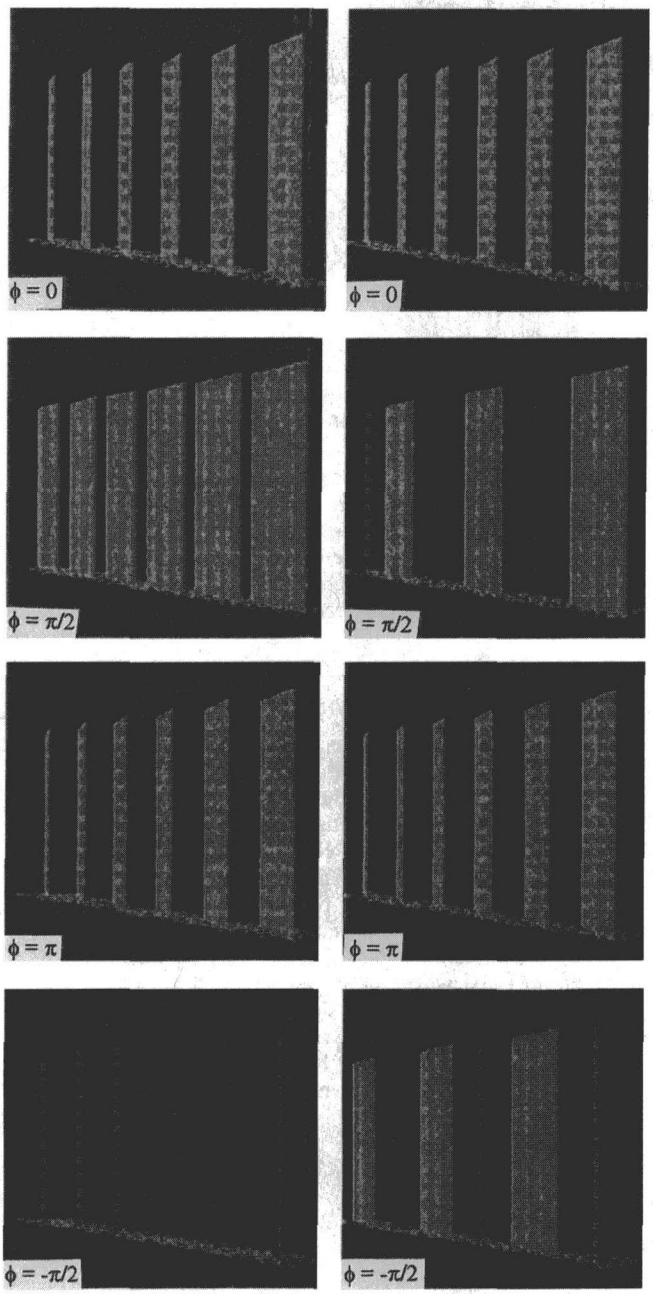

Fig. 1 Schematic of Verdon_A cascade torsional vibration at (*a*) $\beta_r = 0$ deg and (*b*) $\beta_r = 180$ deg

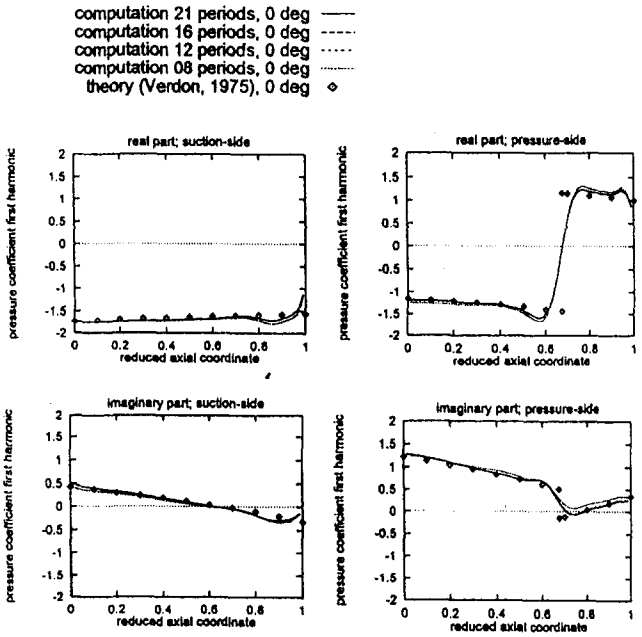

Fig. 2 Unsteady pressure distribution (real and imaginary part) for Verdon_A cascade torsional vibration at $\beta_r = 0$ deg; present numerical computation and analytical theory (Verdon and McCune, 1975)

-85.39 deg and $\beta_{res,2} = -19.35$ deg and hence both computed interblade phase angles $\beta_r = 0$ deg and $\beta_r = 180$ deg are in the subresonant region where propagating waves occur. The torsional vibration amplitude used for the numerical computations was $\alpha = 1$ deg.

The vibratory modes for $\beta_r = 0$ deg and $\beta_r = 180$ deg are presented in Fig. 1 with an amplitude exaggerated 20 times. For the purpose of legibility the blades' spanwise height in Fig. 1 is also 15 times greater than the actual one (very short blades were used in the computation). In Fig. 2 are compared computed and theoretical results of the unsteady pressure coefficient ${}^1C_p = {}^1p/(\frac{1}{2}\rho V^2\alpha)$ distributions, for $\beta_r = 0$ deg. The computational results were identical at every spanwise station. The agreement is quite satisfactory, with the exception of the smearing of the linearized theory discontinuity on the pressure side. Computational results are plotted after the numerical simulation of 8, 12, 16, and 21 periods in order to illustrate the unsteady convergence of the results, which can be considered converged after the simulation of 12 periods. In Fig. 3 are compared computed and theoretical unsteady pressure jump coefficient distributions $\Delta^1C_p = ({}^1C_{p_{\text{pressure}}} - {}^1C_{p_{\text{suction}}})$, for $\beta_r = 180$ deg. Computed results are plotted after the numerical simulation of 8, 16, and 24 periods, showing that the results are practically converged after the numerical simulation of eight periods. Again the computational results agree well with theory, with the exception of the discontinuity smearing.

In Fig. 4 are plotted the unsteady pressures $p(t)/p_t$ where p_t is the steady inflow total pressure) for $\beta_r = 0$ deg (Fig. 4(*a*)) and $\beta_r = 180$ deg (Fig. 4(*b*)) for four different instants in the vibration period. Note that the color map range for $\beta_r = 180$ deg is twice as wide as that for $\beta_r = 0$ deg because as expected the unsteady pressures are higher for $\beta_r = 180$ deg. For both interblade phase angles the Mach wave emanating from the suction-side trailing edge is clearly visible as alternating compression/expansion waves. Both cases are, as already stated, subresonant and pressure waves propagate with undiminished amplitude both upstream and downstream. Before further discussing Fig. 4, it is useful to remind some results concerning the far field of vibrating cascades (Whitehead, 1987; Verdon,

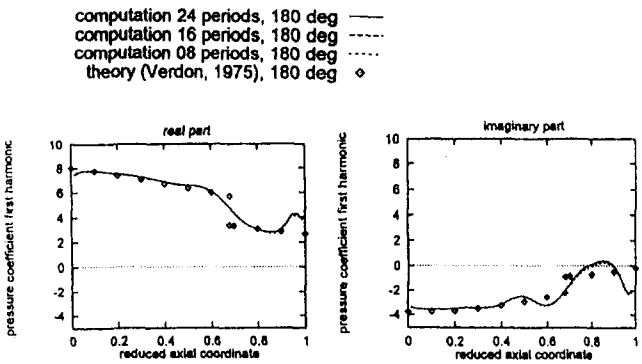

Fig. 3 Unsteady pressure jump distribution (real and imaginary part) for Verdon_A cascade torsional vibration at $\beta_r = 180$ deg; present numerical computation and analytical theory (Verdon and McCune, 1975)

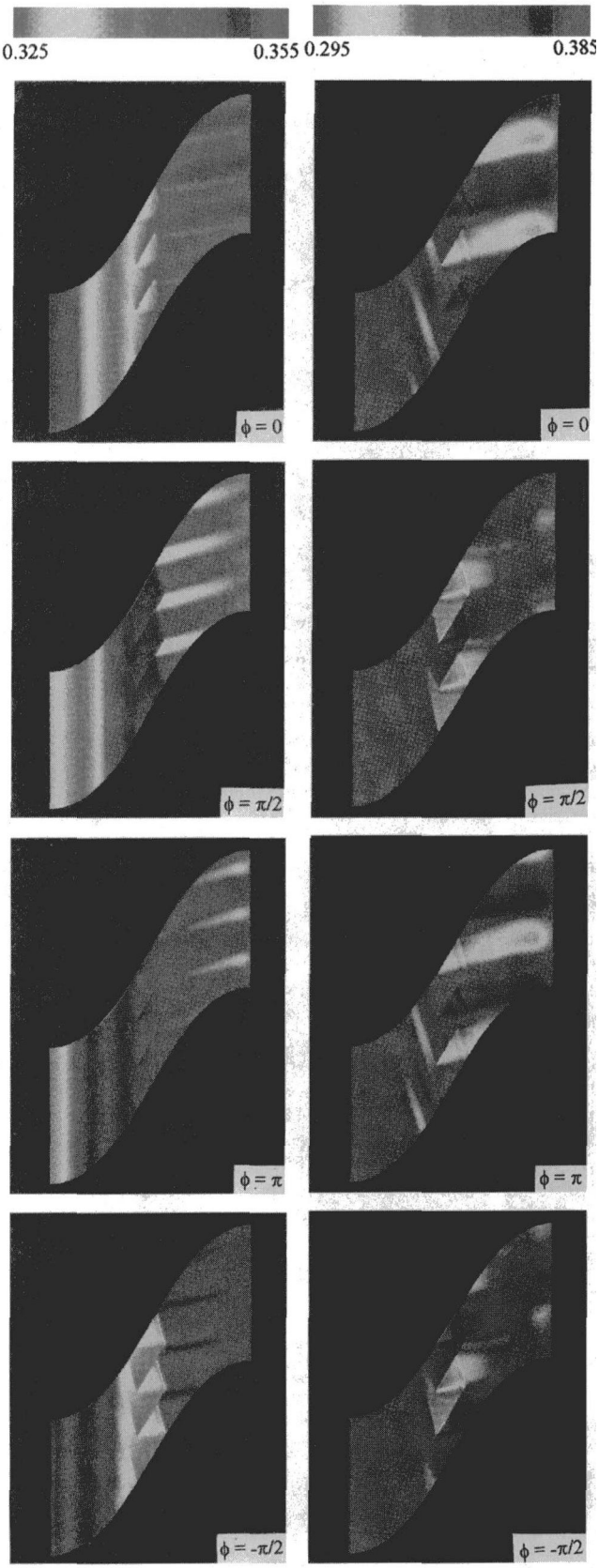

Fig. 4 Unsteady pressure field at various instants for Verdon_A cascade torsional vibration at (*a*) β_r = 0 deg and (*b*) β_r = 180 deg

1989a). Let $\mathbf{k} = (k_x, k_y)$ be the wave vector pointing in the direction of propagation of the waves in the far field of the cascade (x denoting the axial direction, and y the pitchwise direction). The pitchwise wave number k_y is related to the interblade phase angle by $k_y\chi = -\beta_r\,\sigma$, where σ is the solidity of the cascade. Using the dispersion relation of the moving medium wave equation (Whitehead, 1987; Verdon, 1989a) there are two solutions for the axial wave number:

$$k_{x_{1,2}}\chi = -\left(\frac{M_x(\beta_r\sigma M_y + 2\pi M Sr_\chi)}{(1 - M_x^2)} \pm \right.$$

$$\left. \pm \frac{\sqrt{(\beta_r\sigma M_y + 2\pi M Sr_\chi)^2 - (1 - M_x^2)(\beta_r\sigma)^2}}{(1 - M_x^2)}\right) \quad (3)$$

where $M_x = M\cos\beta$ and $M_y = M\sin\beta$ are the axial and pitchwise Mach numbers, respectively. The corresponding wave-propagation directions are computed by

$$\cos\psi_{1,2} = \frac{k_{x_{1,2}}}{\sqrt{k_{x_{1,2}}^2 + k_y^2}}; \quad \sin\psi_{1,2} = \frac{k_y}{\sqrt{k_{x_{1,2}}^2 + k_y^2}} \quad (4)$$

Considering the Doppler frequency shift for an observer moving with the wave the group Mach number in the axial direction can be computed by (Whitehead, 1987; Verdon, 1989a)

$$(M_{\text{group}_x})_{1,2} = M_x + \frac{k_{x_{1,2}}\chi}{2\pi M Sr_\chi - k_{x_{1,2}}\chi M_x + \beta_r\sigma M_y} \quad (5)$$

whose sign determines whether the waves carry energy in the positive or the negative axial direction.

For $\beta_r = 0$ deg (Fig. 4(*a*)) the waves propagate with a purely axial wave vector. The leading-edge compression/expansion waves merge almost immediately in the entrance region of the cascade resulting to plane axial waves propagating upstream. The downstream propagating pressure waves are different in that their amplitude varies circumferentially. For this case ($\beta_r = 0$ deg) the one-dimensional nonreflecting boundary condition is exact since the waves propagate in the direction normal to the boundaries. For $\beta_r = 180$ deg (Fig. 4(*b*)) the direction of the downstream-propagating waves is at $\psi = -67.59$ deg with respect to the axial direction. Upstream the wave direction is at $\psi = +22.07$ deg with respect to the axial direction, corresponding to a $\beta_r = -180$ deg interblade phase angle and their phase velocity is toward the cascade. Computation of their group velocity, however (Eq. (5)), shows that they correspond to energy propagating upstream ($M_{\text{group},x} = -0.24$). The satisfactory agreement of the computations with theory shows that the one-dimensional nonreflecting boundary conditions perform quite well, and probably the complexity of higher-dimensional boundary conditions is not indispensible (Giles, 1990). This is also corroborated by the satisfactory periodic convergence obtained (Figs. 2 and 3). Analogous conclusions were drawn by Gerolymos et al. (1990) over a wide range of interblade phase angles for Verdon_A cascade.

3.3 Linear Namba Cascade With Three-Dimensional Torsional Vibratory Mode. This is a high-aspect ratio linear cascade of untwisted flatplates at a stagger angle $\theta_{stg} = 45$ deg with respect to the axial direction operating of zero incidence with a Mach number M = 0.7. It was first introduced as a test case by He and Denton (1994) and compared very satisfactorily with their three-dimensional Euler code. The steady flow is purely two dimensional but the vibratory mode used was three dimensional, viz. torsion around the leading edge of the cascade with amplitude linearly varying from the hub (zero amplitude) to the tip:

$$z(t) = {}^oz$$

$$x(t) = {}^ox + [{}^ox - x_{TC}({}^oz)]\cos[\alpha({}^oz)\cos\omega t]$$

$$- [{}^oy - y_{TC}({}^oz)]\sin[\alpha({}^oz)\cos\omega t]$$

$$y(t) = {}^{o}y + [{}^{o}x - x_{TC}({}^{o}z)] \sin [\alpha({}^{o}z) \cos \omega t] + [{}^{o}y - y_{TC}({}^{o}z)] \cos [\alpha({}^{o}z) \cos \omega t] \quad (6)$$

where x, y, z is a Cartesian coordinate system with origin at the leading edge of the hub section (x in the axial direction and z in the spanwise direction), $\alpha({}^{0}z) = \alpha_{\text{tip}}({}^{0}z - z_{\text{hub}})/(z_{\text{tip}} - z_{\text{hub}})$ the torsional vibration amplitude, $\alpha_{\text{tip}} = 1$ deg the torsional vibration amplitude at the tip, $\omega = 2\pi f$ the vibration frequency, $x_{\text{TC}}({}^{0}z) = 0$, and $y_{\text{TC}}({}^{0}z) = 0$, $\forall {}^{0}z$ the coordinates of the torsional center (located at the leading edge), and the superscript ${}^{0}(\ )$ denotes the undeflected blade position. As a consequence the unsteady flow is three dimensional. Theoretical results were available for two interblade phase angles $\beta_r = 0$ deg and $\beta_r = 180$ deg (He and Denton, 1994), at a reduced frequency $2\pi f \chi / V = 1$ which for a chord $\chi = 100$ mm and a total temperature $T_t = 288$ K corresponds to a frequency $f = 361.7$ Hz and a Strouhal number $\text{Sr}_\chi = 0.159$. A tip amplitude $\alpha_{\text{tip}} = 1$ deg was used in the computations (the same amplitude was used by He and Denton, 1994).

A schematic representation of the vibration for $\beta_r = 0$ deg and $\beta_r = 180$ deg is depicted in Figs. 5(a) and 5(b), respectively, with an amplitude exaggerated 20 times. Computed and theoretical results are compared in Fig. 6 for $\beta_r = 0$ deg (Fig. 6(a)) and $\beta_r = 180$ deg (Fig. 6(b)). An $81 \times 25 \times 21$ computational grid was used, and computed results are plotted after the numerical simulation of 8 and 16 vibration periods. It is seen that the computational results are already converged after the numerical simulation of 8 periods. Computed and theoretical distributions of $\Delta^1 C_p = ({}^1p_{\text{pressure}} - {}^1p_{\text{suction}})/(\frac{1}{2}\rho V^2 \alpha_{\text{tip}})$ are in quite satisfactory agreement. For $\beta_r = 0$ deg (Fig. 6(a)) there is a small discrepancy in the $\text{Re}[\Delta^1 C_p]$ distribution near the trailing edge at the tip. However, in this region, $\text{Re}[\Delta^1 C_p] \ll \text{Im}[\Delta^1 C_p]$ so that the overall error in the prediction is small. For $\beta_r = 180$ deg (Fig. 6(b)) there are some discrepancies in the $\text{Im}[\Delta^1 C_p]$ distribution for the near-tip stations. Note that again in this region $\text{Re}[\Delta^1 C_p] \gg \text{Im}[\Delta^1 C_p]$ so that the error in amplitude and phase is small (different scales) are used for the $\text{Re}[\Delta^1 C_p]$ and $\text{Im}[\Delta^1 C_p]$ plots in Fig. 6(b). For both interblade phase angles the leading-edge amplitudes are quite satisfactorily predicted. Computations (not presented) with a grid twice as fine in the spanwise direction ($81 \times 25 \times 41$) gave identical results with Fig. 6.

3.4 Annular Chi_D Cascade With Three-Dimensional Torsional Vibratory Mode. This is a wide-chord rotor with 15 helicoïdal twisted flat plates at zero relative incidence, which are stacked on a straight radial axis at their leading edges. This test case was introduced by Chi (1993) who presented semi-analytical linearized theoretical results. The rotor is in forward flight at $M_{\text{abs}} = 0.5$. The relative tip and hub Mach numbers are $M_{\text{rel,hub}} = 0.57$ and $M_{\text{rel,tip}} = 0.94$, with corresponding relative flow angles (and stagger angles) $\beta_{\text{hub}} = \theta_{stg,\text{hub}} = 29.2$ deg and $\beta_{\text{tip}} = \theta_{stg,\text{tip}} = 67.95$ deg. For the dimensions used in this study (Table 1) the rotor has an angular velocity of 265.1 rpm. The vibratory mode is torsional, around the straight stacking axis, which passes through the leading edge, with amplitude linearly varying from hub (zero amplitude) to tip. For a tip chord $\chi_{\text{tip}} = \chi_{\text{hub}} = 330$ mm the vibration frequency is $f = 63.3$ Hz corresponding to a Strouhal number $\text{Sr}_\chi = 0.127$ ($T_{t,abs} = 288$ K). The vibration amplitude at the tip is $\alpha_{\text{tip}} = 1$ deg. The blade displacement is described by

$$R(t) = {}^{o}R$$

$$x(t) = {}^{o}x + [{}^{o}x - x_{\text{TC}}({}^{o}R)] \cos [\alpha({}^{o}R) \cos \omega t] - [{}^{o}R{}^{o}\theta - {}^{o}R\theta_{\text{TC}}({}^{o}R)] \sin [\alpha({}^{o}R) \cos \omega t]$$

$${}^{o}R\theta(t) = {}^{o}R{}^{o}\theta + [{}^{o}x - x_{TC}({}^{o}R)] \sin [\alpha({}^{o}R) \cos \omega t] - [{}^{o}R{}^{o}\theta - {}^{o}R\theta_{TC}({}^{o}R)] \cos [\alpha({}^{o}R) \cos \omega t] \quad (7)$$

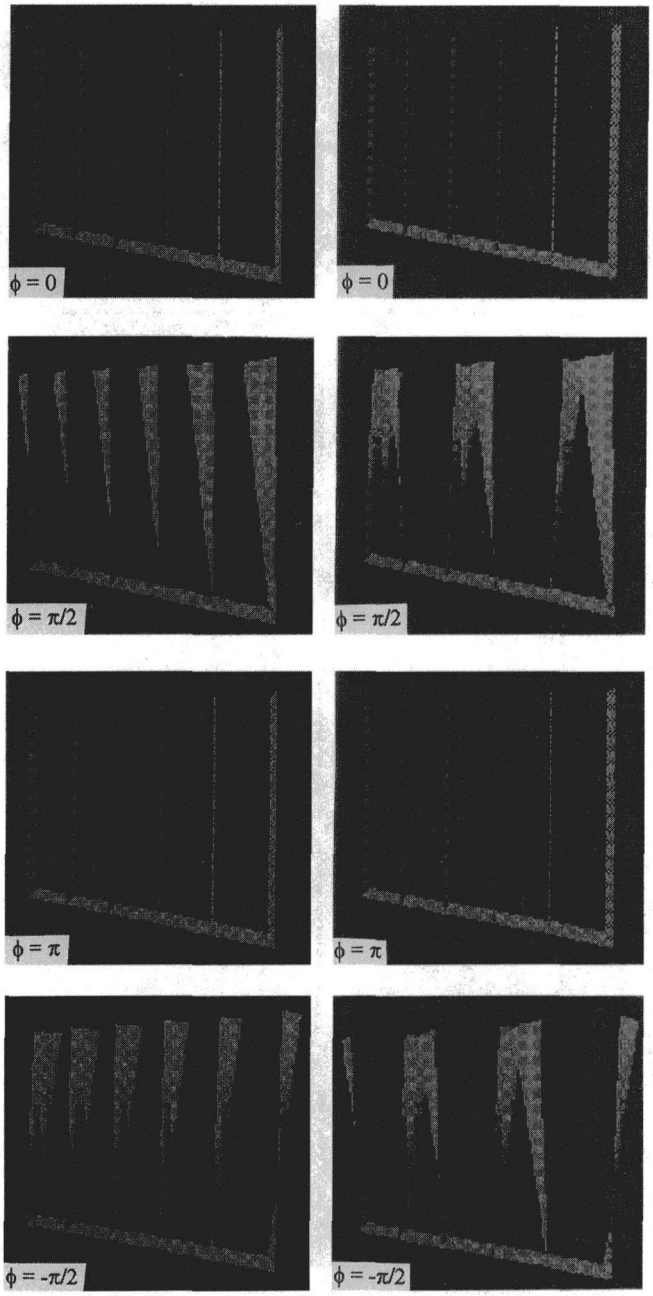

Fig. 5 Schematic of Namba cascade torsional vibration at (a) $\beta_r = 0$ deg and (b) $\beta_r = 180$ deg

where x, R, θ is a cylindrical coordinate system with origin at the leading edge of the hub section (x in the axial direction and z in the spanwise direction), $\alpha({}^{0}R) = \alpha_{\text{tip}}({}^{0}R - R_{\text{hub}})/(R_{\text{tip}} - R_{\text{hub}})$ the torsional vibration amplitude, $\alpha_{\text{tip}} = 1$ deg the torsional vibration amplitude at the tip, $\omega = 2\pi f$ the vibration frequency, and $x_{TC}({}^{0}R) = 0$, ${}^{0}R\theta_{TC}({}^{0}R) = 0$, $\forall {}^{0}R$ the coordinates of the torsional center (at the leading edge), and the superscript ${}^{0}(\ )$ denotes the undeflected blade position. The interblade phase angle is $\beta_r = 0$ deg. The vibratory mode is depicted in Fig. 7 exaggerated 30 times. Computational results using an $121 \times 33 \times 33$ grid and an $81 \times 17 \times 17$ grid for the $\Delta^1 p/\rho W^2 \alpha_{\text{tip}}$ distributions at various spanwise locations are compared with the theoretical ones in Fig. 8 ($W = W({}^{0}R)$ is the relative flow velocity). Computational results are taken after the numerical simulation of 12 periods, which as shown in the convergence test of Fig. 9 (using the coarse grid) are sufficient since computed results are practically converged at four periods. The

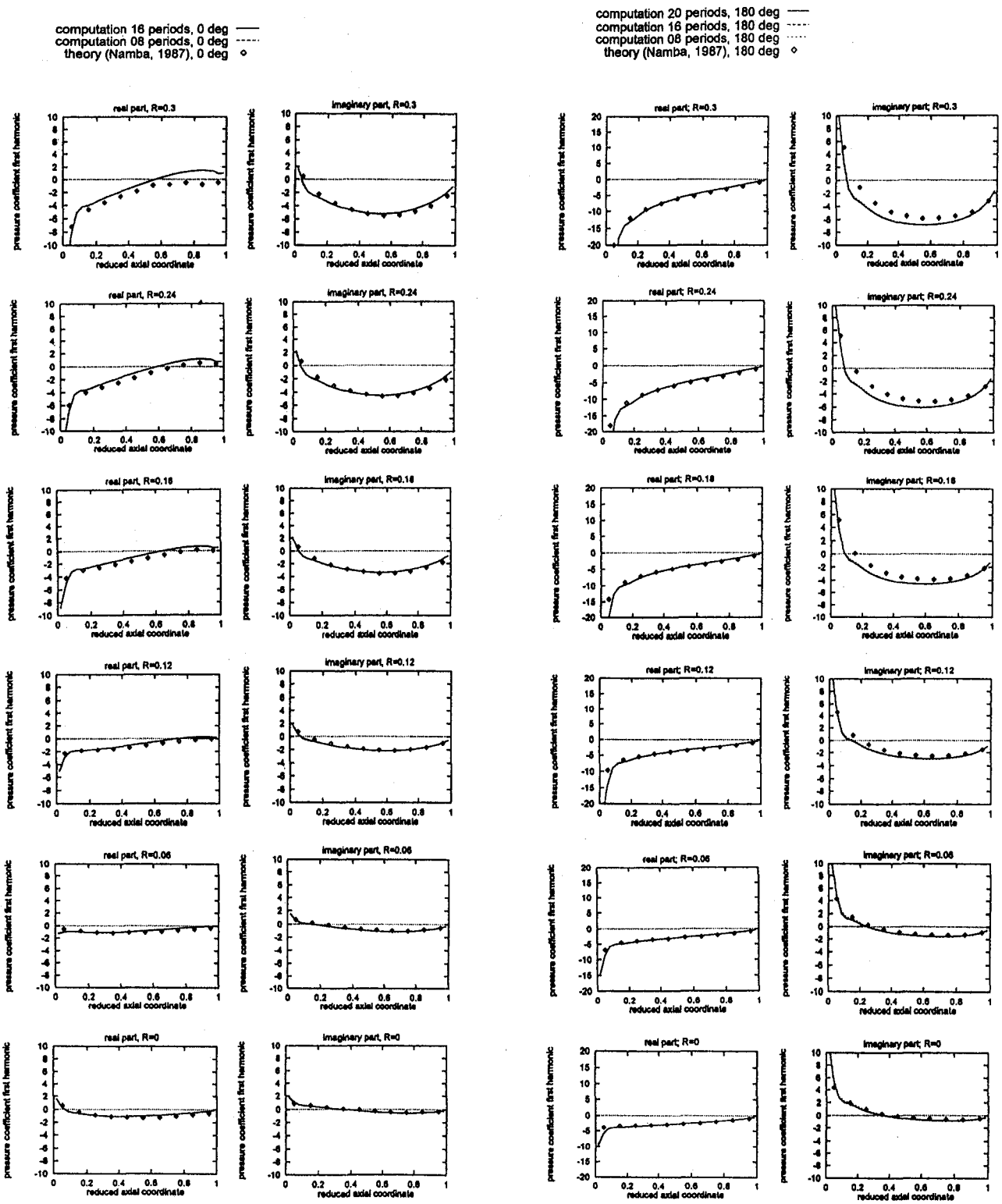

Fig. 6 Unsteady pressure jump distribution (real and imaginary part) for Namba cascade torsional vibration at (*a*) $\beta_r = 0$ deg and (*b*) $\beta_r = 180$ deg; present numerical computation and analytical theory (Namba, 1987; He and Denton, 1994)

comparison of computed and theoretical results in Fig. 8 is quite satisfactory. The finer grid resolves somewhat better the leading edge peak at the tip. A small discrepancy is found at the hub, near the leading edge. Since the hub is fixed the discrepancy is of no aeroelastic consequence.

In order to test the importance of prescribing the exact nonlinear blade motion for torsional vibration, computations were also run on the same grid using a linearized mode

$$x(t) = {}^{o}x - [{}^{o}R{}^{o}\theta - {}^{o}R\theta_{TC}({}^{o}R)]\alpha({}^{o}R)\cos\omega t$$
$$y(t) = {}^{o}y - [{}^{o}x - x_{TC}({}^{o}R)]\alpha({}^{o}R)\cos\omega t \sin {}^{0}\theta$$
$$z(t) = {}^{o}z + [{}^{o}x - x_{TC}({}^{o}R)]\alpha({}^{o}R)\cos\omega t \cos {}^{0}\theta \qquad (8)$$

which is obtained from Eq. (7) for $\alpha({}^{0}R) \ll 1$ rad, $\forall {}^{0}R$. The results are practically identical using the linearized (Eq. (8)) or the nonlinear (Eq. (7)) mode, as shown in Fig. 10.

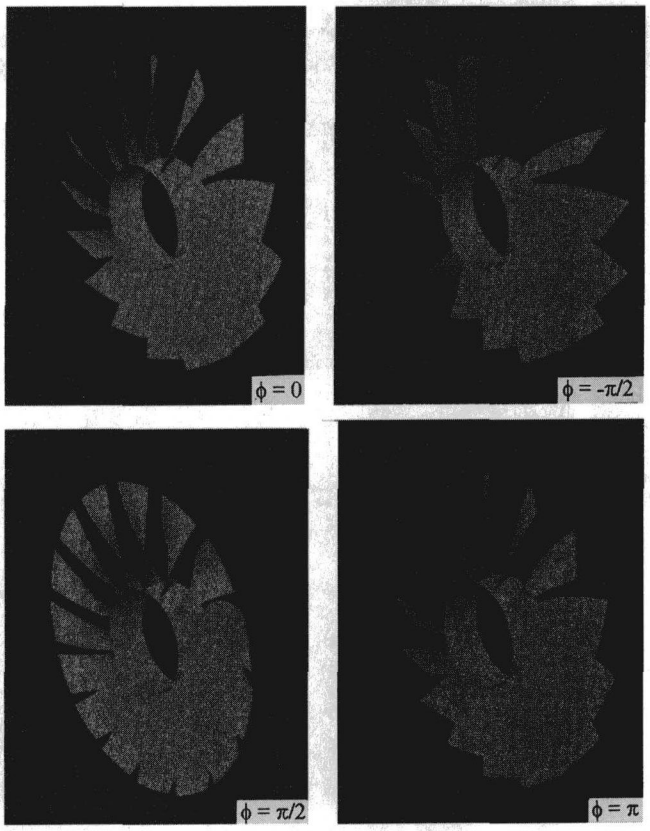

Fig. 7 Schematic of Chi_D cascade torsional vibration at $\beta_r = 0$ deg

3.5 Annular Chi__B Cascade With Three-Dimensional Flexural Vibratory Mode. This is a rotor with 30 high-aspect-ratio helicoïdal twisted flat plates at zero relative incidence, which are stacked on a straight radial axis at their midchord locus. This test case was introduced by Chi (1993) who presented semi-analytical linearized theoretical results. The rotor is in forward flight at $M_{abs} = 0.3$. The relative tip and hub Mach numbers are $M_{rel,hub} = 0.42$ and $M_{rel,tip} = 0.80$, with corresponding relative flow angles (and stagger angles) $\beta_{hub} = \theta_{stg,hub} = 44.7$ deg and $\beta_{tip} = \theta_{stg,tip} = 68$ deg. For the dimensions used in this study (Table 1) the rotor has an angular velocity of 250.29 rpm. The vibratory mode is flexural in the pitchwise direction. The amplitude varies in the spanwise direction from zero at the hub to $h_{tip} = 1$ mm at the tip following the first bending modeshape of a cantilever beam (Meirovitch, 1975)

$$h({}^0R) = \frac{-h_{tip}}{2 \sin \kappa L \sinh \kappa L} \times \begin{bmatrix} (\sin \kappa L - \sinh \kappa L)(\sin \kappa {}^0\bar{r} - \sinh \kappa L) \\ + (\cos \kappa L + \cosh \kappa L)(\cos \kappa {}^0\bar{r} - \cosh \kappa {}^0\bar{r}) \end{bmatrix} \quad (9)$$

where

$${}^0\bar{r} = \frac{{}^0R - R_{hub}}{R_{tip} - R_{hub}};$$

$$L = R_{tip} - R_{hub};$$

$$\kappa L = 1.8751046871 \quad (10)$$

and the superscript ${}^0(\ \ )$ denotes the undeflected blade position. The circumferential bending vibration is described by

$$R(t) = {}^oR$$

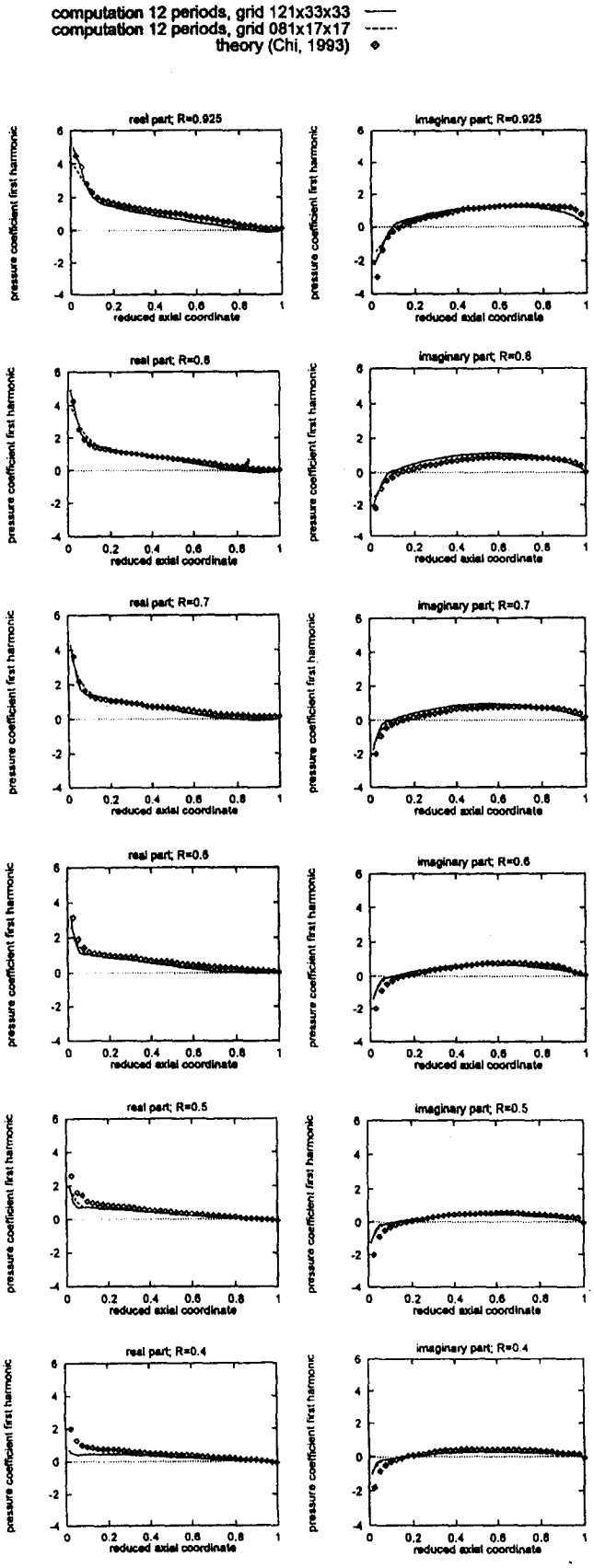

Fig. 8 Unsteady pressure jump distribution (real and imaginary part) for Chi_D cascade torsional vibration at $\beta_r = 0$ deg; grid influence results; present numerical computation and analytical theory (Chi, 1993)

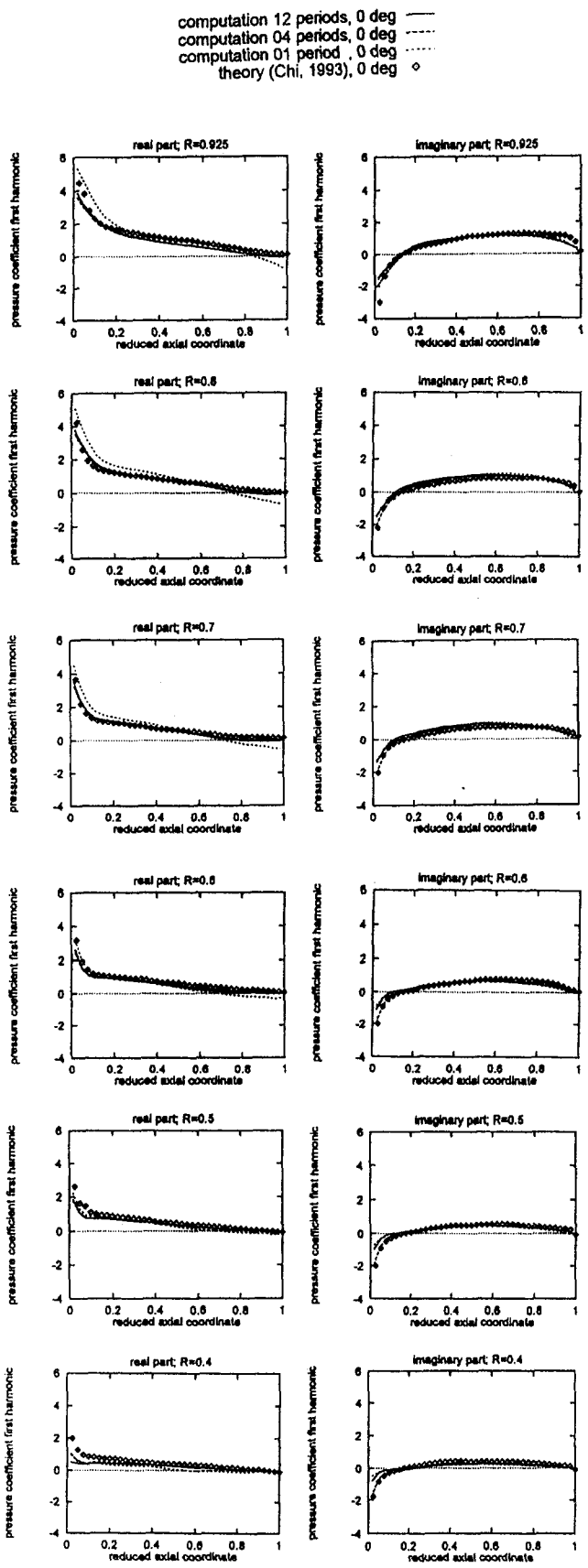

Fig. 9 Unsteady pressure jump distribution (real and imaginary part) for Chi_D cascade torsional vibration at $\beta_r = 0$ deg; present numerical computation and analytical theory (Chi, 1993)

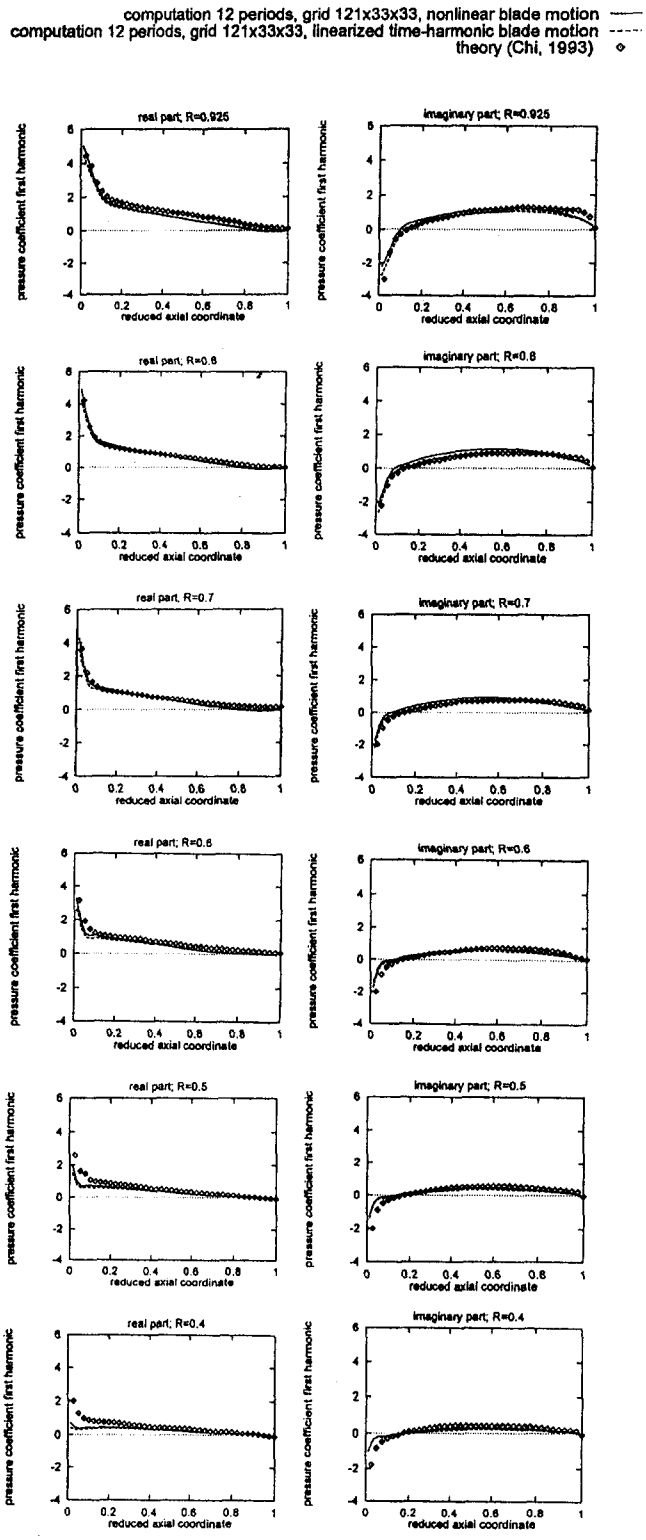

Fig. 10 Unsteady pressure jump distribution (real and imaginary part) for Chi_D cascade torsional vibration at $\beta_r = 0$ deg; effect of mode linearization; present numerical computation and analytical theory (Chi, 1993)

$$x(t) = {}^{o}x$$

$${}^{o}R\theta(t) = {}^{o}R{}^{o}\theta + h({}^{o}R)\cos\omega t \qquad (11)$$

For a tip chord $\chi_{\text{tip}} = 170$ mm the vibration frequency is $f = 48.3$ Hz corresponding to a Strouhal number $\text{Sr}_{\chi,\text{tip}} = 0.085$ ($T_{t,abs} = 288$ K). The interblade phase angle is $\beta_r = 72$ deg corresponding to $r = 6$ nodal diameters. The vibratory mode is

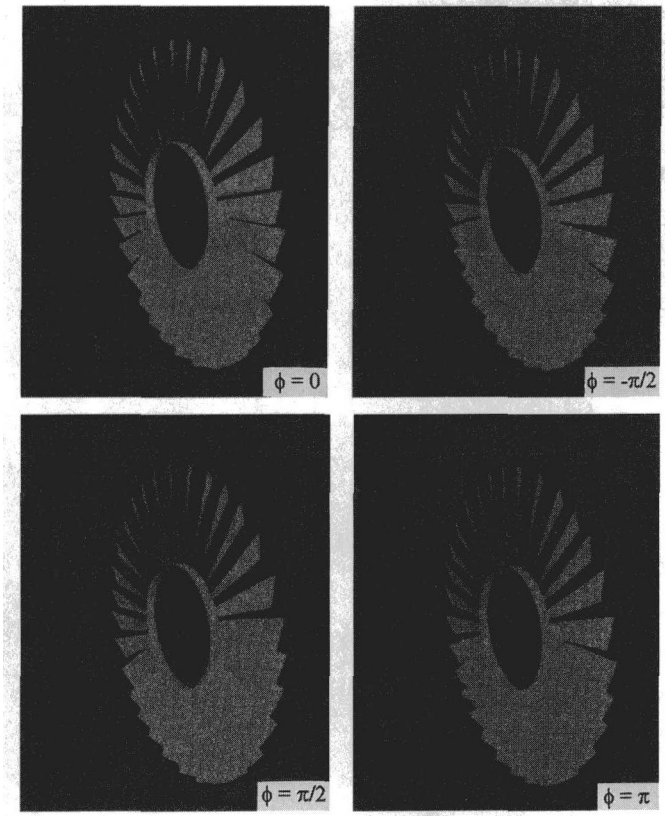

Fig. 11 Schematic of Chi_B cascade bending vibration at β_r = 72 deg

depicted in Fig. 11, exaggerated 30 times. Computational results using an $81 \times 17 \times 17$ grid for the $\Delta^1 p/\rho W^2 h_{\text{tip}}$ distributions are compared with theoretical results in Fig. 12 ($W = W(^0R)$ is the relative flow velocity). Computational results were taken after the numerical simulation of 1, 8, and 16 periods, showing that convergence is obtained after the numerical computation of 8 periods. The agreement between computational and theoretical results is quite satisfactory with the exception of the leading edge region at the tip for the $\text{Re}[\Delta^1 p/\rho W^2 h_{\text{tip}}]$ distributions. This discrepancy was attributed to insufficient radial resolution of the computational grid.

3.5 Convergence and Computing-Time Requirements. The periodic convergence of the unsteady computations was illustrated in the preceding sections by comparing the results after the simulation of a different number of periods. The logarithm of the error norm of the unsteady pressures on the surface of the blades (note a typographical error in Gerolymos, 1993)

$$\text{error} = \sqrt{\frac{f}{\iint_{\partial \mathbf{B}} dS} \left[\iint_{\partial \mathbf{B}} dS \int_{t_0}^{t_0+1/f} \left(\frac{p(t) - p(t - 1/f)}{p(t - 1/f)} \right)^2 \right]} \tag{12}$$

(where $\partial \mathbf{B}$ is the blade surface) is depicted in Fig. 13. Satisfactory convergence is obtained in all cases. The computing-time requirements are presented in Table 2.

4 A Code-to-Code Comparison

Another test case for a subsonic rotor of helicoïdal twisted flat plates has been suggested by Hall and Lorence (1993) who presented results using a time-linearized three-dimensional Euler code. There are unfortunately no semi-analytical theoretical results available for this case, but a code-to-code comparison was undertaken. This test-case is a wide-chord rotor with 18

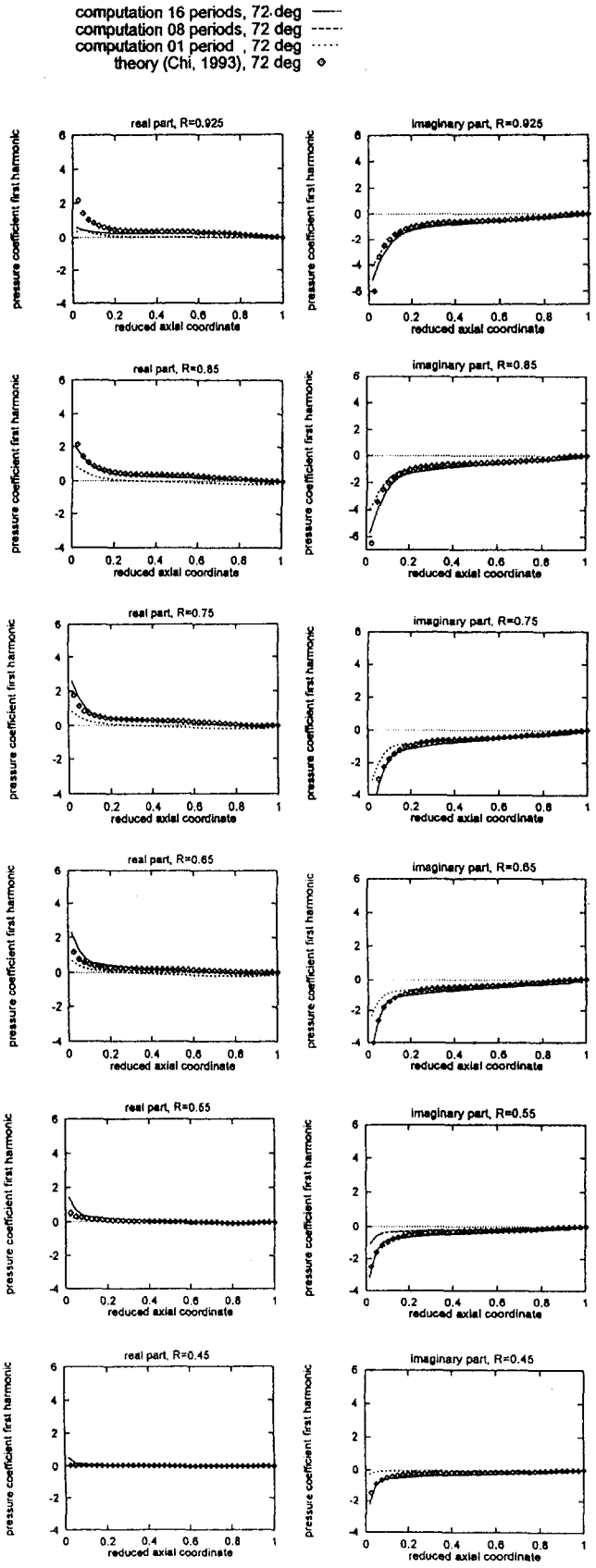

Fig. 12 Unsteady pressure jump distribution (real and imaginary part) for Chi_B cascade bending vibration at β_r = 72 deg; present computation and analytical theory (Chi, 1993)

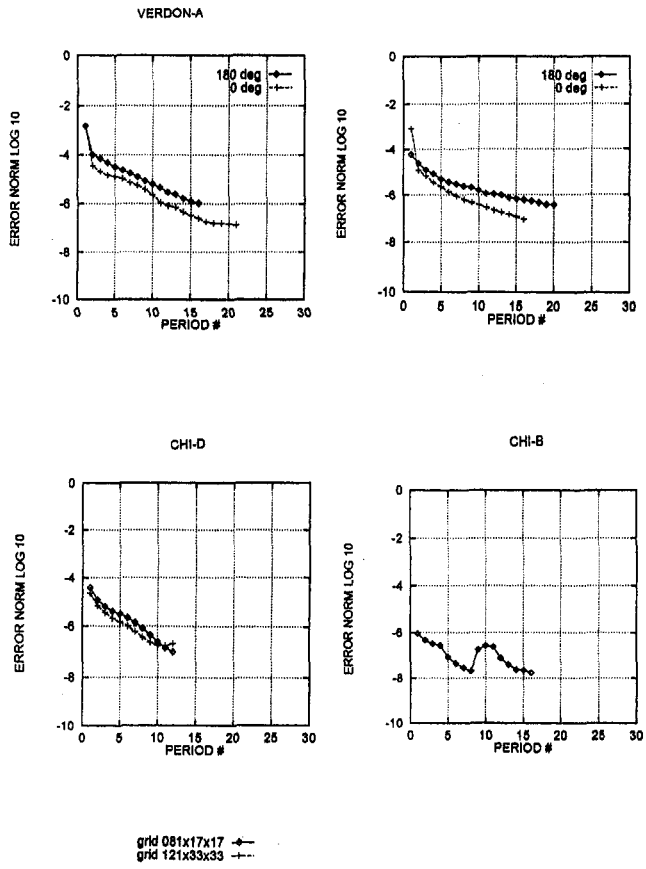

Fig. 13 Unsteady convergence for the four configurations studied; (*a*) Verdon_A, (*b*) Namba, (*c*) Chi__D, (*d*) Chi__B

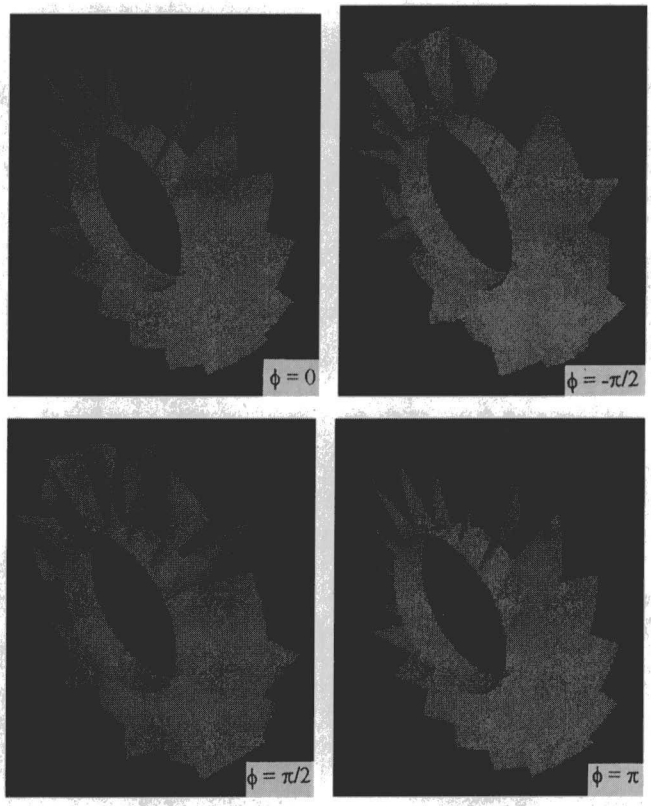

Fig. 14 Schematic of torsional vibration at β_r = 180 deg for the code-to-code comparison test case

helicoïdal twisted flat plates at zero relative incidence, which are stacked on a straight radial axis at their midchord locus. The rotor is in forward flight at $M_{abs} = 0.5$. The relative tip and hub Mach numbers are $M_{rel,hub} = 0.60$ and $M_{rel,tip} = 0.83$, with corresponding relative flow angles (and stagger angles) $\beta_{hub} = \theta_{stg,hub} = 33.69$ deg and $\beta_{tip} = \theta_{stg,tip} = 53.13$ deg. For the dimensions used in this study ($R_{tip} = 4000$ mm, $R_{hub} = 2000$ mm) the rotor has an angular velocity of 528.39 rpm. The vibratory mode is torsional, around the straight stacking axis, which passes through the midchord locus, with amplitude linearly varying from hub (zero amplitude) to tip. For a tip chord $\chi_{tip} = 1666.7$ mm ($\chi_{hub} = 1201.9$ mm) the vibration frequency is $f = 10.57$ Hz, corresponding to a Strouhal number $Sr_{\chi,tip} = 0.063$ ($T_{t,abs} = 288$ K). The vibration amplitude at the tip is $\alpha_{tip} = 1$ deg. The blade displacement is described by

$$R(t) = {}^oR$$

$$x(t) = {}^ox + [{}^ox - x_{TC}({}^oR)] \cos [\alpha({}^oR) \cos \omega t] - [{}^oR{}^o\theta - {}^oR\theta_{TC}({}^oR)] \sin [\alpha({}^oR) \cos \omega t]$$

$${}^oR\theta(t) = {}^oR{}^o\theta + [{}^ox - x_{TC}({}^oR)] \sin [\alpha({}^oR) \cos \omega t] - [{}^oR{}^o\theta - {}^oR\theta_{TC}({}^oR)] \cos [\alpha({}^oR) \cos \omega t] \quad (13)$$

where x, R, θ is a cylindrical coordinate system with origin at midchord of the hub section (x in the axial direction and z in the spanwise direction), $\alpha({}^oR) = \alpha_{tip}({}^oR - R_{hub})/(R_{tip} - R_{hub})$ the torsional vibration amplitude, $\alpha_{tip} = 1$ deg the torsional vibration amplitude at the tip, $\omega = 2\pi f$ the vibration frequency, and $x_{TC}({}^oR) = 0$, ${}^oR\theta_{TC}({}^oR) = 0$, $\forall {}^oR$ the coordinates of the torsional center (at midchord), and the superscript ${}^o(\ )$ denotes the undeflected blade position. The interblade phase angle is $\beta_r = 180$ deg. The vibratory mode is depicted in Fig. 14 exaggerated 30 times. Computational results using an $121 \times 17 \times 17$ grid and an $81 \times 17 \times 17$ grid for the $\Delta^1 p/\rho V^2 \alpha_{tip}$ distributions at various spanwise locations are compared with the computational results of Hall and Lorence (1993) in Fig. 15 (V is the absolute flow velocity, which is in the axial direction, and is constant spanwise). Computational results are taken after the numerical simulation of 16 periods, which as shown in the convergence tests for the theoretical test cases are sufficient for periodic convergence. The comparison of the present nonlinear and the linearized (Hall and Lorence, 1993) computations are quite satisfactory. The finer grid resolves somewhat better the leading edge peak at the tip. The periodic convergence (Eq. (12)) is shown in Fig. 16. The computations (16 periods) required 14143. CPU-s (grid $121 \times 17 \times 17$) and 7370. CPU-s (grid $81 \times 17 \times 17$) on a CRAY C98 computer.

Table 2 Computing-time requirements

case	grid	β_r (deg)	f (Hz)	Periods	CPU-s CRAY2	CPU-s Cray YMP-EL
Verdon_A	121x25x05	0 180	376.41	21 16	18300	56280
Namba	81x25x21	0 180	361.69	16 20	34105	60179
Chi_D	121x33x33 81x17x17	0	63.30	12 12		374916 53508
Chi_B	81x17x17	72	48.29	16		212014

5 Conclusions and Discussion

In the present work an existing unsteady time-nonlinear three-dimensional Euler code was validated by comparison with available semi-analytical theoretical data from linear and annular vibrating flat plate cascades, Verdon_A, Namba, Chi_D and Chi_B, with tip Mach numbers $M_{rel,tip}$ = 1.345, 0.7, 0.94, 0.80, hub Mach numbers $M_{rel,hub}$ = 1.345, 0.7, 0.57, 0.42, and tip Strouhal numbers $Sr_{\chi,tip}$ = 0.096, 0.159, 0.127, 0.085, respectively ($Sr_{\chi,tip} = f\,\chi_{tip}/W_{tip}$). Both torsional and bending modes were simulated at various interblade phase angles. The agreement of computations with theory is quite satisfactory for all the cases studied. In all the computations one-dimensional nonreflecting boundary conditions were used, giving quite satisfactory results. The rapidity of the computations convergence is dependent on the test case, but generally 12 periods are sufficient to obtain converged results for all the cases. A comparison between the use of a nonlinear and a linearized torsional vibratory motion gave pratically identical results for both cases. A first code-to-code comparison on a configuration quite similar with Chi_D also gave very satisfactory results.

The authors believe that this contribution is an interesting step toward the validation of three-dimensional codes for the prediction of the unsteady aerodynamics of vibrating cascades. The validation effort should be continued on more realistic configurations. In the absence of well-documented three-dimensional experimental test cases, code-to-code comparison is an interesting step toward code validation. Nonetheless three-dimensional experiments are urgently needed. An experimental setup resembling the Namba test case, which combines nonrotating cascade simplicity with three-dimensional data, is an interesting alternative to on-engine measurements for the purpose of code validation. Analogous work could be conducted in annular nonrotating cascades. In both cases the blade should be excited in a three-dimensional mode shape.

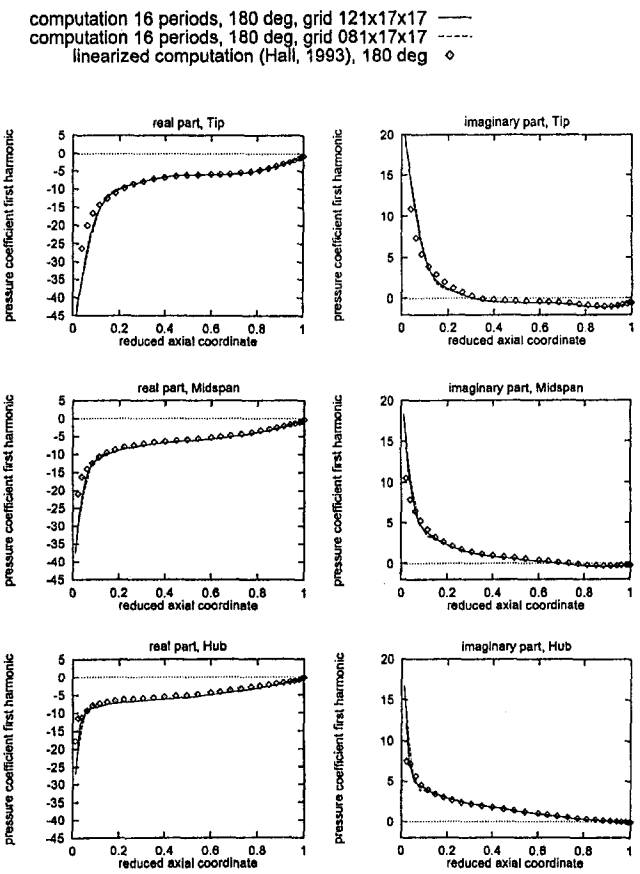

Fig. 15 Unsteady pressure jump distribution (real and imaginary part) for the code-to-code comparison; present computation and time-linearized Euler computations (Hall and Lorence, 1993)

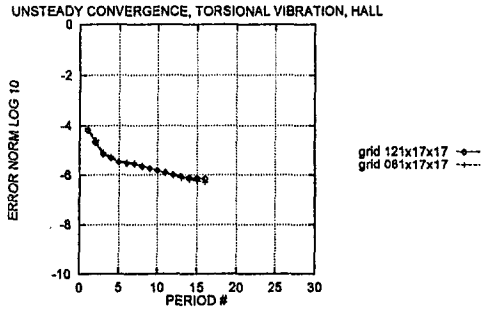

Fig. 16 Unsteady convergence for the code-to-code comparison

Acknowledgments

The computations presented in this paper were run on the CRAY YMP-EL computer of Université Pierre & Marie Curie and on the CRAY 2 computer of CCVR. The code-to-code comparison was run on the CRAY C98 computer of IDRIS. Computer resources at CCVR and IDRIS were allocated by CNRS (Centre National de la Recherche Scientifique).

References

Adamczyk, J. J., and Goldstein, M. E., 1978, "Unsteady Flow in a Supersonic Cascade With Subsonic Leading-Edge Locus," *AIAA J.*, Vol. 16, pp. 1248–1254.

Bölcs, A., and Fransson, T. H., 1986, "Aeroelasticity in Turbomachines: Comparison of Theoritical and Experimental Cascade Results," Communication du Laboratoire de Thermique Appliquée et de Turbomachines No. 13, Ecole Polytechique Fédérale de Lausanne, Switzerland.

Carstens, V., 1991, "Computation of the Unsteady Transonic 2-D Cascade Flow by an Euler Algorithm With Interactive Grid Generation," *AGARD Conf. Proc.*, Vol. 507, pp. 9.1-9.14.

Carstens, V., Bölcs, A., and Körbacher, H., 1993, "Comparison of Experimental and Theoretical Results for Unsteady Transonic Cascade Flow at Design and Off-Design Conditions," ASME Paper No. 93-GT-100.

Chi, R. M., 1993, "An Unsteady Lifting Surface Theory for Ducted Fan Blades," ASME JOURNAL OF TURBOMACHINERY, Vol. 115, pp. 175–188.

Denton, J. D., 1992, "The Calculation of Three-Dimensional Viscous Flow Through Multistage Turbomachines," ASME JOURNAL OF TURBOMACHINERY, Vol. 114, pp. 18–26.

Fleeter, S., and Hoyniak, D., 1989, "Aeroelastic Detuming for Stability Enhancement of Unstalled Supersonic Flutter," *Int. J. Turbo. Jet Eng.*, Vol. 6, pp. 17–26.

Fransson, T. H., and Verdon, J. M., 1991, "Panel Discussion on Standard Configurations for Unsteady Flow Through Vibrating Axial Flow Turbomachine Cascades," Unsteady Aerodynamics, Aeroacoutics, and Aeroelasticity of Turbomachines and Propellers, Notre Dame [USA].

Gerolymos, G. A., 1988, "Numerical Integration of the 3-D Unsteady Euler Equations for Flutter Analysis of Axial Flow Compressors," ASME Paper No. 88-GT-255; *Int. J. Turbo Jet Eng.*, Vol. 7, 1990, pp. 131–142.

Gerolymos, G. A., Blin, E., and Quiniou, H., 1990, "Comparison of Inviscid Computations With Theory and Experiment in Vibrating Transonic Compressor Cascades," ASME Paper No. 90-GT-373; *Rech. Aérosp.*, Vol. 1991.6, 1991, pp. 63–82.

Gerolymos, G. A., 1993, "Advances in the Numerical Integration of the Three-Dimensional Euler Equations in Vibrating Cascades," ASME JOURNAL OF TURBOMACHINERY, Vol. 115, pp. 781–790.

Giles, M. B., 1990, "Nonreflecting Boundary Conditions for Euler Equation Calculations," *AIAA J.*, Vol. 28, pp. 2050–2058.

Goldstein, M. E., Braun, W., and Adamczyk, J. J., 1977, "Unsteady Low in a Supersonic Cascade With Strong in Passage Shocks," *J. Fluid Mech.*, Vol. 83, pp. 569–604.

Goldstein, M. E., 1978, "Unsteady Vortical and Entropic Distortions of Potential Flows Round Arbitrary Obstacles," *J. Fluid. Mech.*, Vol. 89, pp. 433–468.

Hall, K. C., and Lorence, C. B., 1993, "Calculation of Three Dimensional Unsteady Flows in Turbomachinery Using the Linearized Harmonic Euler Equations," ASME JOURNAL OF TURBOMACHINERY, Vol. 115, 1993, pp. 800–809.

Hall, K. C., and Clark, W. S., 1993, "Linearized Euler Predictions of Unsteady Aerodynamic Loads in Cascades," *AIAA J.*, Vol. 31, pp. 540–550.

Hall, K. C., 1993, "Deforming Grid Variational Principle for Unsteady Small Disturbance Flows in Cascades," *AIAA J.*, Vol. 31, pp. 891–900.

Hall, K. C., Clark, W. S., and Lorence, C. B., 1994, "A Linearized Euler Analysis of Unsteady Transonic Flows in Turbomachinery," ASME JOURNAL OF TURBOMACHINERY, Vol. 116, pp. 477–488.

Halliwell, D. G., Newton, S. G., and Lit, K. S., 1984, "A Study of Unsteady Pressures Near the Tip of a Transonic Fan in Unstalled Supersonic Flutter," ASME *J. Vibr. Acoust. Reliab. Design,* Vol. 106, pp. 198–203.

He, L., 1990, "An Euler Solution for Unsteady Flows Around Oscillating Blades," ASME JOURNAL OF TURBOMACHINERY, Vol. 112, pp. 714–722.

He, L., and Denton, J. D., 1993a, "Inviscid–Viscous Coupled Solution for Unsteady Flows Through Vibrating Blades: Part 1—Description of the Method," ASME JOURNAL OF TURBOMACHINERY, Vol. 115, pp. 94–100.

He, L., and Denton, J. D., 1993b, "Inviscid–Viscous Coupled Solution for Unsteady Flows Through Vibrating Blades: Part 2—Computational Results," ASME JOURNAL OF TURBOMACHINERY, Vol. 115, pp. 101–109.

He, L., and Denton, J. D., 1994, "Three-Dimensional Time-Marching Inviscid and Viscous Solutions for Unsteady Flows Around Vibrating Blades," ASME JOURNAL OF TURBOMACHINERY, Vol. 116, pp. 469–478.

Hedstrom, G. W., 1979, "Nonreflecting Boundary Conditions for Nonlinear Hyperbolic Systems," *J. Comp. Phys.,* Vol. 30, pp. 222–237.

Huff, H. L., 1992, "Numerical Analysis of Flow Through Oscillating Cascade Sections," *J. Prop. Power,* Vol. 8, pp. 815–822.

Kodoma, H., and Namba, M., 1990, "Unsteady Lifting Surface Theory for a Rotating Cascade of Swept Blades," ASME JOURNAL OF TURBOMACHINERY, Vol. 112, pp. 411–417.

Lane, F., 1957, "Supersonic Flow Past on Oscillating Cascade With Supersonic Leading-Edge Locus," *J. Aero. Sci.,* Vol. 24, pp. 65–66.

Meirovitch, L., 1975, *Elements of Vibration Analysis,* McGraw-Hill, pp. 210–214.

Namba, M., and Ishikawa, A., 1983, "Three-Dimensional Aerodynamic Characteristics of Oscillating Supersonic and Transonic Annular Cascade," ASME *Journal of Engineering for Power,* Vol. 105, pp. 138–146.

Namba, M., 1987, "Three-Dimensional Flows," AGARDograph 298, pp. 4.1–4.30.

Ni, R. H., 1979, "A Rotational Analysis of Periodic Flow Perturbation in Supersonic Two–Dimensional Cascade," ASME *Journal of Engineering Power,* Vol. 101, pp. 431–439.

Salaün, P., 1987, "Three-Dimensional Flow," AGARDograph 298, pp. 5.1–5.17.

Sidén, L. D. G., 1991, "Numerical Simulation of Unsteady Viscous Compressible Flows Applied to Blade Flutter Analysis," ASME Paper No. 91-GT-203.

Surampudi, S. P., and Adamczyk, J. J., 1986, "Unsteady Transonic Flow Over Cascade Blades," *AIAA J.,* Vol. 24, pp. 293–302.

Usab, W. J., Jr., and Verdon, J. M., 1991, "Advances in the Numerical Analysis of Linearized Unsteady Cascade Flows," ASME JOURNAL OF TURBOMACHINERY, Vol. 119, pp. 633–643.

Venkatakrishnan, V., and Jameson, A., 1988, "Computation of Unsteady Transonic Flows by the Solution of Euler Equations," *AIAA J.,* Vol. 29, pp. 974–981.

Verdon, J. M., 1973, "The Unsteady Aerodynamics of a Finite Supersonic Cascade With Subsonic Axial Flow," ASME *Journal of Applied Mechanics,* Vol. 40, pp. 667–671.

Verdon, J. M., and McCune, J. E., 1975, "Unsteady Supersonic Cascade in Subsonic Axial Flow," *AIAA J.,* Vol. 13, pp. 193–201.

Verdon, J. M., 1975, "Comment on the Issue of Resonance in an Unsteady Supersonic Cascade," *AIAA J.,* Vol. 13, pp. 1542–1543.

Verdon, J. M., 1977a, "Further Developments in the Aerodynamic Analysis of Unsteady Supersonic Cascades: Part 1—The Unsteady Pressure Field," ASME *Journal of Engineering Power,* Vol. 99, pp. 509–516.

Verdon, J. M., 1977b, "Further Developments in the Aerodynamic Analysis of Unsteady Supersonic Cascades: Part 2—Aerodynamic Response Predictions," ASME *Journal of Engineering for Power,* Vol. 99, pp. 517–525.

Verdon, J. M., and Caspar, J. R., 1982, "Development of a Linear Unsteady Aerodynamic Analysis for Finite Deflection Subsonic Cascades," *AIAA J.,* Vol. 20, pp. 1259–1267.

Verdon, J. M., and Caspar, J. R., 1984, "A Linearized Unsteady Aerodynamic Analysis for Transonic Cascades," *J. Fluid Mech.,* Vol. 149, pp. 403–429.

Verdon, J. M., 1989a, "The Unsteady Flow in the Far Field of an Isolated Blade Row," *J. Fluids Struct.,* Vol. 3, pp. 123–149.

Verdon, J. M., 1989b, "The Unsteady Aerodynamic Response to Arbitrary Modes of Blade Motion," *J. Fluids Struct.,* Vol. 3, pp. 255–274.

Verdon, J. M., 1992, "Linearized Unsteady Aerodynamics for Turbomachinery Aeroelastic Applications," *J. Phys. III France,* Vol. 2, pp. 481–506.

Verdon, J. M., 1993, "Review of Unsteady Aerodynamic Methods for Turbomachinery Aeroelastic and Aeroacoustic Applications," *AIAA J.,* Vol. 31, pp. 235–250.

Whitehead, D. S., 1987, "Classical Two-Dimensional Methods," AGARDograph 298, pp. 3.1–3.30.

Whitehead, D. S., 1990, "A Finite Element Solution of Unsteady Two-Dimensional Flows in Cascades," *Int. J. Num. Meth. Fluids,* Vol. 10, pp. 13–34.

Unsteady Numerical Simulations of Radial Temperature Profile Redistribution in a Single-Stage Turbine

D. J. Dorney
Department of Mechanical and Aeronautical Engineering, Western Michigan University, Kalamazoo, MI 49008

J. R. Schwab
Turbomachinery Flow Physics Branch, NASA Lewis Research Center, Cleveland, OH 44135

Experimental data taken from gas turbine combustors indicate that the flow exiting the combustor can contain both circumferential and radial temperature gradients. A significant amount of research recently has been devoted to studying turbine flows with inlet temperature gradients, but no total pressure gradients. Less attention has been given to flows containing both temperature and total pressure gradients at the inlet. The significance of the total pressure gradients is that the secondary flows and the temperature redistribution process in the vane blade row can be significantly altered. Experimental data previously obtained in a single-stage turbine with inlet total temperature and total pressure gradients indicated a redistribution of the warmer fluid to the pressure surface of the airfoils, and a severe underturning of the flow at the exit of the stage. In a concurrent numerical simulation, a steady, inviscid, three-dimensional flow analysis was able to capture the redistribution process, but not the exit flow angle distribution. In the current research program, a series of unsteady two- and three-dimensional Navier–Stokes simulations have been performed to study the redistribution of the radial temperature profile in the turbine stage. The three-dimensional analysis predicts both the temperature redistribution and the flow underturning observed in the experiments.

Introduction

Experimental data taken from gas turbine combustors indicate that the flow exiting the combustor can contain both circumferential and radial temperature gradients. These temperature gradients arise from the combination of the combustor core flow with the combustor bypass and combustor surface cooling flows. It has been shown both experimentally (Butler et al., 1989; Roback and Dring, 1993) and numerically (Krouthen and Giles, 1988; Rai and Dring, 1990; Takahashi and Ni, 1990, 1991; Saxer and Giles, 1990; Dorney et al., 1991, 1992; Dorney and Davis, 1993) that temperature gradients, in the absence of total pressure nonuniformities, do not alter the flow within the first-stage turbine vane but do have significant impact on the secondary flows and wall temperatures of the first-stage rotor (blade). Combustor hot streaks, which can typically have temperatures twice the free-stream stagnation temperature, increase the extent of the secondary flow in the first-stage rotor and significantly alter the rotor surface temperature distribution. A hot streak such as this has a greater streamwise velocity than the surrounding fluid, and therefore a larger positive incidence angle to the rotor as compared to the free stream. Due to this rotor incidence variation through the hot streak, and the slow convection speed on the pressure side of the rotor, the hot streak accumulates on the rotor pressure surface, creating a "hot spot." It has been shown that thermal fatigue due to combustor hot streaks can significantly reduce the life of a turbine blade.

In a related experimental effort, radial total temperature and total pressure profiles were introduced at the inlet of an advanced single-stage axial turbine and the results were compared with those obtained for uniform inlet profiles (Schwab et al., 1983; Stabe et al., 1984). Significant temperature rises were observed at the hub and tip corners at the trailing edge plane near the pressure surface in both the vane and rotor. It was hypothesized that the elevated temperatures were a result of the secondary flows. The inlet temperature profile was mixed out by the time it reached the rotor exit measurement plane. Severe underturning (compared to the design conditions) occurred from the midspan to the tip at the exit of the rotor. An inviscid analysis failed to predict the underturning of the flow (Schwab et al., 1983). In a recent numerical investigation, Saxer and Giles (1990) performed steady three-dimensional Euler simulations for a transonic turbine stage with an inlet radial temperature profile. Harasgama (1990) has used a steady three-dimensional Navier–Stokes code, coupled with a two-dimensional boundary layer analysis, to study the effects of radial temperature distortions in a rotor flow field. Weigand and Harasgama (1994) have also used a three-dimensional viscous analysis to simulate inlet radial temperature profiles and film cooling. Kirtley et al. (1993) have compared the results of steady and unsteady numerical analyses to study the impact of flow unsteadiness on the thermal loads in a turbine stage.

In the current investigation, unsteady two- and three-dimensional viscous simulations have been performed for the geometry and flow conditions described in Schwab et al. (1983) and Stabe et al. (1984). The two- and three-dimensional simulations were performed to determine whether the severe underturning of the flow results from the fluid viscosity, or a combination of fluid viscosity and secondary flows. The use of unsteady simulations allowed the proper modeling of vane–blade interactions, which are known to be important in turbomachinery. The three-dimensional simulations were also used to study the effects of secondary flows on the temperature redistribution process.

Contributed by the International Gas Turbine Institute and presented at the 40th International Gas Turbine and Aeroengine Congress and Exhibition, Houston, Texas, June 5–8, 1995. Manuscript received by the International Gas Turbine Institute February 13, 1995. Paper No. 95-GT-178. Associate Technical Editor: C. J. Russo.

Numerical Integration Procedure

The governing equations considered in this study are the time-dependent, three-dimensional, Reynolds-averaged, Navier–Stokes equations:

$$U_t + (F_i + F_v)_x + (G_i + G_v)_y + (H_i + H_v)_z = 0 \quad (1)$$

where

$$U = \begin{bmatrix} \rho \\ \rho u \\ \rho v \\ \rho w \\ e_t \end{bmatrix} \quad (2)$$

$$F_i = \begin{bmatrix} \rho u \\ \rho u^2 + P \\ \rho uv \\ \rho uw \\ (e_t + P)u \end{bmatrix} \qquad F_v = - \begin{bmatrix} 0 \\ \tau_{xx} \\ \tau_{xy} \\ \tau_{xz} \\ \tau_{hx} \end{bmatrix} \quad (3)$$

$$G_i = \begin{bmatrix} \rho v \\ \rho uv \\ \rho v^2 + P \\ \rho vw \\ (e_t + P)v \end{bmatrix} \qquad G_v = - \begin{bmatrix} 0 \\ \tau_{yx} \\ \tau_{yy} \\ \tau_{yz} \\ \tau_{hy} \end{bmatrix} \quad (4)$$

$$H_i = \begin{bmatrix} \rho w \\ \rho uw \\ \rho vw \\ \rho w^2 + P \\ (e_t + P)w \end{bmatrix} \qquad H_v = - \begin{bmatrix} 0 \\ \tau_{zx} \\ \tau_{zy} \\ \tau_{zz} \\ \tau_{hz} \end{bmatrix} \quad (5)$$

and

$$\tau_{xx} = 2\mu u_x + \lambda(u_x + v_y + w_z)$$

$$\tau_{xy} = \mu(u_y + v_x)$$

$$\tau_{xz} = \mu(u_z + w_x)$$

$$\tau_{yx} = \tau_{xy}$$

$$\tau_{yy} = 2\mu v_y + \lambda(u_x + v_y + w_z)$$

$$\tau_{yz} = \mu(v_z + w_y)$$

$$\tau_{zx} = \tau_{xz}$$

$$\tau_{zy} = \tau_{yz}$$

$$\tau_{zz} = 2\mu w_z + \lambda(u_x + v_y + w_z)$$

$$\tau_{hx} = u\tau_{xx} + v\tau_{xy} + w\tau_{xz} + \gamma\mu P_r^{-1} e_x$$

$$\tau_{hy} = u\tau_{yx} + v\tau_{yy} + w\tau_{yz} + \gamma\mu P_r^{-1} e_y$$

$$\tau_{hz} = u\tau_{zx} + v\tau_{zy} + w\tau_{zz} + \gamma\mu P_r^{-1} e_z$$

$$e = \frac{P}{(\rho(\gamma - 1))}$$

$$e_t = \rho e + \frac{\rho(u^2 + v^2 + w^2)}{2} \quad (6)$$

For the present application, the second coefficient of viscosity is calculated using Stokes' hypothesis, $\lambda = -2/3\mu$. The equations of motion are completed by the perfect gas law.

The viscous fluxes are simplified by incorporating the thin layer assumption (Baldwin and Lomax, 1978). In the current study, viscous terms are retained only in the direction normal to the hub surfaces and in the direction normal to the blade surfaces. To extend the equations of motion to turbulent flows, an eddy viscosity formulation is used. Thus, the effective viscosity and effective thermal conductivity can be defined as:

$$\mu = \mu_L + \mu_T$$

$$\frac{\kappa}{c_p} = \frac{\mu_L}{Pr_L} + \frac{\mu_T}{Pr_T} \quad (7)$$

The turbulent viscosity, μ_T, is calculated using the two-layer Baldwin–Lomax (1978) algebraic turbulence model.

The numerical algorithm used in the three-dimensional computational procedure consists of a time-marching, implicit, finite-difference scheme. The procedure is third-order spatially accurate and first-order temporally accurate. The inviscid fluxes are discretized according to the scheme developed by Roe (1981). The viscous fluxes are calculated using standard central differences. An alternating direction, approximate-factorization technique is used to compute the time rate changes in the primary variables. In addition, Newton subiterations are used at each global time step to increase stability and reduce linearization errors. For all cases investigated in this study, two Newton subiterations were performed at each time step. The numerical algorithm used in the two-dimensional analysis is similar to that used in the three-dimensional analysis, except that the procedure is second-order temporally accurate and the inviscid fluxes are discretized according to the scheme developed by Chakravarthy and Osher (1982). Further details of the numerical techniques can be found in Rai (1989), Dorney et al. (1992), and Dorney and Davis (1993).

Boundary Conditions

The theory of characteristics is used to determine the boundary conditions at the vane inlet and blade exit. For subsonic inlet flow, four quantities are specified, and one is extrapolated from the interior of the computational domain. The total pressure (or entropy, s), v and w velocity components (or the corresponding tangential and meridional angles) and the downstream running Riemann invariant, $R_1 = u + 2a/(\gamma - 1)$ (or the total temperature T_t), are specified as a function of the radius. The

Nomenclature

a = speed of sound
e_t = total energy
M = Mach number
P = static pressure
Re = inlet reference Reynolds number
Sp = blade span
T = static temperature
u, v, w = x, y, z components of velocity
ρ = density
τ = shear stress
Ω = rotor rotational speed

Subscripts

t = stagnation quantity, time derivative
x, y, z = first derivative with respect to x, y, z
0 = vane inlet quantity
1 = vane exit/rotor inlet quantity
2 = rotor exit quantity

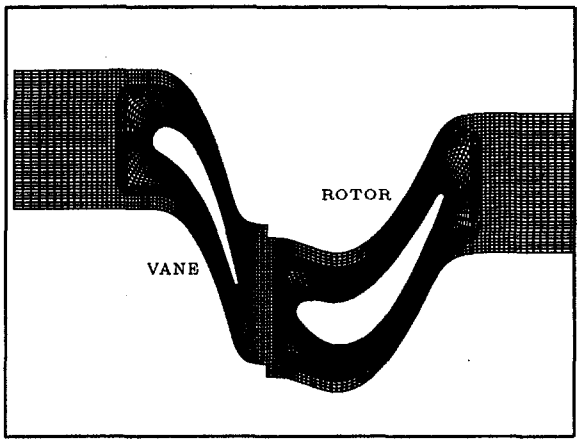

Fig. 1 Midspan section of the three-dimensional computational grid for the turbine

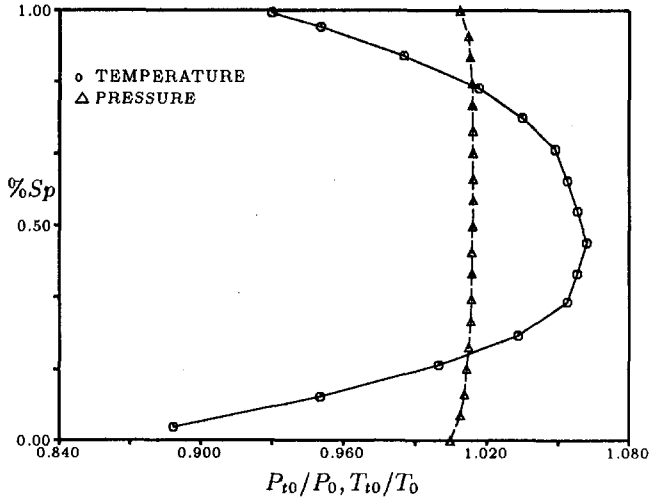

Fig. 2 Experimental radial total temperature, total pressure profiles

upstream running Riemann invariant, $R_2 = u - 2a/(\gamma - 1)$, is extrapolated from the interior of the computational domain.

For subsonic outflow, one flow quantity is specified and four are extrapolated from the interior of the computational domain. The v and w velocity components, entropy, and the downstream running Riemann invariant are extrapolated from the interior of the computational domain. The pressure ratio, P_2/P_{t0}, is specified at midspan of the computational exit and the pressure at all other radial locations at the exit is obtained by integrating the equation for radial equilibrium. Periodicity is enforced along the outer boundaries of the H-grids in the circumferential (θ) direction.

For viscous simulations, no-slip boundary conditions are enforced along the surfaces of the vane and blade airfoils. Absolute no-slip boundary conditions are enforced at the hub and tip endwalls of the vane region, along the surface of the vane, and along the outer casing (tip endwall) of the rotor blade. Relative no-slip boundary conditions are imposed at the hub and along the surface of the rotor blade. It is assumed that the normal derivative of the pressure is zero at solid wall surfaces. In addition, a specified (zero) heat flux distribution is held constant in time along the solid surfaces.

The flow variables of Q at zonal boundaries are explicitly updated after each time step by interpolating values from the adjacent grid. The zonal boundary conditions are nonconservative, but for subsonic flow this should not affect the accuracy of the final flow solution.

Grid Generation

The Navier–Stokes analysis uses overlaid zonal grids to discretize the vane-blade flow field and facilitate relative motion of the rotor (see Fig. 1). A combination of O- and H-grid sections are generated at constant radial spanwise locations in the blade-to-blade direction extending upstream of the vane leading edge to downstream of the rotor blade trailing edge. Algebraically generated H-grids are used in the regions upstream of the leading edge, downstream of the trailing edge, and in the interblade region. The O-grids, which are body-fitted to the surfaces of the airfoils and generated using an elliptic equation solution procedure, are used to resolve the viscous flow in the blade passages properly and to apply the algebraic turbulence model easily. Computational grid lines within the O-grids are stretched in the blade-normal direction with a fine grid spacing at the wall. The combined H- and O-overlaid grid sections are stretched in the spanwise direction away from the hub and tip regions with a fine grid spacing located adjacent to the hub and tip. An O-grid structure is used in the region between the rotor blade and the tip endwall in the tip clearance region. Grid generation for the two-dimensional analysis is similar to that for the three-dimensional procedure.

Numerical Results

A series of two- and three-dimensional numerical simulations have been performed and the predicted results have been com-

Table 1 Design, experimental, and predicted data

	Design	Expt No CERTS Mid-span	Expt CERTS Mid-span	2-D NS No CERTS	2-D NS CERTS	3-D NS CERTS Mid-span 1.2% CL	3-D NS CERTS Mid-span NO CL
T_{t0} (K)	1533	672	712	673	711	710	711
P_{t0} (N/m^2)	1241000	310300	308995	310221	309002	309029	308914
P_0 (N/m^2)	1225000	305947	304679	305573	304529	304157	304267
M_0	0.1422	0.1438	0.1438	0.1487	0.1463	0.1525	0.1492
α_0 (deg)	0.0	0.0	0.0	0.0	0.0	0.0	0.0
T_{t2} (K)	1305	551	557	543	574	565	569
α_2 (deg)	30.2	16.55	16.40	28.84	28.27	17.32	18.87
β_2 (deg)	67.9	61.66	60.95	67.20	67.00	62.90	62.48
V/V_{cr2}	0.394	0.440	0.445	0.414	0.410	0.390	0.410
W/W_{cr2}	0.867	0.845	0.847	0.887	0.879	–	–
η	0.890	0.890	0.890	0.92	0.92	0.87	0.86

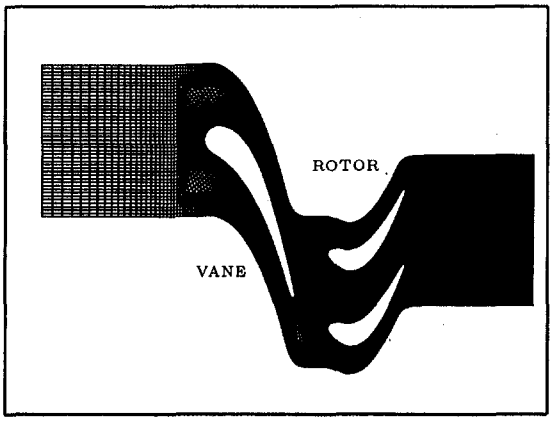

Fig. 3 Two-dimensional computational grid topology

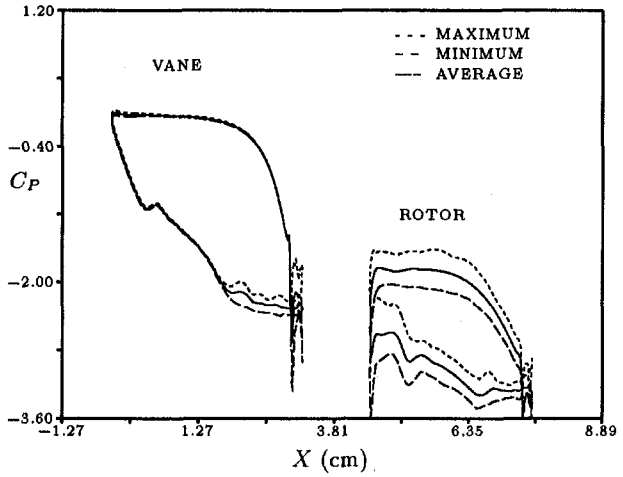

Fig. 4 Unsteady pressure envelopes for the vane and blade, with CERTS

pared with the experimental data reported by Schwab et al. (1983) and Stabe et al. (1984). The geometry used in both the two- and three-dimensional computations consists of the single-stage turbine in the NASA Lewis Research Center (LeRC) Warm Core Turbine Test Facility, which includes 26 vane airfoils and 48 rotor airfoils. An accurately scaled simulation of this configuration would require 13 vane and 24 blade airfoils. To produce reasonable computation times in the three-dimensional simulations, a one-vane/one-rotor rescaling strategy was used. The vane was scaled down by a factor of (26/48) and it was assumed that there were 48 vane airfoils. The pitch-to-chord ratio of the vane was not changed. For the two-dimensional simulations, a one-vane/two-blade rescaling strategy was employed. In this case it was assumed that there were 26 vane airfoils and 52 blade airfoils, and the rotors were scaled down by the factor of (48/52).

The inlet radial total temperature and pressure profiles in the experiment were produced using the Combustor Exit Radial Temperature Simulator (CERTS) at LeRC. The CERTS injects coolant air through circumferential slots in the hub and tip endwalls upstream of the vane. The radial variations in the total temperature and total pressure produced by the CERTS are illustrated in Fig. 2.

Based on the experimental data and the design velocity triangles, the midspan Mach number at the inlet to the vane was approximately equal to 0.14 and the inlet flow was assumed to be axial. The rotor rotational speed was 11,373 rpm. The experimental flow coefficient was $\phi = u_o/U = 0.27$, and the free stream Reynolds number was approximately 5.85×10^6 per meter (150,000 per inch). A pressure ratio of $P_2/P_{t0} \approx 0.385$ was determined from the midspan inlet total pressure and the static pressure measured in the rotor trailing-edge plane. An inviscid quasi-one-dimensional flow analysis was used to determine the remainder of the initial flow conditions for the two- and three-dimensional simulations. A tabulation of the flow parameters with and without the CERTS is presented in Table 1.

Two-Dimensional Simulations. Two-dimensional unsteady simulations were performed, with and without the inclusion of the CERTS, for the midspan section of the turbine.

The computational grids used to discretize the vane flow field in the two-dimensional simulations contained 121 × 41 (streamwise × tangential) grid points in the O-grid and 111 × 45 grid points in the H-grid. The grids used to discretize the rotor flow field contained 121 × 41 points in the O-grid and 119 × 45 grid points in the H-grid. A total of 30,588 grid points were used in the viscous simulations. Figure 3 illustrates the grid topology used in the two-dimensional simulations. The grid extended 2.5 vane axial chord lengths upstream and 2 blade axial chords downstream. Typical viscous simulations required 0.00024 seconds of CPU time per grid point per iteration (with two Newton subiterations) on a DEC 3000-400 workstation. For the unsteady simulations, 15 rotor blade-passing cycles at 3000 iterations (including two Newton iterations) per cycle were performed to ensure a time-periodic solution (in terms of performance quantities). A cycle corresponds to a rotor blade rotating through an angle of $2\pi/N$, where N is the number of vanes used in the simulation (i.e., $N = 1$). The average values of y^+, the nondimensional distance of the first grid point above the surface, were equal to 1.85 for the vane and 1.65 for the blade.

Figures 4 illustrates the minimum, maximum, and time-averaged pressure coefficient distributions along the vane and blade surfaces during one rotor blade passing cycle for the case with the CERTS. The results from the case without the CERTS were nearly identical to those from the case with the CERTS, and therefore have been omitted. In this investigation, the pressure coefficient is defined as

$$C_p = \frac{P_{\text{avg}} - P_{t_1}}{\frac{1}{2}\rho_1 U^2} \tag{8}$$

where P_{avg} is the local (minimum, maximum, or time-averaged) pressure, P_{t_1} is the inlet total pressure, ρ_1 is the average inlet free stream density, and $U = \Omega r$ is the rotor velocity. The unsteadiness in the vane is mainly confined to the uncovered portion of the suction surface and is caused by potential interac-

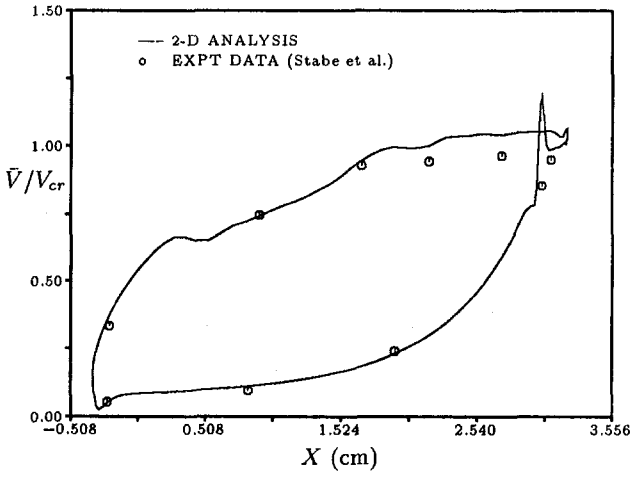

Fig. 5 Velocity ratio distribution for the vane

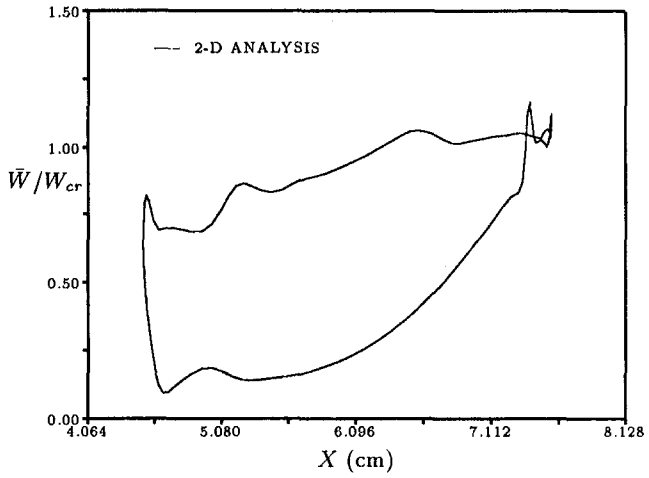

Fig. 6 Velocity ratio distribution for the blade

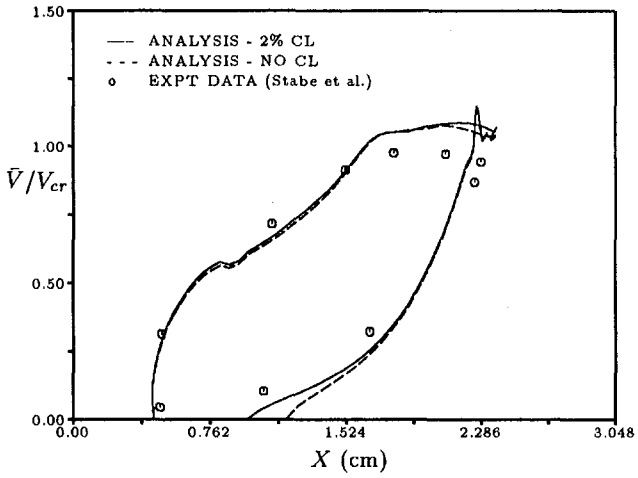

Fig. 8 Velocity ratio distribution at the vane hub

tions with the passing rotor blades. The rotor blade exhibits a large amount of unsteadiness over the entire surface. The unsteadiness in the rotor is caused by potential interactions with the vane (near the blade leading edge) and by the rotor blades passing through the wakes shed by the vanes.

The numerical solutions were compared with the available experimental data in the form of surface velocity ratios (Stabe et al., 1984). In this study, the time-averaged velocity ratio is defined as

$$\bar{V}/V_{cr} = \bar{V} \Big/ \sqrt{\frac{2\gamma}{\gamma + 1} RT_t} \tag{9}$$

where $\bar{V}$ is the time-averaged surface velocity obtained via the isentropic relations, V_{cr} is the critical velocity, and R is the universal gas constant. For rotating blade rows, the absolute velocity ratio is replaced by the relative velocity ratio ($\bar{W}/W_{cr}$) and the absolute total temperature is replaced by the relative total temperature. Figures 5 and 6 illustrate the velocity ratios along the vane and blade surfaces, respectively, for the case including the CERTS. Also included in Fig. 5 is the experimental data reported in Stabe et al. (1984). The predicted results and the experimental data for the vane show good agreement, except along the uncovered portion of the suction surface. Referring back to Fig. 4, this is the portion of the vane that experiences flow unsteadiness due to potential interaction with the blade. The velocity distribution for the blade is similar to the design velocity distribution presented in Stabe et al. (1984).

The convection of the vane and blade wakes is highlighted in Fig. 7, which shows unsteady entropy contours at one instant in time. Additional vane and blade passages have been added to the figure for clarity. Both the vane and the blade exhibit vortex shedding, and the structures remain coherent all the way to the exit boundary. The wake of the vane is cut by the passing rotor blades, and the filaments are stretched between the rotor pressure and suction surfaces due to differences in the flow velocity. Downstream of the rotor blade, a combination of vane and blade wakes are visible.

Table 1 contains the time-averaged inlet and exit quantities from the two-dimensional simulations with and without the CERTS. Both of the two-dimensional simulations exhibit approximately 2 deg of flow underturning compared to the design value, but much less than the 15 deg of underturning observed in the experiments. Therefore, the underturning observed in the experiments may be caused by three-dimensional viscous phenomena.

Three-Dimensional Simulations. A set of three-dimensional simulations have been performed for the turbine stage, including the CERTS. The vane grid system was constructed with 101 × 31 grid points in each spanwise O-grid and 86 × 41 grid points in each spanwise H-grid. The rotor grid system was constructed with 101 × 31 grid points in each spanwise O-grid and 83 × 41 grid points in each spanwise H-grid. A total of 40 O-H grid planes were distributed in the spanwise direction. In the first simulation, the rotor region had a tip clearance grid system that contained 101 × 17 grid points in

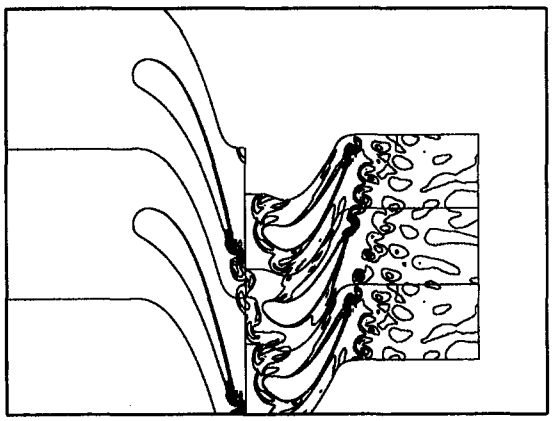

Fig. 7 Unsteady entropy contours in the turbine stage

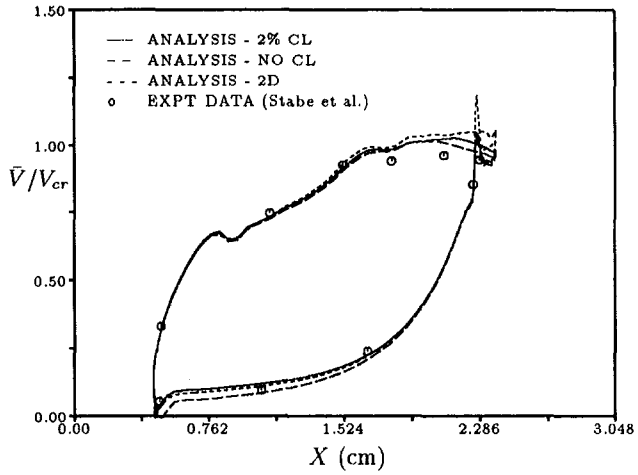

Fig. 9 Velocity ratio distribution at the vane midspan

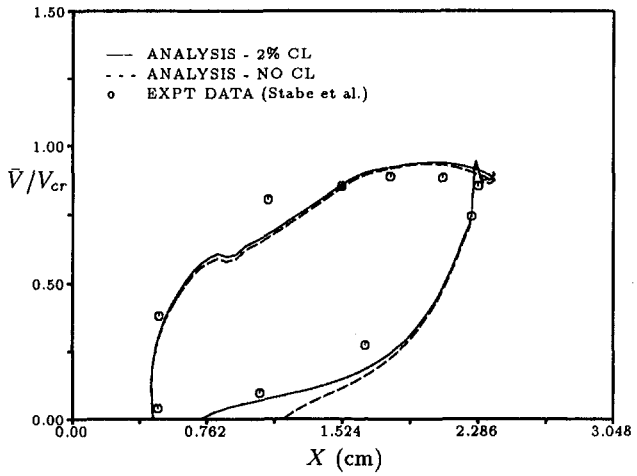

Fig. 10 Velocity ratio distribution at the vane tip

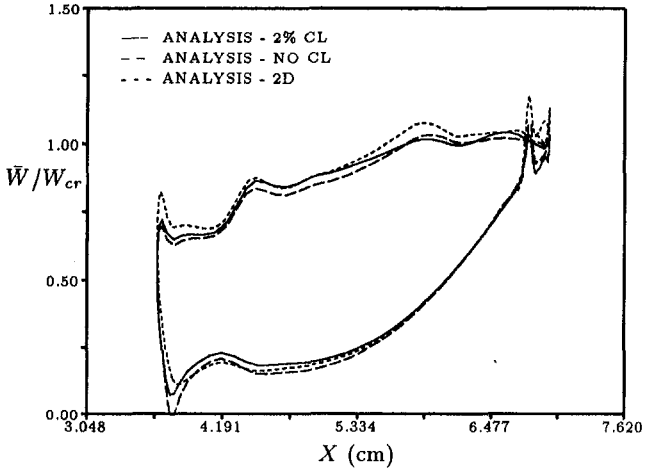

Fig. 12 Velocity ratio distribution at the blade midspan

each of five spanwise locations. A total of 536,730 grid points were used in the first three-dimensional simulation. The experimental rotor had a tip gap equal to 1.2 percent of the rotor span (Schwab et al., 1983), while the tip clearance in the three-dimensional simulation was set equal to 2.0 percent of the rotor span. A larger tip gap was used in the numerical simulation to address the grid density constraints in a practical manner. A second three-dimensional numerical simulation was performed with no tip clearance. The midspan section of the three-dimensional computational grids is illustrated in Fig. 1. The grid extended 1.2 vane axial chord lengths upstream and 1.2 blade axial chords downstream. Typical viscous simulations required 3.0×10^{-5} seconds of CPU time per grid point per iteration (with two Newton subiterations) on a Cray C90 supercomputer. The average value of y^+ along the surface of the vane and blade surfaces was equal to approximately 3.0, while the hub and tip endwalls had average y^+ values of approximately 8.0. Both three-dimensional simulations were run for nine rotor blade-passing cycles, at 4000 iterations per cycle.

Figures 8–10 illustrate the time-averaged velocity ratios along the hub, midspan, and tip sections of the vane, respectively, for the three-dimensional simulations. Also included in Figs. 8–10 are the experimental data presented in Stabe et al. (1984) and the two-dimensional predicted results. At the hub, the predicted results show good agreement with the experimental data (see Fig. 8). Differences are noticeable near the leading edge of the pressure surface and along the uncovered portion of the suction surface. Similar to the results of the two-dimensional simulations, the differences along the uncovered portion of the blade are probably caused by potential interactions with the passing rotor blade. At midspan (Fig. 9), the predicted results and experimental data exhibit very close agreement. At the tip (Fig. 10), the numerical results show fair agreement with the experimental data. A rather large discrepancy exists between the predicted results and the experimental data at approximately 40 percent of the axial chord on the suction surface. Considering the experimental data at the hub and midspan, and the fact that the vane is an untwisted airfoil of constant blade section, it is believed that the experimental data point is anomalous.

The time-averaged relative velocity ratio distributions at the hub, midspan, and tip locations of the rotor blade are illustrated in Figs. 11–13, respectively. The midspan velocity ratio distributions shows excellent agreement with the two-dimensional results, while the hub and tip distributions show significantly reduced loading due to the endwall and tip clearance flows.

Figures 14–16 contain the spanwise distributions of the time-averaged absolute total temperature, absolute total pressure, and absolute flow (tangential) angle at the exit of the blade. Figures 14–16 also contain the experimental data presented in Schwab et al. (1983) and Stabe et al. (1984). The predicted total temperature distributions show fair agreement with the experimental data (see Fig. 14). The solution including tip clearance shows relatively good agreement with the experimental data from the hub endwall to approximately 70 percent of the span. Near the

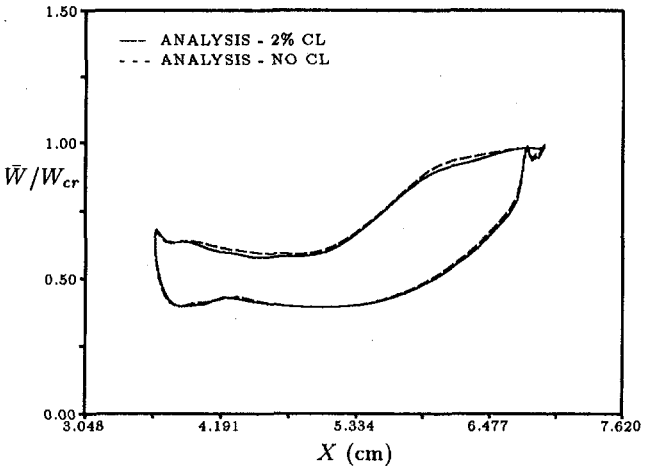

Fig. 11 Velocity ratio distribution at the blade hub

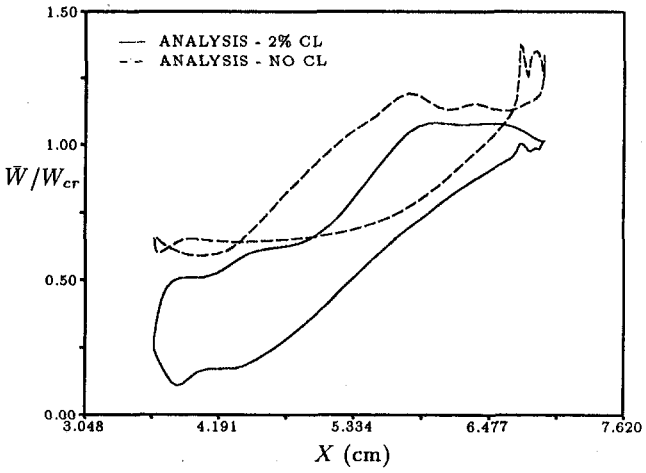

Fig. 13 Velocity ratio distribution at the blade tip

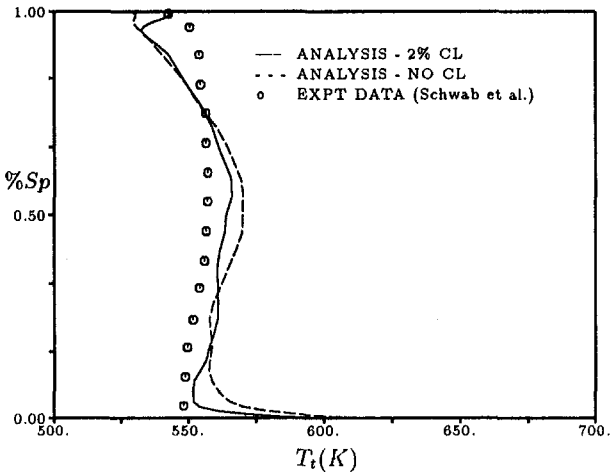

Fig. 14 Absolute total temperature distributions at the blade exit

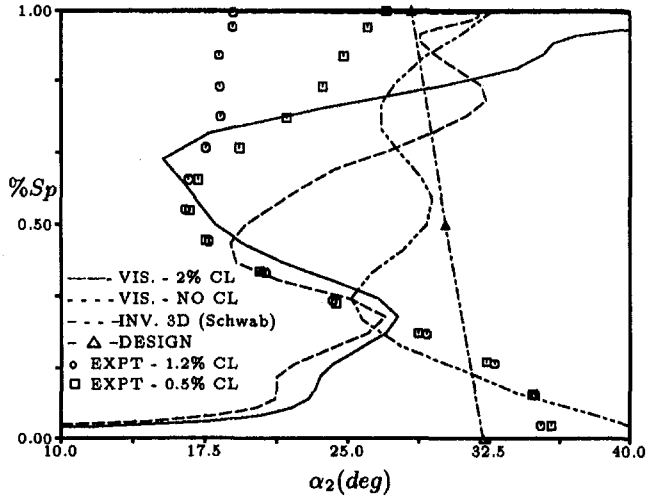

Fig. 16 Absolute flow angle distributions at the blade exit

tip however, the total temperature shows more variation than that indicated by the experimental data. The solution without tip clearance indicates trends similar to those for the case including tip clearance, with small differences noticeable near the hub and midspan. The midspan temperature for the solution without tip clearance is similar to that predicted in the two-dimensional simulation. Note, in both numerical solutions the exit plane is located 1.2 blade axial chord lengths downstream of the blade trailing edge and the hub rotates at the speed of the shaft. The experimental data, however, were obtained at a location 2.5 chord lengths downstream of the blade trailing edge where both the hub and tip endwalls were stationary. Therefore, the numerical results indicate an increase in the absolute total temperature at the hub endwall while the experimental data do not show an increase. In addition, the assumption that the flow is mixed out in the numerical simulations may warrant further examination. The predicted absolute total pressure distributions compare favorably with the experimental data (see Fig. 15). Small discrepancies are noticeable near the hub and tip endwalls in both cases. Figure 16 shows the absolute (tangential) flow angle distributions at the exit of the blade passage. Included in this figure are the predicted flow angle distributions with and without tip clearance, the results of a steady, inviscid three-dimensional simulation (Schwab et al., 1983), experimental data for tip gaps of 0.5 and 1.2 percent (Schwab et al., 1983; Stabe et al., 1984), and the design values. The experimental data show severe underturning near midspan, while the flow angle returns to approximately the design value at the hub endwall. Near the tip endwall, the flow angle is observed to be directly related to the amount of tip clearance. As the tip clearance increases, the amount of flow turning is reduced. Near midspan, the numerical results also indicate substantial underturning of the flow. The simulation including tip clearance shows approximately 2 deg more underturning than the case without tip clearance. The results of both numerical simulations show discrepancies with the experimental data near the hub endwall. These are partly due to the rotation of the hub endwall in the numerical simulations, partly due to the nature of the secondary flows in the hub region, and partly due to grid resolution. Near the tip endwall, the simulation without the inclusion of tip clearance exhibits fair agreement with the experimental data. The simulation including tip clearance shows large deviations from the experimental data. The differences are caused by the increased tip gap in the simulation, which generates a much stronger tip clearance vortex. The underturning predicted in the unsteady three-dimensional simulations was not captured in the current two-dimensional unsteady simulations, or by a previous steady three-dimensional inviscid analysis of the turbine stage (Schwab et al., 1983). Therefore, the underturning is caused by three-dimensional, viscous effects, which will now be discussed in greater detail.

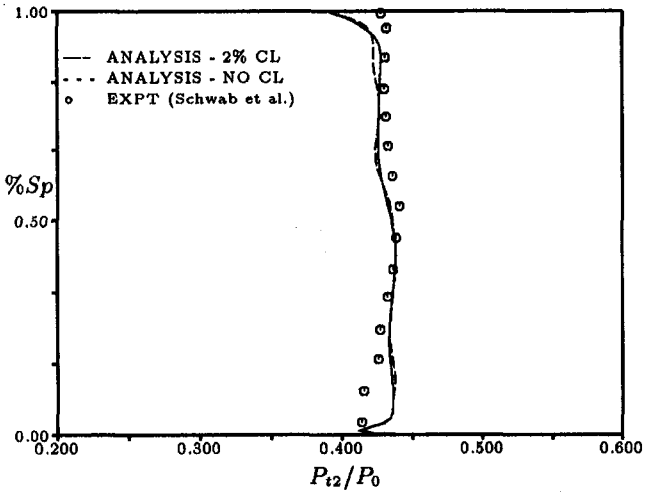

Fig. 15 Absolute total pressure distributions at the blade exit

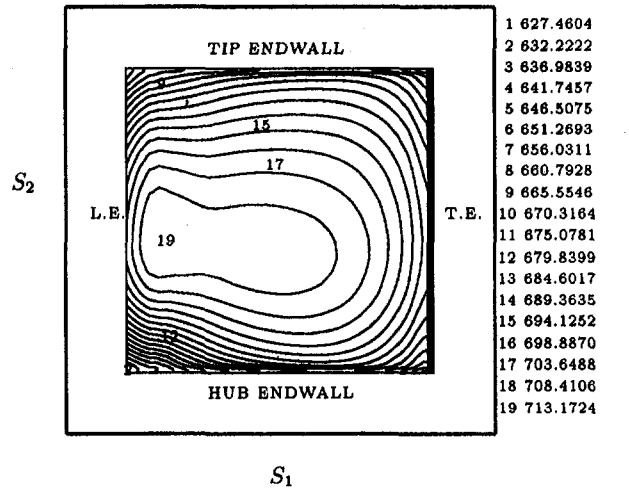

Fig. 17 Absolute total temperature contours on vane pressure surface, with tip clearance

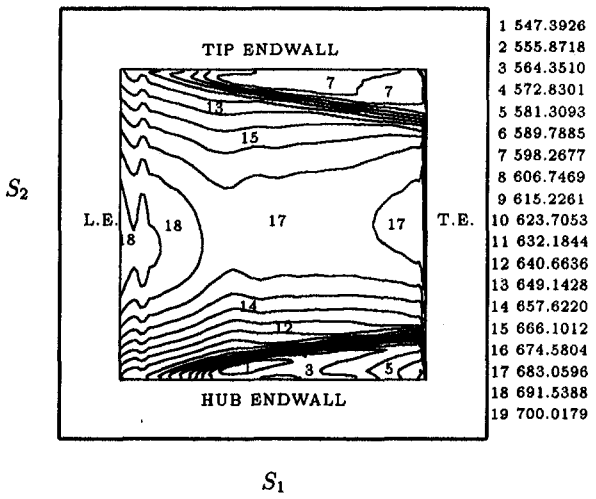

Fig. 18 Absolute total temperature contours on vane suction surface, with tip clearance

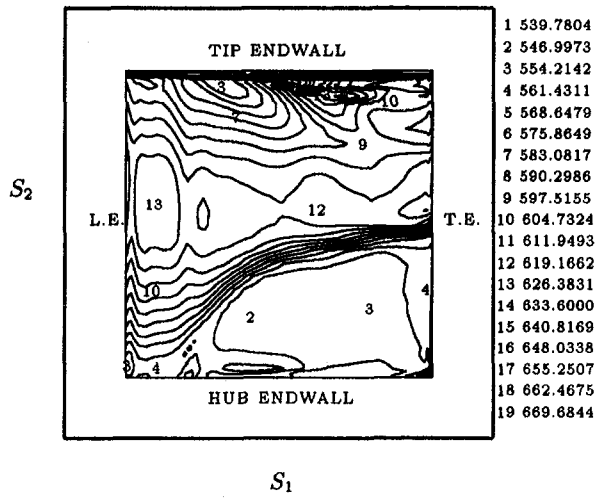

Fig. 20 Relative total temperature contours on blade suction surface, with tip clearance

The time-averaged absolute total temperature contours along the pressure and suction surfaces of the vane are illustrated in Figs. 17 and 18, respectively. The results in these two figures are for the case including tip clearance; the results from the case without tip clearance were very similar for the vane passage. The contours have been plotted as a function of arc length in the streamwise and spanwise directions for clarity of presentation. Along the pressure surface of the vane (Fig. 17), hotter fluid is present in the hub and tip endwall regions at the trailing edge, while cooler pockets are located near the hub and tip endwalls regions at the leading edge. These results are very similar to the results of the inviscid, steady three-dimensional simulation presented by Schwab et al. (1983). On the suction surface of the vane, the total temperature contours reveal the presence of strong hub and tip endwall secondary flows (see Fig. 18). Within the secondary flow regions, the low-momentum fluid has significantly reduced temperatures. In the midspan region of the suction surface, the temperature is almost constant in the streamwise direction.

Figures 19 and 20 contain the time-averaged relative total temperature contours along the pressure and suction surfaces of the blade, respectively, for the case including tip clearance. Along the pressure surface (see Fig. 19) of the blade, the hotter fluid migrates radially toward the hub and tip endwalls. At the tip, some of the hot fluid dumps over onto the suction surface of the blade. In the hub endwall region near the leading edge, there is a cooler pocket of fluid, which was also observed in the simulations of Schwab et al. (1983). This cooler region is probably caused by the secondary flows generated in the vane passage. Along the suction surface of the blade (see Fig. 20), the secondary flows extend to almost 50 percent of the span. The temperature inside the secondary flow region is significantly lower than that of the surrounding flow. The warmer fluid is forced by the secondary and tip clearance flows into a narrow region extending from approximately 50 to 75 percent of the span. Aft of midchord in the tip region, warmer fluid from the pressure surface dumps over the gap onto the suction surface. The results of the current investigation are similar to those of Dorney et al. (1992) and Dorney and Davis (1993) for a three-dimensional circular hot streak; along the pressure surface of the rotor the hot fluid spreads out radially toward the hub and tip, while the hotter fluid on the suction surface is confined to the midspan region by the secondary and tip flows.

Figure 21 contains the time-averaged relative total temperature contours along the suction surface of the blade for the case without tip clearance. The flow features on the pressure surface of the blade were similar to those from the case including tip clearance (see Fig. 19). The warmer fluid migrates radially

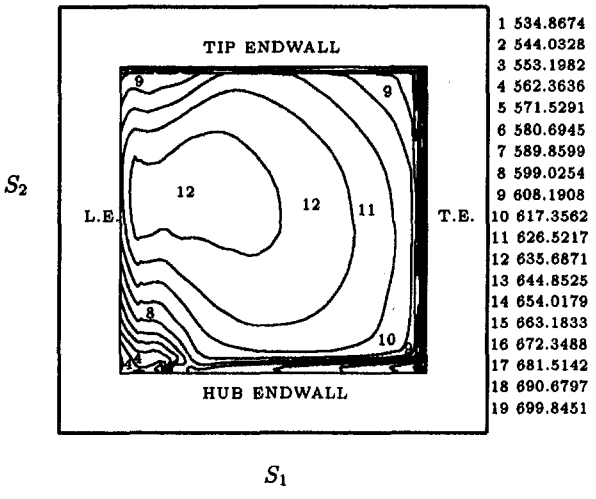

Fig. 19 Relative total temperature contours on blade pressure surface, with tip clearance

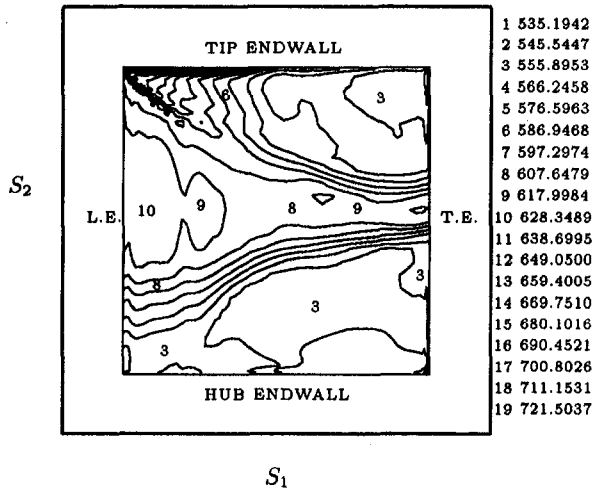

Fig. 21 Relative total temperature contours on blade suction surface, without tip clearance

toward the hub and tip endwalls, with a cooler pocket of fluid located at the hub endwall near the leading edge. On the suction surface of the blade (see Fig. 21), the tip leakage flow has been replaced by a strong endwall boundary layer. The hub and tip endwall boundary layers squeeze the warmer fluid into a very narrow region around midspan. Within the secondary flow regions, the low-momentum fluid is much cooler than in the core-flow region.

It is the secondary flows that appear to account for the severe underturning observed in the experiments of Schwab et al. (1983) and Stabe et al. (1984) (note the underturning was also observed without the inclusion of the CERTS). In the rotor passage, the colder fluid associated with the hub endwall secondary flow moves along the hub from the pressure side to the suction side of the passage. From there the flow moves radially along the suction surface of the blade. At the same time, higher (total) temperature (i.e., higher energy) fluid spreads radially from the midspan of the pressure surface toward the hub and tip endwalls. As the flow progresses through the passage, warmer fluid is entrained into the secondary flow and moves toward the suction surface of the blade. In addition, warmer fluid dumps over the tip clearance region from the pressure surface to the suction surface. It is observed that the flow angle distribution in the blade passage follows patterns similar to the relative total temperature distribution. Larger flow angles are associated with the lower temperature regions, while smaller flow angles are associated with the higher temperature regions. Near the trailing edge the secondary flows have pinched warmer fluid *in the core flow region* toward midspan, resulting in a severe underturning of the flow. The tip clearance flow is seen to have a strong effect on the flow angle from about 50 percent span to the tip.

Finally, Table 1 contains the time-averaged inlet and exit quantities at midspan from the three-dimensional simulations with and without tip clearance, showing good agreement with the experimental data.

Conclusions

A series of two- and three-dimensional, unsteady, viscous numerical simulations have been performed for a turbine stage with total pressure and total temperature profiles introduced at the vane inlet. The numerical simulations were designed to understand the severe underturning observed at the rotor exit in previous experiments. The predicted three-dimensional results showed the redistribution of the warmer fluid to the pressure surface of the airfoils, as well as the underturning of the flow at the exit of the rotor. It was determined that the underturning was caused by strong endwall secondary flows, which were generated on the suction side of the rotor blade. It was also shown that the tip clearance has a significant impact on the rotor exit flow angle from approximately 60 to 100 percent of the span.

Acknowledgments

The three-dimensional simulations were performed on the NAS Cray C90 supercomputer located at NASA Ames Research Center. The authors would like to thank Ms. Jeannine Banks of NASA Lewis Research Center for assistance with the computational aspects of this program.

References

Baldwin, B. S., and Lomax, H., 1978, "Thin-Layer Approximation and Algebraic Model for Separated Turbulent Flows," AIAA Paper No. 78-257.

Butler, T. L., Sharma, O. P., Joslyn, H. D., and Dring, R. P., 1989, "Redistribution of an Inlet Temperature Distortion in an Axial Flow Turbine Stage," *AIAA Journal of Propulsion and Power,* Vol. 5, Jan.–Feb., pp. 64–71.

Chakravarthy, S., and Osher, S., 1982, "Numerical Experiments With the Osher Upwind Scheme for the Euler Equations," AIAA Paper No. 82-0975.

Dorney, D. J., Davis, R. L., and Sharma, O. P., 1991, "Two-Dimensional Inlet Temperature Profile Attenuation in a Turbine Stage," ASME Paper No. 91-GT-406.

Dorney, D. J., Davis, R. L., Edwards, D. E., and Madavan, N. K., 1992, "Unsteady Analysis of Hot Streak Migration in a Turbine Stage," *AIAA Journal of Propulsion and Power,* Vol. 8, No. 2, pp. 520–529.

Dorney, D. J., and Davis, R. L., 1993, "Numerical Simulation of Turbine 'Hot Spot' Alleviation Using Film Cooling," *AIAA Journal of Propulsion and Power,* Vol. 9, No. 3, pp. 329–336.

Harasgama, S. P., 1990, "Combustor Exit Temperature Distortion Effects on Heat Transfer and Aerodynamics Within a Rotating Turbine Blade Passage," ASME Paper No. 90-GT-174.

Kirtley, K. R., Celestina, M. L., and Adamczyk, J. J., 1993, "The Effect of Unsteadiness on the Time-Mean Thermal Loads in a Turbine Stage," SAE Paper 931375 (also to appear in the ASME JOURNAL OF TURBOMACHINERY).

Krouthen, B., and Giles, M. B., 1988, "Numerical Investigation of Hot Streaks in Turbines," AIAA Paper No. 88-3015.

Rai, M. M., 1989, "Three-Dimensional Navier–Stokes Simulations of Turbine Rotor–Stator Interaction," *AIAA Journal of Propulsion and Power,* Vol. 5, pp. 307–319.

Rai, M. M., and Dring, R. P., 1990, "Navier–Stokes Analyses of the Redistribution of Inlet Temperature Distortions in a Turbine," *AIAA Journal of Propulsion and Power,* Vol. 6, pp. 276–282.

Roback, R. J., and Dring, R. P., 1993, "Hot Streaks and Phantom Cooling in a Turbine Rotor Passage: Part 1—Separate Effects," ASME JOURNAL OF TURBOMACHINERY, Vol. 115, pp. 657–666.

Roe, P. L., 1981, "Approximate Riemann Solvers, Parameter Vectors, and Difference Schemes," *Journal of Computational Physics,* Vol. 43, pp. 357–372.

Saxer, A. P., and Giles, M. B., 1990, "Inlet Radial Temperature Redistribution in a Transonic Turbine Stage," AIAA Paper No. 90-1543.

Saxer, A. P., and Felici, H. M., 1996, "Numerical Analysis of Three-Dimensional Unsteady Hot Streak Migration and Shock Interaction in a Turbine Stage," ASME JOURNAL OF TURBOMACHINERY, Vol. 118, pp. 268–277.

Schwab, J. R., Stabe, R. G., and Whitney, W. J., 1983, "Analytical and Experimental Study of Flow Through an Axial Turbine Stage With a Nonuniform Inlet Radial Temperature Profile," AIAA Paper 83-1175; also NASA TM 83431.

Stabe, R. G., Whitney, W. J., and Moffitt, T. P., 1984, "Performance of a High-Work Low Aspect Ratio Turbine With a Realistic Inlet Radial Temperature Profile," AIAA Paper No. 84-1161; also NASA TM 83655.

Takahashi, R. K., and Ni, R. H., 1990, "Unsteady Euler Analysis of the Redistribution of an Inlet Temperature Distortion in a Turbine," AIAA Paper No. 90-2262.

Takahashi, R. K., and Ni, R. H., 1991, "Unsteady Hot Streak Migration Through a 1-1/2 Stage Turbine," AIAA Paper No. 91-3382.

Weigand, B., and Harasgama, S. P., 1994, "Computations of a Film-Cooled Turbine Rotor Blade With Non-uniform Inlet Temperature Distribution Using a Three-Dimensional Viscous Procedure," ASME Paper No. 94-GT-15.

The Design and Performance of a High Work Research Turbine

E. P. Vlasic

S. Girgis

S. H. Moustapha

Turbine Aerodynamics and Cooling,
Pratt & Whitney Canada,
Montréal, Quebéc, Canada

This paper describes the design and performance of a high work single-stage research turbine with a pressure ratio of 5.0, a stage loading of 2.2, and cooled stator and rotor. Tests were carried out in a cold flow rig and as part of a gas generator facility. The performance of the turbine was assessed, through measurements of reaction, rotor exit conditions and efficiency, with and without airfoil cooling. The measured cooled efficiency in the cold rig was 79.9 percent, which, after correcting for temperature and measuring plane location, matched reasonably well the efficiency of 81.5 percent in the gas generator test. The effect of cooling, as measured in the cold rig, was to reduce the turbine efficiency by 2.1 percent. A part-load turbine map was obtained at 100, 110, and 118 percent design speed and at 3.9, 5.0, and 6.0 pressure ratio. The influence of speed and the limit load pattern for transonic turbines are discussed. The effect of the downstream measuring distance on the calculated efficiency was determined using three different locations. An efficiency drop of 3.2 percent was measured between the rotor trailing edge plane and a distance four chords downstream.

Introduction

Research and development on single stage, high work compressor turbines is readily justified by the light weight, low initial cost, and maintenance of such a turbine. For a low-cost, high overall pressure ratio, two-shaft engine, the work duty of a single-stage high-pressure turbine is high in order to achieve acceptable fuel consumption. Yet this work is subject to a maximum speed and annulus area to obtain moderate levels of blade and disk stress so as to maximize engine life. In addition, the high power requirement necessitates a high turbine inlet temperature. These requirements generally lead to a turbine having a high pressure ratio and stage loading as well as cooled airfoils with small aspect ratio and supersonic exit Mach numbers.

A number of detailed experimental studies have been carried out to investigate the performance of transonic turbines. Figure 1 and Table 1 compare the stage parameters for some of these research turbines. Ewen et al. (1973) tested a lightly loaded, $\Delta H/U^2$ of 1.2, turbine with a P.R. of 3.4 (FRDC in Fig. 1). Okapuu (1974) investigated the effect of degree of reaction, nozzle and rotor aspect ratio, tip clearance and nozzle contouring on the performance of a turbine with a P.R. of 3.9 and a $\Delta H/U^2$ of 1.5 (DRB in Fig. 1). Liu et al. (1979) reported on the three-dimensional design and testing of a low aspect ratio turbine with a P.R. of 3.0 and a $\Delta H/U^2$ of 1.7 (LART in Fig. 1). Crow et al. (1980) tested a turbine, uncooled and with stator and rotor cooling, as part of the joint P&WA/NASA Energy Efficient Engine (E^3) program. The high rim speed turbine had a P.R. of 4.0, a low Cx/U of 0.3, and a $\Delta H/U^2$ of 1.6. They demonstrated 90.3 percent uncooled efficiency at a reaction of 35 percent and an efficiency drop of 2.5 percent because of cooling. Bryce et al. (1985) investigated the performance of a turbine with a P.R. of 4.5, a $\Delta H/U^2$ of 2.1, and a hub-to-tip diameter ratio of 0.84 (RAE in Fig. 1). The turbine, designed to have cooling in the stator and the rotor, was tested with solid blading in a cold flow rig and demonstrated an efficiency of 87 percent based on torquemeter temperature drop. Moustapha et al. (1987) described the performance of a highly loaded turbine, $\Delta H/U^2$ of 2.5, with a P.R. of 3.8 (HLT in Fig. 1). They investigated the effect of nozzle contouring and rotor loading on the performance of the nozzle, the rotor, and the stage. The measuring technique of the efficiency and the traversing location were discussed.

Research at Pratt and Whitney Canada has been focused over the years on high pressure ratio, highly loaded and uncooled blade turbines (Okapuu, 1974, Moustapha et al., 1987). This paper describes the aerodynamic design and rig testing of a cooled High Work Research Turbine (HWRT in Fig. 1). The turbine was designed for a pressure ratio of 4.4 (equivalent to 5.0 in the cold flow rig) and a stage loading of 2.2 (El-Fouly and Moustapha, 1990). The cold rig results will be presented for the uncooled and cooled tests at various speeds and pressure ratios. Comparison of the rig (HWRT) results with those obtained for the same turbine tested in an engine environment as part of a High Technology Demonstrator Engine (HTDE) program will be discussed.

Turbine Stage Aerodynamic Design

Stage Design. The research stage (HWRT) was modeled on a realistic compressor turbine for a small, low-cost and advanced aeroengine. This engine (HTDE) would employ a single-stage gas generator turbine operating at sufficiently high inlet gas temperatures to require stator and rotor cooling. Table 1 gives the research stage design point parameters as compared to other published high pressure ratio turbines. Figure 2(a) shows the HWRT cold flow rig including the turbine gas path and instrumentation planes. Because of the difference in the specific heat ratio between the engine and the cold flow rig, the stage pressure ratio is 5.0 in the rig compared to 4.4 in the engine, as shown in Table 1.

The gas path (Fig. 2(b)) shows a slightly contoured outer diameter for the vane to reduce secondary flow and a cylindrical one for the blade for minimum tip clearances. The stator-to-rotor axial gap (0.5 of stator axial chord) was a compromise between aerodynamic, mechanical and blade vibration considerations. The mean reaction (31 percent was limited by the high stage exit swirl angle (39 deg) and Mach number (0.62) on one hand, and the blade metal temperature on the other. Midspan velocity triangles (Fig. 3) show the nozzle and rotor transonic exit Mach numbers and the large amount of flow turning needed for high stage work requirements. A radial work distribution was used to unload the hub and tip sections and hence reduce

Contributed by the International Gas Turbine Institute and presented at the 40th International Gas Turbine and Aeroengine Congress and Exhibition, Houston, Texas, June 5–8, 1995. Manuscript received by the International Gas Turbine Institute February 27, 1995. Paper No. 95-GT-233. Associate Technical Editor: C. J. Russo.

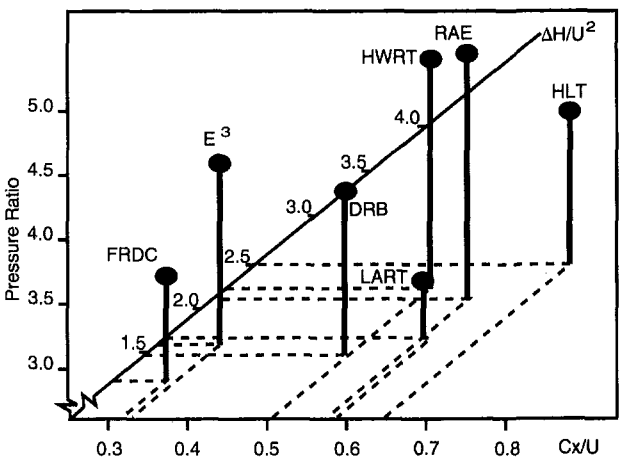

Fig. 1 High pressure research turbine characteristics

Table 1 Comparison of the HWRT with other high pressure ratio turbines

Stage Parameters	HWRT (HTDE)	E3	RAE	HLT	DRB
P.R.	5.0 (4.4)	4.0	4.5	3.8	3.9
$\Delta H/U^2$	2.2	1.6	2.1	2.5	1.5
Cx/U	0.48	0.3	0.65	0.63	0.56
Airfoil count Vane	18	24	40	14	29
Airfoil count Blade	43	54	89	51	54
Reaction	31	35 & 43	30	30	28
Exit swirl, deg.	39	41	37	37	4
Exit Mach number	0.62	0.5	0.62	0.65	0.6
$AN^2 \times 10^{-10}$	1.6 (4.7)	4	0.8	1.3	2.15
Aspect ratio (Vane)	0.7	0.65	0.58	0.7	1.0
Aspect ratio (Blade)	1.4	1.4	1.29	1.44	1.66
T.E. blockage % (Vane)	14	9	10	20	16
T.E. blockage % (Blade)	28	11	11	13	16
Clearance/span %	1.1	0.8	1.4	1.5	1.7
η, cooled %	80.4 (81.9)	87.8			
η, uncooled %	82.0	90.3	87.0	81.4	88.6

the endwall losses. Selection of number of airfoils was based on a compromise between optimum loading (pitch-to-chord ratio), minimum trailing edge blockage, and secondary (aspect ratio) losses. After the mechanical considerations, 18 vanes and 43 blades were chosen. Using the correlation of Kacker and Okapuu (1982) and after accounting for the cooling flow mixing losses, the vane and blade mean total pressure loss coefficients (based on exit dynamic head) were 0.25 and 0.33, respectively. This resulted in a gas path cooled turbine efficiency of 81.9 percent at engine conditions (HTDE, Table 1) for a rotor tip clearance of 1.1 percent of the blade height.

Comparing the HWRT to other similar research turbines in Table 1, having cooled blades (e.g., E^3 and RAE) and uncooled blades (e.g., HLT and DRB), one could see that the present design is aggressive in terms of pressure ratio, stage loading, rotor trailing edge blockage and flow area speed square (AN^2).

Nozzle Design. For a given blade vibration mode, the vane number is selected to avoid dynamic interference with the blade frequency. The vane axial chord was chosen in order to provide a maximum thickness required for the cooling passage insert design. The resulting nozzle had 18 vanes of aspect ratio of 0.7 (based on mean true chord), a pitch-to-chord ratio of 0.85, a turning angle of 79 deg, and a mean exit Mach number of 1.14. Due to the high turbine inlet temperature, the vane cooling scheme called for shower head film cooling and internal cooling passage with pressure surface film ejection. The nozzle meridional leading to trailing edge contraction ratio was limited to 1.05 in order not to increase the rotor hub inlet relative Mach number above the already high value of 0.67. In addition, closing the gas path will increase the vane exit angle above 79 deg, which will result in manufacturing difficulties in sizing the airfoil throat. Different nozzle stacking configurations were analyzed in order to optimize the vane Mach number distributions, to improve the rotor hub inlet conditions and to provide for an inserted cooling scheme. Figure 4 shows the predicted vane surface Mach number distributions as obtained by a three-dimensional Euler flow solver due to Ni and Bogoian (1989).

Rotor Design. A cooled blade design for a high pressure ratio, high stage loading turbine generally poses conflicting design requirements in terms of the selection of the stage reaction. On one hand, a low mean reaction is required to give lower blade metal temperature, low stage exit Mach number and low root stagger angle and hence reduced rotor disk fixing stress and ease of platform fit. On the other hand a high reaction is needed to ensure the required discharge pressure for the cooling scheme, a low rotor hub inlet Mach number, and good blade hub flow acceleration. The rotor had 43 blades of aspect ratio of 1.4 (based on mean true chord) and a pitch-to-chord ratio of 0.7. The cooling scheme was a multipass configuration with trailing edge ejection. The low hub reaction of 19.4 percent resulted in an inlet Mach number of 0.67 and a turning of 137 deg at the root. This made it difficult to fit the hub section on a conventional platform without compromising the surface Mach number distribution. Accordingly, a contoured hub platform was used, as shown in Fig. 5. The blade sections were stacked using the trailing edge as a radial line with some tangential lean and meridional sweep. This stacking resulted in acceptable stress levels and reasonable Mach number distributions as shown in the three-dimensional inviscid solution of Fig. 6.

Experimental Facility and Procedure

The general arrangement of the HWRT is shown in Fig. 2(*a*). The test section is fed by a plenum of air, which is

Nomenclature

A = flow area
A.R. = aspect ratio
B = blade
C_p = average stage heat capacity at constant pressure, J/kg/K
Cx = axial velocity, m/s
H = stagnation enthalpy, J/kg
M = Mach number
N = rotational speed, rpm
P = total pressure, kPa
P.R. = stage total pressure ratio
Q = mass flow parameter = $W\sqrt{T}/P$
T = total temperature, K
T.E. = trailing edge
U = blade speed, m/s
V = vane
W = mass flow rate, kg/s
α = exit flow angle, degrees from axial
Δ = change
η = total to total efficiency = $[(WCp\Delta T)_{ms} + \Sigma(WCp\Delta T)_{cl}]/[(WCpi\Delta T_i)_{ms} + \Sigma(WCpi\Delta Ti)_{cl}]$

Subscripts

1, 2, . . = plane number (Fig. 2(*a*))
cl = cooling flow
i = ideal
ms = mainstream flow
r = relative

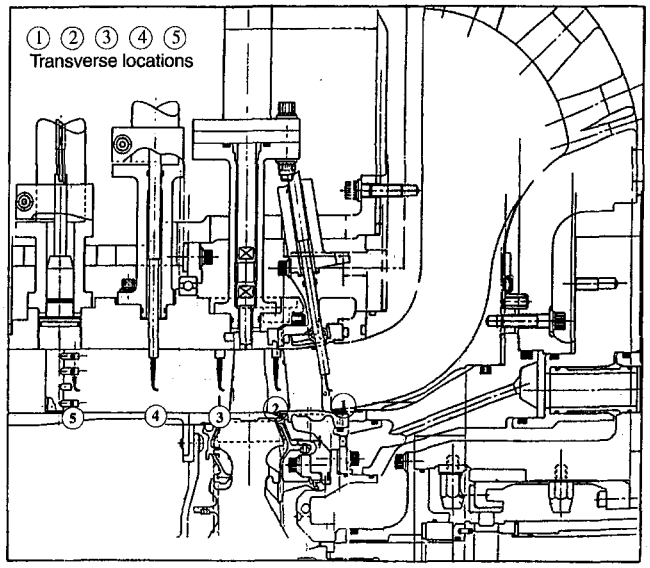

Fig. 2(*a*) High work research turbine rig

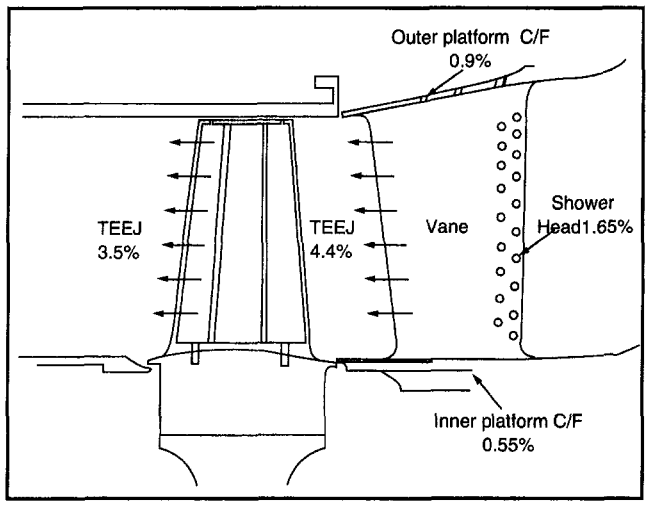

Fig. 2(*b*) High work research turbine cooling flow schematic

pressurized by upstream compressors capable of reaching plenum pressures of 275 kPa. Prior to entering the plenum chamber, the air is heated by heat exchangers. Inlet turbulence is simulated by using a honeycomb screen between the plenum and inlet to the test section. A straight exhaust duct is placed immediately downstream of the turbine to reduce the likelihood of duct loss in the relatively high swirl and Mach number regimes. Air is then exhausted by two compressors located downstream of the test section, which can pull the exhaust pressure down to about 35 kPa. This allows for the range of stage pressure ratios necessary for mapping the turbine characteristics. A dynamometer is used as a means of absorbing the turbine power and controlling its speed. Mainstream and cooling mass flow rates are measured using upstream venturi flow meters. The vane is fed with cooling flow via two cooling plenums, one in the tip location, the other in the hub. The blade cooling is provided by a TOBI system. Cooling flow temperature can be set at test section mainstream or ambient temperature. Thermocouples and static pressure taps are located in each of the three cooling plenums.

The plenum inlet temperature is sensed using 16 pairs of thermocouples equally spaced inside the plenum chamber. Similarly, plenum pressure is sensed using eight static taps. The inlet of the test section (plenum to vane leading edge) is characterized for drops in temperature and pressure using a cobra probe mounted in the plane of the vane leading edge. The rig inlet pressure and temperature were set at 275 kPa and 464 K, respectively.

A rotating shroud assembly permits a variety of probes (cobra, wedge, and touch probes) to be mounted and subsequently perform radial and circumferential traverses in many planes without interfering with one another. Three downstream cobra probe circumferential and radial traversing planes, shown in Fig. 2(*a*) as planes 3, 4, and 5 (0.2, 2, and 4 blade chords downstream, respectively), were used to allow for proper mixing and to measure the change in efficiency versus downstream location. Each of the three planes could accommodate one cobra

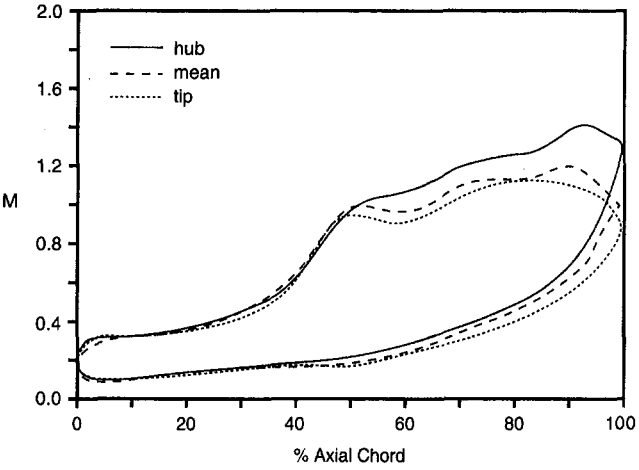

Fig. 4 Predicted vane surface Mach number distributions

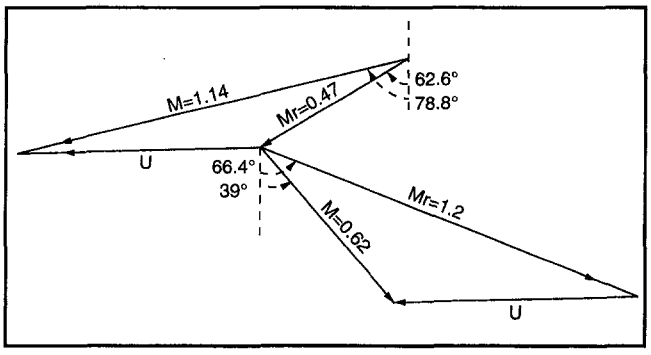

Fig. 3 Design point velocity triangles at midspan

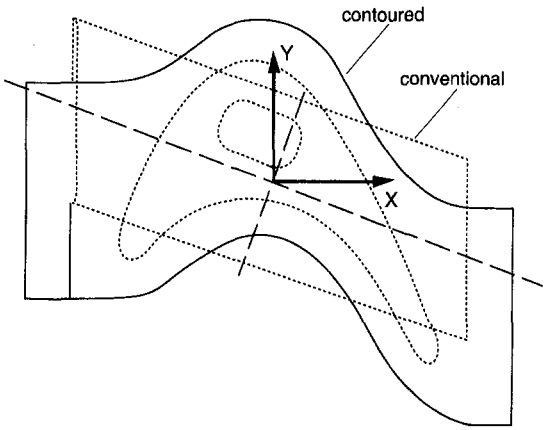

Fig. 5 Rotor hub platform configurations

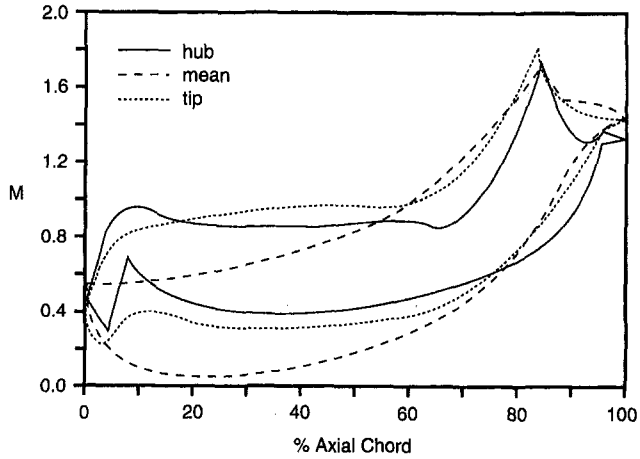

Fig. 6 Predicted blade surface Mach number distributions

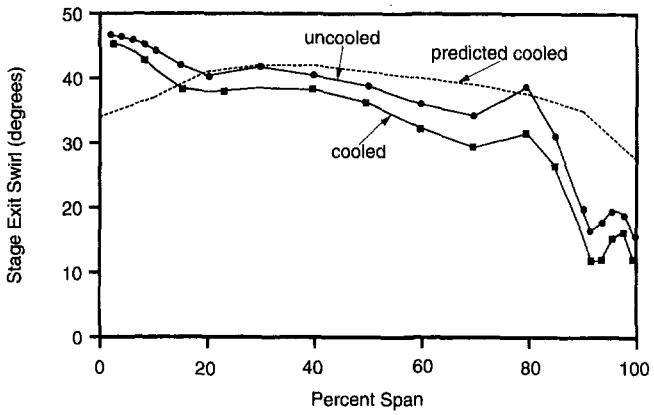

Fig. 7 Radial distribution of stage exit swirl, plane 3

probe at a given circumferential position. Since there was no risk of interference between cobra probes (traversing was done one plane at a time with the other two cobra fully retracted out of the gas path) and the inlet profile was uniform circumferentially, the circumferential positioning of the probes was chosen to facilitate installation. Exit total pressure measurement is accomplished by using four shielded Kiel head rakes. These nontraversing rakes are made and installed 90 deg apart, each with four pressure heads spaced approximately at the centers of equal area. Four exit temperature rakes of five heads each are installed 1 m down-stream of the rotor to ensure a well mixed flow field. However, at such a distance the test section is more susceptible to heat transfer with the test cell. To minimize this, the inlet temperature is set such that the measured average exhaust temperature matched the test cell ambient to within 3°C. As well, insulation is used to cover the entire length of the test section.

Gas path, rotor disk (upstream and downstream), and shroud cavity pressure statics are used to give information on velocity triangles, reactions, separation zones, and potential cooling flow leakages. Running tip clearances are assessed using three Rotadata touch probes spaced every 120 deg.

Effect of Cooling on Turbine Performance at Design Condition

The HWRT stage had, as a percentage of vane inlet flow, 7.5 percent vane and 3.5 percent blade cooling flow, as seen in Fig. 2(*b*). The vane cooling was split between showerhead and platform (2.2 percent) and pressure surface cutback trailing edge and shroud (5.3 percent). The blade cooling was all trailing edge ejection. The coolant to mainflow temperature ratio in the rig was between 0.75 and 0.95 while the engine (HTDE) ratio was between 0.45 and 0.65.

Table 2 summarizes the measured performance of the HWRT with and without the cooling flows at the design point (rig P.R. of 5.0). The absence of the cooling flow, upstream and downstream of the vane throat, created a larger effective vane throat area and therefore a larger nondimensional flow parameter (Q_1). The cooled turbine reactions are higher than their uncooled counterparts (more evident at the hub than the tip). The differences are attributed to the addition of cooling downstream of the vane throat, primarily on the inner platform, where the static pressure is more favorable. This cooling flow effectively increases the vane area and hence the reaction. The measured cooled turbine reaction agreed well with the target at the tip and was higher than target at the hub. With only one cooling feed for the vane, more cooling is provided to the vane exit hub region where the static pressure is lower than the tip region. This cooling, being added downstream of the throat, will increase the hub reaction.

Table 2 Comparison of design target parameters and measurements

Configuration	HWRT	HWRT	HWRT	HTDE	HTDE
Stage Parameters	Design Target	Measured	Measured	Design Target	Measured
	(Cooled)	(Uncooled)	(Cooled)		
P.R.	5.0	5.1	5.1	4.4	4.4
$N/\sqrt{T_1}$	760	760	760	741	737
Q_1	2.93	3.18	2.98	2.82	2.85
Reaction (hub)	21.8	20.5	24.0	19.4	23.3
Reaction (tip)	46.0	45.2	45.6	46.0	44.3
Exit swirl, deg.	36.1	37.1	34.5	39.0	—
η %	80.4	82.0	79.9	81.9	81.5

The measured uncooled efficiency is 82 percent. The control volume cooled efficiency is 79.9 percent at a tip clearance of 1.1 percent of blade span. These efficiencies are based on total pressure measured four blade chords downstream (plane 5) and the far downstream mixed temperature. The cooled efficiency was 0.5 percent lower than the predicted rig meanline target of 80.4 percent, and is within the rig accuracy and the assumptions made about the cooling flows, coolant temperature ratio, and the measuring location. The definition of control volume efficiency includes the potential for the cooling flows to do work. If the cooling flows do work, this will affect the average exit total temperature measured differently than if they do not. No torque measurements were taken. This would have added another, perhaps more correct (based on accurate parasitic loss correlations) check on air flow doing work. The temperature ratio of the coolant to mainstream (0.75 to 0.95 in these experiments) will alter the cooling losses. This was taken into account through the cooled meanline prediction code used to assess turbine efficiency targets. The difference of 1.5 percent between the rig (HWRT) and the engine (HTDE) efficiency targets (Table 2) will be discussed later. The measured cooled stage exit swirl is on target to within two degrees. The uncooled swirl as expected is larger than the cooled value. This is due to the effect of cooling on the axial velocity and hence the velocity triangles.

Figures 7 and 8 show the radial distribution of stage exit swirl and efficiency, at plane 3, for the uncooled and cooled tests. Compared to the target swirl, the measurements showed overturning in the hub region due to the secondary flows and large underturning in the upper 80 percent span indicating strong tip leakage vortices. The cooled and uncooled profiles are of very similar shape but with a slight offset. This could be expected with the type of cooling flows added. Showerhead and trailing edge ejection (by far the bulk of the flows added) are uniformly introduced from hub to tip whereas shroud and platform/disk cavity purging are nonuniform. The offset is probably

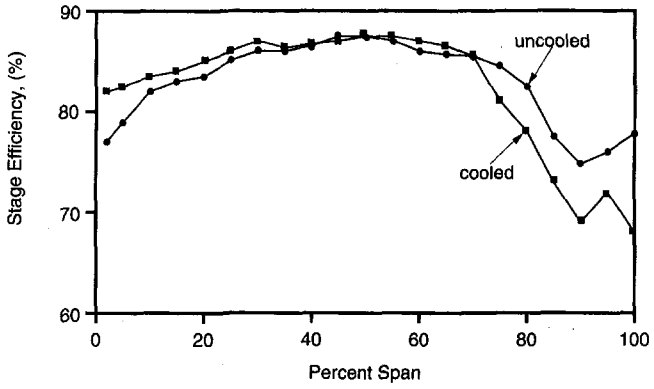

Fig. 8 Radial distribution of stage efficiency, plane 3

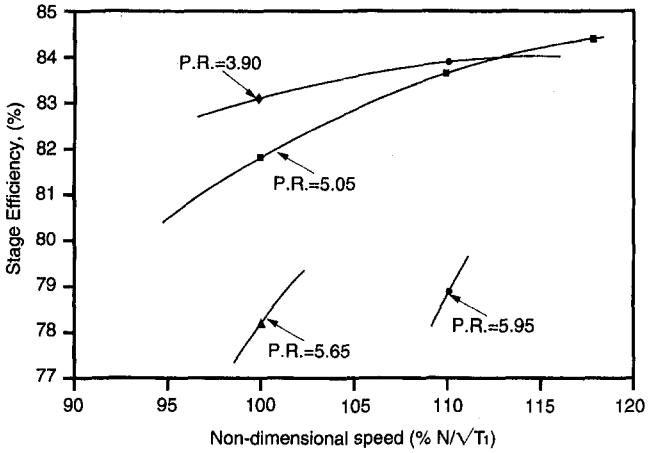

Fig. 10 Variation of efficiency with nondimensional speed (uncooled)

due to the velocity triangle adjustment due to changes in the axial velocity.

Design and Off-Design Performance of the Uncooled Turbine

A part-load turbine performance characteristic was obtained for the stage without cooling flows. The turbine was run at three speeds: 100, 110, and 118 percent of design nondimensional speed and three pressure ratios: approximately 4, 5 (design), and 6. There was only one pressure ratio at 118 percent speed. The turbine performance parameters at the design and off-design conditions are presented in Figs. 9–13.

Figures 9 and 10 show a sharp drop-off in efficiency at pressure ratios of 4.5 and 5.0 for 100 and 110 percent speeds, respectively. The design point lies on a steep slope and is very near limit load, where no extra work is possible with increasing pressure ratio (Fig. 11). The rapid drop in turbine efficiency, at the design speed, starts at a rotor exit relative Mach number (M_{3r}) of about 1.15 corresponding to a P.R. of 4.5. This efficiency drop occurs at higher pressure ratios with increasing speed: At 110 percent speed the P.R. is about 5.3 and M_{3r} is 1.25. The limit load pattern of the HWRT is more evident in Fig. 11, where the stage loading flattens to a certain value at a pressure ratio, which is a function of the turbine speed. The stage exit swirl plots of Fig. 12 illustrate the supersonic expansion that takes place downstream of the rotor. The exit flow is accelerated, through increasing the stage pressure ratio, until a certain M_{3r} is reached. That M_{3r} is 1.15 at 100 percent speed in Fig. 12. Thereafter, instead of the exit swirl increasing as in fully subsonic flow, the swirl decreases as the need for increased area in supersonic expansion takes over.

The HWRT, being very close to limit load, showed a more pronounced drop in efficiency with increase in pressure ratio than other published turbines. At the design speed, an efficiency drop of approximately 4 percent was measured for an increase in P.R. from the design value of 5.1 to 5.65 (Figs. 9 and 10). This compares to 2 percent drop for a P.R. increase from 3.9 to 4.4 for DRB (Okapuu, 1974), 3 percent drop for a P.R. increase from 4 to 5.5 for E^3 (Crow et al., 1980), and only 0.7 percent for a P.R. increase from 4.5 to 5.2 for RAE (Bryce et al., 1985). The characteristics of the HWRT stage (Table 1), and in particular the rotor trailing edge blockage and stage reaction, are the reason for this rapid drop in efficiency. Okapuu (1974) and Crow et al. (1980) showed in their tests that limit loading is reached at a lower pressure ratio with a higher reaction design, due to the higher rotor exit relative Mach number.

The vane of the HWRT operates virtually choked over a wide range of pressure ratios and speeds. Therefore the vane exit Mach number (M_2) and swirl (rotor incidence) are constant. The vane M_2 for the 100 and 110 percent speed lines, estimated from meanline modeling of the HWRT, are 1.14 and 1.08, respectively. The vane exit swirl for the two speed lines induces 0.0 and −4.0 deg rotor incidence, respectively. At a constant pressure ratio, the higher the speed, the lower the exit vane and rotor relative Mach numbers, and the more negative the rotor incidence. For a highly loaded turbine rotor, some negative incidence is generally beneficial. In addition, with the higher

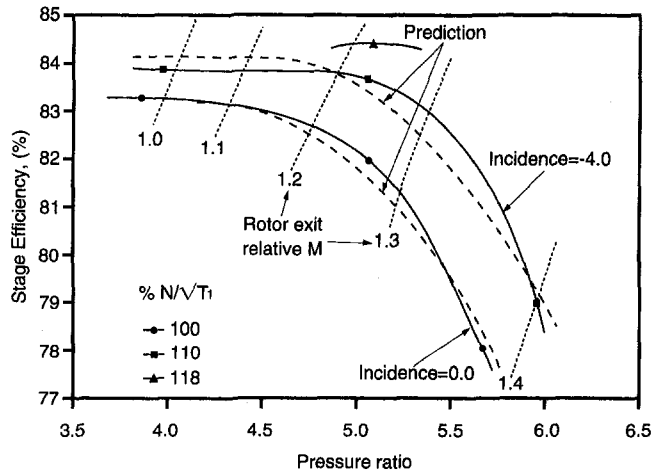

Fig. 9 Variation of efficiency with pressure ratio (uncooled)

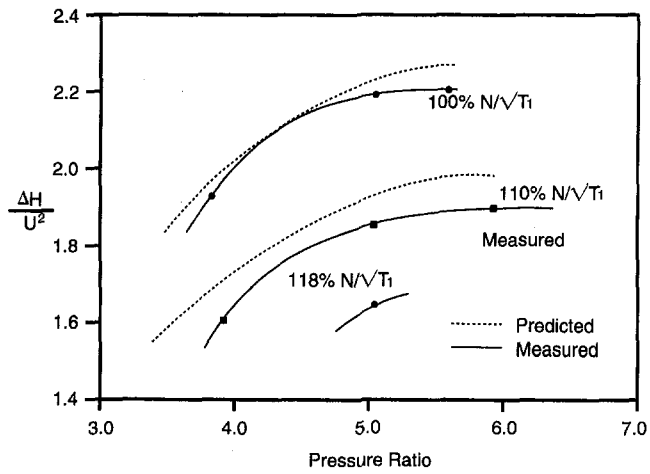

Fig. 11 Variation of stage loading with pressure ratio (uncooled)

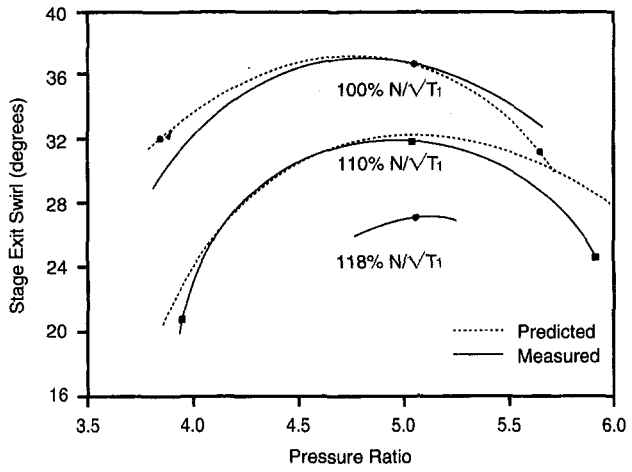

Fig. 12 Variation of stage exit swirl with pressure ratio (uncooled)

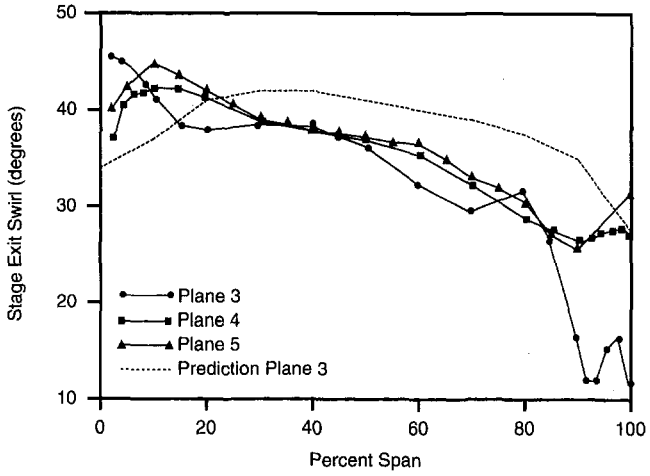

Fig. 14 Radial distribution of stage exit swirl (cooled)

rotational speeds, the stage loading is lower (Fig. 11), the rotor is doing less flow turning, and hence has reduced secondary flow losses. The 2.5 percent increase in turbine efficiency (Figs. 9 and 10), at a pressure ratio of 5.05, for a speed change from 100 to 118 percent is due to the above-mentioned factors.

The measured turbine performance characteristics were compared in Figs. 9, 11, and 12 with the results of a turbine design and off-design prediction model (Kacker and Okapuu, 1982; Moustapha et al., 1990). The model predicted reasonably well the variation of the stage efficiency with speed and pressure ratio, the transonic drag rise as well as the change in exit swirl.

The reaction variation (hub to tip) with pressure ratio at different normalized speeds is illustrated in Fig. 13. The increase in reaction at the hub and tip when pressure ratio is varied through the range tested (3.8 to 5.95) is 14 and 9 percent respectively. There is a more profound pressure ratio effect on reaction than speed. This is due to the fact that at very low pressure ratios the vane takes up most of the available static pressure drop, whereas at increasingly higher pressure ratios (as seen in the tests conducted) the vane becomes choked and the rotor increases its static pressure drop and therefore increases the reaction. Speed does little to alter the reaction because swallowing capacity changes very little in the ranges tested. A similar conclusion was obtained in the tests of Crow et al. (1980) and Moustapha et al. (1987).

Effect of Downstream Traverse Location on Turbine Performance

The location of the exit total pressure rakes downstream of the rotor is important primarily because of the phenomenon of mixing. The downstream mixing and associated increase in losses for turbine cascades have been well documented in the literature. Similar to cascades, losses generated in a turbine stage take some distance to mix fully downstream. This mixing distance is often quoted as the number of rotor axial chords, downstream of a stage, needed for the efficiency roll-off to asymptote. Duct loss begins to play a role if too large a distance is chosen. The location of the measurement plane for the exit total pressure therefore affects the calculated efficiency of a turbine. Moustapha et al. (1987) showed that the derived efficiencies from their rig measurements had a band of 3.6 percent depending on the measuring location, instrumentation accuracy, and averaging techniques.

Three downstream traverse locations: 0.2, 2, and 4 blade axial chords, were selected to investigate the performance of such a high pressure ratio turbine as affected by the mixing process. The rotor exit absolute swirl profiles of Fig. 14 and efficiency profiles of Fig. 15, measured at planes 3, 4, and 5, illustrate the concept of mixing. The efficiency calculated in Fig. 15 uses the mixed-out average total temperature, and not the local radial temperature profile. The swirl and total pressure gradients gen-

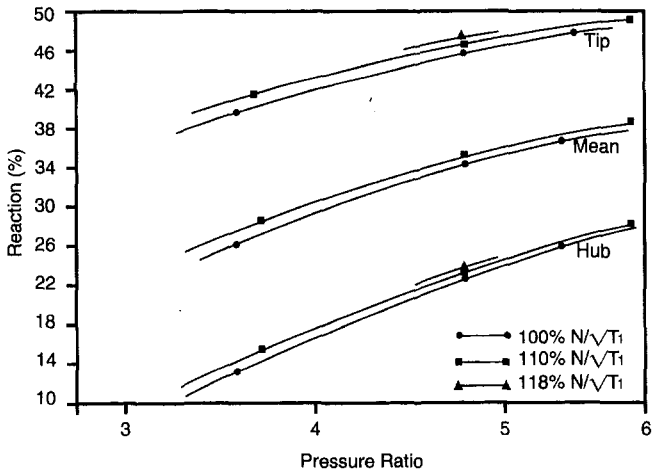

Fig. 13 Variation of reaction with pressure ratio (uncooled)

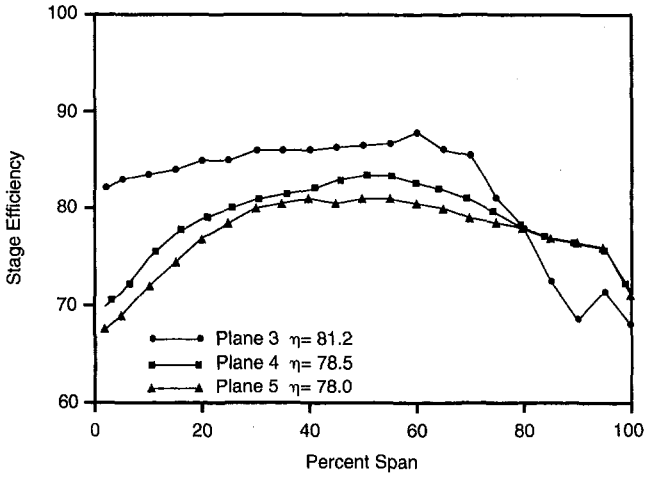

Fig. 15 Radial distribution of stage efficiency (cooled)

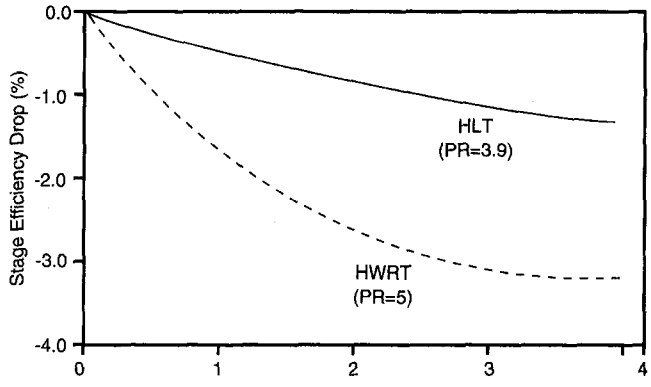

Fig. 16 Variation of stage efficiency with downstream measuring distance

erated in the vane and rotor increase to a maximum just at the rotor trailing edge near the endwalls as loss vortices (tip leakage and secondary) combine. The continued mixing of these vortices downstream creates smoother and more uniform flow but generally lower efficiency as average pressure losses increase.

Figure 16 shows the effect of the downstream measuring plane on the calculated uncooled efficiency. The efficiency drop between the zero and four-chord location is 3.2 percent. The largest portion of this, 2.7 percent, comes in the first two chords. The balance, 0.5 percent is from the two to four-chord location. The estimated duct loss per rotor axial chord is 0.06 percent $\Delta P/P$, which accounts for 0.2 percent points on turbine efficiency. Adding cooling flow increased the efficiency delta at the four chord location, from 3.2 to 3.5 percent. Cooling would probably increase the distance at which fully mixed-out flow would occur. The HLT (Table 1) with a pressure ratio of 3.8 showed a drop of only 1.35 percent. Although at least four chord downstream location was needed for the HLT and the HWRT for full mixing, the effect of stage pressure ratio on the magnitude of the efficiency drop is apparent from Fig. 16. The efficiencies quoted in Table 1 for the HWRT and the HLT are based on four and six chord location, respectively. However, the efficiencies for the DRB and the E^3 are based on one and two chord location, respectively, and the efficiency for RAE is calculated from torquemeter and continuity. According to the present investigation and the study of Moustapha et al. (1987), the efficiencies of the DRB, E^3 and RAE need then to be adjusted downward by 1 to 2 percent for proper comparison with the HWRT.

Comparison of the HWRT With Gas Generator Testing (HTDE)

The HTDE was the gas generator equivalent to the HWRT. The principle objectives of the HTDE were to: assess the aerodynamic performance of both the compressor and high work turbine, investigate combustor characteristics using, among other things, optical pyrometery, and measure stress levels in the rotating components, in an engine environment. The HTDE ran in parallel with the cold flow rig testing of the HWRT and therefore provided a rare opportunity for engine to rig calibration.

The typical differences between an engine and a rig environment are: inlet temperature and turbulence levels, combustor exit temperature, pressure and swirl profiles, steps and gaps created by thermal growth and speed differences, cooling flow amounts, locations and temperature ratios, hardware, fuel-to-air ratios and temperature causing changes to specific heat ratio, measurement accuracy and traverse locations. These differences can be lumped into "an engine to rig target efficiency conversion factor," which is normally obtained as a function of the inlet temperature and through proper meanline efficiency auditing. For the present investigation the engine to rig cooled efficiency delta was 1.5 percent, as shown in Tables 1 and 2.

The results of measurements made in the HTDE and the HWRT are compared with their predictions in Table 2. The relationship between the HTDE and HWRT with each respective predicted efficiencies are consistent. The HTDE was 0.4 percent lower than its target of 81.9 percent. The HWRT was 0.5 percent lower than its predicted rig target. The HTDE and HWRT efficiencies are at 1.1 percent tip clearance to span ratio. Measured reaction levels in both turbines showed a similar trend of being over target at the hub and slightly less than target at the tip. The mean reaction in the HTDE and HWRT were higher than target by approximately the same amount. Nondimensional flow parameters (Q_1) are higher than predicted for both turbines, 1.2 percent for the HTDE and 2.1 percent for the HWRT.

The HWRT and HTDE results demonstrated, that once a suitably logical engine to rig (or vice versa) delta is estimated, that rig experimentation correlates with engine testing very well, even to the level of absolute efficiencies and comparisons with their respective targets.

Conclusions

The performance of a high work cooled research turbine with a pressure ratio of 5.0 and a stage loading of 2.2 has been presented for different pressure ratios and speeds. The effects of cooling and downstream measuring location on the radial distribution of the stage exit performance parameters have been presented. The results lead to the following main conclusions:

1. The measured cooled turbine efficiency was within 0.5 percent of the predicted rig target of 80.4 percent. After correcting for temperature, cooling flows, and measuring location, the cold flow rig efficiency matched reasonably well the measured engine efficiency of 81.5 percent.
2. The stage reaction and exit swirl agreed with the target values. Off-design maps showed that the pressure ratio has a stronger effect on reaction than speed.
3. The effect of cooling flows (7.5 percent for vanes and 3.5 percent for blades) was to reduce the turbine efficiency by 2.1 percent at rig temperature ratios.
4. Radial distribution of the stage exit swirl showed underturning over most of the upper span indicating strong tip leakage vortices.
5. A part-load map indicated that the turbine is operating very near to limit loading. A drop of 4 percent in efficiency was measured at design speed when the pressure ratio was increased from 5.1 to 5.65. The map showed that the roll-off in efficiency occurs at higher pressure ratios with increased speed. The phenomenon of supersonic expansion at the rotor trailing edge, after a pressure ratio of 5.0, was explained by means of the measured exit swirl.
6. An efficiency increase of 2.5 percent was measured for a speed change from 100 to 118 percent. This was mainly due to the lower stage loading and the lower exit vane and blade Mach numbers.
7. The investigation demonstrated the importance of the downstream traverse location when comparing the performance of high pressure ratio turbines. An efficiency drop of 3.2 percent was measured between the rotor trailing edge and a four blade chord downstream plane.

Acknowledgments

The work summarized here is part of a research program jointly sponsored by Industry, Science and Technology Canada (ISTC). The aerodynamic design of the High Work Research Turbine was done by M. El-Fouly under the supervision of

S. H. Moustapha and Ü. Okapuu. Overall coordination of the High Technology Demonstrator Engine program was provided by R. K. Agrawal. The dedication of the two test engineers G. Begin and L. Bourque is gratefully acknowledged.

References

Bryce, J. D., Litchfield, M. R., and Leversuch, N. P., 1985, "The Design, Performance and Analysis of a High Work Capacity Transonic Turbine," ASME *Journal of Engineering for Gas Turbines and Power,* Vol. 107, pp. 931–937.

Crow, D. E., Vanco, M. R., Welna, H., and Singer, I. D., 1980, "Results From Tests on a High Work Transonic Turbine for an Energy Efficient Engine," ASME Paper No. 80-GT-146.

El-Fouly, M., and Moustapha, S. H., 1990, "Application of 3D Flow Analysis to the Design of a High Work Transonic Turbine," *CASI Journal,* Vol. 36, No. 2, pp. 90–96.

Ewen, J. S., Huber, F. W., and Mitchell, J. P., 1973, "Investigation of the Aerodynamic Performance of Small Axial Turbines," ASME Paper No. 73-GT-3.

Kacker, S. C., and Okapuu, Ü., 1982, "A Mean Line Prediction Method for Axial Flow Turbine Efficiency," ASME *Journal of Engineering for Power,* Vol. 104, pp. 111–119.

Liu, H. C., Booth, T. C., and Tall, W. A., 1979, "An Application of 3D Viscous Flow Analysis to the Design of a Low Aspect Ratio Turbine," ASME Paper No. 79-GT-146.

Moustapha, S. H., Kacker, S. C., and Tremblay, B., 1990, "An Improved Incidence Losses Prediction Method for Turbine Airfoils," ASME JOURNAL OF TURBOMACHINERY, Vol. 112, pp. 267–276.

Moustapha, S. H., Okapuu, Ü., and Williamson, R. G., 1987, "The Influence of Rotor Blade Aerodynamic Loading on the Performance of a Highly Loaded Turbine Stage," ASME JOURNAL OF TURBOMACHINERY, Vol. 109, pp. 155–162.

Ni, R. H., and Bogoian, J., 1989, "Prediction of 3D Multi-stage Turbine Flow Field Using a Multiple-Grid Euler Solver," AIAA Paper No. 89-0203.

Okapuu, Ü., 1974, "Some Results From Tests on a High Work Axial Gas Generator Turbine," ASME Paper No. 74-GT-81.

Film Cooling With Compound Angle Holes: Heat Transfer

B. Sen

D. L. Schmidt

D. G. Bogard

Mechanical Engineering Department,
University of Texas at Austin,
Austin, TX 78712

Heat transfer coefficients have been measured for film cooling injection from a single row of holes laterally directed with a compound angle of 60 deg. Two hole configurations were tested, round holes and holes with a diffusing expansion at the exit. Streamwise-directed round holes were also tested as a basis for comparison. All the holes were inclined at 35 deg with respect to the surface. The density ratio was 1.0, momentum flux ratios ranged from $I = 0.16$ to 3.9, and mass flux ratios ranged from $M = 0.4$ to 2.0. Results are presented in terms of h_f/h_0, the ratio of film cooling heat transfer coefficient to the heat transfer coefficient for the undisturbed turbulent boundary layer at the same location. Results indicate that for the streamwise directed holes, the heat transfer rates are close to the levels that exist without injection. Similarly, at low momentum flux ratio, holes with a large compound angle had little effect on heat transfer rates. However, at high momentum flux ratios, holes with a large compound angle had significantly increased heat transfer levels. The results were combined with adiabatic effectiveness results to evaluate the overall performance of the three geometries. It is shown that for evaluation of film cooling performance with compound angle injection, especially at high momentum flux ratios, it is critical to know the heat transfer coefficient, as the adiabatic effectiveness alone does not determine the performance. Compound angle injection at high momentum flux ratios gives higher effectiveness values than streamwise-directed holes, but the higher heat transfer levels result in poorer overall performance.

Introduction

Film cooling is a technique for cooling gas turbine blades to protect them from the high-temperature mainstream. The benefits of film cooling are that it prolongs the life of the blade, and makes higher combustor temperatures (and hence higher efficiency) attainable. Film cooling may be done by injection of a film of cooling air onto the blade surface through discrete holes. These holes are typically inclined at approximately 30 to 40 deg with respect to the surface, and are generally aligned with the direction of the free-stream flow. However, in many cases the holes are aligned at a large angle inclined from the mainstream direction, which is called a compound angle. In this study we have investigated the effect on film cooling heat transfer of using holes with a large compound angle, with and without expansion of the hole exit.

Heat transfer to a film cooled blade may be defined as (Goldstein, 1971):

$$q'' = h_f(T_{aw} - T_w) \tag{1}$$

The adiabatic wall temperature is typically expressed in dimensionless form as the adiabatic effectiveness η. For injection at the free-stream temperature, the adiabatic wall temperature becomes the same as the free-stream (and jet) temperature and hence the heat transfer coefficient can be found from the difference between the wall and free-stream temperatures (Eckert, 1984). It is clear that distributions of both the heat transfer coefficient and the adiabatic wall temperature are required to predict film cooling heat transfer.

The net benefit from film cooling can be quantified as a Net Heat Flux Reduction (NHFR) due to film cooling, or the ratio of reduction in heat transfer to the blade with film cooling to heat transfer without film cooling. This is similar to the Stanton number reduction described by Luckey et al. (1977):

$$\text{NHFR} = 1 - q''/q_0'' = 1 - h_f(T_{aw} - T_w)/h_0(T_\infty - T_w) \tag{2}$$

where the subscript 0 denotes conditions with no film cooling. The objective of film cooling is to increase NHFR by reducing h_f/h_0 and lowering T_{aw} (and hence increasing η). If we define the dimensionless temperature ratio θ by:

$$\theta = (T_\infty - T_c)/(T_\infty - T_w) \tag{3}$$

it can be readily shown that:

$$\text{NHFR} = 1 - h_f/h_0(1 - \eta\theta) \tag{4}$$

Thus, both the adiabatic effectiveness and the heat transfer coefficient are required to evaluate film cooling performance. Note that application of Eq. (4) with an arbitrary value of θ presumes that h_f is not dependent on temperature.

Film cooling performance is affected by a number of flow and geometric parameters. Injection geometry parameters that affect film cooling include the injection angle, pitch-to-diameter ratio, length-to-diameter ratio, hole exit shape, and orientation of hole with respect to mainstream. Flow parameters include the ratios of density, velocity, mass flux and momentum flux between injectant and mainstream, pressure gradient, and free-stream turbulence. (Note that the ratios of jet to mainstream variables, DR, VR, M, and I, are not all independent; specifying any two of them fixes the other two.)

Although there have been many studies of adiabatic effectiveness for discrete hole film cooling, there have been relatively few studies of the associated heat transfer. Studies of isothermal heat transfer with film cooling (using jets at the same temperature as the free stream) using a single row of inclined, streamwise directed holes on a flat plate have been completed by Eriksen and Goldstein (1974); Liess (1975); Goldstein and Yoshida (1982); Hay et al. (1985); and Ammari et al. (1990). Similar studies using heated or cooled jets have been done by Forth et al. (1985), Makki and Jakubowski (1986), and Ligrani et al. (1988). The only previous study of heat transfer associ-

Contributed by the International Gas Turbine Institute and presented at the 39th International Gas Turbine and Aeroengine Congress and Exposition, The Hague, The Netherlands, June 13–16, 1994. Manuscript received by the International Gas Turbine Institute February 9, 1994. Paper No. 94-GT-311. Associate Technical Editor: M. G. Dunn.

ated with compound angle holes was by Ligrani et al. (1992). A brief summary of the major results from these studies relevant to the work presented in this paper is given below.

The consistent trend among all the studies of inclined, streamwise-directed holes is that there is only a slight effect on heat transfer relative to the flow without film cooling. The only significant deviation from $h_f/h_0 = 1.0$ occurs near the hole within $x/D = 10$. All the studies are consistent in showing increases in h_f/h_0 for higher blowing ratios, $1 \leq M \leq 2$, with centerline values increasing as much as 40 to 50 percent very near the hole. For moderate blowing ratio, $M = 0.5$, Eriksen and Goldstein (1974) showed a slight (10 percent) decrease in h_f/h_0, but Liess (1975), Hay et al. (1985), and Ammari et al. (1990) showed slight increases of 10 to 20 percent.

With the exception of Makki and Jakubowski (1986), Forth et al. (1985), and Ammari et al. (1990), all the studies listed above used low density ratios ranging from $DR = 0.85$ to 1.0. Ammari et al. (1990) studied the effect of density ratio on film cooling heat transfer for the same geometries as Hay et al. (1985). They found that increasing the density ratio from $DR = 1.0$ to $DR = 1.52$ at a moderate mass flux ratio of $M = 0.5$ had essentially no effect on the heat transfer. For larger mass flux ratios the laterally averaged heat transfer rate was consistently higher for the lower density ratio. They attributed this to the greater momentum flux ratio of the unit density ratio jet at the same M. Forth et al. (1985) obtained similar results for jets with different density ratios.

Film cooling using compound angle holes was studied by Ligrani et al. (1992). Using one and two rows of round holes, they compared results for $CA = 0$ deg and $CA = 50.5$ deg. However, the injection angles and hole pitch for the $CA = 50.5$ deg and $CA = 0$ deg holes were different (35 and 24 deg, and $P/D = 6.0$ and 7.8 for $CA = 0$ and 50.5 deg, respectively). Their laterally averaged isothermal heat transfer data show negligible differences between the $CA = 0$ deg and $CA = 50.5$ deg holes for the three mass flux ratios, $M = 0.5$, 1.0, and 1.5, they studied. In each case the laterally averaged isothermal heat transfer ranged from $\overline{h}_f/h_0 = 1.0$ to $\overline{h}_f/h_0 = 1.15$, with slightly increasing heat transfer with increase in M.

An important part of this study was determining the net heat transfer reduction by combining the heat transfer results with adiabatic effectiveness results presented in the companion paper (Schmidt et al., 1995). To maximize the accuracy of the heat transfer measurements, heat transfer tests were done with $DR = 1.0$ (coolant at the same temperature as the free stream). The poor accuracy for high density ratio tests was due to the difficulty of maintaining a steady coolant temperature in our facility for very low coolant temperatures (for further details, see Sen, 1995). Heat transfer measurements were related to effectiveness measurements, which were done at $DR = 1.6$, by matching the momentum flux ratio, I. Matching in terms of I rather than M was done based on the adiabatic effectiveness results of Sinha et al. (1991) and the thermal field results of Thole et al. (1992), which showed that I is the appropriate scaling parameter for variable density ratio film cooling at moderate to high blowing ratios. The results of Ammari et al. (1990) also showed that I is a more appropriate scaling parameter. Although Ammari et al. showed a significant variation in heat transfer rates when comparing different density ratios at the same M, when compared at approximately the same I the differences are negligible. For example, comparing the laterally averaged heat transfer results of Ammari et al. at $M = 2.0$ and $DR = 1.5$ with results at $M = 1.5$ and $DR = 1.0$, which are at similar I ($I = 2.6$ and 2.3, respectively), a maximum difference of less than 4 percent was found. These results support use of the momentum flux ratio to match the heat transfer and adiabatic effectiveness results, which were obtained at different density ratios.

Facilities and Instrumentation

Measurements were made in a closed-loop wind tunnel with a 0.61-m-high × 0.61-m-wide × 2.4-m-long test section, and a secondary flow loop for the film cooling jets. Figure 1 shows a schematic of the test section in the facility. For a detailed description of this facility see Pietrzyk et al. (1990). The film cooling jet flow and leading edge suction were provided by a secondary flow loop. The static pressure drop across the contraction upstream of the test section was used to measure the free-stream velocity, and a sharp-edged orifice flow meter was used to measure the flow rate of the coolant jets. Pietrzyk et al. verified uniform distribution of injectant between the film cooling jets. The leading edge suction was adjusted to provide uniform flow without separation at the leading edge. The test plate consisted of three sections, a 12.7-cm-long leading edge plate, a 14-cm-long injection plate with film cooling holes, and a constant heat flux plate described in detail later. This modular construction made it possible to test different hole geometries using the same constant heat flux surface. A 2.4-mm-dia trip wire was installed 9.5 cm downstream of the leading edge. Results are presented in terms of x (streamwise) and z (spanwise) coordinates, where the origin of x is the trailing edge of the film cooling hole and the origin of z is the centerline of the central hole. All distances are nondimensionalized using the hole diameter of $D = 1.11$ cm. Figure 2 shows the test plate arrangement and the coordinate system.

The film cooling holes had a compound angle of $CA = 60$ deg. One set of holes had a round hole, and the other set of

Nomenclature

A = surface area
CA = compound angle
D = film cooling hole diameter
DR = density ratio of coolant to mainstream = ρ_c/ρ_∞
I = momentum flux ratio of coolant to mainstream = $\rho_c U_c^2/\rho_\infty U_\infty^2$
L = hole length
M = mass flux ratio of coolant to mainstream = $\rho_c U_c/\rho_\infty U_\infty$
NHFR = Net Heat Flux Reduction, or ratio of reduction in heat transfer with film cooling to heat transfer without film cooling
P = hole spacing
Re = Reynolds number
T = temperature
Tu = free-stream turbulence intensity
U = velocity
U_c = bulk cooling jet velocity through metering length (inlet) of the hole
h_f = heat transfer coefficient = $q''/(T_{aw} - T_w)$
q'' = heat flux
x = streamwise coordinate originating at downstream edge of film cooling holes
z = spanwise coordinate originating at centerline of central hole
δ_1 = displacement thickness
δ_2 = momentum thickness
ϵ = emissivity
η = adiabatic effectiveness = $(T_{aw} - T_\infty)/(T_c - T_\infty)$
θ = dimensionless temperature ratio = $(T_\infty - T_c)/(T_\infty - T_w)$
ρ = density
σ = Stefan–Boltzmann constant

Subscripts

aw = adiabatic wall
c = coolant
f = with film cooling
r = radiation
s = roof and side walls of test section
w = blade surface (or test plate surface)
0 = no injection
∞ = free stream

Superscripts

$\bar{}$ = lateral average
$\bar{\bar{}}$ = spatial average

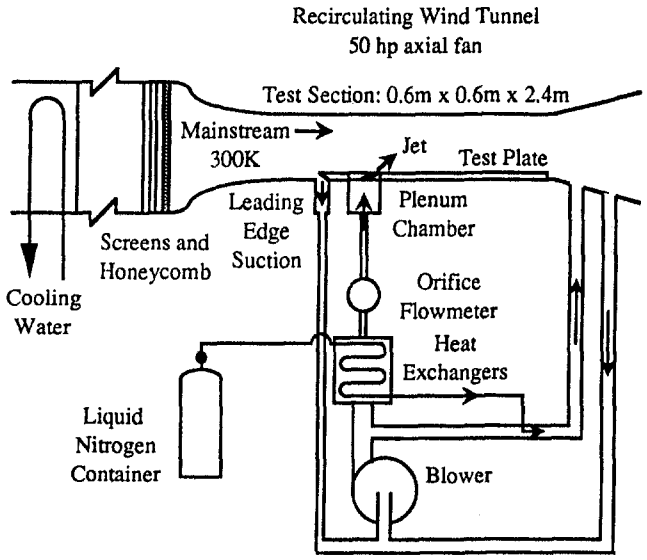

Fig. 1 Film cooling test facility

holes had a diffusing exit with a 15 deg forward expansion. Schematics of the holes are given in Fig. 3. As a basis of comparison, a set of holes aligned with the flow ($CA = 0$ deg) was also tested. Each set of holes had 9 holes inclined at 35 deg with respect to the surface and spaced 3.0 diameters apart, and the hole length was 4 diameters. The values of hole spacing, length, and injection angle were selected to be representative of gas turbine film cooling geometries. The values of compound angle and forward expansion angle were provided by Garrett Engine Division of Allied Signal Aerospace Company, one of the sponsors of this study, and represent geometries in use in Garrett gas turbines.

Temperatures were measured on a constant heat flux surface, 1.37 m long and 0.61 m wide, consisting of a 0.08-mm-thick serpentine monel heating element embedded in a 0.18-mm-thick insulating Kapton film. Except near the lateral edges of the plate, the heating elements were oriented perpendicular to the direction of the mainstream flow, so the heating elements alternated with gaps in between. The heating elements were 10 mm in width and the gaps were 1 mm in width. The effective boundary condition was a periodic heat flux. Numerical analysis of conduction within the plate and convection at the surface showed that this periodic boundary condition did not change the temperature distribution on the heating element significantly from that for a constant flux surface. The top surface of the heater was painted using a paint of known emissivity (ϵ_w = 0.97). The heating film was bonded to a 1.27-cm-thick plate made of a fiberglass composite commercially designated as G-10. Below the G-10 plate were 15.2 cm of Corning fiberglass insulation and 2.54 cm of extruded polystyrene foam (Styrofoam). The thermal conductivities of G-10, Corning fiberglass, and polystyrene foam are 0.29 W/mK, 0.046 W/mK, and 0.027 W/mK, respectively. The heater was powered using two DC power supplies, and the power input was found by measuring the voltage output of the power supplies and the voltage across a calibrated 3.33 mΩ shunt resistor in series with the heater.

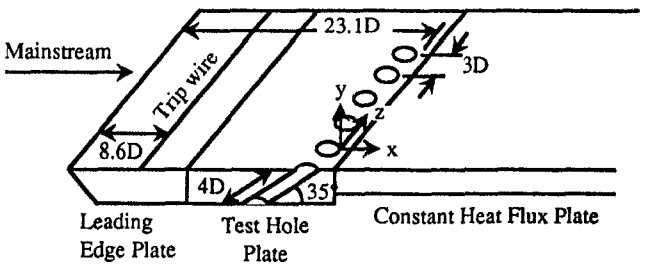

Fig. 2 Test section geometry and coordinate system

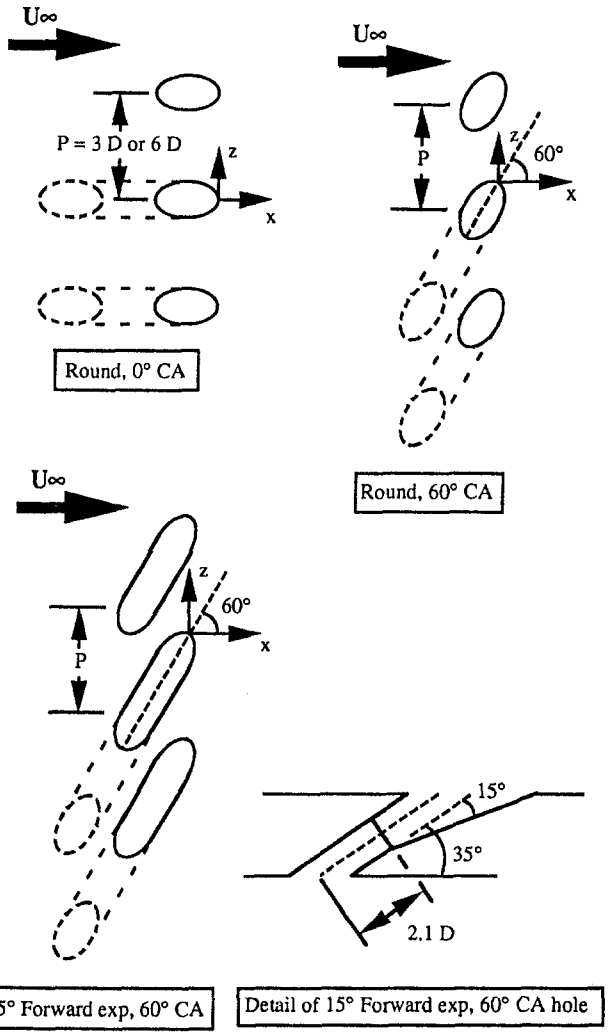

Fig. 3 Injection hole geometry showing the top view of the central three holes for all three geometries, and details of the geometry for the 15 deg forward expansion, 60 deg *CA* holes

Surface temperature measurements were made using an Inframetrics IR camera system calibrated against type E thin ribbon thermocouples permanently installed on the surface at seven streamwise positions ranging from $x/D = 2$ to 50. The thermocouples had a maximum height of $y^+ \leq 5$, which represents a smooth wall flow. Any other unevenness of the surface was significantly smaller than that due to the thermocouples. The thermocouple accuracy of ±0.2°C was confirmed using an ice bath (note that since the reference junction was at room temperature, the ice bath caused a temperature differential similar in magnitude to that occurring during experiments). The ice bath was placed in a metallic container, which was placed in contact with the thermocouples, to minimize thermal contact resistance. The thermocouples were tested to ensure that the proximity of the electrical heater did not affect measurements. During experiments, thermocouple data were acquired and used to verify the IR camera measurements. The centerline measurements reported for $x/D > 22$ are thermocouple measurements, as the viewing window for the IR camera on the test section roof did not permit measurement downstream of $x/D = 22$. Measurements were made behind three jets, the center jet and the jets on either side of the center jet, and these three measurements

were averaged. The h_0 measurements were made with the holes covered with tape. Free-stream and jet temperatures were measured using type E thermocouples. The jet temperatures were taken as the plenum temperatures. Previous tests in our lab have shown that the plenum temperature is a good measure of the jet temperature. The convective heat flux was found by subtracting a radiation correction from the total heat flux. The radiation correction was found from the following relation:

$$q_r'' = \sigma(T_w^4 - T_\infty^4)/(1/\epsilon_w + (A_w/A_s)(1/\epsilon_s - 1)) \quad (5)$$

where A_w, A_s, ϵ_w, and ϵ_s are area of test surface, area of side walls and roof, emissivity of test surface, and emissivity of side walls and roof, respectively. The surface temperature, and hence the radiation loss, increased with streamwise distance. The maximum radiation loss in the x/D range for which measurements were made was 17 percent of the total heat flux (at $x/D = 50$). The heat loss from the back was negligible, as verified using analytical calculations for a simplified one-dimensional model of the plate assembly, a two-dimensional finite difference conduction code, as well as actual measurement of the temperature difference across the G-10 plate. The heat transfer coefficient was found from:

$$h_f = (q'' - q_r'')/(T_w - T_\infty) \quad (6)$$

where q'' is the total heat flux.

The dominant source of uncertainty was the uncertainty in measurement of the temperature differential, ΔT, between the surface and free stream, which was determined as follows. Precision uncertainty, determined statistically based on jet-to-jet variation in temperature for specified x/D and z/D locations at a specified blowing condition for a specified set of holes, was $\delta\Delta T = \pm 0.4$°C. Bias uncertainty due to calibration and drift of the IR camera was $\delta\Delta T = \pm 0.5$°C. The bias uncertainty included contributions from the thermocouples used for calibrating the camera, as well as from the calibration process itself. Combining these uncertainties gave an uncertainty in h_f/h_0 of ± 4, ± 3, and ± 2.5 percent or less at $x/D = 2$, $x/D = 3$, and all downstream locations. Combining these uncertainties for h_f/h_0 with uncertainties in η reported in Schmidt et al. (1996) gave uncertainties in NHFR ranging from ± 0.05 for the $CA = 60$ deg holes for $I \geq 1.0$ to ± 0.03 for the $CA = 0$ deg holes.

The heat transfer results for no injection were compared to prediction using TEXSTAN (Crawford, 1995), a two-dimensional boundary computation code. The agreement was within 16 percent at the first measurement location downstream of the holes, and within 3 percent or less for $x/D \geq 5$.

Experimental Conditions

The free-stream velocity was maintained at $U_\infty = 10$ m/s in all the tests and the free-stream turbulence intensity was $Tu = 0.2$ percent. The spanwise uniformity of flow in the facility and the uniform distribution of flow through the film cooling holes were verified by Pietrzyk et al. (1990). The Reynolds number based on the free-stream velocity and the hole diameter was $\mathrm{Re}_D = 7000$. The momentum thickness Reynolds number at the upstream end of the hole was measured to be $\mathrm{Re}_{\delta_2} = 1160$ and the ratio of displacement thickness to hole diameter was $\delta_1/D = 0.23$.

Table 1 lists the blowing ratios for each hole configuration tested. The last column lists the mass flux ratios for the equivalent condition (i.e., with the same I) from the adiabatic effectiveness tests, which were run with $DR = 1.6$.

Table 1 Test conditions for heat transfer tests

Geometry	I	M	Equivalent M (DR = 1.6)
round, CA = 0°	0.16	0.4	0.5
	0.25	0.5	0.63
	1.0	1.0	1.25
round, CA = 60°	0.25	0.5	0.63
	1.0	1.0	1.25
	3.9	2	2.5
fwd. exp., CA = 60°	1.0	1.0	1.25
	3.9	2.0	2.5

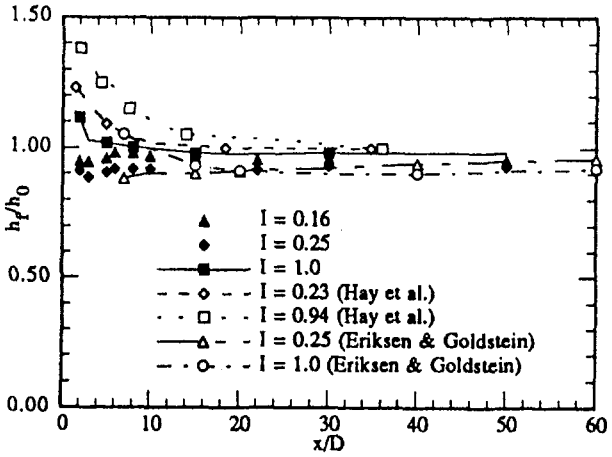

Fig. 4 Centerline h_f/h_0 distribution for round hole, $CA = 0$ deg; present data compared to data of Eriksen and Goldstein (1974) and Hay et al. (1985)

Results and Discussion

The streamwise variation of centerline heat transfer for the round, $CA = 0$ deg holes is shown in Fig. 4. These results show a slight decrease in h_f/h_0 near the hole for lower momentum flux ratios, $I = 0.16$ and $I = 0.25$, but a slight increase for high momentum flux ratio, $I = 1.0$. For both high and low momentum flux ratio, the heat transfer asymptotically approaches $h_f/h_0 = 1.0$ for $x/D > 10$. These results are consistent with those of Eriksen and Goldstein (1974), who had a similar injection angle and δ_1/D ratio, but much larger L/D and Re_D. Hay et al. (1985), who had a similar injection angle, but much larger δ_1/D and L/D ratios and smaller Re_D, found distinctly higher levels close to the hole. A possible reason for this difference is that in the study by Eriksen and Goldstein, and in the present study, the heat transfer surface starts downstream of the injection, while in the study of Hay et al. the mass transfer surface starts upstream of the injection. Note that with the species concentration

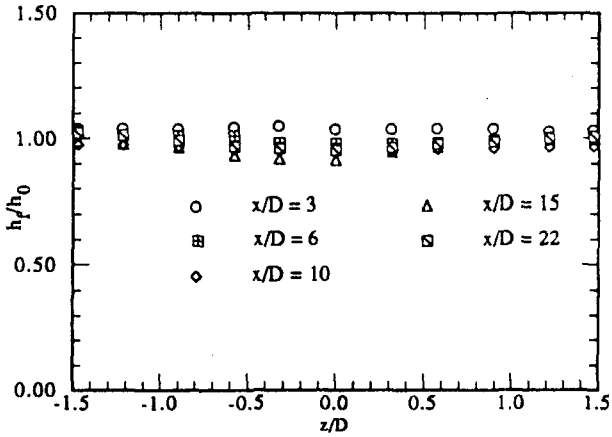

Fig. 5 Lateral h_f/h_0 distribution for round hole, $CA = 0$ deg, $I = 1.0$, $M = 1.0$

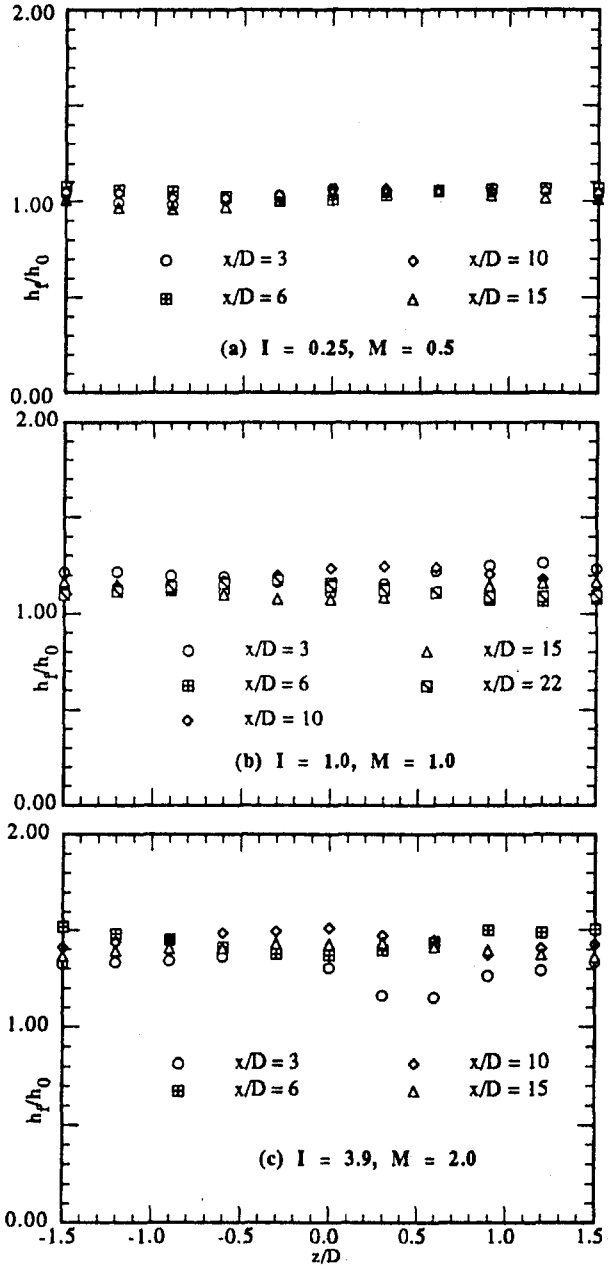

Fig. 6 Lateral h_f/h_0 distribution for round hole, CA = 60 deg: (a) I = 0.25, M = 0.5, (b) I = 1.0, M = 1.0, (c) I = 3.9, M = 2.0

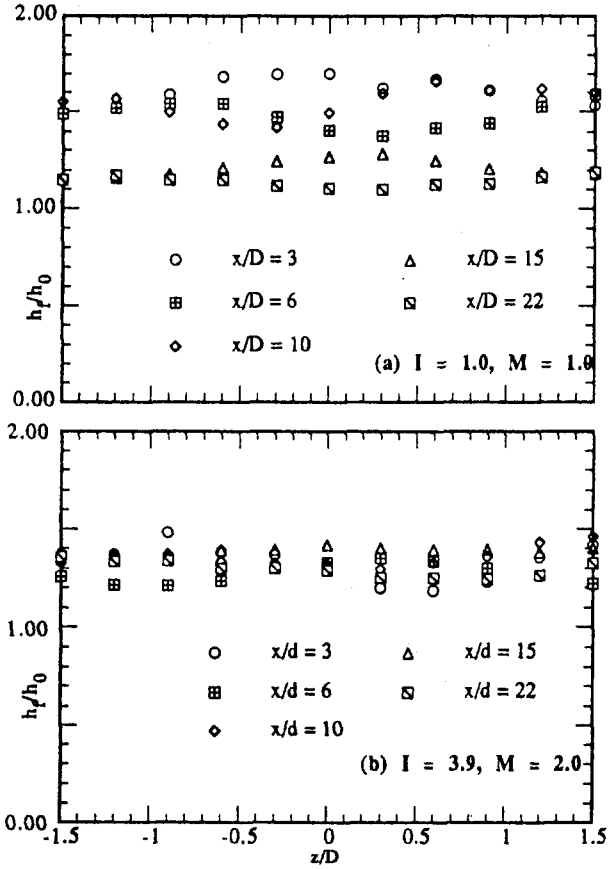

Fig. 7 Lateral h_f/h_0 distribution for 15 deg forward expansion hole, CA = 60 deg: (a) I = 1.0, M = 1.0, (b) I = 3.9, M = 2.0

boundary layer starting upstream of the holes, the reference mass transfer coefficient, h_0, would be lower. Also, a new species concentration boundary layer would start with the injected fluid resulting in a larger h_f mass transfer coefficient.

The lateral variations of h_f/h_0 for the round CA = 0 deg holes are shown for I = 1.0 in Fig. 5. These data show that the maximum deviation from h_f/h_0 = 1.0 occurs at the centerline, and is essentially h_f/h_0 = 1.0 at $z/D = \pm 1.5$ for all streamwise positions measured. There is very little lateral variation. Similar results were obtained at I = 0.16 and I = 0.25.

The lateral h_f/h_0 distributions for the round holes with CA = 60 deg at I = 0.25, I = 1.0, and I = 3.9 are shown in Fig. 6(a), 6(b), and 6(c), respectively. The magnitude of h_f/h_0 increases with increase in momentum flux ratio. Note that at the two higher levels of I, h_f/h_0 is greater than 1.0 at all points in the span. The movement in the lateral location of the heat transfer peak shows the lateral movement of the jet due to the compound angle orientation of the hole.

The forward expansion hole with CA = 60 deg also shows a significantly higher heat transfer level as compared to injection at CA = 0 deg. This is illustrated by the lateral distributions at I = 1.0 and I = 3.9 shown in Figs. 7(a) and 7(b), respectively. Most notable when comparing the CA = 60 deg with and without exit expansion is that h_f/h_0 for I = 1.0 is much greater near the hole for the expanded hole, but relaxes to nominally the same value at x/D = 22. Results for the two compound angle holes were very similar at I = 3.9.

To use the heat transfer results meaningfully, they should be combined with the adiabatic effectiveness results (presented in Schmidt et al., 1996) to find the Net Heat Flux Reduction (NHFR). The heat transfer results were obtained at DR = 1.0

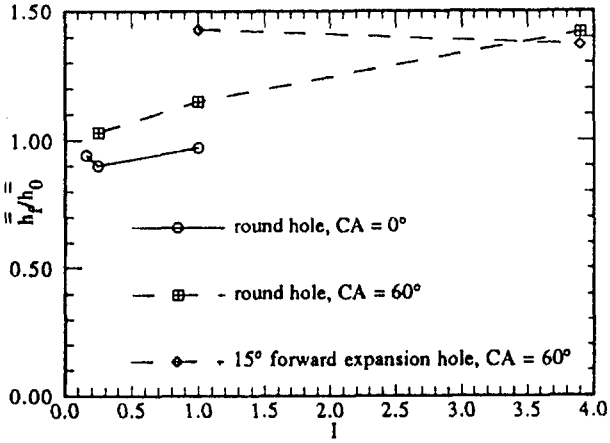

Fig. 8 Variation of spatially averaged $\bar{h}_f/\bar{h}_0$ with I; DR = 1.0

and the effectiveness data was obtained at $DR = 1.6$, but as discussed in the introduction, the density ratio effect at constant momentum flux ratio is not expected to be significant. Spatial averages for the effectiveness, $\bar{\bar{\eta}}$, and for the heat transfer coefficient, $\bar{\bar{h}}_f$, were determined for the surface area bounded by the span between the holes and from $x/D = 3$ to $x/D = 15$. The spatial average heat transfer coefficients as a function of the momentum flux ratio for the different configurations are shown in Fig. 8. These data were used to determine the NHFR for each hole configuration tested, and results are presented in Table 2 and Fig. 9. Calculation of values of NHFR requires that a value for θ be assumed since the actual value of θ is dependent on the real turbine blade conditions. A value of $\theta = 1.6$, which is typical of film cooled turbine blade operation, was used for these calculations. From the standpoint of NHFR, which represents overall performance, all the hole geometries have very similar performance for $I \leq 1.0$. At $I = 3.9$ the expanded exit $CA = 60$ deg holes perform significantly better than the round $CA = 60$ deg holes.

As noted in Schmidt et al. (1996) and evident in Table 2, from an adiabatic effectiveness standpoint, the holes with $CA = 60$ deg are significantly better at larger momentum flux ratios, e.g., $I = 1.0$. However, the heat transfer results from this phase of the study showed that holes with $CA = 60$ deg had a significantly higher heat transfer coefficients at higher momentum flux ratios. As a result, the holes with $CA = 60$ deg and with an expanded exit, which have the largest $\bar{\eta}$ at $I = 1.0$, did not have a net increase in performance as indicated by the similar values of NHFR. Note that the round hole with $CA = 60$ deg has NHFR ≈ 0.0 at $I = 3.9$, which means that the film cooling process is completely ineffective because of the high heat transfer level and the low adiabatic effectiveness. Figure 9 also shows that for all geometries, the performance deteriorated with increasing I, and both increased heat transfer coefficients and lower adiabatic effectiveness contributed to this deterioration.

Conclusions

Heat transfer coefficients for the baseline $CA = 0$ deg holes did not deviate significantly from that for the undisturbed boundary layer flow when operated at typical momentum flux ratios. These results were consistent with previous studies of $CA = 0$ deg holes. The increased interaction between the jets and the mainstream when using $CA = 60$ deg holes results in significantly higher heat transfer rates at higher momentum flux ratios. This increase in heat transfer rate decreases the overall film cooling performance, which was quantified in terms of a net heat flux reduction, NHFR. This study showed the importance of knowing both adiabatic effectiveness and heat transfer coefficient for evaluating overall film cooling performance. The heat transfer coefficient becomes a specially important variable for determining overall performance for compound angle injection at high momentum flux ratios. In particular, Schmidt et al. (1996) showed that the maximum spatially averaged adiabatic effectiveness occurred for the forward expanded $CA = 60$ deg holes at $I = 1.0$, but the overall NHFR at this condition was significantly lower than that obtained at $I = 0.25$ for round holes with $CA = 0$ and 60 deg. Note that the relative performance of the different hole geometries presented here should be viewed in terms of the operating conditions used. For example, differences in the response to high free-stream turbulence or rough walls might well alter the relative performance. The most general conclusion from this study is that ultimately evaluation of film cooling performance should be done in terms of NHFR rather than adiabatic effectiveness alone.

Table 2 Spatial average effectiveness and heat transfer, and NHFR results; $\theta = 1.6$

Geometry	I	$\bar{\bar{\eta}}$	$\bar{\bar{h}}_f/h_0$	NHFR
round,	0.16	0.25	0.94	0.46
CA = 0°	0.25	0.25	0.90	0.44
	1.0	0.13	0.97	0.23
round,	0.25	0.29	1.03	0.45
CA = 60°	1.0	0.24	1.15	0.29
	3.9	0.17	1.42	-0.03
fwd.exp.,	1.0	0.32	1.43	0.30
CA = 60°	3.9	0.28	1.37	0.24

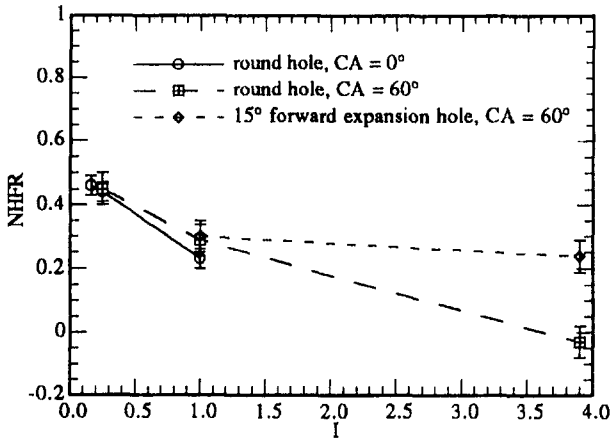

Fig. 9 Variation of NHFR (Net Heat Flux Reduction) with I; h_f/h_0 measurements at $DR = 1.0$, η measurements at $DR = 1.6$

Acknowledgments

The authors would like to thank the sponsors, the Garrett Engine Division of Allied Signal Aerospace Company and the Air Force Wright-Patterson Research and Development Center. We would also like to thank Mr. Noor Sait, Mr. David Dotson, and Dr. Karen Thole for their assistance in conducting experiments, and Prof. Michael Crawford for his assistance in running TEXSTAN.

References

Ammari, H. D., Hay, N., and Lampard, D., 1990, "The Effect of Density Ratio on the Heat Transfer Coefficient for a Film Cooled Flat Plate," ASME JOURNAL OF TURBOMACHINERY, Vol. 112, pp. 444–450.

Crawford, M. E., 1995, Professor at The University of Texas at Austin, private communication.

Eckert, E. R. G., 1984, "Analysis of Film Cooling and Full-Coverage Film Cooling of Gas Turbine Blades," ASME *Journal of Engineering for Gas Turbines and Power*, Vol. 106, pp. 206–213.

Eriksen, V. L., and Goldstein, R. J., 1974, "Heat Transfer and Film Cooling Following Injection Through Inclined Circular Tubes," ASME *Journal of Heat Transfer*, Vol. 96, pp. 239–245.

Forth, C. J. P., Loftus, P. J., and Jones, T. V., 1985, "The Effect of Density Ratio on the Film Cooling of a Flat Plate," Agard Conference Proceedings 390.

Goldstein, R. J., 1971, "Film Cooling," *Advances in Heat Transfer*, T. F. Irvine and J. P. Hartnett, eds., Academic Press, New York, Vol. 7, pp. 321–379.

Goldstein, R. J., and Yoshida, T., 1982, "The Influence of a Laminar Boundary Layer and Laminar Injection on Film Cooling Performance," ASME *Journal of Heat Transfer*, Vol. 104, pp. 355–362.

Hay, N., Lampard, D., and Saluja, C. L., 1985, "Effects of Cooling Films on the Heat Transfer Coefficient on a Flat Plate With Zero Mainstream Pressure Gradient," ASME *Journal of Engineering for Gas Turbines and Power*, Vol. 107, pp. 105–110.

Kays, W. M., and Crawford, M. E., 1993, *Convective Heat and Mass Transfer*, 3rd ed., McGraw-Hill, New York.

Liess, C., 1975, "Experimental Investigation of Film Cooling With Ejection From a Row of Holes for the Application to Gas Turbine Blades," ASME *Journal of Engineering for Power*, Vol. 97, pp. 21–27.

Ligrani, P. M., Ciriello, S., and Bishop, D. T., 1992, "Heat Transfer, Adiabatic Effectiveness, and Injectant Distributions Downstream of a Single Row and Two Staggered Rows of Compound Angle Film Cooling Holes," ASME JOURNAL OF TURBOMACHINERY, Vol. 114, pp. 687–700.

Ligrani, P. M., Ortiz, A., Joseph, S. L., and Evans, D. L., 1989, "Effects of Embedded Vortices on Film-Cooled Turbulent Boundary Layers," ASME JOURNAL OF TURBOMACHINERY, Vol. 111, pp. 71–77.

Luckey, D. W., Winstanley, D. K., Hanus, G. J., and L'Ecuyer, M. R., 1977, "Stagnation Region Gas Film Cooling for Turbine Blade Leading-Edge Applications," AIAA *Journal of Aircraft,* Vol. 14, pp. 494–501.

Makki, Y. H., and Jakubowski, G. S., 1986, "An Experimental Study of Film Cooling From Diffused Trapezoidal Shaped Holes," Paper No. AIAA-86-1326.

Pietrzyk, J. R., Bogard, D. G., and Crawford, M. E., 1990, "Effect of Density Ratio on the Hydrodynamics of Film Cooling," ASME JOURNAL OF TURBOMACHINERY, Vol. 112, pp. 437–443.

Schmidt, D. L., Sen, B., and Bogard, D. G., 1996, "Film Cooling With Compound Angle Holes: Adiabatic Effectiveness," ASME JOURNAL OF TURBOMACHINERY, Vol. 118, this issue, pp. 807–813.

Sen, B., 1995, "Effects of Injection Hole Geometry, Freestream Turbulence, and Surface Roughness on Film Cooling Heat Transfer," Ph.D dissertation, The University of Texas at Austin.

Sinha, A. K., Bogard, D. G., and Crawford, M. E., 1991, "Film Cooling Effectiveness Downstream of a Single Row of Holes With Variable Density Ratio," ASME JOURNAL OF TURBOMACHINERY, Vol. 113, pp. 442–449.

Thole, K. A., Sinha, A. K., Bogard, D. G., and Crawford, M. E., 1992, "Mean Temperature Measurements of Jets With a Crossflow for Gas Turbine Film Cooling Application," *Rotating Machinery Transport Phenomena,* J. H. Kim and W. J. Yang, eds., Hemisphere Pub. Corp., New York.

Film Cooling With Compound Angle Holes: Adiabatic Effectiveness

D. L. Schmidt

B. Sen

D. G. Bogard

Mechanical Engineering Department,
University of Texas at Austin,
Austin, TX 78712

Film cooling effectiveness was studied experimentally in a flat plate test facility with zero pressure gradient using a single row of inclined holes, which injected high-density, cryogenically cooled air. Round holes and holes with a diffusing expanded exit were directed laterally away from the free-stream direction with a compound angle of 60 deg. Comparisons were made with a baseline case of round holes aligned with the free stream. The effects of doubling the hole spacing to six hole diameters for each geometry were also examined. Experiments were performed at a density ratio of 1.6 with a range of blowing ratios from 0.5 to 2.5 and momentum flux ratios from 0.16 to 3.9. Lateral distributions of adiabatic effectiveness results were determined at streamwise distances from 3 D to 15 D downstream of the injection holes. All hole geometries had similar maximum spatially averaged effectiveness at a low momentum flux ratio of $I = 0.25$, but the round and expanded exit holes with compound angle had significantly greater effectiveness at larger momentum flux ratios. The compound angle holes with expanded exits had a much improved lateral distribution of coolant near the hole for all momentum flux ratios.

Introduction

Discrete hole film cooling is an important technique for cooling turbine blades in gas turbine engines. Much of the published research on the effectiveness of film cooling has concentrated on round holes, inclined at approximately 35 deg with respect to the surface, and aligned with the mainstream flow. In this work we used a flat plate test facility with zero pressure gradient to study the effectiveness of a single row of holes directed laterally away from the mainstream direction (i.e., with a nonzero compound angle). Two sets of laterally directed holes were studied; the first had round holes, and the second had holes with a circular metering section and a diffusing forward expansion at the exit of the holes (forward-expanded holes).

Compound angle injection has received renewed attention because this orientation is "believed to produce injectant distributions over surfaces giving better protection and higher film effectivenesses than injectant from holes with simple angle orientations" (Ligrani et al., 1992). However, there are few experimental or computational studies reported in the open literature. Experimental adiabatic effectiveness studies of laterally directed injection from a single row of holes into a zero pressure gradient flow over a flat plate are limited to those by Goldstein et al. (1970) for a single round hole with $\beta = 15$ and 35 deg, $CA = 90$ deg; Ligrani et al. (1992) for a single row of round holes with $\beta = 24$ deg, $CA = 50.5$ deg; and Honami et al. (1994) for a single row of round holes with $\beta = 30$ deg, $CA = 90$ deg. Honami et al. did not include streamwise-directed holes as a basis for comparison, but their near-hole compound angle effectiveness behavior was comparable to the other two studies. Compared to streamwise directed jets, the lateral spread of a compound angle film cooling jet increased, thus improving the laterally averaged effectiveness near the injection location. A significant improvement over streamwise directed jets was found at higher blowing ratio, $M \geq 1$ (all these studies were done at density ratio of $DR \approx 1$, so this corresponds to $I \geq 1$), which indicated that the jets stayed closer to the wall when a compound angle was used. However, far downstream the effectiveness results were different at higher M. Goldstein et al. (1970), who determined effectiveness from adiabatic wall temperature measurements, found that the improvement was sustained far downstream. Ligrani et al. (1992), who deduced adiabatic results from Stanton number extrapolations using superposition, found that the compound angle effectiveness decreased to the values for $CA = 0$ deg holes over a similar streamwise distance.

A computational study of a single row of laterally directed holes was conducted by Sathyamurthy and Patankar (1990), for a streamwise distance to $x/D = 10$ downstream of the holes. Rows of holes with $\beta = 30$ deg, $CA = 45$ and 90 deg, and with spacing between holes from $P/D = 3$ to 5 were investigated with unit density ratio injection. They stated that their analysis should be interpreted as qualitative since there are very limited experimental data with which to validate the computations. For $P/D = 3$ and $M = 1.0$ ($I = 1.0$), the laterally averaged effectiveness was found to improve with increase in compound angle, but at $P/D = 5$ there was very little difference for $CA = 0$, 45, or 90 deg. They also found that for laterally directed holes, the average effectiveness continued to increase with increase in blowing ratio up to $M = 3.0$ ($I = 9.0$), the maximum blowing ratio computed.

The shape of the film cooling hole is also an important geometric variable, but it has received limited attention in the literature. Goldstein et al. (1974) examined holes that had circular metering sections and were widened out at 10 deg near the exits. Makki and Jakubowski (1986) examined holes that had trapezoidal cross sections and were diffused in the direction of the mainstream flow. They used a transient facility, for which film cooling performance was indicated by the ratio of heat transfer coefficients with cooling to those without cooling. Both studies showed that expanding the hole exit improved film cooling performance compared to the round hole base case. However, there are no studies of the effects of compound angle with shaped or expanded holes in the open literature.

The effects of increasing hole spacings were discussed by Brown and Saluja (1979) and Foster and Lampard (1980) for streamwise-directed holes. Spacing of injection holes affects

Contributed by the International Gas Turbine Institute and presented at the 39th International Gas Turbine and Aeroengine Congress and Exposition, The Hague, The Netherlands, June 13–16, 1994. Manuscript received by the International Gas Turbine Institute February 9, 1994. Paper No. 94-GT-312. Associate Technical Editor: M. G. Dunn.

film cooling performance in two ways: The spacing determines the coolant mass per unit span at a given blowing condition, and closer spacing promotes jet merging, thus improving lateral coverage. There have been no studies reported for compound angle holes.

The customary way to describe film cooling performance defines the heat transfer coefficient in terms of adiabatic wall temperature, T_{aw}. In nondimensional form, T_{aw} is expressed as the adiabatic effectiveness. In the present experimental program, adiabatic effectiveness and heat transfer coefficients were determined for laterally directed film cooling holes, round and expanded, and for round streamwise-directed holes (as a basis for comparison). This paper presents the adiabatic effectiveness results. The associated heat transfer coefficients for the different hole configurations are presented in Sen et al. (1996).

Experimental Facilities and Techniques

Experiments were conducted in a closed-loop, subsonic wind tunnel facility, illustrated in Fig. 1. A secondary flow loop provided cryogenically cooled injection air to obtain the desired density ratio. Further details of the facility can be found in Pietrzyk et al. (1990). The flat test plate was a modular design composed of three sections: a 12.7-cm-long, sharp leading edge plate; a 14-cm-long injection plate; and an instrumented downstream plate. The sharp leading edge section had a 45 deg angle cut on the upstream edge. Suction at the leading edge, shown in Fig. 1, was adjusted so that a uniform flow with no separation occurred at the leading edge. The injection plate had a single row of holes with one of three different geometries to be described later. The geometry and coordinate system of the film cooled test plate is shown in Fig. 2.

This study considered three hole geometries, illustrated in Fig. 3, all with injection angle $\beta = 35$ deg, metering inlet diameter $D = 11.1$ mm, and a hole length of $L = 4D$. The test plates were constructed from extruded polystyrene foam (Styrofoam) with nine holes at a hole spacing of 3D; hole spacing was doubled by taping alternate holes closed. The basic geometry parameters of hole length, spacing, and injection angle were selected to be representative of the geometry used for turbine blade film cooling holes. Two compound angles were used: $CA = 0$ deg, with the hole axes aligned with the free-stream direction; and $CA = 60$ deg, with the hole axes at a 60 deg angle to the free stream. The $CA = 0$ deg holes were round holes and were tested as a basis of comparison. Two geometries were constructed with $CA = 60$ deg: a round hole case and a forward expanded exit case. The metering length, measured along the hole axis, was 2.1 D for the expanded exit holes, and the exit was expanded at a 15 deg angle along the line of the laterally directed hole as indicated in Fig. 3. Note that the projected cross-stream exit width of the expanded hole with $CA = 60$ deg was 3.3 D, which resulted in an overlapping of the projected widths, although the holes did not physically overlap.

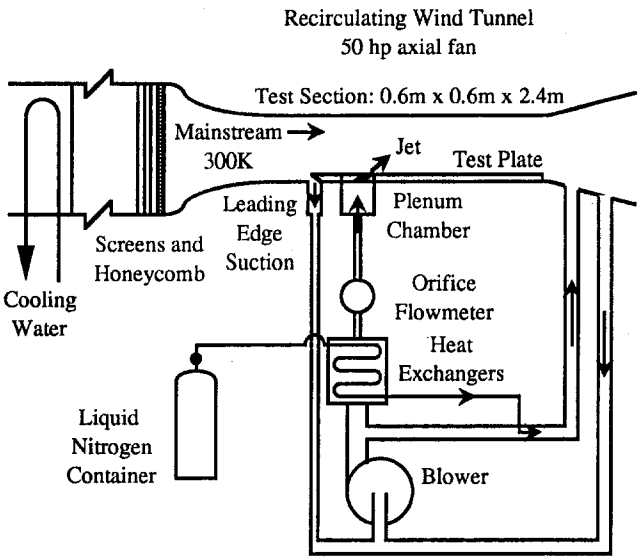

Fig. 1 Film cooling test facility

The 60 deg compound angle and 15 deg forward expansion angle were specified by Garrett Engine Division of AlliedSignal Aerospace and represent geometries in use in Garrett gas turbines. The hole inlets and exits were sharp edged, and the interiors were aerodynamically smooth. The holes were supplied by a common plenum, 48 cm by 12.7 cm in cross section (70 times the inlet area of all nine injection holes) and 48 cm deep, with several screens to promote more uniform flow through the plenum. The coolant temperature was monitored by a thermocouple positioned about 7 D below the entrances to the holes, which was found to give temperatures equivalent to the jet exit temperature.

The downstream plate was constructed from Styrofoam to provide an adiabatic boundary condition. A three-dimensional conduction heat transfer code indicated negligible conduction errors for this plate material (Sinha et al., 1991). The foam was bonded to a fiberglass composite (Extren) for structural rigidity. Below the Extren was 15.2 cm of Corning fiberglass insulation and 2.54 cm of Styrofoam. Surface roughness of the Styrofoam was measured to be less than 0.005 mm, which was much less than $y^+ = 5$ for the boundary layer flow on the test plate, so that the test plate was aerodynamically smooth.

An array of thin ribbon thermocouples was epoxied to the surface for surface temperature measurements. Because the thermocouple ribbons were very thin relative to their width, 38 μm thick and 1.5 mm wide, conduction error was negligible. An IR camera was used to verify that the thermocouple ribbons did not cause a smearing of the large temperature gradients that

Nomenclature

CA = compound angle
D = film cooling hole diameter
DR = density ratio of coolant to mainstream = ρ_c/ρ_∞
H = shape factor = δ_1/δ_2
I = momentum flux ratio of coolant to mainstream = $\rho_c U_c^2/\rho_\infty U_\infty^2$
L = hole length
M = mass flux ratio of coolant to mainstream = $\rho_c U_c/\rho_\infty U_\infty$
P = hole spacing
Re = Reynolds number
T = temperature
U = streamwise velocity
U_c = bulk cooling jet velocity through metering length of hole
x = streamwise coordinate originating at downstream edge of cooling holes
z = spanwise coordinate originating at centerline of central hole
β = angle of injection with respect to the surface
δ_1 = displacement thickness
δ_2 = momentum thickness
η = adiabatic effectiveness = $(T_{aw} - T_\infty)/(T_c - T_\infty)$
ρ = density

Subscripts

aw = adiabatic wall
c = coolant
∞ = free stream

Superscripts

$\bar{}$ = lateral average
$\bar{\bar{}}$ = spatial average

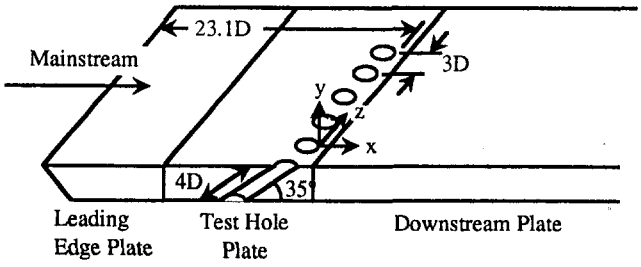

Fig. 2 Test section geometry and coordinate system

occurred during film cooling tests. The junctions formed by welding the ribbons were approximately 0.4 mm in diameter, and the ends of the ribbons were soldered to 0.5 mm thermocouple extension wires, which were routed through the test plate. The thickness of the thermocouple junctions after gluing to the surface ranged from 0.1 to 0.2 mm ($y^+ = 6$ to 12 at the highest velocity), which caused negligible aerodynamic interference. Further details about the thin ribbon thermocouple design are provided by Sinha et al. (1991). Nine thermocouple junctions were located on the central hole centerline from 2 D to 30 D downstream of the trailing edge of the hole. At streamwise locations of 3 D, 6 D, 10 D, and 15 D, seven thermocouple junctions were used, spanning the lateral distance from -1.5 D to $+1.5$ D. These lateral locations were for $P/D = 3$ hole spacing. For $P/D = 6$ spacing two runs were necessary to form a composite picture of the cooling jet performance. In these cases, with the central hole open and adjacent holes taped, data were obtained for -1.5 $D \le z \le 1.5$ D, and with the central hole taped and adjacent holes open data were obtained for 1.5 $D \le z \le 4.5$ D. Thermocouples were used to monitor free-stream and secondary loop temperatures. Acquisition of temperature data and data processing was automated to allow on-line analysis of film cooling effectiveness. Pressure differentials across the wind tunnel contraction and across a sharp-edged orifice plate in the secondary flow loop were used to set free-stream velocity and injection flow rate, respectively.

The operating technique utilized for this study was to set the mass flow rate of the cryogenically cooled injectant, then vary the free-stream velocity to obtain the desired blowing conditions. The coolant-to-mainstream density ratio and the blowing conditions were selected to be representative of the actual film cooling process. The free-stream velocity ranged from $U_\infty = 30$ m/s to 7.5 m/s, providing momentum flux ratios from $I = 0.16$ to 3.9 ($M = 0.5$ to 2.5), with $DR = 1.6$. A comprehensive description of free-stream and boundary layer development and uniformity was given by Pietrzyk et al. (1990) for a 20 m/s free-stream velocity. For this study the boundary layer profiles were measured immediately upstream of the film cooling holes (with no cooling flow), which was a position 21.6 cm downstream of the leading edge. The boundary layers were found to be fully developed turbulent boundary layers at $U_\infty = 20$ m/s and $U_\infty = 10$ m/s. The boundary layer parameters for $U_\infty = 20$ m/s were $\mathrm{Re}_{\delta 2} = 1100$, $\delta_1/D = 0.120$, and $H = 1.48$. At $U_\infty = 10$ m/s, the boundary layer parameters were $\mathrm{Re}_{\delta 2} = 700$, $\delta_1/D = 0.151$, and $H = 1.46$. These values were obtained without using a trip wire, and no trip wire was used for the effectiveness tests. The precision uncertainty on free-stream velocity was $\delta U_\infty = \pm 1$ percent, and the free-stream turbulence level was about $Tu = 0.2$ percent. The Reynolds number based on the free-stream velocity and the hole diameter ranged from $\mathrm{Re}_D = 5000$ to 21,000. The technique of varying free-stream conditions to obtain the various I and M ratios raised concerns about Reynolds number effects. Tests were conducted maintaining a constant I using several injectant mass fluxes and free-stream velocities for one geometry at one low I near the optimum performance condition, and one high I. The variation in the laterally averaged effectiveness was within the uncertainty of $\bar{\eta}$ for injection conditions spanning the range of Re_D.

Pietrzyk et al. (1990) also documented the film cooling loop. The cooling jets were supplied by a common plenum. Pietrzyk et al. performed laser-Doppler anemometry measurements of individual jets and found a mean velocity variation between jets of $\delta U_c = \pm 2.6$ percent. For the data described below, the mass flux ratio was held constant within $\delta M = \pm 4$ percent during experiments. The injectant-to-free stream density ratio was $DR = 1.6$. Maximum variation of density ratio between all experiments was $\delta DR = \pm 4$ percent, although the variation during any one experiment was $\delta DR = \pm 2$ percent. The free-stream temperature was allowed to vary ± 0.5°C and the coolant temperature was allowed to vary ± 2°C during an experimental run.

The low temperature of the dense jets meant a potential for H_2O and CO_2 to solidify and accumulate in the secondary flow loop and on the test plate. Wind tunnel air drying techniques and operating procedures developed by Pietrzyk et al. (1990) to reduce the frosting potential were employed. A new heat exchanger for cooling the jets was installed and the tunnel was sealed to minimize air infiltration to the wind tunnel, although a fully effective seal could not be obtained. This meant that frost could accumulate during an experiment, and it would have to be removed from the test plate between adiabatic effectiveness measurements. Repeated tests showed consistent performance was obtained after frost removal, with the variation in

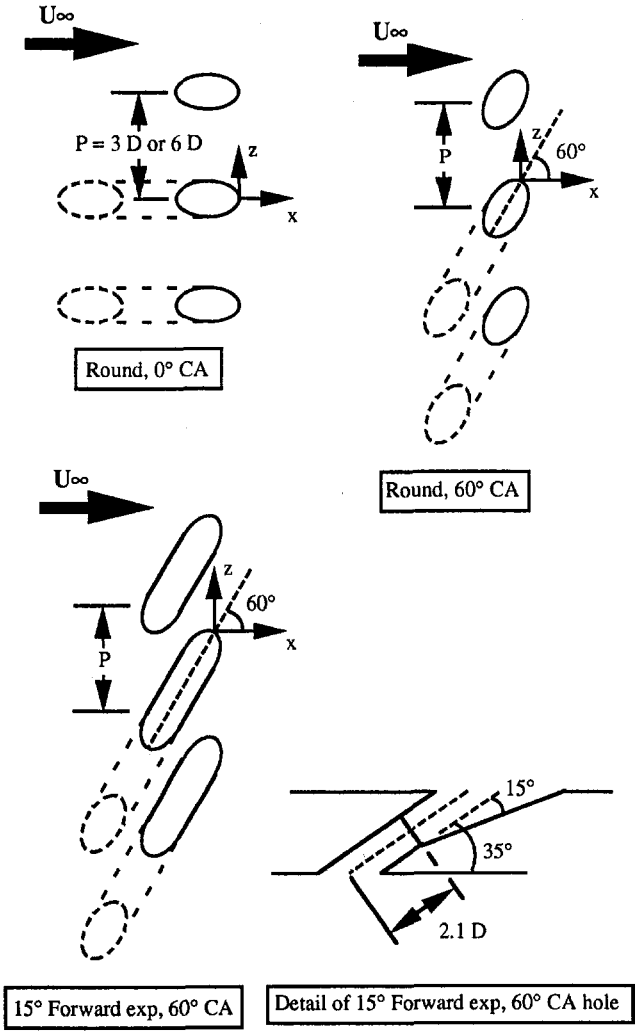

Fig. 3 Injection hole geometry showing the top view of the central three holes for all three geometries, and details of the geometry for the 15 deg forward expansion, 60 deg CA holes

local effectiveness, laterally averaged effectiveness, and spatially averaged effectiveness being $\delta\eta = \pm 0.01$, $\delta\bar{\eta} = \pm 0.01$, and $\delta\bar{\bar{\eta}} = \pm 0.01$, respectively.

Based on the uncertainties for flow conditions and freestream, coolant, and surface temperatures, and the uncertainties due to frost effects, the sequential perturbation technique (Moffat, 1988) was used to estimate the resulting uncertainties for adiabatic effectiveness values. We also obtained a direct measure of the precision uncertainties for adiabatic effectiveness by performing a number of repeatability tests. Most of these were performed with $CA = 0$ deg round holes for which six sets of measurements were made in four separate experiments conducted over a span of three years. The momentum flux ratio for these tests was $I = 0.16$, and similar repeatability tests were conducted with $I = 0.63$ and $I = 1.4$. Statistical analysis of the variation of the local values of η gave an uncertainty of $\delta\eta = 0.03$ for all momentum flux ratios and streamwise positions. The analysis of variations of laterally averaged and spatially averaged effectiveness gave uncertainties of $\delta\bar{\eta} = 0.02$ and $\delta\bar{\bar{\eta}} = 0.02$, for all streamwise positions and momentum flux ratios. The sequential perturbation analysis gave equivalent values for uncertainties for laterally and spatially averaged effectiveness, but a slightly lower value for local effectiveness. Similar uncertainties were obtained using compound angle holes, although not the same compound angle discussed in this paper.

In terms of percentages, the uncertainty of the local effectiveness ranged from 5 percent of the largest centerline value to 15 percent of the smallest centerline value for all data presented. The uncertainty for the laterally averaged effectiveness ranged from 5 to 20 percent for all data presented, except for round holes with $CA = 0$ deg and $P/D = 6$, in which case very low $\bar{\eta}$ values were obtained. For the spatially averaged effectiveness results, the uncertainty ranged from 7 to 20 percent for all data presented, except for round holes with $CA = 0$ deg data at $I > 1.0$, in which case the coolant jets were completely separated, resulting in very low effectiveness values.

The evaluation of film cooling performance discussed below refers to blowing ratio and momentum flux ratio. These ratios are defined using the injectant velocity, U_c, based on the flow rate and the cross section area of the metering length (inlet) of the hole. Studies reported in the literature commonly use the jet velocity in the definitions of M and I. However, expanding the hole exit increases the cross-sectional area after the metering length, hence the jet velocity decreases. In this situation, U_c is used in the description of flow conditions since the correct representative jet velocity is not known.

Results and Discussion

Results for the three hole geometries tested are presented in terms of lateral variations of local effectiveness η, streamwise variation of laterally averaged effectiveness $\bar{\eta}$, and finally the variation of spatially averaged effectiveness $\bar{\bar{\eta}}$ as a function of momentum flux ratio. The results of the 3 D and 6 D hole spacings are presented together to aid in the description of the effects of compound angle injection. For the coordinate system we placed the streamwise coordinate origin, $x = 0$, at the trailing edge of the film cooling hole. The lateral coordinate origin, $z = 0$, was at the centerline of the trailing edge of the central hole. The coordinate system origins are shown in Fig. 3 for each geometry.

The validity of the round hole $CA = 0$ deg results was established by comparing the effectiveness with results from Pedersen et al. (1977) and results from Sinha et al. (1991). Both studies measured effectiveness at high density ratio and had injection geometries similar to the present study, although the injection hole lengths were substantially different. The present study used holes with $L/D = 4.0$, while Pedersen et al. used much longer holes ($L/D \sim 40$) and Sinha et al. used holes with $L/D = 1.75$. For low I, there was good agreement between the present results and the data of Pedersen et al. and Sinha et al., as illustrated by the centerline data in Fig. 4(a). At high I (Fig. 4(b)), for which jet lift-off occurs in the near-hole region, the present results showed some deviation from the data of Pedersen et al. and Sinha et al. The difference was primarily attributed to differences in the film cooling hole length-to-diameter ratio for the different studies.

The lateral movement of the cooling jet expected for compound angle injection is clearly illustrated by comparing in Figs. 5(a) and 5(b), which show lateral η distributions at the four streamwise stations for the round holes with $CA = 0$ and 60 deg. A distinct difference in the initial lateral distribution of coolant for the round holes and expanded exit holes with compound angle is evident when comparing Figs. 5(a), 5(b), and 5(c). The expanded exit holes have an almost uniform lateral distribution of coolant at the first measurement position of $x/D = 3$, while the round holes show a large lateral variation. However, by $x/D = 15$ both round and expanded exit holes with compound angle show similar uniform lateral distributions.

We selected $x/D = 10$ as a representative position for the following comparisons of the lateral distribution of η for the different hole geometries. Results presented in Fig. 6 are representative of low momentum flux ratio ($I < 0.5$), and results presented in Fig. 7 are representative of high momentum flux ratio ($1 \leq I < 4$). Figure 6(a) shows that $\eta > 0.1$ across the span between holes for low I and for $P/D = 3$. This result suggests that there is some merging of the coolant jets for all hole geometries for this hole spacing. For $P/D = 6$, Fig. 6(b) shows a distinct region of zero effectiveness indicating the coolant jets no longer merged (note, data were not taken for $z/D > 1.5$ for round $CA = 0$ deg and the round $CA = 60$ deg holes because it was evident that η would be essentially zero over this range). Also evident from Fig. 6(b) is that the forward expanded $CA = 60$ deg holes deliver a much greater lateral distribution of the coolant. At high I, Fig. 7(a) shows that the round and the forward expanded $CA = 60$ deg holes have similar good lateral distribution of coolant for $P/D = 3$, and both are

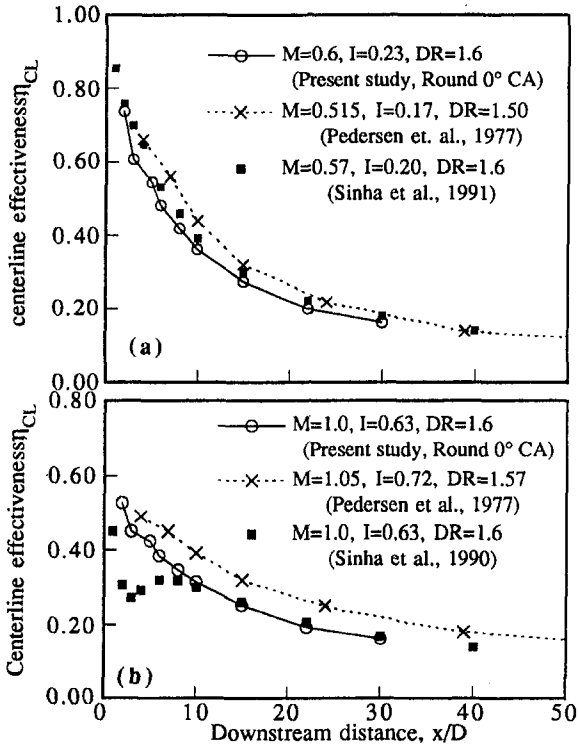

Fig. 4 Comparison of round hole centerline effectiveness to published data: (*a*) $I = 0.23$, $M = 0.6$, (*b*) $I = 0.63$, $M = 1.0$

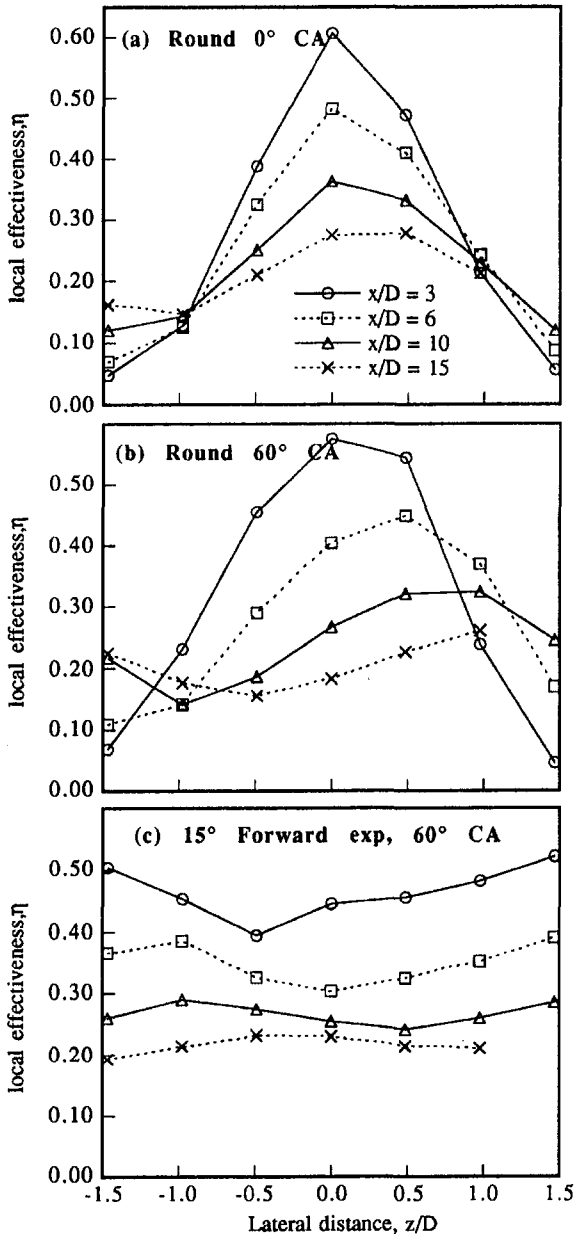

Fig. 5 Local lateral effectiveness for the holes with CA = 60 deg, I = 0.25, M = 0.63

clearly superior to the round CA = 0 deg holes. However, for P/D = 6, Fig. 7(b) shows regions of zero effectiveness, indicating that the coolant jets have not merged, but there is a greater lateral distribution of coolant for both the round and forward expanded compound angle holes. Note that in Fig. 7(b) both compound angle cases also exhibited steep η gradients on the side toward which the jets were directed. We attribute this to the impact of the mainstream on this side of the jet causing a sharp shear layer.

Laterally averaged effectivenesses were determined by integrating the measured lateral distribution of η and dividing by the span between hole centerlines. A simple trapezoidal integration was used since it was found to give the same result as higher order polynomial fits. Results are shown as a function of downstream distance for $I \approx 0.25$ and $I \approx 1.0$ in Figs. 8 and 9, respectively. At the lower I, adding a compound angle to the round hole did not significantly change $\overline{\eta}$ compared to the base case round hole. In contrast, the combination of compound angle with the forward expanded exit caused a significant increase immediately downstream of the hole, but fell to a level equivalent to the round holes by x/D = 10. The initial improved $\overline{\eta}$ value for the forward expanded CA = 60 deg may be attributed to the improved lateral distribution of the coolant discussed previously. Increasing the spacing between holes from P/D = 3 to P/D = 6 caused approximately a factor of two decrease in $\overline{\eta}$, and $\overline{\eta}$ values for each of the holes were very similar.

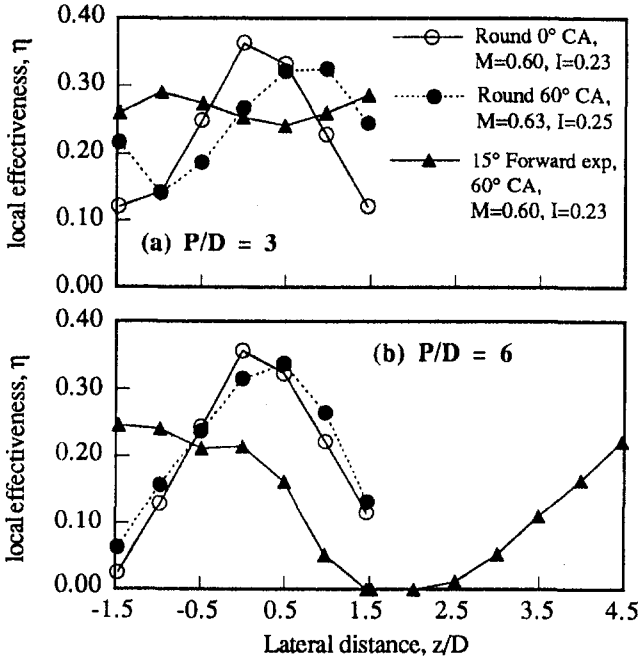

Fig. 6 Local lateral effectiveness at x/D = 10 for the test holes, $I \approx 0.25$, $M \approx 0.6$

Figure 9 shows that at relatively high I, there were distinct differences in the effectiveness for the different hole geometries. Both compound angle holes had significantly greater effectiveness than the baseline case round hole with CA = 0 deg. This is mainly because of a large decrease in $\overline{\eta}$ for the CA = 0 deg

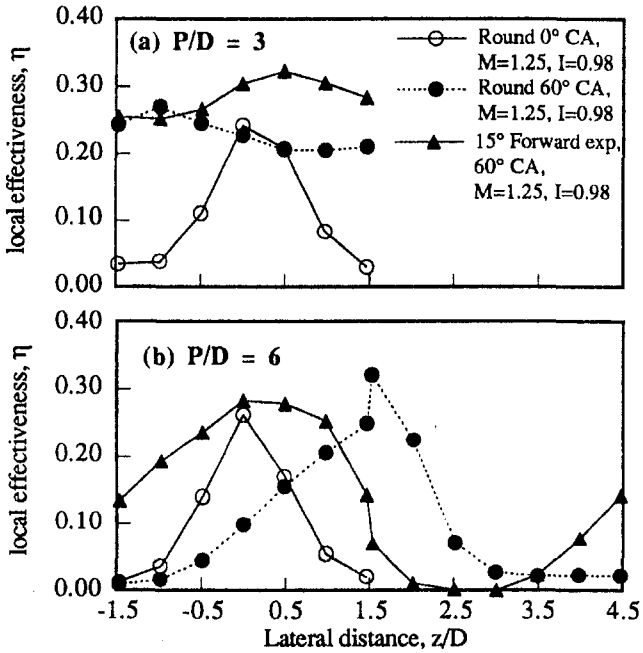

Fig. 7 Local lateral effectiveness at x/D = 10 for the test holes, I = 0.98, M = 1.25

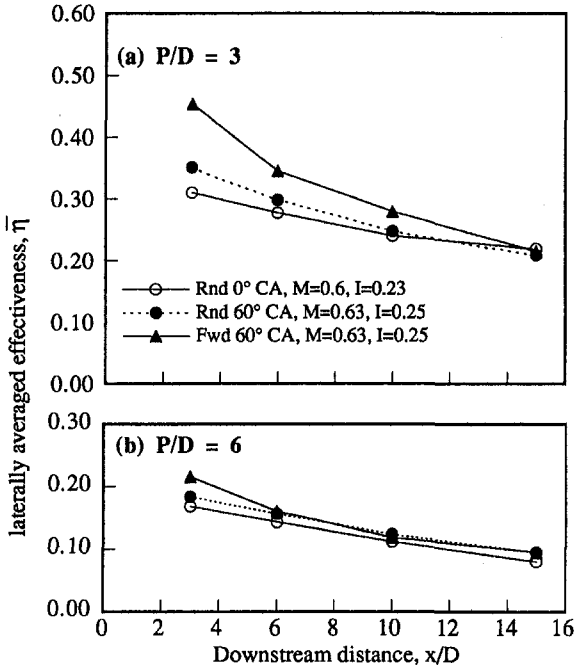

Fig. 8 Laterally averaged effectiveness for the test holes, $I \approx 0.25$, $M \approx 0.6$

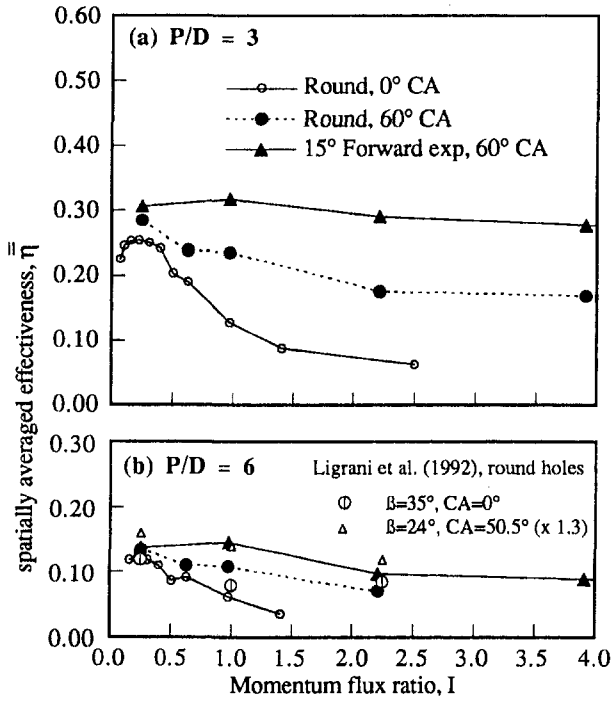

Fig. 10 Spatially averaged effectiveness for the test holes with $DR = 1.6$

round hole, which may be attributed to detachment of the cooling jet from the surface. Detachment of the cooling jet for $CA = 0$ deg round holes at $I = 1.0$ is consistent with the results of Thole et al. (1992), who showed that the coolant jet would be fully detached for $I > 0.8$. Again the forward expanded exit with $CA = 60$ deg significantly increased $\bar{\eta}$ immediately downstream of the holes, but fell to a level comparable to the round $CA = 60$ deg holes by $x/D = 15$. When the hole spacing was doubled, $\bar{\eta}$ was reduced by a factor of two, but the $CA = 60$ deg geometries retained significantly increased effectiveness relative to the $CA = 0$ deg holes.

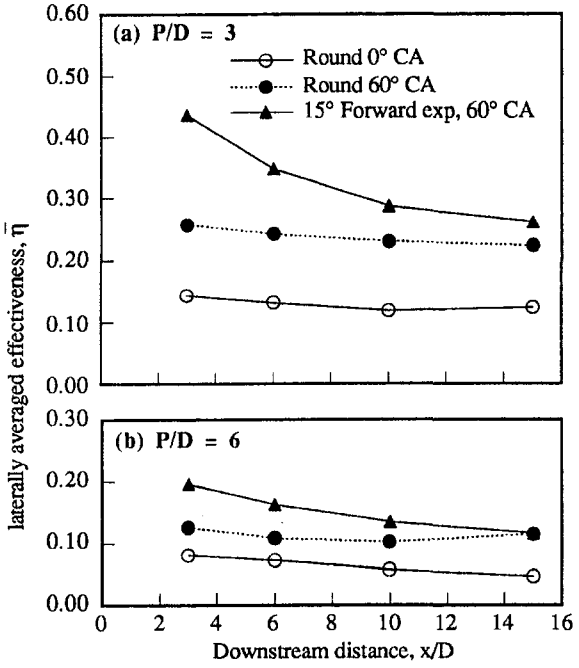

Fig. 9 Laterally averaged effectiveness for the test holes, $I = 0.98$, $M = 1.25$

To compare the effectiveness of the different geometries over a full range of momentum flux ratios, a spatially averaged adiabatic effectiveness, $\bar{\bar{\eta}}$, was used. This quantity was defined as the integral average of the laterally averaged effectiveness from $x/D = 3$ to 15. Results for $\bar{\bar{\eta}}$ for all three geometries as a function of momentum flux ratio are shown in Fig. 10. Immediately obvious from Fig. 10(a) for $P/D = 3$ is that the effectiveness at low I is very similar for the different geometries, but adding a 60 deg compound angle significantly increased the range over which high effectiveness levels were maintained. The forward expanded exit holes with $CA = 60$ deg maintained essentially the same level of $\bar{\bar{\eta}}$ over the full range tested, $0.25 < I < 3.9$, and were significantly better than the round $CA = 60$ deg holes at the larger I. For the round $CA = 60$ deg holes, $\bar{\bar{\eta}}$ decreased slightly with increasing I, but still had reasonably good effectiveness at $I = 3.9$. This decreasing trend for the $CA = 60$ deg round holes is somewhat different from the computational predictions of Sathyamurthy and Patankar (1990), which indicated a constant level of effectiveness for $CA = 45$ deg round holes, and increasing effectiveness with increasing I for $CA = 90$ deg round holes.

The effect of increasing hole spacing to $P/D = 6$ is shown in Fig. 10(b). Both round hole geometries had blowing conditions at which local lateral data for $1.5 < z/D < 4.5$ were not obtained (as noted previously, it was evident that η was essentially zero over this range). For these cases, averaged effectiveness results were calculated assuming $\eta = 0$ over $1.5 < z/D < 4.5$. The results for $P/D = 6$ are somewhat similar to the $P/D = 3$ results with the $\bar{\bar{\eta}}$ levels generally decreased by a factor of two. Results for the round holes with $CA = 0$ and 60 deg can be compared with the results of Ligrani et al. (1992), who used round holes with $CA = 0$ and 50.5 deg, but with an injection angle of $\beta = 24$ deg. The magnitudes of the effectiveness deduced from the data of Ligrani et al. over the range $x/D = 5$ to 15 were very similar to the present results for the range that Ligrani et al. tested, $0.25 < I < 2.2$. Similarly they found that the effectiveness of the compound angle round holes decreased with increasing I, but improved relative to the $CA = 0$ deg holes.

Conclusions

All three geometries had very similar spatially averaged adiabatic effectiveness at low momentum flux ratio, although the forward expansion with $CA = 60$ deg holes had an improved lateral spread of the film cooling jets immediately behind the holes. Adding a compound angle to the baseline round hole geometry significantly improved effectiveness at high momentum flux ratios, and the combination of compound angle and forward expansion provided further improvement. With a hole spacing of $P/D = 3$, the forward expanded $CA = 60$ deg holes maintained essentially the same level of spatially averaged effectiveness for the range of I studied, while the effectiveness level of the round $CA = 60$ deg holes decreased slightly with increasing I. The higher spatially averaged effectiveness obtained for the forward expanded holes was due to significantly higher effectiveness very near the hole, but by $x/D = 15$ the forward expanded and round $CA = 60$ deg holes had essentially the same effectiveness. With $P/D = 6$, both compound angle geometries retained significantly improved effectiveness compared to the streamwise directed round holes. These results indicate that film cooling with compound angle injection does not provide higher adiabatic effectiveness at the optimum momentum flux ratio, but does provide high effectiveness over a considerably larger range of momentum flux ratios. However, these adiabatic effectiveness results must be coupled with the heat transfer coefficients to determine overall performance as discussed in Sen et al. (1996).

Acknowledgments

The authors gratefully acknowledge Garrett Engine Division of the AlliedSignal Aerospace Company and the Air Force Wright-Patterson Research and Development Center for support of this research. We would also like to thank Mr. Noor Sait, Mr. David Dotson, and Dr. Karen Thole for their assistance in conducting experiments.

References

Brown, A., and Saluja, C. L., 1979, "Film Cooling From a Single Hole and a Row of Holes of Variable Pitch to Diameter Ratio," *International Journal of Heat and Mass Transfer,* Vol. 22, pp. 525–533.

Foster, N. W., and Lampard, D., 1980. "The Flow and Film Cooling Effectiveness Following Injection Through a Row of Holes," ASME *Journal of Engineering for Power,* Vol. 102, pp. 584–588.

Goldstein, R. J., Eckert, E. R. G., Eriksen, V. L., and Ramsey, J. W., 1970, "Film Cooling Following Injection Through Inclined Circular Tubes," *Israel Journal of Technology,* Vol. 8, pp. 145–154.

Goldstein, R. J., Eckert, E. R. G., and Burggraf, F., 1974, "Effects of Hole Geometry and Density on Three-Dimensional Film Cooling," *International Journal of Heat and Mass Transfer,* Vol. 17, pp. 595–607.

Honami, S., Shizawa, T., and Uchiyama, A., 1994, "Behavior of the Laterally Injected Jet in Film Cooling: Measurements of Surface Temperature and Velocity/Temperature Field Within the Jet," ASME JOURNAL OF TURBOMACHINERY, Vol. 116, pp. 106–112.

Ligrani, P. M., Ciriello, S., and Bishop, D. T., 1992, "Heat Transfer, Adiabatic Effectiveness, and Injectant Distributions Downstream of a Single Row and Two Staggered Rows of Compound Angle Film Cooling Holes," ASME JOURNAL OF TURBOMACHINERY, Vol. 114, pp. 687–700.

Makki, Y. H., and Jakubowski, G. S., 1986, "An Experimental Study of Film Cooling From Diffused Trapezoidal Shaped Holes," Paper No. AIAA-86-1326.

Moffat, R. J., 1988, "Describing Uncertainties in Experimental Results," *Experimental Thermal and Fluid Science,* Vol. 1, pp. 3–17.

Pedersen, D. R., Eckert, E. R. G., and Goldstein, R. J., 1977, "Film Cooling With Large Density Differences Between the Mainstream and the Secondary Fluid Measured by the Heat–Mass Transfer Analogy," ASME *Journal of Heat Transfer,* Vol. 99, pp. 620–627.

Pietrzyk, J. R., Bogard, D. G., and Crawford, M. E., 1990, "Effects of Density Ratio on the Hydrodynamics of Film Cooling," ASME JOURNAL OF TURBOMACHINERY, Vol. 112, pp. 437–443.

Sathyamurthy, P., and Patankar, S. V., 1990, "Prediction of Film Cooling With Lateral Injection," AIAA/ASME Thermophysics and Heat Transfer Conference, Seattle, WA.

Sen, B., Schmidt, D. L., and Bogard, D. G., 1996, "Film Cooling With Compound Angle Holes: Heat Transfer," ASME JOURNAL OF TURBOMACHINERY, Vol. 118, this issue, pp. 800–806.

Sinha, A. K., Bogard, D. G., and Crawford, M. E., 1991, "Film Cooling Effectiveness Downstream of a Single Row of Holes With Variable Density Ratio," ASME JOURNAL OF TURBOMACHINERY, Vol. 113, pp. 442–449.

Thole, K. A., Sinha, A. K., Bogard, D. G., and Crawford, M. E., 1992, "Mean Temperature Measurements of Jets With a Crossflow for Gas Turbine Film Cooling Application," in: *Rotating Machinery Transport Phenomena,* J. H. Kim and W. J. Yang, eds., Hemisphere Pub. Corp., New York.

The Effect of High Free-Stream Turbulence on Film Cooling Effectiveness

J. P. Bons

C. D. MacArthur

R. B. Rivir

Aero Propulsion and Power Directorate,
US Air Force Wright Laboratory,
Wright-Patterson AFB, OH 45433

This study investigated the adiabatic wall cooling effectiveness of a single row of film cooling holes injecting into a turbulent flat plate boundary layer below a turbulent, zero pressure gradient free stream. Levels of free-stream turbulence (Tu) up to 17.4 percent were generated using a method that simulates conditions at a gas turbine combustor exit. Film cooling was injected from a single row of five 35 deg slant-hole injectors (length/diameter = 3.5, pitch/diameter = 3.0) at blowing ratios from 0.55 to 1.85 and at a nearly constant density ratio (coolant density/free-stream density) of 0.95. Film cooling effectiveness data are presented for Tu levels ranging from 0.9 to 17 percent at a constant free-stream Reynolds number based on injection hole diameter of 19,000. Results show that elevated levels of free-stream turbulence reduce film cooling effectiveness by up to 70 percent in the region directly downstream of the injection hole due to enhanced mixing. At the same time, high free-stream turbulence also produces a 50–100 percent increase in film cooling effectiveness in the region between injection holes. This is due to accelerated spanwise diffusion of the cooling fluid, which also produces an earlier merger of the coolant jets from adjacent holes.

Introduction

Modern trends in aero-engine gas turbine combustor design have resulted in short, high temperature rise combustors, which produce highly turbulent exit flows. As combustor exit temperature is increased to benefit the engine cycle efficiency, effective film cooling of the turbine components downstream of the combustor becomes increasingly important.

Counteracting the increased heat load from the higher temperature gas by increasing the film flow is rarely an acceptable engineering solution because the coolant is usually taken from upstream in the cycle and its extraction can cause unacceptable performance penalties. The film cooling designer is therefore faced with the challenge of obtaining the maximum efficiency from each unit of coolant flow. Accurate information on the effects of the many variables that enter the problem—pressure gradient, curvature, exit hole design, coolant and mass flow rates—is critical.

All gas turbine combustors, and in particular, the newer low aspect ratio designs, produce complex exit flows, which contain turbulence of varying intensity, scale, and isotropy. Recent research has shown free-stream turbulence to have a significant effect on boundary layer flows. Therefore it may be expected that film cooling will also be significantly influenced by turbulence in the mainstream. Although there exists a large body of film cooling effectiveness data documenting the effects of many design parameters, there have been relatively few comprehensive studies of the effect of free-stream turbulence. No study to date has investigated the effect of turbulence of the type associated with gas turbine combustors on film cooling. This may be in part because, until recently, few quantitative data have been available in the open literature on combustor exit turbulence. The work of Goebel et al. (1993) and Moss and Oldfield (1991) has begun to provide details of turbulence for actual combustors. Information on many additional quantities, in particular length scales, is yet to be reported. Goebel et al. found the ranges of axial and swirl turbulence intensities to be generally between 5 and 20 percent. Also, these values vary considerably with radial position and the amount of swirl induced in the flow by the fuel injection. Such significant intensities would be expected to affect film cooling behavior greatly. While these studies provide information on older combustor geometries, as previously noted, new combustors are shorter, with less pressure drop, and anticipated to have more severe exit turbulence.

The objective of this work is to further the understanding of how film cooling effectiveness is influenced by mainstream turbulent flow. A single row of angled injection holes is used with diameter-to-spacing and length-to-diameter ratios typical of current cooling schemes. Free-stream turbulence is created by jets in crossflow, an arrangement designed to simulate the dilution jets located near or at the exit of virtually all combustors. This work concentrates on effectiveness (a measure of the mixing rate of the film with the free stream as determined from the adiabatic wall "recovery" temperature) because of its importance in most common methods of predicting gas-to-surface heat transfer.

The most comprehensive published work documenting the effects of free-stream turbulence on film cooling is that of Kadotani and Goldstein (1979a, b). These authors used turbulence-generating grids in a low-speed, zero pressure gradient flow to create free-stream intensity fluctuations of up to about 20 percent and turbulent integral length scales (average eddy sizes) of 0.06 to 0.33, expressed as fractions of the film ejection hole diameter. The film cooling arrangement was a single row of angled holes similar to the present study. Kadotani and Goldstein found varying degrees of turbulence influence, which, when expressed as a ratio of disturbed effectiveness to effectiveness with a (nearly) laminar free stream, ranged from −30 to +15 percent. The authors concluded that three general parameters were of greatest importance in changing the effectiveness: the turbulence intensity, the blowing ratio, and the ratios of length scale to hole diameter and length scale to mainstream boundary layer thickness at the hole location. All three parameters appear to alter the mixing rate between the mainstream and the film coolant.

Contributed by the International Gas Turbine Institute and presented at the 39th International Gas Turbine and Aeroengine Congress and Exposition, The Hague, The Netherlands, June 13–16, 1994. Manuscript received by the International Gas Turbine Institute February 16, 1994. Paper No. 94-GT-51. Associate Technical Editor: E. M. Greitzer.

Other studies of the effect of free-stream turbulence on film cooling have been presented by Jumper et al. (1989), and Brown and Saluja (1979). Jumper et al. presented effectiveness results for one nearly constant turbulence level of 16 percent generated using a wall jet as the mainstream flow. This turbulence level was achieved in the initial period of the wall jet velocity decay. The wall jet has velocity and turbulence profiles somewhat distinct from those of a conventional flat plate boundary layer, which makes comparison of these results to other work difficult. Nevertheless the same general trends in enhancement or decrease of effectiveness with blowing ratio as seen in Kadotani and Goldstein were observed, but at a greater rate. Brown and Saluja studied film cooling from a single hole and a row of holes exiting into accelerating and decelerating flows. Free-stream turbulence was generated with a grid, giving levels of 1.7 and 8 percent. In general, increasing turbulence intensity resulted in a decrease of centerline effectiveness at all downstream locations. The spanwise-averaged effectiveness values, however, increased with higher Tu for blowing ratios above 0.7.

The focus of this report is the influence of turbulence intensity on film effectiveness. Turbulent length scales were measured at the film injection location and are reported. The current experiment lacks the means to vary this parameter independently. Thus the effect of length scale on effectiveness downstream of the injection point was not addressed as an independent parameter. The facility has been carefully constructed to simulate the actual turbine environment, providing, in particular, levels of free-stream turbulence higher than that generated by the injected film flow in the boundary layer. When the turbulence in the free stream is greater than the turbulence in the boundary layer, the transport of $u'v'$ and $v'T'$ throughout the boundary layer is significantly altered from the values achieved beneath a quiescent free stream. This is evidenced by the nonconstant values of the Reynolds analogy factor with Tu observed by MacMullin et al. (1989) and Maciejewski and Moffat (1992). This condition, lacking in all previously published work, is necessary to reproduce actual engine conditions properly.

Experimental Facility

The research facility used for the experiments is shown in Fig. 1. The open loop wind tunnel uses a main flow blower with an external intake to provide a nominal mass flow of 1.5 kg/s to the test section. A heat exchanger at the main flow blower discharge can be used to vary the flow temperature from 18 to 54°C (depending on local atmospheric temperature). The main flow enters a conditioning plenum of 0.6 m diameter before reaching the rectangular test section. This conditioning plenum has one layer of perforated aluminum plate followed by 7.6 cm of honeycomb straightener, and three layers of fine screen. A circular-to-rectangular nozzle constructed of polystyrene foam conducts the flow from the 0.6 m diameter plenum cross section to the 0.24 m × 0.38 m test section. With this conditioning, flow uniformity of ±2.5 percent in velocity (at U_{fs} = 16 m/s) is obtained over the center 0.23 m (spanwise dimension) by 0.22 m (vertical dimension) of the test section (the region with coolant injection). Without employing turbulence generation devices, a free-stream turbulence level of 0.9 percent (±0.05) was achieved over this center region.

Boundary layer bleeds are employed at the top and bottom of the test section 12.07 cm upstream of the downstream lip of the film cooling injection holes (designated as $x/d = 0$ in Figs. 1 and 2). At 1.22 m from the plenum exit, a knife edge bleed clips off the bottom 1.27 cm of the growing boundary layer. On the top of the test section (and at the same streamwise location), a circular leading edge bleeds off an additional 1.27 cm of the flow, making the aspect ratio of the final test section (aspect ratio = span/height) approximately 1.76. The circular leading edge bleed is the upstream end of the adjustable top wall. The top wall pivots about this forward end in order to adjust the pressure gradient in the tunnel. For the tests presented here, constant pressure was desired and the wall was adjusted until a nondimensional pressure gradient $(L/\rho U_{fs}^2)(dP/dx)$ of 0.0182 was achieved down the test section.

Figure 2 shows a top view of the test section, indicating boundary layer bleed, trip, film cooling holes, and thermocouple placement. At 0.64 cm from the downstream lip of the coolant holes ($x/d = 0.33$), an adiabatic surface with imbedded thermocouples spans the 0.38 m width and the 1.82 m streamwise length of the test section. The surface consists of a top layer of 0.051-mm-thick Inconel foil epoxied to a 0.16-cm-thick epoxy board, which is in turn affixed to a 10-cm-thick insulating urethane foam. For the present experiments, no voltage potential was placed across the Inconel foils, and the surface is essentially adiabatic. The 80 (0.94 mm bead diameter) iron-constant thermocouples are mounted from the underside of the epoxy panel

Nomenclature

H = shape factor = δ^*/θ
L = streamwise test section length = 1.82 m
Lgx = longitudinal integral length scale, cm
Lgy = vertical integral length scale, cm
M = blowing ratio = $\rho_{fc}U_{fc}/\rho_{fs}U_{fs}$
Re_d = Reynolds number based on cooling hole diameter
T = static temperature
Tu = turbulence intensity = u'/U, percent
U = mean local streamwise velocity, m/s
U_{fs} = mean free-stream streamwise velocity, m/s
b = turbulence grid bar width = 1.34 cm
d = film cooling hole diameter = 1.905 cm
d_{TJ} = turbulence generator hole diameter = 1.11 cm
dP/dx = streamwise pressure gradient, Pa/m
u' = fluctuating streamwise velocity component
v' = fluctuating vertical velocity component
x = streamwise distance measured from downstream lip of injection hole
y = vertical distance measured from injection surface
z = spanwise distance measured from center injection hole
Δ_{eff} = effectiveness deficit = $1 - \eta_{hiTu}/\eta_{loTu}$, percent
δ = boundary layer thickness
δ^* = boundary layer displacement thickness
η = film cooling effectiveness = $(Tw - Taw)/(Tfc - Taw)$
η_c = centerline film cooling effectiveness
η_m = midline film cooling effectiveness
θ = boundary layer momentum thickness
ρ = fluid density

Subscripts

aw = adiabatic wall
dTJ = Reynolds number based on turbulence hole diameter
fc = in the film cooling fluid
fs = in the free-stream fluid
$hiTu$ = $Tu > 0.9$ percent free-stream conditions
$loTu$ = $Tu = 0.9$ percent free-stream conditions
w = at the wall
θ = Reynolds number based on momentum thickness

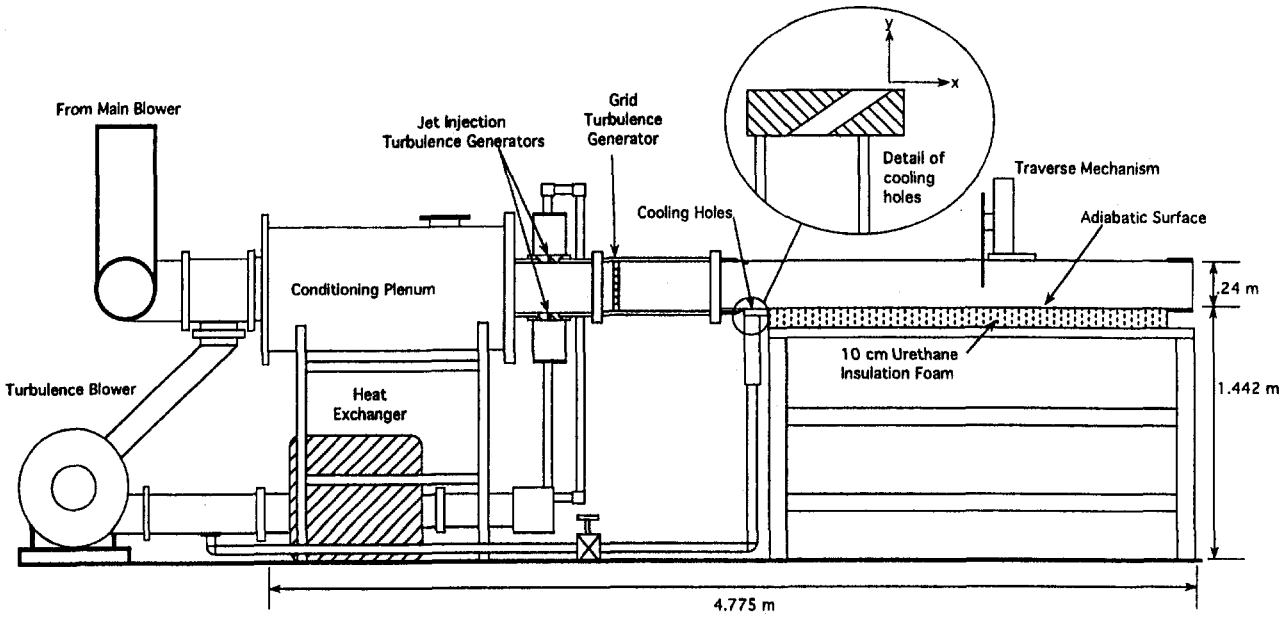

Fig. 1 Side view of experimental film cooling facility

to within 0.051 mm of the backside of the foil. The boundary layer trip is a 1.59 mm diameter steel rod located 2.54 cm from the knife-edge bleed. This is approximately the height of a fictitious turbulent boundary layer starting from the knife edge, and insures a spanwise uniform turbulent boundary layer profile at the injection point, $x/d = 0$ (9.53 cm downstream of the trip).

A principal requirement of the facility is the generation of high levels of free-stream turbulence. This is accomplished by two methods for the present experimental data. A 0.15 m diameter "Tee" located 0.61 m upstream of the inlet to the conditioning plenum leads to a bypass blower, which boosts the bypass flow pressure by 7 kPa. This bypass flow is then re-injected from two opposing rows of eleven 1.11 cm diameter holes located on the top and bottom of the test section 1.02 m upstream of the boundary layer bleed. A heat exchanger in the bypass line is used to remove the 25°C heat of compression from the bypass blower. This type of turbulence generation device was pioneered by Bogard et al. (1992), who successfully varied the velocity ratio (jet velocity/free-stream velocity) and the Reynolds number (based on hole diameter) to obtain uniform Tu levels from 5 to 25 percent.

In the present facility, a velocity ratio of 14 produced a turbulence level of 17 percent (± 0.85) at the injection station ($x/d_{TJ} = 103$ downstream of the turbulence generator holes). The Reynolds number based on d_{TJ} for this case is 7800 for the nominal operating conditions of $U_{fs} = 16$ m/s in the film cooling test section. The attainable Tu level varies with both velocity ratio and Re_{dTJ}, and decays down the plate slightly slower than the characteristic $-5/7$ power law for grid-generated turbulence (Fig. 4). By throttling the bypass flow down to a velocity ratio of 4.5 (and $\mathrm{Re}_{dTJ} = 9400$), an 11.5 percent Tu level at the

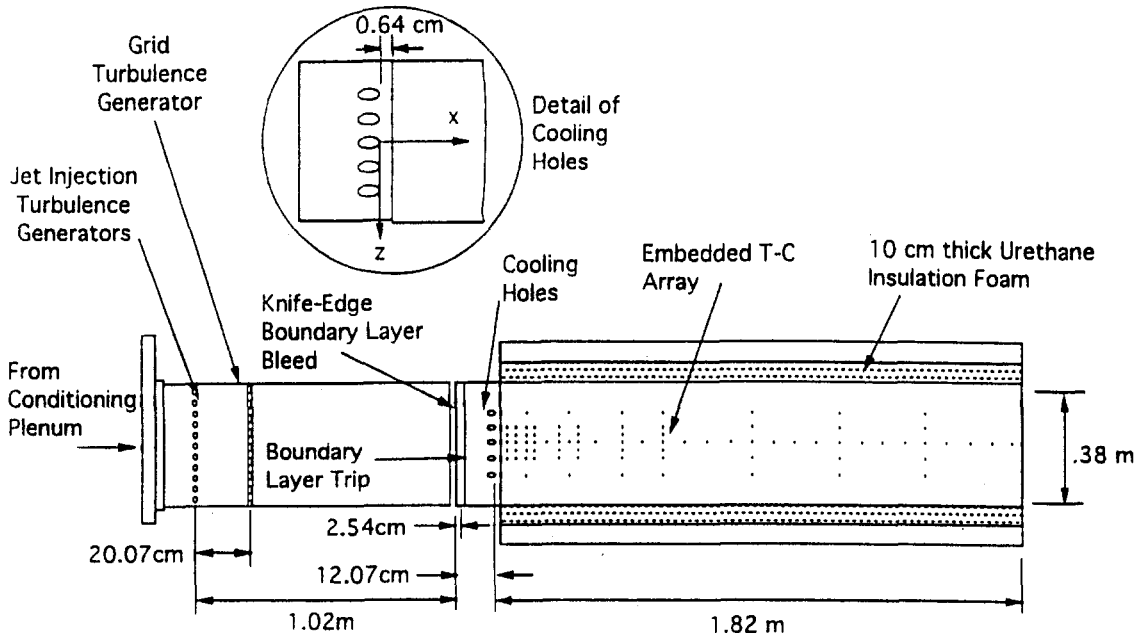

Fig. 2 Top view of experimental film cooling facility

injection point was achieved with a uniformity of ±0.94 in the bottom 5 cm of the flow (below $y/d = 2.63$). This was considered adequate uniformity for the present study as the coolant fluid never rises above the lower 5 cm of the flow before $x/d = 10$, and only marginally thereafter.

To provide comparison with the bulk of elevated free-stream turbulence film cooling literature, which uses grid-generated turbulence, a standard square grid was installed 0.94 m upstream of the coolant injection point. The grid is made of square bars with a width of 1.34 cm and a spacing-to-width ratio of 4.5. The grid provided a turbulence level of 6.5 percent (±0.3) at the injection point. The turbulent jets and grid were never employed simultaneously. Figure 3 shows typical fluctuating velocity boundary layer profiles at the injection station for the different turbulence generation modes without film cooling injection (injection holes taped). Figure 4 shows the streamwise decay of the generated free-stream turbulence (arrows denote the film cooling injection station). Boundary layer data corresponding to the four fluctuating velocity profiles in Fig. 3 are tabulated in Table 1. Turbulence levels and length scales for the free stream ($y/d = 2.63$) are included in the table for comparison.

The source of the film cooling flow is a "Wye" located at the exit of the turbulence flow blower (and before the turbulence flow heat exchanger). The blower heat of compression provides an elevated temperature of approximately 20°C over the free-stream temperature at the injection point. Due to heat loss in the film cooling flow piping, the exit temperature drops with decreasing mass flow and the temperature rise was as low as 9°C for the lowest blowing ratio tested ($M = 0.55$). The facility is thus run in the "film heating" versus the "film cooling" mode with a density ratio of approximately 0.95 ("film heating" and "film cooling" are used interchangeably in this report). The row of five 1.9 cm diameter injection holes is centered in the test section width. The 35 deg inclined holes are spaced at three hole diameters and the injection pipe length from the coolant access plenum to the exit is 3.5 hole diameters. Comparing velocity and temperature profiles from the center three holes shows uniformity to within ±5 percent nominally for both parameters.

Instrumentation

The data presented in this report were taken using a single 4 μm diameter tungsten hot wire and an array of thermocouples. The hot wire and a flow temperature thermocouple (0.33 mm bead diameter) located 0.5 cm downstream (and at the same y and z) from the hot wire probe are both mounted on a vertical traverse. A magnetically encoded linear position indicator (Sony model #SR50-030A) affixed to the traverse was used to determine the probe position to within 2.5 μm. National Instruments data acquisition and Labview software were used to acquire and process the hot wire and thermocouple voltages. Hot wire voltages were obtained using a TSI Model #IFA-100 anemometer and a National Instruments NB-MIO-16X A-to-D board. Each mean velocity measurement is obtained from the average of 1000 points taken at 200 samples per second, from which the fluctuating component of velocity, u', was also calculated. The velocity computation algorithm corrects for local variations in pressure, temperature, and humidity. Length scales were calculated by integrating to the first zero crossing of the autocorrelation coefficient function for the velocity obtained from the hot wire signal. Each length scale represents the average of 20 autocorrelations (each with 2048 velocity data points taken at 2000 samples per second). The temperature measurements were made using an integrating voltmeter with an integration period of 0.017 s for each sample.

To calculate the film effectiveness, the facility was run without film cooling to determine the adiabatic wall temperature, T_{aw}, for each setting of free-stream turbulence. The film cooling fluid temperature was determined from a vertical temperature

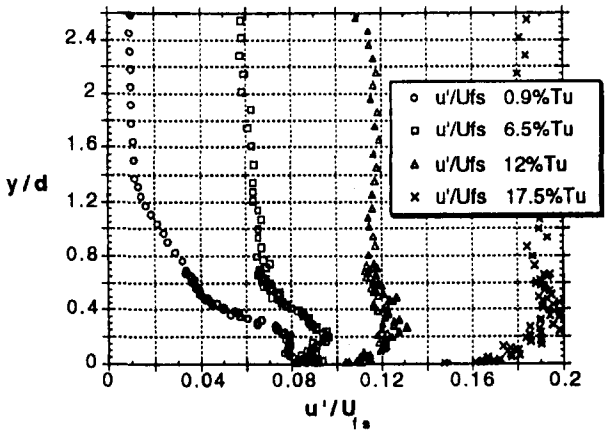

Fig. 3 Nondimensional fluctuating velocity component profiles for the mainstream at the injection point ($x/d = 0$) without film cooling. Four levels of *Tu* shown: 17.5, 12, 6.5, and 0.9 percent.

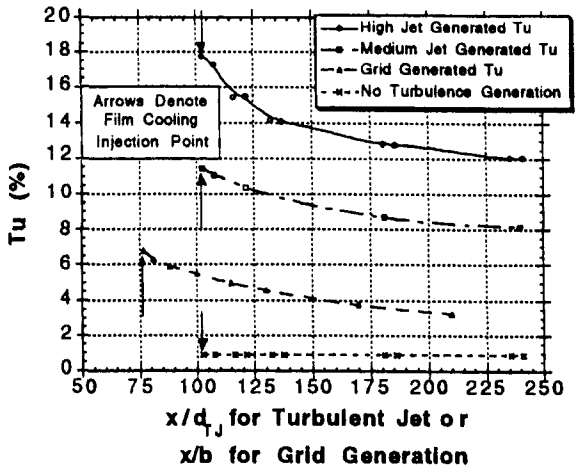

Fig. 4 Streamwise decay of turbulence intensity behind turbulent jets and grid (*Tu* measured at $y/d = 2.6$). Turbulent jet hole diameter (d_{TJ}) = 1.11 cm. Grid bar width (b) = 1.34 cm.

Table 1 Classification of experimental test conditions ($x/d = 0$, $z/d = +1.5$)

	No Turbulence Generation	Grid Generated Turbulence (bar grid)	Jet Generated Turbulence (Velocity Ratio = 4.5)	Jet Generated Turbulence (Velocity Ratio = 14)
Data at y/d = 2.6				
Tu (%)	0.96	6.76	12.01	17.3
Lgx (cm)	6.77	3.65	6.04	7.73
Data at y = δ				
U(m/s)	16.03	14.35	13.96	16.82
Re_d	19085	17085	16621	20026
u' (m/s)	0.59	1.1	1.875	3.16
Tu (%)	3.68	7.67	13.43	18.79
Lgx (cm)	3.94	5.48	6.09	8.05
Lgx/d	2.07	2.88	3.20	4.23
δ (cm)	1.22	1.31	1.28	1.26
δ* (cm)	0.123	0.121	0.130	0.123
θ (cm)	0.0927	0.0917	0.0991	0.0965
H	1.33	1.32	1.31	1.27
θ/d	0.0487	0.0481	0.052	0.051
Re_θ	929	822	864	1015

profile at $x/d = 0$ and the maximum temperature recorded was designated as T_{fc}. To determine the injection jet mean velocity a vertical velocity profile at $x/d = 0$ was integrated from the wall to the point of maximum u' (which corresponded approximately to the edge of the film cooling fluid). This average velocity, U, and the local free-stream velocity, U_{fs}, were used to determine the film cooling blowing ratio.

The experimental uncertainties are calculated based on knowledge of the instrumentation used and a simple root-mean-squared error analysis (Kline and McClintock, 1953). This method assumes contributions to uncertainties arise mainly from unbiased and random sources. For the film effectiveness calculation, the uncertainties in thermocouple measurements come from two distinct sources: the error of the thermocouple device and random fluctuations in the actual local temperature being sensed while at a constant operating point. The latter of these two is greater (±0.11°C) and yields an uncertainty in η of ±0.008 at $M = 1$, and ±0.016 at $M = 0.5$ (using a histogram of experimental results). The insulated test surface downstream of the film cooling injection point is considered to be essentially adiabatic. The ratio of the convective heat flux at the test surface to conduction along any path below the surface for typical flow conditions is of order 100. This indicates that the local temperature on the surface is dominated by the convection process and is an accurate indicator of film effectiveness. Uncertainty in the velocity measurement stems primarily from the calibration fit accuracy. When compared to a co-located Kiel probe velocity measurement, the error is within ±1.0 percent at flow rates of interest. Due to the 0.5 cm streamwise displacement of the hot wire and the flow thermocouple, in regions of steep temperature gradients (near $x/d = 0$) the temperature from the thermocouple used in the velocity computation algorithm is as much as 1.2°C lower than the actual temperature at the hot-wire probe. This results in a maximum additional error in U of 2 percent very near the injection hole (decreasing rapidly with x/d), and was not corrected for.

Results and Discussion

The data presented in this section are divided into two subheadings. The first subheading deals with the centerline film cooling effectiveness, η_c, directly downstream of the injection point. Temperature and velocity (both U and u') profiles are used to characterize the evolving film cooling flow over first low, then high, blowing ratios. The second subheading treats the area between coolant holes, up to the point where the adjacent coolant streams merge. Together, the results explore the regions of both decreased and increased film cooling effectiveness due to high free-stream turbulence.

Effectiveness Along the Hole Centerline ($z/d = 0$). This research is motivated by the understanding that high levels of free-stream turbulence are a reality in the environments where film cooling is used (for example: turbine airfoils and casings), and thus the interaction of free-stream turbulence and film cooling should be understood. Freestream turbulence is a measure of the level of random motion of a fluid flow. It would thus be natural to expect that when elevated levels of random motion in an enclosed flow come in contact with mass injection from an adjacent surface, the injected mass will be rapidly mixed into the surrounding fluid. This first-order effect would imply a reduced film cooling effectiveness for elevated levels of free-stream turbulence, a result that has been reported by other researchers (namely, Kadotani and Goldstein, 1979b).

To explore the magnitude and limitations of this expected degradation in film cooling effectiveness for the current facility, wall temperature (and thus film cooling effectiveness) data were taken along the insulated surface downstream from the coolant holes. Blowing ratios from 0.55 to 1.85 were studied for four markedly different flows: (a) a quiescent (0.9 percent Tu) free stream; (b) 6.5 percent grid-generated free-stream turbulence; (c) 11.5 percent mixing jet generated free-stream turbulence; and (d) 17 percent mixing jet generated free-stream turbulence. In the paper, flows are referenced by the level of Tu at the coolant injection plane; naturally this decays to lower values downstream (Fig. 4). Figure 5 shows η_c as a function of blowing ratio for the four different levels of free-stream turbulence. Centerline effectiveness data from the middle three holes agree to within ±5 percent, though only data for the center hole ($z/d = 0$) are shown. As expected, the increasing levels of Tu in the free stream generally decrease the centerline effectiveness of the cooling fluid. This decrease, or deficit (defined here as $\Delta_{\text{eff}} = 1 - \eta_{hiTu}/\eta_{loTu}$), reaches a maximum of 70 percent for $0.55 < M < 0.95$ ($Tu = 17$ percent and $x/d = 22$) with the effect becoming less pronounced as M increases. The jet lift off from the cooled surface is responsible for this change in the observed deficit with higher M, and will be addressed in section B, below.

A deficit of this magnitude is considerably larger than that observed by Kadotani and Goldstein (1979b), who saw a deficit of up to 28 percent at $M = 0.35$ for grid generated free-stream turbulence levels of 20.6 percent. Part of this disparity may be due to the nature of free-stream turbulence generation in the two facilities. The jet generated free-stream turbulence is fairly uniform through the boundary layer (Fig. 3), whereas the 20.6 percent Tu case for Kadotani and Goldstein could only be obtained by placing the turbulence generation grid in close proximity to the film cooling injection point. This resulted in a rather nonuniform turbulence profile at $x/d = 0$, with an actual Tu level of 12.9 percent at the boundary layer edge. In addition to the nonuniform vertical distribution of Tu, the axial distribution also varies rapidly with x in Kadotani and Goldstein's experiment because the injection point is still in the initial decay of the grid generated turbulence. The effectiveness deficit (Δ_{eff}) for the present work at a more comparable Tu level of 11.5 percent and at the lowest blowing ratio studied ($M = 0.55$) is 49 percent.

Another important variable in the Kadotani and Goldstein data is the vertical length scale, Lgy. By varying this parameter, they found that the Δ_{eff} for 8.2 percent free-stream turbulence with $Lgy = 0.39$ cm was comparable to the Δ_{eff} for the 12.9 percent turbulence with $Lgy = 0.07$ cm quoted above, at a constant blowing ratio. This demonstrates the importance of turbulent length scale in completely characterizing the effect of free-stream turbulence on film cooling effectiveness. By comparison, in the present study the longitudinal length scale for the jet-generated turbulence is 50 percent larger than the scale of the 6.5 percent grid-generated turbulence in the boundary layer. This difference grows to as large as 110 percent at $y/d = 2.63$, Table 1. This "larger" jet turbulence scale may contribute to larger Δ_{eff} with high levels of free-stream turbulence in the present study. No definitive conclusions can be reached with the present data, though, since turbulence scale and intensity were not varied independently. Other factors contributing to the difference in results will be discussed in the succeeding sections.

(A) Low Blowing Ratios ($0.5 < M < 0.95$). Han and Mehendale (1986) reported the optimum blowing ratio range to be from 0.5 to 0.7 ($x/d \leq 20$) for single row film cooling at a Reynolds number based on hole diameter of 20,000. The Reynolds number of the data presented here is approximately the same (19,000), and so it is instructive to compare the optimum blowing ratio and the effect of free-stream turbulence. From Fig. 5, though the data are not sufficient to determine precisely, it appears that the optimum M shifts to higher M as Tu increases. The elevated turbulence also appears to flatten the region of optimum effectiveness, resulting in a considerably wider range of blowing ratios over which the effectiveness remains within a 10 percent band of the optimum effectiveness point.

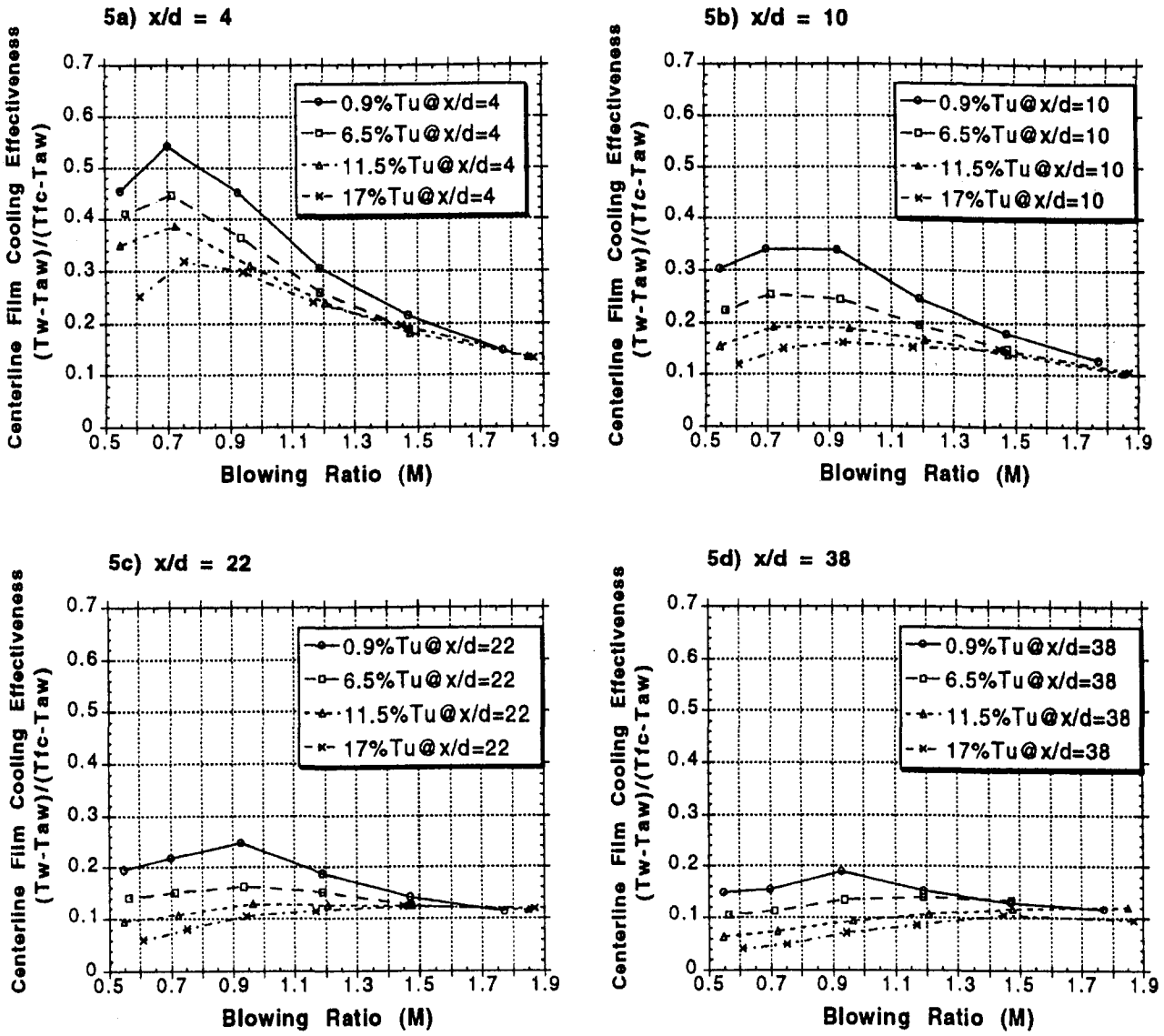

Fig. 5 Centerline film cooling effectiveness at four different x/d stations: 4, 10, 22, and 38 (z/d = 0). Data for four levels of Tu: 17, 11.5, 6.5, and 0.9 percent. U_{fs} = 16 m/s (Re_d = 19,000).

In this range of blowing ratios ($0.55 < M < 0.95$), before blow-off becomes a significant factor, film cooling effectiveness decreases monotonically with free-stream turbulence. A rudimentary attempt to correlate the loss in effectiveness to the Tu level at the point of injection results in the following empirical form:

$$\Delta_{\text{eff}} = \left(1 - \frac{\eta_{hiTu}}{\eta_{loTu}}\right) = B\left(1 - \exp\left(-m\frac{x}{d}\right)\right) \quad [Tu \text{ in percent}]$$

where n and B are functions of blowing ratio. Values of B = 1.05, m = 0.5, and n = 0.05 fit the data presented in this paper for $x/d < 38$ and $0.55 < M < 0.95$ to within ±17 percent. The form of this expression is intuitive, and without physical basis. Though the empirical expression implies that Tu is the only parameter that influences effectiveness, other characteristics of the free-stream turbulence generated for the different cases presented here (for example, integral length scale) may play a significant role in effectiveness reductions. Notably, it is evident from Fig. 5 that film cooling effectiveness data based solely on grid generated turbulence (with its inherent maximum of uniform $Tu \approx 8$ percent) would be inadequate for predicting the trend at high Tu levels ($Tu > 10$ percent) accurately. This is the fundamental reason for the development of the present experimental facility.

To understand the underlying reason for the loss in cooling effectiveness with increasing Tu, it is instructive to examine temperature and velocity (mean and fluctuating components) boundary layer profiles at various x/d locations downstream of the injection hole. Figures 6(a–h) show these profiles at four x/d stations for M = 0.95 and two Tu levels (0.9 and 17.4 percent). U and u' are nondimensionalized by the free-stream mean velocity U_{fs}. The static temperature is shown as a ratio of the difference between local temperature and free-stream temperature and the difference between the film cooling temperature and the free-stream temperature. The nondimensional fluctuating velocity component, u'/U_{fs}, is shown with a factor of 5 to facilitate presentation on the same scale with the nondimensional mean velocity.

Of particular note is the slanted shape of the coolant fluid velocity profile in both cases (see the $y/d < 0.4$ region of velocity profiles on Figs. 6(a) and 6(b)). This nonparabolic shape is discussed in detail by Leylek and Zerkle (1994) and is due to the flow internal to the film cooling hole and access plenum. Separation off the downstream edge at the inlet to the film cooling injection tube causes the fluid to hug the upstream

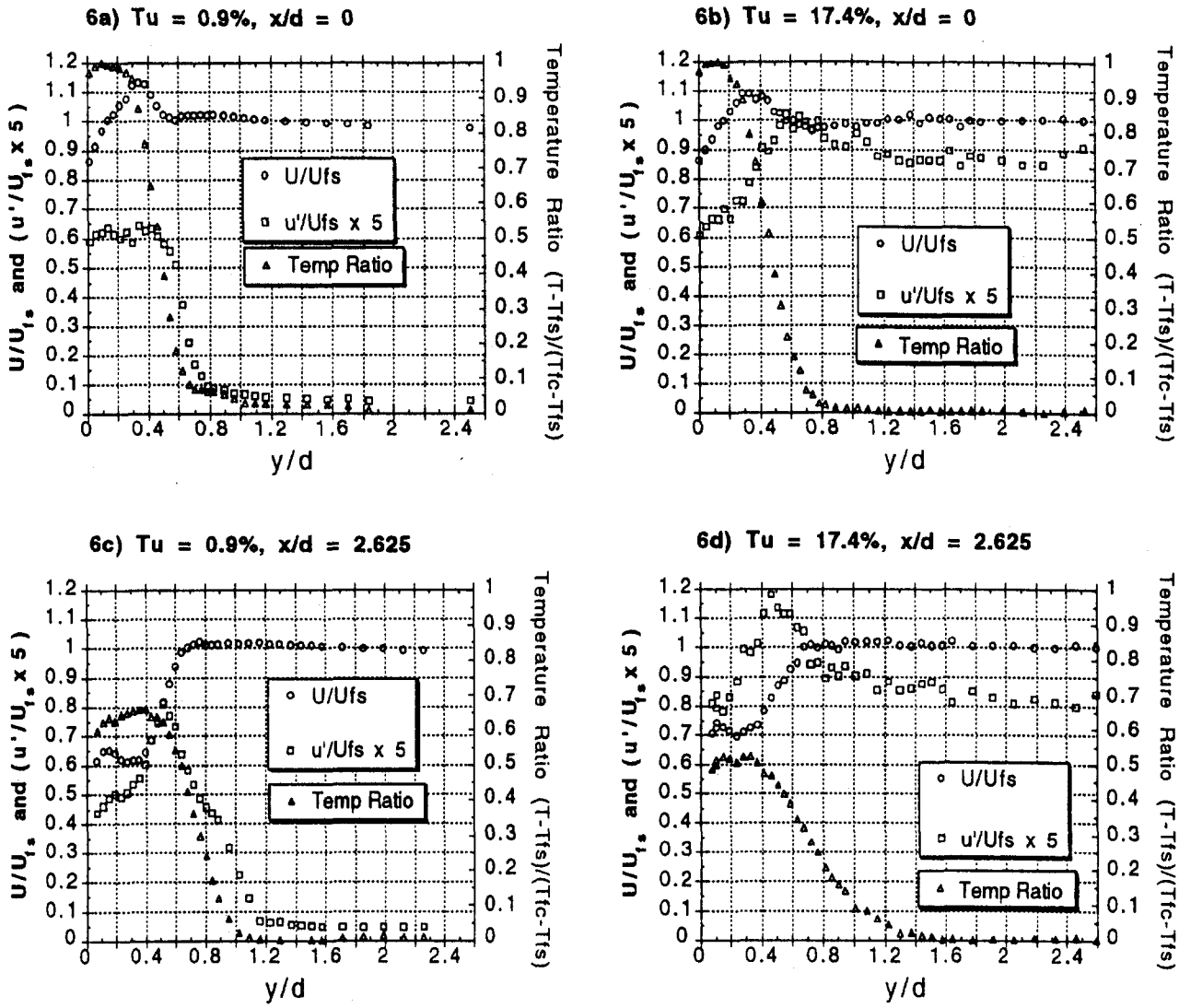

Fig. 6(*a–d*) U/U_{fs}, u'/U_{fs}, and temperature ratio boundary layer profiles at two x/d: 0 and 2.625 (z/d = 0). Data for *Tu* = 0.9 percent and *M* = 0.99 compared to *Tu* = 17.4 percent and *M* = 0.95.

wall of the tube. For tubes with short L/d, representative of modern film cooling applications, the flow has insufficient length to establish a traditional pipe flow velocity profile, resulting in a skewed velocity profile at exit. This effect brings the injected momentum apex further away from the wall and closer to the high-*Tu* free stream. In the presence of elevated free-stream turbulence, this unique feature of short L/d cooling tubes could result in a larger Δ_{eff} than for cooling injected with long L/d tubes. Since the momentum core is closer to the turbulent shear layer and the free stream, it may experience an accelerated dissipation compared to the long L/d case where the velocity profile is more symmetric. This effect may help partly to explain the lower Δ_{eff} values observed by Kadotani and Goldstein (1979b), who used a facility with L/d = 62 compared to L/d = 3.5 in the present facility. Exit velocity profiles taken at M = 0.55 and M = 1.87 show the "skewness" of this film cooling velocity profile to increase with M (also noted by Leylek and Zerkle, 1994).

Proceeding downstream from the injection location (Figs. 6(c–h)), significant differences develop between the high and low-*Tu* flows. For the low-*Tu* case, the film cooling fluid and the free stream merge in a strong shear region located at approximately y/d = 0.5 from the wall. Below this shear region, the fluctuating velocity component of the film cooling flow is remarkably flat, with the maximum of $(u'/U_{fs} \times 5)$ = 0.6 at x/d = 0 decaying rapidly (with a nearly linear decay rate of 4.4 [m/s]/m from x/d = 0 to x/d = 10) with x/d due to the strong damping effect of the surrounding quiescent free stream. The diffusion of the thermal energy in the film cooling flow is also retarded by the relatively inactive freestream, and the temperature profile retains its shape (and thus effectiveness) well beyond x/d = 20.

The situation is markedly different in the high-*Tu* case, where the formation of two distinct flow regimes is impeded immediately by a high level of mixing. At the injection plane (x/d = 0), the peak velocity of the injected fluid is reduced from U/U_{fs} = 1.12 for low *Tu* to U/U_{fs} = 1.09 for high *Tu*. The u' level in the film cooling fluid rises dramatically from a value of $(u'/U_{fs} \times 5)$ = 0.6 at the wall to $(u'/U_{fs} \times 5)$ = 1.0 at the velocity peak. Of greater concern for effectiveness, the temperature profile at x/d = 0 is already partially dissipated. The maximum temperature begins to drop at y/d = 0.17 for the high-*Tu* case versus y/d = 0.27 for the low-*Tu* case. This lower temperature in the shear region is indicative of heightened mixing with the free stream. By x/d = 2.6, the film cooling flow for the high-*Tu* case has lost 48 percent of its effectiveness versus 34 percent for the low-*Tu* case. The original free-stream velocity profile recovers quickly from the disruption caused by the mass

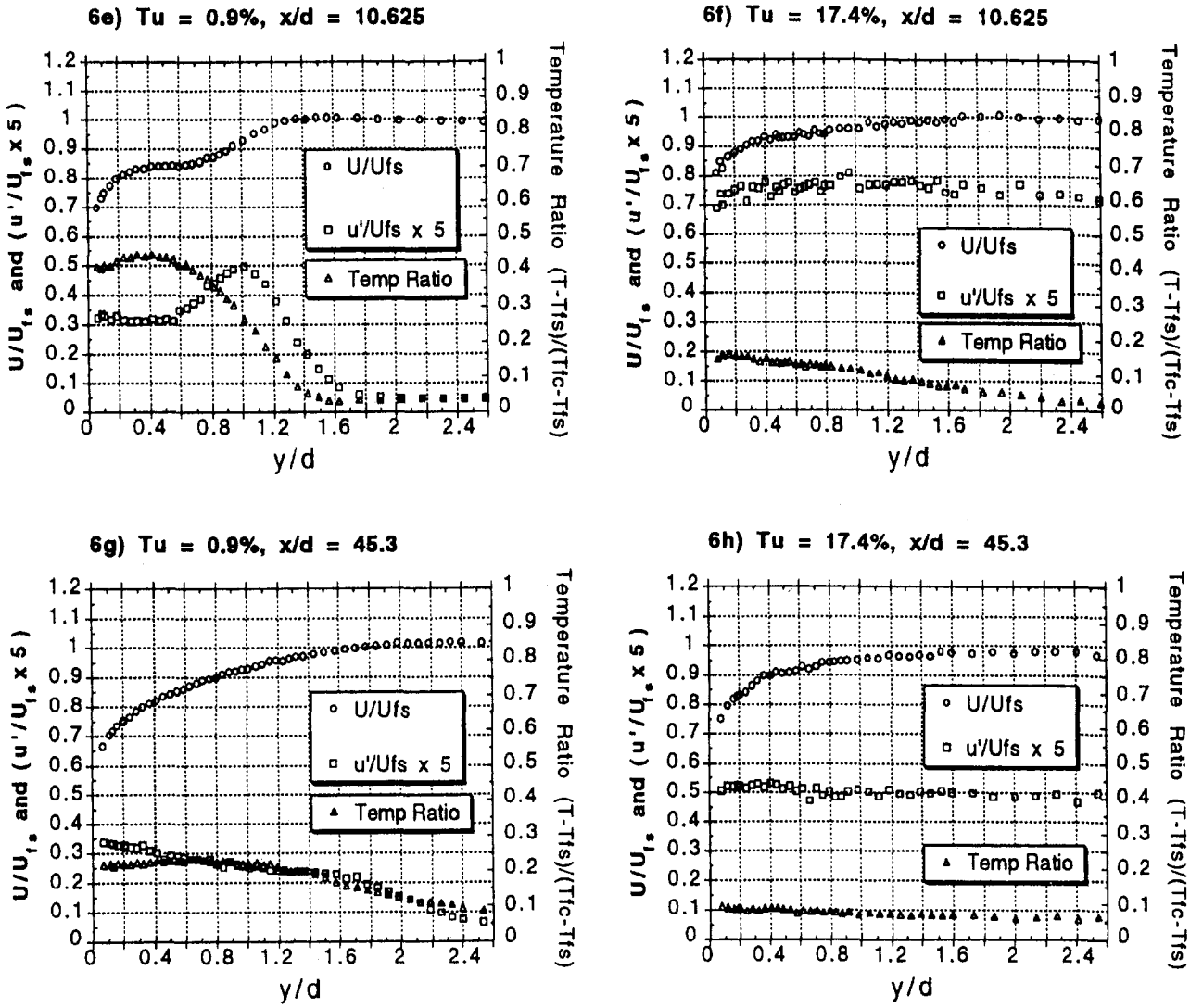

Fig. 6(*e–h*) U/U_{fs}, u'/U_{fs}, and temperature ratio boundary layer profiles at two x/d: 10.625 and 45.3 (z/d = 0). Data for Tu = 0.9 percent and M = 0.99 compared to Tu = 17.4 percent and M = 0.95.

injection and by x/d = 10.6 there is little trace of the film cooling fluid (u'/U_{fs} is nearly constant down to the wall).

In summary, free-stream turbulence has a profound mixing effect resulting in accelerated break-up of the injected film cooling flow. This is the underlying cause of the loss of centerline effectiveness. The trends in Figs. 6(a–h) are similar for the two intermediate levels of Tu, though less pronounced.

(B) High Blowing Ratios ($M > 0.95$). From Fig. 5, it is evident that the loss in η_c due to high free-stream turbulence becomes less pronounced as M increases. This is due to the film cooling fluid's separation from the surface (blow-off). This blow-off is well documented in the literature, but little has been reported on the effect of elevated free-stream turbulence on the blow-off phenomenon. For M = 1.5, Kadotani and Goldstein (1979b) reported that η_c increased everywhere with elevated free-stream turbulence. By comparison, high free-stream turbulence levels appear to have two noteworthy influences on the separated film cooling flow in this study. Figure 7 is a close-up of η_c versus x/d for M = 1.47 and two different Tu levels. As shown, the first several wall thermocouples exhibit a rising temperature with x/d and then fall off as expected after reaching a maximum at x_1 and x_2 (for the high and low-Tu cases, respectively). This region of positive dT/dx is indicative of separated film cooling fluid, which is gradually reattaching to the wall. From the distances noted on Fig. 7 ($x_2 > x_1$), it is clear that higher free-stream turbulence lessens the streamwise extent of the initial blow-off region.

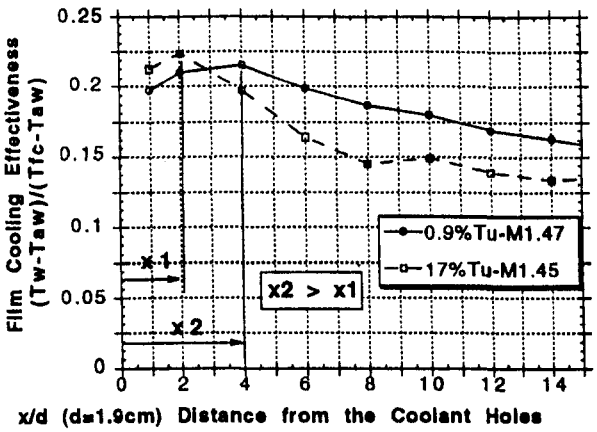

Fig. 7 Centerline film cooling effectiveness for two levels of Tu: 17.0 and 0.9 percent (blowing ratios of 1.45 and 1.47, respectively). U_{fs} = 16 m/s (Re_d = 19,000) close-up of blow-off region for z/d = 0.

This observation is supported by Fig. 8's mean velocity and temperature profile data at $x/d = 0$ and 2.625 for two levels of Tu and $M = 1.47$. As shown, the elevated Tu of the surrounding fluid rapidly diffuses the injected coolant fluid, dropping the peak in U and T dramatically as the flow progresses from $x/d = 0$ to 2.625. By conservation of energy, this lost thermodynamic energy must be transported elsewhere in the flow, and (as will be discussed in the succeeding section) a significant amount mixes laterally. Some of the energy also appears to mix vertically, as is evidenced by the slightly higher T and U for high Tu versus low Tu above and below the greatly reduced peak ($x/d = 2.625$). The vertical diffusion caused by the high free-stream turbulence brings the film cooling fluid in contact with the surface more quickly than for the case with low Tu. Though the fluid that comes in contact with the wall is at a lower, mixed-out temperature, the contact is made at a smaller x/d (approximately $x/d = 2$) in the presence of 17 percent Tu versus the 0.9 percent Tu case ($x/d \approx 4$, Fig. 7).

The second effect of elevated free-stream turbulence on film cooling blow-off is apparent beyond $x/d = 30$ on Fig. 9, which

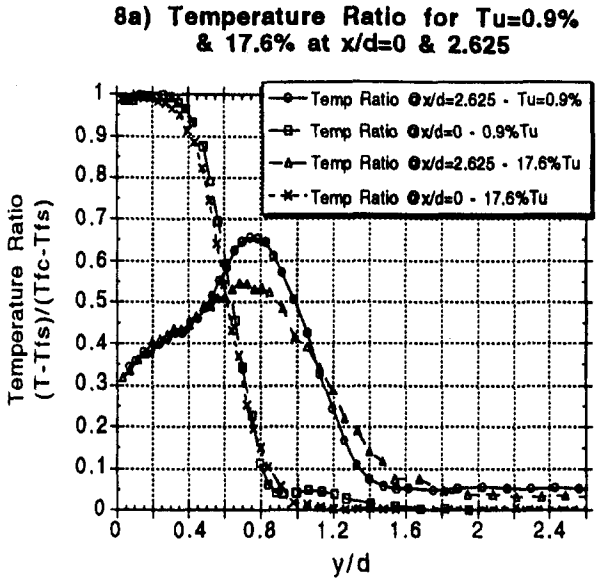

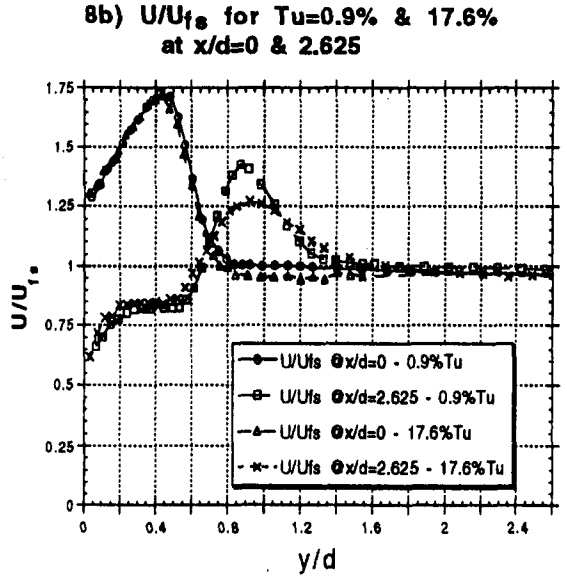

Fig. 8 Temperature ratio and U/U_{fs} boundary layer profiles at two x/d stations: 0 and 2.625 ($z/d = 0$). Data shown for $Tu = 0.9$ percent and $M = 1.47$ versus $Tu = 17.6$ percent and $M = 1.45$.

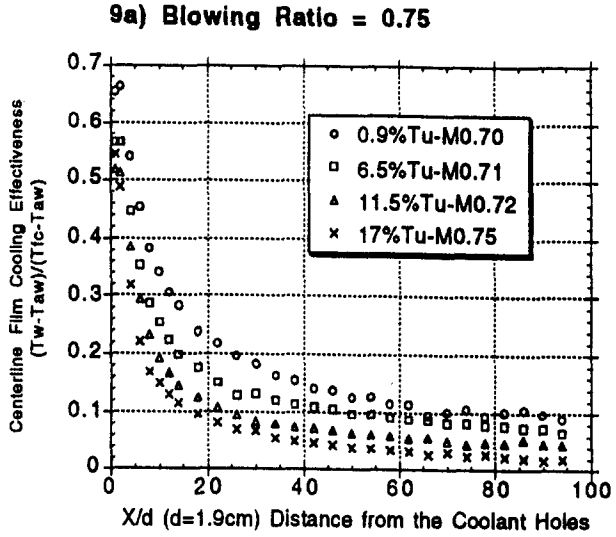

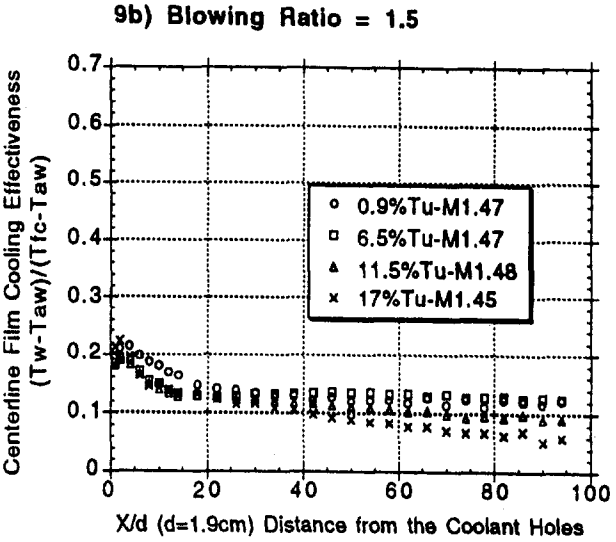

Fig. 9 Centerline film cooling effectiveness versus x/d for two blowing ratios ($M = 0.75$ and 1.5) and four free-stream turbulence levels: 17.0, 11.5, 6.5, and 0.9 percent. $U_{fs} = 16$ m/s ($Re_d = 19{,}000$). $z/d = 0$.

shows the centerline effectiveness down the adiabatic surface for four turbulence levels and two blowing ratios: $M = 0.75$ (minimal blow-off) and $M = 1.5$ (significant blow-off). Looking closely at the $M = 1.5$ plot, a significant change in the η_c trend with x/d is detected at $x/d \approx 15$. Upstream of this location, the low-Tu η_c data are clearly superior. After $x/d = 15$, the η_c decay with x/d is arrested for the $Tu = 6.5$ percent case, and η_c remains essentially flat thereafter. Figure 10 compares the centerline and midline effectiveness data for high and low turbulence at $M = 0.75$ and 1.2. From this figure it is clear that the point of spanwise film uniformity (adjacent stream merger) occurs at approximately $x/d = 10$ for high Tu versus beyond $x/d = 30$ for low Tu. The change in η_c decay rate noted in Fig. 9(b) at $x/d = 15$ is due to this earlier merger of the adjacent cooling jets for high Tu. After the merger, the film is essentially spanwise uniform. Without any further spanwise dissipation due to high free-stream turbulence, the η_c decay flattens for $Tu = 6.5$ percent. The merger doesn't occur for the low-Tu flow before $x/d = 30$, and a slow η_c decay continues well down the adiabatic surface for this case. The accelerated spanwise diffusion caused by high free-stream turbulence makes the coolant "more effective" beyond $x/d \approx 30$ for the $Tu = 6.5$ percent

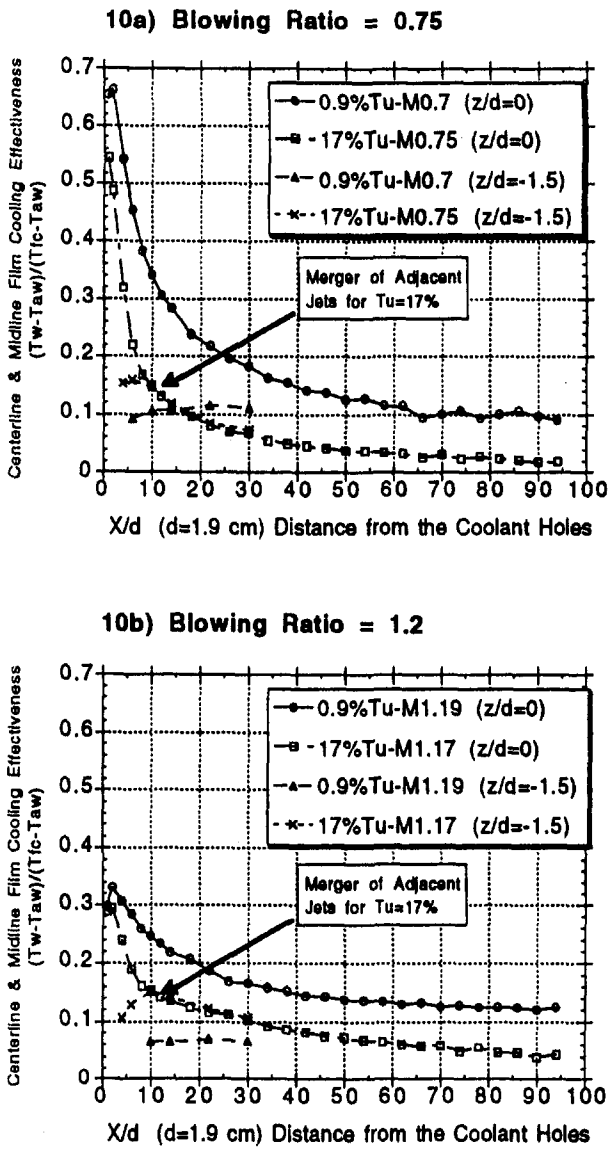

Fig. 10 Centerline and midline film cooling effectiveness (z/d = 0 and −1.5) versus x/d for two blowing ratios: 0.75 and 1.2. Data for Tu = 0.9 and 17.0 percent. U_{fs} = 16 m/s (Re_d = 19,000).

case. A similar change in η_c decay is noted at $x/d = 15$ for the two higher Tu levels of 11.5 and 17 percent. These higher levels create enough vertical dissipation beyond this point to continue decreasing the cooling effectiveness with x/d (unlike the η_c for $Tu = 6.5$ percent, which is flat). There appears to be an optimum level of Tu for this unexpected effectiveness enhancement at large x/d.

Effectiveness Along the Hole Midline (z/d = 1.5). The previous data have documented the behavior of the film cooling fluid directly downstream of the injection hole ($z/d = 0$). These data are representative of the spanwise-averaged effectiveness downstream of the point at which the adjacent streams merge. The point of spanwise uniformity (stream merger) is, however, greatly dependent on the level of free-stream turbulence in the surrounding fluid (as noted earlier from Fig. 10). The effect of free-stream turbulence on the effectiveness of film cooling fluid *between* the coolant holes is of equal interest to the designer.

Figure 11 shows data obtained from the surface thermocouples located exactly between the center cooling hole and its $-z$ neighbor (the $z/d = +1.5$ and $z/d = -1.5$ data agree to within ±4 percent nominally, but only the $-z$ data are shown as the η_c data from the $-z$ hole are closest to the η_c data from the center hole). The data are presented in a format identical to that in Fig. 5, though at x/d locations of 6, 14, and 30. Except at very low blowing ratios, the elevated free-stream turbulence data show a greatly improved effectiveness, even as far down the surface as $x/d = 30$ for some high blowing ratios. Brown and Saluja (1978) also observed an increase in midline effectiveness with increased Tu. The mixing of film cooling fluid that resulted

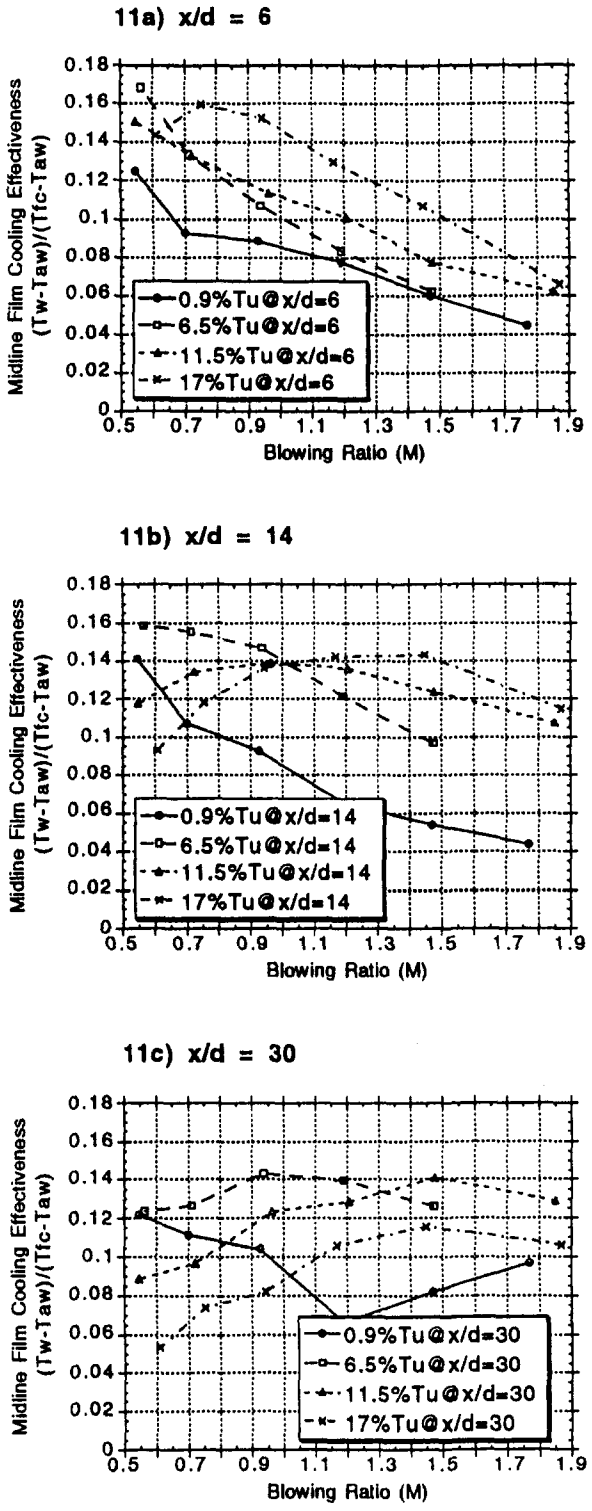

Fig. 11 Midline film cooling effectiveness (z/d = −1.5) at three x/d: 6, 14, and 30. Data for four levels of Tu: 0.9, 6.5, 11.5, and 17.0 percent. U_{fs} = 16 m/s (Re_d = 19,000).

in a dramatically reduced η_c has brought some of that effectiveness spanwise. By conservation of energy, η_m is enhanced by the high turbulence in the free stream, up to 100 percent at $M = 1.5$ and $x/d = 14$. The data also reveal the complexity of the effects that free-stream turbulence has on η_m in that the observed effect is not always monotonic with Tu. For example, in Fig. 11(a) the 6.5 percent Tu data are more effective than the 11.5 percent data at low blowing ratios. In Fig. 11(b), the $Tu = 6.5$ percent data are most effective for low blowing ratios while the $Tu = 17$ percent data are best at high blowing ratios. Also, at $x/d = 30$ (Fig. 11(c)), the $Tu = 6.5$ percent data are superior for low blowing ratios while the $Tu = 11.5$ percent data are best at high blowing ratios. The characteristics of turbulence that are responsible for these "inconsistencies" are not fully understood, although comparisons of integral length scale provide some additional insight.

The measured length scale of the grid-generated turbulence given in Table 1 is considerably smaller than the jet-generated length scales and approximately equal to the distance between adjacent holes ($Lgx/d = 2.88$ versus hole spacing/$d = 3$). Though this is a streamwise length scale, the associated spanwise length scale will also be relatively "smaller" than in the jet-generated case, and may be better suited to dissipating the film fluid laterally. Kadotani and Goldstein (1979a) also reported a greater lateral spread of cooling fluid for "smaller" scale versus "larger" scale free-stream turbulence. Figure 12 presents the Fig. 11 data in an η_m versus x/d format and shows the same trends more clearly (data for $M = 0.75$ and 1.2 only). Clearly, there is some optimization of M, Tu, and possibly Lgx/d that must be performed by the turbine designer to achieve a unique design requirement.

Summary and Conclusions

Effectiveness data has been presented for a practical range of blowing ratios and four levels of free-stream turbulence. Markedly different results are obtained for effectiveness directly in line with the coolant holes compared to effectiveness in the space between adjacent coolant holes, with a strong dependence on blowing ratio. It appears that the simple conclusion "high free-stream turbulence decreases the effectiveness of discrete hole film cooling" is not altogether correct. Figure 10 summarizes the composite result for effectiveness at both spanwise locations, comparing the effect of 0.9 percent Tu to 17 percent Tu at $M = 0.75$ and 1.2. Free-stream turbulence drastically reduces the effectiveness of film cooling directly behind the injection holes at low to moderate blowing ratios, At high blowing ratios, however, free-stream turbulence reduces the extent of blow-off, and diffuses the separated fluid down to the wall more quickly, resulting in higher effectiveness for $x/d > 30$. Also, the diffusion of coolant fluid with high Tu results in a dramatic increase in the lateral spread of the adjacent streams. High Tu creates a more uniform film more quickly and increases the resulting effectiveness between the coolant holes. Changes in effectiveness by a factor of two (both up and down) at practical values of blowing ratio, and over significant regions, are documented for Tu in the range from 0.9 to 17 percent. An empirical correlation is offered that predicts the centerline effectiveness deficit for high turbulence levels to a reasonable degree of accuracy. However, this correlation does not include the effects of such additional variables as turbulent length scales, streamwise pressure gradient, and curvature. The influences of these parameters have not been investigated or documented at the present time. Future plans include parametric studies of these variables also.

The density ratio between the coolant and the free stream was held constant throughout this study at approximately 0.95. In typical turbine engine applications, the film cooling fluid is at times 500°C cooler than the core flow, with a density ratio of 1.5 to 2.0. Investigations by Goldstein et al. (1974) and Sinha et al. (1991) show that centerline film cooling effectiveness generally increases with higher density ratio for the same blowing ratio (M). This trend is more evident at higher blowing ratios, $M > 0.7$. There is still considerable discussion over the mechanism for this influence and the effect of elevated free-stream turbulence has not been investigated. The authors intend to make this an area of future research.

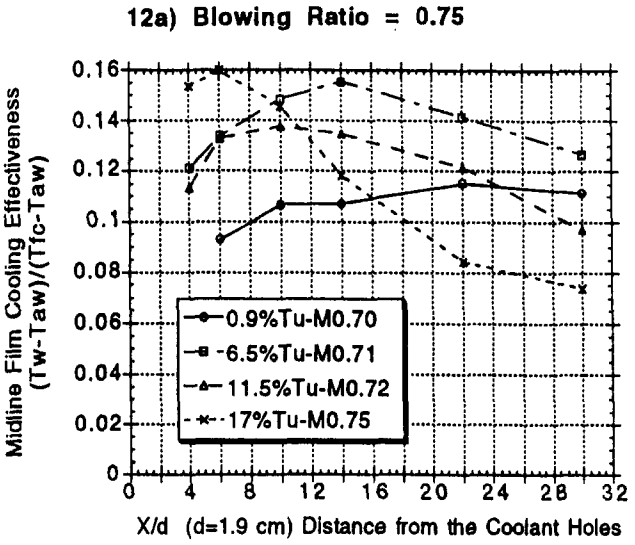

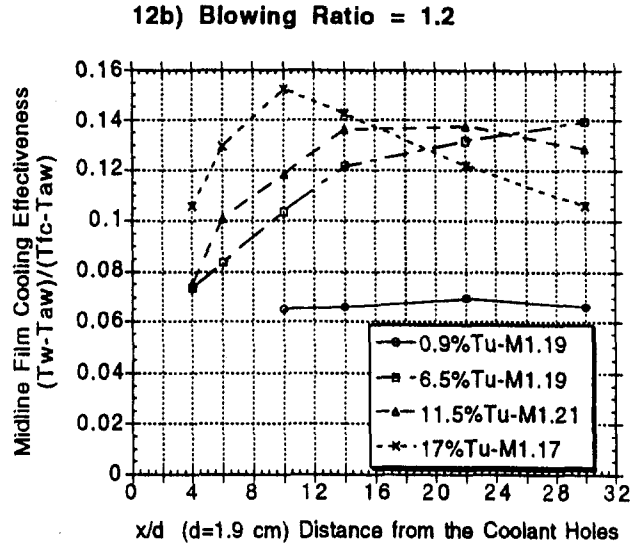

Fig. 12 Midline film cooling effectiveness ($z/d = -1.5$) versus x/d for two blowing ratios: 0.75 and 1.2. Data for four levels of Tu: 0.9, 6.5, 11.5, and 17.0 percent. $U_{fs} = 16$ m/s ($Re_d = 19{,}000$).

In summary, free-stream turbulence is an important flow parameter that must be properly understood and simulated to design appropriate film cooling flows for a given application. From the data presented, it appears that certain features of cooling flows (blowing ratio, diameter, spacing/d, L/d) can be tailored to optimize film cooling effectiveness for a given turbulent environment.

Acknowledgments

The authors wish to recognize the assistance and expert craftsmanship of the Aeronautical Systems Center's Development, Manufacturing, and Modification Facility (Zone Shop 1), specifically Mr. Larry Foland and Mr. Jerry Reed, for the construction of the test facility. Also, we would acknowledge

the professional advice and assistance offered by the other members of the Wright Laboratory Aerothermal Research team; namely Mr. Gregory Cala, Mr. Edward Michaels, Mr. David Pestian, and Dr. Shichuan Ou. This work was performed under partial sponsorship from the Air Force Office of Scientific Research. Dr. James McMichael is the project manager.

References

Bogard, D. G., Thole, K. A., and Crawford, M. E., 1992, "Hydrodynamic Effects on Heat Transfer for Film-Cooled Turbine Blades," Technical Report No. WL-TR-92-2035, U.S. Air Force Wright Laboratory, Wright-Patterson AFB, OH.

Brown, A., and Saluja, C. L., 1979, "Film Cooling From a Single Hole and a Row of Holes of Variable Pitch to Diameter Ratio," *Int. J. Heat Mass Transfer,* Vol. 22, pp. 525–533.

Goebel, S. G., Abuaf, N., Lovett, J. A., and Lee, C.-P., 1993, "Measurements of Combustor Velocity and Turbulence Profiles," ASME Paper No. 93-GT-228.

Goldstein, R. J., Eckert, E. R. G., and Burggraf, F., 1974, "Effects of Hole Geometry and Density on Three-Dimensional Film Cooling," *Int. J. Heat Mass Transfer,* Vol. 17, pp. 595–607.

Han, J. C., and Mehendale, A. B., 1986, "Flat Plate Film Cooling With Steam Injection Through One Row and Two Rows of Inclined Holes," ASME JOURNAL OF TURBOMACHINERY, Vol. 108, pp. 137–144.

Jumper, G. W., Elrod, W. C., and Rivir, R. B., 1991, "Film Cooling Effectiveness in High-Turbulence Flow," ASME JOURNAL OF TURBOMACHINERY, Vol. 113, pp. 479–483.

Kadotani, K., and Goldstein, R. J., 1979a, "On the Nature of Jets Entering a Turbulent Flow: Part A—Jet-Mainstream Interaction," ASME *Journal of Engineering for Power,* Vol. 101, pp. 459–465.

Kadotani, K., and Goldstein, R. J., 1979b, "On the Nature of Jets Entering a Turbulent Flow: Part B—Film Cooling Performance," ASME *Journal of Engineering for Power,* Vol. 101, pp. 466–470.

Kline, S. J., and McClintock, F. S., 1953, "Describing Uncertainties in Single-Sample Experiments," *Mechanical Engineering,* Jan., pp. 3–8.

Leylek, J. H., and Zerkle, R. D., 1994, "Discrete-Jet Film Cooling: A Comparison of Computational Results With Experiments," ASME JOURNAL OF TURBOMACHINERY, Vol. 116, pp. 358–368.

Maciejewski, P. K., and Moffat, R. J., 1992, "Heat Transfer With Very High Free-Stream Turbulence: Part II—Analysis of Results," ASME *Journal of Heat Transfer,* Vol. 114, pp. 834–839.

MacMullin, R., Elrod, W., and Rivir, R., 1989, "Free-Stream Turbulence From a Circular Wall Jet on a Flat Plate Heat Transfer and Boundary Layer Flow," ASME JOURNAL OF TURBOMACHINERY, Vol. 111, pp. 78–86.

Moss, R. W., and Oldfield, M. L. G., 1991, "Measurements of Hot Combustor Turbulence Spectra," ASME Paper No. 91-GT-351.

Sinha, A. K., Bogard, D. G., and Crawford, M. E., 1991, "Film-Cooling Effectiveness Downstream of a Single Row of Holes With Variable Density Ratio," ASME JOURNAL OF TURBOMACHINERY, Vol. 113, pp. 442–449.

Assessment of Two- and Three-Scale $k-\epsilon$ Models for Rotating Cavity Flows

Z. Guo

D. L. Rhode

Turbomachinery Laboratories,
Department of Mechanical Engineering,
Texas A&M University,
College Station, Texas 77843-3123

A three-scale $k-\epsilon$ turbulence model was recently developed for complex flows such as the rotor–rotor and rotor–stator cavities found in gas turbine engines. The three-scale model is a logical extension of the previous two-scale $k-\epsilon$ model of Ko and Rhode (1990). Both multiscale turbulence models are presented and assessed via comparison with measurements for possible adoption in future cavity computations. A single computer code solving the two-dimensional axisymmetric Navier–Stokes equations with a "switch" for selecting among the various turbulence models being compared was used. It was found for both cavity cases that the three-scale model gives a marginal improvement over the two-scale model. Further, both multiscale models give a substantial improvement over the standard $k-\epsilon$ model for the rotor–stator case, especially in the near-wall region where different eddy sizes are found. However, the feasibility of using a multiscale model for the rotor–rotor case is unclear since it gives improved values over the standard high-Re model in some regions but worse values in other regions. In addition, the solutions provide enhanced insight concerning the large changes in flow pattern previously photographed in the rotor–rotor case as rotation increases. In particular, it is shown how: (a) the number of recirculation zones increase with increasing rotation rate and (b) the recirculation zones decrease in size with a decreasing G ratio.

1 Introduction

1.1 Rotating Cavities. The design trend of the compressor section of the gas turbine engine is toward high pressure ratios. The result is that compressor exit temperatures are as high as 650°C. Compressor air is often extracted for the cooling of compressor disks as well as turbine blades and disks. The designer must accurately predict the thermal growth and fatigue life of the compressor disks, for example. Thus, a good understanding of pertinent flow patterns and thermal distributions in both the rotor–rotor compressor cavities and rotor–stator turbine rim seal cavities is quite important. Upon extraction, the secondary cooling air generally flows axially through the center bore of a series of corotating compressor disks. The geometry of the disks is often complicated, although substantial insight regarding important flow structure may be gained by studying an idealized configuration such as that shown in Fig. 1(*a*) for the rotor–rotor case, for example.

The axial flow of coolant through corotating compressor disks, for which the throughflow enters and exits through the center bore, induces secondary flow inside the cavity. A complete collection of pertinent results is given by Owen and Rogers (1989). The resulting flow pattern can be very complicated, and asymmetries are commonly found. For example, Owen and Bilimoria (1977) and Owen and Onur (1983) found that, for such heated cavities, an asymmetric vortex breakdown occurs at certain values of the Rossby number. Specifically, the axial jet passing through the rotor–rotor cavity begins to precess about the cavity rotation axis. Similar findings were reported by Yu et al. (1973) for a heated rotor–stator cavity. More recently Farthing et al. (1992) studied the flow structure complexities of rotor–rotor cavities, both isothermal and heated, over a wide range of geometries and Rossby numbers. Surprising changes were found, using flow visualization and LDA velocity measurements, as the cavity rotation was increased. Very recently, the effects of axial coolant flow rate, rotation speed and the disk surface heating condition on the local heat transfer coefficient within the rotor–rotor cavity were obtained by Kim and Metzger (1992).

1.2 $k-\epsilon$ Model Variations. It is well known that turbulence is generated by mean flow shear, which produces eddies of large size. The eddy then undergoes complex interactions, which ultimately reduce the eddy to smaller sizes, until eventually its turbulent energy is dissipated into heat, primarily at the smallest (i.e., Kolmogorov) size. It is also known that different eddy sizes should be treated separately to allow the proper modeling of the interactions between the different sizes.

The approximation that a single length scale can represent the entire range of eddy sizes in a turbulent flow is inherent in the standard (high-Re) $k-\epsilon$ turbulence model (Launder and Spalding, 1972). This approximation invokes the assumption that the length scale of the energy-containing (i.e., large) eddies is universally proportional to the length scale of the energy-dissipation (smallest) eddies. However, for complex turbulent flows where the energy spectrum is not in equilibrium and where a flow particle undergoes rapid changes, the different sizes of turbulent eddies show greatly different rates of development. That is, the energy spectrum should be partitioned into several zones of eddy size, and the interactions among them appropriately modeled. Thus, one advantage of multiscale turbulence models is that each eddy size is characterized by a single length scale, which allows that eddy size to respond at its own (appropriate) rate to sudden changes in the mean flow field experienced by a fluid particle. Fluid particles are well known to undergo abrupt changes throughout turbomachinery fluid flows.

Although there are countless papers dealing with non-multiscale $k-\epsilon$ versions, only a few focus on the multiscale approach. A two-scale $k-\epsilon$ model involving model coefficients that depend on the partitioning of the spectrum was developed by Hanjalic et al. (1980). It was found that the particular choice

Contributed by the International Gas Turbine Institute and presented at the 40th International Gas Turbine and Aeroengine Congress and Exhibition, Houston, Texas, June 5–8, 1995. Manuscript received by the International Gas Turbine Institute February 22, 1995. Paper No. 95-GT-300. Associate Technical Editor: C. J. Russo.

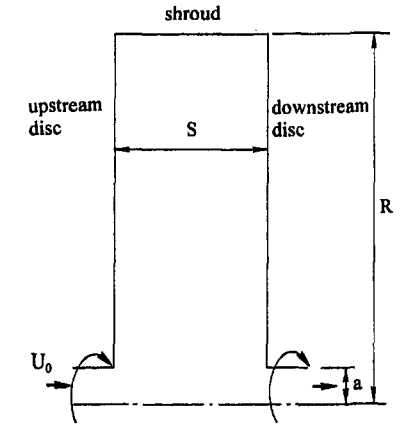

(A) CO-ROTATING CAVITY WITH AN AXIAL THROUGH-FLOW

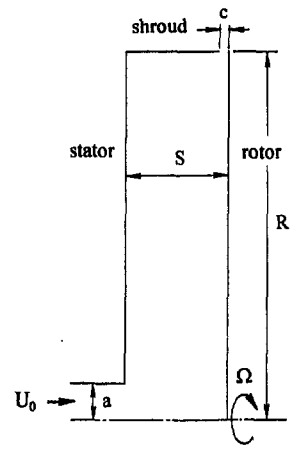

(B) ROTOR-STATOR CAVITY WITH A RADIALLY OUTWARD THROUGHFLOW

Fig. 1 Schematic showing: (*A*) the corotating cavity and (*B*) the rotor–stator cavity

of partition boundaries did not significantly affect the solutions. Improvement over the standard $k-\epsilon$ model and Reynolds stress transport models was found for: (*a*) decaying grid turbulence in a sudden contraction, (*b*) the spreading rate of plane and axisymmetric free jets, and (*c*) boundary layers with an adverse as well as a zero pressure gradient. Also, Kim and Chen (1987) developed a two-scale turbulence model, as outlined by Schiestel (1983), using a variable partitioning of the turbulence kinetic energy spectrum.

In addition, the multiscale model of Hanjalic et al. was applied to a variety of flows pertaining to the scramjet combustor by Fabris et al. (1981). The results show reliable predictions of round jets, wakes, and shear layers. More recently, Chen and Guo (1991) developed another two-scale turbulence model. The direct modeling of Reynolds stresses and split-spectrum concepts was utilized in the model to predict rotating flows, free shear flows and recirculating flows. Further, Ko and Rhode (1990) derived and tested a new two-scale $k-\epsilon$ turbulence model, starting the derivation from a different fundamental equation than previous derivations. This model was first applied to rim seal cavities by Ko and Rhode (1992). It was shown that such multiscale models give closer agreement with rotor–stator cavity measurements than does the standard $k-\epsilon$ model for flows exhibiting a recirculation zone, whereas the multiscale model and the standard model agree equally well with measurements for simpler flows such as free jets and boundary layers.

The next section gives the objective. The following one summarizes the equations, boundary conditions and previous assessments of the two multiscale models being considered. The fourth section assesses the multiscale models for the rotor–rotor and rotor–stator test cases.

2 Objective

The rotor–rotor cavity is known to exhibit a variety of complicated flow patterns consisting of numerous recirculation zones. Thus the feasibility of using the multiscale $k-\epsilon$ model, as compared to the standard $k-\epsilon$ model, to predict this challenging type of cavity flow is of significant interest. The primary objective of the present paper is to assess and analyze the capability of the two- and three-scale $k-\epsilon$ models, for rotor–rotor as well as rotor–stator cavity computations, via comparison with measurements. A secondary objective is to provide enhanced insight into the increase of flow pattern complexity with cavity rotation for the rotor–rotor case.

3 Turbulence Modeling

The new three-scale $k-\epsilon$ model was implemented in a finite-volume computer code that solves the fully elliptic form of the two-dimensional, axisymmetric Navier–Stokes equations for compressible, turbulent flow. All of the solutions for the various turbulence models were obtained using one computer code, which has a turbulence model "switch." The continuity and momentum equations are, respectively,

Nomenclature

a = radial width of cavity inlet
c = stator shroud gap axial width
C_w = volumetric flow rate parameter = $Q/(\nu R)$
E = law-of-the-wall constant = 9.793
G = gap ratio = s/R
G_c = seal clearance ratio = c/R
H = stagnation enthalpy
k = total turbulent kinetic energy = $k^{(1)} + k^{(2)} + k^{(3)}$
$k^{(1)}$, $k^{(2)}$, $k^{(3)}$ = partial turbulence kinetic energies
K = wavenumber
L_e = characteristic length scale
p = static pressure
p_a = ambient pressure
R = outer radius of disk
Re_x = axial Reynolds number = $2\rho Ua/\mu$
Re_θ = rotational Reynolds number = $\rho\Omega R^2/\mu$
Ro = Rossby number = $U/\Omega a$ = $1/2R^2\ \mathrm{Re}_x/a^2\ \mathrm{Re}_\theta$
S = axial width of cavity
U, V, W = mean velocities in x, r, θ directions
U_o = bulk mean axial velocity at domain inlet
V_t = characteristic velocity
x, r, θ = axial radial and tangential coordinates
x_i = spatial coordinate in tensor notation
y^+ = dimensionless distance of near-wall grid point = yU_τ/ν
ϵ = turbulent energy dissipation rate
$\epsilon^{(1)}$, $\epsilon^{(2)}$, $\epsilon^{(3)}$ = turbulence energy fluxes
κ = von Kármán constant
μ = absolute viscosity
ν = kinematic viscosity
ν_t = turbulence kinematic viscosity
ρ = fluid density
τ_w = wall shear stress
Ω = rotational speed

$$\frac{\partial(\rho U_i)}{\partial x_i} = 0 \tag{1}$$

$$\frac{\partial(\rho U_i U_j)}{\partial x_i} = -\frac{\partial p}{\partial x_j} + \frac{\partial \tau_{ij}}{\partial x_i}. \tag{2}$$

The primitive variables are solved on a system of three staggered grids using the SIMPLER algorithm of Patankar (1980). The QUICK differencing scheme developed by Léonard (1979) is used for all convective terms in the momentum equations to reduce false diffusion numerical error.

Virr et al. (1993) found that high-Re turbulence models with the wall function give correct results for rotating cavities if: (*a*) the near-wall mesh spacing is small enough to resolve the radial velocity peak located there and (*b*) the near-wall y^+ value is in the logarithmic range. The same conclusion was reached by Williams et al. (1991) and Avva et al. (1989). Thus, high-Re modeling was used for both multiscale models since low-Re approaches: (*a*) require approximately 75 percent more grid points than that for high-Re and (*b*) considerably complicate the multiscale model derivation.

3.1 Standard $k-\epsilon$ Model. The turbulent kinetic energy k and turbulent energy dissipation rate ϵ are evaluated from the following transport equations:

$$\frac{Dk}{Dt} - \frac{\partial}{\partial x_i}\left(\frac{\nu_{\text{eff}}}{\sigma_k}\frac{\partial k}{\partial x_i}\right) = P - \epsilon \tag{3}$$

$$\frac{D\epsilon}{Dt} - \frac{\partial}{\partial x_i}\left(\frac{\nu_{\text{eff}}}{\sigma_\epsilon}\frac{\partial \epsilon}{\partial x_i}\right) = \frac{\epsilon}{k}(C_1 P - C_2\epsilon), \tag{4}$$

where P is the rate of production of turbulence kinetic energy, and $C_1 = 1.44$, $C_2 = 1.92$, $C_\mu = 0.09$, $\sigma_k = 1.0$, and $\sigma_\epsilon = 1.3$. This model was developed (Launder and Spalding, 1972) for the high-Reynolds-number flow region (i.e., away from walls) where the turbulent viscosity is much larger than the molecular viscosity.

3.2 Two-Scale $k-\epsilon$ Model. In the two-scale model of Ko and Rhode (1990), the energy spectrum is partitioned into two energy-containing zones, each having its own turbulent length and velocity scales. In addition, there is the dissipation zone, which contains eddies of negligible energy. Further, assuming the algebraic form of the source/sink terms in the ϵ equations based merely on physical/dimensional arguments has been circumvented. Specifically, by incorporating the normalized energy spectrum shape of von Kármán (1948) in the derivation, the algebraic form of each source/sink term emerges directly from the algebra so that physical reasoning is not required, in contrast to the standard (high-Re) model. Because of this new feature, the physical meaning of each source/sink term in the ϵ equations is irrelevant to the derivation. The governing equations for $k^{(1)}$ and $K^{(2)}$ are

$$\frac{Dk^{(1)}}{Dt} - \frac{\partial}{\partial x_i}\left(\frac{\nu_{\text{eff}}}{\sigma_k}\frac{\partial k^{(1)}}{\partial x_i}\right) = P - \epsilon^{(1)} \tag{5}$$

$$\frac{Dk^{(2)}}{Dt} - \frac{\partial}{\partial x_i}\left(\frac{\nu_{\text{eff}}}{\sigma_k}\frac{\partial k^{(2)}}{\partial x_i}\right) = \epsilon^{(1)} - \epsilon^{(2)}, \tag{6}$$

where $k^{(1)}$ and $k^{(2)}$ are the large- and intermediate-eddy partial turbulence energies found in the production and transfer zones of the turbulence energy spectrum, respectively. Note that the turbulence energy is the sum of the partial energies, i.e., $k = k^{(1)} + k^{(2)}$. The governing equations for the energy transfer rates are:

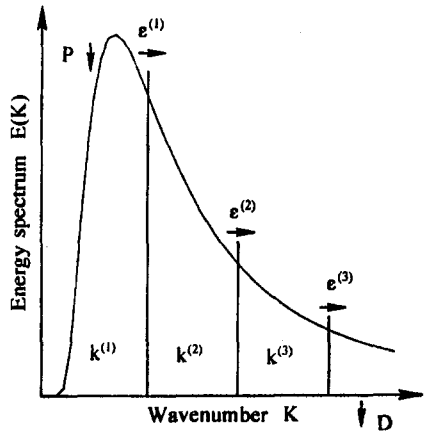

Fig. 2 Turbulence kinetic energy spectrum for the three-scale turbulence model partitioning

$$\frac{D\epsilon^{(1)}}{Dt} - \frac{\partial}{\partial x_i}\left(\frac{\nu_{\text{eff}}}{\sigma_\epsilon}\frac{\partial \epsilon^{(1)}}{\partial x_i}\right) = C_1^{(1)}\frac{\epsilon^{(1)}P}{k^{(1)}} - C_2^{(1)}\frac{\epsilon^{(1)^2}}{k^{(1)}} \tag{7}$$

$$\frac{D\epsilon^{(2)}}{Dt} - \frac{\partial}{\partial x_i}\left(\frac{\nu_{\text{eff}}}{\sigma_\epsilon}\frac{\partial \epsilon^{(2)}}{\partial x_i}\right) = -C_1^{(2)}\frac{\epsilon^{(2)^2}}{k^{(2)}} + C_2^{(2)}\frac{\epsilon^{(1)}\epsilon^{(2)}}{k^{(2)}} + C_3^{(2)}\frac{P\epsilon^{(2)}}{k^{(2)}} - C_4^{(2)}\frac{P\epsilon^{(2)}}{k^{(1)}} + C_5^{(2)}\frac{\epsilon^{(1)}\epsilon^{(2)}}{k^{(1)}}, \tag{8}$$

where the coefficients are:

$$C_1^{(1)} = 1.603, \quad C_2^{(1)} = 1.840, \quad C_1^{(2)} = 1.633,$$

$$C_2^{(2)} = 1.152, \quad C_3^{(2)} = 0.146, \quad C_4^{(2)} = 0.024,$$

$$C_5^{(2)} = 0.080, \quad C_\mu = 0.09, \quad \sigma_k = 1.0, \quad \text{and} \quad \sigma_\epsilon = 1.3.$$

Here $\epsilon^{(1)}$ and $\epsilon^{(2)}$ are interpreted as the turbulence energy fluxes leaving the large- and intermediate-eddy zones, respectively. Note here that $\epsilon = \epsilon^{(2)}$, where it has been assumed that turbulence energy leaves the intermediate-eddy zone at the Kolmogorov eddy size. The turbulent viscosity for the two-scale model is

$$\nu_t = \frac{C_\mu(k^{(1)} + k^{(2)})^2}{\epsilon^{(2)}}. \tag{9}$$

3.3 Three-Scale $k-\epsilon$ Model. The three-scale $k-\epsilon$ model basically follows the theory of the two-scale model of Ko and Rhode (1990). The modeling strategy used in the three-scale model is to add an additional energy transfer zone in the energy spectrum partitioning. Figure 2 shows the partitioning of the energy spectrum for the three-scale model. The wavenumber is indicative of the inverse eddy size, so the first zone represents the large (production) eddies and so on.

The partial turbulence kinetic energies $k^{(1)}$, $k^{(2)}$, and $k^{(3)}$ are computed at each grid point from

$$\frac{Dk^{(1)}}{Dt} - \frac{\partial}{\partial x_i}\left(\frac{\nu_{\text{eff}}}{\sigma_k}\frac{\partial k^{(1)}}{\partial x_i}\right) = P - \epsilon^{(1)} \tag{10}$$

$$\frac{Dk^{(2)}}{Dt} - \frac{\partial}{\partial x_i}\left(\frac{\nu_{\text{eff}}}{\sigma_k}\frac{\partial k^{(2)}}{\partial x_i}\right) = \epsilon^{(1)} - \epsilon^{(2)} \tag{11}$$

$$\frac{Dk^{(3)}}{Dt} - \frac{\partial}{\partial x_i}\left(\frac{\nu_{\text{eff}}}{\sigma_k}\frac{\partial k^{(3)}}{\partial x_i}\right) = \epsilon^{(2)} - \epsilon^{(3)}. \tag{12}$$

The governing equation for the energy transfer rate leaving each of the three zones $\epsilon^{(1)}$, $\epsilon^{(2)}$, and $\epsilon^{(3)}$ is given as:

$$\frac{D\epsilon^{(1)}}{Dt} - \frac{\partial}{\partial x_i}\left(\frac{\nu_{\text{eff}}}{\sigma_\epsilon}\frac{\partial \epsilon^{(1)}}{\partial x_i}\right) = C_1^{(1)}\frac{\epsilon^{(1)}P}{k^{(1)}} - C_2^{(1)}\frac{\epsilon^{(1)^2}}{k^{(1)}} \quad (13)$$

$$\frac{D\epsilon^{(2)}}{Dt} - \frac{\partial}{\partial x_i}\left(\frac{\nu_{\text{eff}}}{\sigma_\epsilon}\frac{\partial \epsilon^{(2)}}{\partial x_i}\right) = -C_1^{(2)}\frac{\epsilon^{(2)^2}}{k^{(2)}} + C_2^{(2)}\frac{\epsilon^{(1)}\epsilon^{(2)}}{k^{(2)}} + C_3^{(2)}\frac{P\epsilon^{(2)}}{k^{(2)}} - C_4^{(2)}\frac{P\epsilon^{(2)}}{k^{(1)}} + C_5^{(2)}\frac{\epsilon^{(1)}\epsilon^{(2)}}{k^{(1)}} \quad (14)$$

$$\frac{D\epsilon^{(3)}}{Dt} - \frac{\partial}{\partial x_i}\left(\frac{\nu_{\text{eff}}}{\sigma_\epsilon}\frac{\partial \epsilon^{(3)}}{\partial x_i}\right) = -C_1^{(3)}\frac{P\epsilon^{(3)}}{k^{(1)}} - C_2^{(3)}\frac{P\epsilon^{(3)}}{k^{(2)}} + C_3^{(3)}\frac{P\epsilon^{(3)}}{k^{(3)}} + C_4^{(3)}\frac{\epsilon^{(1)}\epsilon^{(3)}}{k^{(1)}} + C_5^{(3)}\frac{\epsilon^{(1)}\epsilon^{(3)}}{k^{(2)}} - C_6^{(3)}\frac{\epsilon^{(1)}\epsilon^{(3)}}{k^{(3)}} + C_7^{(3)}\frac{\epsilon^{(2)}\epsilon^{(3)}}{k^{(2)}} + C_8^{(3)}\frac{\epsilon^{(2)}\epsilon^{(3)}}{k^{(3)}} - C_9^{(3)}\frac{\epsilon^{(3)^2}}{k^{(3)}}. \quad (15)$$

The derivation of the model coefficients is similar to that of Ko and Rhode (1990) and will be reported elsewhere due to space constraints. The constants σ_k, σ_ϵ, and C_μ are kept at their original values as in the standard $k-\epsilon$ model. The model coefficients are:

$$C_1^{(1)} = 1.618, \quad C_2^{(1)} = 1.840$$

$$C_1^{(2)} = 1.649, \quad C_2^{(2)} = 1.228, \quad C_3^{(2)} = 0.146,$$

$$C_4^{(2)} = 0.065, \quad C_5^{(2)} = 0.190$$

$$C_1^{(3)} = 0.030, \quad C_2^{(3)} = 0.085, \quad C_3^{(3)} = 0.101,$$

$$C_4^{(3)} = 0.088, \quad C_5^{(3)} = 0.159, \quad C_6^{(3)} = 0.280,$$

$$C_7^{(3)} = 0.087, \quad C_8^{(3)} = 1.649, \quad C_9^{(3)} = 1.660$$

$$C_\mu = 0.09, \quad \sigma_k = 1.0, \quad \sigma_\epsilon = 1.3.$$

The expression for the turbulent eddy viscosity is given as

$$\nu_t = \frac{C_\mu(k^{(1)} + k^{(2)} + k^{(3)})^2}{\epsilon^{(3)}}. \quad (16)$$

Note that $k = k^{(1)} + k^{(2)} + k^{(3)}$, and $\epsilon = \epsilon^{(3)}$ was also maintained.

3.4 Boundary Conditions. The wall function was used for both velocity components tangential to the wall. It was also used for evaluating the turbulence production term in the $k^{(1)}$ equation to "bridge over" the wall layer to the fully turbulent region. The first grid point near the wall is to be located in the fully turbulent log-law region. The momentum flux at such a grid point satisfies the following relation by Launder and Spalding (1972):

$$\frac{U}{(\tau/\rho)_w}C_\mu^{1/4}k^{1/2} = \frac{1}{\kappa}\ln\left[Ey\frac{(C_\mu^{1/2}k)^{1/2}}{\nu}\right], \quad (17)$$

where $C_\mu = 0.09$, $\kappa = 0.41$, and $E = 9.793$. Here τ_w is the shear stress at the wall in the opposing direction of U, and it is evaluated in terms of the above constants. U, k, and y are the values at the near-wall grid point. The modification incorporated for a rotating wall is based on the swirling pipe flow measurements of Backshall and Landis (1969). It entails replacing the near-wall grid point value of U with the corresponding vector value $V_r = (U^2 + W^2)^{1/2}$ for walls that are parallel to the axial direction. The wall shear stress τ_w is then the vector sum of the axial and tangential stress components. These components, which are what actually enters into the computations, are then evaluated from:

$$\tau_{r\theta} = \tau_w W/V_r \quad (18)$$

$$\tau_{rx} = \tau_w U/V_r. \quad (19)$$

Walls parallel to the radial direction are treated similarly. It has been assumed that the turbulence energy added by the mean flow equals that dissipated by the viscosity, so that the energy transfer rate is constant across each wavenumber. Thus the near-wall values of the turbulence energy transfer quantities $\epsilon^{(1)}$, $\epsilon^{(2)}$, and $\epsilon^{(3)}$ are evaluated, assuming production equals dissipation near the wall, as

$$\epsilon^{(1)} = \epsilon^{(2)} = \epsilon^{(3)} = \frac{C_\mu^{0.75}k^{1.5}}{\kappa y}, \quad (20)$$

where y is the normal distance from the wall, and k is the total turbulent kinetic energy at the near-wall grid point.

At the inlet, $\epsilon^{(1)}$, $\epsilon^{(2)}$, and $\epsilon^{(3)}$ are evaluated from

$$\epsilon^{(1)} = \epsilon^{(2)} = \epsilon^{(3)} = \frac{k^{1.5}}{L_e}, \quad (21)$$

where L_e is the characteristic length scale of the flow, which currently is equal to 30 percent of the inlet passage radial width.

3.5 Previous Multiscale Model Testing. The multiscale models above have been tested over a wide range of popular test cases (Guo, 1995). For example, the three-scale model overpredicted the measured spreading rate of the axisymmetric free jet (Capp, 1983) by 16 percent rather than 23 percent for the standard model. Similarly, the three-scale model underpredicted the spreading rate of the swirling free jet (Pratte and Keffer, 1972) by 1.6 percent versus approximately 10.2 percent for the standard model. For the wake recirculation zone behind a disk, measured by Carmody (1964), the three-scale model gave an 11.6 percent underprediction versus 25.6 percent underprediction for the standard model. Further, the three-scale model overpredicted the skin friction coefficient for the boundary layer with an adverse pressure gradient (Samuel and Joubert, 1974) by 16.1 percent, whereas the standard model underpredicted it by 19.7 percent. For the defying case of the recirculation zone length of the annular free jet, measured by Durao and Whitelaw (1978), all three turbulence models considered gave a 21 percent underprediction.

Model testing using the rotor–stator cases of Daily et al. (1964) was also conducted. Since it was found that the three-scale model gives the same solution as the two-scale model for such a rotor–stator cavity case in particular, the three-scale model is being designated as "multiscale" for this case. Numerous computations were made for Re_θ ranging from 2×10^6 to 9.5×10^6 and a volumetric flow rate C_w ranging from 1500 to 13,000. The multiscale wall shear stress was considerably improved over that of the single-scale model, yielding a friction moment coefficient that was approximately 4 percent rather than 25 percent underpredicted over the entire Re_θ range above.

4 Results and Discussion

The present three-scale turbulence model is assessed by examining two rotating cavity systems: (*a*) a rotor–rotor cavity with axial throughflow and (*b*) a rotor–stator cavity with radial throughflow. Solutions using the three-scale model are compared with experimental data, as well as that of the two-scale model (Ko and Rhode, 1990) and the standard $k-\epsilon$ model.

4.1 Rotor–Rotor Cavity With Axial Throughflow. The experimental data of the isothermal corotating cavity recently presented by Farthing et al. (1992) was selected for this test case. A schematic of the test section is shown in Fig. 1(*a*) with inner and outer radii of $a = 19$ mm and $R = 190$ mm, respec-

tively. The range of cavity width ratio (G ratio) considered is between 0.267 and 0.533. Flow visualization by Farthing et al. (1992) showed that the flow structure for $G = 0.4$ and $G = 0.533$ is similar at substantial Rossby numbers, whereas that for $G = 0.267$ is generally different. Thus the detailed comparisons among the three turbulence models will focus on $G = 0.4$ and $G = 0.267$. The radial velocity measurements for large G ratios showed that the radial velocity increases with increasing radius until $r/R = 0.8$, and thereafter falls to zero. Further, no inviscid core occurs and only the outer portion ($r/R \geq 0.8$) of the cavity is in solid body rotation.

Insight regarding the Ro effect on the overall flow field structure is obtained from the streamline patterns shown in Figs. $3(a)$–$3(c)$ for the case of $G = 0.4$. Figure $3(a)$ shows that the case of Ro = 160 and $\mathrm{Re}_x = 8 \times 10^4$ is almost identical to the nonswirling case (not shown here) sketched by Farthing et al. That is, the vortex is almost centered axially within the cavity at a radial location of approximately $r/R = 0.8$. The higher rotor speed giving Ro = 80 is seen in Fig. $3(b)$ as being quite different with: (a) outward centrifugally pumped flow along both side-walls and (b) the center of the large vortex moved inward to $r/R = 0.33$ and moved axially to $x/S = 0.80$. Also, two counterrotating vortices occur as shown. The axial relocation of the vortex center is attributed to the intense shear in the free shear layer near $r/R = 0.1$, which produces a stagnation point flow near $x/S = 1.0$ and $r/R = 0.1$ and a very thin boundary layer on the downstream disk. Thus the resulting intense shear on the downstream disk causes the centrifugal pumping effect there to overpower that along the upstream disk. This results in radially outward flow along the downstream disk and inward flow along most of the upstream disk. The streamline plots agree with those of the flow visualization portion of the experiment (Farthing et al., 1992).

At still higher rpm giving Ro = 40, we find in Fig. $3(c)$ a third recirculation zone and the center of the largest vortex relocated farther inward to approximately $r/R = 0.27$. Not shown are the streamline plots from the standard model for $G = 0.4$, which are similar to the corresponding cases of Fig. 3, except that the small recirculation zone near the upstream disk is larger. For the Ro = 80 case, for example, the small zone of the standard model extends axially (on average) from $x/S = 0$ to approximately $x/S = 0.7$, rather than to $x/S = 0.4$ as for the three-scale model result shown in Fig. $3(b)$.

The effect of Ro on the flow pattern is given for the narrow cavity in Figs. $4(a)$–$4(c)$. The influence of Ro is similar to that in Fig. 3. The only significant difference in the flow structure between these two cavities is that the large recirculation zone shrinks radially as the gap ratio G decreases. As found for Fig. 3, the standard model streamline plots for the $G = 0.267$ case generally show a significantly wider small recirculation zone along the upstream disk.

Solution comparisons with measurements using the turbulence models discussed are herein considered for: (a) the axial distribution of the radial velocity component for $\mathrm{Re}_x = 8 \times 10^4$ and $r/R = 0.8$ as well as (b) the radial distribution of the tangential velocity component for $\mathrm{Re}_x = 4 \times 10^4$ and $x/S = 0.5$. After grid independence testing involving a 90×92 grid, a 62×62 grid of almost uniform mesh spacing was used for a computational domain height of 190 mm and domain widths between 131 and 181 mm, according to the value of G. Eight uniformly spaced grid lines of constant r value covered the radial extent of the inlet and exit regions, and the remaining constant r value lines were spaced almost uniformly across the cavity. The constant x value lines were almost uniformly spaced across the domain. The inlet of the domain is located 20 mm upstream of the upstream disk. However, the required inlet values (radial profiles) are not known there from the experiment. Therefore, a preliminary computation of the long, rotating entrance pipe was conducted first in order to obtain the required values 20 mm upstream of the upstream disk to be used as inlet

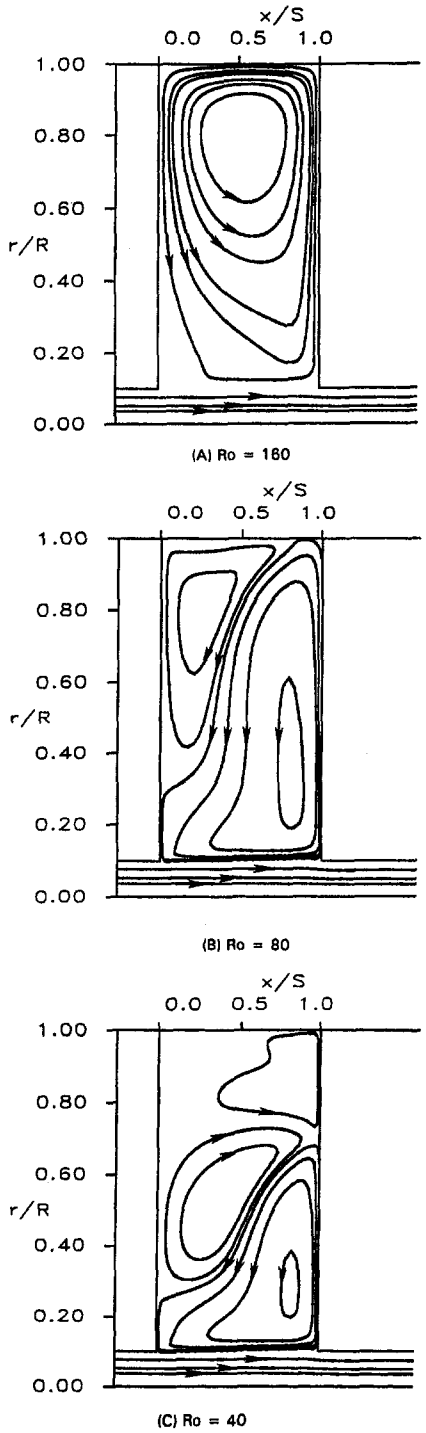

Fig. 3 Streamline pattern for the $G = 0.4$ rotating cavity using the three-scale model ($\mathrm{Re}_x = 8 \times 10^4$)

boundary values for the cavity domain. Flat radial profiles of all quantities were assumed at the pipe entrance. Further, the downstream boundary was located at a distance of 0.45 R downstream of the downstream disk in order to allow the exit boundary conditions: (a) axial velocity based on a global mass balance and (b) zero axial gradient for other quantities.

The predictions of the radial velocity, normalized by the radially averaged axial velocity at the domain inlet, for all three models are compared with the experimental data in Fig. 5 for $G = 0.4$ and Ro = 160. The three-scale, two-scale, and standard models give discrepancies with measurements of approximately 4 percent, 9 percent, and 60 percent, respectively, at the near-

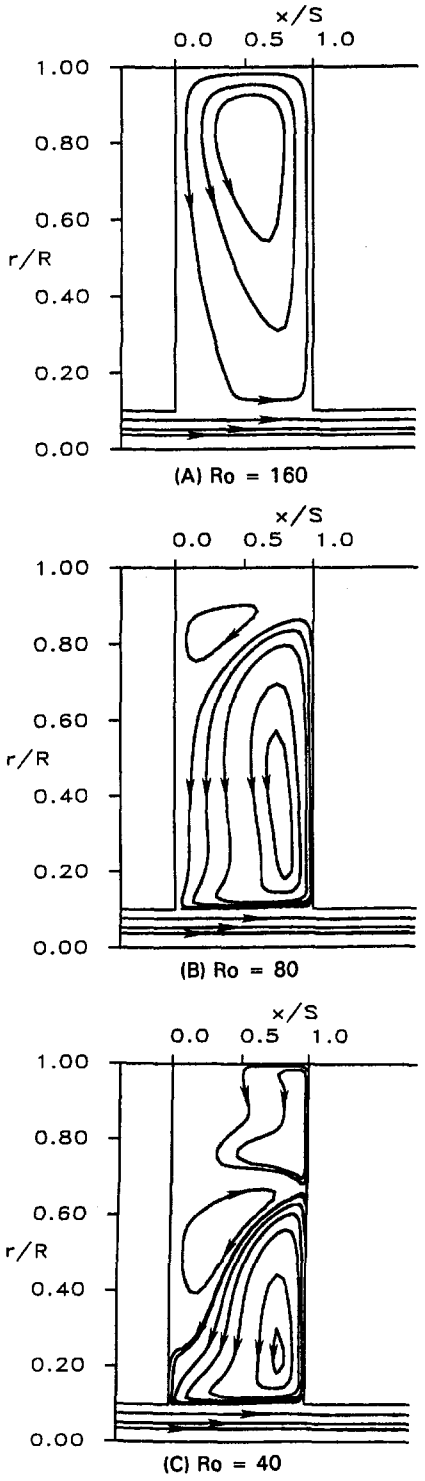

Fig. 4 Streamline pattern for the $G = 0.267$ rotating cavity using the three-scale model ($Re_x = 8 \times 10^4$)

wall measurement location on the downstream disk. On the upstream disk these discrepancies are 4 percent, 8 percent, and 80 percent respectively. Interestingly, the standard $k-\epsilon$ model gives improved velocities for x/S between 0.35 and 0.9, whereas for x/S between 0.0 and 0.35 and also between 0.9 and 1.0, the three-scale results are better. Figure 5 also indicates that the profile predicted by the three-scale model agrees with the experimental data slightly better overall than that predicted by the two-scale model. A note of uncertainty, however, is that even this case of Ro number as high as 160 is found to exhibit a

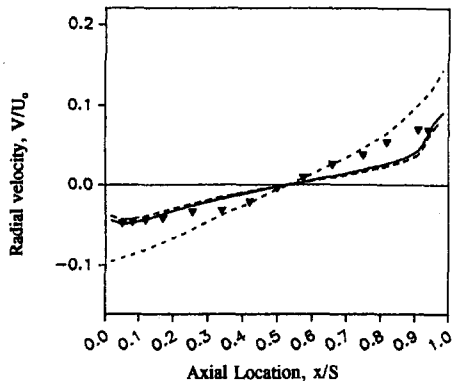

Fig. 5 Axial distribution of mean radial velocity for the rotating cavity at $r/R = 0.8$ with: (A) —— three-scale model, (B) ---- two-scale model, (C) – – – standard model, and (D) measurements ($G = 0.4$, $Re_x = 8 \times 10^4$, Ro = 160)

degree of three dimensionality in the measurements. Specifically, the radially outward mass flow and radially inward mass flow are not in global mass balance at the radial location shown ($r/R = 0.8$). That is, since there are no inflows or outflows for locations of radius larger than $r/R = 0.8$, a global mass balance dictates that the radial outward mass flow rate must equal the radial inward mass flow rate at any radial location.

The distribution of radial velocity for the narrow cavity case of $G = 0.267$ is shown in Fig. 6. The result is very similar to the case of $G = 0.4$ except that a smaller magnitude of V is found here, as was expected from earlier work (Farthing et al., 1992). The three-scale model gives the best agreement with measurements on the upstream side wall and for x/S between 0.0 and 0.61; the standard $k-\epsilon$ model is preferred for x/S between 0.6 and 0.90; and the two-scale model is preferred on the downstream wall.

The effect of Ro on the level of agreement between the three-scale model and measurements is presented in Fig. 7 for $G = 0.4$ and $Re_x = 8 \times 10^4$ ($r/R = 0.8$). The prediction of the radial velocity at infinite Ro generally gives the best agreement with measurements as expected, and the agreement worsens as Ro decreases for all of the turbulence models considered.

This was not surprising because all of the models suffer from not accounting for "extra" strain rates due to the presence of swirl velocity. Figure 8 shows the similar Ro effect on the level of three-scale model agreement with measurements for the narrow cavity of $G = 0.267$ and $Re_x = 8 \times 10^4$. Also, note that the significant differences between these two cases are that: (a) the radial velocities for the narrow cavity are considerably

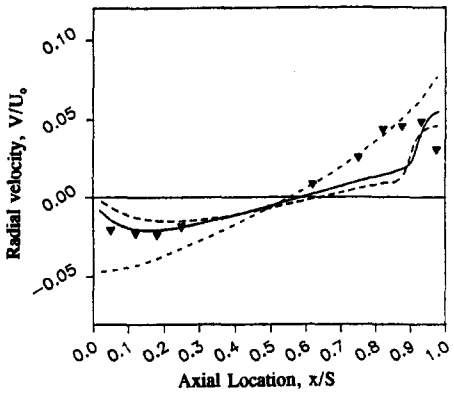

Fig. 6 Axial distribution of mean radial velocity for the rotating cavity at $r/R = 0.8$ with: (A) —— three-scale model, (B) ---- two-scale model, (C) – – – standard model, and (D) measurements ($G = 0.267$, $Re_x = 8 \times 10^4$, Ro = 160)

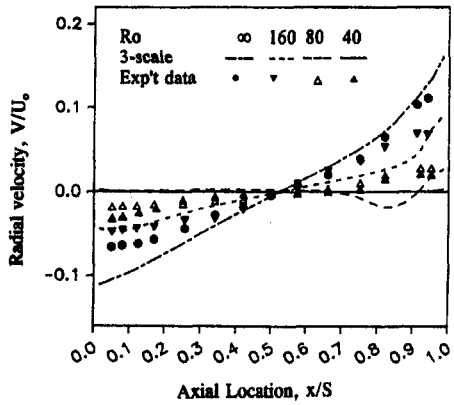

Fig. 7 Axial distribution of mean radial velocity for the rotating cavity at $r/R = 0.8$ using the three-scale model ($G = 0.4$ and $Re_x = 8 \times 10^4$)

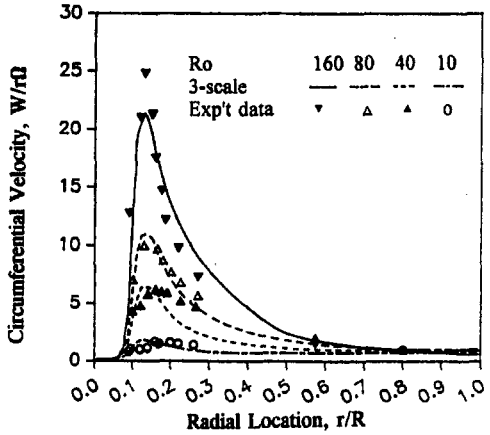

Fig. 9 Radial distribution of mean circumferential velocity for the rotating cavity at $x/S = 0.5$ using the three-scale model ($G = 0.4$ and $Re_x = 4 \times 10^4$)

smaller in magnitude and (b) the solution for Ro = 80 at $x/S = 0.85$ does not exhibit a peak of radially inward velocity, as was found for $G = 0.4$ in Fig. 7.

The effect of Ro on the swirl velocity is shown in Fig. 9 for $G = 0.4$ and $Re_x = 4 \times 10^4$. The three-scale, two-scale, and standard $k-\epsilon$ models exhibit very similar results for the circumferential velocity distributions, and only the three-scale solution is shown here. The radial peak of swirl velocity occurs at a constant radial location of $r/R = 0.13$ for the entire range of Ro considered. Once again it is seen that the agreement with measurements is surprisingly good, considering that all of these models have no accounting for extra strain rates. It is also seen that the outer portion of the flow is nearly a free vortex. Only for $r/R > 0.8$ is the flow in solid body rotation. The high values of W/rQ near $r/R = 0.13$ are due to the conservation of angular momentum within the toroidal vortex, whose center is at $r/R = 0.8$. That is, when a particle is near $r/R = 0.13$, its W/rQ must be much larger than when it is near $r/R = 0.9$.

The agreement of the swirl velocity with measurements for the narrow cavity case (Fig. 10) is better for Ro = 10 and Ro = 40, but worse than that for the wider cavity at greater Ro. The radial peak of the circumferential velocity appears to be significantly overpredicted for Ro = 160, whereas it is underpredicted for the wider cavity.

4.2 Rotor–Stator Cavity With Radial Throughflow. Phadke and Owen (1988) provided measurements of the circumferential velocity and the static pressure distributions for rotor–stator systems with the rotational Reynolds number as high as 10^6. The geometry of the test section is shown schematically in Fig. 1(b). The throughflow coefficient C_w of 2950, the seal clearance ratio G_c of 0.01, and the gap ratio G of 0.1 have been selected for model testing within this flow category. After grid independence testing, a nonuniformly spaced grid of 40 constant x value and 70 constant r value lines was used. Fourteen constant r value lines cover the radial extent of the inlet with a spacing that contracts at an 8.6 percent rate. The remaining constant r value lines are located to expand and then contract at an 8.3 percent rate from the inlet radius to the disk outer radius. Seven constant x value lines cover the axial region upstream of the cavity and are almost uniform. Next, the remaining constant x value lines give an expanding and then contracting mesh spacing of 8.1 percent across the cavity.

The static pressure outside the cavity is higher than that inside, indicating a tendency for flow ingress into the cavity. The effect of Re_θ on the pressure drop is shown in Fig. 11. The pressure drop is increasingly negative as the rotation increases. This is due to the centrifugal pumping effect. It is interesting to see that solutions involving the three-scale model have a smaller discrepancy with measurements than those using the standard model at high Re_θ, whereas both turbulence models give the same discrepancy at low or zero Re_θ. Specifically, the three-scale model gives an 8 percent discrepancy, whereas the standard model gives a 27 percent discrepancy at $r/R = 0.4$ and $Re_\theta = 1 \times 10^6$. The two-scale model gives almost the same solution as the three-scale model, and thus the two-scale model

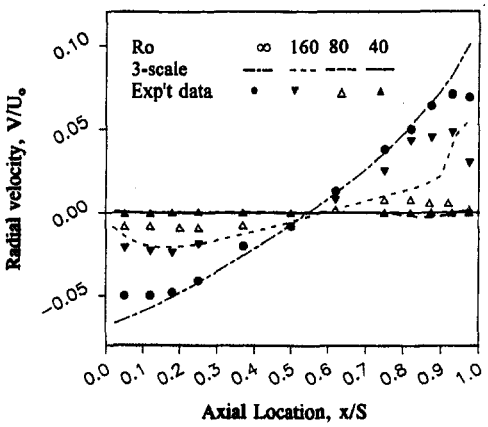

Fig. 8 Axial distribution of mean radial velocity for the rotating cavity at $r/R = 0.8$ using the three-scale model ($G = 0.267$ and $Re_x = 8 \times 10^4$)

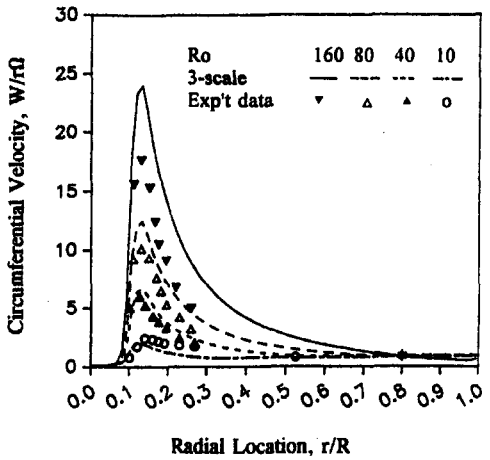

Fig. 10 Radial distribution of mean circumferential velocity for the rotating cavity at $x/S = 0.5$ using the three-scale model ($G = 0.267$ and $Re_x = 4 \times 10^4$)

results have been deleted in favor of clarity of the figure. The expected solution improvement over the standard $k-\epsilon$ model resulting from the use of the multiscale model is seen here once again for the more complex turbulent flows, while they have little effect for simpler flows.

Figure 12 shows the comparison of these two models with measurements of the circumferential velocity. Specifically, the axial distribution of the circumferential velocity at $r/R = 0.81$ is displayed for $Re_\theta = 1 \times 10^6$. Here the predictions from the three-scale model are clearly in better agreement with the experimental data across the entire cavity width, including the important region near the disk.

5 Conclusion

The two-scale $k-\epsilon$ model of Ko and Rhode had previously given a substantial improvement over the standard $k-\epsilon$ model for flows exhibiting complex turbulence characteristics. A three-scale $k-\epsilon$ turbulence model was recently developed to predict such flows as that found in rotor–rotor and rotor–stator cavities. The new model was derived in a similar fashion as the two-scale $k-\epsilon$ model, except that the turbulence energy spectrum is partitioned into three (rather than two) energy-containing zones along with a dissipation zone of negligible energy eddies.

For the rotor–stator test case, comparisons with measurements generally show a marginally improved capability of the three-scale model over the two-scale model. As expected, both multiscale models give a significant improvement over the standard $k-\epsilon$ model, especially in the near-wall region where a wide range of eddy size is found. In addition, all three models give essentially the same overall level of swirl velocity, although the multiscale models give a much more realistic rotor shear stress and friction moment coefficient. For example, the discrepancy with the friction moment coefficient measurements of Daily et al. (1964) was 4 percent with the multiscale model versus 25 percent with the standard model.

Multiscale feasibility for the rotor–rotor case, however, is less certain. Both multiscale models give improved results over the standard model for $x/S < 0.65$ and $x/S > 0.93$; however, they give an unrealistic sharp change in the slope of the radial velocity near $x/S = 0.88$. It should be noted here that the measurements apparently exhibit a degree of three dimensionality. Note further that heretofore the multiscale models have consistently given improved or identical results compared with the standard model for several previous cavity test cases. This is also true for numerous other cases such as free jets with and without swirl, boundary layers with and without an adverse pressure gradient, the near-wake flow behind a disk, etc. The reason for the unexpected outcome of the assessment for the rotor–rotor test case is unclear.

The streamline plots provide an enhanced understanding of the increase of flow pattern complexity for two G ratios with increasing rotation rate for the rotor-rotor cavity case. More recirculation zones are formed as Ro decreases apparently because vortex breakdown occurs at low Ro due to the outward centrifugally pumped flow along both side walls. The effect of a decreasing gap ratio G on the flow structure in the cavity space results in the reduction of the recirculation zone size. Further, solution convergence was found to be increasingly challenging with decreasing Ro. In fact, convergence became unobtainable for approximately Ro < 10. This is attributed to the fact that the flow visualization study of Farthing et al. (1992) shows increasing tendencies toward flow asymmetry as Ro decreases.

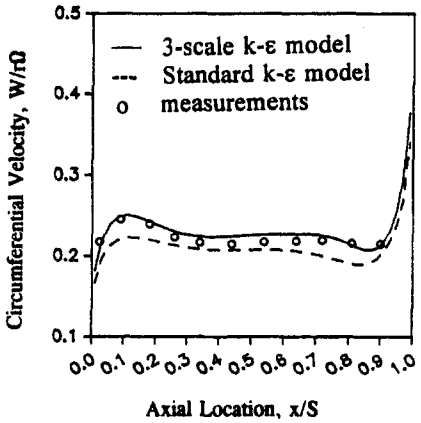

Fig. 12 Axial distribution of mean circumferential velocity for the rotor–stator cavity at $r/R = 0.81$ ($Re_\theta = 10^6$, $C_w = 2950$, $G_c = 0.01$, $G = 0.1$)

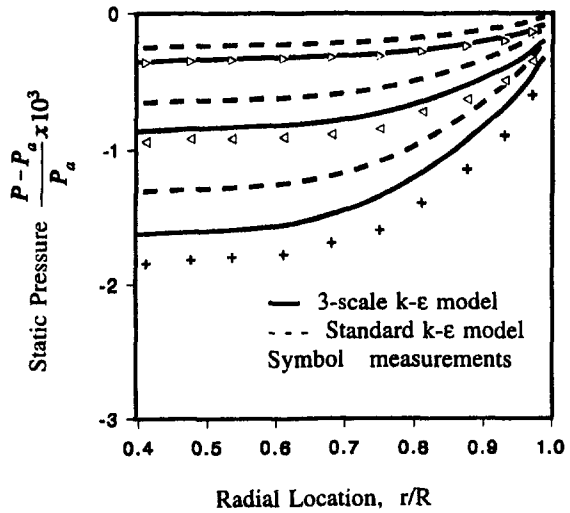

Fig. 11 Radial distribution of mean static pressure for the rotor–stator cavity using the three-scale model ($C_w = 2950$, $G_c = 0.01$, $G = 0.1$)

$Re_\theta/10^6$	0.6	0.8	1.0
SYMBOL	▷	▷	+

Acknowledgments

The authors are indebted to both the NASA Center for Space Power and the Texas Advanced Technology Program for financial support.

References

Avva, R. K., Ratcliff, M. L., and Leonard, A. D., 1989, "CFD Analysis of Rotating Disk Flows," *Proc. ASME Winter Annual Meeting*, O. Baysal, ed., ASME FED-Vol. 103, pp. 99–105.

Backshall, R. G., and Landis, F., 1969, "The Boundary-Layer Velocity Distribution in Turbulent Swirling Pipe Flow," ASME *Journal of Basic Engineering*, Vol. 91, pp. 728–733.

Capp, S. P., 1983, "Experimental Investigation of the Turbulent Axisymmetric Jet," Ph.D. Thesis, State University of New York, Buffalo, NY.

Carmody, T., 1964, "Establishment of the Wake Behind a Disk," ASME *Journal of Basic Engineering*, Vol. 86, pp. 869–882.

Chen, C. P., and Guo, Kuan-liang, 1991, "A Non-isotropic Multiple-Scale Turbulence Model," *Applied Mathematics and Mechanics* [English ed.], Vol. 12, No. 10, pp. 981–991.

Daily, J. W., Ernst, W. D., and Asbedian, V. V., 1964, "Enclosed Rotating Disks With Superposed Throughflow," Hydrodynamics Laboratory, MIT, Report No. 64.

Durao, D. F. G., and Whitelaw, J. H., 1978, "Velocity Characteristics of the Flow in the Near Wake of a Disk," *Journal of Fluid Mechanics*, Vol. 85, Part 2, pp. 369–385.

Fabris, G., Harsha, P. T., and Edelman, R. B., 1981, "Multiple-Scale Turbulence Modeling of Boundary Layer Flows for Scramjet Applications," NASA CR-3433.

Farthing, P. R., Long, C. A., Owen, J. M., and Pincombe, J. R., 1992, "Rotating Cavity With Axial Throughflow of Cooling Air: Flow Structure," ASME JOURNAL OF TURBOMACHINERY, Vol. 114, pp. 237–246.

Guo, Z., 1995, "Development and Assessment of a Three-Scale $k-\epsilon$ Turbulence Model for Turbomachinery Applications," Ph.D. Thesis, Texas A&M University, College Station, TX.

Hanjalic, K., Launder, B. E., and Schiestel, R., 1980, "Multiple-Time-Scale Concepts in Turbulent Transport Modeling," *Turbulent Shear Flows,* L. J. S. Bradbury et al., eds., Springer-Verlag, New York, Vol. 2, pp. 36–49.

Jones, W. P., and Launder, B. E., 1973, "The Prediction of Laminarization With a Two-Equation Model of Turbulence," *Int. J. Heat Mass Transfer,* Vol. 5, pp. 301–314.

Kim, S.-W., and Chen, C.-P., 1987, "A Multiple-Time-Scale Turbulence Model Based on Variable Partitioning of Turbulent Kinetic Energy Spectrum," NASA CR-179222.

Kim, Y. W., and Metzger, D. E., 1992, "Comparison of Central Axis and Jet Ring Coolant Supply for Turbine Disk Cooling on a SSME-HPOTP Model," Paper No. AIAA 92-0255.

Ko, S. H., and Rhode, D. L., 1990, "Derivation and Testing of a New Multi-scale $k-\epsilon$ Turbulence Model," Paper No. AIAA-90-0243.

Ko, S. H., and Rhode, D. L., 1992, "Thermal Details in a Rotor–Stator Cavity at Engine Conditions With a Mainstream," ASME JOURNAL OF TURBOMACHINERY, Vol. 114, pp. 446–453.

Launder, B. E., and Spalding, D. B., 1972, *Mathematical Models of Turbulence,* Academic Press, London.

Leonard, B. P., 1979, "A Stable and Accurate Convective Modeling Procedure Based on Quadratic Upstream Interpolation," *Computer Methods in Applied Mechanics and Engineering,* Vol. 19, pp. 59–98.

Owen, J. M., and Bilimoria, E. D., 1977, "Heat Transfer in Rotating Cylindrical Cavities," *Journal of Mech. Engr. Sci.,* Vol. 19, pp. 175–187.

Owen, J. M., and Onur, H. S., 1983, "Convective Heat Transfer in a Rotating Cylindrical Cavity," ASME JOURNAL OF ENGINEERING FOR POWER, Vol. 105, pp. 265–271.

Owen, J. M., and Rogers, R. H., 1989, *Flow and Heat Transfer in Rotating-Disc Systems: Vol. 1, Rotor–Stator Systems,* Research Studies Press, Taunton.

Patankar, S. V., 1980, *Numerical Heat Transfer and Fluid Flow,* McGraw-Hill, New York.

Phadke, U. P., and Owen, J. M., 1988, "Aerodynamic Aspects of the Sealing of Gas-Turbine Rotor–Stator Systems, Part 1: The Behavior of Simple Shrouded Rotating-Disk Systems in a Quiescent Environment," *Int. J. Heat Fluid Flow,* Vol. 9, No. 2, pp. 98–105.

Pratte, B. D., and Keffer, J. F., 1972, "The Swirling Turbulent Jet," ASME *Journal of Basic Engineering,* Vol. 94, pp. 739–748.

Samuel, A. E., and Joubert, P. N., 1974, "A Boundary-Layer Developing in an Increasingly Adverse Pressure Gradient," *Journal of Fluid Mechanics,* Vol. 66, pp. 481–505.

Schiestel, R., 1983, "Multi-Scale Concept in Turbulence Modeling," *Journal de Mechanique Theorique et Appliquee,* Vol. 2, pp. 417–449.

Virr, G. P., Chew, J. W., and Coupland, J., 1993, "Application of Computational Fluid Dynamics to Turbine Disc Cavities," ASME Paper No. 93-GT-89.

Williams, M., Chen, W. C., Bache, G., and Eastland, A., 1991, "An Analysis Methodology for Internal Swirling Flow Systems With a Rotating Wall," ASME JOURNAL OF TURBOMACHINERY, Vol. 113, pp. 83–90.

Yu, J. M., Sparrow, E. M., and Eckert, E. R. G., 1973, "Experiments on a Shrouded, Parallel Disk System With Rotation and Coolant Throughflow," *Int. J. Heat Mass Transfer,* Vol. 16, pp. 311–328.

Experimental and Numerical Investigation of Stator Exit Flow Field of an Automotive Torque Converter

B. V. Marathe

B. Lakshminarayana

Y. Dong

Department of Aerospace Engineering,
Pennsylvania State University,
University Park, PA 16802

The objective of this investigation is to understand the nature of the complex flow field inside each element of the torque converter through a systematic experimental and numerical investigation of the flow field. A miniature five-hole probe was used to acquire the data at the exit of the stator at several operating conditions. The flow field is found to be highly three dimensional with substantial flow deviations, and secondary flow at the exit of the stator. The secondary flow structure, caused by the upstream radial variation of the through flow, induces flow overturning near the core. Flow separation near the shell causes flow underturning in this region. The rate of decay of stator wake is found to be slower than that observed in the wakes of axial flow turbine nozzles. The flow predictions by a Navier–Stokes code are in good agreement with the pressure and the flow field measured at the exit of the stator at the design and the off-design conditions.

Introduction

Very little is known about the flow field inside automotive torque converters. Lack of information on this flow field could be attributed to the severe limitations and difficulties associated with the size, configuration, and closely coupled blade rows in these torque converters. Some early experiments conducted by Adrian (1985) were performed in a modified torque converter geometry. The blade surface pressure measurements performed by By and Lakshminarayana (1991) and By (1993) and LDV measurements performed by Bahr et al. (1990) and Flack et al. (1993) indicate the presence of a highly three-dimensional flow field with large flow separation zones inside the torque converter components. The torque converter flow field is complex due to highly three-dimensional flow path geometries, large variations in the operating conditions, and viscous interactions between closely spaced blade elements. Improvements in the performance of the torque converter could be achieved by a systematic investigation of the flow field in these torque converters.

The objective of the experimental investigation reported in this paper is to improve the performance of the torque converter through a systematic experimental and numerical investigation. The focus of the program is on the measurement of the steady and unsteady flow field upstream and downstream of each element of the torque converter. These measurements will provide insight into the flow phenomena in each blade component. Specifically, they will provide information on losses, torque, and the interaction effects between each component. The flow field information could be incorporated into the design procedure to improve the torque converter performance and efficiency.

The steady and unsteady measurements were performed downstream of the stator using a miniature five-hole probe. However, only the steady-state flow measurements are reported in this paper.

Experimental Facility and Instrumentation

The torque converter test facility used in this research is shown in Fig. 1. Detailed descriptions of the experimental facility and the static pressure distribution on the stator blade are given by By and Lakshminarayana (1991) and By (1993). This facility has five components: driver and absorption dynamometer, test section, oil system, and control system. The driver dynamometer is a 30 hp DC motor, which delivers the precise amount of torque or rpm specified by the control system and drives the pump. The turbine is connected to the absorption dynamometer, which is controlled to maintain constant torque or rpm. The cross section of the torque converter flow path is an elliptical torus formed by pump, turbine, and stator blades. The inner boundary of the torus is called the core, and the outer boundary is called the shell. It has been observed that high oil pressure prevents cavitation, and maintaining elevated temperatures enables stable flow conditions with repeatable performance. Hence an oil system is used to keep the oil pressure and temperature constant at 14 psi and 60°C, respectively. The performance of a torque converter is expressed in terms of torque ratio (TR) and speed ratio (SR), defined in the Nomenclature.

Tests were conducted at SR = 0.0, 0.2, 0.4, 0.6, and 0.8 in order to simulate all the conditions the torque converter experiences in actual automatic transmission. The design speed ratio of the torque converter is 0.6. It has a maximum efficiency at SR = 0.8 and minimum efficiency at SR = 0.0. Data at only these two speed ratios (0.0 and 0.8) will be reported here. The blade geometry, blade angles, and inlet flow angles (obtained from one-dimensional analysis) at various speed ratios are presented in Fig. 2.

A miniature five-hole probe (1.67 mm tip diameter) was designed and fabricated to facilitate the measurements of the flow properties upstream and downstream of each of the blade rows. The measurements are carried out at 5 radial positions and 11 tangential positions in one blade passage at 0.36 axial chords downstream, as shown in Fig. 2. The radial position at the shell will be designated by H = 0.0 and the core will be designated by H = 1.0. Measurements were also performed at two additional tangential positions in an adjacent blade passage to check for periodicity of the flow field. Two static pressures on the stator were used as reference pressures for normalizing the total and static pressures obtained from the five-hole probe. The data processing technique for the five-hole probe is de-

Contributed by the International Gas Turbine Institute and presented at the 39th International Gas Turbine and Aeroengine Congress and Exposition, The Hague, The Netherlands, June 13–16, 1994. Manuscript received by the International Gas Turbine Institute February 4, 1994. Paper No. 94-GT-32. Associate Technical Editor: E. M. Greitzer.

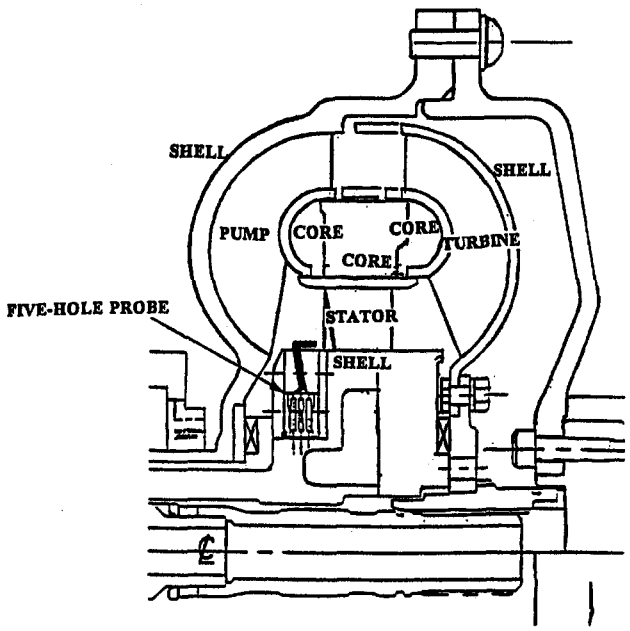

Fig. 1 Schematic of the torque converter facility

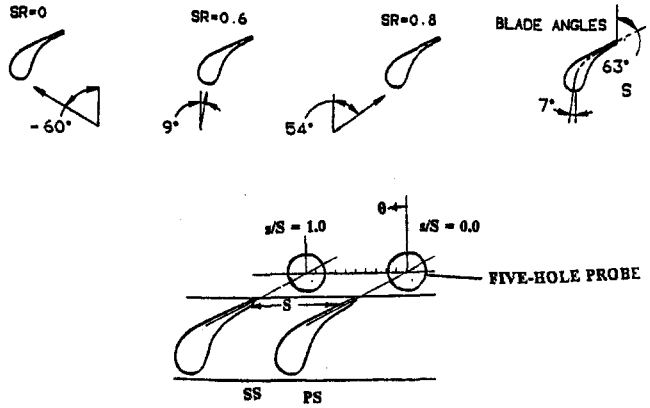

Fig. 2 Blade profile, inlet flow conditions, and measurement stations

scribed by Treaster and Yocum (1979). A thermocouple was installed on the hub of the stator for accurate reference temperature. The probe calibration has an accuracy of ±1 deg in angle measurement. The pressure measurements are obtained to an accuracy of ±0.01 psi. The transducer drift introduces a maximum error of 0.5 percent. This results in a maximum 1–2 percent error in the velocities and 0.5 percent error in the static and total pressures. The corrections to the probe due to blockage and the pressure gradient are incorporated into the data processing. The maximum cumulative error in the velocity and pressure measurements is 2–3 percent.

Results and Discussion

The tangential and radial distributions of important flow parameters at the exit of stator 2 are discussed in this section. All the velocities are normalized by the mass-averaged mean throughflow (axial) velocity $\bar{V}_x$. Total and static pressures measured by the five-hole probe are normalized by subtracting the reference hub static pressure and dividing it by the average dynamic head of the throughflow ($1/2\ \rho\bar{V}_x^2$).

Stagnation Pressure Coefficient at Stator Exit. The distribution of stagnation pressure coefficient (C_{PO}) is shown in Fig. 3 for $SR = 0.8$. The presence of an inviscid core, where the stagnation pressure is nearly uniform, is evident at this speed ratio. The shell region ($H = 0.2$) shows a fully developed profile, caused by the thick boundary layers in the corner formed by the suction surface and the endwall. The secondary flow, discussed later in the paper, interacts with the blade boundary layer in the shell region, resulting in thick corner boundary layer or corner separation (corner stall). The data presented later do not indicate any flow separation in this region. Hence the major phenomenon here is the accumulation of low-energy fluid swept by the secondary flow. However, a substantial difference in the stagnation pressure distribution between $H = 0.2$ and 0.35 indicates that this phenomenon does not extend beyond $H = 0.35$ and ends somewhere between these two locations. The flow periodicity is maintained at this speed ratio. The wake thickness varies from nearly 70 percent of passage at $H = 0.2$ (shell region) to about 50 percent of the passage at $H = 0.5$. The poor definition of wake near the core endwall can be attributed to the faster wake decay near the core endwall. It is also possible that the boundary layer on the core endwall separates due to the low-momentum fluid at the exit of the turbine near the core region. The wake width at midspan and shell is large compared to the wakes of nozzle vanes in other types of turbomachinery.

The distribution of stagnation pressure coefficient at $SR = 0.0$, shown in Fig. 3, reveals a large region of low stagnation pressure extending from the core to the shell. This low-pressure region indicates massive flow separation near the suction side.

Nomenclature

C = chord length
$C_{PO} = 2(P_o - p_{hub})/\rho\bar{V}_x^2$
$C_{PS} = 2(p_s - p_{hub})/\rho\bar{V}_x^2$
H = radial distance from stator shell (hub) normalized by the stator blade span; $H = 0$ (shell), $H = 1.0$ (core)
P = pressure normalized by $\rho\bar{V}_x^2/2$
p_{hub} = reference pressure on the hub
PS, SS = pressure and suction side
r = radius
s = tangential distance measured from the suction surface (Fig. 2)
S = blade spacing
SR = speed ratio (turbine rpm/pump rpm)
TR = torque ratio (turbine torque/pump torque)
V = absolute flow velocity/total velocity normalized by $\bar{V}_x$
V_c = defect in wake centerline velocity
$\bar{V}_x$ = mass-averaged axial velocity downstream of stator
U = blade speed
Z = distance downstream of trailing edge
α = pitch angle = arc tan (V_r/V_x)
β = yaw angle (measured from the axial direction, arc tan (V_θ/V_x))
ξ = total pressure loss coefficient (Eq. (2))
ρ = density of the fluid

Subscripts

1, 2 = inlet and exit
0, s = total, static
x, R, θ = axial, radial, and tangential components
hub, tip = property at the hub and tip, respectively
max = maximum value

Superscripts

$\bar{}$ = passage-averaged value

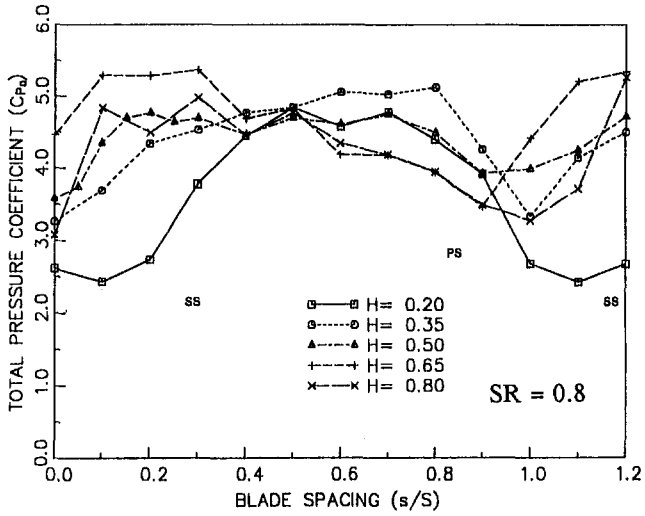

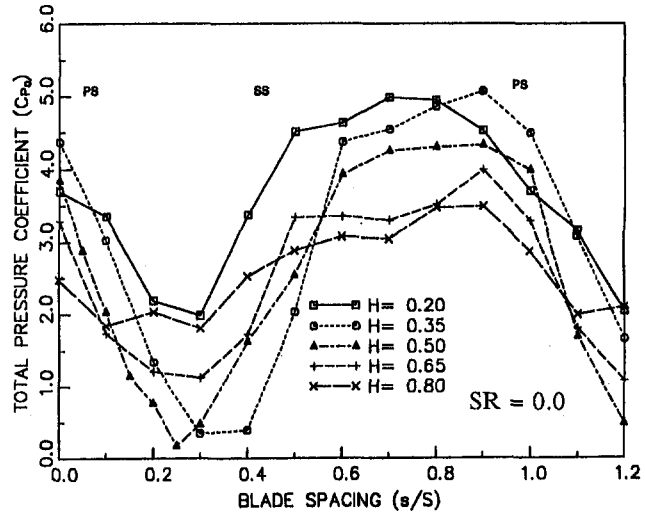

Fig. 3 Profiles of total pressure coefficient

The zone of low stagnation pressure and the wake region covers approximately 50 percent of the blade spacing at all radii. The inviscid core is less than 20 percent of the blade spacing at this speed ratio. In the inviscid core, the stagnation pressure increases slightly from the core to the shell, indicating an increase in the total velocity from the core to the shell. The lowest stagnation pressures and largest wake widths are observed near the midspan, indicating a rapid deterioration of flow at midspan as compared to the core or the shell. Another important feature is that the center of the low-pressure region is at a different tangential position for each radius, indicating that the wake is skewed. The reason for the skewness of the wake is discussed later in this paper. Due to high positive incidence angle (Fig. 2), both the flow blockage and the flow turning are high (approximately 120 deg) at this speed. As a result, the blade boundary layers are thick on the suction side at this speed ratio. This is also confirmed by the numerical analysis, presented later. The flow separation near the trailing edge of the stator shifts the position of the wake. Also, the flow blockage due to separation affects the secondary flow structure induced by the radial gradient of throughflow velocity upstream of the stator. The interaction of the blockage caused by the flow separation, secondary flow induced by the upstream normal vorticity, and the secondary flow induced by endwall boundary layers generate a very complex flow structure at this speed ratio.

The radial distribution of the mass-averaged stagnation pressure coefficient is plotted in Fig. 4. The average stagnation pressure coefficient at $SR = 0.8$ is nearly uniform, with the

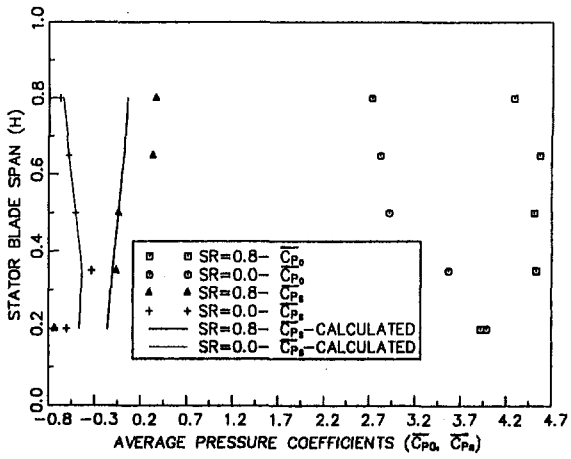

Fig. 4 Radial variation of mass-averaged pressure coefficient ($\bar{C}_{PO}$ and $\bar{C}_{PS}$)

exception of the hub and the tip regions. This is caused by the shell and the core boundary layers. At $SR = 0.0$, the stagnation pressure coefficient decreases from the shell to the core, indicating high losses near the core. These losses could be due to the flow separation on the core endwall of the upstream turbine rotor. However, this hypothesis cannot be confirmed due to lack of information on the flow field upstream of the stator. The axial velocities in this region, described later, are also found to be small.

Static Pressure Coefficient at Stator Exit. The radial distribution of the mass averaged static pressure coefficient, plotted in Fig. 4, shows very nonuniform distribution. For $SR = 0.8$, the static pressure increases with radius. Very high static pressure gradients are observed between $H = 0.2$ and 0.35 and $H = 0.5$ and 0.65. At $SR = 0.0$, the static pressure coefficient increases from location $H = 0.2$ to 0.35 and decreases from $H = 0.35$ to 0.8. The physical reasoning for such a distribution is given below:

The fluid particles experience centrifugal forces in two directions, as shown in Fig. 5. It should be noted that the streamlines have curvature in the meridional as well as azimuthal directions. As a result, a simplified radial equilibrium equation cannot be used to determine the radial pressure gradient. A streamline

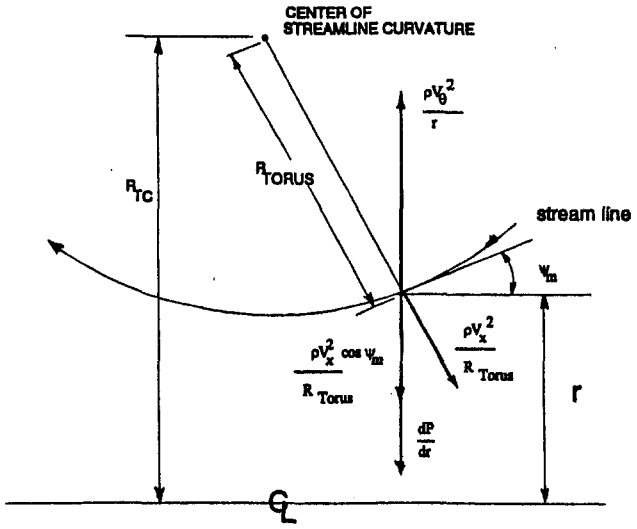

Fig. 5 Effect of streamline curvature on static pressure coefficient

curvature equation should be used to calculate the pressure gradient. This equation is given by:

$$\frac{\partial P}{\partial r} = \rho \frac{V_\theta^2}{r} - \rho \frac{V_x^2}{(R_{TC} - r)} \cos \Psi_M \qquad (1)$$

where R_{TC} is the distance between the center of the torus (or center of curvature of the streamlines in torus plane, as shown in Fig. 5), and the axis of rotation; r is the radius from the axis of rotation, and Ψ_M is the angle between the streamlines and axial flow direction at exit of the stator. This equation can be integrated to obtain the static pressure distribution.

A comparison of the radial distribution of the static pressure coefficient derived from the streamline curvature equations and the experimental data, shown in Fig. 4, reveals good agreement between the estimated and the measured distribution of $\bar{C}_{ps}$ for $SR = 0.0$. The positive pressure gradient between $H = 0.2$ and 0.35 and negative pressure gradient between $H = 0.35$ and 0.8 are predicted accurately for $SR = 0.0$. The estimation is poor for $SR = 0.8$. The pressure gradient for $SR = 0.8$ between $H = 0.35$ and 0.5 and $H = 0.65$ and 0.8 are estimated accurately, even though the magnitudes are not predicted well near the core. However, the estimation of the gradient between $H = 0.2$ and 0.35 and $H = 0.5$ and 0.65 is poor. This confirms the influence of both the meridional and the azimuthal curvatures on the radial static pressure gradient measured.

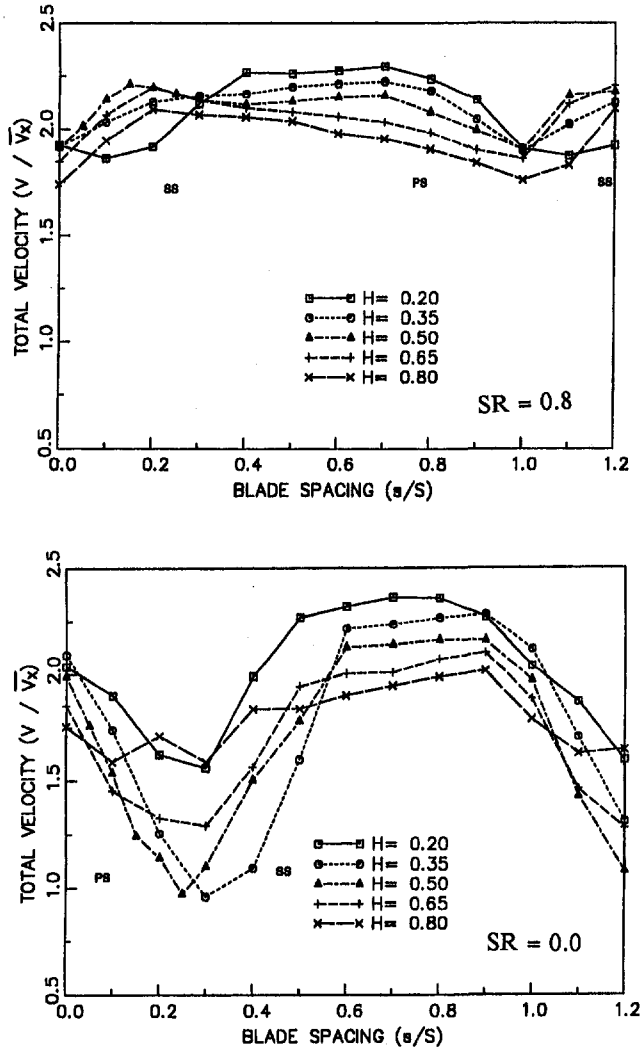

Fig. 6 Profiles of total velocity

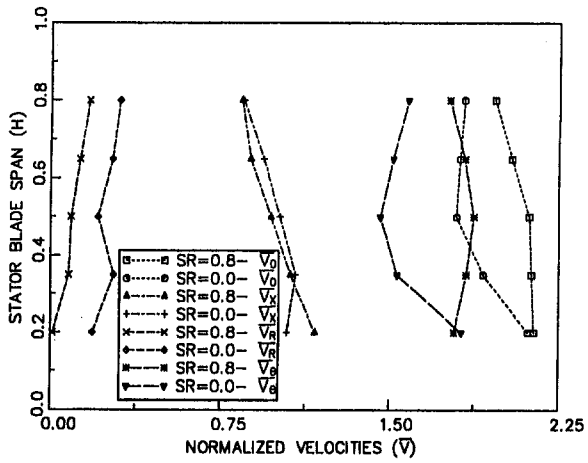

Fig. 7 Radial variation of mass-averaged normalized velocities

Velocity Profiles at the Stator Exit. The distribution of nondimensionalized total velocity behind the stator blade is shown in Fig. 6 for $SR = 0.8$ and 0. The velocity distribution is nearly uniform over the entire blade passage at speed ratio 0.8. At $SR = 0.8$ the stator wake is thin due to thin boundary layers on the blade surface and the wake decays rapidly due to high turbulence and mixing of the flow downstream of the stator. As indicated earlier, the wake thickness is about 70 percent of passage at $H = 0.2$ and is relatively thin at other locations.

At $SR = 0.0$, the wake trajectory is skewed from the core to the shell (Fig. 6). The wake is very thick at this speed and it occupies nearly 70–80 percent of the blade passage in the entire annulus. However, it should be noted that the flow mixes rapidly downstream of the blade and the velocity defect varies from 25–50 percent of the free-stream velocity. It is also clear, despite the fully developed nature of the flow, that the total velocity distribution is periodic in the blade-to-blade direction.

The radial distribution of the mass-averaged nondimensional total velocity (Fig. 7) shows that the average total velocity decreases from the shell to the core, especially at $SR = 0$. The low-velocity region near the core is attributed to the separation on the core surface in turbine rotors. Flack et al. (1993) have also observed a similar variation of the flow velocity downstream of the pump and turbine in the torque converter. The dominant component at the stator exit is the tangential velocity, whose mass-averaged values are also shown in Fig. 7. Large values of V_θ and V in the shell region at $SR = 0$ are caused by secondary flow, which induces overturning. The low-velocity region at midspan at $SR = 0$ is due to flow separation on the suction side, as shown in Fig. 6. The tangential velocity distribution at $SR = 0.8$ indicates no major influence of secondary flow. It should be noted here that no measurements are taken from $H = 0$ to 0.2, and from $H = 0.8$ to 1.0. At $SR = 0.0$, the tangential velocity is lower at midspan and higher near the core and the shell.

The radial distribution of the mass-averaged axial velocity (Fig. 7) indicates an almost linear variation in the axial velocity from the shell to the core for $SR = 0.0$ and 0.8. The mass-averaged axial velocity decreases from the shell to the core. This observation is in conformity with the data acquired by Flack et al. (1993). The distribution of mass-averaged axial velocity is identical for $SR = 0.8$ and 0.0, except at $H = 0.2$. The radial distribution of the mass-averaged axial velocity was also found to be identical for the speed ratios 0.6, 0.4, and 0.2. Thus the change in incidence angle, speed ratio, and Reynolds number does not affect radial distribution of average axial velocity. Hence, it can be concluded that the nondimensionalized

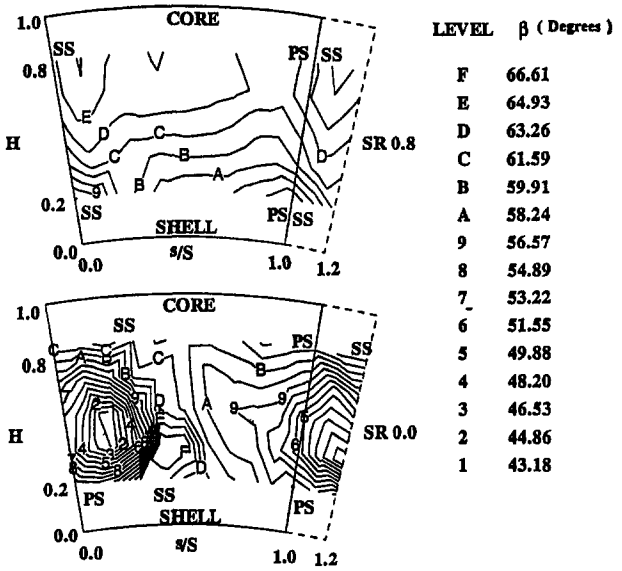

Fig. 8 Contours of yaw angle (β) in degrees

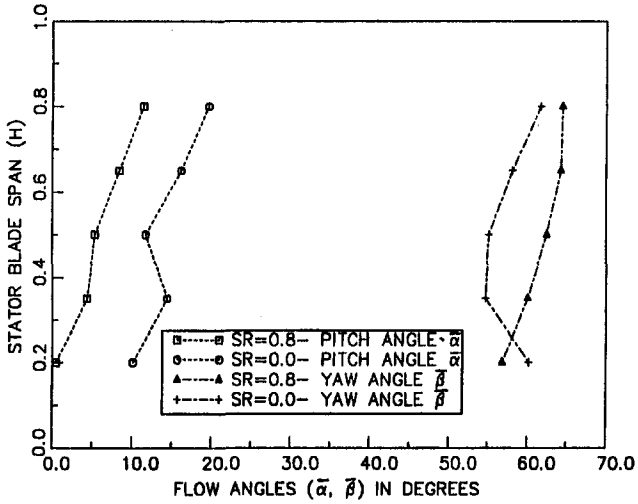

Fig. 9 Radial variation of average flow angles (derived from mass-averaged velocities)

throughflow velocity distribution is dependent only on the geometric parameters and not on the operating conditions.

Yaw Angle Profiles at Stator Exit. The contours of yaw angle (measured from the axial direction) are shown in Fig. 8. As indicated in Fig. 2, the blade outlet angle is 63 deg. The distribution at $SR = 0.8$ indicates that the flow angles are nearly uniform across the passage, with large variations occurring across the wake. The turning is lower on the pressure side and higher on the suction side of the wake. This is consistent with measurements across the wake in a compressor reported by Prato and Lakshminarayana (1993).

The contours of yaw angle at $SR = 0.8$ show flow overturning near the core and underturning near the shell. The overturning is caused by the secondary flow resulting from the nonuniform radial distribution of the throughflow velocity upstream of the stator. The throughflow velocity decreases from shell to core. As a result, the flow overturns near the core. Also, corner separation on the shell suction side induces underturning of the flow.

The yaw angle distribution at $SR = 0$ shows considerable departure from the design conditions. The flow inside the loss core (wake or separated region) near the suction side has very low turning angles, especially near the midspan. The midspan region perceives flow acceleration brought about by the separation near the core and the shell. The turning angle at almost all of the locations at $SR = 0$ is considerably less than the blade angle.

The radial distribution of the average yaw angles (Fig. 9), calculated from the mass-averaged velocities (Fig. 7), indicates a smooth variation at $SR = 0.8$. The radial distribution of yaw angles at $SR = 0.0$ indicates high yaw angles at both the core and the shell regions and low yaw angles at $H = 0.35$. This type of distribution can be attributed to the flow separation zone on suction surface of the blade near $H = 0.35$. Also the secondary flow generated by the shell boundary layer causes overturning at $H = 0.2$ and underturning at $H = 0.35$. The details of this flow structure are discussed earlier in the paper and will not be repeated here.

Radial Velocity Profiles at Stator Exit. The contour plots of radial velocity are shown in Fig. 10. For $SR = 0.8$, negative radial velocities (inward) are observed in the wake regions. These velocities are induced by a strong positive static pressure gradient (toward the shell) discussed earlier in the paper (Fig. 4). Small positive radial velocities are observed in the inviscid core. These velocities result from primary inviscid flow features. The radially positive velocities in the inviscid core region and the radially negative velocities inside the wake region result in a strong secondary flow pattern near the blade regions.

The radial velocity distribution at $SR = 0$ shows some complex features. The negative radial velocities induced by the secondary flow are observed only in a small region located near the core, near the pressure surface. Most of the blade passage shows high positive radial velocities (toward the core). The blockage, generated by the flow separation, causes the flow to go around the separation zone inducing high radial velocities in the inviscid core. Also, since the pressure gradient is negative (toward the core), positive radial velocities are induced in the separation and the wake regions.

As a result, the radial distributions of the mass-averaged radial velocity, shown in Fig. 7, are much higher at $SR = 0.0$ than at $SR = 0.8$. For $SR = 0.8$, the mass-averaged radial velocity increases linearly with radius from the shell to the core. This increase is due to the differences in the torus curvature from the shell to the core. For $SR = 0.0$, the radial distribution of

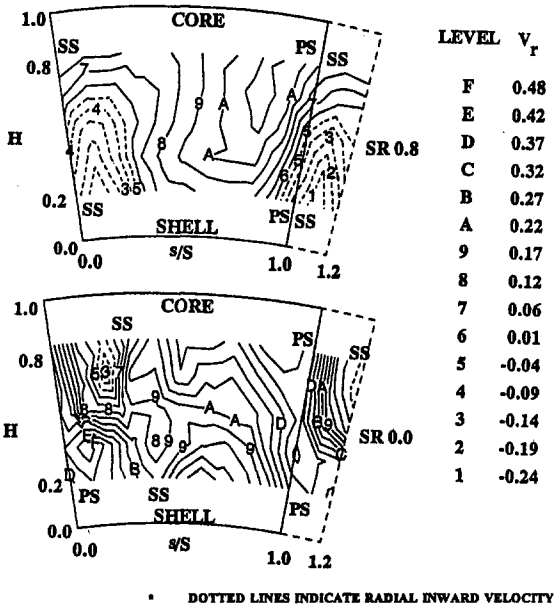

Fig. 10 Contours of radial velocity

average radial velocity is uniform except at $H = 0.35$. This discrepancy is attributed to high radial velocities in the region surrounding the separation zone. For $SR = 0$ at $H = 0.35$, $\partial p/\partial r$ changes sign. It is positive for $H < 0.35$ and negative for $H > 0.35$ (Fig. 4).

The radial distribution of average pitch angles calculated from the mass-averaged velocities are shown in Fig. 9. The average pitch angles increase from the shell to the core due to differential bending of the stream lines in torus plane. The pitch angles derived from mass averaged velocity vary by approximately 10 deg from the shell to the core for both $SR = 0.8$ and $SR = 0.0$. The pitch angles are generally higher for $SR = 0.0$.

As mentioned earlier, the radius of the torus introduces three dimensionality as evidenced by the magnitude of the radial velocities and pitch angles. Hence, some of the three dimensionality is due to inviscid effects. The fact that the pitch angles are substantially higher at $SR = 0$ indicates the presence of highly three-dimensional nature of the flow at zero speed ratio.

Wake Decay. The defect in velocity inside the wake depends on several factors, including the axial distance from the trailing edge, turbulence level, Reynolds number, secondary flows, and the pressure gradients. A knowledge of the stator wake is essential for improvement in the performance of torque converters, as these interact with the pump rotor resulting in unsteady flow and vibration. The wake width and the maximum velocity defect are of interest. Magnitude of wake width was discussed earlier. The maximum velocity defect (normalized the local maximum velocity) is shown plotted as a function of distance from trailing edge in Fig. 11. It is also compared with Raj and Lakshminarayana's (1973) correlation for a cascade, the nozzle wake data of Zaccaria et al. (1992), Sitaram and Govardhan's (1986) rotor cascade data, as well as Goldman and Seaholtz's (1992) data on annular turbine cascade. The wake decay at $SR = 0.8$ follows the trend observed in other cascades, but the decay of the wake is slower at $SR = 0.6$. This is due to high inlet incidence and blade loading.

Composite Flow Field at the Exit of the Stator. A schematic of the composite flow field, based on the data presented earlier, is shown in Fig. 12. The flow field at $SR = 0.8$ is well behaved. The wake is thin and uniform at all radii except near the shell at $H = 0.2$. The secondary flow causes flow overturning near the core. The underturning near the shell is due to possible corner separation. The positive static pressure gradient induces radial inward velocities in the wake and curvature of the streamlines in azimuthal direction causes radial outward velocities in the inviscid core region. As a result, a weak secondary flow structure could be observed, as shown in Fig. 12.

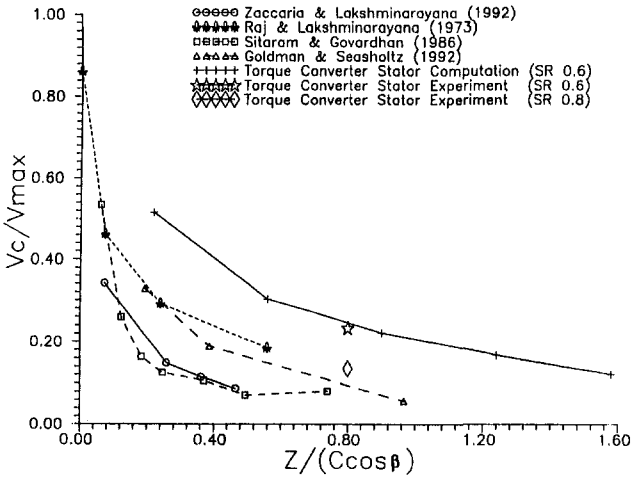

Fig. 11 Decay of total velocity defect with streamwise distance ($H = 0.5$)

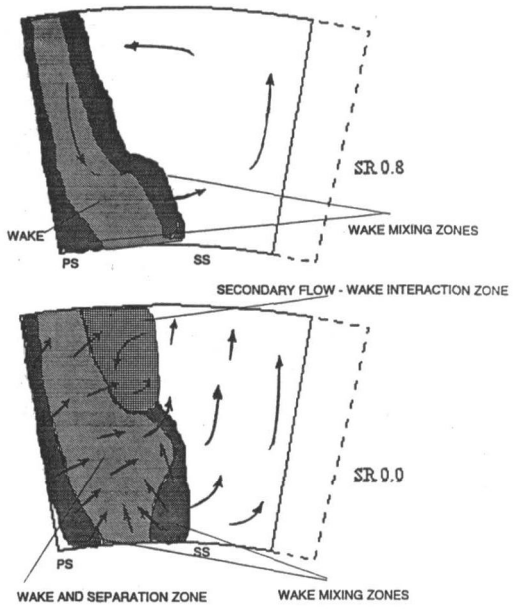

Fig. 12 Schematic of secondary flow pattern

At $SR = 0.0$, the flow field can be generally divided into four regions. The wake region, with possible separation, is the largest region near the suction surface. The secondary flow induced by the upstream radial gradient in velocity interacts with the wake near the core to generate an interaction zone where radial inward velocities and flow overturning are observed. The flow mixing adjacent to the wake entrains the main flow, causing large secondary flow and mixing. These zones are marked as wake mixing zones. The inviscid core is small and exhibits high radial velocities due to the curvature of streamlines in the meridional direction. The displacement of streamlines, due to the flow blockage, also contributes to the radial velocities.

The flow field at the stall condition ($SR = 0.0$) is highly three dimensional at the exit of the stator. The incidence angle is approximately 60 deg and the turning angle is about 120 deg. The mass flow rate is maximum and the secondary flow is very strong; the flow separation and wake dominate the flow in the entire passage at this speed ratio. The flow near the middle span is no longer two dimensional, but the flow properties at the inlet of the stator are more uniform than the design condition since the turbine is stationary.

Predictions From Navier–Stokes Analysis

A two-dimensional steady, incompressible Navier–Stokes code was used to predict the flow field at midspan of the stator. The analysis and code, which utilize a pressure-based method, were developed by Basson and Lakshminarayana (1995) at Penn State. The artificial dissipation terms are included directly and controlled for each case. A $k-\epsilon$ low Reynolds number turbulence model (Chien, 1982) was employed. The flow field was computed for all speed ratios. The prediction for the design point ($SR = 0.6$) and extreme off-design conditions ($SR = 0$) are presented and interpreted in detail. The incidence angle and velocity are specified from the one-dimensional analysis. It is assumed to be steady and uniform across the inlet plane located far upstream. The computation does not include unsteadiness in turbine exit flow field.

The inlet flow is assumed to be turbulent with a free-stream turbulence intensity of 5 percent. The blade pressure coefficient, the exit flow field, the wake decay, and the losses are computed and compared with the experimental data.

The computational grids were generated using a hybrid algebraic and elliptic grid. This method enables a strict control over

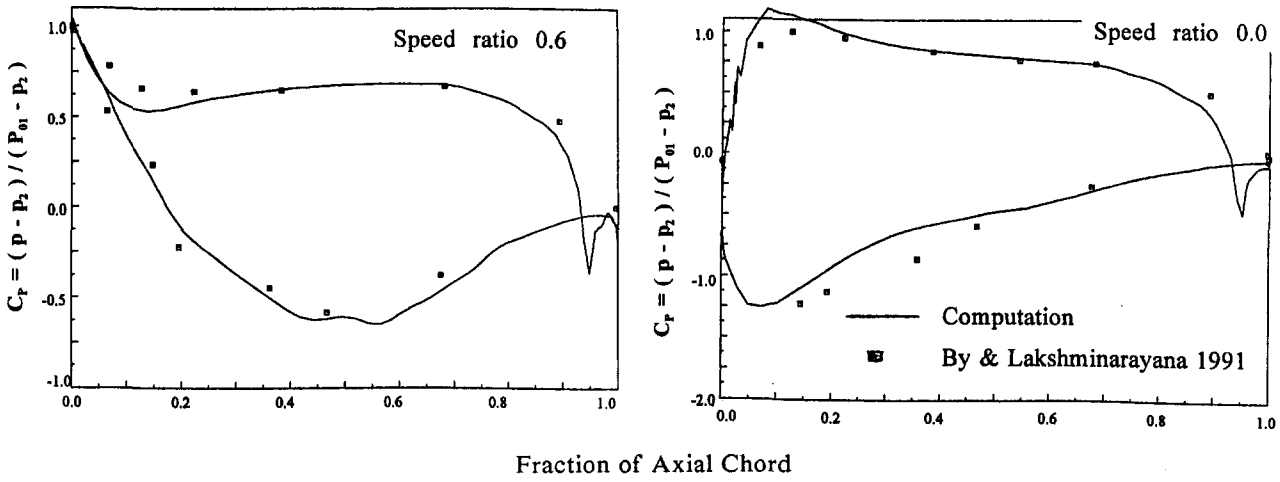

Fig. 13 Blade surface pressure distribution (H = 0.5)

the grid spacing and orthogonality near the solid boundaries. The convergence was sensitive to the grid. A 139 × 55 grid was found to be necessary to capture the flow phenomena accurately near the leading and trailing edges, as velocity and pressure gradients are very large in these regions. The convergence was also sensitive to the inlet turbulence intensity and the artificial dissipation rate.

The incidence angle is 9 deg at the design point (SR = 0.6), the turning angle is about 65 deg and the secondary flow is relatively weak. The flow near the leading edge is relatively smooth and there is no flow separation. Furthermore, the wake is thin and the flow is nearly two dimensional in the middle third of the span. Hence the predictions from the two-dimensional Navier–Stokes code should be valid near the midspan at design conditions.

The blade surface pressure distribution at the design (SR = 0.6) and the stall conditions (SR = 0.0) are shown in Fig. 13. The agreement between the data (By and Lakshminarayana, 1991) and the prediction is excellent for both the design and the off-design conditions. Small discrepancies near the leading and trailing edges are caused mainly by the lack of sufficient grid points. The grid size was systematically decreased to obtain improved performance.

The measured and predicted stagnation and static pressure coefficients for SR = 0.6 are compared in Fig. 14. The agreement between measured and predicted C_{po} is very good except in the wake region. The stagnation pressures are captured exactly in the inviscid region. The static pressure, on the other hand, was predicted accurately in the wake region and discrepancies exist in the inviscid region. Both the data and the computation show that the static pressure is almost uniform in the tangential direction at this location (0.36 axial chord length downstream). Considering the complexity of the flow, these predictions provide confidence in the ability of Navier–Stokes codes to simulate the flow field.

The stagnation and static pressure coefficients at the exit of the stator at SR = 0 are shown in Fig. 14. The stagnation pressure coefficients are predicted reasonably well, including the wake region, which covers nearly 70 percent of the passage. The prediction of the inviscid region agrees well with the data, but the maximum defect in the wake is overpredicted. The static pressure coefficient is not predicted well.

The measured and computed velocity profiles at SR = 0.6 are shown in Fig. 15. Here again, the agreement between predicted and measured velocity components is excellent. The flow angle, the axial, tangential, and total velocity components are

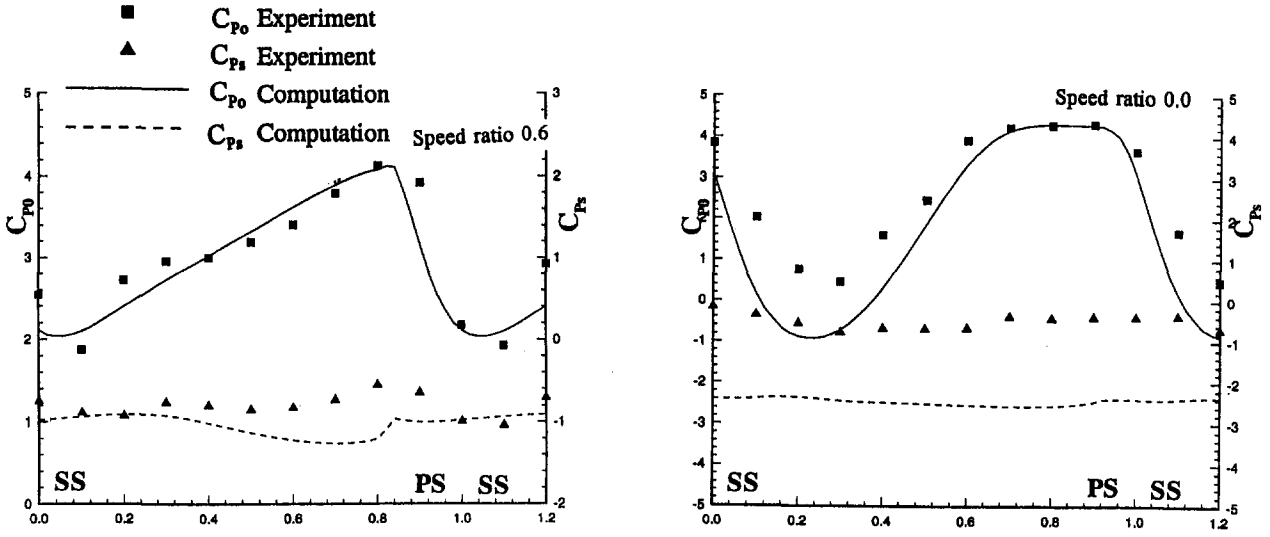

Fig. 14 Exit pressure coefficient (H = 0.5)

predicted well both in the inviscid region and in the wake. The velocities are nearly uniform in the inviscid region at this operating condition. The axial, tangential and the total velocity profiles for $SR = 0$ are shown plotted in Fig. 15. The agreement with axial velocity is excellent and surprisingly, the total velocity prediction is good in the wake but deviates appreciably in the inviscid region.

The flow field in a torque converter is inherently unsteady due to close coupling of stator–pump, pump–turbine, and turbine–stator. One of the major causes of unsteadiness is the wake of stator interacting with the pump rotor, and hence an attempt is made to assess the predictive capability of the code to resolve the wake structure. The maximum velocity defect in the wake at $SR = 0.6$ is shown compared with data from other turbine stators, nozzles and cascades, and correlations in Fig. 11. The predicted wake defect compares very well with the measured data at $SR = 0.6$. No attempt is made to carry out such correlation for $SR = 0$, as the flow is highly three-dimensional and two-dimensional codes are not accurate at this speed.

The predicted stagnation pressure coefficients and velocities are used to compute the overall stagnation pressure loss at midradius, using the equation:

$$\xi = \frac{\int_0^1 P_{01} V_{x_1} d\left(\frac{s}{S}\right) - \int_0^1 P_{02} V_{x_2} \left(d\frac{s}{S}\right)}{\int_0^1 P_{01} V_{x_1} d(s/S)} \qquad (2)$$

The predictions are shown compared with the data (based on $P_{01} = P_{o\max}$ at station 2) in Fig. 16. The agreement near the design condition ($SR = 0.8$ and 0.6) is excellent as the code is exactly valid at this speed ratio, as the flow is two-dimensional at midradius. The agreement is poor at $SR = 0.4$, 0.2, and 0 and one of the major reasons for this is the fact that the flow is highly three-dimensional even at midradius at this speed ratio.

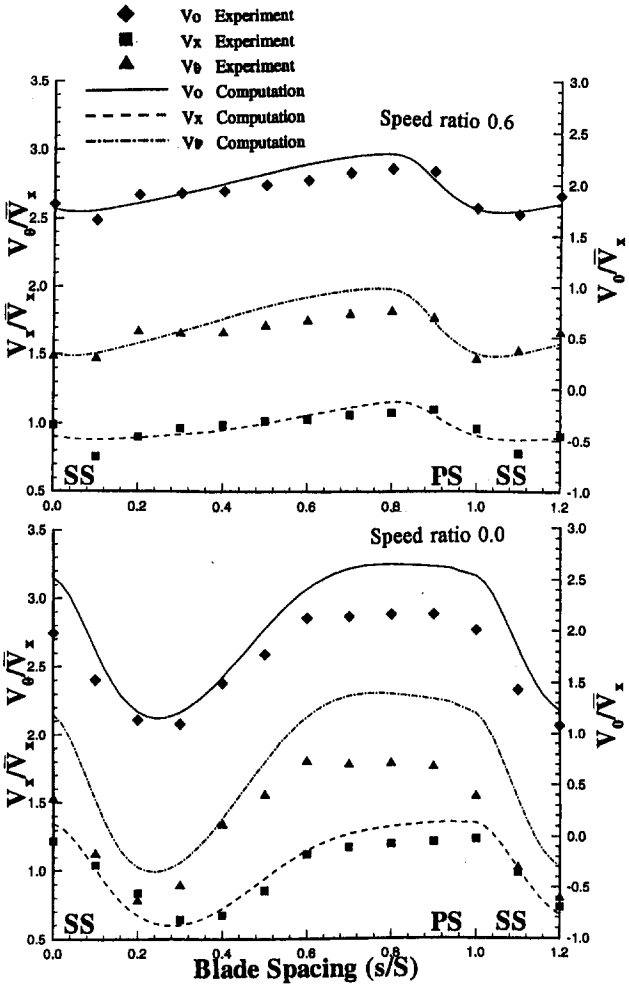

Fig. 15 Exit velocity distribution ($H = 0.5$)

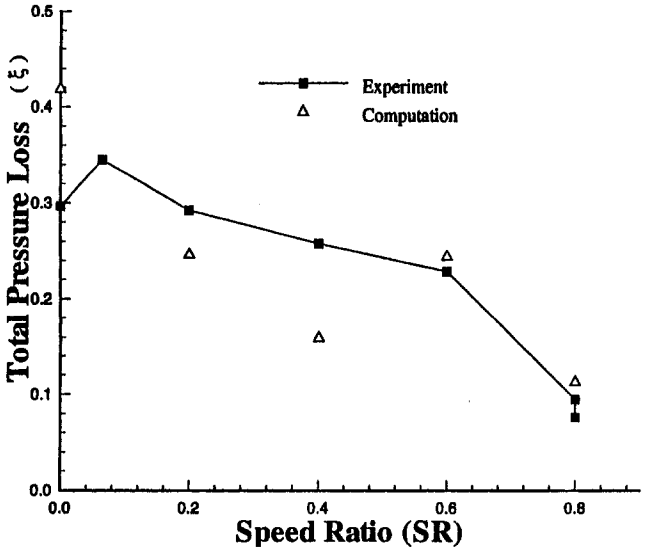

Fig. 16 Total pressure loss ($H = 0.5$)

Conclusions

A comprehensive investigation of the flow field at the exit of the stator is reported in this paper. The following conclusions are drawn from the data presented:

1 At low flow turning angles (9 deg at $SR = 0.8$), the growth of the blade surface boundary layer and the resulting wakes are thin. The wake decays rapidly before it reaches the measurement plane. At higher flow turning angles (120 deg at $SR = 0.0$) the boundary layer growth on the suction surface is large and the wake width covers a large extent of the blade passage. The defect in maximum velocity in the wake agrees well with the data from similar blade rows. The wake width is found to be a substantial portion of the blade passage, and this will generate large unsteadiness in the pump blade passage.

2 The throughflow velocities are highest near the shell and lowest near the core. This type of throughflow velocity distribution is similar to those observed in other mixed flow turbomachinery. The core-to-shell distribution of the throughflow velocity is identical at the design and the off-design conditions.

3 The flow overturning and underturning are observed adjacent to wakes at both the speed ratios.

4 The stagnation pressure, static pressure, and velocities are found to be nearly uniform from pressure to suction surface, with the exception of wakes, at $SR = 0.8$ and 0.6. Substantial variation is observed only near the shell. On the contrary, large nonuniformities are observed in distribution of flow property for $SR = 0.0$.

5 Negative radial velocities are observed inside the wake, due to radial gradient in static pressure. Positive radial velocities are observed in the inviscid core. This is due to the meridional streamline curvature. The radial velocity and hence three-dimensionality in the flow are found to be appreciable for $SR = 0.8$ and substantial for $SR = 0$. The maximum variation in the radial velocity for the design condition is found to be 10 percent of the total velocity.

6 The radial distribution of static pressure is influenced not only by the swirl velocity but also by the meridional streamline curvature.

7 The flow at the midspan is predicted accurately at the design condition by the two-dimensional Navier–Stokes code. The blade-to-blade distribution of the stagnation and static pressure coefficients, axial and tangential velocities are predicted accurately. At off-design conditions ($SR = 0$), the axial velocity and stagnation pressure are predicted reasonably well, with qualitative prediction for the static pressure. The computed and measured losses at midspan are in agreement with the data at $SR = 0.8$ and 0.6, but the comparison is not good at $SR = 0.0$.

Acknowledgments

This project was sponsored by Hydromatic Division and Technical Center of General Motors Corporation. Helpful discussions and assistance in the experimental program by D. Maddock and R. By are gratefully acknowledged. J. F. Gallardo's help in the computational effort is also acknowledged.

References

Adrian, F. W., 1985, "Investigations and Analysis of Flow in Hydrodynamic Torque Converters," Ph.D Thesis, The Ruhr University, Bochum, Germany.

Bahr, H. M., et al., 1990, "Laser Velocimeter Measurements in the Stator of a Torque Converter," SAE Paper No. 901769.

Basson, A., and Lakshminarayana, B., 1995, "Numerical Simulation of Tip Clearance Effects in Turbomachinery," ASME JOURNAL OF TURBOMACHINERY, Vol. 117, pp. 348–359.

By, R. R., and Lakshminarayana, B., 1991, "Static Pressure Measurements in a Torque Converter," SAE Paper No. 911934.

By, R. R., 1993, "An Investigation of Three-Dimensional Flow Fields in the Automotive Torque Converter," Ph.D Thesis, Penn State University.

Chien, K. Y., 1982, "Predictions of Channel and Boundary-Layer Flows With a Low-Reynolds-Number Turbulence Model," *AIAA Journal*, Vol. 20, pp. 33–38.

Flack, R., et al., 1993, University of Virginia, personal communication.

Goldman, L. J., and Seaholtz, R. G., 1992, "Laser Anemometer Measurements and Computations in an Annular Cascade of High Turning Core Turbine Vanes," NASA TP 3252.

Prato, J., and Lakshminarayana, B., 1993, "Investigation of Compressor Rotor Wake Structure at Peak Pressure Rise Coefficient and Effects of Loading," ASME JOURNAL OF TURBOMACHINERY, Vol. 115, pp. 487–500.

Raj, R., and Lakshminarayana, B., 1973, "Characteristics of the Wake Behind a Cascade of Airfoils," *J. Fluid Mech.*, Vol. 61, part 4, pp. 707–730.

Sitaram, N., and Govardhan, M., 1986, "Effect of Incidence Angle on Wake Characteristics of High Deflection Turbine Rotor Linear Cascade," presented at 9th Australasian Fluid Mechanics Conference, Aukland.

Treaster, A. L., and Yocum, A. M., 1979, "The Calibration and Application of Five-Hole Probes," *ISA Transactions*, Vol. 18, No. 3, pp. 23–34.

Zaccaria, M., and Lakshminarayana, B., 1992, "Investigation of Three-Dimensional Flow Field in a Turbine Including Rotor/Stator Interaction. Part 2: Three-Dimensional Flow Field at the Exit of the Nozzle," AIAA Paper No. 92-3326.